Automatisierung bioinformatischer Analysen von sFIDA-generierten Bilddaten zur Diagnose von Proteinfehlfaltungserkrankungen

Inaugural-Dissertation

zur Erlangung des Doktorgrades
der Mathematisch-Naturwissenschaftlichen Fakultät
der Heinrich-Heine-Universität Düsseldorf

vorgelegt von

Fabian Rehn
aus Köln

Bergheim, März 2025

Aus dem Institut für Physikalische Biologie

der Heinrich-Heine-Universität Düsseldorf

Gedruckt mit der Genehmigung der

Mathematisch-Naturwissenschaftlichen Fakultät der

Heinrich-Heine-Universität Düsseldorf

Berichterstatter:

1. Prof. Dr. Dieter Willbold

2. Prof. Dr. Henrike Heise

3. Prof. Dr. Peter Bayer

Tag der mündlichen Prüfung: 29.09.2025

Eidesstattliche Erklärung

Ich versichere an Eides Statt, dass die Dissertation von mir selbständig und ohne unzulässige fremde Hilfe unter Beachtung der „Grundsätze zur Sicherung guter wissenschaftlicher Praxis an der Heinrich-Heine-Universität Düsseldorf“ erstellt worden ist. Ferner erkläre ich, dass ich in keinem anderen Dissertationsverfahren mit oder ohne Erfolg versucht habe, diese Dissertation einzureichen.

---------- ----------

Ort, Datum Fabian Rehn

Danksagung

An dieser Stelle möchte ich mich herzlich bei den vielen Menschen bedanken, die mich während meiner Promotion unterstützt haben.

Mein besonderer Dank gilt meinem Doktorvater, Prof. Dr. Dieter Willbold für die Möglichkeit, meine Forschung am Institut für Strukturbiochemie des Forschungszentrums Jülich und an der Heinrich-Heine-Universität Düsseldorf durchführen zu können. Ich danke ihm für die Vielzahl interessanter Projekte, den Freiraum eigene Ideen zu entwickeln und zu verfolgen, spannende fachliche Diskussionen sowie die anhaltende Unterstützung. Des Weiteren möchte ich Prof. Dr. Henrike Heise für die Übernahme des Zweitgutachtens danken.

Ein besonderer Dank gilt Dr. Oliver Bannach für die engagierte Betreuung meiner Promotion. Bei Fragen und Problemen war er aufgrund seiner optimistischen Art und fachlichen Kompetenz stets eine enorme Hilfe. Danke für die Unterstützung bei der Umsetzung zahlreicher Projekte, bei denen ich viel gelernt habe sowie für das Korrekturlesen dieser Arbeit. Mein Dank gilt ebenso der sFIDA- und suFIDA-Gruppe. Ich konnte mich jederzeit mit meinen Fragen an euch wenden und habe bei Problemen immer wertvolle Unterstützung erhalten. Insbesondere bedanke ich mich bei Dr. Lara Blömeke und Victoria Kraemer-Schulien, von denen ich viel gelernt habe und die mir den Einstieg am Forschungszentrum sehr erleichtert haben. Unsere gemeinsame Arbeit hat diese Zeit besonders bereichert. Meiner ehemaligen und erneuten Kollegin Dr. Marlene Pils danke ich für ihre kontinuierliche Unterstützung, das Testen diverser Methoden sowie das sorgfältige Korrekturlesen dieser Arbeit. Prof. Dr. Erdem Tamgüney und Dr. Tuyen Bujnicki danke ich für die wertvollen fachlichen Diskussionen. Bei allen weiteren Mitgliedern des Instituts für Strukturbiochemie am Forschungszentrum Jülich bedanke ich mich ebenfalls für das angenehme Arbeitsklima und die konstruktive Zusammenarbeit in den letzten Jahren.

Abschließend möchte ich meinen Eltern für ihre anhaltende Unterstützung und ihren unerschütterlichen Rückhalt danken. Mein größter Dank gilt jedoch Kim für das Vertrauen, die Motivation sowie die unermüdliche Unterstützung.

Gender-Hinweis

Die in dieser Arbeit verwendeten Personenbezeichnungen beziehen sich, sofern nicht anders vermerkt, auf alle Geschlechter gleichermaßen. Aus Gründen der besseren Lesbarkeit wird auf eine doppelte Nennung oder spezielle Genderformen verzichtet.

Kurzzusammenfassung

Das Risiko, an einer Proteinfehlfaltungserkrankung wie der Alzheimer-Krankheit oder dem Typ-2-Diabetes zu erkranken, steigt mit zunehmendem Alter. Infolge der steigenden Lebenserwartung nehmen daher auch die Fallzahlen kontinuierlich zu, was die Gesundheitssysteme vor erhebliche finanzielle Herausforderungen stellt. Charakteristisch für diese Erkrankungen ist die Aggregation verschiedener Peptide und Proteine zu Oligomeren, Fibrillen und Plaques, die aufgrund ihrer toxischen Eigenschaften eine zentrale Rolle in der Pathologie einnehmen. Die löslichen Oligomere gelten dabei als die toxischste Spezies, weshalb eine möglichst genaue Quantifizierung essenziell ist, um die Krankheitsmechanismen genauer zu verstehen und gezielt Wirkstoffe zu entwickeln. Die Quantifizierung stellt jedoch eine erhebliche Herausforderung dar, da die eingesetzte Methode hochsensitiv für Oligomere, aber gleichzeitig unempfindlich gegenüber den chemisch identischen Monomeren sein muss. Eine Technologie, welche diesen Anforderungen gerecht wird, ist die sFIDA-Technologie (englisch: surface-based fluorescence intensity distribution analysis).

Ziel der vorliegenden Dissertation war es, die Messgenauigkeit und Präzision der sFIDA-Technologie durch die Entwicklung neuer Methoden zu steigern sowie den Automatisierungsgrad zu erhöhen. Durch die Kombination der sFIDA-Technologie mit den entwickelten Methoden sowie etablierten Ansätzen aus dem Data-Science-Bereich sollten zudem neue Erkenntnisse zur Pathologie verschiedener Proteinfehlfaltungserkrankungen gewonnen werden. Durch die Entwicklung einer Methode zur post-hoc-Reduktion falsch-positiver Signale konnte die Präzision und Genauigkeit der sFIDA-Technologie in einem ersten Schritt gesteigert werden. Die Analyse mehrerer Studien, in denen die sFIDA-Technologie Anwendung fand, untermauerte den explorativen, diagnostischen sowie pharmakologischen Nutzen der Technologie. So konnte beispielsweise gezeigt werden, dass die Aβ-Oligomer-Level bereits früh im Verlauf der Alzheimer-Krankheit wieder abfallen, was das therapeutische Zeitfenster für oligomer-auflösende Wirkstoffe begrenzt. Um dieses Potenzial zu nutzen sowie die Effizienz und Anwendbarkeit der sFIDA-Technologie zu optimieren, wurden verschiedene Automatisierungsmethoden entwickelt. Dazu gehörten ein Verfahren zur automatischen Bestimmung eines Grenzwerts zur Trennung von Hintergrundrauschen und Signal sowie die Entwicklung einer automatischen Artefaktdetektion. Da nun alle Komponenten für eine vollständige Automatisierung des Analyseprozesses etabliert sind, erscheint die vollständige Automatisierung der sFIDA-Technologie als ein vielversprechender nächster Schritt.

Abstract

The risk of developing a protein misfolding disease, such as Alzheimer's disease or type 2 diabetes, increases with age. As life expectancy continues to rise, the number of cases is also steadily increasing, creating major financial challenges for healthcare systems. A characteristic feature of these diseases is the aggregation of various peptides and proteins into oligomers, fibrils, and plaques, which play a central role in pathology due to their toxic properties. Soluble oligomers are considered the most toxic species, making their precise quantification essential for a better understanding of disease mechanisms and the targeted development of therapeutics. However, quantification presents a considerable challenge, as the applied method must be highly sensitive to oligomers while remaining insensitive to chemically identical monomers. A technology that meets these requirements is the sFIDA technology (surface-based fluorescence intensity distribution analysis).

The objective of this dissertation was to enhance the measurement accuracy and precision of the sFIDA technology by developing new methods and increasing the degree of automation. By combining the sFIDA technology with the developed methods as well as established approaches from the field of data science, new insights into the pathology of various protein misfolding diseases were also to be gained. In an initial step, the development of a method for post-hoc reduction of false-positive signals improved the precision and accuracy of the sFIDA technology. The analysis of multiple studies in which the sFIDA technology was applied further substantiated its exploratory, diagnostic, and pharmacological utility. For instance, it was demonstrated that Aβ oligomer levels decrease again early in the course of Alzheimer's disease, thereby limiting the therapeutic window for oligomer dissolving drugs. To harness this potential and optimize the efficiency and applicability of the sFIDA technology, various automation methods were developed. These included a procedure for the automatic determination of a threshold to distinguish background noise from signal, as well as the development of an automatic artifact detection algorithm. Since all components necessary for a fully automated analysis process have now been established, the complete automation of the sFIDA technology appears to be a promising next step.

Abkürzungsverzeichnis

Aβ	Amyloid-β
AD	Alzheimer-Krankheit (Alzheimer's disease)
AE-HL	Ausreißerentfernung-Hodges-Lehmann
AE-MdM	Ausreißerentfernung-Mittelwert der Mittelwerte
AF	Autofluoreszenz
APOE	Apolipoprotein-E
APP	Amyloid-Vorläuferprotein (Amyloid precursor protein)
aSyn	Alpha-Synuclein
CAE	Convolutional Autoencoder
CSF	Cerebrospinalflüssigkeit
CU	Cognitively unimpaired
CV%	Variationskoeffizienten (coefficient of variation)
DELCODE	DZNE-longitudinal cognitive impairment and dementia study
ELISA	Enzyme-linked Immunosorbent Assay
EOAD	Early-onset Alzheimer's disease
FPS	Falsch-positives Signal
HL	Hodges-Lehman
IAPP	Inselzellen-Amyloid-Polypeptid
IQC	Interne Qualitätskontrolle (internal quality control)
LOAD	Late-onset Alzheimer's disease
MCI	Mild cognitive impairment
MdM	Mittelwert der Mittelwerte
ML	Maschinelles Lernen
MME-MdM	Min-Max-Entfernung- Mittelwert der Mittelwerte
MPC	Maximaler Pixel Count
MRT	Magnetresonanztomographie
MTP	Mikrotiterplatte
NFT	Neurofibrillenbündel (neurofibrillary tangles)
MVP	Minimum Viable Product
PET	Positronen-Emissions-Tomographie
pTau	Hyperphosphoryliertes Tau-Protein

SCD	Subjective cognitive decline
SD	Standardabweichung
sFIDA	Surface-based Fluorescence Intensity Distribution Analysis
SiNaPs	Siliziumdioxid-Nanopartikeln
T1D	Typ-1-Diabetes
T2D	Typ-2-Diabetes
TIRF	Total Internal Reflection Fluorescence
tTau	Gesamt Tau-Protein (total tau)
VDL	Verdünnungslinearität
wMSE	Weighted mean squared error

Abbildungsverzeichnis

Tabellenverzeichnis

Liste der Publikationen

* Autoren sind gleichberechtigt

- Blömeke, L.*, **Rehn, F.***, Kraemer-Schulien, V.*, Kutzsche, J., Pils, M., Bujnicki, T., Lewczuk, P., Freiesleben, S.D., Schneider, L.-S., Preis, L., Priller, J., Spruth, E.J., Altenstein, S., Lohse, A., Schneider, A., Fliessbach, K., Wiltfang, J., Hansen, N., Rostamzadeh, A., Düzel, E., Glanz, W., Incesoy, E.I., Butryn, M., Buerger, K., Janowitz, D., Ewers, M., Perneczky, R., Rauchmann, B.-S., Teipel, S., Kilimann, I., Goerss, D., Laske, C., Munk, M.H., Sanzenbacher, C., Spottke, A., Roy-Kluth, N., Heneka, M.T., Brosseron, F., Wagner, M., Wolfsgruber, S., Kleineidam, L., Stark, M., Schmid, M., Jessen, F., Bannach, O., Willbold, D., Peters, O. (2024). Aβ oligomers peak in early stages of Alzheimer's disease preceding tau pathology. *Alzheimer's & Dementia: Diagnosis, Assessment & Disease Monitoring,* 16(2), e12589.
  https://doi.org/10.1002/dad2.12589

- Blömeke, L., **Rehn, F.**, Pils, M., Kraemer-Schulien, V., Cousin, A., Kutzsche, J., Bujnicki, T., Freiesleben, S.D., Schneider, L.-S., Preis, L., Cetindag, A.C., Gref, D., Cosma, N.C., Keles, D., Wang, X., Priller, J., Spruth, E.J., Altenstein, S., Schneider, A., Fliessbach, K., Wiltfang, J., Hansen, N., Rostamzahdeh, A., Düzel, E., Glanz, W., Incesoy, E. I., Buerger, K., Janowitz, D., Ewers, M., Perneczky, R., Rauchmann, B.-S., Teipel, S., Kilimann, I., Laske, C., Munk, M.H., Spottke, A., Roy, N., Heneka, M. T., Brosseron, F., Wagner, M., Roeske, S., Ramirez, A., Schmid, M., Jessen, F., Bannach, O., Peters, O., Willbold, D. (2024). Blood-based quantification of Aβ oligomers indicates impaired clearance from brain in ApoE ε4 positive subjects. *Communications Medicine*, 4(1), 1-13.
  https://doi.org/10.1038/s43856-024-00690-w

- Pils, M., Dybala, A., Schaffrath, A., **Rehn, F.**, Kutzsche, J., Blömeke, L., Tusche, M., Özdüzenciler, P., Bujnicki, T., Kraemer-Schulien, V., Gramespacher, H., Schmieschek, M.H.T., Barbe, M.T., Onur, O.A., Fink, G.R., Tamgüney, G., Bannach, O., Willbold, D. (2024). Elevated Aβ aggregates in feces from Alzheimer's disease patients: a proof-of-concept study. Alzheimer's Research & Therapy, 16(1), 223.
  https://doi.org/10.1186/s13195-024-01597-3

- **Rehn, F.***, Kraemer-Schulien, V.*, Bujnicki, T., Bannach, O., Tschoepe, D., Stratmann, B., Willbold, D. (2024). IAPP-oligomerisation levels in plasma of people with type 2 diabetes. *Scientific Reports, 14(1), 19556.*
  https://doi.org/10.1038/s41598-024-70255-3

- Blömeke, L., Pils, M., Kraemer-Schulien, V., Dybala, A., Schaffrath, A., Kulawik, A., **Rehn, F.**, Cousin, A., Nischwitz, V., Willbold, J., Zack, R., Tropea, TF., Bujnicki, T., Tamgüney, G., Weintraub, D., Irwin, D., Grossman, M., Wolk, DA., Trojanowski, JQ., Bannach, O., Chen-Plotkin, A., Willbold, D. (2022). Quantitative detection of α-Synuclein and Tau oligomers and other aggregates by digital single particle counting. *npj Parkinson's Disease*, 8(1), 68.
  https://doi.org/10.1038/s41531-022-00330-x

- Pils, M., Dybala, A., **Rehn, F.**, Blömeke, L., Bujnicki, T., Kraemer-Schulien, V., Hoyer, W., Riesner, D., Willbold, D., Bannach, O. (2023). Development and implementation of an internal quality control sample to standardize oligomer-based diagnostics of Alzheimer's disease. *Diagnostics*, 13(10), 1702. https://doi.org/10.3390/diagnostics13101702

- Bujnicki, T., Cousin, A., Schwarten, M., Hänel, K., **Rehn, F.**, König, B., Kraemer-Schulien, V., Pils, M., Blömeke, L., Bannach, O., Cukkemane, A., Willbold D. (2025). Digital direct detection of single biomolecules revealed femtomolar sensitivity. (Eingereicht - *The Journal of Molecular Diagnostics*)

- **Rehn, F.**, Pils M., Bujnicki B., Bannach O., Willbold D. (2024). Artifact detection in fluorescence microscopy using convolutional autoencoder. (Eingereicht - *Scientific Reports*)

Inhaltsverzeichnis

1 Einleitung

1.1 Proteinfehlfaltung

Proteine spielen eine essenzielle Rolle in nahezu allen biochemischen Reaktionen in lebenden Organismen und fungieren darüber hinaus als funktionelle Regulatoren und strukturelle Komponenten[1]. Um die Funktion einer Zelle zu erhalten, müssen sich Proteinsynthese, -faltung und -abbau daher im Gleichgewicht befinden und korrekt ablaufen[2]. Die bei der Proteinsynthese erzeugte lineare Sequenz von Aminosäuren bestimmt die durch Faltung entstandene, dreidimensionale Struktur (Konformation) und somit die Funktion des Proteins[3,4]. Konformationen unterscheiden sich unter anderem durch den Grad der Rotation um die Bindungen des Rückgrats[3], wodurch die Anzahl der theoretisch möglichen Konformationen mit zunehmender Kettenlänge exponentiell ansteigt. Letztlich nimmt ein Protein die Konformation an, welche die Menge der freien Energie minimiert[5]. Die im Organismus auftretende und funktionelle Konformation wird als nativer Zustand bezeichnet. Die Stabilität dieses nativen Zustandes ist jedoch unter physiologischen Bedingungen oft nur in begrenztem Maße belastbar, was unter bestimmten Umständen zur Fehlfaltung der Proteine führen kann, die mit einer zunehmenden Anzahl an Krankheiten assoziiert ist[2]. Im Verlauf dieser sogenannten Proteinfehlfaltungserkrankungen sind spezifische Proteine in der Lage stabile Konformationen anzunehmen, welche vom nativen Zustand abweichen und zur Aggregation neigen[6,7]. Dies kann zum Verlust der ursprünglichen biologischen Funktion („loss-of-function“) führen und dem Protein toxische Eigenschaften („toxic-gain-of-function“) verleihen[7]. Letzteres wird meist mit der Formation von β-Faltblatt-reichen Sekundärstrukturen in Verbindung gebracht, die intermolekulare Aggregation begünstigen[2]. Die Ursachen für Fehlfaltung und Aggregation sind bisher nicht abschließend geklärt.

Die Polymerisierungshypothese besagt, dass die Proteinfehlfaltung durch die Aggregation ausgelöst wird, während die Konformationshypothese besagt, dass die Fehlfaltung unabhängig von der Aggregation auftritt[7]. Aufgrund dieser Hypothese wäre eine Aggregation der fehlgefalteten Proteine möglich, aber nicht zwingend erforderlich, um einen stabilen Zustand zu erreichen[7]. Eine Kombination dieser beiden Hypothesen stellt die Konformations/Oligomerisierungs-Hypothese dar, welche die Proteinfehlfaltung als Auslöser der Aggregation benennt, jedoch postuliert, dass die Aggregation notwendig ist, um die angenommene Konformation zu stabilisieren[7].

Insgesamt sind über 25 Proteine bekannt, die im Kontext von Proteinfehlfaltungserkrankungen zur Aggregation neigen[8]. Die entstandenen Aggregate können sich hierbei in Bezug auf Struktur, Löslichkeit, biologische bzw. chemische Funktion und Lokalisation (intra- oder extrazellulär) unterscheiden[9]. Bei den meisten Proteinfehlfaltungserkrankungen erfolgt die Aggregation jedoch über mehrere Zwischenschritte, wobei zunächst lösliche Oligomere und Protofibrillen entstehen, die sich anschließend zu hochorganisierten, β-Faltblatt-reichen Fibrillen akkumulieren können (siehe Abbildung 1)[6,8]. Lagern sich diese extrazellulär ab, werden sie häufig als Plaques bezeichnet[6]. Entstandene Aggregate können darüber hinaus als sogenannte Keime (englisch: Seeds) fungieren, die native Proteine dazu veranlassen, nicht native Konformation anzunehmen, wodurch sie die Aggregation in bisher unbetroffenen Zellen initiieren können[10].

Ein Großteil der Proteinfehlfaltungserkrankungen tritt sporadisch auf (85 %), sie können jedoch auch genetisch bedingt oder in seltenen Fällen übertragbar sein[6]. Zu den bekannten Vertretern zählen Morbus Parkinson, Demenz mit Lewy-Körperchen, sowie die Progressive supranukleäre Blickparese, bei denen die Aggregation von Alpha-Synuclein (aSyn) bzw. des Tau-Proteins charakteristisch sind[11]. Weitere prominente Beispiele sind die neurodegenerative Alzheimer-Krankheit (englisch: Alzheimer's disease, AD), bei der die Aggregation von Amyloid-β (Aβ) und phosphoryliertem Tau-Protein (pTau) auftritt, sowie der Typ-2-Diabetes (T2D), eine Stoffwechselerkrankung, die mit der Aggregation des Inselzellen-Amyloid-Polypeptids (IAPP) assoziiert ist[2]. Letztere werden in den folgenden Abschnitten genauer erläutert.

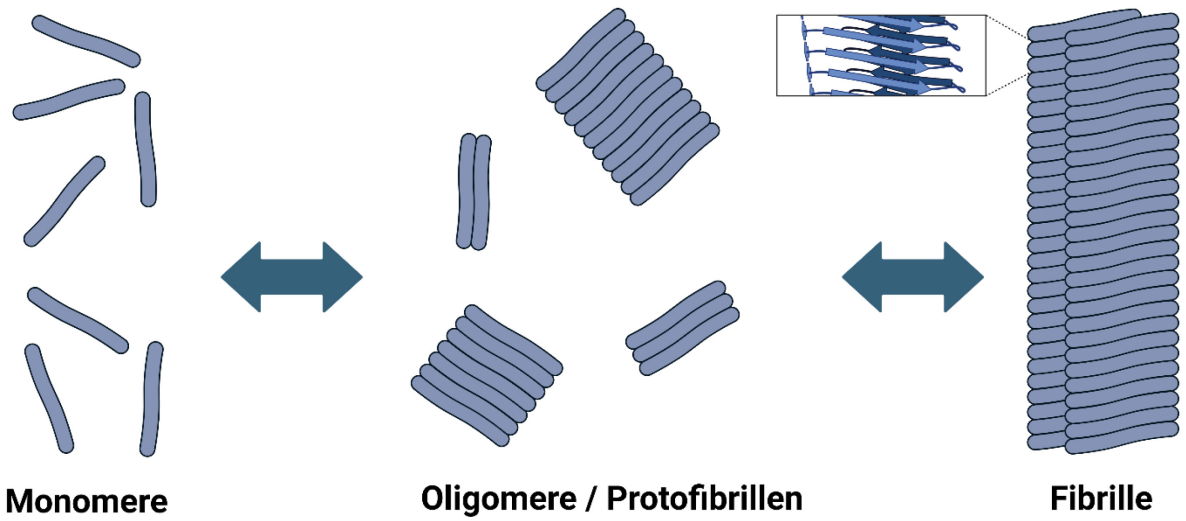

Abbildung 1: Generischer Aggregationsprozess. Fehlgefaltete Monomere können durch Aggregation Oligomere oder größere Protofibrillen bilden. Durch Anlagerung weiterer Bausteine entstehen wiederum β-Faltblatt-reiche Fibrillen. Bereits entstandene Aggregate können ebenso wieder zerfallen. Erstellt mit BioRender.com.

1.2 Alzheimer-Krankheit

Zu den Demenzerkrankungen zählen verschiedene Krankheitsformen, die sowohl Verhaltensänderungen als auch kognitive Beeinträchtigungen verursachen[12]. Prognosen zufolge wird die Zahl der Demenzerkrankungen weltweit bis 2040 auf über 80 Millionen ansteigen[13], was die Gesundheitssysteme mit erheblichen finanziellen Belastungen im Umfang von mehreren Billionen Dollar konfrontieren wird[14]. Unter den verschiedenen Demenzformen ist die AD die am häufigsten auftretende Form[13,15].

1.2.1 Subtypen der Alzheimer-Krankheit

Die AD lässt sich in zwei Subtypen unterteilen. Die seltenere early-onset AD (EOAD), die weniger als 6 % aller AD Fälle umfasst und die häufiger auftretende late-onset AD (LOAD)[16]. Obwohl es keine eindeutige Definition für die EOAD gibt, wird sie üblicherweise mit dem Auftreten erster Symptome vor dem 65. Lebensjahr und einer aggressiveren Progression assoziiert, wohingegen die LOAD sich typischerweise erst nach dem 65. Lebensjahr klinisch manifestiert[17,18]. Auch wenn das Aβ-Peptid in beiden AD-Formen eine wichtige Rolle in der Pathologie einnimmt, ist es im EOAD von besonderem Interesse. Aβ-Monomere entstehen während der Proteolyse des Membranproteins Amyloid-Vorläuferprotein (englisch: amyloid percursor protein, APP) durch γ-Sekretasen[19]. Die extrazellulär entstandenen Monomere können sich dabei hinsichtlich der Länge ihrer Aminosäurensequenz unterscheiden, wobei $A\beta_{42}$ (Aβ-Peptid mit 42 Aminosäuren) im Kontext der AD besonders relevant ist[20]. Die EOAD wird häufig mit autosomal-dominanten Mutationen in den Genen des APP sowie Presenilin-1 und Presenilin-2 assoziiert[8], welche die Funktion der γ-Sekretasen beeinträchtigen, was zu einer vermehrten Produktion von Aβ-Monomeren mit längeren Aminosäuresequenzen, wie $A\beta_{42}$ führt[21]. Im Vergleich zu Formen mit kürzeren Sequenzen, wie $A\beta_{40,}$ weist $A\beta_{42}$ ein erhöhtes Aggregationspotenzial auf[21]. $A\beta_{42}$ kann darüber hinaus als Seed für die Aggregation anderer Aβ-Formen fungieren, welche dann ebenfalls zur Pathogenese der Krankheit beitragen können[22]. Angesichts dessen werden diese Genmutationen als ein Auslöser der EOAD angesehen[23]. Neuere Ergebnisse zeigten jedoch, dass diese Mutationen nur in bis zu 15 % der EOAD-Fälle auftreten, während die restlichen Fälle durch eine Kombination bekannter und bisher unbekannter Gen-Varianten ausgelöst werden[24]. Während die EOAD fast ausschließlich genetisch bedingt ist[25], wurden für die LOAD bisher noch keine ursächlichen Genmutationen identifiziert[18]. Es wird daher angenommen, dass es sich bei der LOAD um eine sporadische, stark polygenetische Erkrankung handelt, bei deren Pathogenese eine Vielzahl genetischer sowie nicht-genetischer Faktoren involviert sind[19,23,25]. Zu den bekannten genetischen

Risikofaktoren zählt dabei das Vorhandensein einer oder zweier Kopien des ε4-Alleles des Apolipoprotein-E (APOE)-Genes, welches nicht nur das Risiko einer AD deutlich erhöht, sondern gleichzeitig das durchschnittliche Alter für das Auftreten erster Symptome senkt[26,27]. Zusätzlich tragen vaskuläre und diverse lebensstilbedingte Faktoren zur Pathogenese bei[28]. Zuletzt kann das Risiko einer AD durch das Vorliegen von Komorbiditäten, wie beispielsweise T2D, weiter erhöht werden[29,30].

Unabhängig vom Subtyp ist für die AD eine fortschreitende Abnahme kognitiver Fähigkeiten, wie des Gedächtnisses und der Konzentrationsfähigkeit charakteristisch[31]. Zudem sind die Wortfindung und die Fähigkeit zur Durchführung alltäglicher Aktivitäten mit fortschreitender Progression zunehmend beeinträchtig[31], und das Risiko für eine Vielzahl psychischer Symptome ist erhöht[12]. Im Falle einiger, nicht-gedächtnisbezogener Symptome ist dabei das Risiko im LOAD deutlich geringer ausgeprägt als in der EOAD[32]. Schließlich erhöht die AD das Mortalitätsrisiko, was zu einer Zeitspanne von oft wenigen Jahren zwischen Diagnose und Tod führt[33,34]. Ein Heilmittel existiert derzeit nicht.

1.2.2 Klinische Diagnose

Obwohl die Symptome der AD ausreichend dokumentiert sind, ist ihre zugrunde liegende Pathologie noch nicht vollständig verstanden. Für deren Erforschung und die Entwicklung wirksamer Behandlungsstrategien ist es daher hilfreich, Patienten möglichst präzise anhand ihrer individuellen Charakteristika zu gruppieren. Hierdurch können mögliche vorübergehende Effekte klarer erkannt und Patientengruppen identifiziert werden, bei denen die Behandlung mit bestimmten Wirkstoffen besonders vielversprechend erscheint. Einen Ansatz hierfür bietet das Framework des National Institute on Aging and Alzheimer's Association, welches die Progression einer AD anhand der klinischen Symptome in sechs Phasen unterteilt[20,35]. Die ersten beiden Phasen stellen präklinische Phasen dar, in denen die kognitive Leistung nicht objektiv beeinflusst ist (englisch: cognitively unimpaired, CU), sodass die Resultate kognitiver Tests folglich im normalen Bereich liegen. In der zweiten Phase manifestiert sich jedoch eine subjektiv wahrgenommene kognitive Beeinträchtigung (englisch: subjective cognitive decline, SCD)[36]. Die nachfolgenden Phasen drei bis sechs sind durch eine fortschreitende Abnahme der kognitiven Fähigkeiten und Zunahme der zuvor genannten Symptome gekennzeichnet[20,35]. Sie erstrecken sich von milder kognitiver Beeinträchtigung (englisch: mild cognitive impairment, MCI) über die milde, die moderate, bis hin zur schweren Demenzform.

1.2.3 Pathologie und Biomarker

Die Prodromalphase der AD beginnt häufig bereits Jahrzehnte vor dem Auftreten erster klinischer Symptome[37]. Mögliche auslösende Effekte könnten bei Studienteilnehmern, die aufgrund ihrer klinischen Symptome ausgewählt wurden, somit bereits abgeklungen sein und Personen in der Prodromalphase könnten aufgrund des asymptomatischen Zustandes fälschlicherweise in Kontrollgruppen aufgenommen werden. Aufgrund der symptomatischen Überlappung mit anderen Demenzformen besteht darüber hinaus das Risiko für Fehldiagnosen. Dies kann potenzielle Unterschiede zwischen Patienten- und Kontrollgruppen maskieren und somit die Gewinnung neuer Erkenntnisse erschweren. Um darüber hinaus eine frühestmögliche Behandlung mit potenziellen Wirkstoffen zu ermöglichen, ist eine frühzeitige Diagnose, vor dem Auftreten der ersten Symptome entscheidend. Eine Möglichkeit hierfür bietet die Verwendung verschiedener Biomarker, wie der monomeren Konzentration des $A\beta_{42}$-Peptids sowie des Tau-Proteins, gemessen in der Cerebrospinalflüssigkeit (CSF)[18,23].

Eine weit verbreitete Annahme besagt, dass die AD durch ein Ungleichgewicht zwischen Produktion und Clearance des Aβ-Monomers entsteht[37–39]. Bedingt durch pathologische Fehlfaltungen kommt es zudem vermehrt zur Aggregation von Aβ-Monomeren in unterschiedliche Strukturen[19]. Es bilden sich Oligomere, die unverändert bleiben, oder sequenziell zu Protofibrillen und darauffolgend zu Fibrillen aggregieren können[19,40]. Während dieser Aggregation können diverse Konformationen, wie α-Helix- oder β-Faltblatt-Konformere entstehen und schnelle Konformationsänderungen können auftreten[41]. Im weiteren Verlauf der AD akkumuliert ein Teil der Fibrillen in den sogenannten Senilen- oder β-Plaques[42]. Durch die abnormale Aggregation und Ablagerung in den β-Plaques sinkt die monomere $A\beta_{42}$-Konzentration im CSF, wodurch diese als Biomarker verwendet werden kann[20].

Eine frühe Theorie, welche die Forschung maßgeblich beeinflusste und kontinuierlich weiterentwickelt wurde, ist die Kaskadentheorie von Hardy und Higgins (1992)[39]. Diese besagt, dass die β-Plaques neurotoxische Eigenschaften aufweisen und als initialer Faktor für die weitere Pathologie fungieren. Durch die Beeinträchtigung der Kalziumhomöostase führen sie zu erhöhten intraneuronalen Kalziumkonzentrationen, was wiederum die Aggregation des Tau-Proteins in den Neuronen auslöst[39]. Tau ist ein natürlich vorkommendes Protein, welches zur Struktur und Stabilität der Mikrotubuli beiträgt[42]. Im Verlauf der AD kommt es jedoch aufgrund der erhöhten intraneuronalen Kalziumkonzentration zur Hyperphosphorylierung des Tau-Proteins, wodurch dieses toxische Eigenschaften entwickelt[39,43]. Das Neuron synthetisiert daraufhin fortlaufend neues, natives Tau-Protein und versucht das pTau in inerte Polymere

einzuschließen, was zur Bildung von Neurofibrillärenbündeln (englisch: neurofibrillar tangles, NFTs) führt[43]. Da jedoch auch das zum Ausgleich synthetisierte, native Tau hyperphosphoryliert, wird die Mikrotubuli zunehmend geschädigt, wodurch der axonale Transport beeinträchtigt wird[42]. Zusammen mit der zunehmenden Menge an NFTs, beeinträchtigt dies die synaptische und neuronale Funktion zunehmend, was letztlich, gemeinsam mit dem durch das steigende Volumen der NFTs einhergehenden Druck, zur retrograden Degeneration und schließlich zum Zelltod führt[42,43]. NFTs treten bei einer Vielzahl neurodegenerativer Krankheiten in Erscheinung und korrelieren im Gegensatz zu β-Plaques mit dem Schweregrad der demenziellen Symptome[44]. Da unter anderem nach dem Zelltod unterschiedliche Formen des Tau-Proteins in den extrazellulären Raum und ins CSF gelangen, können erhöhte Konzentrationen dieses Proteins als Biomarker zur Diagnose verschiedener neurodegenerativer Erkrankungen verwendet werden[45].

Obwohl auch Aβ-Fibrillen und β-Plaques neurotoxische Eigenschaften aufweisen, werden gegenwärtig lösliche Aβ-Oligomere, welche sich aufgrund ihrer geringen Größe leicht im Gehirn verbreiten können[19], als die neurotoxischste Form angesehen[40,46]. Die Toxizität der Oligomere wird dabei ebenfalls auf die Störung der Kalziumhomöostase zurückgeführt, die eine erhöhte, intraneuronale Kalziumkonzentration zur Folge hat[40]. Ebenso können Oligomere Zellmembranen schädigen, diverse Entzündungs- und Stressreaktionen auslösen sowie die synaptische Signalübertragung beeinträchtigen[19,40,47].

1.2.4 Biomarker-basierte Diagnose

Das AT(N) Research Framework nutzt die zuvor beschriebenen Biomarker für eine Klassifizierung, mittels derer Personen eindeutig in eins von acht Profilen eingeordnet werden können (siehe Abbildung 2)[20]. Die Klassifizierung kann dabei auf den Werten der Biomarker $A\beta_{42}$, pTau und der Gesamtmenge an Tau-Proteinen (tTau) basieren. Die Konzentration von $A\beta_{42}$ im CSF dient der Prüfung einer möglichen Amyloidose (A), während die pTau-Konzentration Aufschluss über das Vorliegen einer Tauopathie (T) gibt und die tTau-Konzentration eine neurologische Schädigung (N) anzeigt. Unterschreitet die $A\beta_{42}$-Konzentration, oder überschreiten pTau- und tTau-Konzentrationen einen definierten Grenzwert wird die entsprechende Kategorie als positiv gewertet (A+, T+, N+). Unabhängig vom T- und N-Status muss eine Amyloidose vorliegen (A+), um eine Person einem AD-assoziierten Profil zuzuordnen. Eine Klassifikation in das AD-Profil erfordert darüber hinaus eine vorliegende Tauopathie (T+). Ein großer Vorteil gegenüber der klinischen Diagnose ist, dass Patienten, deren Demenz-Symptome nicht durch eine AD bedingt sind (beispielsweise

A-T+N+) leichter identifiziert und somit aus Studien ausgeschlossen werden können. Durch die somit erhöhte Homogenität der Studiengruppen wird das Aufzeigen AD-spezifischer Effekte erleichtert.

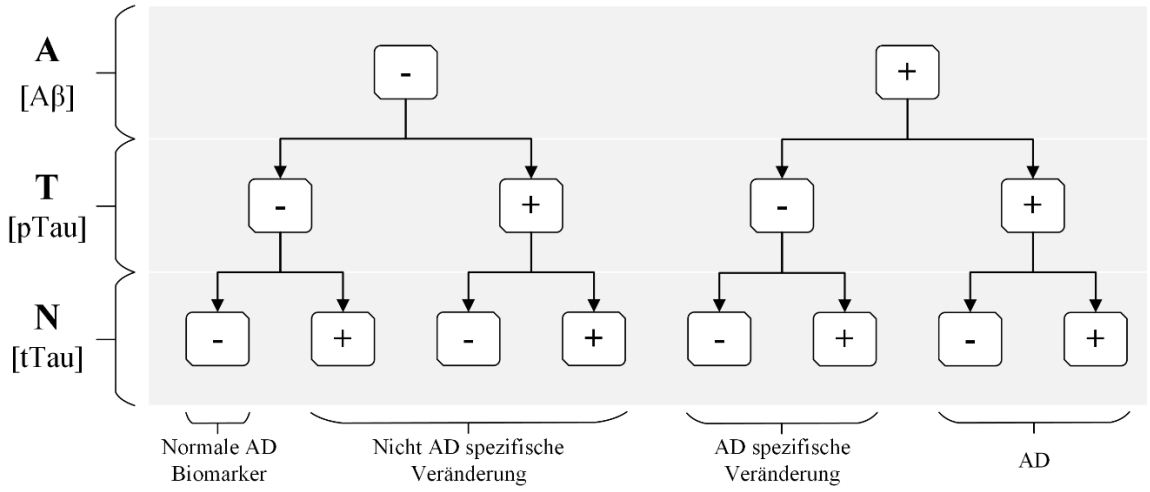

Abbildung 2: AT(N) Research Framework. Verändert nach Jack et al. (2018)[20]**.** Zur Vereinfachung der Darstellung wurden beide Profile unter A+T- zusammengefasst. Das Profil A-T-N+ weist neben AD-spezifischen auch nicht AD-spezifische Veränderungen auf.

Jack et al. (2010) entwickelten ein Modell, das die pathologische Abfolge der zuvor genannten Biomarker und Symptome mit den klinischen Diagnosegruppen kombiniert[37]. Wie in der Kaskadentheorie tritt die Aggregation von Aβ als Erstes auf, gefolgt von abnormalen Tau-Konzentrationen[37]. Die Konzentrationen beider Biomarker verändern sich dabei schon vor dem Auftreten erster Symptome (Phase 1 und 2) und sind bei Eintritt in die dritte Phase (MCI) bereits zu einem hohen Grad abnormal verändert. Die Gehirnstruktur sowie kognitive Fähigkeiten erreichen erst im Verlauf des MCI oder in späteren Phasen einen hohen Grad an Abnormalität. Es ist jedoch wichtig zu beachten, dass der Verlauf einer AD in seinem zeitlichen Fortschreiten individuell variiert. Es gibt somit keine einheitliche Dauer für die einzelnen Phasen. Des Weiteren kann es vorkommen, dass Verläufe stagnieren. So entwickeln nicht alle Personen, welche der SCD-Phase zugeordnet wurden vor ihrem Ableben klinische Symptome[37].

1.2.5 Weitere Diagnosemethoden

Neben der Verwendung von CSF-Biomarkern können auch nicht-invasive Bildgebungsverfahren wie die Positronen-Emissions-Tomographie (PET) zu diagnostischen Zwecken eingesetzt werden[20]. Mithilfe radioaktiver Amyloid-Tracer lässt sich eine erhöhte Retention nachweisen, was auf eine verstärkte Amyloid-Akkumulation hinweist, während eine synaptische Fehlfunktion aufgrund eines detektierten Hypometabolismus angenommen werden

kann[48]. Andere Verfahren, wie die Magnetresonanztomographie (MRT), ermöglichen zudem die Erkennung von Atrophie in verschiedenen Gehirnbereichen sowie von Läsionen der weißen Substanz, die über altersbedingte Veränderungen hinausgehen[49]. Die Atrophie der medialen Temporallappen wird hierbei als aussagekräftigster Marker für eine AD betrachtet[50]. Da bildgebende Verfahren erst nach CSF-Biomarkern Hinweise auf eine sich entwickelnde AD geben, sollten sie unterstützend eingesetzt werden[37].

1.3 Diabetes mellitus

Unter normalen physiologischen Bedingungen unterliegt der Blutzuckerspiegel Schwankungen, bewegt sich aber innerhalb eines eng regulierten Bereichs. Dies wird durch die aufeinander abgestimmte Interaktion (Glukosehomöostase) zwischen der Insulinsekretion, der Glukoseaufnahme durch Muskeln und Leber sowie der Unterdrückung der hepatischen Glukoseproduktion erreicht[51]. Insulin spielt dabei eine zentrale Rolle, da es als Hormon die Aufnahme der Glukose reguliert. Im Falle einer Diabeteserkrankung sind ein oder mehrere dieser Mechanismen gestört, wodurch die Glukosehomöostase nicht oder nur eingeschränkt aufrechterhalten werden kann[51]. Infolgedessen tritt häufig ein erhöhter Blutzuckerspiegel (Hyperglykämie) auf. Eine Diabeteserkrankung kann des Weiteren eine Reihe von Komplikationen verursachen, die zu Funktionsbeeinträchtigung oder Schäden an den Augen, Nerven, Nieren, den Blutgefäßen, sowie dem Herzen führen[52]. Durch die Kontrolle und Behandlung von Hyperglykämie, Blutdruck und Hypercholesterinämie kann die Wahrscheinlichkeit von Komplikationen reduziert oder deren Entwicklung verlangsamt werden[53,54]. Unbehandelt kann Diabetes jedoch ein ketoazidotisches Koma herbeiführen.

Weltweit sind im Jahr 2021 537 Millionen Menschen von Diabetes mellitus betroffen[55], wodurch dieser zu den häufigsten Stoffwechselerkrankungen zählt[56]. Prognosen zufolge wird die Fallzahl bis zum Jahr 2040 auf 642 Millionen ansteigen, wodurch die Gesundheitssysteme mit direkten Kosten von über einer Billion USD konfrontiert werden würden[57]. Die Gesamtanzahl der Diabetesfälle verteilt sich dabei auf verschiedene Diabetes-Typen. Typ-1-Diabetes (T1D) sowie T2D sind dabei die am häufigsten auftretenden Formen[58], wobei T2D rund 90 % aller Diabetesfälle ausmacht[59].

1.3.1 T1D und T2D

Der T1D ist eine Autoimmunerkrankung, welche sowohl genetisch bedingt als auch durch spezifische Viruserkrankungen in der Kindheit ausgelöst werden kann[58,60]. Durch Autoimmunreaktionen wird ein großer Anteil der β-Zellen, welche sich in den Langerhans-Inseln des Pankreas befinden, durch T-Zellen zerstört[60]. In einer Metaanalyse mehrerer

Autopsiestudien konnte gezeigt werden, dass die β-Zellmasse in Individuen mit T1D um 70-100 % gegenüber den gesunden Kontrollgruppen zurückging[61]. Da das Insulin in den β-Zellen produziert wird, können die verbleibenden Zellen nach Zerstörung eines ausreichend großen Anteils den Insulinbedarf nicht mehr durch eine erhöhte Sekretion kompensieren, wodurch die Glukosehomöostase nicht weiter aufrechterhalten werden kann. Ab diesem Zeitpunkt ist eine Insulintherapie notwendig, um den Blutzuckerspiegel zu regulieren. Bei Primaten wurde dieser Punkt bei einem Verlust von etwa 50 % der β-Zellmasse erreicht[62].

Zu den Risikofaktoren für den T2D zählen neben polygenetischen Auslösern auch umwelt- und lebensstilbedingte Faktoren wie Übergewicht und mangelnde körperliche Aktivität sowie ein fortschreitendes Alter[56,58,63]. Auch bestimmte Erkrankungen, darunter die AD, erhöhen das Risiko[64]. Der T2D ist durch eine fortschreitende Insulinresistenz sowie Beeinträchtigung der Insulinsekretion gekennzeichnet[59]. Infolge der zunehmenden Resistenz wird die Glukoseaufnahme in Muskeln und Leber reduziert, wodurch eine steigende Menge an Insulin zur Regulation des Blutzuckerspiegels benötigt wird. Unter normalen physiologischen Bedingungen würden Organismen mit einer gesteigerten Insulinsekretion (Hyperinsulinämie) sowie einer möglichen Zunahme der β-Zellmasse reagieren[65]. Während der Progression des T2D tritt jedoch eine abnormale Reaktion in Form einer beeinträchtigten Insulinsekretion und nachfolgender β-Zell-Apoptose auf[61,66]. Im Vergleich zu gesunden Individuen steigert sich die Apoptoserate um das Drei- bis Zehn-fache, während die Cytokineserate unverändert bleibt, was letztlich zu einer Abnahme der β-Zellmasse führt[65]. Die genaue Ursache der beeinträchtigten Insulinsekretion sowie der folgenden Apoptose ist nicht abschließend geklärt. Es gibt jedoch eine Vielzahl an Faktoren, die damit in Verbindung gebracht werden. Zu diesen gehören β-Zellstress, Reaktionen auf oxidativen Stress sowie Entzündungsprozesse[59]. Im Vergleich zu dem T1D findet die Abnahme der β-Zellmasse verlangsamt statt und ein größerer Anteil der β-Zellen unterliegt nicht der Apoptose. Eine Metastudie verschiedener Autopsiestudien konnte zeigen, dass die β-Zellmasse von Individuen mit T2D um bis zu 65 % gegenüber der Kontrollgruppe abnimmt[61]. Nichtsdestotrotz kann es auch bei dem T2D zu einer relativ abrupt einsetzenden Symptomatik sowie zum Zusammenbruch der Glukosehomöostase kommen[61], wodurch eine Insulintherapie erforderlich wird.

1.3.2 Aggregation von IAPP

Eine weitere mögliche Ursache für die Abnahme der β-Zellmasse im T2D ist die Insulinresistenz-bedingte Hypersekretion von IAPP und dessen nachfolgende Aggregation und Akkumulation. IAPP ist ein Peptidhormon, das mit Insulin durch die β-Zellen co-sekretiert

wird[67]. Bedingt durch die erhöhte Insulinresistenz steigt im frühen Krankheitsstadium die Sekretion von Insulin und folglich ebenfalls von IAPP, wobei letzteres in einem überproportionalen Verhältnis sekretiert wird[68]. Ähnlich wie die Aggregation von Aβ in der AD ist auch die Aggregation von IAPP im T2D pathologisch. Das IAPP-Monomer aggregiert analog zunächst zu löslichen Oligomeren, die wiederum Fibrillen bilden können, welche dann zu unlöslichen Plaques, dem sogenannten Amyloid akkumulieren können[69]. Dieses befindet sich extrazellulär zwischen β-Zellen sowie β-Zellen und Endothelzellen[70]. Obwohl die IAPP-Plaques als pathologisch angesehen werden, können sie ebenso in gesunden Individuen vorkommen (~10 % der Fälle) oder in einigen Fällen von T2D ausbleiben[65]. Die kleineren, löslichen Oligomere bilden sich hingegen auch intrazellulär, in den β-Zellen[71,72].

Der Grund für die übermäßige Aggregation ist noch nicht abschließend geklärt. Eine mögliche Hypothese besagt, dass intrazelluläre Aggregation durch die Hypersekretion von IAPP ausgelöst wird[69,73]. Da monomeres IAPP auch in gesunden Individuen intrazellulär vorhanden ist, wird die Existenz von Mechanismen angenommen, welche die Aggregation verhindern oder fehlgefaltetes IAPP entsorgen. Aufgrund des Hyperinsulinismus und der dadurch bedingten hohen Konzentration an co-sekretiertem IAPP-Monomer werden diese Schutzmechanismen jedoch überlastet[69,73]. Zusätzlich wird es als möglich erachtet, dass die Wirksamkeit der Mechanismen durch den T2D reduziert wird[73].

Eine weitere Parallele zwischen der AD und dem T2D besteht in der Zytotoxizität der Aggregate. Analog zur AD wird angenommen, dass die in unlöslichen Plaques abgelagerten Fibrillen im T2D eine geringere Toxizität aufweisen als Oligomere und somit wahrscheinlich nicht primär für die abnehmende β-Zellmasse verantwortlich sind[69]. Modelstudien an Mäusen zeigten, dass die Abnahme der β-Zellmasse nicht allein durch IAPP-Plaques bedingt sein kann, da sich diese zum Zeitpunkt der stärksten Reduzierung noch nicht gebildet hatten[69]. Ein weiteres Argument ist, dass nicht alle Individuen im Verlauf der T2D IAPP-Plaques entwickeln[65]. Nichtsdestotrotz sind auch extrazelluläre Fibrillen und Plaques in der Lage, die Integrität von Zellmembranen zu beeinträchtigen und sind somit zytotoxisch[74]. Den kleineren, löslichen Oligomeren wird eine stärkere toxische Wirkung zugeschrieben. Obwohl nachgewiesen werden konnte, dass IAPP-Oligomere verschiedene Zellmembranen beeinträchtigen oder schädigen und sowohl Entzündungsprozesse als auch oxidativen Stress hervorrufen können, ist die genaue Ursache der Zytotoxizität bislang nicht abschließend geklärt[72,74–76]. Neben der Zytotoxizität wird des Weiteren davon ausgegangen, dass IAPP-Oligomere die Clearance-Mechanismen beeinträchtigen, wodurch die Bildung weiterer

Oligomere sowie die Ausbreitung über Seeding-Mechanismen begünstigt wird[73]. Darüber hinaus gibt es weitere Faktoren, welche die Aggregation beeinflussen. So konnte gezeigt werden, dass Glukose und Fruktose gebildete Aggregate stabilisieren können[77], während Insulin inhibitorische Eigenschaften in Bezug auf die Aggregation von IAPP aufweist[78,79]. Da eine insulinresistenzbedingte Steigerung der Insulinsekretion im frühen Krankheitsstadium jedoch im Gegensatz zu der während einer T2D-Erkrankung auftretenden IAPP-Aggregation steht, wird vermutet, dass durch den T2D die Bindung von Insulin an IAPP beeinträchtigt wird oder weitere Faktoren eine Rolle spielen.

Zur Diagnose des T2D können die Plasmaglukosewerte genutzt werden. Die Integration zusätzlicher Plasmaprotein-Biomarker kann jedoch die Genauigkeit erhöhen und eine frühere Diagnose erlauben[80]. Ein Heilmittel für T1D und T2D existiert derzeit nicht. Während die Symptome behandelbar sind, muss eine Insulintherapie, falls notwendig geworden, fortgesetzt werden.

1.4 Quantifizierung von Oligomeren mit sFIDA

Wie in den vorhergehenden Kapiteln beschrieben, gibt es diverse Proteinfehlfaltungserkrankungen, in denen die Aggregation von Proteinen zu Oligomeren, Fibrillen und Plaques eine zentrale Rolle in der Pathologie einnimmt[2]. Aufgrund dessen ist die Auflösung dieser Aggregate ein vielversprechendes Ziel in der Entwicklung von Medikamenten. Frühere Studien zeigten, dass durch die Anwendung monoklonaler Antikörper Aβ-Plaques in AD-Patienten aufgelöst werden konnten[81]. Allerdings konnte eine resultierende Verlangsamung der Progression nur bedingt belegt werden[81,82]. Neuere Ansätze fokussieren sich daher auf die Auflösung der kleineren, löslichen Oligomere, da diese bereits in frühen Krankheitsphasen auftreten und zugleich eine hohe Toxizität aufweisen[40,46,69,83]. Sowohl für die Entwicklung von Wirkstoffen, die auf die Auflösung der Oligomere abzielen, als auch für diagnostische Zwecke ist eine präzise Quantifizierung der Oligomere unabdingbar. Im Gegensatz zu den Plaques lassen sich Oligomere aufgrund ihrer geringen Größe, welche im einstelligen Nanometerbereich liegen kann[83], jedoch nicht durch visuelle Methoden wie MRT oder PET in-vivo quantifizieren. Folglich sind Methoden zur Quantifizierung von Oligomeren in Körperflüssigkeiten wie CSF oder Plasma sowie in Ausscheidungen notwendig.

Eine zentrale Herausforderung bei der Entwicklung solcher Assays besteht in der geringen Konzentration von Oligomeren in Körperflüssigkeiten im Vergleich zu den hohen Konzentrationen an Monomeren. So wird beispielsweise angenommen, dass Aβ-Oligomere weniger als einen Prozent der Gesamtmenge an Aβ in CSF ausmachen[84]. Aufgrund dessen ist

die Unempfindlichkeit gegenüber Monomeren sowie eine hohe Sensitivität und Spezifität des Assays erforderlich, um aussagekräftige Messwerte zu gewährleisten. Die *Surface-based Fluorescence Intensity Distribution Analysis* (sFIDA) Technologie, welche ursprünglich aus einer Methode zur Quantifizierung von Prionen entwickelt wurde[85], ist gezielt an diese Anforderungen adaptiert und für die Quantifizierung von Aggregaten und Oligomeren weiter optimiert worden[86,87].

1.4.1 sFIDA - Grundprinzip

Ein Enzyme-linked Immunosorbent Assay (ELISA) nutzt das Konzept der Antikörperbindung, um verschiedene Antigene, insbesondere Proteine, zu detektieren und zu quantifizieren[88]. Die ELISA haben gemeinsam, dass sie über mindestens drei Komponenten verfügen. Diese umfassen den Analyten, der die zu detektierenden Antigene enthält, einen Fänger zur Fixierung der Antigene und eine Detektionskomponente[88]. Die genaue Form dieser Komponenten variiert je nach ELISA-Typ, die sich in ihrer Komplexität, ihren spezifischen Vor- und Nachteilen sowie ihren Einsatzvoraussetzungen unterscheiden[89]. Der Sandwich-ELISA bietet unter den ELISA-Typen eine besonders hohe Sensitivität und Spezifität[88,89], weshalb er als Grundlage für die sFIDA-Technologie genutzt wird. Der Ansatz wird durch hochauflösende Fluoreszenzmikroskopie ergänzt, die neben quantitativen Messungen eine umfassendere Datenerhebung ermöglicht. Da die Grundprinzipien des Sandwich-ELISAs sowie der Fluoreszenzmikroskopie unabhängig vom spezifischen Antigen und der Probenmatrix sind, stellt die sFIDA-Technologie eine flexible Plattformtechnologie dar. Abbildung 3 veranschaulicht das Grundprinzip des sFIDA-Assays.

Wie für einen Sandwich-ELISA üblich werden auch im sFIDA-Assay die Fängerantikörper auf einer Mikrotiterplatte (MTP) immobilisiert. Dabei werden für sFIDA-Assays MTPs mit Glasboden verwendet, um die anschließende Fluoreszenzmikroskopie mit einem inversen Mikroskop zu ermöglichen[90]. Durch die anschließende Auftragung einer Blockierlösung wird die verbleibende freie Glasoberfläche gesättigt, sodass spätere unspezifische Bindungen und somit potenzielle falsch-positive Signale minimiert werden. Nach Zugabe der Proben findet eine Inkubationsphase statt, in welcher die in der Probe enthaltenen Antigene, sowohl in monomerer als auch in aggregierter Form an die Fängerantikörper gebunden werden. Nach einem Waschschritt werden die mit Fluoreszenzfarbstoff-markierten Detektionsantikörper eingesetzt, wobei Fluorochrome mit hoher Quantenausbeute und Photostabilität genutzt werden. Da der Fänger- sowie der Detektionsantikörper identische oder überlappende Epitope erkennen, können die Detektionsantikörper nicht an die Monomere binden, da deren Epitope

bereits durch die Fängerantikörper maskiert sind[90]. Die Detektionsantikörper können folglich nur an aggregierte Formen des Antigens, wie Oligomere, binden, wodurch eine Unempfindlichkeit gegenüber den chemisch identischen Monomeren gewährleistet wird. Die Anzahl der verwendeten Antikörper sowie die Emissionsbereiche der zur Markierung eingesetzten Fluorochrome sind variabel, wodurch es möglich ist, in einem einzelnen Experiment verschiedene Antigene zu detektieren. Ebenso können mehrere Detektionsantikörper mit unterschiedlichen Fluorochromen verwendet werden, welche jedoch auf dasselbe Antigen abzielen. Durch die Überlagerung beider Fluoreszenzkanäle (Kolokalisation) wird die Spezifität des Assays erhöht, da wellenlängenspezifische, disjunkte Autofluoreszenz (AF) herausgefiltert werden kann. Die Anwendung der Kolokalisation führt jedoch ebenfalls zu einer Verringerung der quantitativen Analyseergebnisse (Readouts). Da dieser Effekt in einigen Assays stärker ausfällt als in anderen, kann die Kolokalisation nicht in allen Assays angewendet werden.

1.4.2 Datenakquise

Mit einem Total Internal Reflection Fluorescence (TIRF) Mikroskop werden für jedes Well der MTP 25 Bilder im 14-Bit-Format mit einer Auflösung von 1000×1000 Pixeln aufgenommen, wobei jeder Pixel etwa 114 nm abbildet. Die 25 Bilder erfassen kumuliert somit etwa 3 % der gesamten Well-Fläche. Werden verschiedene Fluorochrome verwendet, werden die Emissionen der unterschiedlichen Wellenlängenbereiche (üblicherweise rot (705 nm) und grün (525 nm)) in separaten Bilddateien gespeichert. Abbildung 3 zeigt ein Beispiel eines durch den sFIDA-Assay erfassten Well-Ausschnittes durch zwei Fluoreszenzkanäle sowie die Kolokalisation der Einzelkanäle. Jeder einzelne Pixel nimmt dabei einen Graustufenwert zwischen 0 und 16383 an, der im Folgenden als Intensität bezeichnet wird. Jeder Pixel, dessen Intensität oberhalb eines definierten Intensitätsgrenzwertes (Cutoff) liegt und sich somit vom Hintergrund abgrenzen lässt, wird im Folgenden als Signal bezeichnet. Stellen angrenzende Pixel Signal dar, wird die gesamte direkt zusammenhängende Signal-Fläche (ohne diagonale Verbindungen) als Partikel bezeichnet. Zur Unterscheidung des Signals, das durch spezifisch gebundene Detektionsantikörper erzeugt wird, von Signalen, die auf andere Quellen zurückzuführen sind, wird im Folgenden der Begriff Nutzsignal verwendet, wenn eine Abgrenzung erforderlich ist.

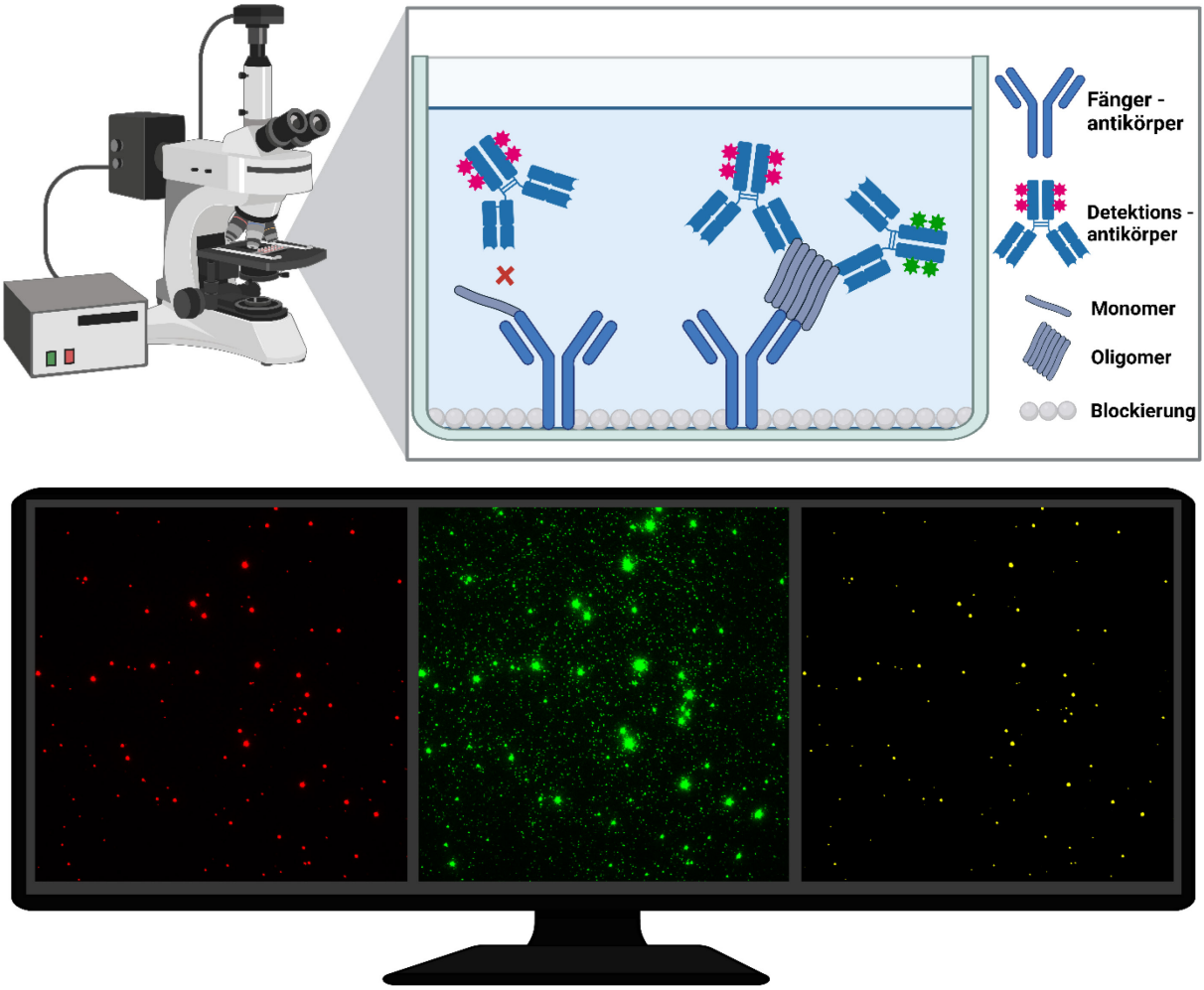

Abbildung 3: Schematische Darstellung des sFIDA-Assays. Die schematische Darstellung verdeutlicht, dass Detektionsantikörper ausschließlich an Aggregate wie Oligomere, aber nicht an Monomere binden können. Folglich sind nur diese in der Lage Nutzsignal zu erzeugen. Das Beispielbild zeigt eingefärbte Signale in den einzelnen Fluoreszenzkanälen (rot und grün) sowie die Kolokalisation (gelb). Partikel im grünen Fluoreszenzkanal sind ausgedehnter als im roten Fluoreszenzkanal und der Hintergrund weist eine höhere Intensität auf. Erstellt mit BioRender.com.

Wie bereits ausgeführt, ist das Grundprinzip des sFIDA-Assays unabhängig von der spezifischen Probenmatrix und den nachzuweisenden Antigenen. Die einzelnen Assay-Komponenten und das Assay-Protokoll müssen jedoch für jeden Assay im Rahmen der Assay-Entwicklung individuell bestimmt und optimiert werden, um eine bestmögliche Leistung hinsichtlich Sensitivität und Spezifität zu erreichen. Um den Assay robuster gegenüber Intra-Assay-Varianz zu gestalten, hat sich die Verwendung von vier Replikaten jeder Probe bewährt, die in separate Wells pipettiert werden. Durch Aggregation der einzelnen Well-Readouts wird der Readout der Probe ermittelt.

1.4.3 Bildanalyse-Prozess

Der Prozess der Bildanalyse umfasst im Wesentlichen vier zentrale Schritte (siehe Abbildung 4). Zunächst erfolgt die Artefaktdetektion, bei der Bilder auf potenzielle Artefakte überprüft werden. Artefaktbelastete Bilder werden hierbei aussortiert, um eine Verfälschung der nachfolgenden Berechnungen zu vermeiden. Im anschließenden Schritt wird der Cutoff bestimmt, welcher die Abgrenzung des Signals vom Hintergrundrauschen, bestehend aus Streulicht und dem Dunkelrauschen des Detektors, ermöglichen soll. Danach erfolgt die quantitative Analyse, bei der die in den Bildern enthaltenen Signale oder Partikel in numerische Readouts umgewandelt werden. Abschließend sollte eine Kalibration, oder im Falle dessen, dass dies nicht möglich ist, eine Normierung der Readouts stattfinden.

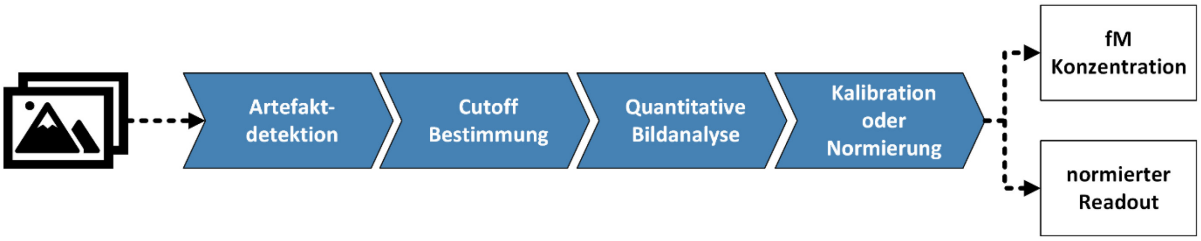

Abbildung 4: Bildanalyse-Prozess. Prozess der Bildanalyse von sFIDA-generierten Rohdaten bis hin zu experimentübergreifend vergleichbaren Ergebnissen.

Für die ersten drei Prozessschritte spielt AF eine wichtige Rolle, da sie zum Hintergrundrauschen beiträgt, falsch-positive Signale erzeugt sowie in Form von Artefakten auftreten kann. Wird die AF in den verschiedenen Formen nicht entfernt, können die Ergebnisse der quantitativen Analyse verfälscht werden.

1.4.3.1 AF und falsch-positive Signale

Unabhängig davon, ob es sich um Proben aus Körperflüssigkeiten oder Gewebehomogenaten handelt, bestehen diese aus komplexen Zusammensetzungen vieler unterschiedlicher Komponenten. Einige der enthaltenen endogenen Moleküle besitzen autofluoreszierende Eigenschaften und können somit nach Anregung durch Licht in bestimmten Wellenlängenbereichen auch ohne Markierung durch exogene Fluorochrome AF emittieren[91–93]. Obwohl viele dieser Moleküle nur in schmalen Wellenlängenbereichen mit einer Breite unter 200 nm autofluoreszieren, sind auch breitere Bereiche von über 300 nm möglich[94]. Die Emission liegt dabei häufig im blauen Wellenlängenbereich, es existieren jedoch auch endogene Moleküle die Licht im grünen oder roten Bereich und somit im Emissionsbereich der Detektionsantikörper, emittieren[94]. Obwohl die endogene AF für diverse explorative und diagnostische Zwecke genutzt wird, da sie Hinweise auf pathologische oder metabolische

Veränderungen geben kann[93], führt sie bei der Verwendung exogener Fluorochrome zu ungewollten Signalen, was die Genauigkeit (Maß der Abweichung zum tatsächlichen Wert) und Präzision (Maß der Streuung einzelner Messpunkte) der Messung verringert[95].

Im Rahmen des sFIDA-Assays wird das Auftreten von AF durch endogene Moleküle weitestgehend reduziert, indem durch einen Waschschritt alle nicht spezifisch an die Fängerantikörper gebundenen Matrixkomponenten entfernt werden[90]. Ist die Oberfläche des Wells jedoch nicht vollständig blockiert oder treten Kreuzreaktionen zwischen Fängerantikörpern und Matrixkomponenten auf, kann es zu unspezifischen Bindungen kommen, wodurch autofluoreszierende Matrixkomponenten in geringem Umfang verbleiben können. Die Intensität der AF variiert dabei abhängig von der spezifischen Emissionsquelle sowie der Anzahl unspezifischer Bindungen auf begrenzter Fläche. Ist die Intensität dieser Emissionen niedrig (unterhalb des Cutoffs), werden sie im Folgenden gemeinsam mit weiteren Störfaktoren, wie dem Dunkelrauschen des Detektors, als Hintergrundrauschen bezeichnet. Neben komplexen mathematischen Methoden zur Entfernung des Hintergrundrauschens, beispielsweise auf Basis der Wavelet-Funktion[96], kann es auch scheinbar simpel durch die Anwendung eines Cutoffs entfernt werden. Erzeugt die unerwünschte Emission hingegen ein Signal, kann dieses allein auf Grundlage der Intensität nicht mehr vom Nutzsignal unterschieden werden, was die Identifikation und Entfernung erheblich erschwert.

Es gibt mehrere Ansätze, um den Einfluss AF-bedingter Signale auf die Analyseergebnisse zu reduzieren. Diese umfassen direkte Maßnahmen, welche die AF bei Aufnahme der Bilder verringern sollen, sowie indirekte bzw. post-hoc Methoden, um die AF aus bereits generierten Bildern zu entfernen. Zu den direkten Maßnahmen gehört die chemische Behandlung der Probe, die häufig bei der Analyse von Gewebe Anwendung findet und die AF sehr effektiv reduzieren bzw. in einigen Fällen nahezu vollständig eliminieren kann[97,98]. Ebenfalls direkten Einfluss hat das sogenannte Photobleaching, bei dem die Fluorochrome durch Bestrahlung zerstört werden sollen[99]. Für den sFIDA-Assay sind jedoch beide Ansätze nicht praktikabel, da eine Beeinflussung der Struktur der Proteinaggregate nicht ausgeschlossen werden kann. Zudem kann besonders im Falle des Photobleachings der Prozess zeitaufwändig ausfallen[99]. Indirekte Ansätze zur Reduzierung der AF umfassen die Optimierung des zeitlichen Abstands zwischen der Anregung der Fluorochrome und der Detektion der Emission, die auf den unterschiedlichen Emissionsdauern von exogenen und endogenen Fluorochromen basieren[100,101], sowie die Spektralanalyse der Signale[102]. Beide Ansätze erfordern jedoch für jeden Assay eine erneute Optimierung, was sie sehr aufwendig macht. Ein weiterer indirekter Ansatz ist die Optimierung

der exogenen Fluorochrome mit dem Ziel, ihre Quantenausbeute zu erhöhen, um das Signal-Rausch-Verhältnis zu maximieren[95].

Post-hoc-Methoden zur Identifikation von AF-bedingten Signalen umfassen unter anderem differenzielle Fluoreszenz-Korrekturverfahren, welche einen zweiten Anregungs- bzw. Detektionsbereich im Rahmen einer zusätzlichen Messung verwenden[103,104]. In beiden Fällen basiert das Grundprinzip darauf, dass exogene Fluorochrome nur in einem spezifischen und schmalen Wellenlängenbereich emittieren, während AF endogener Moleküle auch über breitere Wellenlängenbereiche auftreten kann[94]. Bei Verwendung mehrerer Anregungsbereiche wird die Probe sowohl im für das exogene Fluorochrom spezifischen Wellenlängenbereich als auch in einem disjunkten Bereich angeregt[103]. Die aus der Anregung resultierende Fluoreszenz wird hingegen nur im für das exogene Fluorochrom spezifischen Wellenlängenbereich detektiert. Die erste Messung soll dabei das Nutzsignal inklusive der AF detektieren, während die zweite Messung reine AF detektiert. Durch Subtraktion der zweiten Messung wird das Nutzsignal anschließend von der AF bereinigt. Eine abgewandelte Form stellt die Verwendung zweier Detektionsbereiche bei identischem Anregungsbereich dar[104]. In diesem Fall wird die Probe ausschließlich im für das exogene Fluorochrom spezifischen Wellenlängenbereich angeregt. Das Signal wird sowohl im spezifischen Bereich als auch in einem davon abweichenden Bereich detektiert, wobei das Prinzip dem der vorherigen Methode entspricht. Während die erste Messung sowohl das Nutzsignal als auch die AF erfasst, repräsentiert die zweite Messung ausschließlich die AF. Auch in diesem Ansatz wird die AF von der gesamten Fluoreszenz subtrahiert, um das reine Nutzsignal zu extrahieren. Die Subtraktion erfordert jedoch stets eine präzise Abstimmung der Wellenlängenbereiche mittels eines Korrekturfaktors[104], was die Anwendung anspruchsvoll macht[99].

Neben endogenen Molekülen können auch die exogenen Detektionsantikörper unspezifisch an nicht blockierte Flächen oder aufgrund von Kreuzreaktivitäten an unspezifisch gebundene endogene Moleküle binden. Analog zur AF kann die hieraus resultierende Emission sowohl mit niedriger Intensität zum Hintergrundrauschen beitragen als auch Signal erzeugen. Da diese unerwünschte Fluoreszenz jedoch im spezifischen Detektionsbereich auftritt, lassen sich die resultierenden Signale weder anhand des Fluoreszenzbereichs noch anhand der Intensität vom Nutzsignal differenzieren.

Im Folgenden werden alle unerwünschten Signale, unabhängig von ihrer Quelle, als falsch-positives Signal (FPS) bezeichnet. Obwohl die genauen Quellen der Emissionen nicht eindeutig bestimmt werden können, deutet die Signalreduktion in Negativkontrollen ohne

eingesetzte Detektionsantikörper darauf hin, dass ein beträchtlicher Teil der FPS auf unspezifisch gebundene Detektionsantikörper zurückzuführen ist[105,106]. Dies ist insbesondere problematisch, da alle zuvor vorgestellten Ansätze ausschließlich die endogene AF reduzieren, jedoch keine durch unspezifisch gebundene Detektionsantikörper erzeugten Signale abschwächen bzw. entfernen können. Folglich kann nur ein Bruchteil der FPS, etwa bei abnormal großen oder abnormal geformten Partikeln, vom Nutzsignal differenziert werden. Partikel, die visuell klassifizierbar sind, werden im Folgenden als Artefakte bezeichnet.

1.4.3.2 Artefaktdetektion

Zusätzlich zu den bereits beschriebenen Artefakten, die auf Matrixkomponenten bzw. den Assay zurückzuführen sind, existieren weitere potenzielle Artefaktquellen. Dazu gehören Kontaminationen der Proben mit Bakterien, die AF unterschiedlicher Intensität erzeugen können[107]. Ebenso besteht die Möglichkeit einer Kontamination mit Aerosolen, die unterschiedlichste Größen von ca. 10 nm bis 100 µm aufweisen und sowohl biologischen als auch nicht-biologischen Ursprungs sein können[108,109]. Unabhängig von ihrem Ursprung können Aerosole jedoch autofluoreszierende Eigenschaften aufweisen[108]. Neben der direkten AF, die durch Bakterien und Aerosole verursacht wird, kann zusätzlich AF durch die unspezifische Bindung von endogenen Molekülen oder Detektionsantikörpern auftreten. Im Fall von Aerosolen ist zudem eine Beeinträchtigung durch Lichtstreuung oder Reflexion nicht auszuschließen.

Während die Gefahr einer Kontamination mit Bakterien vor allem auf das Pipettieren, sowie die Waschschritte beschränkt ist, besteht das Risiko einer Aerosolkontamination potenziell in allen Prozessschritten. Auch das verwendete Material, insbesondere die MTP, können Quellen von Artefakten darstellen. Dies ist dann der Fall, wenn die Platten Verschmutzungen oder Beschädigungen, wie beispielsweise Kratzer, oder Rückstände des Klebers aufweisen[110]. Diese können, analog zu Aerosolen, unspezifische Bindungen sowie Streuung und Reflexion des Lichts verursachen. Zuletzt gibt es bestimmte Artefakte, welche typisch für das verwendete Mikroskop, bzw. die angewandte Mikroskopie-Methode sind. Im Fall der TIRF-Mikroskopie können beispielsweise Luftblasen oder Kontaminationen im Immersionsöl auftreten, welche Streulicht verursachen[111]. Ein ungleichmäßig dicker Ölfilm oder Staub auf dem Mikroskopobjektiv oder der Optik im Revolverkopf kann darüber hinaus Streifen sowie konzentrische Interferenzringmuster erzeugen[111]. Im Gegensatz zu den zuvor genannten Artefakten verursachen diese jedoch teilweise keine AF, sondern dunkle Bereiche (falsch-negative Signale). Bewegungsunschärfe, entstanden durch die Aufnahme des Bildes in

Bewegung oder während des Fokussierens, kann hingegen in einer Vielzahl an Mikroskopie-Methoden auftreten[112–114].

Unabhängig vom konkreten Artefakt und dessen Ursache ist die Detektion und Entfernung in der Mikroskopie von zentraler Bedeutung. Dies gilt insbesondere für quantitative, fluoreszenzmikroskopische Assays, bei denen die Anzahl fluoreszierender Partikel oder die Gesamtfläche des Signals ermittelt und ausgewertet werden soll. Artefakte können hier die Messergebnisse erheblich verfälschen, was zu einer Verringerung der Präzision und Genauigkeit des Assays führt und dadurch die Verlässlichkeit der nachfolgenden Analyse gefährdet. Folglich ist eine effektive Artefaktdetektion für den sFIDA-Assay von großer Bedeutung.

Die Artefaktdetektion für sFIDA-generierte Bilddateien wurde bislang teilautomatisiert durchgeführt. Die dabei verwendeten Methoden identifizieren Artefakte über die Größe und Form und erkennen darüber hinaus unscharfe Bilder. Bei ersterer wird zunächst das Originalbild mithilfe eines Grenzwertes in ein hintergrundfreies Binärbild konvertiert, bei dem Werte oberhalb des Grenzwertes den Wert eins erhalten. Der Grenzwert wird dabei durch den Mittelwert plus die Standardabweichung (englisch: standard deviation, SD) der Intensität aller Pixel ermittelt. Anschließend werden durch morphologische Operationen kleinere Partikel entfernt und schwach verbundene Partikel voneinander getrennt[115]. In einem Kernel-basierten Verfahren (auch als Filter-basiertes Verfahren bekannt) werden Partikel identifiziert, die eine vom Analysten festgelegte Mindestfläche überschreiten. Dazu wird ein sogenannter Kernel, ein Element definierter Form und Größe, über das Bild bewegt. Wenn ein Partikel so groß ist, dass alle unter dem Kernel liegenden Pixel den Wert eins aufweisen, wird es als potenzielles Artefakt identifiziert. Wenn zudem der Mittelwert, die SD und die Schiefe der Intensitäten eines Partikels im Originalbild die vom Analysten definierten Grenzwerte übertrafen, wurde das Artefakt bestätigt und das entsprechende Bild nicht in die weitere Analyse einbezogen[115]. Zusätzlich wurden die Bilder durch Verwendung einer Laplace-Operation auf Unschärfe geprüft.

Der Laplace-Operator ist ein Filter, der zur Detektion von Kanten in einem Bild eingesetzt wird, indem er Intensitätsänderungen im Bild durch die Berechnung der zweiten partiellen Ableitung hervorhebt[116]. Seine Anwendung zur Erkennung von Unschärfe basiert auf der Annahme, dass scharfe Kanten starke Intensitätsgradienten erzeugen, die bei verschwommenen Bildern ausbleiben[117]. Der Laplace-Operator, angewendet als Filter, erzeugt durch seine Bewegung über das Bild eine Matrix, in welcher sich starke Intensitätsgradienten im originalen Bild als hohe positive oder negative Werte manifestieren, während niedrige Intensitätsgradienten nur geringe

Werte hervorrufen[116]. Die Varianz der resultierenden Matrix dient als Maß zur Bewertung der Bildschärfe, wobei eine niedrige Varianz auf ein verschwommenes Bild hindeutet[117]. Mittels eines durch den Analysten definierten Grenzwertes werden Bilder, deren Varianz diesen nicht überschreiten aussortiert.

Beide Detektionsmethoden sind jedoch anfällig für verschiedene potenzielle Fehlerquellen und bringen empfindliche Nachteile mit sich. So ist die Bestimmung der akzeptablen Partikelgrößen stark vom jeweiligen Assay, den eingesetzten Probenkonzentrationen sowie externen Einflüssen während der Messung abhängig. Dies macht es unmöglich, einen allgemeingültigen Grenzwert für die Partikelgröße festzulegen, was für jedes Experiment einen erneuten Optimierungsprozess nach sich zieht. Auch die Unschärfeerkennung erfordert die manuelle Festlegung eines Grenzwertes durch den Analysten und somit ebenfalls wiederholte Optimierungsprozesse. Dazu kommt, dass die Methode eine inhärente Problematik aufweist. So ist die aus der Laplace-Operation resultierende Varianz nicht nur von der Unschärfe, sondern ebenfalls von der Anzahl an Kanten abhängig[117]. Bilder mit wenig Signal beinhalten entsprechend wenige Kanten, was in einer niedrigen Varianz resultiert. Im Gegensatz dazu weisen Bilder mit viel Signal viele Kanten auf, was wiederum eine hohe Varianz nach sich zieht. Hieraus folgt, dass in Abhängigkeit von der Signalmenge in verschwommenen Bildern eine höhere Varianz auftreten kann als in scharfen Bildern.

Für den Analysten bedeuten die wiederholten Parameter-Optimierungsprozesse der beiden Methoden einen hohen Zeitaufwand sowie die Notwendigkeit umfassender Erfahrung. Zudem wird ein Interpretationsfreiraum für den Analysten geschaffen, der subjektive Entscheidungen ermöglicht, wodurch die Auswertung einem menschlichen Bias unterliegt und die Reproduzierbarkeit des Assays negativ beeinflusst wird. Angesichts der potenziellen Fehlerquellen, der eingeschränkten Reproduzierbarkeit und der wirtschaftlichen Faktoren erscheint ein parameterfreies und vollautomatisiertes Verfahren als eine erstrebenswerte Lösung. Die Nutzung maschinellen Lernens (ML) bietet dabei eine vielversprechende Möglichkeit, diese Anforderungen zu erfüllen.

Das Konzept des ML hat bereits in zahlreichen biologischen und medizinischen Bereichen breite Anwendung gefunden. Insbesondere wurde ML häufig zur Analyse bildgebender Verfahren wie der Röntgenbildgebung, der Computertomographie oder der MRT eingesetzt. Dabei kamen verschiedene Modelle wie *Neural Networks, Support Vector Machines und Random Forests* zu diagnostischen Zwecken zum Einsatz[118,119]. In vielen Anwendungsfällen spielt dabei die Detektion spezifischer Objekte, wie beispielsweise von Tumoren, eine zentrale

Rolle[118]. Auch die für diese Arbeit relevante Detektion von Artefakten fällt im weiteren Sinne in den Bereich der Objektdetektion.

Die Detektion von Artefakten kann auf verschiedenen Ebenen erfolgen. Sie reicht von der grundlegenden Feststellung, ob ein Bild oder Bildausschnitt Artefakte enthält, bis hin zur präzisen Lokalisierung der Artefakte innerhalb des Bildes. Werden Methoden des überwachten Lernens eingesetzt (Verwendung eines Datensatzes, der für jeden Eingabewert einen vordefinierten Ausgabewert enthält, der im Trainingsprozess erlernt werden soll[120]), erfordert die genaue Lokalisierung in der Regel einen höheren Aufwand beim Training, da nicht nur ein Label pro Bild („artefaktfrei“ oder „artefaktbelastet“) benötigt wird, sondern jeder Pixel eines Trainingsbildes mit einem entsprechenden Label versehen werden muss. Obwohl dieser Ansatz zeitintensiv ist, bildet er in vielen ML-Modellen die Grundlage für eine nachfolgende Entfernung der Artefakte.

Unabhängig von der Label-Ebene basieren alle Modelle, die dem überwachten Lernen zuzuordnen sind und zur Detektion von Artefakten eingesetzt werden sollen, auf demselben Prinzip. Artefakte im Trainingsdatensatz werden erlernt, um sie später in Bildern wiederzuerkennen. Erkennen die Algorithmen Strukturen mit ausreichender Übereinstimmung zu den erlernten Artefakten, werden diese entsprechend klassifiziert und können potenziell entfernt werden. Bildartefakte, die keine ausreichende Übereinstimmung zum Erlernten aufweisen, bleiben hingegen unerkannt. Eine künstliche Erweiterung des Datensatzes (Daten Augmentation), beispielsweise durch Rotation, Spiegelung oder Farbveränderung der original Bilder, kann helfen, die Robustheit des Modells durch Vermeidung von Überanpassung zu erhöhen[121], eine deutliche Steigerung der Spezifität für stark abweichende Artefakte ist jedoch nicht zu erwarten. Folglich werden Artefakte, die im Trainingsdatensatz nicht enthalten sind, wie beispielsweise spezifische Kontaminationen oder Materialbeschädigungen, nicht erkannt. Treten in einem bereits skalierten und automatisierten Prozess dem Modell bisher unbekannte Kontaminationen oder Materialbeschädigungen auf, kann die Genauigkeit und Präzision der erzeugten Readouts somit anhaltend beeinträchtigt werden. Aufgrund der großen Vielfalt möglicher Erscheinungsformen von Artefakten sind komplexe Modelle notwendig, um diese umfassend zu erlernen, weshalb sich viele Ansätze auf spezifische Artefakttypen, wie beispielsweise Streifen, Luftblasen oder Bewegungsartefakte beschränken[112,122,123]. Ebenso entscheidend für die Leistungsfähigkeit des Modells ist ein umfangreicher und diversifizierter Datensatz artefaktbelasteter Bilder[124]. Die Kombination dieser Anforderungen führt jedoch zu einem zeitintensiven Trainingsprozess, da sowohl die Architektur des ML-Modells als auch der

Umfang des Trainingsdatensatzes die Trainingsdauer beeinflussen. Neben dem Trainingsprozess selbst ist auch die Erstellung des Trainingsdatensatzes, besonders bei Verwendung von Pixel-Labeln, mit erheblichem Aufwand verbunden. Dies trifft insbesondere auf neu implementierte Methoden zu, da in solchen Fällen keine historischen Daten verfügbar sind. Selbst bei etablierten Methoden gestaltet sich die Datensatzerstellung aufwendig, da nur wenige frei zugängliche Artefakt-Datensätze existieren[125].

Neben dem Ansatz der direkten Detektion existiert auch ein indirekter Ansatz, bei dem nicht die Artefakte, sondern die zu analysierenden Objekte bzw. Segmente (zusammenhängende Bildbereiche, die aufgrund gemeinsamer Eigenschaften gruppiert wurden), im Fokus des Trainingsprozesses stehen. Im Falle eines sFIDA-Assays sind dies die aus Nutzsignal bestehenden Partikel. Dabei werden zunächst alle im Bild vorhandenen Segmente mithilfe eines Segmentierungsalgorithmus isoliert und anschließend separat klassifiziert[126]. Im Gegensatz zum Ansatz der direkten Erkennung von Artefakten konzentriert sich dieser Ansatz auf das Erlernen der aus Nutzsignal bestehenden Partikel anstelle der Artefakte. Durch die Erkennung der aus Nutzsignal bestehenden Partikel ist es möglich, im Bild vorhandene Artefakte während der quantitativen Analysen zu ignorieren. Alternativ erlaubt der Ansatz in bestimmten Szenarien nicht erkannte Segmente als Artefakte zu interpretieren und somit zu detektieren. Der Vorteil des indirekten Ansatzes besteht darin, dass aus Nutzsignal bestehende Partikel aufgrund ihrer spezifischen und definierten Charakteristika zuverlässiger identifiziert werden können als Artefakte, deren heterogene und variierende Strukturen die Erkennung erschweren. Zudem gestaltet sich die Erstellung eines Trainingsdatensatzes für die Detektion der aus Nutzsignal bestehenden Partikel wesentlich einfacher und kann in kürzerer Zeit realisiert werden. Ein Nachteil der Methode liegt in der Notwendigkeit zweier Modelle (Segmentierung, Klassifikation), die sequentiell angewendet werden müssen, was das Fehlerpotenzial selbst bei hoher Leistungsfähigkeit der Einzelmodelle stark erhöht. Zudem ist der zweistufige Prozess zeitaufwendig, da nach der Segmentierung jedes erkannte Segment einzeln klassifiziert werden muss.

1.4.3.3 Cutoff-Bestimmung

Wie in den vorausgehenden Kapiteln erläutert, wird jedes fluoreszenzmikroskopische Bild durch Hintergrundrauschen beeinflusst, wodurch die Intensität der Pixel stets größer als Null ist. Für quantitative Analysen ist es daher erforderlich, einen Cutoff zu definieren, der das Hintergrundrauschen vom Signal trennt. Der Cutoff fungiert somit als ein Schwellenwert für die Pixelintensität, wobei nur Pixel, deren Intensität diesen Wert überschreiten, in die

quantitative Analyse einfließen. Die übrigen Pixel werden hingegen als Hintergrundrauschen interpretiert und nicht in nachfolgende Analysen einbezogen. Wird der Cutoff zu niedrig angesetzt, führt dies dazu, dass Hintergrundrauschen in die Berechnung der Readouts einfließt und die Ergebnisse verfälscht. Ein zu hoch angesetzter Cutoff kann hingegen dazu führen, dass potenzielles Nutzsignal verloren geht, was die Sensitivität der Analyse beeinträchtigt. Obwohl die TIRF-Technologie ein hohes Signal-Rausch-Verhältnis bietet[111], erschweren die zuvor beschriebenen AF- und FPS-Quellen, kombiniert mit der hohen Variabilität der Signalintensität und geringen Partikeldichte, die Bestimmung eines geeigneten Cutoffs erheblich. Abbildung 5 zeigt beispielhaft die Intensitätsverteilung eines Kalibrationsstandards in zwei Konzentrationen in Form eines Histogramms. Die Verteilung weist eine positive Schiefe auf und der Peak lässt sich dem Hintergrundrauschen zuordnen. Da selbst bei Konzentrationen oberhalb der für die meisten Protein- und Peptid-Oligomere zu erwartenden physiologischen Konzentrationen kein zusätzlicher Peak mit höherer Intensität erkennbar ist, der den Signalen zugeordnet werden könnte, lässt sich der optimale Cutoff nicht visuell bestimmen.

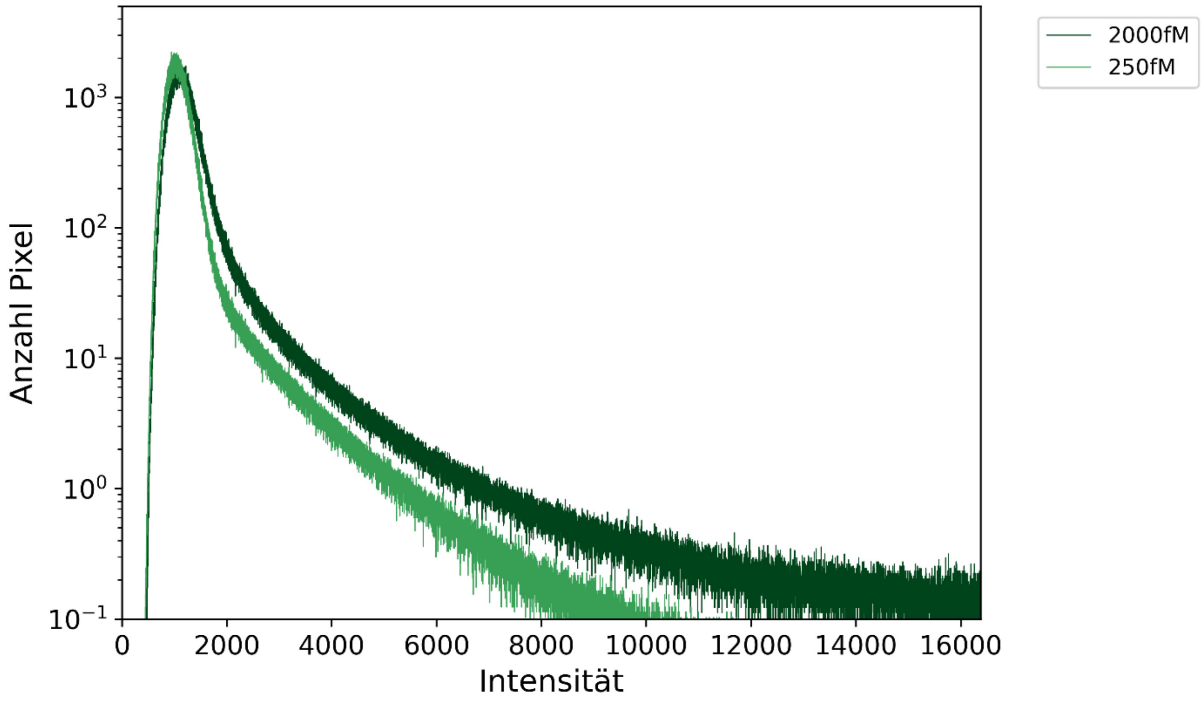

Abbildung 5: Intensitätsverteilungs-Histogramme. Histogramme der Intensitätsverteilung von Siliziumdioxid-Nanopartikeln (siehe Kapitel 1.4.3.5) in Konzentrationen von 250 fM und 2000 fM.

In bisherigen sFIDA-Experimenten wurde der Cutoff auf Grundlage verschiedener Perzentile der Pixelintensitäten verschiedener Kontrollproben ermittelt[115]. Dies bedeutet, dass ein Cutoff gewählt wurde, der eine definierte Anzahl an Signalen in den Kontrollen tolerierte. Es kristallisierte sich jedoch kein experimentübergreifendes Optimum für das zugrunde liegende

Perzentil heraus. Stattdessen erwies sich eine diskrete Menge von Perzentilen {99.9999, 99.9995, 99.999, 99.995, 99.99, 99.95} als häufig geeignet, was zu einer Spannbreite an Werten führte, die große Teile des gesamten Graustufenbereichs abdecken konnten. Obwohl sich in den meisten Experimenten die Auswahl geeigneter Perzentile schnell eingegrenzt ließ, war es dennoch erforderlich, die Daten mit unterschiedlichen Cutoffs zu analysieren. Letztendlich wurde häufig der Cutoff gewählt, der zur höchsten Verdünnungslinearität oder dem höchsten Signal-Rausch-Verhältnis führte. Ähnlich wie bei der Artefaktdetektion ist dieser Prozess jedoch mit einem hohen Zeitaufwand und einem potenziellen menschlichen Bias verbunden.

1.4.3.4 Quantitative Analyse

Nachdem die artefaktbelasteten Bilder aussortiert wurden und ein Cutoff zur Entfernung des Hintergrundrauschens festgelegt wurden, können die Bilder quantitativ analysiert werden. Dabei stehen verschiedene Analysemethode zur Verfügung, die entweder auf den Signalen oder auf der Anzahl und den Charakteristika einzelner Partikel basieren. Als besonders aussagekräftig haben sich dabei die direkte Quantifizierung der Signale (Pixel Count) sowie der Partikel (Particle Count) erwiesen. Für die Bestimmung des Pixel Counts wird dabei lediglich die Anzahl an Pixeln, welche Signal darstellen, ermittelt[115]. Für die Partikelzählung werden hingegen die einzelnen Partikel mithilfe eines Floodfill-Algorithmus identifiziert und deren Anzahl bestimmt. Nach der Berechnung des Readouts für jedes Bild wird, unabhängig von der gewählten Analysemethode, zunächst der Mittelwert der Readouts aller Bilder eines Wells ermittelt. Da der Mittelwert jedoch anfällig gegenüber Ausreißern ist, wird in einigen sFIDA-Assays eine Min/Max-Operation angewendet. Dabei wird ein variabler Prozentsatz der höchsten und niedrigsten Werte von der Mittelwertberechnung ausgeschlossen. Da diese Methode jedoch unabhängig von der tatsächlichen Präsenz von Ausreißern in den Wells die fest definierte Anzahl an Bildern exkludiert ist es wahrscheinlich, dass unauffällige Werte ebenfalls ausgeschlossen werden. Liegen darüber hinaus die Ausreißer nur in einer Richtung vor, kann dies die Ergebnisse verzerren. Durch die Berechnung des Mittelwertes aller Replikate derselben Probe, wird das endgültige Ergebnis bestimmt.

1.4.3.5 Kalibration und Normierung

Nach der Durchführung einer quantitativen Analyse ist es empfehlenswert, die resultierenden Readouts entweder zu kalibrieren oder, falls eine Kalibration nicht realisierbar ist, eine Normierung durchzuführen. Diese Schritte erleichtern nicht nur die Interpretation der Daten, insbesondere im interdisziplinären wissenschaftlichen Kontext, sondern gewährleisten auch die Vergleichbarkeit der Ergebnisse zwischen einzelnen Experimenten[90]. Ohne eine Kalibration oder Normierung kann die Vergleichbarkeit aufgrund der Inter-Assay-Varianz erheblich

beeinträchtigt sein, da externe Einflussfaktoren während der Messung, wie beispielsweise die Temperatur, die Intensität des Hintergrundrauschens verändern und somit den Cutoff und folglich die Readouts beeinflussen können.

Zur Sicherstellung einer verlässlichen Kalibration wurde von Hülsemann et al. (2016) ein Kalibrationsstandard mit definierten Eigenschaften entwickelt[127], der hohe Ähnlichkeit mit dem zu quantifizierenden Antigen aufweist[90]. Dieser basiert auf Siliziumdioxid-Nanopartikeln (SiNaPs), deren Oberflächen gezielt mit Antigenen, beispielsweise Peptiden, funktionalisiert werden können. Diese Funktionalisierung kann mit verschiedenen Antigenen durchgeführt werden, wodurch die SiNaPs für unterschiedliche sFIDA-Assays adaptierbar sind[127,128]. Die Verwendung der SiNaPs in Form einer Verdünnungsreihe, die üblicherweise aus zehn oder mehr bekannten Konzentrationen besteht, ermöglicht die Umrechnung der Readouts in Konzentrationen mittels einer Regression. Da sowohl die SiNaPs als auch die Proben identischen externen Einflüssen unterliegen, erlaubt dieses Verfahren eine quantitative Bewertung, die weitgehend unabhängig von externen Störfaktoren ist.

Sollte eine Kalibration nicht möglich sein, beispielsweise wenn die Readouts der Proben außerhalb des von der SiNaPs-Verdünnungsreihe abgedeckten Bereiches liegen, stellt eine Normierung eine alternative Vorgehensweise dar. Hierbei werden alle Readouts relativ zu einer definierten Kontrolle skaliert, indem sie durch deren Readout dividiert werden. Hinsichtlich der Vergleichbarkeit erfüllt die Normierung denselben Zweck wie die Kalibration, allerdings sind normierte Readouts weniger intuitiv interpretierbar als Konzentrationen, weshalb, sofern möglich, die Kalibration bevorzugt werden sollte.

1.5 sFIDAta

Üblicherweise werden in einem sFIDA-Assay 384-Well-MTP verwendet. Bei 25 Messbereichen pro Well ergibt sich eine Gesamtanzahl von 9600 Messbereichen pro Experiment. Werden zwei Fluoreszenzkanäle sowie deren Kolokalisation analysiert, die jeweils als eigenständiges Bild behandelt werden, resultiert daraus eine maximale Anzahl von 28800 Bildern. Diese Menge an Einzelbildern verdeutlicht nicht nur die Notwendigkeit, manuelle Prozessschritte aufgrund qualitativer Nachteile zu vermeiden, sondern macht eine manuelle Herangehensweise auch aufgrund des enormen Zeitaufwands praktisch unmöglich.

Zu diesem Zweck wurde am Forschungszentrum Jülich die sFIDAta-Software entwickelt, die den Analysten bei der Datenanalyse unterstützt. Die Software automatisiert die Schritte des Bildanalyseprozesses bis zu einem gewissen Grad und bietet zudem verschiedene Ansätze zur

Bildvisualisierung, wie etwa die Anpassung von Kontrasten sowie nichtlineare Helligkeitseinstellungen. Diese Funktionen ermöglichen es, einen ersten Eindruck der Messung zu gewinnen und potenzielle Probleme, die eine weitere Auswertung obsolet machen, frühzeitig zu identifizieren. Ebenso unterstützen sie bei der manuellen Identifikation von Artefakten in Bildern. Die Software bietet neben der Visualisierung die Möglichkeit, die zuvor beschriebenen Artefaktdetektionen (basierend auf Größe und Unschärfe) durchzuführen. Dabei müssen jedoch alle relevanten Parameter, wie die Form und Größe des Kernels sowie die Kriterien zur Validierung von Artefakten (siehe Kapitel 1.4.3.2), manuell festgelegt werden. Dies gilt ebenfalls für die Festlegung des Grenzwerts, der zur Unschärfeerkennung verwendet wird.

Die Software ermöglicht darüber hinaus die Bestimmung eines Cutoffs basierend auf einem vom Analysten definierten Perzentil sowie die anschließende automatisierte Analyse der Bilder.

Der sFIDA-Assay hat sich seit der Veröffentlichung der sFIDAta-Software kontinuierlich weiterentwickelt, was zu einer stetigen Anpassung und Erweiterung der Anforderungen an die Software führte. Im Laufe der Zeit ist sFIDAta daher historisch gewachsen und wurde im Rahmen mehrerer Entwicklerwechsel kontinuierlich modifiziert, was zu einer kontinuierlichen Zunahme der Komplexität des Programm-Codes führte.

1.6 Zielsetzung

Die Zielsetzung dieser Arbeit umfasst die assayübergreifende i) Erhöhung der Genauigkeit und Präzision der sFIDA-Technologie sowie die ii) Entwicklung von Methoden zur Steigerung des Automationsgrades des Analyseprozesses. Darüber hinaus iii) sollen durch Anwendung der entwickelten Methoden sowie bereits etablierter Ansätze aus dem Data-Science-Bereiche neue Erkenntnisse zur Pathologie verschiedener Proteinfehlfaltungserkrankungen gewonnen werden.

Das erste Ziel fokussiert sich auf die Reduktion von FPS, welches in die Analyse einfließt und dadurch die Readouts verfälscht, wodurch sowohl die Präzision als auch die Genauigkeit des Assays beeinträchtigt wird. Im sFIDA-Assay kann durch die bereits implementierten Maßnahmen ausschließlich das durch AF-bedingte FPS mittels einer Kolokalisation reduziert werden. Die Kolokalisation entfernt die AF jedoch nicht zwangsläufig vollständig und ist aufgrund des experimentellen Designs oder unerwarteter Komplikationen während der Messung nicht in jedem Experiment anwendbar. Darüber hinaus eignet sich die Kolokalisation nicht zur Identifikation von FPS, das durch unspezifisch gebundene Detektionsantikörper erzeugt wurde. Um das nach der Kolokalisation verbleibende FPS weiter zu reduzieren und die

Lücke für Einzelkanalanalysen zu schließen, soll eine Methode entwickelt werden, die sowohl in Einzelkanalanalysen als auch in der Kolokalisation anwendbar ist und nicht auf durch AF-bedingte FPS beschränkt ist. Neben dem FPS kann die Messgenauigkeit einzelner Replikate sowie die Varianz aller Replikate einer Probe durch Ausreißer in den Readouts einzelner Bilder beeinflusst werden. Um dies zu vermeiden, sollen unterschiedliche Aggregationsmethoden für die Readouts einzelner Wells identifiziert werden, welche robust gegenüber einzelnen Ausreißern sind.

Das zweite Ziel ist eng mit dem ersten verknüpft und zielt auf die Automatisierung bislang nicht oder nur teilweise automatisierter Analyseschritte ab. Dies soll die Reproduzierbarkeit der Analysen erhöhen, menschliche Fehler und potenziellen Bias minimieren sowie die Bearbeitungszeit pro Experiment verkürzen. Dies trägt zu einer Steigerung des potenziellen Durchsatzes bei und ermöglicht eine breitere sowie effizientere Anwendung der sFIDA-Technologie. Konkret beinhaltet dieses Ziel die Entwicklung einer Methode zur automatischen Artefaktdetektion und zur automatischen Bestimmung eines geeigneten Cutoffs. Beide Verfahren sollen dabei auf Grundlage objektiver Kriterien agieren und vollständig ohne manuell festzulegende Parameter auskommen.

Neben der Methodenentwicklung sollen im Rahmen dieser Arbeit Messergebnisse verschiedener sFIDA-Assays zur Quantifizierung von diversen Oligomer-Spezies analysiert werden. Durch die Verwendung statistischer Analysen und Data-Science-Ansätze sollen dabei neue Erkenntnisse zur Rolle der Aggregation in verschiedenen Proteinfehlfaltungserkrankungen gewonnen werden. Der Fokus liegt hierbei auf der AD sowie dem T2D.

2 Ergebnisse

In diesem Kapitel werden die Ergebnisse der Arbeit präsentiert, die sowohl veröffentlichte als auch eingereichte Manuskripte sowie bislang unveröffentlichte Daten umfassen. Die Manuskripte fokussieren biologische und medizinische Fragestellungen, behandeln jedoch die im Rahmen dieser Dissertation entwickelten Methoden zur Erhöhung der Genauigkeit und Präzision der sFIDA-Technologie oft nur oberflächlich. Daher beginnt dieses Kapitel mit der Vorstellung unveröffentlichter Daten, welche die Entwicklung der neuen Methoden dokumentieren und deren Funktionalität belegen. Anschließend folgen Manuskripte, die entweder die Anwendung der zuvor entwickelten Methoden demonstrieren, sich ausschließlich der Entwicklung weiterer Methoden widmen oder deren analytische Auswertung im Kontext dieser Arbeit im Fokus steht.

2.1 Unveröffentlichte Ergebnisse

In diesem Abschnitt werden die Ergebnisse der Methodenentwicklung dargestellt. Zunächst wird eine Methode zur Reduktion der FPS beschrieben, gefolgt von einer Methode zur objektiven sowie automatischen Bestimmung eines Cutoffs.

2.1.1 Reduktion der FPS

Wie im Einleitungskapitel erläutert, werden die Genauigkeit und Präzision der Analyse fluoreszenzmikroskopischer Bilder durch Hintergrundrauschen sowie FPS erheblich beeinträchtigt. Während Hintergrundrauschen durch die Anwendung eines Cutoffs effektiv unterdrückt werden kann, gestaltet sich die Entfernung von FPS deutlich schwieriger. Besonders herausfordernd sind FPS, die weder großflächig noch als auffällige Strukturen in Erscheinung treten. Ihre Eigenschaften ähneln daher stark denen der Nutzsignale, wodurch eine eindeutige visuelle Abgrenzung nicht möglich ist. Um dieses Problem zu adressieren, wurde im Rahmen dieser Arbeit eine Methode zur Identifikation und anschließenden Entfernung von FPS in sFIDA-generierten Bilddaten entwickelt. Diese basiert auf der Adaption von differenziellen Fluoreszenz-Korrekturverfahren (siehe Kapitel 1.4.3.1). In diesen Korrekturverfahren wird typischerweise ein zweiter Anregungs- oder ein zweiter Detektionsbereich im Rahmen einer zusätzlichen Messung verwendet, wobei eine Messung die Summe des Nutzsignals und der AF darstellt, während die andere reine AF repräsentiert[103,104]. Durch Subtraktion der AF-Intensität kann im Anschluss das reine Nutzsignal extrahiert werden. Aufgrund der deutlichen Signalreduktion in Negativkontrollen ohne eingesetzte Detektionsantikörper ist jedoch im sFIDA-Assay davon auszugehen, dass ein großer Teil der FPS durch unspezifisch gebundene Detektionsantikörper hervorgerufen wird[105,106]. Da die vorgestellten Korrekturverfahren jedoch

lediglich endogene AF entfernen können, würden diese somit nur einen begrenzten Nutzen aufweisen. Dies gilt insbesondere bei der Verwendung von zwei identischen Detektionsantikörpern mit unterschiedlichen Fluorochromen und nachfolgender Kolokalisation, da dies bereits eine Methode zur Entfernung endogener AF darstellt. Folglich müssen die Korrekturverfahren so adaptiert werden, dass sie in der Lage sind, unspezifisch gebundene Detektionsantikörper zu detektieren. Hierfür muss zunächst analysiert werden, unter welchen Umständen die unspezifische Bindung der Detektionsantikörper eintreten kann.

Im sFIDA-Assay zielt der Waschschritt darauf ab, die Matrixkomponenten, mit Ausnahme der Antigene, welche spezifisch an die Fängerantikörper gebunden sind, weitestgehend zu entfernen. Unspezifische Bindungen sowohl verbliebener Matrixkomponenten als auch von Detektionsantikörpern, beispielsweise aufgrund von Bereichen mit unvollständiger Blockierung der Glasoberfläche oder kontaminationsbedingter Kreuzreaktivität, können jedoch nicht vollständig ausgeschlossen werden. Diese Bereiche gilt es daher zu identifizieren. Da die Proben vor der Zugabe der Detektionsantikörper appliziert werden, ist mit hoher Wahrscheinlichkeit anzunehmen, dass in den gesuchten Bereichen endogene Moleküle unspezifisch gebunden sind. Die später zugegebenen Detektionsantikörper müssen folglich entweder an die verbleibende freie Fläche oder an die unspezifisch gebundenen endogenen Moleküle binden, was die Grundlage für die Identifikation des FPS schafft.

Es ist bekannt, dass endogene Fluorochrome typischerweise im niedrigeren Wellenlängenbereich (u.a. blau) emittieren[94], während die Detektionsantikörper in spezifischen, höheren Wellenlängenbereichen (z. B. rot oder grün) fluoreszieren. Da die Antigene selbst keine AF zeigen, sollte bei Abwesenheit unspezifischer Bindungen im blauen Wellenlängenbereich kein Signal detektierbar sein. Wird dennoch Signal im blauen Fluoreszenzkanal detektiert, deutet dies auf Bereiche hin, in denen unspezifische Bindungen der Detektionsantikörper und somit FPS möglich sind. Um diese Bereiche zu lokalisieren, wird daher der markierungsbasierte sFIDA-Assay um eine nachgeschaltete Messung erweitert, bei der potenzielle kurzwellige AF im blauen Wellenlängenbereich (405 nm) angeregt und detektiert wird. Da für diese Wellenlänge kein spezifisch markierter Detektionsantikörper verwendet wird, repräsentiert diese Messung ausschließlich die AF. Im Gegensatz zu herkömmlichen differenziellen Fluoreszenz-Korrekturverfahren wird somit weder im spezifischen Wellenlängenbereich angeregt noch detektiert, da das Ziel verfolgt wird, möglichst viel AF zu lokalisieren. Zudem soll die Intensität der markierungsbasierten Messung nicht direkt korrigiert werden. Stattdessen wird für den blauen Kanal ein eigener Cutoff definiert, um das Hintergrundrauschen zu

eliminieren. Durch eine Kolokalisation mit den detektionsantikörperspezifischen Fluoreszenzkanälen können Bereiche potenziell möglicher unspezifischer Bindung lokalisiert, somit die FPS identifiziert und durch eine inverse Kolokalisation aus den Bildern entfernt werden. Die Abbildung 6 zeigt beispielhaft, anhand eines Bildausschnitts, dass durch die Messung des markierungsfreien, blauen Wellenlängenbereichs Signal als FPS identifiziert werden kann, welches anderenfalls, aufgrund fehlender Möglichkeiten zur Differenzierung, als Nutzsignal interpretiert werden würde.

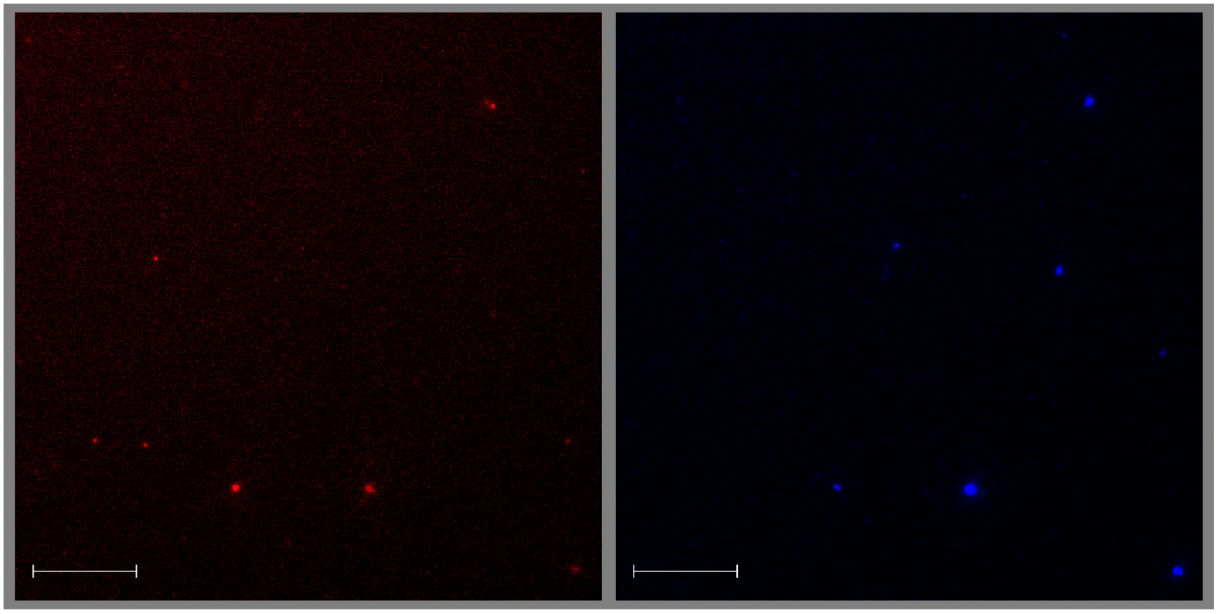

Abbildung 6: Ausschnitt eines sFIDA-generierten Bildes. Links ist der rote Fluoreszenzkanal mit spezifisch markierten Detektionsantikörpern dargestellt. Die Signale können sowohl Nutzsignal als auch FPS darstellen. Rechts ist der blaue Fluoreszenzkanal dargestellt, für den keine spezifisch markierten Detektionsantikörper zugegeben wurden. Die Signale resultieren folglich ausschließlich aus AF. Die Maßstabsleiste entspricht 20 µm. Die Signale wurden in der Farbe des jeweiligen Detektionskanals eingefärbt.

Da jedoch nicht garantiert werden kann, dass ausreichend endogene Fluorochrome an unspezifischen Bindungsstellen vorhanden sind, um eine Intensität oberhalb des Cutoffs zu erreichen, kann keine vollständige Entfernung der FPS sichergestellt werden, weshalb das Verfahren im Folgenden als FPS-Reduktion bezeichnet wird. Bei Anwendung der FPS-Reduktion sollte die Messung des markierungsfreien Kanals nach den antikörperspezifischen Kanälen erfolgen, um Intensitätsverluste durch Photobleichung zu vermeiden[129]. Eine Missachtung dieser Reihenfolge könnte das Signal-Rausch-Verhältnis und somit die Effektivität des Cutoffs beeinträchtigen.

Die FPS-Reduktion wurde im Vorfeld der ersten sFIDA-Messungen von Aβ-Oligomeren in humanem Plasma von Spendern der DELCODE (DZNE-longitudinal cognitive impairment and

dementia study)-Kohorte entwickelt und im Rahmen des ersten durchgeführten Experiments validiert[130,131]. Das Experiment umfasste die Messung einer SiNaPs-Verdünnungsreihe mit einer Ausgangskonzentration von 2 pM, welche seriell zweifach verdünnt wurde sowie 62 humane Proben (siehe Kapitel 2.2.2). Für jede humane Probe sowie jede SiNaPs-Konzentration wurden jeweils vier Replikate verwendet. Die Bilddaten wurden vor der Auswertung einer Artefaktdetektion unterzogen, wobei alle artefaktbelasteten Bilder aussortiert wurden. Zur Bestimmung der Pixel Counts wurden für jeden Fluoreszenzkanal, basierend auf dem 99.5-Perzentil einer Nullkontrolle ein Cutoff berechnet. Die Nullkontrolle bestand aus Plasma ohne eingesetzte Detektionsantikörper. Alle Analysen wurden auf Well-Ebene, das heißt für einzelne Replikate ausgeführt. Aufgrund vorhandener Ausreißer in den Daten und da keine Normalverteilung der relevanten Parameter festgestellt werden konnte (siehe Anhang 1, Tabelle A1), wurden nichtparametrische Tests verwendet.

Zunächst wurde der potenzielle Einfluss der FPS untersucht, indem der Pixel Count im AF-spezifischen (blauen) Fluoreszenzkanal ermittelt und mit den Signalen der detektionsantikörperspezifischen Fluoreszenzkanäle kolokalisiert wurde. Die resultierenden FPS-Level sind in Abbildung 7 dargestellt. Im roten Fluoreszenzkanal konnten die höchsten FPS-Level identifiziert werden. Der grüne Fluoreszenzkanal sowie die Kolokalisation der beiden Fluoreszenzkanäle zeigten hingegen deutlich niedrigere FPS-Level, obwohl auch hier einige Ausreißer nach oben zu verzeichnen waren. Während die FPS-Level im roten Fluoreszenzkanal und bei der Kolokalisation für SiNaPs im Vergleich zu den humanen Proben nahezu signifikant bzw. signifikant höher ausfielen, zeigte sich im grünen Fluoreszenzkanal kein deutlicher Unterschied (*P*-Werte der zweiseitigen Mann-Whitney-U Tests bei gewählten Signifikanzniveau von 0.05: 0.072 (rot); 0.442 (grün); 0.003 (Kolokalisation)). Durch die Berechnung des FPS-Anteils am gesamten Signal der jeweiligen Detektionskanäle wurde ersichtlich, dass quantitative Auswertungen des roten Fluoreszenzkanals sowie der Kolokalisation durch FPS verzerrt wurden (siehe Abbildung 7). Dieser Effekt zeigte sich insbesondere bei den humanen Proben, die im Median einen prozentualen FPS-Anteil von 12.8 % bzw. 19.5 % aufwiesen. Die Exklusion des FPS führt folglich zu einer erhöhten Genauigkeit des Assays, da unspezifische Störfaktoren verringert werden, was durch eine erhöhte Verdünnungslinearität der SiNaPs belegt werden konnte. Nach Anwendung der FPS-Reduktion verringerte sich die Abweichung vom optimalen Wert in den einzelnen Fluoreszenzkanälen zwischen 6.4 % und 57.1 % (siehe Abbildung 7, sowie Anhang 1, Abbildung A1 und A2, sowie Tabelle A2). Wurde die SiNaPs-Verdünnungsreihe auf Konzentrationen oberhalb von 15 fM begrenzt und damit die stärker vom Hintergrundrauschen

beeinflussten Konzentrationen ausgeschlossen, erhöhte sich die Reduktion auf Werte zwischen 13.3 % und 71.1 % (siehe Anhang 1 Tabelle A2). Die deutlichste Verringerung wurde dabei in der Kolokalisation erzielt, welche gemessen an der Verdünnungslinearität den Fluoreszenzkanal mit der höchsten Genauigkeit darstellte. Eine quantitative Bewertung des Einflusses der FPS-Reduktion auf die Genauigkeit der Messung von humanen Proben ist aufgrund der unbekannten realen Messgröße nicht möglich.

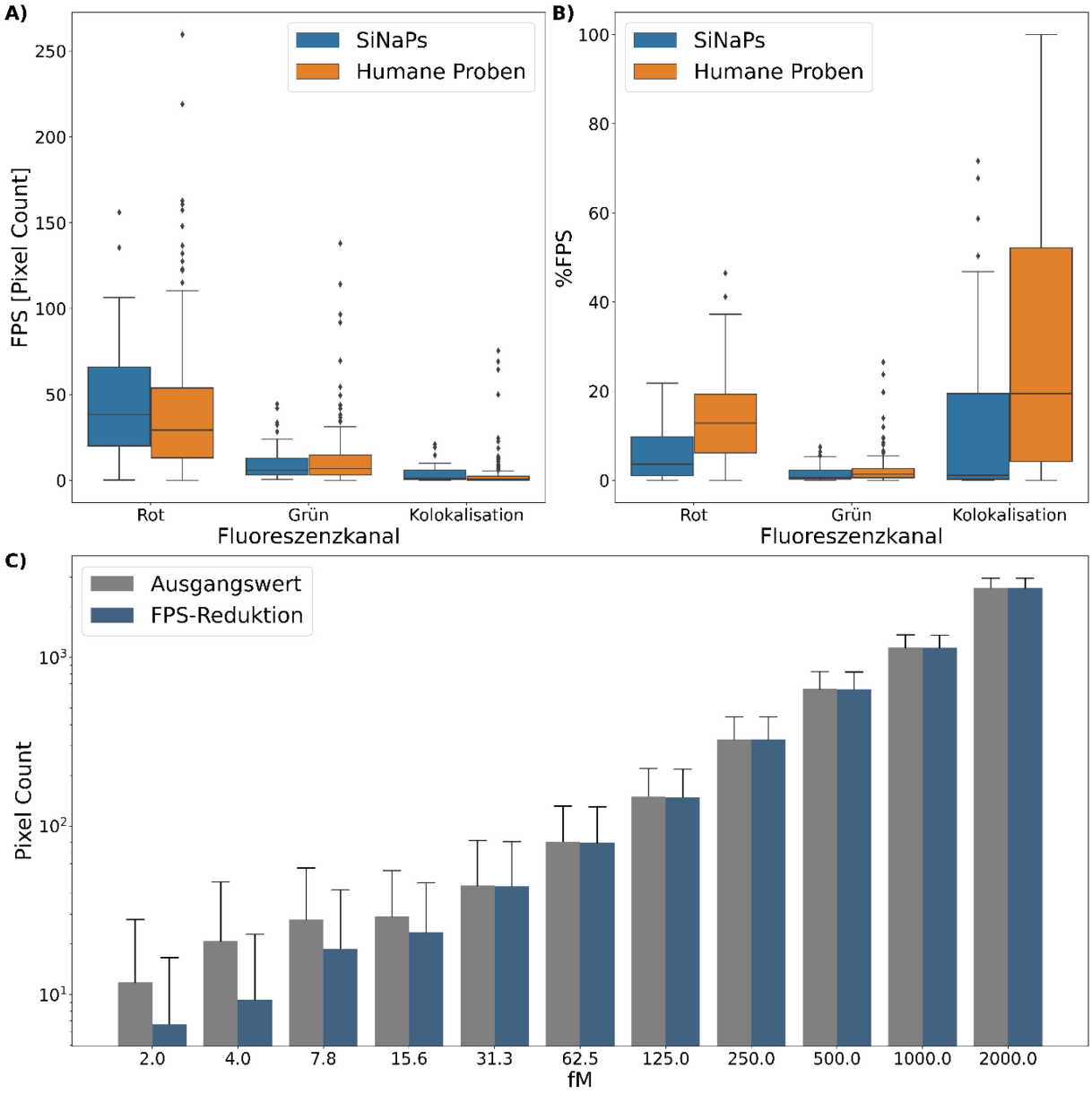

Abbildung 7: Potential der FPS-Reduktion. A) Anzahl der FPS-Pixel. Einzelne Datenpunkte stellen den Mittelwert eines Wells dar. **B)** Anteil der FPS am gesamten Signal. Einzelne Datenpunkte stellen den Mittelwert eines Wells dar. **C)** Kolokalisation der SiNaPs-Verdünnungsreihe. Die Balken spiegeln den Mittelwert aller Wells wider. Anmerkung: Sowohl in **A)**, **B)** als auch **C)** zeigen die Whisker die SD an.

Neben der Auswirkung der FPS-Reduktion auf die Genauigkeit wurde ebenso der Einfluss auf die Präzision untersucht. Zu diesem Zweck wurde die SD der einzelnen Bilder eines jeden Wells

analysiert. Die SD wurde hierbei dem prozentualen Variationskoeffizienten (englisch: percentage coefficient of variation, CV%) vorgezogen, da die FPS-Reduktion zwangsläufig eine Verringerung des Mittelwerts der Pixel Counts nach sich zieht, der in die Berechnung des CV% einfließt, wodurch mögliche positive Effekte verschleiert werden könnten. Die FPS-Reduktion führte in den SiNaPs-Messungen in zwei von drei Fluoreszenzkanälen zu einer signifikanten Verringerung der SD (siehe Tabelle 1). Lediglich im grünen Fluoreszenzkanal wurde keine signifikante Verringerung beobachtet, wobei das Signifikanzniveau nur knapp überschritten wurde. Im Gegensatz dazu reduzierte sich die SD der humanen Proben in jedem Fluoreszenzkanal, einschließlich der Kolokalisation, signifikant. Darüber hinaus wurde gezeigt, dass die durchschnittliche Reduktion der SD in allen Anwendungsfällen die Reduktion des Mittelwerts übertraf. Durchschnittlich entsprach diese 267 % der Reduktion des Mittelwerts.

Tabelle 1: Auswirkung der FPS-Reduktion. Die Mittelwerte der durch die FPS-Reduktion bedingten Verringerung des Mittelwerts sowie der SD der Readouts einzelner Wells. Durch einen zweiseitigen Wilcoxon-Vorzeichen-Rang-Tests wurde die Signifikanz der SD-Reduktion geprüft. Hierzu wurden die SD-Werte der Wells mit und ohne die Anwendung der FPS-Reduktion gegenübergestellt. Das gewählte Signifikanzniveau beträgt 0.05.

Typ	Fluoreszenzkanal	Reduktion des Mittelwerts	Reduktion der SD	FPS-Reduktion [*P*-Wert]
SiNaPs	Rot	2.2 %	8.1 %	3.173e-09
	Grün	0.9 %	2.1 %	0.081
	Kolokalisation	0.8 %	2.5 %	0.002
Humane	Rot	14.9 %	39.7 %	2.722e-40
Proben	Grün	2.1 %	6.4 %	5.334e-25
	Kolokalisation	33.1 %	38.8 %	2.213e-33

Anschließend wurde die Korrelation zwischen der SD vor der FPS-Reduktion sowie die daraus resultierende Verringerung der SD untersucht. Für die Readouts der SiNaPs zeigten sich dabei negative, jedoch außer in der Kolokalisation nicht signifikante Korrelationen (siehe Tabelle 2). In den Readouts der humanen Proben zeigte sich ein gegenteiliger Effekt. Unabhängig vom Fluoreszenzkanal wurden hochsignifikante und positive Korrelationen festgestellt, was darauf hinweist, dass in Wells mit ursprünglich höherer SD die Verringerung der SD stärker ausgeprägt war.

Tabelle 2: Wirkungsschwerpunkt der FPS-Reduktion. Korrelationen zwischen der SD-Reduktion durch die Entfernung des FPS und der ursprünglichen SD. Der Korrelationskoeffizient sowie der *P*-Wert wurden mittels der Spearman-Rangkorrelation ermittelt. Das gewählte Signifikanzniveau beträgt 0.05.

Typ	Fluoreszenzkanal	Korrelationskoeffizient	*P*-Wert
SiNaPs	Rot	-0.029	0.849
	Grün	-0.123	0.426
	Kolokalisation	-0.544	1.350e-04
Humane	Rot	0.772	1.586e-49
Proben	Grün	0.211	0.001
	Kolokalisation	0.469	2.143e-13

Abschließend wurde untersucht, ob eine Korrelation zwischen der Anzahl als FPS identifizierter Pixel und der SD-Reduktion vorlag. Tabelle 3 zeigt, dass unabhängig davon, ob SiNaPs oder humane Proben gemessen wurden und unabhängig vom Fluoreszenzkanal, moderate bis starke, hochsignifikante Korrelationen vorlagen.

Tabelle 3: Evaluierung der FPS. Korrelation zwischen der SD-Reduktion und der Anzahl an FPS-Pixeln. Der Korrelationskoeffizient, sowie der *P*-Wert wurden mittels der Spearman Rangkorrelation ermittelt. Das gewählte Signifikanzniveau beträgt 0.05.

Typ	**Fluoreszenzkanal**	**Korrelationskoeffizient**	***P*-Wert**
SiNaPs	Rot	0.637	3.282e-06
	Grün	0.465	0.001
	Kolokalisation	0.548	1.000e-04
Humane	Rot	0.880	2.215e-80
Proben	Grün	0.604	8.644e-26
	Kolokalisation	0.879	3.734e-72

Neben der Reduktion des FPS bietet die Messung des blauen Kanals ohne entsprechend markierte Antikörper einen zusätzlichen Vorteil. Es wurde beobachtet, dass bestimmte Artefakte nach Anregung durch den Laser im blauen Wellenlängenbereich in diesem ebenfalls detektierbar waren, wodurch die Artefaktdetektion unterstützt werden kann. Neben der Validierung potenzieller Artefakte konnten auch Artefakte identifiziert werden, die nicht in beiden Fluoreszenzkanälen auftreten (siehe Spalte eins und zwei des in Abbildung 8 dargestellten Bildrasters) oder leicht übersehen werden könnten (siehe Spalte drei). Besonders die Fälle, in denen Artefakte nicht in jedem Fluoreszenzkanal auftreten, sind hierbei von Interesse für Einkanalanalysen, da resultierende Readouts zwar nicht durch zusätzliches Signal verfälscht werden, aber möglicherweise eine Reduktion der mit funktionalen Fängerantikörpern bedeckten Fläche zu einer Verfälschung führen kann.

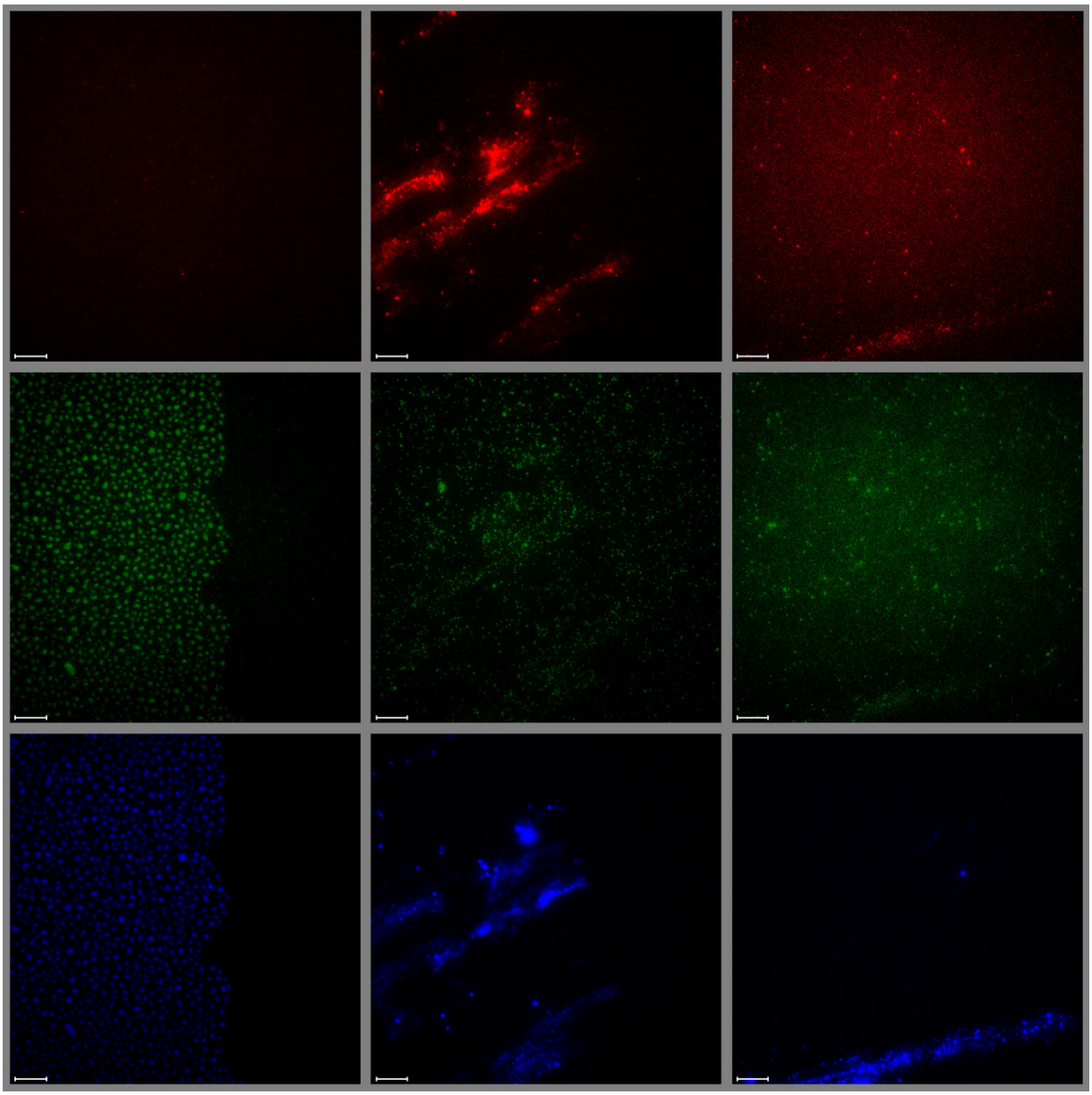

Abbildung 8: Bilderraster verschiedener Artefakte. Die Zeilen stellen die jeweiligen TIRF-Fluoreszenzkanäle dar. Spezifisch markierte Detektionsantikörper wurden nur für den roten und grünen Fluoreszenzkanal eingesetzt. Alle Signale wurden entsprechen des Fluoreszenzkanals eingefärbt. Der Kontrast wurde erhöht, um schwache Emissionen besser sichtbar zu machen. Die Maßstabsleiste entspricht 10 µm.

2.1.2 Cutoff-Bestimmung

Ein weiteres Ziel dieser Arbeit war die Entwicklung einer Methode zur automatisierten Bestimmung eines Cutoffs, der zur Abgrenzung des Signals vom Hintergrundrauschen dient. Diese Methode wird im Folgenden als Auto-Cutoff bezeichnet. Im Gegensatz zum bisher verwendeten Ansatz zur Cutoff-Bestimmung soll der Auto-Cutoff ohne vom Analysten vorgegebene Parameter auskommen, in Bezug auf die erwarteten Ergebnisse eines Experiments unbiased und vollkommen objektiv sein. Um dieses Ziel zu erreichen, wurden die zur Bestimmung des Cutoffs herangezogenen Daten auf Standard-Verdünnungsreihen beschränkt, die in den Experimenten mitgeführt werden können. Die humanen Proben des jeweiligen Experiments werden nicht in die Bestimmung des Cutoffs mit einbezogen.

Da für den Analyten repräsentative Standard-Verdünnungsreihen unter anderem zur Optimierung und Qualitätssicherung im Rahmen der Assay-Entwicklung genutzt werden, kann die grundlegende Annahme getroffen werden, dass ein Cutoff, der das Hintergrundrauschen in Messungen einer solchen Verdünnungsreihe effektiv entfernt, bei humanen Proben gleichermaßen wirksam ist[90]. Folglich kann angenommen werden, dass die Qualität der aus dem Cutoff resultierenden Readouts von humanen Proben und Standard-Verdünnungsreihen, definiert durch die Genauigkeit und Präzision, korrelieren. Eine Optimierung der Qualität der Standard-Verdünnungsreihen hinsichtlich dieser Faktoren durch den Cutoff kann daher die Genauigkeit und Präzision der Readouts humaner Proben sicherstellen. In initialen Versuchen wurden sowohl die zur Kalibration mitgeführte SiNaPs-Verdünnungsreihe, als auch eine Verdünnungsreihe einer internen Qualitätskontrolle (englisch: internal quality control, IQC, siehe Kapitel 2.2.6) als Datengrundlage geprüft. Da im Gegensatz zu den SiNaPs nicht in jedem Experiment eine vollständige IQC-Verdünnungsreihe mitgeführt wird und die zusätzliche Verwendung der IQC zu keinem objektiven Vorteil führte, wurde die Datengrundlage für den Auto-Cutoff auf die SiNaPs-Verdünnungsreihe, einschließlich einer Nullkontrolle beschränkt.

Neben der Notwendigkeit einer Qualitätsmetrik zur Bewertung einer SiNaPs-Verdünnungsreihe nach Berechnung der Pixel Counts mit einem bestimmten Cutoff, ist ein effektives Vorgehen bei der Auswahl möglicher Cutoff-Kandidaten erforderlich. Da die Berechnung dieser Qualitätsmetrik die vorausgehende Analyse aller Bilddaten mit dem jeweiligen Cutoff erfordert, wäre eine Überprüfung aller möglichen Cutoffs aus Laufzeitgründen, besonders im Kontext eines High-Throughput Assays nicht zielführend. Aufgrund der 16384 möglichen Graustufen, die als potenzielle Cutoff-Kandidaten dienen, und in Abhängigkeit von der Anzahl der nach der Artefaktdetektion verbliebenen Bilder n ergibt sich bereits bei der Nutzung eines einzelnen

Fluoreszenzkanals (k=1) eine Anzahl von bis zu 1.57×10^8 notwendigen Bildauswertungen (Gleichung 1). Sollen die Cutoffs zweier Fluoreszenzkanäle (k=2) aufeinander abgestimmt optimiert werden, steigt die erforderliche Anzahl an Bildauswertungen auf bis zu 2.58×10^{12} an.

$$\text{Bildauswertungen} = n \times 16384^k \quad (1)$$

2.1.2.1 Qualitätsbewertung (QScore)

Zu Beginn der Entwicklung wurden diverse potenzielle Metriken gesammelt, um die Qualität einer Verdünnungsreihe zu bewerten. Diese wurden auf die folgende Liste beschränkt.

1. **Der gewichtete (englisch: weighted) Mean Squared Error (wMSE):** Der wMSE basiert auf einer gewichteten linearen Regression, die an die SiNaPs-Verdünnungsreihe angepasst wird und somit zur Kalibration verwendet werden kann. Sowohl die Gewichtung der Regression während der Anpassung als auch die Gewichtung des MSE erfolgt durch den Kehrwert der jeweiligen Konzentration, wodurch die Residuen im niedrigen Konzentrationsbereich stärker berücksichtigt werden. Dies ist notwendig, da humane Proben häufig nur niedrige Konzentrationen des Analyten enthalten. Durch die Minimierung des wMSE wird sichergestellt, dass die Regression die vorgegebenen Kalibrationspunkte so genau wie möglich trifft. Ein niedriger wMSE gewährleistet somit die Genauigkeit und Anwendbarkeit der Regressionsgeraden. Dies ist insbesondere bei experimentübergreifenden Analysen von Bedeutung, da andernfalls beobachtete Unterschiede potenziell auf eine unzureichende Kalibration zurückzuführen wären. Um den wMSE mit den anderen Metriken vergleichbar zu machen, wird er mittels einer *MinMax-Skalierung* auf ein Intervall zwischen null und eins normalisiert (siehe Gleichung 2). Die dazu verwendeten Min- und Max-Werte sind in Anhang 1, Tabelle A3 aufgelistet. Ein Wert von eins entspricht somit einer vollständigen Übereinstimmung der Kalibrationspunkte mit der Regressionsfunktion. Werte, die den definierten Maximalwert erreichen oder überschreiten, werden hingegen auf null gesetzt.

$$x' = \frac{max - x}{max - min} \quad (2)$$

Im Anschluss wird die finale Wertung der Metrik erstellt, indem die normalisierten Werte durch eine nichtlineare Funktion umgewandelt werden. Diese Anpassung berücksichtigt, dass Verringerungen des wMSE bei weiterhin hohen wMSE-Werten weniger bedeutend

sind und eine Wertung nahe eins nur durch einen besonders niedrigen wMSE erreicht wird, was die Notwendigkeit einer hohen Genauigkeit betont. Die verwendete Funktion f(x) wird in Abbildung 9 dargestellt.

2. **Verdünnungslinearität (VDL):** Ein niedriger wMSE allein kann die Qualität einer Verdünnungsreihe nicht ausreichend belegen. Ein Beispiel hierfür stellt eine SiNaPs-Verdünnungsreihe dar, die in allen Verdünnungsstufen nahezu identische Pixel Counts aufweist. Obwohl diese Reihe einen sehr niedrigen wMSE und somit eine hohe Wertung aufweisen würde, wäre der zugrundeliegende Cutoff nicht geeignet, da die Pixel Counts mit hoher Wahrscheinlichkeit nur Hintergrundrauschen widerspiegeln. Die VDL, gemessen an der absoluten Abweichung zum Idealwert (100 %), wird zur Sicherstellung der Funktionalität des Cutoffs sowie einer ausreichenden Genauigkeit verwendet. Analog zum Vorgehen beim wMSE wird auch für die Normalisierung der VDL eine *MinMax-Skalierung* eingesetzt (siehe Gleichung 2). Die dazu verwendeten Min- und Max-Werte sind in Anhang 1, Tabelle A3 aufgelistet. Mittels einer Sigmoid-Funktion wird im Anschluss die finale Wertung der Metrik ermittelt (siehe Abbildung 9, Funktion g(x)). Eine Sigmoid-Funktion wurde gewählt, da weder Verringerungen nahe null noch nahe eins eine große Auswirkung aufwiesen. Wie bei der Wertung des wMSE wird auch bei der Wertung der VDL das bestmögliche Ergebnis durch den Wert eins repräsentiert.

3. **Prozentualer Variationskoeffizient (CV%):** Zusätzlich zur Sicherstellung einer hohen Genauigkeit der Pixel Counts ist auch eine ausreichende Präzision entscheidend, um valide und aussagekräftige Messergebnisse zu erzielen. Diese kann durch den prozentualen CV% quantifiziert werden[132]. Analog zur VDL wird auch der CV% mittels einer *MinMax-Skalierung* (siehe Gleichung 2) und nachfolgender Transformation durch eine Sigmoid-Funktion in eine finale Wertung umgewandelt. Die verwendeten Min- und Max-Werte sind in Anhang 1, Tabelle A3 aufgeführt. Die verwendete Sigmoid-Funktion wird in Abbildung 9, Funktion g(x) dargestellt. Wie bei den vorherigen Wertungen wird auch bei der Wertung des CV% das bestmögliche Ergebnis durch den Wert eins repräsentiert.

4. **Maximaler Pixel Count (MPC):** Aufgrund der niedrigen physiologischen Konzentrationen der untersuchten Antigene steigt bei hohen Pixel Counts die Wahrscheinlichkeit, dass Hintergrundrauschen fälschlicherweise als Signal interpretiert wurde. Wenn der minimale Pixel Count der SiNaPs-Verdünnungsreihe bzw. der

Nullkontrolle unter 1000 liegt, beträgt die Wertung eins. Liegt der minimale Pixel Count jedoch darüber, wird die Wertung auf null gesetzt.

5. **Gültigkeit:** Diese binäre Metrik zeigt an, ob ein Cutoff die grundlegenden Anforderungen erfüllt und somit als gültig und anwendbar angesehen werden kann. Es nimmt den Wert eins an, wenn die folgenden Kriterien erfüllt sind:

   5.1 Die zur Bestimmung des wMSE verwendete Regression strebt gegen unendlich ($\rightarrow+\infty$). Dieses Kriterium stellt zusammen mit der VDL die Plausibilität der SiNaPs-Verdünnungsreihe sicher.

   5.2 Bei einem zu niedrigen Cutoff resultiert ein Großteil des Signals aus Hintergrundrauschen. Da die Intensität des Hintergrundrauschens in allen Bildern nahezu identisch ist, führen sehr niedrige Cutoffs folglich zu einem niedrigen CV%. Mit zunehmender Höhe des Cutoff sinkt der Einfluss des Hintergrundrauschens, wodurch der CV% zunächst stark ansteigt. An einem gewissen Cutoff endet dieser Anstieg, da die eigentliche Varianz zu Tage tritt. Der Cutoff, bei dem dieser Anstieg endet, wird als Cutoff-Minimalwert festgelegt, da davon ausgegangen wird, dass unterhalb dieses Cutoffs Hintergrundrauschen zu einer deutlichen Verzerrung der Messergebnisse führt.

   5.3 Messwerte humaner Proben können aufgrund von Matrixeffekten, wie zum Beispiel Epitopmaskierungen durch Matrixkomponenten, niedriger ausfallen als die in Puffer verdünnten SiNaPs. Um sicherzustellen, dass der Cutoff nicht zu restriktiv gewählt wird und Messungen humaner Proben ohne detektierbares Signal vermieden werden, muss der niedrigste Pixel Count der SiNaPs-Verdünnungsreihe bzw. der Nullkontrolle größer als zehn sein.

   5.4 Im Fall einer Kolokalisation muss der niedrigere Cutoff mindestens 20 % des höheren Cutoffs betragen. Dies vermeidet „dysfunktionale“ Kolokalisationen (später erläutert).

Die finale Qualitätsbewertung (QScore) der SiNaPs-Verdünnungsreihe, die zur Auswahl des Cutoffs dient, wird anhand der Gleichung 3 berechnet. Da sowohl die einzelnen Wertungen der Metriken als auch der Binärwert im Bereich zwischen null und eins liegen, fällt auch der QScore in diesen Bereich. Für die Analyse der humanen Proben wird der Cutoff gewählt, der auf der SiNaPs-Verdünnungsreihe den höchsten QScore erzielt.

$$QScore = \frac{(Wertung_{wMSE}+Wertung_{VDL}+Wertung_{CV\%}+Wertung_{MPC})}{4} \times \text{Gültigkeit} \qquad (3)$$

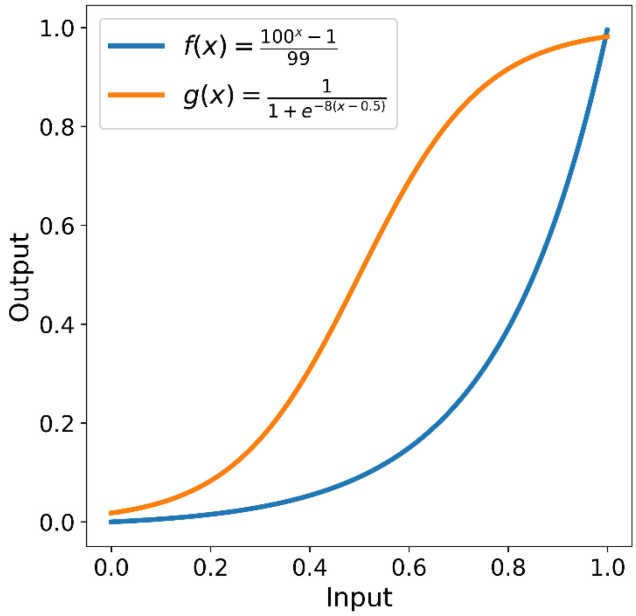

Abbildung 9: Funktionen zur Konvertierung normalisierter Werte. Formel f(x) wird zur Konvertierung des wMSE verwendet, Formel g(x) wird zur Konvertierung der VDL sowie des CV% verwendet.

Im Rahmen der Entwicklung des Auto-Cutoffs wurde des Weiteren untersucht, ob verschiedene Aggregationsmethoden zu Unterschieden in Präzision (gemessen am CV%) und Genauigkeit (gemessen an wMSE und VDL) führen. Hierzu wurden neben den bereits etablierten Methoden drei Alternativen evaluiert (siehe Tabelle 4). Die Berechnung der Metriken sowie des QScores kann unabhängig von der Aggregationsmethode ausgeführt werden.

Tabelle 4: Aggregationsmethoden. Die Tabelle zeigt die verschiedenen Aggregationsmethoden, welche für die folgenden Auswertungen des Optimierungs- sowie Validierungsdatensatzes angewendet wurden.

Aggregationsmethode	Beschreibung
Mittelwert der Mittelwerte [MdM]	Eine etablierte Methode, bei der zunächst der Mittelwert aller Bilder eines Replikates (Wells) und anschließend der Mittelwert aller Replikate einer Probe berechnet wird.
Min-Max-Entfernung-MdM [MME-MdM]	Ebenfalls eine etablierte Methode, bei der Bilder, deren Pixel Count zu den höchsten und niedrigsten 10 % eines Wells gehört, ausgeschlossen werden. Die anschließende Aggregation erfolgt analog zur MdM-Methode.
Ausreißerentfernung-MdM [AE-MdM]	Mittels des 1.5-fachen Interquartilsabstands zum Median der Pixel Counts werden alle statistischen Ausreißer innerhalb eines Wells entfernt. Die nachfolgende Aggregation erfolgt analog zu MdM.
Hodges-Lehman [HL]	Anwendung des Hodges-Lehman-Schätzers auf die Pixel Counts der Bilder eines Wells. Hierbei wird zunächst der Mittelwert aller möglichen Pixel Count Paare ermittelt. Im Anschluss wird der Median aller Mittelwerte als finaler Wert des Wells übernommen. Analog zu den früheren Methoden wird im Anschluss der Mittelwert aller Replikate einer Probe berechnet.
Ausreißerentfernung – Hodges-Lehman [AE-HL]	Kombination aus Ausreißerentfernung und HL. Zunächst werden mittels des 1.5-fachen Interquartilsabstands zum Median der Pixel Counts alle Ausreißer eines Wells entfernt. Anschließend analog zu HL.

Das Konzept des Auto-Cutoffs wurde auf Grundlage verschiedener SiNaPs-Verdünnungsreihen entwickelt. Die Optimierung und Validierung des Auto-Cutoffs erfolgten nachfolgend anhand zweier sFIDA-Experimente zur Quantifizierung von Aβ-Oligomeren in humanem Plasma sowie den zugehörigen SiNaPs-Verdünnungsreihen. Der zur Optimierung verwendete Datensatz (Optimierungsdatensatz) umfasste Proben von vier Personen, die in vier Schritten sequenziell im Verhältnis 1:2 mit Puffer verdünnt wurden. Da eine initiale Auswertung der Daten eine Tendenz zur Halbierung des Pixel Counts durch jede Verdünnung aufzeigte, wurde der halbierte Pixel Count der jeweils vorausgehenden Verdünnungsstufe erwartet. Der zweite Datensatz (Validierungsdatensatz) wurde ausschließlich zur Validierung verwendet. Er umfasste Plasma eines Kontrollspenders, welches mit Aβ-Aggregaten in unterschiedlichen, sich sequenziell verdoppelnden Konzentrationen von 0.24 pM bis 4000 pM angereichert wurde. Aufgrund der Applikation von Aggregaten wurde in diesem Fall eine Verdopplung des Signals zwischen den einzelnen Spike-Schritten erwartet. Die einzelnen Schritte wurden zu diesem Zweck um das Signal-Grundniveau durch endogenes Aβ-Oligomer bereinigt.

Zur Bewertung der Funktionalität des Auto-Cutoffs wurden für die Einzelkanäle (roter und grüner Fluoreszenzkanal) die Pixel Counts aller Cutoff-Möglichkeiten im Intensitätsbereich von 500 bis 15000 in Schritten von 50 berechnet. Die Grenzwerte wurden so festgelegt, dass die minimale Intensität des Hintergrundrauschens den unteren Grenzwert überschritt, während nach Überschreiten des oberen Grenzwerts nur noch sporadisches Signal vorhanden war. Eine Schrittweite von 50 wurde gewählt, da geringe Änderungen des Cutoffs nur vernachlässigbare Änderungen am QScore nach sich zogen (siehe Kapitel 2.1.2.2), die Anzahl notwendiger Analysen pro Bild und Fluoreszenzkanal jedoch auf 290 reduziert wurde. Die Pixel Counts aller individuellen Cutoffs wurden im Anschluss durch die fünf Aggregationsmethoden (siehe Tabelle 4) aggregiert und die jeweiligen Metriken sowie der resultierende QScore berechnet. Für die Kolokalisation beider Fluoreszenzkanäle wurden die Pixel-Counts aller Cutoff-Möglichkeiten im Bereich zwischen 500 und 12000 berechnet, wobei Intensitätsschritte von 250 verwendet wurden. Dies führte zu über 2000 Analysen aller Bilder, deren resultierende Pixel Counts anschließend ebenfalls mit allen Aggregationsmethoden aggregiert wurden. Die Verringerung der Intensitätsschrittweite war aufgrund der sonst zu hohen Anzahl erforderlicher Berechnungen, in Kombination mit den durch die Kolokalisation ohnehin erhöhten Anforderungen an die Rechenleistung notwendig. Nach Abschluss der Aggregation durch alle Methoden wurden die Pixel Counts, die aus der jeweiligen Kombination von Cutoff und Aggregationsmethode resultierten, zur Berechnung der einzelnen Metriken sowie des QScores verwendet.

Im Fokus der Optimierung stand die Differenzierbarkeit zwischen den einzelnen Verdünnungs- bzw. Spike-Schritten der humanen Proben, die aufgrund der geringen Anzahl anhand eines einseitigen Mann-Whitney-U-Tests zwischen den Replikaten aufeinanderfolgender Schritte bewertet wurde. Zusätzlich wurde für die humanen Proben ebenfalls die VDL sowie der CV% berechnet, um die zentrale Annahme des Modells, den Zusammenhang zwischen Genauigkeit und Präzision von SiNaPs-Verdünnungsreihen und humanen Proben bewerten zu können, sowie eine umfassendere Evaluierung des durch den QScore gewählten Cutoffs zu ermöglichen. Für den Validierungsdatensatz wurden zur Berechnung der Verdünnungslinearität die Pixel Counts aller Spike-Konzentrationen um den Pixel Count der niedrigsten Spike-Konzentration korrigiert, um das Grundlevel, bedingt durch endogenes Aβ-Oligomer, auszuschließen. Um die Datensätze trotz der unterschiedlichen Personenanzahl vergleichbar zu machen, wurde jede Metrik auf Basis einer einzelnen Person berechnet. Für den Optimierungsdatensatz wurden anschließend die Mittelwerte aller Personen gebildet.

Zu Beginn wurde auf Grundlage des Validierungsdatensatzes die zentrale Annahme des Modells geprüft, welche die Korrelation zwischen den einzelnen Metriken der SiNaPs-Verdünnungsreihe und der humanen Proben postuliert. Zusätzlich wurde untersucht, ob die gewählten Metriken der SiNaPs-Verdünnungsreihe mit der Differenzierbarkeit der humanen Proben in Verbindung standen. Zu diesem Zweck wurden die jeweiligen Spearman-Korrelationen analysiert. Tabelle 5 zeigt die Mittelwerte der Korrelationen aller Aggregationsmethoden, während die nach den Aggregationsmethoden aufgeschlüsselten Korrelationen in Anhang 1, Tabelle A4 präsentiert werden. Der QScore und die Wertung des wMSE korrelierten stark negativ und hochsignifikant mit dem *P*-Wert, der die Differenzierbarkeit der Spike-Konzentrationsstufen humaner Proben widerspiegelt. Im Gegensatz dazu zeigt die Wertung des VDL lediglich eine schwache, jedoch signifikante, negative Korrelation. Die Wertung des CV% weist hingegen keine nennenswerte Korrelation zum *P*-Wert auf. Ein Vergleich der unbehandelten (weder normalisiert noch transformiert) VDL und CV% zwischen SiNaPs-Verdünnungsreihen und humanen Proben ergab moderate bis starke, hochsignifikante positive Korrelationen.

Tabelle 5: Korrelationen zwischen Metriken der humanen Proben und SiNaPs-Verdünnungsreihen in Einzelkanälen. Die Korrelationen wurden mittels eines zweiseitigen Spearman-Tests ermittelt. Die präsentierten Daten stellen die Mittelwerte aller Aggregationsmethoden des Validierungsdatensatzes dar. Es wurden nur gültige Cutoffs berücksichtigt. Beim Vergleich einer Metrik mit dem *P*-Wert wurde die Wertung der jeweiligen Metrik verwendet, andernfalls die unbehandelten Werte (weder normalisiert noch transformiert). Anmerkung: r-Wert = Rangkorrelationskoeffizient, Signifikanzniveau: 0.05.

Metrik (Humane Probe)	**Metrik (SiNaPs)**	**r-Wert**	***P*-Wert**
P-Wert	QScore	-0.864	5.283e-93
P-Wert	wMSE (Wertung)	-0.692	2.730e-36
P-Wert	VDL (Wertung)	-0.177	2.319e-02
P-Wert	CV% (Wertung)	0.097	2.170e-01
VDL	VDL	0.902	9.284e-142
CV%	CV%	0.334	1.437e-07

Nachdem signifikante Korrelationen sowohl zwischen den einzelnen Metriken humaner Proben und der SiNaPs-Verdünnungsreihe als auch zwischen den Metriken der SiNaPs-Verdünnungsreihe und der Differenzierbarkeit der humanen Proben nachgewiesen wurden, konnte sowohl die Grundannahme als auch die Funktionalität des Auto-Cutoffs belegt werden. Dennoch wurde ein qualitativer Vergleich der durch den Auto-Cutoff ausgewählten Cutoffs mit allen anderen berechneten Cutoffs durchgeführt. Die Abbildung 10 ermöglicht eine direkte Einschätzung hinsichtlich der *P*-Werte, VDL und CV% der humanen Proben sowie der Genauigkeit der Kalibration, gemessen am wMSE. Es ist wichtig zu berücksichtigen, dass es nicht möglich ist, in allen Metriken gleichzeitig optimale Ergebnisse zu erzielen, da die einzelnen Metriken teils positiv, teils negativ mit dem Cutoff korrelieren, weshalb stets ein Kompromiss gefunden werden muss (siehe Tabelle 6).

Tabelle 6: Korrelationen der einzelnen Metriken mit dem Cutoff in Einzelkanälen. Der wMSE basiert auf der SiNaPs-Verdünnungsreihe. VDL und CV% beziehen sich hingegen auf die humanen Proben. Alle Daten beziehen sich auf die Einzelkanäle des Validierungsdatensatzes und stellen den Mittelwert aller Aggregationsmethoden dar. Es werden die unbehandelten Metriken (weder normalisiert noch transformiert) zur Berechnung der Spearman-Korrelation verwendet. Anmerkung: r-Wert = Rangkorrelationskoeffizient, Signifikanzniveau: 0.05.

Metrik	**r-Wert**	***P*-Wert**
wMSE	-0.613	1.658e-299
VDL	-0.452	6.962e-146
CV%	0.448	2.620e-143

Die Einordnung der aus der Auto-Cutoff-Methode resultierenden Cutoffs ergab, dass etwa 60 % der gewählten Cutoffs zu *P*-Werten führten, die unterhalb des 25 %-Quantils der aus allen anderen Cutoffs resultierenden *P*-Werte lagen. Dabei wurde nur in wenigen Fällen der Median-Wert überschritten (siehe Abbildung 10). Bei Verwendung des HL-Schätzers zur

Aggregation lagen die *P*-Werte stets deutlich unter dem Median. Alle Aggregationsmethoden mit Ausnahme des MdM, der anfällig für Ausreißer ist, zeigten weitgehend übereinstimmende Bestwerte. Bei Verwendung der MdM-Aggregationsmethode konnten vergleichbar niedrige *P*-Werte jedoch nur in Ausnahmefällen erreicht werden. Für die VDL befanden sich alle aus den gewählten Cutoffs resultierenden Werte unter dem Median, wohingegen beim wMSE ein einzelner Wert oberhalb des Medians lag. In beiden Fällen lag etwa die Hälfte der aus den gewählten Cutoffs resultierenden Werte auf oder unterhalb der 25 %-Quantile. Die aus den gewählten Cutoffs resultierenden CV%-Werte lagen hingegen meist nahe des Medians (siehe Abbildung 10).

Durch die Verwendung einer Kolokalisation lässt sich der Einfluss von AF auf die Readouts häufig reduzieren, wodurch die Spezifität des sFIDA-Assays erhöht wird. Kann die Kolokalisation angewendet werden, müssen folglich Cutoffs für zwei Kanäle statt eines einzelnen bestimmt werden. Ziel des Auto-Cutoffs ist es, diese Werte in Abhängigkeit zueinander zu optimieren, um auch bei der Kolokalisation höchstmögliche Genauigkeit und Präzision zu erzielen. Das zugrundeliegende Prinzip des Auto-Cutoffs bleibt hierfür unverändert; es wurde lediglich eine zusätzliche Bedingung für die Metrik *Gültig* hinzugefügt. Diese besagt, dass bei der Kolokalisation eine Cutoff-Kombination nur dann als gültig betrachtet wird, wenn der niedrigere Cutoff mindestens 20 % des höheren Cutoffs beträgt. Diese Bedingung stellt sicher, dass eine funktionale Kolokalisation erfolgt. Ohne diese Einschränkung könnten in einem Fluoreszenzkanal ein Cutoff unterhalb der Intensität des Hintergrundrauschens gewählt werden, was dazu führen würde, dass sämtliche Signale des anderen Fluoreszenzkanals übernommen werden. Dies würde de facto zu einer Einzelkanalanalyse mit deutlich erhöhtem Rechenaufwand führen. Da die Intensitätsniveaus des Hintergrundrauschens zwischen verschiedenen Experimenten variieren, wurde diese dynamische Bedingung anstelle einer allgemeinen Einschränkung für niedrige Cutoffs eingeführt.

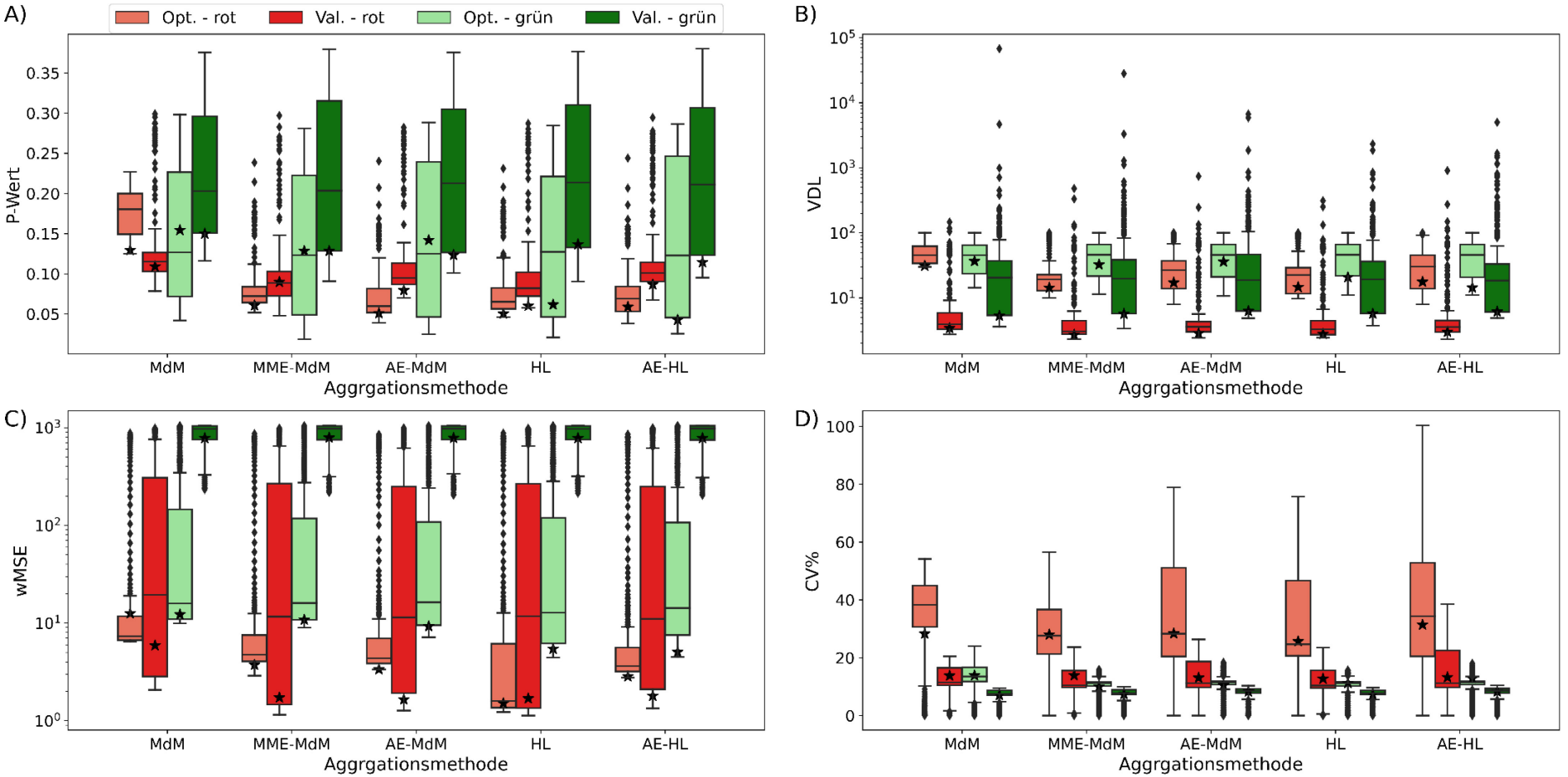

Abbildung 10: Einordnung der ermittelten Cutoffs in den Einzelkanälen. Der Stern markiert den Wert, der aus dem Cutoff resultiert, welcher durch die Auto-Cutoff-Methode bestimmt wurde. Die Boxplots zeigen die Werte der Metriken für alle untersuchten Cutoffs. Die Rauten stellen Ausreißer gemäß dem 1.5-fachen Interquartilsabstandes dar. Die Legende oberhalb von **A)** ist ebenfalls für **B)**, **C)** und **D)** gültig.

Analog zu den Einzelkanalanalysen wurden für die Kolokalisation zunächst die Grundannahmen überprüft, wobei eine hohe Übereinstimmung der Resultate festgestellt wurde. Auch hier zeigten sich stark negative, hochsignifikante Korrelationen zwischen dem *P*-Wert und dem QScore, sowie der Wertung des wMSE. Des Weiteren konnten erneut hochsignifikante Korrelationen zwischen den unbehandelten (weder normalisiert noch transformiert) VDL und CV% in SiNaPs-Verdünnungsreihen und humanen Proben festgestellt werden. Ein deutlicher Unterschied trat hingegen bei der Korrelation des *P*-Wertes mit der Wertung des CV% auf, welche für die Kolokalisation stark positiv ausfällt (siehe Tabelle 7).

Tabelle 7: Korrelationen zwischen Metriken der humanen Proben und SiNaPs-Verdünnungsreihen in der Kolokalisation. Die Korrelationen wurden mittels eines zweiseitigen Spearman-Tests ermittelt. Die präsentierten Korrelationen stellen die Mittelwerte aller Aggregationsmethoden des Validierungsdatensatz dar. Es wurden nur gültige Cutoffs berücksichtigt. Beim Vergleich einer Metrik mit dem *P*-Wert wurde die Wertung der jeweiligen Metrik verwendet, andernfalls der unbehandelte Wert (weder normalisiert noch transformiert). Eine nach Aggregationsmethode aufgeschlüsselte Tabelle, sowie eine analoge für beide Datensätze befindet sich im Anhang 1 (siehe Tabelle A4 und A5). Anmerkung: r-Wert = Rangkorrelationskoeffizient, Signifikanzniveau: 0.05.

Metrik (Human)	**Metrik (SiNaPs)**	**r-Wert**	***P*-Wert**
P-Wert	QScore	-0.735	2.669e-97
P-Wert	wMSE (Wertung)	-0.824	3.778e-131
P-Wert	VDL (Wertung)	-0.354	8.889e-19
P-Wert	CV% (Wertung)	0.832	3.023e-153
VDL	VDL	0.602	2.701e-49
CV%	CV%	0.874	1.102e-192

Ebenso analog zu den Einzelkanälen zeigten sich auch bei der Kolokalisation Korrelationen zwischen Metriken und Cutoff, welche unterschiedliche Richtungen (positiv, negativ) aufwiesen (siehe Tabelle 8). Aus diesem Grund war auch in diesem Fall kein gleichzeitiges, optimales Abschneiden in allen Metriken zu erwarten.

Tabelle 8: Korrelationen der einzelnen Metriken mit dem Cutoff in der Kolokalisation. Die wMSE-Metrik bezieht auf die SiNaPs-Verdünnungsreihe. VDL und CV% auf die humanen Proben. Alle Daten beziehen sich auf die Kolokalisation des Validierungsdatensatzes und stellen den Mittelwert aller Aggregationsmethoden dar. Es werden die unbehandelten Metriken (weder normalisiert noch transformiert) zur Berechnung der Spearman-Korrelation verwendet. Anmerkung: r-Wert = Rangkorrelationskoeffizient, Signifikanzniveau: 0.05.

Metrik	**r-Wert**	***P*-Wert**
wMSE	-0.613	1.658e-299
VDL	-0.452	6.962e-146
CV%	0.448	2.620e-143

Wie zuvor für die Einzelkanalanalyse in Abbildung 10 erlaubt Abbildung 11 eine Metrik übergreifende Bewertung des durch den QScore bestimmten Cutoffs der Kolokalisation. Es wird deutlich, dass die aus dem Auto-Cutoff resultierenden Werte in den meisten Metriken niedrig ausfallen. Die einzige Ausnahme stellt der wMSE dar, wobei die Werte im Verhältnis zwar hoch erscheinen mögen, absolut gesehen jedoch niedrig ausfallen.

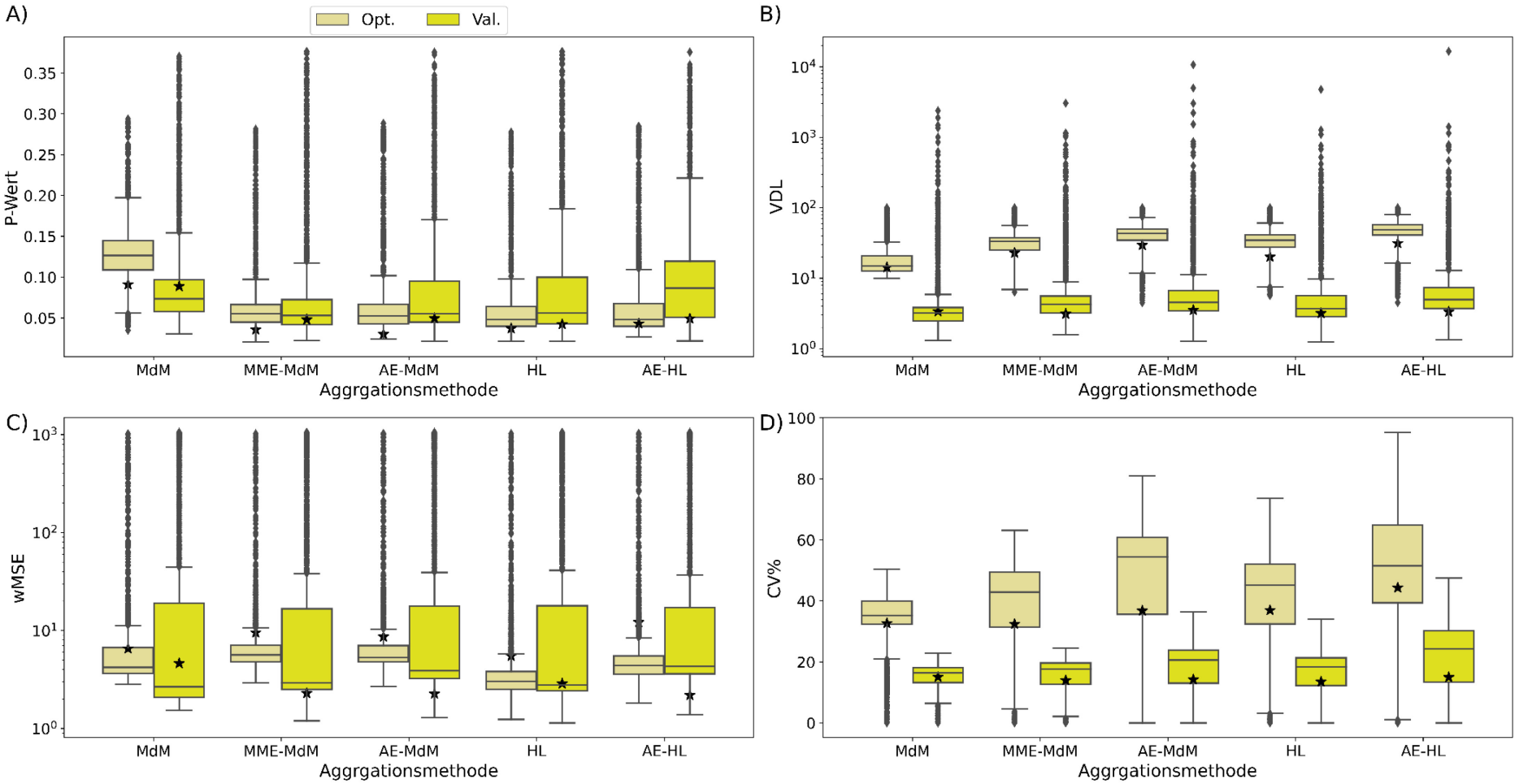

Abbildung 11: Einordnung der ermittelten Cutoffs in der Kolokalisation. Der Stern markiert den Wert, der aus dem Cutoff resultiert, welcher durch die Auto-Cutoff-Methode bestimmt wurde. Die Boxplots zeigen die Werte der Metriken für alle untersuchten Cutoffs. Die Rauten stellen Ausreißer gemäß dem 1.5-fachen Interquartilsabstandes dar. Die Legende oberhalb von **A)** ist ebenfalls für **B)**, **C)** und **D)** gültig.

2.1.2.2 Auswahl potenzieller Cutoffs

Nachdem die Eignung des QScores zur Bestimmung der Cutoffs sowohl in Einzelkanälen als auch für die Kolokalisation belegt werden konnte, musste ein Verfahren zur effizienten Bestimmung potenzieller Cutoff-Kandidaten eingeführt werden. Da der QScore mit Ausnahme von Verletzungen der Gültigkeitsbedingungen in den Randbereichen bei geringfügigen Anpassungen des Cutoffs lediglich marginale Veränderungen aufwies (siehe Abbildung 12), konnte die Berechnung der QScores in definierten Intensitätsabständen erfolgen, wodurch die Anzahl der notwendigen Durchläufe der Analysepipeline auf 290 bzw. 2116 reduziert wurde.

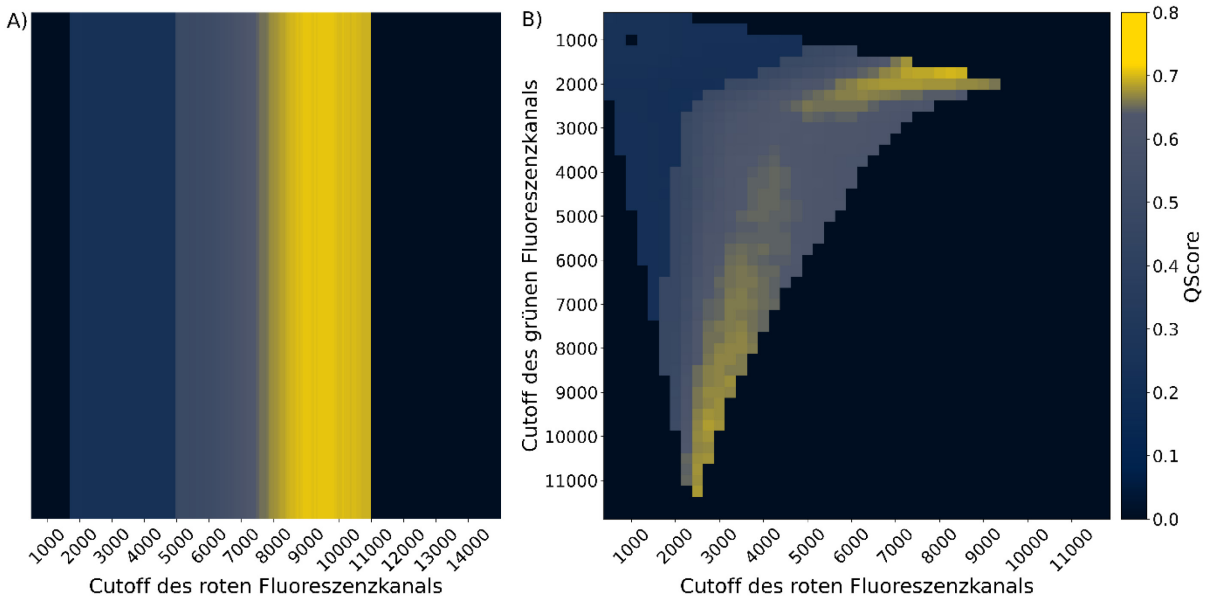

Abbildung 12: QScores in Abhängigkeit zum Cutoff. QScores der jeweiligen Cutoffs im **A)** eindimensionalen Szenario (roter Fluoreszenzkanal) und im **B)** zweidimensionalen Szenario (Kolokalisation). Die Farbskala ist sowohl für **A)** als auch für **B)** gültig. Die präsentierten QScores wurden mittels der AE-HL Aggregationsmethode für den Validierungsdatensatz berechnet.

Obwohl die Anzahl der QScore-Berechnungen bereits stark reduziert wurde, stand die resultierende Verarbeitungszeit, insbesondere im Fall der Kolokalisation, weiterhin nicht im Einklang mit den Erwartungen an einen High-Throughput-Assay. Eine weitere Reduktion der Verarbeitungszeit war daher wünschenswert. Um dies zu ermöglichen, wurde der Suchraum als ein- bzw. zweidimensionaler Raum betrachtet, wobei jede Position (Cutoff) mit einem Lösungswert (QScore) verknüpft wurde (siehe Abbildung 12). Ziel war es, durch möglichst wenige Bewegungen im jeweiligen Raum eine Position zu finden, die einen höchstmöglichen Lösungswert lieferte. Zwei geeignete Optimierungsmethoden wurden zu diesem Zwecke ausgewählt: ein Multi-Start-Hill-Climbing-Algorithmus sowie ein modifizierter Firefly-Algorithmus. Um die Vorteile beider Ansätze zu kombinieren, wurde darüber hinaus

eine hybride Methode implementiert, die beide Algorithmen vereint. Im Folgenden werden die drei Algorithmen und ihre Eigenschaften detailliert beschrieben.

Der Hill-Climbing-Algorithmus ist eine einfache, jedoch effektive Optimierungsmethode, die in unterschiedlichsten Anwendungsbereichen eingesetzt wird[133]. Der Algorithmus beginnt an einer definierten Startposition und evaluiert die Lösungen der benachbarten Positionen. Wenn eine oder mehrere benachbarte Lösungen höhere Werte erzielen als die der aktuellen Position, wird die Position übernommen, welche die größte Erhöhung des Lösungswertes bietet. Die Überprüfung der benachbarten Positionen und die folgende Anpassung der aktuellen Position, werden so lange iterativ wiederholt, bis der Lösungswert der aktuellen Position höher oder gleich dem aller benachbarten Positionen ist. In diesem Fall terminiert der Algorithmus und ein lokales Maximum wurde gefunden. Im konkreten Anwendungsfall der QScore-Optimierung wird zunächst ein Cutoff (für einen Einzelkanal) oder eine Kombination von Cutoffs (bei der Kolokalisation) als Ausgangspunkt definiert und der zugehörigen QScores berechnet. Anschließend werden die QScores für die benachbarten Cutoffs bzw. Cutoff-Kombinationen bestimmt. Falls einer dieser QScores höher ist als der QScore der aktuellen Position, wird der Cutoff oder die Cutoff-Kombination mit dem höchsten QScore als neue Position übernommen. Andernfalls terminiert der Algorithmus.

Die Einfachheit des Hill-Climbing-Algorithmus geht mit der Einschränkung einher, dass lediglich das Auffinden lokaler Maxima garantiert werden kann. Dies führt dazu, dass die Qualität des Ergebnisses stark von der gewählten Startposition abhängt. In mehrdimensionalen Suchräumen kann es zudem vorkommen, dass ein lokales Maximum nicht auf direktem Weg erreicht wird, was die Anzahl der Iterationen und somit Cutoff-Berechnungen erhöht[133]. Darüber hinaus versagt der Algorithmus in Szenarien, in denen sowohl die Startposition als auch deren benachbarte Lösungen identische Werte liefern. Diese Problematik ist in der QScore-Optimierung kein rein theoretischer Fall, da ungünstige Startkonstellationen beispielsweise durch die Nichteinhaltung von Gültigkeitsbedingungen entstehen können (siehe Abbildung 12). Zur Vermeidung dieser Probleme wurde eine Multi-Start-Strategie für die Optimierung des QScores implementiert. Dabei erfolgt die iterative Optimierung aus mehreren Startpositionen und nicht nur von einer einzigen Position aus. Dies ermöglicht es, Vorteile populationsbasierter Algorithmen zu nutzen. So wurde das Risiko durch ungünstige Startpositionen verringert und die Wahrscheinlichkeit, das globale Maximum zu finden, erhöht[134].

Populationsbasierte Algorithmen, die das Verhalten von Tieren oder natürlichen Systemen nachahmen, finden vielfältige Anwendung in der Optimierung[135–138]. Ein weit verbreiteter Vertreter dieser Kategorie ist der Firefly-Algorithmus, der das Sozialverhalten von Fireflies (Glühwürmchen) modelliert[138]. Bei der Initialisierung des Algorithmus wird eine definierte Anzahl an Fireflies im Suchraum platziert und anschließend iterativ bewegt. Im Gegensatz zum Hill-Climbing-Algorithmus erfolgt diese Bewegung nicht aufgrund der Prüfung benachbarter Cutoffs. Stattdessen wird das Verhalten der Fireflies simuliert, bei dem sie durch die Biolumineszenz ihrer Artgenossen angelockt werden. Umso heller ein Firefly leuchtet, desto attraktiver ist es für andere. Die Helligkeit eines Fireflies entspricht dabei dem Lösungswert (QScore) der spezifischen Position (Cutoff), an dem es sich befindet. Die Helligkeit β nimmt jedoch mit zunehmender Entfernung r ab. Die Gleichung 4 beschreibt die entfernungsabhängige Helligkeit, wobei β_0 die Helligkeit aus einer Distanz von null repräsentiert[138]. Für die Implementierung des Algorithmus wurde der Parameter $\gamma = 1$ verwendet. Die Entfernung *r* wurde durch die maximal mögliche Differenz im spezifischen Suchraum normiert.

$$\beta(r) = \beta_0 e^{-\gamma r^2} \qquad (4)$$

Ein Firefly an Position x_i bewegt sich iterativ in Richtung der Position des für ihn attraktivsten Artgenossen x_j. Die Schrittweite ist dabei nicht fest definiert, sondern wird dynamisch berechnet. Ebenso wie die Attraktivität wird die Schrittweite durch die Helligkeit sowie die Entfernung beeinflusst[138]. Yang (2009) verwendete darüber hinaus eine Zufallskomponente, welche in dieser Implementation jedoch nicht genutzt wird, um die Reproduzierbarkeit der Ergebnisse zu gewährleistet (Gleichung 5)[138].

$$x_i' = x_i + \beta_0 e^{-\gamma r_{i,j}^2}(x_j - x_i) \qquad (5)$$

Der Algorithmus terminiert, wenn alle Fireflies den für sie attraktivsten Partner erreicht haben oder eine definierte Anzahl an Schritten absolviert wurde. Das Auffinden lokaler Maxima kann im Firefly-Algorithmus nicht garantiert werden. Wenn dies jedoch der Fall ist, können Fireflies diese im Gegensatz zum Hill-Climbing-Algorithmus überwinden, wodurch die Wahrscheinlichkeit, das globale Maximum zu finden potenziell steigt. Durch die Optimierung für unterschiedlichste Anwendungsfelder entstanden zahlreiche weitere Varianten des ursprünglichen Algorithmus, welche unterschiedliche Vor- und Nachteile aufweisen[139]. In dieser Arbeit wurde weitestgehend der ursprüngliche Algorithmus verwendet, wobei aus Gründen der Reproduzierbarkeit auf sämtliche Zufallskomponenten verzichtet wurde.

Als dritter Optimierungsalgorithmus wurde der Firefly-Algorithmus durch die Integration des Hill-Climbing-Algorithmus erweitert, um die Stärken beider Ansätze zu vereinen. Dabei kombiniert er die effiziente Exploration des Suchraums durch den Firefly-Algorithmus mit der gezielten Suche nach lokalen Maxima, die der Hill-Climbing-Algorithmus ermöglicht. Im Hybridansatz wechseln alle Fireflies, deren zugehöriger QScore mindestens 85 % des aktuell höchsten QScores erreicht hat, ihren Bewegungsmodus. Anstatt weiterhin dem attraktivsten Firefly zu folgen, nutzen sie den Hill-Climbing-Algorithmus, um ihre Position gezielt zu optimieren. Durch die Kombination gelangen die Fireflies schnell in vielversprechende Bereiche mit hohen QScores und können dort lokale Maxima identifizieren.

Um die Leistung der Optimierungsalgorithmen vergleichbar zu machen, wurden für alle Algorithmen dieselben Startpositionen verwendet. Dabei wurde bewusst eine hohe Anzahl an Positionen gewählt. Dies führt zwar in der Regel zu mehr Optimierungsschritten, Bildanalysen, sowie QScore-Berechnungen, steigert jedoch häufig die Qualität der ermittelten Lösung. Um die Anzahl der notwendigen Cutoff-Berechnungen möglichst gering zu halten, wurden alle Algorithmen mit einem globalen Gedächtnis ausgestattet. Dieses verhindert die wiederholte Berechnung einzelner Cutoffs. In Abbildung 13 sind die einzelnen Startpositionen dargestellt.

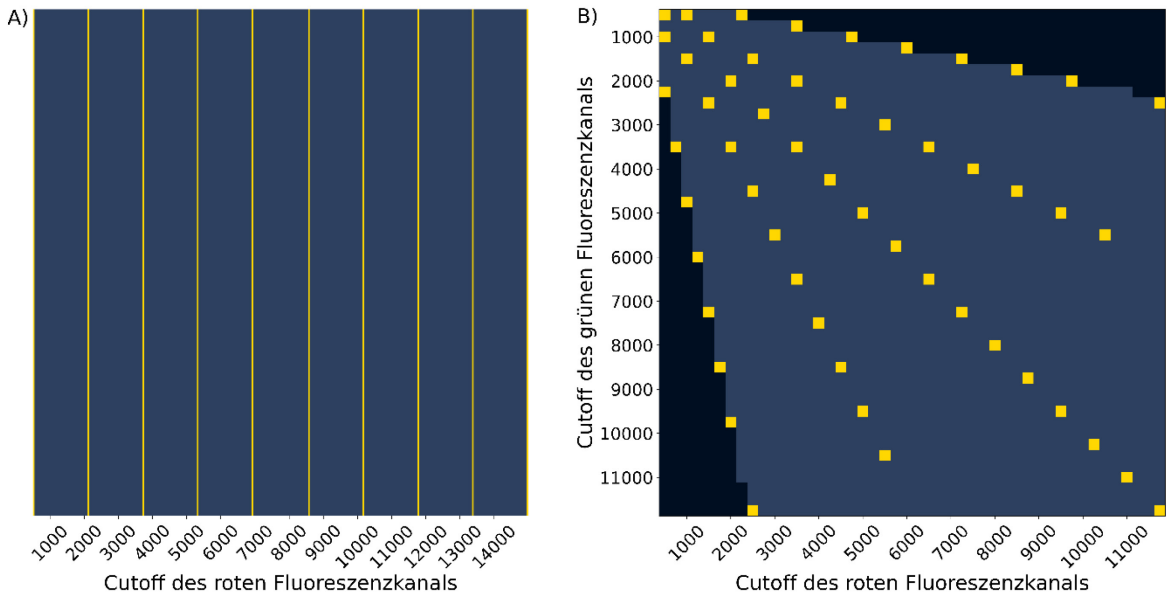

Abbildung 13: Startpositionen im ein- und zweidimensionalen Suchraum. Die Startpositionen befinden sich an Stelle der gelben Markierungen. Die dunklen Bereiche in B) sind aufgrund der zusätzlichen Gültigkeitsbedingung im Fall der Kolokalisation (der niedrigere Cutoff muss mindestens 20 % des höheren betragen), ungültig.

Im zweidimensionalen Raum wurde darauf geachtet, die Randbereiche abzudecken. Dies ist notwendig, da ohne eine Zufallskomponente in der Bewegung der Fireflies Maxima am Rand des gültigen Bereichs möglicherweise nicht gefunden werden könnten. Tabelle 9 und Tabelle 10 zeigen die durchschnittlichen Ergebnisse aller Aggregationsmethoden, die mithilfe der drei untersuchten Optimierungsalgorithmen auf den jeweiligen Datensätzen erzielt wurden. Unabhängig von der Dimensionalität des Suchraums und den spezifischen Datensätzen identifizierten alle Algorithmen hohe QScores zwischen 99.37 % und 100 % des maximal möglichen QScores. Die Abweichung von der optimalen Lösung beträgt somit weniger als 0.7 %. Mit Ausnahme des Optimierungsdatensatzes erreichen der Hill-Climb-Algorithmus sowie der hybride Firefly-Hill-Climb-Algorithmus stets die höchsten QScores. Dabei benötigt der hybride Ansatz im Durchschnitt 45 % weniger Cutoff-Berechnungen als der Hill-Climb-Algorithmus. Der effizienteste Algorithmus ist der Firefly-Algorithmus, der durchschnittlich nur 5 % der möglichen Cutoffs berechnet, bevor er terminiert.

Tabelle 9: Evaluierung der Optimierungsalgorithmen für eindimensionale Suchräume. Die Tabelle zeigt die Mittelwerte der Ergebnisse der unterschiedlichen Datensätze und Kanäle. Die QScores wurden mittels der AE-HL Aggregationsmethode berechnet.

Datensatz	Optimierungs-algorithmus	Cutoff-Berechnungen	Ersparnis Berechnungen	Erreichter QScore
Optimierung	Hill-Climb-Algorithmus	74.9	74.17 %	99.43 %
Optimierung	Firefly-Algorithmus	15.2	94.76 %	99.62 %
Optimierung	Firefly-Hill-Climb - Algorithmus	36.8	87.31 %	99.42 %
Validierung	Hill-Climb-Algorithmus	89.3	69.21 %	99.68 %
Validierung	Firefly-Algorithmus	12.6	95.66 %	99.37 %
Validierung	Firefly-Hill-Climb – Algorithmus	46.2	84.07 %	99.68 %

Tabelle 10: **Evaluierung der Optimierungsalgorithmen für zweidimensionale Suchräume.** Die Tabelle zeigt die Mittelwerte der Ergebnisse der unterschiedlichen Datensätze. Die QScores wurden mittels der AE-HL Aggregationsmethode berechnet.

Datensatz	**Optimierungs-algorithmus**	**Cutoff-Berechnungen**	**Ersparnis Berechnungen**	**Erreichter QScore**
Optimierung	Hill-Climb-Algorithmus	390.8	81.53 %	100 %
Optimierung	Firefly-Algorithmus	120.2	94.32 %	99.37 %
Optimierung	Firefly-Hill-Climb – Algorithmus	220.2	89.59 %	100 %
Validierung	Hill-Climb-Algorithmus	504.4	76.16 %	100 %
Validierung	Firefly-Algorithmus	136.6	93.53 %	99.92 %
Validierung	Firefly-Hill-Climb – Algorithmus	324.8	84.65 %	100 %

2.2 Manuskripte

2.2.1 Aβ oligomers peak in early stages of Alzheimer's disease preceding Tau pathology

Autoren:	Lara Blömeke*, **Fabian Rehn*,** Victoria Kraemer-Schulien*, Janine Kutzsche, Marlene Pils, Tuyen Bujnicki, Piotr Lewczuk, Johannes Kornhuber, Silka D. Freiesleben Luisa-Sophie Schneider, Lukas Preis, Josef Priller, Eike J. Spruth, Slawek Altenstein, Andrea Lohse, Anja Schneider, Klaus Fliessbach, Jens Wiltfang, Niels Hansen, Ayda Rostamzadeh, Emrah Düzel, Wenzel Glanz, Enise I. Incesoy, Michaela Butryn, Katharina Buerger, Daniel Janowitz, Michael Ewers, Robert Perneczky, Boris-Stephan Rauchmann, Stefan Teipel, Ingo Kilimann, Doreen Goerss, Christoph Laske, Matthias H. Munk, Carolin Sanzenbacher, Annika Spottke, Nina Roy-Kluth, Michael T. Heneka, Frederic Brosseron, Michael Wagner, Steffen Wolfsgruber, Luca Kleineidam, Melina Stark, Matthias Schmid, Frank Jessen, Oliver Bannach, Dieter Willbold, Oliver Peters ***Autoren sind gleichberechtigt**
Journal:	*Alzheimer's and Dementia- Diagnosis, Assessment & Disease Monitoring 16(2), e12589 (April, 2024)* *DOI: 10.1002/dad2.12589*
Beitrag:	Normierung und Aufbereitung der Rohdaten Konzeption und Entwicklung des Models zur Bestimmung der Oligomer-Kurven Statistische Analyse Anfertigung von Abbildungen Verfassen des Manuskripts
Druckgenehmigung:	Siehe Anhang 11.

Received: 19 December 2023 | Revised: 11 March 2024 | Accepted: 15 March 2024

DOI: 10.1002/dad2.12589

RESEARCH ARTICLE

Alzheimer's Association Diagnosis, Assessment & Disease Monitoring

Aβ oligomers peak in early stages of Alzheimer's disease preceding tau pathology

Lara Blömeke[1,2,3] | Fabian Rehn[1,2,3] | Victoria Kraemer-Schulien[1] | Janine Kutzsche[1] | Marlene Pils[1,2,3] | Tuyen Bujnicki[1] | Piotr Lewczuk[4] | Johannes Kornhuber[4] | Silka D. Freiesleben[5,6] | Luisa-Sophie Schneider[5] | Lukas Preis[5] | Josef Priller[5,6,7,8] | Eike J. Spruth[5,6] | Slawek Altenstein[5,6] | Andrea Lohse[5] | Anja Schneider[9,10] | Klaus Fliessbach[9,10] | Jens Wiltfang[11,12,13] | Niels Hansen[12] | Ayda Rostamzadeh[14] | Emrah Düzel[15,16] | Wenzel Glanz[15] | Enise I. Incesoy[15,16,17] | Michaela Butryn[15] | Katharina Buerger[18,19] | Daniel Janowitz[19] | Michael Ewers[18,19] | Robert Perneczky[18,20,21,22] | Boris-Stephan Rauchmann[20,23,24] | Stefan Teipel[25,26] | Ingo Kilimann[25,26] | Doreen Goerss[25,26] | Christoph Laske[27,28] | Matthias H. Munk[27,29] | Carolin Sanzenbacher[27] | Annika Spottke[9,30] | Nina Roy-Kluth[9] | Michael T. Heneka[31] | Frederic Brosseron[9] | Michael Wagner[9,10] | Steffen Wolfsgruber[9,10] | Luca Kleineidam[9,10] | Melina Stark[10] | Matthias Schmid[9,32] | Frank Jessen[9,14,33] | Oliver Bannach[1,2] | Dieter Willbold[1,2,3] | Oliver Peters[5,6]

[1]Institute of Biological Information Processing (Structural Biochemistry: IBI-7), Forschungszentrum Jülich GmbH, Jülich, Germany

[2]attyloid GmbH, Düsseldorf, Germany

[3]Institut für Physikalische Biologie, Heinrich-Heine-Universität Düsseldorf, Düsseldorf, Germany

[4]Department of Psychiatry and Psychotherapy, Universitätsklinikum Erlangen and Friedrich-Alexander-Universität Erlangen-Nürnberg, Erlangen, Germany

[5]Department of Psychiatry and Psychotherapy, Charité, Berlin, Germany

[6]German Center for Neurodegenerative Diseases (DZNE), Berlin, Germany

[7]School of Medicine, Department of Psychiatry and Psychotherapy, Technical University of Munich, Munich, Germany

[8]University of Edinburgh and UK DRI, Edinburgh, UK

[9]German Center for Neurodegenerative Diseases (DZNE), Bonn, Germany

[10]Department of Neurodegenerative Disease and Geriatric Psychiatry/Psychiatry, University of Bonn Medical Center, Bonn, Germany

[11]German Center for Neurodegenerative Diseases (DZNE), Göttingen, Germany

[12]Department of Psychiatry and Psychotherapy, University Medical Center Göttingen, University of Göttingen, Göttingen, Germany

[13]Department of Medical Sciences, Neurosciences and Signaling Group, Institute of Biomedicine (iBiMED), University of Aveiro, Aveiro, Portugal

[14]Department of Psychiatry, Medical Faculty, University of Cologne, Cologne, Germany

[15]German Center for Neurodegenerative Diseases (DZNE), Magdeburg, Germany

[16]Institute of Cognitive Neurology and Dementia Research (IKND), Otto-von-Guericke University, Magdeburg, Germany

[17]Department for Psychiatry and Psychotherapy, University Clinic Magdeburg, Magdeburg, Germany

[18]German Center for Neurodegenerative Diseases (DZNE, Munich), Munich, Germany

Lara Blömeke, Fabian Rehn, and Victoria Kraemer-Schulien contributed equally to this study.

[19]Institute for Stroke and Dementia Research (ISD), University Hospital, LMU Munich, Munich, Germany

[20]Department of Psychiatry and Psychotherapy, University Hospital, LMU Munich, Munich, Germany

[21]Munich Cluster for Systems Neurology (SyNergy) Munich, Munich, Germany

[22]Ageing Epidemiology Research Unit (AGE), School of Public Health, Imperial College London, London, UK

[23]Sheffield Institute for Translational Neuroscience (SITraN), University of Sheffield, Sheffield, UK

[24]Department of Neuroradiology, University Hospital LMU, Munich, Germany

[25]German Center for Neurodegenerative Diseases (DZNE), Rostock, Germany

[26]Department of Psychosomatic Medicine, Rostock University Medical Center, Rostock, Germany

[27]German Center for Neurodegenerative Diseases (DZNE), Tübingen, Germany

[28]Section for Dementia Research, Hertie Institute for Clinical Brain Research and Department of Psychiatry and Psychotherapy, University of Tübingen, Tübingen, Germany

[29]Department of Psychiatry and Psychotherapy, University of Tübingen, Tübingen, Germany

[30]Department of Neurology, University of Bonn, Bonn, Germany

[31]Luxembourg Centre for Systems Biomedicine (LCSB), University of Luxembourg, Belvaux, Luxemburg

[32]Institute for Medical Biometry, University Hospital Bonn, Bonn, Germany

[33]Excellence Cluster on Cellular Stress Responses in Aging-Associated Diseases (CECAD), University of Cologne, Köln, Germany

Correspondence
Oliver Peters, Charité – Universitätsmedizin Berlin, Klinik für Psychiatrie und Psychotherapie CBF, Hindenburgdamm 30, 12203 Berlin, Germany.
Email: oliver.peters@charite.de

Oliver Bannach, attyloid GmbH, Merowingerplatz 1a, 40225 Düsseldorf, Germany.
Email: o.bannach@attyloid.com

Dieter Willbold, Institute of Biological Information Processing (IBI-7), Forschungszentrum Jülich, Wilhelm-Johnen-Straße, 52428 Jülich, Germany.
Email: d.willbold@fz-juelich.de

Funding information
"Biomarkers Across Neurodegenerative Diseases I + II" of The Alzheimer's Association; Alzheimer's Research UK and the Weston Brain Institute, Grant/Award Numbers: 11084, BAND-19-614337; The Michael J. Fox Foundation for Parkinson's Research, Grant/Award Numbers: 14977, 009889; ALS Association, Grant/Award Number: 19-SI-476; Packard Center, Grant/Award Number: 19-SI-476; Deutsche Forschungsgemeinschaft, Grant/Award Numbers: INST 208/616-1 FUGG, INST 208/794-1 FUGG; Helmholtz Association, Grant/Award Number: HVF0079

Abstract

INTRODUCTION: Soluble amyloid beta (Aβ) oligomers have been suggested as initiating Aβ related neuropathologic change in Alzheimer's disease (AD) but their quantitative distribution and chronological sequence within the AD continuum remain unclear.

METHODS: A total of 526 participants in early clinical stages of AD and controls from a longitudinal cohort were neurobiologically classified for amyloid and tau pathology applying the AT(N) system. Aβ and tau oligomers in the quantified cerebrospinal fluid (CSF) were measured using surface-based fluorescence intensity distribution analysis (sFIDA) technology.

RESULTS: Across groups, highest Aβ oligomer levels were found in A+ with subjective cognitive decline and mild cognitive impairment. Aβ oligomers were significantly higher in A+T− compared to A−T− and A+T+. *APOE* ε4 allele carriers showed significantly higher Aβ oligomer levels. No differences in tau oligomers were detected.

DISCUSSION: The accumulation of Aβ oligomers in the CSF peaks early within the AD continuum, preceding tau pathology. Disease-modifying treatments targeting Aβ oligomers might have the highest therapeutic effect in these disease stages.

KEYWORDS
Alzheimer's disease, *APOE*, AT(N) classification, Aβ, cerebrospinal fluid, oligomers, preclinical, prodromal, sFIDA, tau

Highlights

- Using surface-based fluorescence intensity distribution analysis (sFIDA) technology, we quantified Aβ oligomers in cerebrospinal fluid (CSF) samples of the DZNE-Longitudinal Cognitive Impairment and Dementia (DELCODE) cohort
- Aβ oligomers were significantly elevated in mild cognitive impairment (MCI)
- Amyloid-positive subjects in the subjective cognitive decline (SCD) group increased compared to the amyloid-negative control group

- Interestingly, levels of Aβ oligomers decrease at advanced stages of the disease (A+T+), which might be explained by altered clearing mechanisms

1 | BACKGROUND

Alzheimer's disease (AD) is a neuropathological disorder accompanied by abnormal protein deposits such as amyloid plaques and neurofibrillary tangles (NFTs)[1] which may occur up to 20 years before the onset of clinical symptoms.[2,3]

Soluble amyloid beta (Aβ) oligomers are neuro- and synaptotoxic Aβ aggregates implicated in triggering AD-related Aβ pathology that are derived from the sequential cleavage of the transmembrane amyloid precursor protein (APP).[4,5] A growing body of research indicates that deficient clearing mechanisms prevent Aβ oligomer degradation and facilitate the accumulation of Aβ species into insoluble plaques.[4,6–9] Furthermore, the formation of toxic Aβ oligomers and fibrils in the cerebrospinal fluid (CSF) has been associated with a decreased ratio of Aβ42/Aβ40, and an increased amyloid plaque burden as measured by positron emission tomography (PET).[10,11] Thus, increased Aβ oligomer levels and increasing Aβ plaque burden might act as a surrogate marker for deficient Aβ monomer clearance. Furthermore, in a series of experiments that included human brain autopsy and rat models, tau pathology measured by phosphorylated tau (pTau) in the CSF or by PET was found to act downstream of synaptic Aβ oligomer accumulation.[12] Consequently, examining potential differences in Aβ oligomer concentrations in different biomarker profiles across the AD spectrum might help identify individuals in the earliest stages of AD, thereby allowing to identify a unique window of opportunity for effective therapeutic intervention.[13] Yet, little is known how the levels of Aβ oligomers in the CSF correlate with the stages of AD, or whether they could serve as reliable biomarkers for disease progression.[14] In order to investigate the role of Aβ oligomer concentrations, the National Institute on Aging and the Alzheimer's Association (NIA-AA) research framework provide a unified biological definition of Alzheimer's disease, capable of identifying early pathological changes and biomarker interactions related to the disease.[1,15]

According to the NIA-AA research framework, individuals can be placed on the Alzheimer continuum once pathological Aβ aggregation (ie, A+) arises, regardless of their cognitive status.[1,15] In the revised NIA-AA research framework, six symptom stages of AD are defined,[16] with stages 1 and 2 characterizing individuals with preclinical AD that are cognitively unimpaired (CU).[15,16] In stage 1, experiencing subjective cognitive decline (SCD) has to be absent, whereas individuals can experience SCD or newly acquired neurobehavioral symptoms in stage 2.[16] Stages 3, 4, 5, and 6 correspond to mild cognitive impairment (MCI), and mild, moderate and severe AD dementia, respectively. Although the revised research framework is closely linked to the AT(N) (A, amyloid; T, tau; N, neurodegeneration) classification system for AD biomarkers, the presence of pTau pathology (ie, T+) is not essential to be placed on the AD continuum, as pTau pathology has been suggested to be a downstream event of amyloid pathology, and may therefore arise at later disease stages.[1] Consequently, individuals on the AD continuum can have varying biomarker profiles (eg, A+T− or A+T+), where A+T− indicates early pathologic change, whereas full-blown AD pathology (ie, the presence of both pathological amyloid and pTau deposition; A+T+) might occur at a later time[1].

Accordingly, the present study aims to elucidate the role of CSF Aβ and tau oligomers in individuals along the AD continuum stratified for different biomarker profiles (ie, A−T−, A−T+, A+T−, and A+T+), assuming that these different cross-sectional profiles reflect the temporal evolution of AD, with subjects being in one of these biological disease stages. Using surface-based fluorescence intensity distribution analysis (sFIDA), a platform technology for the quantitation of protein aggregates in biofluids,[17–21] we specifically aimed to investigate whether oligomer titers differ between biomarker profiles, and whether there is an association between amyloid positivity (ie, A+), oligomer concentrations, and diagnostic status. Lastly, as carrying the ε4 allele of the apolipoprotein E (*APOE*) gene is the most important genetic risk factor in sporadic AD,[22] we examined whether the concentrations of Aβ and tau oligomers are increased in *APOE* ε4 carriers.

2 | METHODS

2.1 | Samples and design

In the present study, demographic and clinical information and CSF baseline samples from 526 participants of the DZNE-Longitudinal Cognitive Impairment and Dementia (DELCODE) study[23] were included. Details on the overall DELCODE study design, definition of patient groups including criteria for patient enrollment, and execution of cognitive, neuropsychological tests as well as biomaterial sampling, *APOE*-genotyping, PET, magnetic resonance imaging (MRI) and CSF biomarker assessment are described in Jessen et al.[23] All participants provided their written informed consent. Only participants with a minimum of 18 points on the Mini-Mental State Examination (MMSE) qualified for the AD group in the DELCODE study.[23] In short, participants were recruited from 10 memory clinics throughout Germany and allocated to 5 participant groups, that is, the cognitively unimpaired control (C) group, SCD, MCI, mild AD dementia, and healthy first-degree relatives of AD patients (REL). To increase the number of controls in the present study, the REL were integrated into the control group. In order to classify participants according to the AT(N) classification system, we used cutoffs established within the DELCODE cohort, that is, Aβ42 ≤ 638.7 pg/mL, total tau (tTau) > 510.9 pg/mL,

and pTau ≥ 73.65 pg/mL.[24] CSF samples were stored at −80°C and did not undergo a freeze-thaw cycle. All 526 samples were blinded at the timepoint of sFIDA measurement.

2.2 | Oligomer measurement using sFIDA

We previously developed sFIDA to specifically and sensitively measure protein oligomers and aggregates in biofluids.[17–19] sFIDA uses a sandwich-like biochemistry employing the same capture and detection antibodies with linear epitopes to reliably measure the whole fraction of Aβ or tau oligomers and larger, but still soluble, aggregates even in the presence of excessive monomers. Due to the use of fluorescence microscopy and sophisticated image analysis, sFIDA yields single particle sensitivity.

2.3 | Synthesis of protein conjugated silica nanoparticles

For assay development and as assay control we used our previously developed silica nanoparticle (SiNaP) standard standard.[25,26] Aβ SiNaPs were coated with amino acids 1–15 of the Aβ protein (peptides and elephants, Henningsdorf, Germany) as described in Blömeke et al.[19] Shortly, SiNaPs were synthetized using the Stöber process and afterwards aminated using (3-aminopropyl)triethoxysilane (APTES, Sigma-Aldrich, St. Louis, MO, USA).[25,26] In the next step, activated maleimidohexanoic acid (MIHA, abcr GmbH, Karlsruhe, Germany) was allowed to react covalently with the amines. Finally, Aβ1–15 functionalized with cysteamine at the C-terminus was added to react with the maleimide groups of the particles.

Tau SiNaPs were coated with full-length tau protein (2N4R). Here, we used a different approach which was previously described in Hülsemann et al.[25] In this approach, synthesized and aminated SiNaPs were further functionalized with succinic anhydride (Sigma-Aldrich). To enable reaction, the pellet of aminated SiNaPs was redispersed in 0.1 M succinic acid anhydride in N,N-dimethylformamide anhydrous (DMF) and incubated for 2 hours at 70°C and afterwards for 2 days at room temperature (RT) when stirring. The carboxylated SiNaPs were washed three times with ddH_2O by centrifugation (7 minutes at 10,000 × *g*) and redispersion. For biofunctionalization, carboxylated SiNaPs were activated with 20 mM 1-ethyl-3-(3-dimethylaminopropyl)carbodiimide (EDC; Sigma-Aldrich) and 5 mM N-hydroxysuccinimide (NHS; Sigma-Aldrich) in a buffer of 0.1 M 2-(N-Morpholino)ethanesulfonic acid (MES; Carl Roth, Karlsruhe, Germany) while shaking for 1 hour at RT. After two washing steps (centrifugation at 18,200 × *g* for 10 minutes) and redispersion in phosphate-buffered saline (PBS), full-length tau protein was added. The next day, biofunctionalized SiNaPs were washed twice with ddH_2O as described before.

SiNaPs were characterized based on particle size and shape as previously described.[19,25] Size and shape of the particles were determined using transmission electron microscopy while concentrations were determined using inductively coupled plasma-mass spectrometry (ICP-MS).

RESEARCH IN CONTEXT

1. **Systematic review**: Aβ oligomers are the most toxic Aβ species. They disrupt synaptic communication and may thereby initiate neurodegeneration in Alzheimer's disease (AD). In order to elucidate the temporal order of amyloid (A) and tau (T) pathology along the AD continuum, we quantified cerebrospinal fluid (CSF) Aβ and tau oligomers in different disease stages.
2. **Interpretation**: CSF Aβ oligomers were significantly higher in participants with subjective cognitive decline (stage 2) and mild cognitive impairment (stage 3) classified as A+. Interestingly, A+T+ showed comparably lower Aβ oligomer levels, which might be due to increased binding to amyloid plaques over time.
3. **Future directions**: Further research examining the underlying mechanisms of the rise and fall of Aβ oligomers along the AD continuum is needed.

2.4 | Labeling of antibodies

To detect oligomers in samples, we labeled the antibodies Nab228 (Sigma-Aldrich) and Tau12 (BioLegend, San Diego, CA, USA) with the fluorescent dyes CF633 (Sigma-Aldrich) and CF488A (Sigma-Aldrich) according to manufacturer's protocol. The principle of reaction, the purification, and the determination of concentration and degree of labeling were previously described.[19]

2.5 | Assay protocol

The biochemical principle of sFIDA has been reported elsewhere.[27,28] In the present study, we used Nunc MicroWell 384-well plates for each experiment (Thermo Fisher Scientific, Waltham, MA, USA) functionalized with N-terminal monoclonal antibodies Nab228 (Sigma-Aldrich) and Tau12 (BioLegend) at a concentration of 2.5 µg/mL in 0.1 M NaHCO3. After overnight incubation at 4°C, we washed the plates five times with 80 µL tris-buffered saline (TBS)-T (1×TBS; Serva Electrophoresis, Duisburg, Germany) containing 0.05% Tween20 (AppliChem, Darmstadt, Germany) and afterwards five times with TBS (405 LS Microplate Washer, BioTek, VT, USA). To block remaining binding sides of the glass surface, 1% bovine serum albumin (BSA; AppliChem) in TBS with 0.03% ProClin (Sigma-Aldrich) were incubated for 1.5 h at RT. After washing five times with TBS-T and TBS as described above, we diluted a mix of Aβ and tau SiNaPs in PBS (Sigma-Aldrich) containing 0.5% BSA and 0.05% Tween (dilution factor 1:2) and applied 20 µL of each dilution and 20 µL of undiluted samples to the plate. The plate was incubated for 2 hours at RT and thereafter washed five times with TBS. Then 20 µL of fluorescent detection antibodies Nab228 CF633 (0.156 µg/mL) and Tau12 CF488A

(0.312 µg/mL) diluted in TBS were applied and incubated for 1 hour at RT. Finally, the plate was washed five times with TBS and the buffer was exchanged against TBS-ProClin. In order to obtain a sufficient number of replicates, each dilution and all samples were applied in a quadruple determination.

2.6 | Image data acquisition

For imaging of the assay surface, we used total internal reflection microscopy (TIRF-M; Leica, Wetzlar, Germany)[27] (excitation: 635 nm, emission filter: 705/22 nm; excitation: 488 nm, emission filter: 525/36 nm; exposure time: 1500 ms; gain: 800). In total, 25 images per well were measured with 1000 × 1000 pixels each.

2.7 | Quantification and statistical analyses

Quantification and general statistical analyses were carried out using Python 3.9.7 (Python software foundation, Wilmington, USA; packages: scipy version 1.7.3) and Origin 2020 (OriginLab Corporation, Northampton, USA). Data were further analyzed for normal distribution and in the case of not normally distributed data, nonparametric tests, for example, Spearman correlation or Mann–Whitney *U*-test, were used for further analyses.

2.8 | Image data analysis

For analysis of the images, the in-house developed software tool sFIDAta was used including the detection and elimination of artefact-containing images.[26,27] The analysis itself is based on the number of pixels above a defined cutoff value, which is defined as the pixel count. The cutoff is defined as the grayscale value at which the blank control exceeds a number of 100 pixels (0.01% of total pixels). The cutoff value is determined for each experiment individually. Moreover, 10% of images per well with the highest and lowest pixel counts were excluded from analysis to ensure that no artificial images influence the readouts.[28,29] Given pixel counts were calculated as the mean of the four sample wells.

2.9 | Analytical validation

To assess intra-assay variability of SiNaPs and samples, the coefficient of variation (CV) percentage of the four test replicates within the same run was calculated (Table S1). Furthermore, analytical selectivity of the assay was investigated applying different assay control setups as described previously.[18,19,30] In this study, we investigate if 2 pM of Aβ or tau SiNaPs interfere with the assay surface in the absence of capture antibodies (capture control), show false-positive signals due to autofluorescence component of the used assay buffers (autofluorescence control, no detection probe), or show cross-reactivity with anti-α-synuclein detection antibodies. In addition, the selectivity of the used assay antibodies was analyzed using equimolar concentrations of α-synuclein-coated SiNaPs. Since monomeric species of Aβ and tau are present in excess compared to synthetic oligomers and therefore can falsify the measurement signals, we have additionally compared equimolar concentrations of monomeric as well as oligomeric species, that is, 1 nM of synthetic Aβ oligomers[30] and 250 pM tau oligomers[19] (Figure S1). Afterward, the signal reduction of each assay control was calculated based on the normalized pixel counts according to Equation (1).

$$\text{Signal reduction } [\%] = \left(1 - \frac{\text{pixel count}_{\text{assay control}} - \text{pixel count}_{\text{blank control}}}{\text{pixel count}_{\text{reference}} - \text{pixel count}_{\text{blank control}}}\right) \times 100\% \quad (1)$$

2.10 | Data scaling

Since oligomer levels in samples were lower than suggested, not enough data points of the SiNaPs concentration series were available to create a suitable calibration curve. However, as it was not possible to use the raw data directly without distorting the statistical results, a scaling method was used to compensate for differences between the experiments. This method was based on the samples of the control group and was carried out separately for Aβ and tau oligomers. For each oligomer type, a cross-plate median *globalMedian* of all control group samples was calculated. Subsequently, a separate medium *plateMedian* was formed for each plate *p*. Using these values, a scaling factor (Table S2) was calculated for each plate *p* according to Equation (2).

$$scaleFactor_p = \frac{globalMedian}{plateMedian_p} \quad (2)$$

Finally, all measurement results of a plate were multiplied by the corresponding $scaleFactor_p$. The scaled pixel counts for Aβ and tau oligomers, in the following referred to as Aβ and tau oligomer pixel counts, were used for all analyses. Figure S2 and Figure S3 show the data before and after scaling, respectively.

2.11 | Descriptive analysis

Using Spearman correlations and two-sided Mann–Whitney *U*-tests, we examined the association of oligomer pixel counts with demographic variables and known risk factors for AD, including age, sex, and *APOE* status,[31,32] as well as associations with further CSF biomarkers.

2.12 | Differences in Aβ and tau oligomer levels

To test for differences between participant groups, we performed a two-sided Mann–Whitney *U*-test. For this purpose, we regrouped the samples stepwise, based first on clinical diagnosis. However, symptoms used for the clinical diagnosis of AD can also be caused by other

forms of dementia, which leads to a clinical diagnosis not necessarily being free of errors. Therefore, we subsequently subdivided the four clinically defined groups based on the amyloid status using Aβ42 biomarker data. Afterward, the samples were analyzed independently of their clinical diagnosis using the AT(N) classification. To this end, cutoffs established within the study of Jessen et al.[24] can be used to classify the participants according to AT(N) system. In the present study, the cut-offs for Aβ42 (≤ 638.7 pg/mL), pTau (≥ 73.65 pg/mL) and tTau (> 510.9 pg/mL) positivity were applied to determine amyloid positivity or tau positivity or neurodegeneration. In addition, we also regrouped the samples based on *APOE* status with carrying at least one *APOE* ε4 allele defining *APOE* positivity (ε2/ε4, ε3/ε4, or ε4/ε4) since the *APOE* ε4 allele is an important genetic risk factor for AD.[22]

2.13 | Modeling Aβ oligomer levels in the AD continuum

In an effort to model levels of Aβ oligomers in the course of AD, a regression pipeline was designed to anticipate the Aβ oligomers utilizing Aβ42 and pTau monomers as features. The pipeline is made up of a standard scaler and a bagging model, the latter comprising three support vector regression models with radial basis function (RBF) kernels that are trained on various data subsets. Given the presumption that the relationship between the features and target might vary depending on the *APOE* ε4 status, three different instances of this pipeline were created using solely *APOE* ε4 carrier data, *APOE* ε4 noncarrier data, and all-encompassing data.

To generate continuous oligomer curves describing the progression of AD with these pipelines, it is necessary to establish a probable trajectory of Aβ42 and pTau monomers throughout the AD stages. In order to exclude bias arising from disproportionate representation of AT groups, equal numbers of samples were randomly chosen from the A−T−, A+T−, and A+T+ sets. Following this, data were scaled employing a min-max scaler, centered, and aligned to the antidiagonal. The trajectory was finally ascertained by applying a second-degree polynomial regression, and subsequently reverse transformed. The resulting trajectory was utilized as input to predict oligomer curves for *APOE* ε4 carrier, *APOE* ε4 noncarrier, and all data by the three system instances, which were later refined by a moving average. Given their relationship to Aβ42 and pTau, these curves can be integrated into other models. With this feature in mind, the curves were deliberately superimposed on a biomarker model for AD progression.[33]

All of the above was achieved using the scikit-learn Python package, version 1.0.2.

3 | RESULTS

The aim of the present study was to investigate Aβ and tau oligomer levels in human CSF samples of patients across the clinical and neurobiological continuum of AD.

3.1 | Descriptive analysis of patient and control groups

In the present study, 526 CSF samples from DELCODE, that is, 137 samples from controls, 211 samples from SCD participants, 112 samples from MCI patients, and 66 samples from AD patients, were screened for Aβ and tau oligomer levels. Demographic and clinical information for these four groups on age, gender, neuropsychological tests, amyloid-, tau-, and *APOE* ε4-status is available in Table 1.

To avoid misinterpretation of the statistical results due to demographic characteristics, we checked for correlations of age and gender with oligomer levels. Since the Shapiro–Wilk test showed that neither Aβ nor tau oligomer values were normally distributed ($p = 9.22 \times 10^{-42}$ and 1.44×10^{-34}, respectively), nonparametric tests were used. No significant Spearman correlation was found between age and oligomer pixel counts (Aβ: $r = .033$, $p = .446$; tau: $r = .016$, $p = .709$). Results from two-sided Mann–Whitney *U*-tests showed that Aβ and tau oligomer pixel counts did not significantly differ between genders, even if the significance is nearly reached for Aβ oligomers ($p = .063$; tau $p = .973$). Furthermore, as age and gender are equally distributed for all combinations of groupings by AT(N) classification as well as *APOE* ε4 genotpye, it can be assumed that there is no respective bias for the analysis.

3.2 | Clinically diagnosed MCI patients showed significantly higher levels of Aβ oligomers compared to controls

First, we investigated if Aβ and tau oligomer levels differ between clinical diagnosis groups, using two-tailed Mann–Whitney *U*-tests (Figure 1). In the case of MCI patients, significantly higher Aβ oligomer levels were found compared to the control group ($p = .017$, Figure 1A). Although Aβ and tau oligomer levels showed a highly significant correlation (Spearman $r = .541$, $p = 2.7 \times 10^{-41}$), no increase of tau oligomer levels regarding the disease stage was observed (Figure 1B).

Next, we divided the four clinical groups based on presence of amyloid pathology into amyloid negative (A−) and amyloid positive (A+) cases to analyze if differences in Aβ oligomer levels are due to underlying AD pathology. When comparing these refined groups with the A− control group, it became apparent that SCD ($p = .014$) and MCI ($p = .003$) participants with underlying amyloid pathology, but not those without evidence for AD, showed significantly increased Aβ oligomer levels (Figure 1C). Furthermore, SCD participants with amyloid positive states showed elevated Aβ oligomer levels compared to SCD individuals without diagnosed amyloid pathology ($p = .048$). However, even after the additional breakdown by A, there was no difference in tau oligomer levels (Figure 1D).

3.3 | Differences in Aβ oligomer levels based on AT(N) profiles and *APOE* ε4 status

As the results of Section 3.2 indicate the importance of the underlying pathologies for increases of Aβ oligomers, we regrouped and analyzed

TABLE 1 Demographic information and study characteristics of participants grouped by clinical diagnosis.

	Control	SCD	MCI	AD
Number	137	211	112	66
Age, years (SD)	68.2 (4.9)	71.4 (5.8)	72.3 (5.4)	75.5 (6.3)
Female	54%	43%	43%	65%
MMSE (SD)	29.3 (0.9)	29.1 (1.1)	27.5 (1.9)	23.2 (3.1)
A+	27.7%	40.8%	72.3%	92.4%
T+	7.3%	15.2%	37.5%	68.2%
APOE ε4[a]	27.6%	34.6%	50.5%	64.5%

Abbreviations: A+, amyloid pathology above cut-off; AD, Alzheimer's disease; *APOE ε4*, apolipoprotein E ε4 allele; MCI, mild cognitive impairment; MMSE, Mini-Mental State Examination; SCD, subjective cognitive decline; SD, standard deviation; T+, tau pathology above cut-off.
[a]No *APOE* data were available for 17 participants.

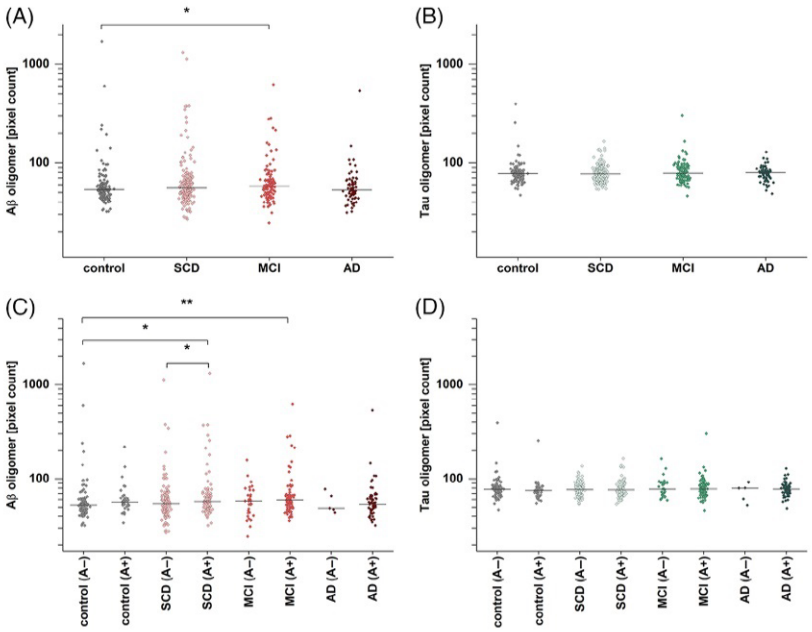

FIGURE 1 Amyloid beta (Aβ) and tau oligomer pixel count based on amyloid pathology (A+/A−). (A) Aβ oligomer pixel counts in mild cognitive impairment (MCI) are significantly increased compared to the controls ($p = .017$). (B) By contrast, no significant changes were detected for tau oligomer pixel count. (C) After dividing groups along amyloid status, significantly higher levels in subjective cognitive decline (SCD) (A+) and MCI (A+) compared to controls (A−) were observed ($p = .014$ and $p = .0028$, respectively). Furthermore, SCD (A+) is significantly elevated compared to SCD (A−) ($p = .048$). (D) Tau oligomers in subgroups show no significant differences when divided in A+ and A−. Effect sizes for the significantly differing groups are provided in Table S3, while receiver operating characteristic curves and area under the curve scores are presented in Figure S4 and Table S5. Horizontal lines indicate the median; y-axis scales are logarithmic. A two-sided Mann–Whitney *U*-test (confidence interval = .05) was carried out to investigate differences between the groups. Abbreviation: AD, Alzheimer's disease. $^{*}p \leq .05$, $^{**}p \leq .01$.

the results based on the AT classification proposed by the NIA-AA research framework and the currently established cutoff values by Jessen et al. for Aβ42 and pTau[24] (Figure 2). Furthermore, demographic information was regrouped based on AT classification (Table 2). Since again no differences in tau oligomer levels between the sample groups were observed, the subsequent analyses were only described with respect to Aβ oligomer levels.

Applying this classification, samples of participants with amyloid pathology without tau pathology (A+T−) had significantly increased levels of Aβ oligomers compared to A+T+ participants with amyloid and tau pathology ($p = 5.8 \times 10^{-5}$). This applied to participants with (A+T−N+) and without (A+T−N−), a concomitant non-Alzheimer's pathologic change (A+T−N+: $p = .032$; A+T−N−: $P = 1.8 \times 10^{-4}$). Aβ oligomer levels of participants classified as A+T+ did not differ

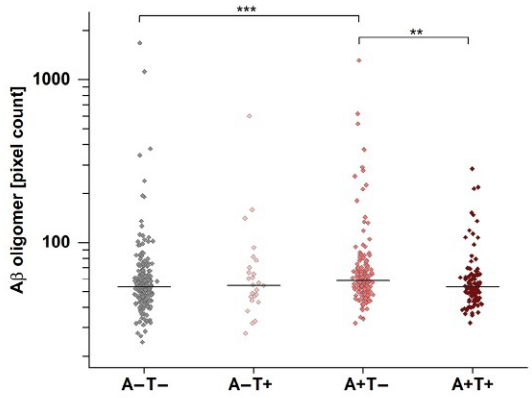

FIGURE 2 Amyloid beta (Aβ) oligomers in quantified cerebrospinal fluid (CSF) samples after AT (amyloid/tau) classification. Aβ oligomer pixel counts in CSF of A+T− patients are significantly increased compared to the reference group A−T− ($p = 5.8 \times 10^{-5}$) and to A+T+ ($p = .0026$). Effect sizes for the significantly differing groups are provided in Table S3, while receiver operating characteristic curves and area under the curve scores are presented in Figure S4 and Table S5. Horizontal lines indicate the median; y-axis scale is logarithmic. A two-sided Mann–Whitney *U*-test (confidence interval = .05) was carried out to investigate differences between the groups. $^{**}p \leq .01$, $^{***}p$ value $\leq .001$.

significantly from control group participants but compared to A+T− participants ($p = .0026$).

Because the *APOE* ε4 allele is an important genetic risk factor for AD,[22] we also investigated Aβ oligomer levels in *APOE* ε4 carriers. Here, significantly increased Aβ oligomer levels were found compared *APOE* ε4 noncarriers independent of the disease stage ($p = .02$). For further evaluation, receiver operating characteristic (ROC) curves, area under the curve (AUC) scores, and effect sizes were presented in Figure S4, Tables S3 and S4.

3.4 | Aβ oligomer levels are elevated in early disease stages

To investigate how Aβ oligomers fit into the AD continuum, we established a regression model that predicts Aβ oligomer levels based on monomeric Aβ42 and pTau concentrations. This model was validated by normalized mean absolute error (Table S5) and by comparing the binned raw data and the binned regression model predictions (Figure S5). As displayed in Figure 3A, increased oligomer levels were only found at low Aβ42 and pTau concentrations in early AD stages. Furthermore, we also investigated if the observed increase and later decrease of Aβ oligomer levels depends on *APOE* ε4 status. To this end, we classified samples into *APOE* ε4 carriers (Figure 3B) and noncarriers (Figure 3C). The predicted Aβ oligomer levels in context of different *APOE* ε4 states indicated that the levels of Aβ oligomers are increased in *APOE* ε4 carriers, and that the peak shifted to higher pTau concentrations (red areas in Figure 3B,C). To provide a more specific statement about the probable level of the Aβ oligomer in the AD continuum, the prediction was reduced to the most likely trajectory of Aβ42 and pTau monomer through the AD stages, as described in 2.3.6 and displayed in Figure 4A. The model of Jack et al.[33] supplemented by the modeled Aβ oligomer curves revealed that in *APOE* ε4

TABLE 2 Demographic information of participants based on the AT classification.

Characteristic	A−T−	A−T+	A+T−	A+T+
number	234	26	163	103
Age, years (SD)	69.62 (5.61)	73.08 (5.15)	71.61 (6.00)	74.08 (5.78)
Female	48.7%	53.8%	61.0%	51.5%
MMSE (SD)	29.1 (1.3)	28.3 (2.9)	28.2 (2.4)	25.7 (3.4)
Aβ42, pg/mL (SD)	960.9 (212.2)	1218.9 (471.2)	445.3 (122.9)	419.8 (116.4)
Aβ42/40 ratio (SD)	0.108 (0.015)	0.094 (0.029)	0.071 (0.023)	0.046 (0.009)
pTau, pg/mL (SD)	47.7 (10.9)	102.2 (45.3)	46.4 (16.3)	108.3 (35.8)
tTau, pg/mL (SD)	333.0 (120.2)	696.8 (361.0)	353.0 (153.3)	849.8 (273.3)
APOE ε4[a]	20.0%	23.1%	48.1%	73.0%
Clinical diagnosis in percentage of subgroups				
Control	39.7%	23.1%	20.9%	3.9%
SCD	48.3%	46.2%	40.5%	19.4%
MCI	10.7%	23.1%	27.6%	35.0%
AD	1.3%	7.7%	11.0%	41.7%
	100%	100%	100%	100%

Abbreviations: A+, amyloid pathology above cut-off; Aβ, amyloid beta; AD, Alzheimer's disease; *APOE* ε4, apolipoprotein E ε4 allele; AT, amyloid/tau; MCI, mild cognitive impairment; MMSE, Mini-Mental State Examination; SCD, subjective cognitive decline; SD, standard deviation; T+, tau pathology above cut-off.
[a]No *APOE* data were available for 17 participants.

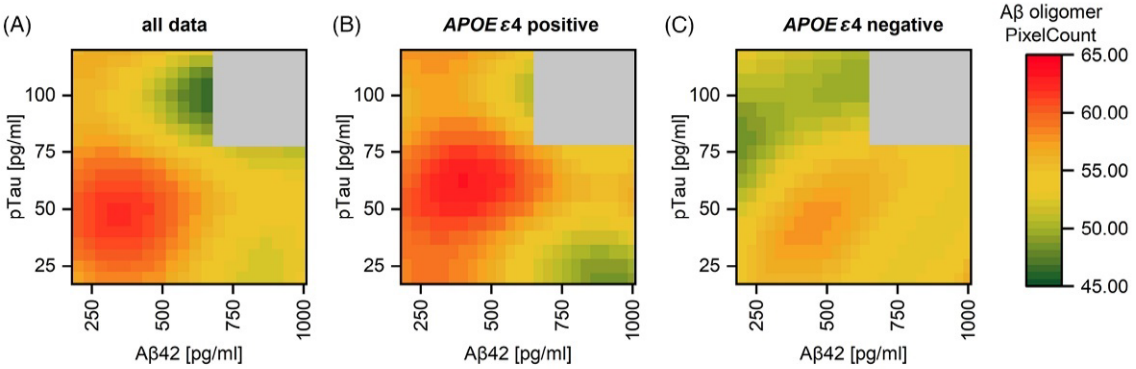

FIGURE 3 Regression model for the interrelationship of amyloid beta (Aβ) oligomers pixel count, Aβ42, and phosphorylated tau (pTau) in cerebrospinal fluid (CSF). Based on Aβ42, pTau, and Aβ oligomer levels in CSF, regression models for prediction of Aβ oligomers pixel count were performed. Highest Aβ oligomer levels can be expected in patients with low Aβ42 while pTau is relatively low in (A) all patients, (B) apolipoprotein E (*APOE*) gene ε4 allele carriers, and (C) *APOE* ε4 noncarriers. Aβ42 oligomer levels in *APOE* ε4-positive participants are overall higher and shifted toward higher pTau concentrations compared to those who were *APOE* ε4 negative.

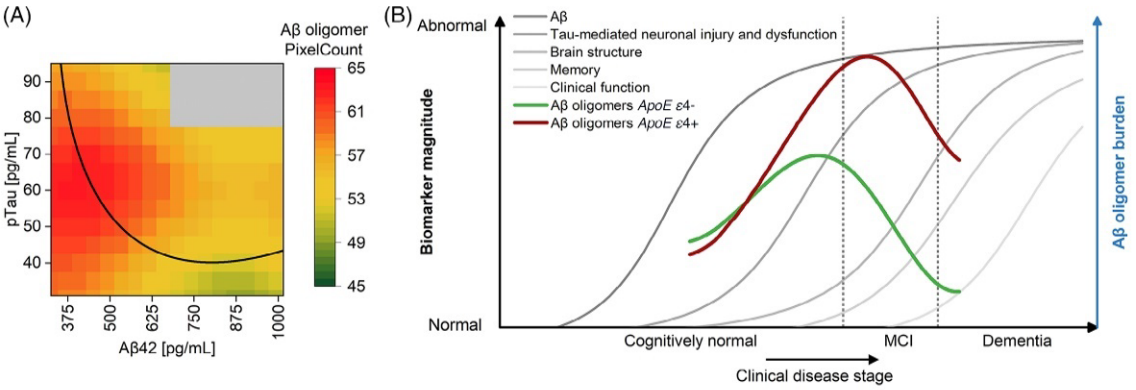

FIGURE 4 Hypothetical model of amyloid beta (Aβ) oligomers in cerebrospinal fluid (CSF) within the Alzheimer's disease (AD) continuum. (A) Along the trajectory of biomarkers during AD progression from high Aβ42 and low pTau (A−T−) to lowered Aβ42 first (A+T−) followed by elevated pTau (A+T+), Aβ oligomers start to rise until a turning point is reached. Soon after pTau starts to increase, Aβ oligomer concentrations decrease. This panel is a zoomed-in portion of Figure 3B. Data are represented in a binned form. (B) Hypothetical changes of Aβ oligomers during disease progression are transferred to the model of AD biomarker changes according to Jack et al.[1] Apolipoprotein E (*APOE*) gene ε4 allele carriers show higher oligomer concentrations with a peak at a more advanced disease stage but still in the early stages of the disease. Due to the high age of the cohort (60+) and the absence of persons with advanced AD, it was not possible to cover the entire x-axis with the curves. For validation of the model, Figure S5 shows a comparison between the measured oligomer level and the oligomer level determined by regression. Figure modified after Jack et al.[33]

noncarriers the peak is reached during the SCD stage, whereas in *APOE* ε4 carriers it is reached at the MCI stage (Figure 4B). Regardless of the *APOE* ε4 status, Aβ oligomer levels already decrease within the MCI stage.

4 | DISCUSSION

In the present study we measured Aβ oligomers in CSF aiming to allocate the presence of these most neurotoxic Aβ species within the neurobiological continuum of AD and thereby elucidate the temporal sequence of Aβ oligomers in AD pathology. Our work provides novel evidence for the importance of Aβ oligomers in early biological and symptomatic disease stages, as we found the highest levels of Aβ oligomers in participants with the clinical diagnosis of MCI. However, 59.8% of SCD and 27.7% of MCI participants did not have evidence for amyloid pathology and might therefore not suffer from AD. Stratification for amyloid positivity (ie, A+ vs A−) alone yielded significant differences within the SCD group and enhanced the discrimination of SCD and MCI to controls. Strikingly, stratification of participants by A/T

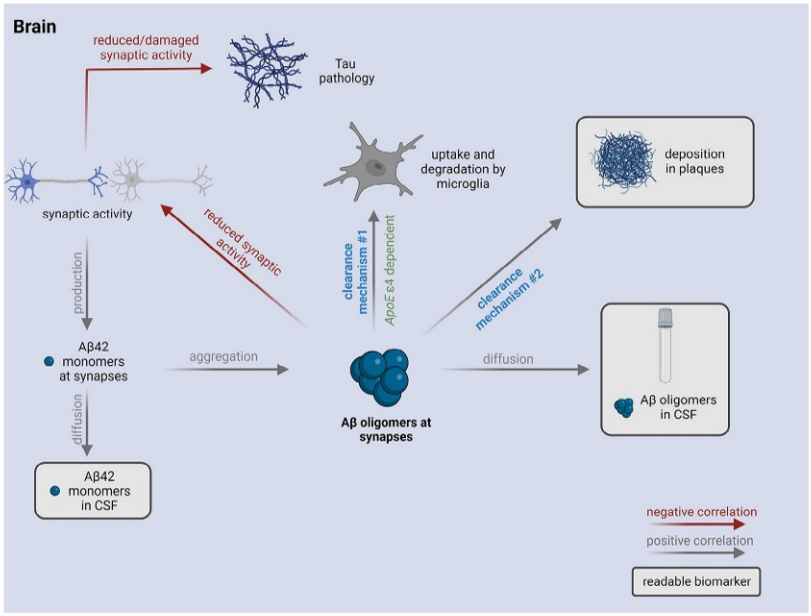

FIGURE 5 Proposed clearance mechanisms for amyloid beta (Aβ) oligomers and the influence on the use of Aβ oligomers as biomarker. Hypothetic scenario: Aβ monomer production at synapses is dependent on synaptic activity. At a certain time point, aggregation of Aβ monomers leads to the formation of toxic Aβ oligomers which can be cleared by different mechanisms. Aβ oligomers can be degraded by microglia (clearance mechanism #1), diffuse into cerebrospinal fluid (CSF), or be deposited into plaques (clearance mechanism #2) as soon as there are plaques. Formation of plaques in patients with amyloid pathology allows oligomers to be deposited there (clearance mechanism #2), which may well become the preferred fate of Aβ oligomers. Figure created with BioRender.com. *APOE* ε4, apolipoprotein E ε4 allele.

biomarker profiles, thereby also taking tau pathology as reflected by CSF pTau into account, yielded significantly elevated Aβ oligomer levels in individuals with an A+/T− biomarker profile compared to participants with nonpathological AD biomarkers (A−/T−) on the one hand, and full-blown AD neuropathological changes (A+/T+ profile) on the other. Consequently, Aβ oligomers in our cohort peak in early disease stages, where tau pathology is still inconspicuous (A+T−). Intuitively, one may assume that while Aβ aggregation is increasing in the brain during early disease stages, the Aβ oligomer level is also rising in the CSF. That is exactly what we observed in the present study when comparing A−T− with A+T− subjects. Rather surprisingly, we observed reduced Aβ oligomer levels in the more advanced disease stage A+T+ compared to the earlier A+T− stage. Deposition of oligomer species into plaques or breakdown of active clearance mechanisms from brain to CSF are just two of many possible explanations (Figure 5). To elucidate the relationship of Aβ oligomers, Aβ42, and pTau (Figure 3), we calculated a chronological sequence of Aβ oligomer levels based on the regression model and superimposed it to key biomarkers of AD as depicted in Figure 4. With respect to the limited range of disease stages within our cohort, lacking very early and advanced disease stages, no statements about oligomer levels over the whole spectrum of disease stages can be made. A limitation of the study is the low number of samples from stage 1 of AD to determine the age at which Aβ oligomer levels start to rise. According to our model, Aβ oligomers start to rise approximately at the beginning of stage 2 and reach their peak early in stage 3 before the oligomer level decreases again, which is in line with previous studies.[34,35] However, other studies, which did not include early stages, reported increased Aβ oligomer concentrations in CSF samples of demented patients compared to the control group[21,34,36] or no differences between dementia or MCI and controls.[37] In addition to differences in patient preanalytical variables such as freeze-thaw cycles, storage period, or centrifugation of the samples,[38] different results may be caused by the choice of assay setups, especially regarding the selection of antibodies,[35] targeting different epitopes and oligomer structures. More recent publications focused on blood-based detection reported increased Aβ oligomer levels in plasma over the course of the disease or a correlation with amyloid-PET positivity.[39–41]

We further investigated the effect of *APOE* ε4 positivity on Aβ oligomer levels. As can be seen in the regression model (Figure 3) and the hypothetical model of Aβ oligomer changes (Figure 4), *APOE* ε4 carriers showed higher oligomer levels. Notably, in *APOE* ε4 carriers, the Aβ oligomer level in CSF peaks further right of the peak in *APOE* ε4 noncarriers. This is not later in time, but further down in disease progression strengthening the view that *APOE* ε4 carriers start earlier into the Alzheimer's continuum.[22,42]

Although Aβ and tau oligomers show a highly significant correlation, no differences of tau oligomers with respect to the biomarker

profile or the clinical syndrome were observed, which is in line with previous findings from our lab.[19] In the present study, we investigated patients who were at mild disease stages when enrolled in the DELCODE study.[23] Presumably, tau oligomers in CSF might be increased and detectable in late stages of dementia. Indeed, a previous study from Sengupta et al. reported elevated tau oligomers only at moderate to severe dementia.[43]

Our results emphasize the relevance of the biologically based definition of Alzheimer's disease, as Aβ oligomers, which are thought to be the major toxic species in the disease, are only increased in patients with abnormal Aβ42. Moreover, we have previously demonstrated that sFIDA is now a robust method to quantitate aggregates from tau, α-synuclein, and Aβ in body fluids.[17–20,30] To further understand the differences between assay outcomes and investigate setups or antibodies which are best suited for diagnosis, it will be of great interest to measure a pool of samples with diverse Aβ oligomer assays. Probably, the combination of different oligomer biomarkers improves the understanding of the underlying pathology and the diagnostic accuracy as calculated by the probability analysis of Lewczuk et al.[44] In particular, longitudinal analysis of Aβ and tau oligomer concentrations over a longer period of time may support our model of Aβ oligomer concentration changes and add to our understanding about which patients at a predementia stage will develop AD in the future. Besides the diagnostic aspects, Aβ oligomers measured by sFIDA are promising biomarkers for clinical drug development to easily monitor their effects.[20]

AUTHOR CONTRIBUTIONS

Victoria Kraemer-Schulien, Lara Blömeke, and Marlene Pils developed the assay. Victoria Kraemer-Schulien performed the experiments together with Lara Blömeke and Marlene Pils. Fabian Rehn, Victoria Kraemer-Schulien, and Lara Blömeke analyzed the data and carried out the statistics. Lara Blömeke, Fabian Rehn, and Victoria Kraemer-Schulien wrote the manuscript together with Oliver Peters, Marlene Pils, Oliver Bannach, and Dieter Willbold. Oliver Bannach, Dieter Willbold, and Oliver Peters supervised the project. Piotr Lewczuk and Johannes Kornhuber were involved in the establishment of the assay. Janine Kutzsche, Tuyen Bujnicki, Luisa-Sophie Schneider, Silka D. Freiesleben, and Michael Wagner carefully revised the manuscript. Lukas Preis, Josef Priller, Eike J. Spruth, Slawek Altenstein, Anja Schneider, Klaus Fliessbach, Jens Wiltfang, Frank Jessen, Wenzel Glanz, Katharina Buerger, Daniel Janowitz, Robert Perneczky, Boris-Stephan Rauchmann, Stefan Teipel, Ingo Kilimann, Doreen Goerss, Christoph Laske, Matthias H. Munk, Michael Ewers, Emrah Düzel, Andrea Lohse, Niels Hansen, Ayda Rostamzadeh, Enise I. Incesoy, Michaela Butryn, Carolin Sanzenbacher, Matthias Schmid were responsible for the management of the DELCODE study at the various sites. Oliver Peters, Frank Jessen, Annika Spottke, Nina Roy-Kluth, Michael T. Heneka, Frederic Brosseron, Steffen Wolfsgruber, Luca Kleineidam, Melina Stark, Michaela Butryn, and Emrah Düzel were responsible for methodological core central data management and quality control of the DELCODE study.

ACKNOWLEDGMENTS

We received funding from the programs "Biomarkers Across Neurodegenerative Diseases I + II" of The Alzheimer's Association, Alzheimer's Research UK and the Weston Brain Institute (11084 and BAND-19-614337). We are also grateful for support from The Michael J. Fox Foundation for Parkinson's Research (14977, 009889), from the ALS Association, and from the Packard Center (19-SI-476). We further received funding from the Deutsche Forschungsgemeinschaft (INST 208/616-1 FUGG, INST 208/794-1 FUGG) and the Helmholtz Association (HVF0079).

Open access funding enabled and organized by Projekt DEAL.

CONFLICTS OF INTERESTS STATEMENT

Dieter Willbold and Oliver Bannach are co-founders and shareholders of attyloid GmbH. This had no influence of the interpretation of the data. All other authors declare no competing interests related to this work. The sFIDA method is protected by patents EP3271724A1, EP3014279B1 and EP2794655B1. Author disclosures are available in the supporting information.

CODE AVAILABILITY STATEMENT

For image data analysis, we used the sFIDAta software tool which can be made available upon request.

DATA AVAILABILITY STATEMENT

The authors confirm that the data supporting the findings of this study are available within the article and its supplementary materials.

CONSENT STATEMENT

All local institutional review boards and ethical committees approved the study protocol. All participants gave written informed consent before inclusion in the study. DELCODE is registered at the German clinical trials register (drks00007966) (04/may/2015).

REFERENCES

1. Jack CR Jr, Bennett DA, Blennow K, et al. NIA-AA Research framework: toward a biological definition of Alzheimer's disease. *Alzheimer's Dement*. 2018;14:535-562.
2. Jack CR Jr, Holtzman DM. Biomarker modeling of Alzheimer's disease. *Neuron*. 2013;80:1347-1358.
3. Villemagne VL, Burnham S, Bourgeat P, et al. Amyloid beta deposition, neurodegeneration, and cognitive decline in sporadic Alzheimer's disease: a prospective cohort study. *Lancet Neurol*. 2013;12:357-367.
4. Tolar M, Hey J, Power A, Abushakra S. Neurotoxic soluble amyloid oligomers drive Alzheimer's pathogenesis and represent a clinically validated target for slowing disease progression. *Int J Mol Sci*. 2021;22(12):6355.
5. Larson ME, Lesné SE. Soluble Aβ oligomer production and toxicity. *J Neurochem*. 2012;120(supp l):125-139.
6. Brinkmalm G, Hong W, Wang Z, et al. Identification of neurotoxic cross-linked amyloid-beta dimers in the Alzheimer's brain. *Brain*. 2019;142:1441-1457.
7. Gaspar RC, Villarreal SA, Bowles N, Hepler RW, Joyce JG, Shughrue PJ. Oligomers of beta-amyloid are sequestered into and seed new plaques in the brains of an AD mouse model. *Exp Neurol*. 2010;223:394-400.
8. Iljina M, Garcia GA, Dear AJ, et al. Quantitative analysis of co-oligomer formation by amyloid-beta peptide isoforms. *Sci Rep*. 2016;6:28658.

9. O'Brien RJ, Wong PC. Amyloid precursor protein processing and Alzheimer's disease. *Annu Rev Neurosci*. 2011;34:185-204.
10. Olsson B, Lautner R, Andreasson U, et al. CSF and blood biomarkers for the diagnosis of Alzheimer's disease: a systematic review and meta-analysis. *Lancet Neurol*. 2016;15:673-684.
11. Lewczuk P, Lukaszewicz-Zajac M, Mroczko P, Kornhuber J. Clinical significance of fluid biomarkers in Alzheimer's disease. *Pharmacol Rep*. 2020;72:528-542.
12. Bilousova T, Miller CA, Poon WW, et al. Synaptic amyloid-β oligomers precede p-Tau and differentiate high pathology control cases. *Am J Pathol*. 2016;186:185-198.
13. Hefti F, Goure WF, Jerecic J, Iverson KS, Walicke PA, Krafft GA. The case for soluble Aβ oligomers as a drug target in Alzheimer's disease. *Trends Pharmacol Sci*. 2013;34:261-266.
14. Hayden EY, Teplow DB. Amyloid β-protein oligomers and Alzheimer's disease. *Alzheimer's Res Ther*. 2013;5:60.
15. Kiselica AM. Empirically defining the preclinical stages of the Alzheimer's continuum in the Alzheimer's disease neuroimaging initiative. *Psychogeriatrics*. 2021;21:491-502.
16. Knopman DS, Haeberlein SB, Carrillo MC, et al. The National Institute on Aging and the Alzheimer's Association Research Framework for Alzheimer's disease: perspectives from the research roundtable. *Alzheimer's Dement*. 2018;14:563-575.
17. Pils M, Rutsch J, Eren F, et al. Disrupted-in-schizophrenia 1 (DISC1) protein aggregates in cerebrospinal fluid are elevated in first-episode psychosis patients. *Psychiatry Clin Neurosci*. 2023;77:665-671.
18. Schaffrath A, Schleyken S, Seger A, et al. Patients with isolated REM-sleep behavior disorder have elevated levels of alpha-synuclein aggregates in stool. *NPJ Parkinson's Dis*. 2023;9:14.
19. Bloemeke L, Pils M, Kraemer-Schulien V, et al. Quantitative detection of alpha-synuclein and Tau oligomers and other aggregates by digital single particle counting. *NPJ Parkinsons Dis*. 2022;8:68.
20. Kass B, Schemmert S, Zafiu C, et al. Abeta oligomer concentration in mouse and human brain and its drug-induced reduction ex vivo. *Cell Rep Med*. 2022;3:100630.
21. Wang-Dietrich L, Funke SA, Kuhbach K, et al. The amyloid-beta oligomer count in cerebrospinal fluid is a biomarker for Alzheimer's disease. *J Alzheimer's Dis*. 2013;34:985-994.
22. Yamazaki Y, Zhao N, Caulfield TR, Liu CC, Bu G. Apolipoprotein E and Alzheimer disease: pathobiology and targeting strategies. *Nat Rev Neurol*. 2019;15:501-518.
23. Jessen F, Spottke A, Boecker H, et al. Design and first baseline data of the DZNE multicenter observational study on predementia Alzheimer's disease (DELCODE). *Alzheimer's Res Ther*. 2018;10:15.
24. Jessen F, Wolfsgruber S, Kleineindam L, et al. Subjective cognitive decline and stage 2 of Alzheimer disease in patients from memory centers. *Alzheimer's Dement*. 2022;19(2):487-497.
25. Hülsemann M, Zafiu C, Kühbach K, et al. Biofunctionalized silica nanoparticles: standards in amyloid-beta oligomer-based diagnosis of Alzheimer's disease. *J Alzheimer's Dis*. 2016;54:79-88.
26. Kühbach K, Hülsemann M, Herrmann Y, et al. Application of an amyloid beta oligomer standard in the sFIDA assay. *Front Neurosci*. 2016;10:8.
27. Kravchenko K, Kulawik A, Hülsemann M, et al. Analysis of anticoagulants for blood-based quantitation of amyloid beta oligomers in the sFIDA assay. *Biol Chem*. 2017;398:465-475.
28. Herrmann Y, Bujnicki T, Zafiu C, et al. Nanoparticle standards for immuno-based quantitation of alpha-synuclein oligomers in diagnostics of Parkinson's disease and other synucleinopathies. *Clin Chim Acta*. 2017;466:152-159.
29. Herrmann Y, Kulawik A, Kuhbach K, et al. sFIDA automation yields sub-femtomolar limit of detection for Aβ aggregates in body fluids. *Clin Biochem*. 2017;50:244-247.
30. Pils M, Dybala A, Rehn F, et al. Development and implementation of an internal quality control sample to standardize oligomer-based diagnostics of Alzheimer's disease. *Diagnostics*. 2023;13:1702.
31. Vermunt L, Sikkes SAM, van den Hout A, et al. Duration of preclinical, prodromal, and dementia stages of Alzheimer's disease in relation to age, sex, and APOE genotype. *Alzheimer's Dement*. 2019;15:888-898.
32. Alzheimer's Association. 2022 Alzheimer's disease facts and figures. *Alzheimer's Dement*. 2022;18:700-789.
33. Jack CR, Knopman DS, Jagust WJ, et al. Hypothetical model of dynamic biomarkers of the Alzheimer's pathological cascade. *The Lancet Neurology*. 2010;9:119-128.
34. Holtta M, Hansson O, Andreasson U, et al. Evaluating amyloid-beta oligomers in cerebrospinal fluid as a biomarker for Alzheimer's disease. *PLOS ONE*. 2013;8:e66381.
35. Yang T, O'Malley TT, Kanmert D, et al. A highly sensitive novel immunoassay specifically detects low levels of soluble Aβ oligomers in human cerebrospinal fluid. *Alzheimer's Res Ther*. 2015;7:14.
36. Savage MJ, Kalinina J, Wolfe A, et al. A sensitive Aβ oligomer assay discriminates Alzheimer's and aged control cerebrospinal fluid. *J Neurosci*. 2014;34:2884-2897.
37. Jongbloed W, Bruggink KA, Kester MI, et al. Amyloid-beta oligomers relate to cognitive decline in Alzheimer's disease. *J Alzheimer's Dis*. 2015;45:35-43.
38. Dulewicz M, Kulczynska-Przybik A, Mroczko P, Kornhuber J, Lewczuk P, Mroczko B. Biomarkers for the diagnosis of Alzheimer's disease in clinical practice: the role of CSF biomarkers during the evolution of diagnostic criteria. *Int J Mol Sci*. 2022:23:8598.
39. Babapour Mofrad R, Scheltens P, Kim S, et al. Plasma amyloid-beta oligomerization assay as a pre-screening test for amyloid status. *Alzheimer's Res Ther*. 2021;13:133.
40. Liu L, Kwak H, Lawton TL, et al. An ultra-sensitive immunoassay detects and quantifies soluble Aβ oligomers in human plasma. *Alzheimer's Dement*. 2022;18:1186-1202.
41. Shea D, Colasurdo E, Smith A, et al. SOBA: development and testing of a soluble oligomer binding assay for detection of amyloidogenic toxic oligomers. *Proc Natl Acad Sci U S A*. 2022;119:e2213157119.
42. Leoni V. The effect of apolipoprotein E (ApoE) genotype on biomarkers of amyloidogenesis, tau pathology and neurodegeneration in Alzheimer's disease. *Clin Chem Lab Med*. 2011;49:375-383.
43. Sengupta U, Portelius E, Hansson O, et al. Tau oligomers in cerebrospinal fluid in Alzheimer's disease. *Ann Clin Transl Neurol*. 2017;4:226-235.
44. Lewczuk P, Wiltfang J, Kornhuber J, Verhasselt A. Distributions of Aβ42 and Aβ42/40 in the cerebrospinal fluid in view of the probability theory. *Diagnostics*. 2021;11:2372.

SUPPORTING INFORMATION

Additional supporting information can be found online in the Supporting Information section at the end of this article.

How to cite this article: Blömeke L, Rehn F, Kraemer-Schulien V, et al. Aβ oligomers peak in early stages of Alzheimer's disease preceding tau pathology. *Alzheimer's Dement*. 2024;16:e12589. https://doi.org/10.1002/dad2.12589

2.2.2 Blood-based quantification of Aβ oligomers indicates impaired clearance from brain in ApoE ε4 positive subjects

Autoren:	Lara Blömeke, **Fabian Rehn**, Marlene Pils, Victoria Kraemer-Schulien, Anne Cousin, Janine Kutzsche, Tuyen Bujnicki, Silke Dawn Freiesleben, Luisa-Sophie Schneider, Lukas Preis, Josef Priller, Eike Jakob Spruth, Slawek Altenstein, Anja Schneider, Klaus Fliessbach, Jens Wiltfang, Niels Hansen, Ayda Rostamzahdeh, Emrah Düzel, Wenzel Glanz, Enise I. Incesoy, Katharina Buerger, Daniel Janowitz, Michael Ewers, Robert Perneczky, Boris-Stephan Rauchmann, Stefan Teipel, Ingo Kilimann, Christoph Laske, Matthias H. Munk, Annika Spottke, Nina Roy, Michael T. Heneka, Frederic Brosseron, Michael Wagner, Sandra Roeske, Alfredo Raminez, Matthias Schmid, Frank Jessen, Oliver Bannach, Oliver Peter, Dieter Willbold
Journal:	*Communications Medicine 4(2), 1-13 (Dezember, 2024)* *DOI: 10.1038/s43856-024-00690-w*
Beitrag:	Entwicklung und Durchführung der FPS-Reduzierung Aufbereitung und Kalibration der Rohdaten Statistische Analysen Diskussion der Ergebnisse
Druckgenehmigung:	Siehe Anhang 11.

communications medicine

Article

https://doi.org/10.1038/s43856-024-00690-w

Blood-based quantification of Aβ oligomers indicates impaired clearance from brain in *ApoE* ε4 positive subjects

Lara Blömeke[1,2], Fabian Rehn[1,2], Marlene Pils[1,2], Victoria Kraemer-Schulien[1], Anneliese Cousin[1], Janine Kutzsche[1], Tuyen Bujnicki[1], Silka D. Freiesleben[3,4], Luisa-Sophie Schneider[3,4], Lukas Preis[3,4], Josef Priller[3,5,6,7], Eike J. Spruth[3,5], Slawek Altenstein[3,5], Anja Schneider[8,9], Klaus Fliessbach[8,9], Jens Wiltfang[10,11,12], Niels Hansen[11], Ayda Rostamzadeh[13], Emrah Düzel[14,15], Wenzel Glanz[14], Enise I. Incesoy[14,15,16], Katharina Buerger[17,18], Daniel Janowitz[18], Michael Ewers[17,18], Robert Perneczky[17,19,20,21], Boris-Stephan Rauchmann[19,22,23], Stefan Teipel[24,25], Ingo Kilimann[24,25], Christoph Laske[26,27], Matthias H. Munk[26,28], Annika Spottke[8,9,29], Nina Roy[8], Michael T. Heneka[30], Frederic Brosseron[8], Michael Wagner[8,9], Sandra Roeske[8], Alfredo Ramirez[8,9,31,32,33], Matthias Schmid[8,34], Frank Jessen[8,11,31], Oliver Bannach[1,2], Oliver Peters[3,4] & Dieter Willbold[1,2,35] ✉

Abstract

Background Quantification of Amyloid beta (Aβ) oligomers in plasma enables early diagnosis of Alzheimer's Disease (AD) and improves our understanding of underlying pathologies. However, quantification necessitates an extremely sensitive and selective technology because of very low Aβ oligomer concentrations and possible interference from matrix components.

Methods In this report, we developed and validated a surface-based fluorescence distribution analysis (sFIDA) assay for quantification of Aβ oligomers in plasma.

Results The blood-based sFIDA assay delivers a sensitivity of 1.8 fM, an inter- and intra-assay variation below 20% for oligomer calibration standards and no interference with matrix components. Quantification of Aβ oligomers in 359 plasma samples from the DELCODE cohort reveals lower oligomer concentrations in subjective cognitive decline and AD patients than healthy Control participants.

Conclusions Correlation analysis between CSF and plasma oligomer concentrations indicates an impaired clearance of Aβ oligomers that is dependent on the *ApoE* ε4 status.

Plain language summary

People with Alzheimer's disease have difficulties with reasoning and communication. In Alzheimer's disease, small proteins called amyloid beta (Aβ) stick together, forming tiny clusters in the brain that eventually grow larger. In this study, we aimed to measure these clusters in the blood. When we tested our method on blood samples from 359 people, we surprisingly found that people with Alzheimer's disease and memory problems had fewer clusters of Aβ compared to healthy individuals. Our finding suggests that genetic factors may influence the body's ability to clear these clusters from the brain.

Although Alzheimer's Disease (AD) is the most prominent neurodegenerative disorder affecting 50 million people worldwide[1], there remains a lack of therapeutic options and diagnostic tools, such as a blood-based test suitable for use in primary care. As increasing evidence supports the role of Amyloid beta (Aβ) oligomers as the most toxic component in AD progression[2–4], these oligomers represent a promising biomarker candidate for diagnosis of AD and drug development. The level of Aβ oligomers in the brains of AD patients are higher and, because of the direct connection to brain parenchyma and liquor[5], also in cerebrospinal fluid (CSF), as supported by previous studies[6–9]. Moreover, more than 50% of monomeric brain Aβ is transferred and cleared in the periphery[10], reaching the blood via blood-brain-barrier (BBB), blood-CSF barrier (BCSFB) or perivascular and glymphatic clearance[11].

Although the exact clearance mechanisms of Aβ oligomers from the brain and CSF to plasma remain largely unknown, earlier studies have confirmed the presence of Aβ oligomer species in plasma samples[12].

However, disease progression may lead to a reduction in Aβ oligomers in plasma samples because of their deposition in amyloid plaques and impaired clearance from the brain into the blood stream[13]. For example, an inverse correlation between efficiency of glymphatic clearance and oligomer size has been described[2]. Additionally, transport of Aβ across the BBB is affected in AD patients, especially in carriers of the AD risk gene allele

A full list of affiliations appears at the end of the paper. ✉e-mail: d.willbold@fz-juelich.de

https://doi.org/10.1038/s43856-024-00690-w

apolipoprotein E (*ApoE*) ε4[2,14]. Quantification of Aβ oligomer concentrations in plasma samples, especially in early disease stages, and in-depth analysis of dependencies between Aβ oligomers and different biomarkers will improve our understanding of the role of amyloid pathology in AD.

Previous studies have reported higher oligomer concentrations in AD patients[13,15–17]. All of the methods applied in these studies detect specific subtypes of Aβ oligomers, depending on the respective antibody used. For Aβ oligomers derived from the brain, a broad range of species was described, ranging from small molecular weight oligomers like dimers and trimers via 56mers and spherical oligomers like Aβ derived diffusible ligands (ADDLs) to high-molecular weight oligomers and protofibrils[18,19]. For these species, differences have been claimed for their neurotoxicity and pathologic mechanisms, like impairment of mitochondrial dysfunction, Ca^{2+} homeostasis dysregulation and induction of tau pathology[18].

The most widely described method for detection of Aβ oligomers in plasma is the multimer detection system (MDS) which uses $Aβ_{1-42}$ to amplify the signal and is therefore a tool to measure the oligomerization tendency of on-pathway oligomers. Using this method, AD patients showed significantly increased MDS signal compared to the control group[15,20,21] and the correlation with cognitive decline using neuropsychological tests like MMSE and CERAD[20,22,23]. Other methods used oligomer specific antibodies to quantify those oligomer species that are recognized by the respective specific antibody[12,17,24]. A third method claimed to quantify the alpha-sheet content of oligomers in plasma using specifically designed alpha-sheet peptides[25].

In contrast to these methods, the surface-based fluorescence intensity distribution analysis (sFIDA) technology aims to quantify all oligomer species, irrespective of their conformation, morphology and size, all of them potentially relevant for disease development and progression. sFIDA is a versatile platform for quantification of protein aggregates in biofluids that features single particle sensitivity due to a microscopy-based readout and selectivity for aggregated Aβ because of the use of antibodies with overlapping or even identical linear epitopes at the N-terminus of Aβ (principle of sFIDA in Fig. 1a). Quantifying the total amount of oligomeric species is crucial for quantitation of target engagement in the development of anti-oligomeric drugs. New therapies aim to eliminate Aβ oligomers. Using a diagnostic tool that captures all oligomer species may show the effect of this anti-oligomeric drug irrespective of the exact mechanism of action and the target oligomer species.

As calibration standard for oligomer-based assay, we previously established protein conjugated silica nanoparticles (SiNaPs)[26–28]. Additionally, we demonstrated that sFIDA sensitively and specifically detects alpha synuclein (αSyn), Tau and Aβ oligomers in CSF samples[9,29]. Nonetheless, the reliable quantification of Aβ oligomers in plasma samples poses an even greater challenge, as plasma typically contains a 200-fold higher total protein

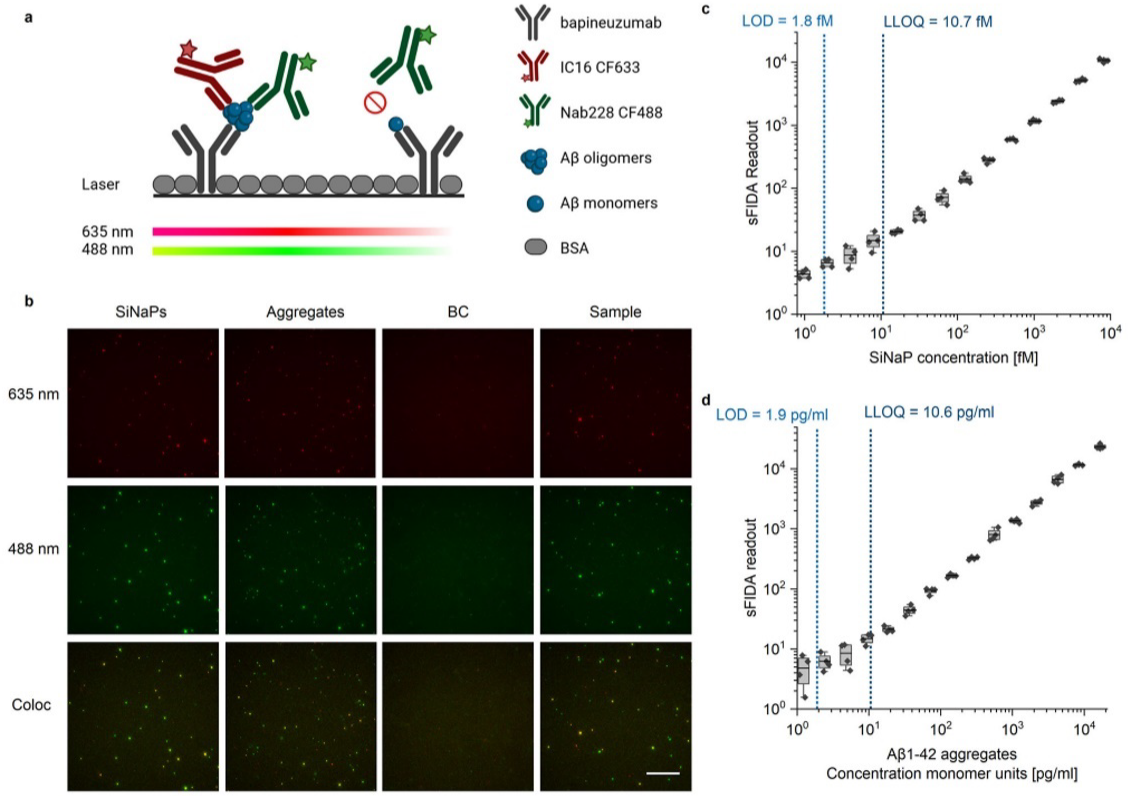

Fig. 1 | Principle of sFIDA setup, imaging and calibration. a The biochemical principle of sFIDA is similar to a sandwich ELISA with capture and detection antibodies directed against overlapping epitopes of the Aβ N-terminus. Therefore, monomers can be captured but not detected as the epitope is already occupied. After preparation, the assay surface is imaged using dual colour fluorescence microscopy (635 and 488 nm, respectively). *Created with biorender.com*. **b** Exemplary images of 500 fM SiNaPs coated with $Aβ_{1-15}$, aggregates composed of 564 pg/ml $Aβ_{1-42}$, a blank plasma (blank control, BC) and an AD plasma sample for the red (illumination with 635 nm) and green (illumination with 488 nm) fluorescence channels and colocalization. For imaging, the gray-scale value of 14-bit images was adjusted to min and max values of 750 and 7500, respectively. The scale bar is 50 µm. **c** Calibration curve of 1 fM to 8 pM $Aβ_{1-15}$ SiNaPs for the colocalization. **d** Dilution series of $Aβ_{1-42}$ aggregates consisting of 1.1 to 18,060 pg/ml $Aβ_{1-42}$ monomers. Boxplots include 25-50% intervals with a line for the mean. Whiskers present 1.5x the interquartile range. Limit of detection (LOD) and lower limit of quantification (LLOQ) were calculated as BC with a single- or ten-fold standard deviation. Standard deviations were calculated across the four replicates. Please note the logarithmic scale.

https://doi.org/10.1038/s43856-024-00690-w

concentration than CSF[5]. This high protein background can lead to false negative readouts because of epitope masking, or false positive readouts because of interferences with human anti-mouse-antibodies[30]. Moreover, Aβ oligomer concentrations are expected to be in the low femto- to even attomolar range[31], thus requiring an extremely sensitive method for detection.

In this report, an sFIDA assay for quantification of Aβ oligomers in plasma samples was developed and validated as a basic research project. We intended to quantitate the total Aβ oligomer levels in plasma samples of the DELCODE cohort to investigate the development of their concentrations during disease progression and their dependency from the *ApoE* ε4 status of the donors.

The sFIDA technology applied for quantifying Aβ oligomers in plasma samples demonstrated femtomolar sensitivity with negligible interference from matrix components making it suitable for quantitation of Aβ oligomers in plasma. Plasma samples from SCD and AD patients exhibited significantly lower Aβ oligomer concentrations compared to controls, particularly in amyloid-positive subjects. Correlation analyses between Aβ oligomers in CSF and plasma revealed a relationship between the two body compartments, influenced by disease progression, the presence of amyloid pathology, and the ApoE ε4 status of the donors.

Methods

SiNaPs

We used our previously developed silica nanoparticle standard (SiNaPs) as an assay control and for calibration. SiNaPs are small, spherical particles with a diameter of ~18.5 nm, which are functionalized with amino acids 1–15 of the Aβ peptide. Synthesis and characterization of the particles have been described previously[28,29] (Supplementary Fig. 1). The silica core of the particles was synthesized via the Stöber process and subsequently modified with APTES (3-aminopropyl(triethoxysilane), Sigma-Aldrich, St. Louis, USA) to create an aminated surface. As a crosslinker between protein and aminated particles, we used maleimido hexanoic acid (MIHA, abcr, Karlsruhe, Germany), which was activated using EDC (1-ethyl-3-(3-dimethylaminopropyl)carbodiimide, Sigma-Aldrich) and NHS (N-hydroxysuccinimide, Sigma-Aldrich). After washing, $Aβ_{1-15}$ (Peptides and Elephants, Henningsdorf, Germany) functionalized with cysteamine at the C-terminus was reacted with the maleimide group of SiNaPs to form a covalent attachment. $Aβ_{1-15}$ was added to achieve a theoretical protein load of ~18 $Aβ_{1-15}$ peptides per SiNaP. After 1 h, TCEP (Tris-(2-carboxyethyl)-phosphine, abcr, Karlsruhe, Germany) was added to prevent oxidation of the cysteamine-functionalized protein, and 1 h later, the reaction was terminated by adding 2-mercaptoethanol. SiNaPs were washed twice with ddH_2O. Prior to use, SiNaPs were subjected to ultrasonication for 15 s at 50% amplitude with a 1 s pulse - 1 s pause cycle.

Aggregates

Aβ aggregates. $Aβ_{1-42}$ was purchased from Bachem AG (Bubendorf, Switzerland). 50 µg aliquots of $Aβ_{1-42}$ were dissolved in 1,1,1,3,3,3-hexafluoroisopropanol (HFIP, Sigma-Aldrich) and divided in 5 µg aliquots. HFIP was then evaporated in a vacuum concentrator (Vacufuge concentrator, Eppendorf, Hamburg, Germany) and stored at RT. 5 µg of $Aβ_{1-42}$ was dissolved in 5 µl dimethyl sulfoxide (DMSO, Sigma-Aldrich) for 10 min with shaking at 650 rpm (Thermomixer, Eppendorf). PBS and 1% sodium azide (AppliChem, Darmstadt, Germany) were added to achieve a concentration of 10 µM $Aβ_{1-42}$ containing 0.04% sodium azide. $Aβ_{1-42}$ was allowed to aggregate for 16 h at RT with shaking at 650 rpm. Aggregates were used directly or stored at −80 °C in 5 µl aliquots. Aβ aggregates have previously been characterized in Pils et al. using Thioflavin T assay (THT) and atomic force microscopy (AFM). Aggregates showed a monodisperse size distribution with a mean diameter of 2.7 nm[32]. We focused on $Aβ_{1-42}$ to prepare artificial aggregates, because in our hands their preparation is more robust and reproducible, and, because the capture and detection antibodies used here do not discriminate between $Aβ_{1-40}$ and $Aβ_{1-42}$.

αSyn aggregates. αSyn (expressed and purified in-house) was dissolved to 1 mg/ml in 20 mM Tris-HCl containing 100 mM sodium chloride (pH 7.4) and incubated for seven days at 37 °C with shaking at 1000 rpm. Aggregates were then sonicated for 60 s in 15 s intervals with a 1 s sonication pulse and a 1 s pause. Aggregates were aliquoted and stored at −80 °C. Preparation of α-Syn aggregates was based on Lohmann et al.[33]. For characterization, AFM measurements were used[33].

Tau aggregates. Full-length Tau (expressed and purified in-house) was dissolved in TBS buffer (Serva, Duisburg, Germany) containing 10-fold excess TCEP. Tau was centrifuged at 18,213 *g* for 1 h at RT and the Tau concentration in the supernatant was determined using UV-Vis spectroscopy. For aggregation, 8 µM heparin and 0.05% sodium azide were added to 15 µM Tau. The mixture was incubated at 37 °C with shaking at 300 rpm every 10 min for 10 days. Tau aggregates were characterized previously including AFM measurement and THT[34].

Fluorescent antibodies

Fluorescently labelled detection antibodies were used for detection of SiNaPs and aggregates. IC16 (Heinrich-Heine-Universität Düsseldorf) was labelled with a red-fluorescent dye (CF633, Sigma-Aldrich), whereas Nab228 (Sigma-Aldrich) was labelled with a green-fluorescent dye (CF488, Sigma-Aldrich). The labelling process, the determination of concentration and degree of labelling are described in the manufacturer's protocol. Purification was carried out with a polyacrylamide bead suspension (Bio-Gel P-30, Bio-Rad Laboratories, Hercules, USA).

Assay setup

Greiner BioOne 384 well plates (Kremsmünster, Austria) were used to ensure an adequate sample and replicate number within one assay. The biochemical principle of sFIDA was described previously[27]. The time course of the sFIDA workflow was illustrated in Fig. 2. For capturing, 40 µl of the humanized monoclonal antibody bapineuzumab (ProteoGenix, Schiltigheim, France) was used at a concentration of 0.625 µg/ml in 0.1 M carbonate buffer (Carl Roth, Karlsruhe, Germany) overnight at 4°C. Wells were washed using an automated microplate washer (405 LS Microplate Washer, BioTec, VT, USA), with five washing cycles with 80 µl TBS-T (TBS (Serva) containing 0.05% Tween (AppliChem)) and five washing cycles with 80 µl TBS. Washing with TBS-T and TBS was performed after each incubation step. After washing, the remaining binding sites were blocking using 0.5% BSA (AppliChem) in TBS containing 0.03% ProClin (Sigma-Aldrich) for 1.5 h at RT. After washing, we first applied 15 µl of LowCross buffer strong (Candor Bioscience, Wangen, Germany) to the wells to reduce matrix effects and then added 15 µl sample or SiNaPs and aggregates spiked in plasma. Samples were centrifuged at 2500 *g* for 5 min prior to analysis. The supernatant was transferred to a new tube and incubated on the plate for 2 h at RT. Fluorescently labelled IC16 CF633 and Nab228 CF488, each at 0.625 µg/ml in TBS containing 0.03% ProClin were first diluted in 0.1% BSA and 0.05% Tween and then centrifuged for 1 h at 100'000 xg. For detection, 20 µl per well of the probes were incubated for 1 h at RT. The TBS buffer was exchanged with 80 µl TBS-ProClin prior to measurement to prevent bacterial growth during measurement and storage. Calibration standards (SiNaPs and aggregates) were spiked and analysed in plasma to prevent plasma matrix effects on the calibration of the results.

Influence of monomeric $Aβ_{1-40}$ and $Aβ_{1-42}$. $Aβ_{1-40}$ was dissolved at 0.1 µg/ml in HFIP, whereas $Aβ_{1-42}$ was dissolved to 10 µM (approximately 45 µg/ml) and shaken for 24 h at RT and 600 rpm. Prior to analysis, monomeric Aβ was diluted to 25 nM in LowCross buffer strong and then to 100 pM in plasma.

Influence of heterophilic anti-mouse antibodies (HAMA). HAMA interference was analysed by spiking different concentrations of goat anti-mouse antibody (Thermo Fisher Scientific, Waltham, USA) in neat plasma. In addition to the capture antibody bapineuzumab, the Nab228 antibody was coated at 2.5 µg/ml in 0.1 M carbonate buffer to the glass surface to compare their HAMA interference in sFIDA.

https://doi.org/10.1038/s43856-024-00690-w **Article**

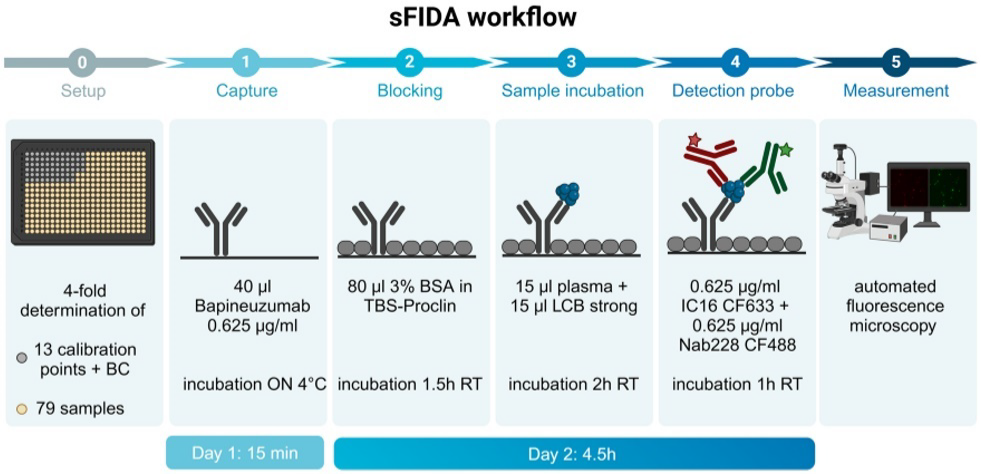

Fig. 2 | Time course of the sFIDA workflow. The use of 384 well plates allow a close-meshed concentration series and the determination of 79 patient samples on one plate in 4-fold replicate determination. The individual steps consist of an over night (ON) incubation of the capture antibody at 4 °C, a 1.5 h blocking step following by 2 h incubation of the plasma samples and 1 h incubation of detection antibodies. The final measurement is conducted by an automated fluorescence microscope. *Created with BioRender.com.*

Influence of haemolysis. Non-haemolytic plasma was spiked with different concentrations of haemolytic plasma to examine the effects of red blood cell haemolysis on assay results. Haemolytic plasma was prepared by freezing whole blood at −80 °C for 24 h and centrifugation at 1200 *g* for 15 min after thawing. Plasma prepared using this procedure is referred to as 100% haemolytic.

Measurement

Measurement of the sFIDA assay surface was performed using total internal reflection microscopy (TIRF-M, Leica DMI6000B, Wetzlar, Germany) with 100x magnification, as described previously (excitation: 635 nm, emission filter: 705 nm; excitation: 488 nm, emission filter: 525 nm; exposure time both channels: 1000 ms; gain 1300)[35]. Each image consisted of 1,000,000 pixels (1000 × 1000 pixels) and in total, 100 images per sample (25 images per well) were measured, which covers 3.14% of the total well surface.

For measurement and calibration of the DELCODE cohort plasma samples, a third fluorescence channel was added (excitation: 405 nm, emission filter: 450 nm) for automated detection and elimination of artificial pixels, as described in statistics.

sFIDAta

The in-house software tool sFIDAta was used for analysis of the images. sFIDAta enables automated detection and elimination of artefact-containing images and counting of pixels above a cutoff value. The cutoff value is defined as the grey-scale value, at which a predefined number of pixels in the blank control are counted and is determined individually for each fluorescence channel and for each experiment to compensate for fluorescence fluctuations. For analysis, a cutoff value of 0.05% (blank control exceeds 500 pixel) was chosen. PixelCount refers to the average number of pixels in an image above the cutoff value for each fluorescent channel, whereas the sFIDA readout describes the number of colocalized pixels that exceed the cutoff value in both fluorescence channels. Min-max filtering was applied to prevent possible remaining artificial images influencing outcomes after artefact detection. Min-max filtering excluded 10% of images per well with the highest fluorescence and 10% of images per well with the lowest PixelCounts[29].

The measurement procedure was extended by an additional step for analysis of DELCODE cohort samples and for inter-assay measurements. After using a red laser (635 nm) and a green laser (488 nm) to detect the IC16 CF633 and Nab228 CF488 antibodies, respectively, a blue laser (405 nm) was used, which does not target any specific antibody. By comparing the colocalized signals with the signals resulting from the blue laser, artificial autofluorescence signals can be detected and removed. This was performed by subtracting the number of autofluorescence pixels above the calculated cutoff from the number of colocalized pixels (corrected sFIDA readouts).

Statistics

Statistical analyses were performed using Excel 2020 (Microsoft corporation, Redmond, USA), Matlab 2019b (The MathWorks, Natick, USA), OriginPro 2020 (OriginLab Corporation, Northhampton, USA) and python 3.9.7 (Python software foundation, Wilmington, USA; packages: pandas 1.3.4, scipy 1.7.1, seaborn 0.11.2).

All samples mentioned in the respective chapters were used for the analyses without further exclusion. As described above, each value is made up of at least 4 replicates.

Intra-assay precision. The PixelCount, coefficient of variation (CV %) and the sFIDA readout were calculated based on the mean value and standard deviation of the four replicates.

Calibration. Linear regression was performed for dilution experiments and to determine the concentration of aggregates in plasma samples. To this end, PixelCounts of the silica nanoparticles and the aggregate standards were weighted with 1/readout.

Corrected sFIDA readouts were used for calibration of DELCODE plasma samples: Based on these adjusted PixelCounts, the calibration of the samples was carried out using the SiNaPs dilution series between 0 and 125 fM for each of the six plates. After regression, the y-intercept of the regression models was subtracted from the respective calibrated values.

The limit of detection (LOD) and die lower limit of quantification (LLOQ) is described in Eqs. (1) and (2) and subsequently converted to a molar concentration using linear regression.

$$LOD[pixel] = PixelCount(blank\ control) + 1\sigma \quad (1)$$

$$LLOQ[pixel] = PixelCount(blank\ control) + 10\sigma \quad (2)$$

https://doi.org/10.1038/s43856-024-00690-w

Analysis of the assay controls is mainly based on colocalization (sFIDA readout).

Inter-assay precision. Inter-assay precision was calculated among six individual experiments. Inter-assay variation for SiNaPs was calculated based on the mean coefficient of variation (CV %) for each concentration and thereafter by calculating the mean among the whole calibration curve. For inter-assay variation of aggregates and samples, we first determined the molar concentrations and afterwards proceeded as described above for inter-assay variation of SiNaPs. The potential significance of experimental differences was further examined by performing ANOVA of repeated measurements for SiNaPs, aggregates and samples with a 5% level of significance.

Dilution linearity. Two-fold dilutions were performed to analyse the influence of dilution on the calibration standard and a simulated plasma sample (aggregates spiked in plasma). sFIDA readouts were calibrated to molar concentrations and corrected by the dilution factor.

Tube transfer. For analysis of the effect of repeated tube transfers on sFIDA readout, 100 µl of plasma were transferred to a new tube, incubated for 5 min at RT and transferred once again (repeated according to the number of tube transfers).

Spike and recovery. A blank plasma sample (reference) and three plasma samples of Control, MCI or AD patients were analysed directly (unspiked) and after spiking with a low (31.3 fM), medium (250 fM) and high (2 pM) concentration of $A\beta_{1-15}$ SiNaPs. Recovery was calculated based on Eq. 3:

$$Recovery[\%] = \frac{sFIDA\ Readout_{spiked\ sample} - sFIDA\ Readout_{non-spiked\ sample}}{sFIDA\ Readout_{spiked\ BC} - sFIDA\ Readout_{non-spiked\ BC}} \quad (3)$$

Pre-analytical and selectivity studies. The effect of freeze-thaw cycles was evaluated using aliquots of six plasma samples, which were thawed repeatedly for 2 h at RT and frozen again[36]. The remaining signal (recovery) and signal reduction for sFIDA readouts of tube transfer, capture control (CC), autofluorescence control (AF), other probes (OP) and immunodepletion (IP) was calculated according to Eq. 4 and Eq. 5 directly, whereas PixelCounts were initially normalized with the blank control.

$$Recovery\ and\ remaining\ signal[\%] = \frac{sFIDA\ readout_{assay\ control}}{sFIDA\ readout_{reference}} * 100\% \quad (4)$$

$$signal\ reduction[\%] = 100\% - remaining\ signal[\%] \quad (5)$$

Capture control. For the capture control, no capture antibody was added in the first incubation step to analyze unspecific binding of the analyte to the assay surface. All other steps were performed as described in Assay setup. For comparison of capture control in plasma and buffer, a cutoff of 0.01% was chosen to reduce the influence of background noise from the different matrices. Capture control refers to the signal of the analyte compared to the assay setup with capture antibody according to Eq. (4).

DELCODE plasma samples. After calibration, samples below the LOD were set to zero. Calibrated concentrations were first tested for normal distribution. For non-normally distributed data, non-parametric tests like Mann-Whitney-U test and Spearman correlation tests were performed.

Bootstrapping. For testing the significance of the Spearman correlation, bootstrapping was applied to all samples with Aβ oligomer concentrations above LOD. This was achieved by performing 5000 replications of the bootstrapping with replacement and calculating the mean Spearman *r* value of the results. After normalization of the standard deviation, bootstrapping *p*-values were calculated using a normal distribution.

Plasma samples

Plasma of validation cohort. Samples of Control, MCI and AD patients were kindly provided by the working group of Oliver Peters at Charité Berlin from patients. Plasma samples were centrifuged, aliquoted to 500 µl and stored at -80 °C. Samples did not undergo a freeze-thaw cycle prior to analysis. Written, informed consent was obtained from all participants. We obtained ethical approval from the Charité Berlin Institutional Review Board, approval number EA2/118/15.

Plasma of DELCODE cohort. Plasma samples were collected as part of the multicentre DZNE-Longitudinal Cognitive Impairment and Dementia Study (DELCODE) at ten clinical centres in Germany, according to a standard operating procedure. After processing, plasma samples were stored at -80 °C[37]. The project was approved by the ethical committee of the Charité Berlin (EA1/074/21 and EA4/066/17). Written, informed consent was obtained from all participants[37].

We received plasma samples from 429 patients, including healthy Controls ($n = 44$), SCD ($n = 148$), MCI ($n = 92$), AD patients ($n = 52$) and first-degree relatives of AD patients ($n = 30$). Sixty-two samples were excluded from analysis because of contamination in one experiment, one sample was excluded because of missing data and seven samples were excluded because of haemolysis. Besides testing cognitive function using different neuropsychological tests (i.e., mini mental state examination (MMSE), Alzheimer's disease assessment scale (ADAS), clinical dementia rating), CSF and plasma biomarkers like $A\beta_{1-40}$, $A\beta_{1-42}$, tau phosphorylated at threonine 181 (pTau) and total tau (tTau) were determined. Information on patient selection, sampling of blood and CSF, neuropathological tests and biomarker quantification are described in Jessen et al.[37]. Subdivision of patient groups by amyloid pathology is based on the $A\beta_{1-42}/A\beta_{1-40}$ ratio with previously established limits[38].

Reporting summary

Further information on research design is available in the Nature Portfolio Reporting Summary linked to this article.

Results

Initially, we validated the sFIDA assay using our $A\beta_{1-15}$-coated silica nanoparticle (SiNaPs) standard[28]. Additionally, Aβ aggregates were used to simulate a positive plasma sample, referred to as internal quality control (IQC). To this end, control plasma samples were spiked with different concentrations of Aβ oligomers. The synthesis and characterization of these aggregates is described in Pils et al. including a setup image in the supplement[32].

Additionally, we confirmed the sensitivity and selectivity of the assay for Aβ oligomers in a validation cohort comprising 20 plasma samples of control subjects (Control), mild cognitive impairment (MCI) and AD patients. Exemplary raw data images for the red and green fluorescence channels and colocalization are shown in Fig. 1b. We then applied the assay to a larger set of plasma samples of the DELCODE cohort, which comprises a control group, subjective cognitive decline (SCD), MCI, AD patients and first-degree relatives of AD patients (Table 1).

sFIDA features high sensitivity and precision

Analytical sensitivity. Quantification of Aβ oligomers in plasma requires extreme sensitivity. Therefore, we initially investigated analytical sensitivity of sFIDA using $A\beta_{1-15}$-coated SiNaPs spiked in plasma and calculated a limit of detection (LOD) of 1.8 fM for the colocalization (Fig. 1c). Dilution linearity of SiNaPs was demonstrated between 2 fM to 8 pM with a mean dilution linearity of 100.6% and coefficient of

https://doi.org/10.1038/s43856-024-00690-w **Article**

Table 1 | Demographic information and biomarker concentrations of participants from the DELCODE cohort (mean ± standard deviation)

	Controls	Relatives	SCD	MCI	AD
Patient information					
number	44	30	146	88	51
% female	45%	63%	42%	45%	67%
Age [years]	68.7 ± 5.2	65.7 ± 5.0	70.8 ± 6.0	71.4 ± 5.0	75.9 ± 5.7
Education [years]	14.5 ± 2.5	14.4 ± 2.7	15.2 ± 2.8	13.6 ± 2.8	13.1 ± 3.1
MMSE	29.6 ± 0.6	29.2 ± 1.1	29.2 ± 1.1	27.5 ± 2.0	23.2 ± 3.3
ApoE ε4 positive	8 (18.2%)	11 (36.7%)	46 (31.5%)	40 (46.0%)[a]	31 (60.8%)
ε2/4	0	1 (3.3%)	4 (2.7%)	3 (3.4%)[a]	2 (3.9%)
ε3/4	8 (18.2%)	10 (33.3%)	39 (26.7%)	32 (36.8%)[a]	21 (41.2%)
ε 4/4	0	0	3 (2.1%)	5 (5.7%)[a]	8 (15.7%)
CSF biomarkers					
$Aβ_{1-40}$ [pg/ml]	9321.1 ± 2617.7	8675.0 ± 2412.6	8679.5 ± 2213.3	8158.6 ± 2378.5[b]	8179.5 ± 2475.2[a]
$Aβ_{1-42}$ [pg/ml]	875.2 ± 344.4	903.6 ± 353.1	808.6 ± 355.3	604.7 ± 309.7[b]	426.6 ± 211.9[a]
$Aβ_{1-42}/Aβ_{1-40}$	0.094 ± 0.024	0.103 ± 0.024	0.092 ± 0.028	0.075 ± 0.030[b]	0.053 ± 0.018[a]
tTau [pg/ml]	413.3 ± 185.1	333.0 ± 135.9	379.1 ± 194.3	532.5 ± 287.4[b]	744.2 ± 344.2[a]
pTau [pg/ml]	54.9 ± 22.6	49.8 ± 20.3	55.9 ± 24.1	69.7 ± 43.3[b]	89.7 ± 34.1[a]
Plasma biomarkers					
$Aβ_{1-40}$ [pg/ml]	76.9 ± 18.7	74.6 ± 19.0	84.3 ± 20.0	86.1 ± 20.8[b]	94.5 ± 28.0[a]
$Aβ_{1-42}$ [pg/ml]	8.8 ± 1.9	8.5 ± 1.7	9.1 ± 1.9	8.5 ± 2.1[b]	9.1 ± 2.5[a]
$Aβ_{1-42}/Aβ_{1-40}$	0.117 ± 0.022	0.115 ± 0.013	0.110 ± 0.015	0.099 ± 0.014[b]	0.094 ± 0.019[a]

SCD subjective cognitive decline, *MCI* mild cognitive impairment, *AD* Alzheimer's Disease.
[a]data not available for one patient.
[b]data not available for two patients.

determination of 0.994. Moreover, an upper limit of quantification (ULOQ) for SiNaPs was determined to be 256 pM, showing a 5-log dynamic range of sFIDA (Supplementary Fig. 2). For recombinant Aβ aggregates as IQC, an LOD of 1.9 pg/ml (monomer unit concentration) and a mean dilution linearity of 98.2% was calculated (Fig. 1d). Colocalization enhances the analytical sensitivity by two-fold for SiNaPs and ten-fold for recombinant aggregates compared to the individual channels red and green (Supplementary Fig. 3). Thus, colocalization was used unless otherwise stated. In a small proof-of-concept study including 20 plasma samples of healthy Control, MCI and AD patients, we measured Aβ oligomer concentrations ranging from 0 to 500 fM, confirming sufficient sensitivity of sFIDA for in vivo Aβ oligomers (sFIDA readouts in Supplementary Fig. 4a). Moreover, these oligomers showed a similar size distribution and amount of colocalization compared to synthetic Aβ-SiNaPs and aggregates (Fig. 1b). Pre-analytical studies indicated that tube transfers and freeze-thaw-cycles should be avoided (Supplementary Fig. 5).

Intra-assay precision. Mean intra-assay variation of SiNaPs among all concentrations was 9.4% for the red fluorescence channel (IC16 CF633), 4.9% for the green fluorescence channel (Nab228 CF488) and 15.5% for colocalization based on four replicates (Fig. 1c). Recombinant aggregates showed a mean intra-assay variation of 19.1% for the colocalization (Fig. 1d).

Inter-assay precision. Repeated measurements of SiNaPs spiked in plasma yielded a mean inter-assay variation of 19.3% for all concentrations tested (Fig. 3a). Calibrated concentrations of BC, two IQC and seven plasma samples showed a mean inter-assay variation of 41.9%. Using repeated measures ANOVA, the individual experiments for measurement of SiNaPs, IQC and plasma samples did not differ significantly (p-value > 0.05).

Aβ oligomer quantification is not influenced by endogenous substances

Recovery and dilution linearity. We spiked three concentrations of SiNaPs in plasma samples from three individual patients to investigate matrix effects and calculated a mean percent recovery of 92% (excluding one concentration/sample) (Supplementary Fig. 6a, b). Additionally, the calibrated concentrations of SiNaPs and aggregates spiked in plasma were not affected by dilution with buffer (Supplementary Fig. 6c, d). The observed negligible effects of the sample matrix in both experiments showed that quantification of Aβ oligomers in individual plasma samples is accurate.

Monomers. In plasma, concentrations of approximately 300 pg/ml $Aβ_{1-40}$ and 20 pg/ml $Aβ_{1-42}$ have been determined[39]. Interference from Aβ monomers on sFIDA measurements was investigated by spiking 452 pg/ml Aβ monomers in a blank plasma sample. As a positive control, the same concentration of aggregated $Aβ_{1-42}$ was used. Monomer samples yielded a signal equivalent to the non-spiked blank control, whereas $Aβ_{1-42}$ aggregates yielded a nearly 100x stronger signal (Fig. 3d), indicating negligible interference from monomeric Aβ at physiologically relevant concentrations in our assay.

HAMA. In sandwich ELISAs, heterophilic antibodies (HA) can crosslink capture and detection antibodies, causing false-positive signals[30]. By changing the capture antibody Nab228, which gave false positive signals at concentrations of 10 ng/ml or higher (Fig. 3e), to bapineuzumab (humanized equivalent to 3D6[40]), interference from the spiked anti-mouse antibody was reduced to <0.005% at the highest concentration tested. Although a false-positive signal was observed at 1000 ng/ml HA, such concentrations are unlikely to be present in human plasma[41].

Cross-reaction with αSyn and Tau aggregates. We next investigated whether other protein aggregates composed of Tau or αSyn cross-reacted

https://doi.org/10.1038/s43856-024-00690-w **Article**

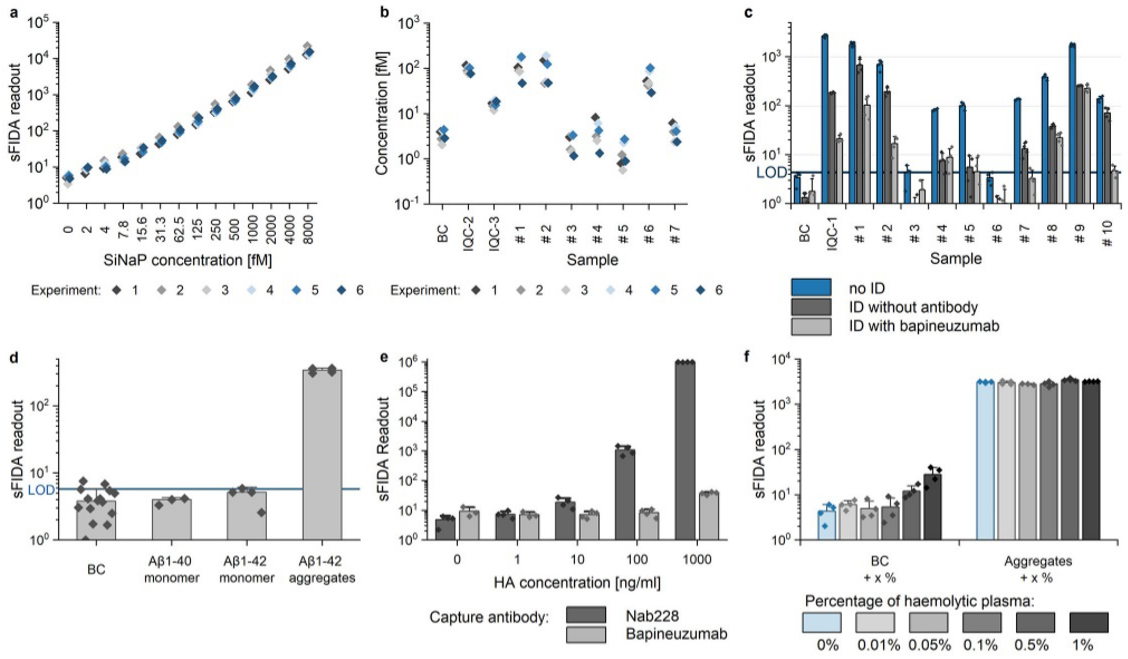

Fig. 3 | Inter-assay variation and specificity controls for Aβ oligomer quantification in plasma. a Repeated preparation of SiNaP calibration in six individual experiments showed an inter-assay variation of 19.3%. **b** Repeated measurements of seven samples of the validation cohort, a blank plasma (BC) and two internal quality controls (IQC, refers to aggregates at 141 pg/ml (IQC-2) and 17.6 pg/ml $Aβ_{1-42}$ monomers (IQC-3), respectively) were calibrated and mean inter-assay variation was calculated as 41.9%. **c** A blank control, $Aβ_{1-42}$ aggregates (IQC-1 with 18 ng/ml $Aβ_{1-42}$ monomer concentration) and 10 plasma samples of Control, MCI and AD patients were subjected to immunodepletion (ID). Unspecific ID (beads without antibody conjugation) resulted in a signal reduction to 6.9% for IQC-1 and to 20.2% for plasma samples for signals above the LOD (limit of detection). However, with specific immunodepletion using bapineuzumab, the signal of IQC-1 was eliminated (signal <1% compared to the non-depleted sample) and that of the samples was reduced on average to 5.1%. **d** Blank plasma (BC) was spiked with 452 pg/ml of $Aβ_{1-40}$, $Aβ_{1-42}$ monomer and aggregates formed from 452 pg/ml $Aβ_{1-42}$ monomer. Samples were analysed by sFIDA. **e** Plasma was spiked with different concentrations of heterophilic antibody (HA) and analysed in two different assay setups, i.e., with monoclonal mouse antibody Nab228 as the capture antibody or with monoclonal humanized antibody bapineuzumab, respectively, to investigate heterophilic antibody interference. **f** Blank plasma and 18 ng/ml Aβ aggregates (concentration based on the monomer unit concentration) were spiked with haemolytic plasma and the effect on detection of aggregates was analysed. Standard deviations were calculated across the four replicates. Please, note the logarithmic scaling.

with our Aβ-specific detection system. The presence of αSyn or Tau aggregates gave no false-positive (BC spiked with αSyn or Tau aggregates) or false-negative signals ($Aβ_{1-42}$ aggregates spiked with αSyn or Tau aggregates), as all signals were ±20% from the non-spiked sample (Supplementary Fig. 4b).

Haemolytic plasma. During blood donation, erythrocytes may be damaged, leading to the release of haemoglobin through haemolysis[42]. As erythrocytes bind Aβ[43], their disruption may affect the sFIDA readout. This potential interference was examined by spiking a non-haemolytic sample with different concentrations of haemolytic plasma. Concentrations of 0.5% and 1% of haemolytic plasma produced a higher background signal, but did not affect aggregate detection (Fig. 2e). However, haemolytic plasma at a concentration of 0.5% gave a visibly reddish colour, indicating that these samples should be excluded from analysis.

sFIDA readouts in plasma samples are solely attributed to Aβ oligomers

Immunodepletion. Immunodepletion was used to further demonstrate that the sFIDA-based Aβ oligomer signal does not originate from the plasma matrix. We removed Aβ species using magnetic beads coated with bapineuzumab, and used magnetic beads that were not coated with antibodies as a control. Non-specific immunodepletion reduced the signal for the recombinant aggregates (IQC-1) by 93.1% and on average by 79.8% for patient samples. In contrast, immunodepletion with bapineuzumab reduced the signal for Aβ aggregates by 99.3% and that of the clinical samples by 94.9% for samples above LOD. Moreover, specific immunodepletion with bapineuzumab yielded a lower signal compared to unspecific immunodepletion for almost every sample tested with a mean signal reduction of 50.3% (Fig. 3c).

Detection probe control. The validation cohort was subjected to sFIDA in the absence of detection antibodies to exclude false-positive signals because of plasma sample autofluorescence. The autofluorescence signal was below the LOD for each sample tested with a mean signal reduction of >99% compared to the signal with detection antibodies (Supplementary Fig. 7a). Possible matrix interferences with IgG detection antibodies in general was investigated by probing plasma samples with an IgG isotype control (MOPC CF633) and an anti-αSyn antibody (211 CF488). The signals of the 20 plasma samples with these non-Aβ-specific probes were also reduced by >97% for the individual channels and colocalization (values of the colocalization are plotted in Supplementary Fig. 4a). Assay specificity was further increased by choosing an assay setup with two different anti-Aβ-probes and analysing only colocalized pixels.

Capture control. As non-specific adherence of Aβ oligomers to surfaces was reported previously[44], we investigated the unspecific binding of the analyte to the sFIDA assay surface by introducing a control where we skip the capture antibody (capture control). In the absence of a capture antibody, SiNaPs and aggregates spiked in plasma showed a signal of

https://doi.org/10.1038/s43856-024-00690-w **Article**

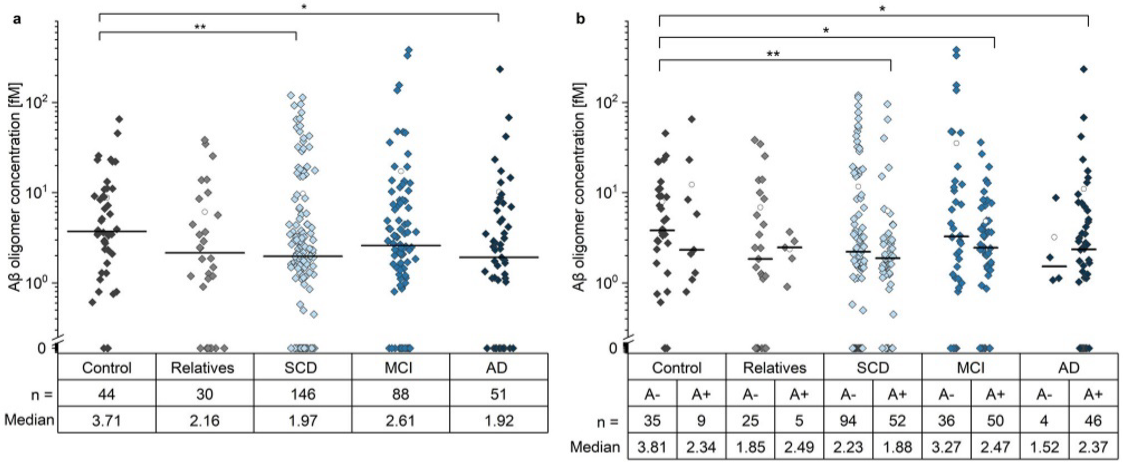

	Control	Relatives	SCD	MCI	AD
n =	44	30	146	88	51
Median	3.71	2.16	1.97	2.61	1.92

	Control		Relatives		SCD		MCI		AD	
	A-	A+	A-	A+	A-	A+	A-	A+	A-	A+
n =	35	9	25	5	94	52	36	50	4	46
Median	3.81	2.34	1.85	2.49	2.23	1.88	3.27	2.47	1.52	2.37

Fig. 4 | Concentrations of Aβ oligomers in plasma samples. a Aβ oligomer concentrations in plasma decreased significantly in SCD and AD patients compared to the Control group (p value SCD: 0.008; AD: 0.017). **b** After subdivision by amyloid pathology (A, based on CSF $Aβ_{1-42}/Aβ_{1-40}$ ratio[37]), SCD, MCI and AD patients positive for amyloid pathology (A +) showed significantly decreased Aβ oligomer concentrations in plasma compared to the amyloid negative (A-) Control group (p value for Control (A-) vs. amyloid positive SCD: 0.002; MCI: 0.041; AD: 0.031). Please note the logarithmic scale. Samples that fell below LOD were set to zero. For reasons of clarity, the median Aβ oligomer concentrations are given for each analysis group below the logarithmically scaled figures (Median; values in fM). Number of samples in each group is referenced as n. SCD subjective cognitive decline, MCI mild cognitive impairment, AD Alzheimer's disease; open circle: mean; line: median, * p-value of Mann-Whitney-U test 0.01 - 0.05; ** p-value of Mann-Whitney-U test 0.001 - 0.01.

33.5% and 54.7%, respectively. However, the signals of SiNaPs and aggregates spiked in buffer were reduced by >99.9% in absence of a capture antibody (Supplementary Fig. 7b), indicating that surface binding is mediated by plasma matrix components. Similar to the calibration standards, five plasma samples tested showed non-specific binding of the analyte to the assay surface, indicated by a signal still at 77.2% (Supplementary Fig. 7c).

Aβ oligomer concentrations in plasma samples are in the low femtomolar range

After analysing the sensitivity and selectivity of the analytical assay and investigating differences among the 20-sample validation cohort, we examined the disease-relevance and correlation with other AD-related biomarkers. Thus, we subjected 359 plasma samples from the DELCODE cohort to sFIDA analysis.

Like the validation cohort, Aβ oligomer concentrations determined in the samples from the DELCODE cohort spanned three orders of magnitude, ranging from 0.4 to 400 fM. Unexpectedly, AD (p-value: 0.017) and SCD (p-value: 0.008) subjects showed a significantly lower plasma Aβ oligomer concentration compared to control subjects using Mann-Whitney-U test, whereas samples of first-degree relatives and MCI patients did not show any significant differences (Fig. 4a). Interestingly, after subdividing groups according to their CSF amyloid pathology status (A + /A-, based on CSF $Aβ_{1-42}/Aβ_{1-40}$ ratio[37]), it became evident that oligomer concentrations are reduced in amyloid positive SCD, MCI and AD patients only (Fig. 4b, p value for Control (A-) vs. amyloid positive SCD: 0.002; MCI: 0.041; AD: 0.031).

Correlations of Aβ oligomers in CSF and plasma depend on cognitive staging, amyloid pathology and *ApoE* status

We performed several correlation analyses to explore the pathophysiological basis for determining Aβ oligomer concentrations in plasma. We performed bootstrapping (re-sampling with replacement, see statistics) to enhance the reliability of our correlation analysis. Moreover, we grouped Control, relatives and SCD patients as well as MCI and AD patients for correlation analysis to enhance clarity and meaningfulness of our statistical analyses. No correlations of Aβ oligomers with Aβ monomers in plasma or with age or MMSE were observed (Supplementary Table 1). In contrast, Aβ oligomers in plasma of MCI and AD patients showed a significant correlation with monomeric Aβ in CSF. We also analysed the correlation of Aβ oligomer concentrations in plasma versus CSF, which were recently measured by sFIDA[45]. Although oligomer concentrations in Control, relatives and SCD patients showed a direct correlation between CSF and plasma, oligomer concentrations in MCI and AD patients showed an inverse correlation (Fig. 5a). In AD, clearance of Aβ species from the brain is hypothesised to be impaired[2], which is probably dependent on the *ApoE* ε4 status or TREM-2 mutations affecting microglia activity[16,17]. Thus, we examined the dependency of Aβ oligomers in CSF and plasma on amyloid pathology or *ApoE* ε4 status. For both Control, relatives and SCD and MCI and AD patient groups, significant correlations were only observed for amyloid negative and *ApoE* ε4 negative patients, respectively. In contrast, when patients are *ApoE* ε4 positive or amyloid positive (A +), no significant correlations were found (Fig. 5b, c).

Discussion

In the present study we adapted the sFIDA technology to quantify Aβ oligomers in human plasma samples. We demonstrated femtomolar sensitivity and low inter- and intra-assay variations for SiNaPs spiked in plasma. In contrast, plasma samples showed an increased inter-assay variation suggesting a yet unknown, possibly pre-analytical influence. However, taking into consideration the inherently high inter-assay variations at low concentrations[48], the 3-log difference between individual samples and the limited effect on the individual ranking of the samples, intra-assay variation was considered to be acceptable currently. Nevertheless, intra- and inter-assay variation may be improved in the future, by in-depth analyses of pre-analytical influences, and by applying full automation of the sFIDA assay to avoid human operator dependent variations, as has been partially applied previously[35].

Investigation of possible interfering factors, such as monomers and HAMA, and analysis of patient plasma samples from the validation cohort confirmed the sensitivity and selectivity of the sFIDA assay for quantification of Aβ oligomers. Although non-specific binding of Aβ oligomers to experimental surfaces did not influence the interpretation of the results, future efforts aim to reduce this issue to avoid signal loss in pre-analytical steps.

https://doi.org/10.1038/s43856-024-00690-w **Article**

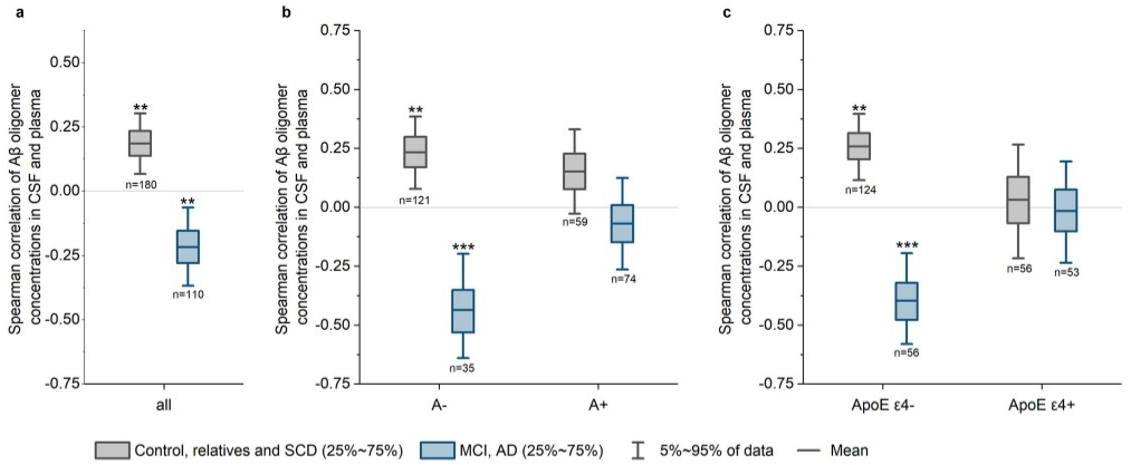

Fig. 5 | Box plots for the bootstrap distribution of the Spearman coefficient of correlation r between Aβ oligomer levels in CSF and plasma. **a** The combined group of Controls, relatives and SCD patients (grey) showed a weak, but significant direct correlation of Aβ oligomer levels in CSF and plasma (Spearman $r = 0.186$, p-value = 0.005), whereas MCI and AD patients (blue) showed an inverse correlation (Spearman $r = -0.217$, p-value = 0.009). **b** The groups were sub-divided by the presence of CSF amyloid pathology (A-/A +) based on the ratio of $A\beta_{1-42}/A\beta_{1-40}$. **c** The groups were sub-divided based on their *ApoE* ε4 status where carrying at least one *ApoE* ε4 allele defines positivity (*ApoE* ε4 +). Only for amyloid negative (A-) or *ApoE* ε4 negative patients, significant correlations between oligomers in CSF and plasma were observed with the Control, relatives and SCD patients showing a direct correlation (A-: Spearman $r = 0.233$, p-value = 0.007; ApoE ε4 negative: Spearman $r = 0.257$, p-value = 0.001) and MCI and AD patients an inverse correlation (A-: Spearman $r = -0.436$, p-value = <0.001; ApoE ε4 negative: Spearman $r = -0.396$, p-value = <0.001). Boxplots include 25-50% intervals with a line for the mean. Whiskers present the 5-95% intervals. p-value of Spearman r distribution: * p-value 0.01 - 0.05, ** p-value 0.001 - 0.01, *** p-value < 0.001.

As the validation experiments showed the suitability of sFIDA to sensitively and specifically quantitate Aβ oligomers in plasma samples, we investigated Aβ oligomer concentrations in 359 plasma samples of the DELCODE cohort. Remarkably, we observed significantly reduced oligomer concentrations in SCD and AD patients compared to the Control group, which is in contrast to previous studies reporting increased Aβ oligomer concentrations in the plasma of AD patients[13,21,25] and a correlation of plasma Aβ oligomer concentration with SCD symptoms[49]. SCD is a heterogeneous condition with many potentially underlying causes – one of them is an early stage of AD[50]. In our cohort, 35.6% of SCD patients were amyloid positive and therefore fulfilling the NIA-AA research framework criteria for an underlying AD[51]. Although at a very early stage of AD, presumably the same mechanisms apply as with MCI and AD patients as discussed below. To interpret the differences to previous studies, it is important to point out, that most of these previous studies detected various oligomeric sub-species because of the use of structure-specific antibodies[17,24], detection of seeding-competent oligomers[21] or α-sheet content[25], whereas sFIDA quantifies the total amount of Aβ oligomers in plasma. It can be hypothesized that the Aβ oligomer subfractions examined by other studies might be subject to different formation and clearing mechanism compared to those described in the present study. Exploring whether differences in patient enrolment or pre-analytical aspects are responsible for these inconsistencies or alternative subpopulations of Aβ oligomers are measured by different assays is essential, and comparative studies using the same set of samples should be conducted. These varying outcomes across different assay setups emphasize the importance of such investigations.

This study aimed to quantify and better understand the potential origin of total Aβ oligomer concentrations in plasma samples. We observed that monomeric Aβ in plasma did not correlate with Aβ oligomers in plasma, whereas a correlation with CSF monomers and oligomers was observed. This observation indicates that Aβ oligomers, at least partially, originate from CSF (Fig. 6 clearance mechanism #4) or directly from the brain (Fig. 6 clearance mechanism #3). Therefore, it is possible that elevated oligomer concentrations in plasma may result from an increase in oligomer concentrations in CSF. Indeed, we observed a positive correlation of Aβ oligomers between CSF and plasma in Controls, relatives and SCD patients. However, this correlation was only evident for patients without amyloid pathology (A-, classification based on CSF $A\beta_{1-42}/A\beta_{1-40}$ ratio[37]) or without the genetic risk factor. We hypothesize that once amyloid positivity becomes evident (A +), Aβ oligomers are preferentially deposited in plaques (clearance mechanism #2), leading to a reduced clearance via other pathways (clearance mechanisms #1, #3, #4). This may explain the absence of a correlation between Aβ oligomers in the CSF and plasma, and the decrease in oligomer concentrations in the plasma of amyloid positive patients. Additionally, impaired clearance mechanisms for Aβ monomers across the BBB, BCSFB and perivascular drainage, and impaired degradation by microglia, have been reported for *ApoE* ε4 carriers (clearance mechanisms #1 and probably #3 and #4)[10,47]. Assuming similar pathological effects for oligomers, the most likely clearance mechanism in *ApoE* ε4 carriers is the deposition of Aβ oligomers into plaques (clearance mechanism #2), which limits the transport and results in a weaker correlation between CSF and plasma.

When interpreting correlations of Aβ oligomers between CSF and plasma in MCI and AD patients, it is important to consider previous sFIDA studies that have quantified Aβ oligomers in CSF. These studies have shown that Aβ oligomer concentrations in CSF are highest in the early stages of the disease and decrease as the disease progresses, particularly in *ApoE* ε4 carriers who have a higher Aβ oligomer burden during the early stages of the disease[45]. Decreasing concentrations of oligomers in CSF in advanced disease stages may arise from negative feedback mechanisms initiated by Aβ oligomers at synapses, resulting in reduced synaptic activity and consequently reduced production of Aβ monomers and replenishment of Aβ oligomers. Additionally, enhanced clearance through other pathways, such as deposition in plaques (clearance mechanism #2) or transport to the blood in a CSF-independent manner, may also contribute to reduced oligomer concentrations in CSF. We observed an inverse correlation of Aβ oligomer concentrations in CSF and plasma indicating an impaired clearance via CSF pathways (clearance mechanism #4) and an uncoupling of Aβ oligomer concentrations in blood and CSF. Moreover, this correlation was not observed for *ApoE* ε4 carriers, which supports the idea that *ApoE* ε4 plays a role in

https://doi.org/10.1038/s43856-024-00690-w **Article**

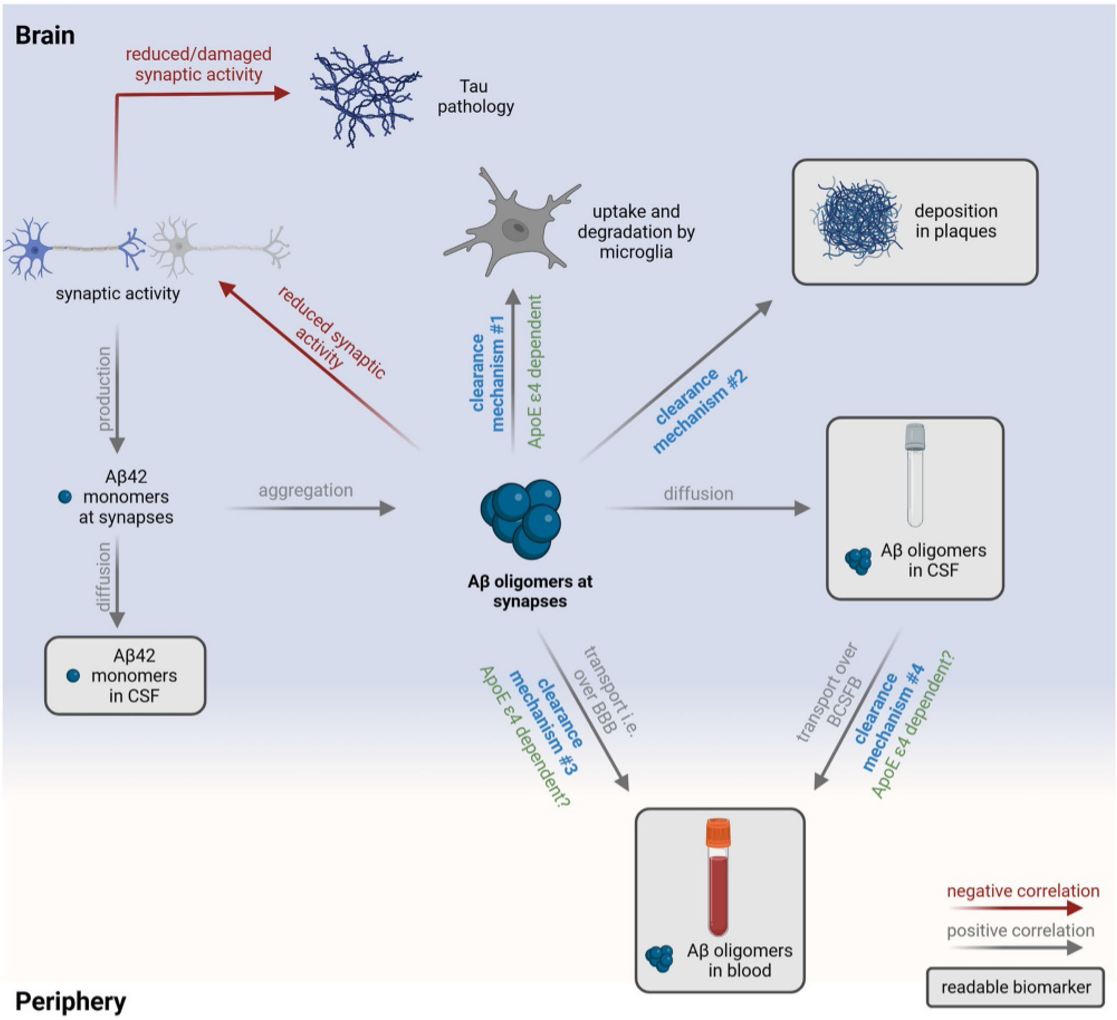

Fig. 6 | Model of the clearance mechanisms for Aβ oligomers and the influence on the use of Aβ oligomers as biomarker. Aβ monomer production at synapses is dependent on synaptic activity[55,56]. At a certain time point, aggregation of Aβ monomers leads to the formation of toxic Aβ oligomers that can be cleared by different mechanisms: Aβ oligomers can be degraded by microglia (clearance mechanism #1), diffuse into CSF or deposited into plaques (clearance mechanism #2). Moreover, Aβ oligomers may be transported to blood either directly across the BBB via glymphatic clearance or interstitial flow (clearance mechanism #3), or after diffusion into CSF and reaching blood via BCSFB (clearance mechanism #4). Formation of plaques in patients with amyloid pathology allows oligomers to be deposited (clearance mechanism #2), which may become the preferred fate of Aβ oligomers. This may lead to reduced clearance to blood and reduced Aβ oligomer concentrations in plasma. Additionally, transport of Aβ oligomers from the brain and CSF to plasma may be inefficient in *ApoE* ε4 carriers influencing correlation analysis. *Created with BioRender.com.*

transporting Aβ oligomers from the brain and thus an increase in oligomer concentrations in CSF for these carriers. However, these are only a few factors that influence Aβ oligomer clearance. Activation of microglia have also been associated with TREM-2 variants[46], which should be analyzed in future studies, as well as the weakly pronounced differences in oligomer concentrations and correlations, which has previously been observed in studies measuring plasma Aβ monomer concentrations[52]. Moreover, monomer concentrations in plasma were reported to depend on co-pathologies like hypertension, dyslipidemia, diabetes, liver function and chronic kidney disease[53]. These co-pathologies might be determinants of Aβ oligomer concentrations in plasma and should be considered in future studies.

Full interpretation of the results requires a better understanding of how Aβ oligomers are distributed and cleared from the brain and peripheral tissues during disease progression. Although we demonstrate here that the sFIDA assay accurately measures total Aβ oligomer concentrations in plasma, the potential for using bloodborne Aβ oligomers as a diagnostic biomarker is limited due to the substantial overlap of individual readouts. Nevertheless, the statistically significant differences between the tested groups allow us to study the underlying pathophysiological role of Aβ oligomers. Owing to their central role in AD pathology, oligomers are a plausible therapeutic target to prohibit disease progression or even cure AD[54]. In pre-clinical and clinical development of anti-oligomer compounds, the quantification of plasma Aβ oligomers is a valuable tool to determine target engagement and to monitor therapeutic success at the molecular level.

Data availability

The authors confirm that the data supporting the findings of this study are available within the article and its supplementary materials or can be made

available upon request. The source data for Figs. 1, 3, 4, 5, Supplementary Figs. 1, 2, 3, 4, 5 and 7 are included in the Supplementary Data file.

Received: 3 July 2023; Accepted: 28 November 2024;
Published online: 10 December 2024

References

1. Cummings, J. et al. *Alzheimer's disease drug development pipeline*: 2022. Alzheimers Dement (N Y 8, e12295 (2022). .
2. Cline, E. N., Bicca, M. A., Viola, K. L. & Klein, W. L. The Amyloid-β Oligomer Hypothesis: Beginning of the Third Decade. *J Alzheimers Dis* **64**, S567–s610 (2018).
3. Hampel, H. et al. The Amyloid-β Pathway in Alzheimer's Disease. *Molecular Psychiatry* **26**, 5481–5503 (2021).
4. Mroczko, B., Groblewska, M., Litman-Zawadzka, A., Kornhuber, J. & Lewczuk, P. Amyloid beta oligomers (AbetaOs) in Alzheimer's disease. *J Neural Transm (Vienna)* **125**, 177–191 (2018).
5. Hladky, S. B. & Barrand, M. A. Mechanisms of fluid movement into, through and out of the brain: evaluation of the evidence. *Fluids Barriers CNS* **11**, 26 (2014).
6. Holtta, M. et al. Evaluating amyloid-beta oligomers in cerebrospinal fluid as a biomarker for Alzheimer's disease. *PLoS One* **8**, e66381 (2013).
7. Savage, M. J. et al. A sensitive abeta oligomer assay discriminates Alzheimer's and aged control cerebrospinal fluid. *J Neurosci* **34**, 2884–2897 (2014).
8. Herskovits, A. Z., Locascio, J. J., Peskind, E. R., Li, G. & Hyman, B. T. A Luminex assay detects amyloid beta oligomers in Alzheimer's disease cerebrospinal fluid. *PLoS One* **8**, e67898 (2013).
9. Wang-Dietrich, L. et al. The amyloid-beta oligomer count in cerebrospinal fluid is a biomarker for Alzheimer's disease. *J Alzheimers Dis* **34**, 985–994 (2013).
10. Xin, S. H., Tan, L., Cao, X., Yu, J. T. & Tan, L. Clearance of Amyloid Beta and Tau in Alzheimer's Disease: from Mechanisms to Therapy. *Neurotox Res* **34**, 733–748 (2018).
11. Wang, J., Gu, B. J., Masters, C. L. & Wang, Y. J. A systemic view of Alzheimer disease - insights from amyloid-β metabolism beyond the brain. *Nat Rev Neurol* **13**, 612–623 (2017).
12. Liu, L. et al. An ultra-sensitive immunoassay detects and quantifies soluble Aβ oligomers in human plasma. *Alzheimers Dement* **18**, 1186–1202 (2022).
13. Xia, W. et al. A specific enzyme-linked immunosorbent assay for measuring beta-amyloid protein oligomers in human plasma and brain tissue of patients with Alzheimer disease. *Arch Neurol* **66**, 190–199 (2009).
14. Kurz, C., Walker, L., Rauchmann, B. S. & Perneczky, R. Dysfunction of the blood-brain barrier in Alzheimer's disease: Evidence from human studies. *Neuropathol Appl Neurobiol* **48**, e12782 (2022).
15. An, S. S. A. et al. Dynamic changes of oligomeric amyloid β levels in plasma induced by spiked synthetic Aβ(42). *Alzheimers Res Ther* **9**, 86 (2017).
16. Dominguez, J. C. et al. Multimer Detection System-Oligomerized Amyloid Beta (MDS-OAβ): A Plasma-Based Biomarker Differentiates Alzheimer's Disease from Other Etiologies of Dementia. *Int J Alzheimers Dis* **2022**, 9960832 (2022).
17. Santos, A. N., Simm, A., Holthoff, V. & Boehm, G. A method for the detection of amyloid-beta1-40, amyloid-beta1-42 and amyloid-beta oligomers in blood using magnetic beads in combination with Flow cytometry and its application in the diagnostics of Alzheimer's disease. *J Alzheimers Dis* **14**, 127–131 (2008).
18. Huang, Y. R. & Liu, R. T. The Toxicity and Polymorphism of β-Amyloid Oligomers. *Int J Mol Sci* **21**, https://doi.org/10.3390/ijms21124477 (2020).
19. Fändrich, M. Oligomeric intermediates in amyloid formation: structure determination and mechanisms of toxicity. *J Mol Biol* **421**, 427–440 (2012).
20. Meng, X. et al. Association between increased levels of amyloid-β oligomers in plasma and episodic memory loss in Alzheimer's disease. *Alzheimers Res Ther* **11**, 89 (2019).
21. Wang, M. J. et al. Oligomeric forms of amyloid-β protein in plasma as a potential blood-based biomarker for Alzheimer's disease. *Alzheimers Res Ther* **9**, 98 (2017).
22. Lee, J. C., Kim, S. J., Hong, S. & Kim, Y. Diagnosis of Alzheimer's disease utilizing amyloid and tau as fluid biomarkers. *Experimental & Molecular Medicine* **51**, 1–10 (2019).
23. Babapour Mofrad, R. et al. Plasma amyloid-β oligomerization assay as a pre-screening test for amyloid status. *Alzheimers Res Ther* **13**, 133 (2021).
24. Zhou, L. et al. Plasma amyloid-β oligomers level is a biomarker for Alzheimer's disease diagnosis. *Biochem Biophys Res Commun* **423**, 697–702 (2012).
25. Shea, D. et al. SOBA: Development and testing of a soluble oligomer binding assay for detection of amyloidogenic toxic oligomers. *Proc Natl Acad Sci USA* **119**, e2213157119 (2022).
26. Kulawik, A., Heise, H., Zafiu, C., Willbold, D. & Bannach, O. Advancements of the sFIDA method for oligomer-based diagnostics of neurodegenerative diseases. *FEBS Lett* **592**, 516–534 (2018).
27. Herrmann, Y. et al. Nanoparticle standards for immuno-based quantitation of alpha-synuclein oligomers in diagnostics of Parkinson's disease and other synucleinopathies. *Clin Chim Acta* **466**, 152–159 (2017).
28. Hülsemann, M. et al. Biofunctionalized Silica Nanoparticles: Standards in Amyloid-beta Oligomer-Based Diagnosis of Alzheimer's Disease. *J Alzheimers Dis* **54**, 79–88 (2016).
29. Bloemeke, L. et al. Quantitative detection of alpha-Synuclein and Tau oligomers and other aggregates by digital single particle counting. *NPJ Parkinsons Dis* **8**, 68 (2022).
30. Sehlin, D. et al. Interference from heterophilic antibodies in amyloid-beta oligomer ELISAs. *J Alzheimers Dis* **21**, 1295–1301 (2010).
31. Kulenkampff, K., Wolf Perez, A.-M., Sormanni, P., Habchi, J. & Vendruscolo, M. Quantifying misfolded protein oligomers as drug targets and biomarkers in Alzheimer and Parkinson diseases. *Nature Reviews Chemistry* **5**, 277–294 (2021).
32. Pils, M. et al. Development and Implementation of an Internal Quality Control Sample to Standardize Oligomer-Based Diagnostics of Alzheimer's Disease. *Diagnostics* **13**, 1702 (2023).
33. Lohmann, S. et al. Oral and intravenous transmission of α-synuclein fibrils to mice. *Acta Neuropathol* **138**, 515–533 (2019).
34. Altendorf, T. et al. Stabilization of Monomeric Tau Protein by All D-Enantiomeric Peptide Ligands as Therapeutic Strategy for Alzheimer's Disease and Other Tauopathies. *Int J Mol Sci* **24**, https://doi.org/10.3390/ijms24032161 (2023).
35. Herrmann, Y. et al. sFIDA automation yields sub-femtomolar limit of detection for Abeta aggregates in body fluids. *Clin Biochem* **50**, 244–247 (2017).
36. Andreasson, U. et al. A Practical Guide to Immunoassay Method Validation. *Front Neurol* **6**, 179 (2015).
37. Jessen, F. et al. Design and first baseline data of the DZNE multicenter observational study on predementia Alzheimer's disease (DELCODE). *Alzheimers Res Ther* **10**, 15 (2018).
38. Jessen, F. et al. Subjective cognitive decline and stage 2 of Alzheimer disease in patients from memory centers. *Alzheimers Dement*, https://doi.org/10.1002/alz.12674 (2022).
39. Janelidze, S. et al. Plasma β-amyloid in Alzheimer's disease and vascular disease. *Sci Rep* **6**, 26801 (2016).
40. Miles, L. A., Crespi, G. A., Doughty, L. & Parker, M. W. Bapineuzumab captures the N-terminus of the Alzheimer's disease amyloid-beta peptide in a helical conformation. *Sci Rep* **3**, 1302 (2013).
41. Mohammadi, M. M. & Bozorgi, S. Investigating the presence of human anti-mouse antibodies (HAMA) in the blood of laboratory animal care workers. *Journal of Laboratory Medicine* **43**, 87–91 (2019).

https://doi.org/10.1038/s43856-024-00690-w **Article**

42. Hsieh, S.-Y., Chen, R.-K., Pan, Y.-H. & Lee, H.-L. Systematical evaluation of the effects of sample collection procedures on low-molecular-weight serum/plasma proteome profiling. *PROTEOMICS* **6**, 3189–3198 (2006).
43. Kuo, Y. M. et al. Amyloid-beta peptides interact with plasma proteins and erythrocytes: implications for their quantitation in plasma. *Biochem Biophys Res Commun* **268**, 750–756 (2000).
44. Willemse, E. et al. How to handle adsorption of cerebrospinal fluid amyloid β (1-42) in laboratory practice? Identifying problematic handlings and resolving the issue by use of the Aβ(42)/Aβ(40) ratio. *Alzheimers Dement* **13**, 885–892 (2017).
45. Blömeke, L. et al. Aβ oligomers peak in early stages of Alzheimer's disease preceding tau pathology. *Alzheimers Dement* (Amst 16, e12589 (2024). .
46. Gratuze, M., Leyns, C. E. G. & Holtzman, D. M. New insights into the role of TREM2 in Alzheimer's disease. *Mol Neurodegener* **13**, 66 (2018).
47. Yamazaki, Y., Zhao, N., Caulfield, T. R., Liu, C. C. & Bu, G. Apolipoprotein E and Alzheimer disease: pathobiology and targeting strategies. *Nat Rev Neurol* **15**, 501–518 (2019).
48. Horwitz, W. & Albert, R. The Horwitz ratio (HorRat): A useful index of method performance with respect to precision. *J AOAC Int* **89**, 1095–1109 (2006).
49. Kim, K. Y. et al. Plasma amyloid-beta oligomer is related to subjective cognitive decline and brain amyloid status. *Alzheimer's Research & Therapy* **14**, 162 (2022).
50. Jessen, F. et al. The characterisation of subjective cognitive decline. *Lancet Neurol* **19**, 271–278 (2020).
51. Jack, C. R. Jr et al. NIA-AA Research Framework: Toward a biological definition of Alzheimer's disease. *Alzheimers Dement* **14**, 535–562 (2018).
52. Olsson, B. et al. CSF and blood biomarkers for the diagnosis of Alzheimer's disease: a systematic review and meta-analysis. *Lancet Neurol* **15**, 673–684 (2016).
53. O'Bryant, S. E., Petersen, M., Hall, J. & Johnson, L. A. Medical comorbidities and ethnicity impact plasma Alzheimer's disease biomarkers: Important considerations for clinical trials and practice. *Alzheimers Dement*, https://doi.org/10.1002/alz.12647 (2022).
54. Kutzsche, J. et al. Safety and pharmacokinetics of the orally available antiprionic compound PRI-002: A single and multiple ascending dose phase I study. *Alzheimers Dement* (N Y 6, e12001 (2020). .
55. Lucey, B. P. & Bateman, R. J. Amyloid-β diurnal pattern: possible role of sleep in Alzheimer's disease pathogenesis. *Neurobiology of Aging* **35**, S29–S34 (2014).
56. Lucey, B. P. et al. Effect of sleep on overnight cerebrospinal fluid amyloid β kinetics. *Ann Neurol* **83**, 197–204 (2018).

Acknowledgements

We thank Dr. Carsten Korth (Institute of Neuropathology, Universitätsklinikum Düsseldorf, 40225 Düsseldorf, Germany) who kindly provided the IC16 antibody. We thank Dr. Volker Nischwitz (Central Institute of Engineering, Electronics and Analytics (ZEA-3), Forschungszentrum Jülich, 52428 Jülich, Germany) for ICP-MS measurements of silica nanoparticles. We thank Dr. Andrew Dingley for proof-reding the manuscript. This work was supported by the Helmholtz Association [grant number HVF0079].

Author contributions

L.B. developed the assay with support of M.P. L.B. performed the experiments and L.B. and F.R. analysed the data and carried out the statistics. V.K., A.C. and T.B. aid in experimental work and evaluation of the data. J.K. supported organization of the samples. L.B., O.B. and D.W. wrote the manuscript. O.B., D.W. and O.P. supervised the project. O.P., S.D.F., L.S.S., L.P., J.P., E.J.S., S.A., A.S., K.F., J.W., N.H., F.J., A.R., E.D., W.G., E.I.I., K.B., D.J., M.E., R.P., B.S.R., S.T., I.K., C.L., M.H.M., A.S., N.R., M.T.H., F.B., M.W., S.R., A.R., M.S. were responsible for overall design, implementation and collection of data for the DELCODE study at the respective study sites. All authors approved the final version of this manuscript.

Funding

Open Access funding enabled and organized by Projekt DEAL.

Competing interests

D.W. and O.B. are co-founders and shareholders of attyloid GmbH. This affiliation had no influence of the interpretation of the data. All other authors declare no competing interests related to this work.

Additional information

Supplementary information The online version contains supplementary material available at https://doi.org/10.1038/s43856-024-00690-w.

Correspondence and requests for materials should be addressed to Dieter Willbold.

Peer review information *Communications Medicine* thanks Gianluigi Forloni and the other, anonymous, reviewer(s) for their contribution to the peer review of this work. A peer review file is available.

[1]Institute of Biological Information Processing (Structural Biochemistry: IBI-7), Forschungszentrum Jülich, 52428 Jülich, Germany. [2]attyloid GmbH, 40225 Düsseldorf, Germany. [3]German Center for Neurodegenerative Diseases (DZNE), 10117 Berlin, Germany. [4]Department of Psychiatry and Neuroscience, Campus Benjamin Franklin, Charité – Universitätsmedizin Berlin, corporate member of Freie Universität Berlin and Humboldt-Universität zu Berlin, 12203 Berlin, Germany. [5]Department of Psychiatry and Psychotherapy, Charité – Universitätsmedizin Berlin, corporate member of Freie Universität Berlin and Humboldt-Universität zu Berlin, 10117 Berlin, Germany. [6]School of Medicine, Technical University of Munich; Department of Psychiatry and Psychotherapy, 81675 Munich, Germany. [7]University of Edinburgh and UK DRI, Edinburgh, UK. [8]German Center for Neurodegenerative Diseases (DZNE), Bonn 53127 Bonn, Germany. [9]University of Bonn Medical Center, Dept. of Neurodegenerative Disease and Geriatric Psychiatry/Psychiatry, 53127 Bonn, Germany. [10]German Center for Neurodegenerative Diseases

https://doi.org/10.1038/s43856-024-00690-w **Article**

(DZNE), 37075 Goettingen, Germany. [11]Department of Psychiatry and Psychotherapy, University Medical Center Goettingen, University of Goettingen, 37075 Goettingen, Germany. [12]Neurosciences and Signaling Group, Institute of Biomedicine (iBiMED), Department of Medical Sciences, University of Aveiro, 3810-193 Aveiro, Portugal. [13]Department of Psychiatry, University of Cologne, Medical Faculty, 50924 Cologne, Germany. [14]German Center for Neurodegenerative Diseases (DZNE), 39120 Magdeburg, Germany. [15]Institute of Cognitive Neurology and Dementia Research (IKND), Otto-von-Guericke University, 39106 Magdeburg, Germany. [16]Department for Psychiatry and Psychotherapy, University Clinic Magdeburg, 39120 Magdeburg, Germany. [17]German Center for Neurodegenerative Diseases (DZNE, Munich), 81377 Munich, Germany. [18]Institute for Stroke and Dementia Research (ISD), University Hospital, LMU Munich, 81377 Munich, Germany. [19]Department of Psychiatry and Psychotherapy, University Hospital, LMU Munich, 81377 Munich, Germany. [20]Munich Cluster for Systems Neurology (SyNergy) Munich, 81377 Munich, Germany. [21]Ageing Epidemiology Research Unit (AGE), School of Public Health, Imperial College London, London, UK. [22]Sheffield Institute for Translational Neuroscience (SITraN), University of Sheffield, Sheffield, UK. [23]Department of Neuroradiology, University Hospital LMU, 81377 Munich, Germany. [24]German Center for Neurodegenerative Diseases (DZNE), 18147 Rostock, Germany. [25]Department of Psychosomatic Medicine, Rostock University Medical Center, 18147 Rostock, Germany. [26]German Center for Neurodegenerative Diseases (DZNE), 72076 Tübingen, Germany. [27]Section for Dementia Research, Hertie Institute for Clinical Brain Research and Department of Psychiatry and Psychotherapy, University of Tübingen, 72076 Tübingen, Germany. [28]Department of Psychiatry and Psychotherapy, University of Tübingen, 72076 Tübingen, Germany. [29]University of Bonn Medical Center, Dept. of Neurology, 53217 Bonn, Germany. [30]Luxembourg Centre for Systems Biomedicine (LCSB), University of Luxembourg, L-4367 Belvaux, Luxembourg. [31]Excellence Cluster on Cellular Stress Responses in Aging-Associated Diseases (CECAD), University of Cologne, 50931 Cologne, Germany. [32]Division of Neurogenetics and Molecular Psychiatry, Department of Psychiatry and Psychotherapy, Faculty of Medicine and University Hospital Cologne, University of Cologne, 50931 Cologne, Germany. [33]Department of Psychiatry & Glenn Biggs Institute for Alzheimer's and Neurodegenerative Diseases, San Antonio, TX, USA. [34]Institute for Medical Biometry, University Hospital Bonn, 53127 Bonn, Germany. [35]Institut für Physikalische Biologie, Heinrich-Heine-Universität Düsseldorf, 40225 Düsseldorf, Germany.
✉e-mail: d.willbold@fz-juelich.de

2.2.3 Elevated Aβ aggregates in feces from Alzheimer's disease patients: a proof-of-concept study

Autoren:	Marlene Pils, Alexandra Dybala, Anja Schaffrath, **Fabian Rehn**, Janine Kutzsche, Lara Blömeke, Markus Tusche, Pelin Özdüzenciler, Tuyen Bujnicki, Victoria Kraemer-Schulien, Hannes Gramespacher, Maximilan H.T. Schmieschek, Michael T.Barbe, Oezguer A. Onur, Gereon R. Fink, Gültekin Tamgüney, Oliver Bannach & Dieter Willbold
Journal:	*Alzheimer's Research & Therapy, 16(1), 223 (Oktober, 2024)* *DOI: 10.1186/s13195-024-01597-3*
Beitrag:	Aufbereitung der Rohdaten Datenauswertung Diskussion der Ergebnisse Prüfung des Manuskriptes
Druckgenehmigung:	Siehe Anhang 11.

Pils *et al. Alzheimer's Research & Therapy* (2024) 16:223
https://doi.org/10.1186/s13195-024-01597-3

Alzheimer's Research & Therapy

RESEARCH Open Access

Elevated Aβ aggregates in feces from Alzheimer's disease patients: a proof-of-concept study

Marlene Pils[1,2], Alexandra Dybala[3], Anja Schaffrath[1], Fabian Rehn[1,2], Janine Kutzsche[1], Lara Blömeke[1], Markus Tusche[1], Pelin Özdüzenciler[1], Tuyen Bujnicki[1], Victoria Kraemer-Schulien[1], Hannes Gramespacher[4], Maximilian H.T. Schmieschek[4], Michael T. Barbe[4], Oezguer A. Onur[4,5], Gereon R. Fink[4,5], Gültekin Tamgüney[1,3], Oliver Bannach[1,2] and Dieter Willbold[1,2,3*]

Abstract

Background Misfolding and aggregation of amyloid β (Aβ), along with neurofibrillary tangles consisting of aggregated Tau species, are pathological hallmarks of Alzheimer's disease (AD) onset and progression. In this study, we hypothesized the clearance of Aβ aggregates from the brain and body into the gut.

Methods To investigate this, we used surface-based fluorescence intensity distribution analysis (sFIDA) to determine the Aβ aggregate concentrations in feces from 26 AD patients and 31 healthy controls (HC).

Results Aβ aggregates were detectable in human feces and their concentrations were elevated in AD patients compared to HC (specificity 90.3%, sensitivity 53.8%).

Conclusion Thus, fecal Aβ aggregates constitute a non-invasive biomarker candidate for diagnosing AD. Whether digestion-resistant Aβ aggregates in feces are secreted via the liver and bile or directly from the enteric neuronal system remains to be elucidated.

Keywords Amyloidosis, Aβ oligomer quantitation, sFIDA, Brain-gut-microbiota axis, Leaky gut, Fecal/stool samples, Clearance

Background

Alzheimer's disease (AD) is the most prevalent age-related cause of dementia, characterized by neurodegenerative processes ultimately leading to neuronal loss in the hippocampus and cerebral cortex. Due to neurodegeneration, a progressive decline of cognitive functions, especially learning and memory, is observed [1]. AD is neuropathologically characterized by the progressive accumulation of extracellular senile plaques composed of fibrillar amyloid β (Aβ) peptides and of intracellular neurofibrillary tangles composed of tau proteins [2, 3]. Furthermore, recent evidence indicates that smaller soluble

*Correspondence:
Dieter Willbold
d.willbold@fz-juelich.de
[1]Institute of Biological Information Processing, Structural Biochemistry (IBI-7), Forschungszentrum Jülich, 52428 Jülich, Germany
[2]attyloid GmbH, 40225 Düsseldorf, Germany
[3]Institut für Physikalische Biologie, Heinrich-Heine-Universität Düsseldorf, 40225 Düsseldorf, Germany
[4]Department of Neurology, Faculty of Medicine and University Hospital Cologne, University of Cologne, 50923 Köln, Germany
[5]Cognitive Neuroscience, Institute of Neuroscience and Medicine (INM-3), Jülich Research Centre, 52428 Jülich, Germany

Aβ protein and tau aggregates like oligomers cause and promote pathological processes due to neurotoxicity [3, 4].

There is a growing body of experimental and clinical data confirming a link between the gut, gut microbiota, and neurodegeneration in various neurodegenerative diseases such as AD. In particular, the gut microbiota as a source of a large amount of bacterial amyloids, lipopolysaccharides, short fatty acids and secondary bile acids may promote system inflammation and increase the permeability of physiological barriers. There is even evidence that the gut microbiota is altered both taxonomically and functionally in AD, even before the onset of amyloid pathology in the CNS [5–8]. However, knowledge about changes of intestinal/fecal Aβ is limited. Considering additional factors like disturbances along the brain-gut-microbiota axis [5, 6, 9–11], liver-mediated Aβ clearance and elimination by bile [12–14], and the consequences of a disturbed blood-brain barrier and a permeable intestinal barrier [5, 10, 15, 16], the presence of Aβ aggregates in feces can be assumed. Initial studies have confirmed an association between AD and increased intestinal or fecal Aβ concentrations, irrespectively of conformational structure [17–20]. Protein aggregation occurs in various neurodegenerative disorders, and it often precedes the appearance of clinical symptoms for several years or even decades [21]. Therefore, we hypothesized that clearance mechanisms must exist that reduce the aggregate load in the brain and body by disposing Aβ aggregates via gut. Consequently, fecal Aβ aggregates may also serve as a biomarker candidate for non-invasive AD diagnosis.

We previously developed surface-based fluorescence intensity distribution analysis (sFIDA), a platform technology for quantitating single protein aggregates [22]. While the biochemical setup of the sFIDA assay is similar to a sandwich ELISA (Fig. 1), the readout is microscopy-based featuring sub-femtomolar sensitivity [22, 23]. To avoid monomer interference, sFIDA uses capture and detection antibodies directed against the same or overlapping epitopes. After probing, the glass surface is imaged by total internal reflection fluorescence microscopy (TIRFM), illuminating fluorescence-labeled detection antibodies bound to the captured aggregates. Individual particles are counted by image-data analysis of pixels with fluorescence intensities above background noise. Our previous work established the technical concept of sFIDA [23–25] and demonstrated that sFIDA is useful for diagnosing neurodegenerative diseases [26–28] and drug development [29].

This study did not intend to investigate the gut microbiome, but to investigate, whether Aβ aggregates are found in human feces and whether their levels are different in AD diseased donors versus healthy controls (HC). Therefore, we developed and analytically validated the sFIDA assay to detect and quantify Aβ aggregates in human fecal samples. We also assessed its applicability as an explorative biomarker for non-invasive AD diagnosis in a small proof-of-concept study including samples from 26 AD patients and 31 HC.

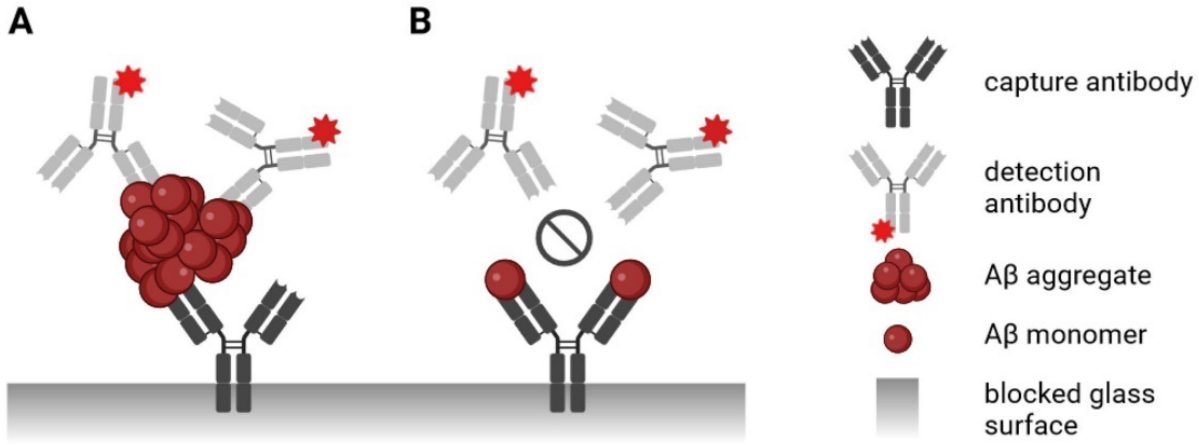

Fig. 1 Scheme of sFIDA principle. In sFIDA, capture antibodies directed against a linear epitope on Aβ (Nab228, directed against epitope amino acids 1 – 11) are immobilized on a glass surface, and unoccupied surface area is blocked with bovine serum albumin to reduce unspecific binding events. During sample incubation, monomeric and aggregated Aβ species are bound to the capture antibody. (**A**) Because sFIDA uses the same or overlapping epitopes for capture and detection, only Aβ aggregates are subsequently detected with fluorescence-labeled antibodies IC16-CF633, which is overlapping with the epitope of the capture antibody (directed against epitope amino acids 2 – 8). (**B**) For monomeric Aβ, this epitope is already masked by the capture antibody and cannot be bound by the detection antibody. Afterward, the assay surface is imaged by fluorescence microscopy, and pixels above a defined cutoff threshold are counted by image-data analysis (called pixel count). Finally, pixel-based readouts are calibrated into molar particle concentrations using silica nanoparticles (SiNaPs) coated with Aβ as calibration standards. Created with BioRender.com

Methods

Human fecal samples

Fecal samples of study participants were collected between October 2019 and June 2022. The Ethics Commission of the Faculty of Medicine of the University of Cologne approved patient recruitment (19-1644). Informed consent was obtained from each participant. A schematic illustration of the sample collection process is shown in Fig. 2.

HC had no known neurological disease, were not subjectively cognitively impaired, and showed complete functional abilities in daily living (ADL). The participants showing cognitive decline were diagnosed by an interdisciplinary team of clinicians with extensive experience in dementia care and research. The neuropsychological classification of the patients involved the following test procedures: DemTect [30], used as a screening tool to identify patients with mild cognitive impairment (MCI) and early-stage dementia; the Beck Depression Inventory II (BDI-II) [31] to evaluate the presence and severity of depression; the Memory Assessment Clinic-Questionnaire (MAC-Q) [32], a brief questionnaire for assessing age-related memory decline; and the Functional Activities Questionnaire (FAQ) to evaluate the ability to perform ADL [33]. The results of the neuropsychological tests for each cognitively impaired participant are listed in Supplementary Table S1. Cognitive impaired participants had to show the typical clinical syndrome according to the National Institute on Aging and Alzheimer's Association (NIA-AA) guidelines [34]. These guidelines specify that patients should have a subtle onset and slow progression of cognitive impairment (either self-reported or reported by a third party) and memory deficits greater than 1.5 standard deviations below the average in any neuropsychological testing results, adjusted for age, sex, and education. In this study, the cognitively impaired participants with preserved functional ADL, as assessed by the FAQ [33] or, in the absence of the FAQ, based on

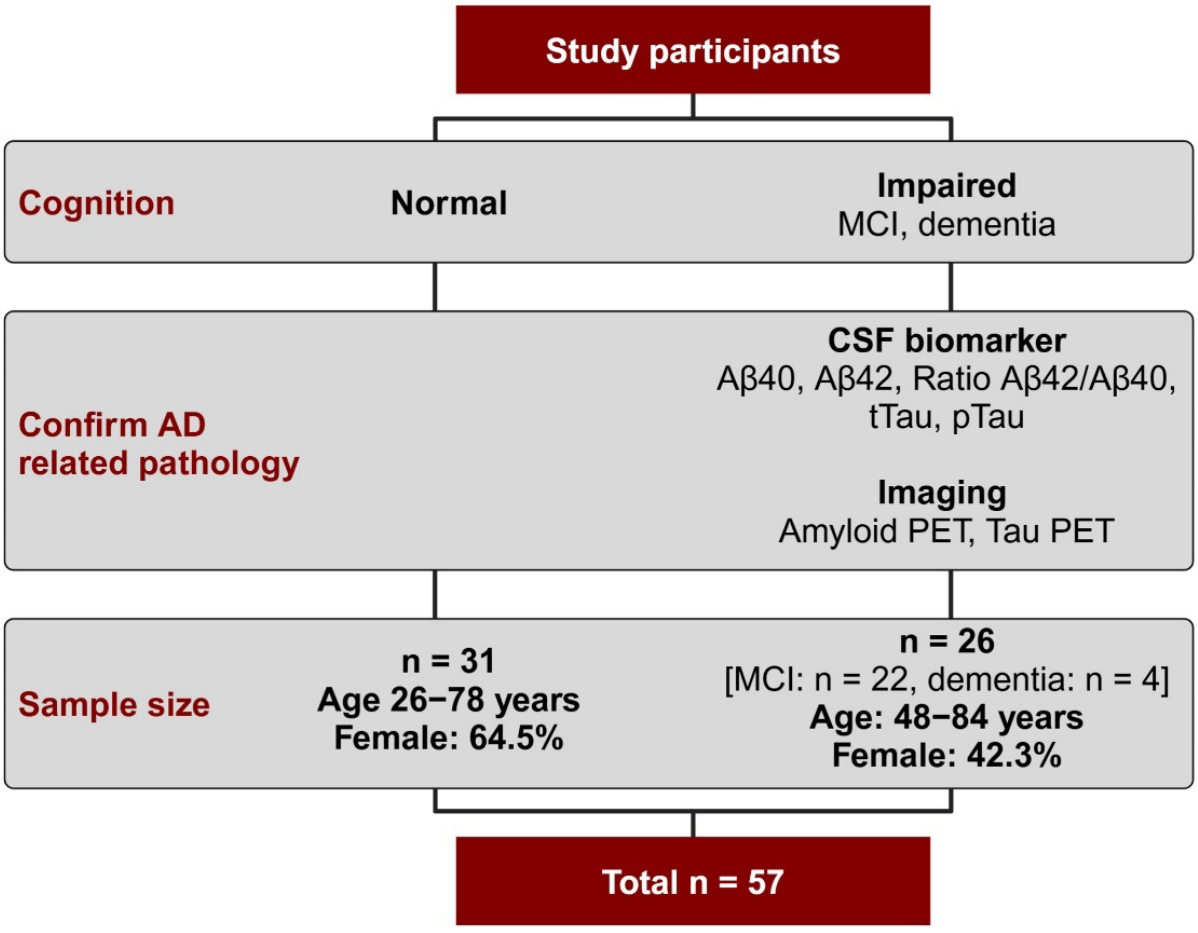

Fig. 2 Schematic illustration of the sample collection process. Study participants were divided into two groups (normal cognition, impaired cognition) based in their clinical symptoms. CSF analyses or imaging were performed for the participants with impaired cognition, to confirm AD related pathology. In total, 31 HC and 26 participants with impaired cognition due to amyloid pathology were included into this study. Created with BioRender.com

the medical history and interview of the caregiver by an experienced clinician, were classified as having MCI. If there were indications of impaired ADL, cognitively impaired participants were classified as having dementia. In order to check whether MCI and dementia are due to AD, biomarker-based diagnostics were carried out.

As described in the research framework of the NIA-AA, AD can be uniformly defined biologically, capable of identifying early pathological changes and biomarker interactions associated with the disease. Therefore, individuals can now be placed in the AD continuum as soon as pathological Aβ aggregation occurs, regardless of their cognitive status [1]. Reduced levels of Aβ42, a reduced ratio between Aβ42 and Aβ40 as well as the image-based detection of senile plaques using amyloid PET serve as evidence for the presence of Aβ aggregation. In the present study, positive amyloid PET (by visual read) and/or CSF levels of Aβ42 less than 630 pg/mL (ELISA kit of Euroimmun AG, Lübeck, Germany, product ID EQ 6511-9601-L, grey zone 570−630 pg/mL) and/or a CSF ration between Aβ42 and Aβ40 less than 0.095 (ELISA kit of Euroimmun AG, product ID EQ 6521-9601-L) confirmed amyloid positivity of cognitively impaired participants and classified them as clinical diagnosed AD patients. To confirm tauopathy, we determined levels of pTau (Fujirebio Europe N.V., Gent, Belgium, product ID 81574, cut-off >61 pg/mL) and tTau (Euroimmun AG, product ID EQ 6531-9601-L, cut-off >452 pg/mL, grey zone 290−452 pg/mL) in CSF as well as tau positivity via PET scan (by visual read).

Based on amyloid positivity, 26 patients (48−84 years of age at sample collection, 42.3% females) were enrolled as clinically defined Alzheimer's disease patients with varying degrees of cognitive impairment ($n=22$ patients with mild cognitive impairment (MCI), $n=4$ patients with dementia). In total, 31 samples from HC were collected (26−78 years of age at sample collection, 64.5% females) and were transferred to sFIDA laboratory without disclosing the names of the donors.

Sample collection

Fecal samples were collected using polypropylene sample tubes with a screwcap-integrated spoon (megro, Wesel, Germany) and a paper-based collection aid (Med Auxil analysis aids, Seesen, Germany) to avoid contamination. In order not to endanger sample stability, samples were stored and transported on ice. After receiving the fecal samples, samples were classified according to their consistency and shape using the Bristol scale [35] and were aliquoted into polypropylene protein low-binding tubes (Sarstedt, Nümbrecht, Germany). Samples were stored at −80 °C until further use.

Homogenization of fecal samples for sFIDA analysis

For sample homogenization, we have developed a sample homogenization buffer and established a suitable homogenization method. A detailed description can be found in the Supplementary method section and Supplementary Figure S1. Fecal homogenates were stored at −80 °C until further use.

sFIDA Assay

Synthesis of Aβ1 – 15 coated silica nanoparticles

For assay calibration, we have previously introduced silica nanoparticle (SiNaP) standards coated with multiple Aβ-derived epitopes to mimic Aβ aggregates [24]. To this end, bare SiNaPs were synthesized via the Stöber process, functionalized, and activated as described previously by Blömeke et al. [26]. Briefly, synthesized SiNaPs were silanized with 3aminopropyl(triethoxysilane) (APTES, Sigma-Aldrich, St. Louis, MO, USA) to functionalize the surface with primary amino groups. Afterward, crosslinking of Aβ1−15 peptides to aminated SiNaPs surface was enabled using maleimido hexanoic acid (MIHA, abcr GmbH, Karlsruhe, Germany), preactivated with 1-ethyl-3-(3-dimethylaminopropyl)carbodiimide (EDC, Sigma-Aldrich) and N-hydroxysuccinimid (NHS, Sigma-Aldrich). Using C-terminal functionalized Aβ1−15 peptides with cysteamine, crosslinking between Aβ and maleimide groups was enabled. Finally, molar concentration of Aβ-coated SiNaPs was calculated based on silicon concentration determined by inductively coupled plasma-mass spectrometry, density of SiNaPs and size and shape of the particles, as determined by transmission electron microscopy.

Aβ1 – 42 oligomer-based IQC sample

We have previously introduced synthetic Aβ1−42 oligomers as internal quality control (IQC) sample [25]. To this end, 5 µg of monomeric Aβ1−42 (Bachem, Bubendorf, Switzerland) was dissolved in 1,1,1,3,3,3-hexafluoro-2-propanol (HFIP, Sigma-Aldrich) and evaporated. Afterward, the Aβ pellet was resolved with 5 µL dimethyl sulfoxide (DMSO, Sigma-Aldrich), agitated for 10 min at 650 rpm at RT and diluted with 1× PBS containing 0.04% NaN_3 to a final stock concentration of 10 µM. Following an overnight incubation on a shaker at 650 rpm and RT, the IQC sample was sonicated for 20 min in an ultrasonic bath before dilution and use in sFIDA assay.

Labeling of antibody

For detection of captured Aβ aggregates, fluorescence-labeled anti-Aβ antibody IC16 (directed against epitope amino acid 2−8, kindly provided by Carsten Korth, Universitätsklinikum Düsseldorf, Germany) [36] was applied on the assay surface. To this end, the antibody was labeled according to the manufacturer's protocol using

CF633 dye (Biotium, Freemont, CA, USA). In carbonate buffer, the succinimidyl ester groups of the preactivated dye bind covalently to the amines of the IC16 antibody. Purification was performed using a polyacrylamide bead suspension (Bio-Gel P-30 Gel, Bio-Rad Laboratories Inc, Hercules, CA, USA), and afterward, concentration and degree of labeling of the probe were calculated as described in manufacturer's protocol. Finally, the detection probe was stored at 4 °C, diluted, and centrifuged for 1 h at 4 °C and 100,000× *g* just before usage.

Assay protocol

The biochemical principle of sFIDA was reported previously [23, 24, 26]. In this study, 384-well-plates (SensoPlate plus, Greiner Bio-One, Frickenhausen, Germany) were functionalized with 40 µL of Nab228 monoclonal anti-Aβ antibody (Sigma-Aldrich) at 2.5 µg/mL in 0.1 M $NaHCO_3$. After overnight incubation at 4 °C, the wells were washed five times with TBST (1× Tris-buffered saline, TBS (Serva, Duisburg, Germany), 0.05% Tween20 (AppliChem, Darmstadt, Germany)) and five times with TBS. Non-coated glass area was blocked with 0.5% bovine serum albumin (BSA, AppliChem) in TBS-ProClin (TBS with 0.03% ProClin (Sigma-Aldrich)) for 1.5 h at RT. After washing five times with TBST and TBS, 20 µL samples were applied in 4-fold determination and incubated for 2 h at RT. For this, Aβ-coated SiNaPs as calibration standard and synthetic Aβ1−42 oligomers as IQC were diluted in sample buffer (1× phosphate-buffered saline (PBS, Sigma-Aldrich), 0.05% Tween, 0.095% NaN_3 (AppliChem) and 0.5% BSA). For fecal samples, an assay-specific 1:5 dilution in sample buffer was performed. After washing five times with TBS, 20 µL of IC16-CF633 (0.625 µg/mL in TBST+0.1% BSA) were applied and incubated for 1 h at RT. Finally, wells were washed five times with TBS, and buffer was changed against TBS-ProClin.

Image data acquisition

Using TIRFM (Leica DMI6000B, Leica microsystems, Wetzlar, Germany), 3.15% of the well surface were imaged at 25 different positions (14-bit grayscale, excitation: 635 nm, emission filter: 705/72 nm, exposure time: 1000 ms, gain: 1000). Imaging of 3.15% of the complete surface area accounts for avoiding edge regions and has been shown to be representative for the well [23, 25, 26]. Each image consists of 1000×1000 pixels and represents an area of 113.76×113.76 µm.

Quantification and statistical analysis

Analysis of image data

Image data analysis was performed using the in-house developed software sFIDAta [23, 26]. All images containing artifacts or images that were out of focus were excluded from analysis. For the exclusion of background signal, an intensity cutoff was determined at which 0.001% of all pixels remain positive in the blank control (unspiked sample buffer, BC). The number of pixels above the respective cutoff is referred to as pixel count. sFIDAta calculated the mean value, standard deviation, and coefficient of variation (CV%) for each sample based on the four replicates. Statistical analyses were performed using OriginPro (OriginLab Corporation, Northampton, MA, USA) and matlab2019b (The MathWorks, Natick, MA, USA) were used for calculations and graphs.

Calibration

To convert pixel counts into femtomolar particle concentration, we used readouts of Aβ-coated SiNaPs to calculate the calibration curve. To this end, only those Aβ-coated SiNaPs concentrations which significantly differed from BC and were within linear range were included in the calculation. A one-sided Mann−Whitney U test with a confidence interval of 5% was performed to investigate significant differences. Linear regression was executed with matlab2019b software, where pixel counts were weighted with 1/readout.

Preanalytics

As it was the first time that we analyzed stool samples to quantify Aβ aggregates using sFIDA, we performed several studies to confirm reproducibility of the preanalytical processes, including fecal sample homogenization and sample dilution. We also investigated the effect of different transport conditions as well as the effect of repeated freeze-thaw cycles on sample stability. A detailed description of these preanalytical study designs is listed in the Supplementary Methods.

Analytical validation

Assay selectivity To evaluate the selectivity of the sFIDA assay in detecting Aβ-coated SiNaPs (molar particle concentration of 10.26 pM), IQC samples (100 nM, Aβ monomer subunit concentration), and three fecal samples with intermediate to high readouts, we measured the percent signal reduction of capture, autofluorescence, and cross-reactivity control, and compared it to a standard assay setup. In addition, we also performed immunodepletion experiments to determine if the observed pixel counts were specifically attributed to Aβ aggregates and not to interfering fecal matrix components. A detailed description of the experiments is listed in the Supplementary Method section.

Influence of Bristol scale Recent studies have demonstrated that microbiome composition and species richness change during AD progression and might impact

cognition [6, 7, 37, 38]. Microbiome composition and species richness also affect feces consistency. Therefore, changes in both water content and pH value are directly reflected in the Bristol scale [35, 39]. The latter may also act as a non-analyte-specific interfering factor [40], altering the quantification of the analyte through dilution or pH-dependent changes in assay kinetics. At sample receipt, all samples were assessed according to their consistency and shape using the Bristol scale. We performed a Mann–Whitney U test and a Spearman correlation analysis to determine whether the Bristol scale influences the fecal Aβ aggregate concentration or whether a cognition-based influence is present.

Influence of matrix components The presence of interfering endogenous substances in fecal samples may falsely alter assay results, either falsely positive or falsely negative [41, 42]. Because disturbances of the brain-gut-microbiota axis, including gut inflammation and increased permeability of the intestinal barrier, may contribute to AD pathology [5], levels of fecal biomarkers indicating pathological processes of the gut, i.e., fecal albumin, hemoglobin, α-1-antitrypsin, calprotectin, IgA, lipids, and bile acid were determined for a set of 15 fecal samples (AD $n=7$, HC $n=8$). Biomarker analyses were performed by the Medizinisches Versorgungszentrum Limbach (Heidelberg, Germany). Afterward, Spearman correlation was conducted to investigate possible interfering effects of those biomarkers on fecal Aβ aggregate concentrations. In addition, Mann–Whitney U tests were used to determine whether levels of all seven biomarkers differ in AD patients and HC.

Intra- and inter-assay variability The precision of an analytical method refers to the consistency of the measured values of several replicates of the same sample. This precision can be categorized as intra-assay variability when considering measurements within a single assay, or inter-assay variability when comparing measurements across different assays [43]. In this study, each sample was analyzed in fourfold determination. For each sample, mean and standard deviation were calculated based on the pixel counts of the four replicates. The intra-assay variation is reflected by CV% value, while for synthetic Aβ species such as Aβ-coated SiNaPs and IQC sample values below 20% were accepted. In case of human fecal samples, CV% below 25% were accepted. Normally, inter-assay variance is determined through a comprehensive validation study. However, due to the limited sample volume available in the present study, we were unable to conduct such an extensive validation. Instead, we assessed the comparability of two independent measurements using Spearman correlation analysis, with Spearman's ρ above 0.9 indicating low inter-assay variability.

Calculation of LoD In order to describe the smallest concentration of Aβ aggregates that can be measured reliably with the sFIDA assay, the limit of detection (LoD) was estimated for each experiment by measuring 24 replicates of BC. First, LoD was calculated according to Armbruster et al. using Eq. 1 [44] and then calibrated into femtomolar concentrations using the determined calibration line.

$$\text{Limit of detection (LoD)} = \text{pixel count}_{\text{BC}} + 2\sigma \quad (1)$$

Proof-of-concept study

For the proof-of-concept, the whole set of 57 fecal samples was subjected to sFIDA. At the time of measurements, all patient-related data was anonymized and researchers were aware of the clinical data at the time of the sFIDA measurements since HC samples were transferred to the sFIDA laboratory without the names of the donors. Pixel counts were generated and calibrated. Data of fecal samples were subsequently tested for normal distribution using Shapiro–Wilk, Lilliefors, Kolmogorov Smirnov, and Anderson–Darling tests. In the case of non-normally distributed data, non-parametric tests, e.g., the Mann–Whitney U test or Spearman correlation, were conducted for further analyses. A receiver operating characteristic (ROC) analysis was performed to evaluate the effectiveness of fecal Aβ aggregates as diagnostic biomarker to differentiate between AD patients and HC. Using maximized Youden's index, the optimal combination of sensitivity and specificity and the area under the curve (AUC) were calculated.

Results

Homogenization and sample dilution of fecal samples are reproducible

Because fecal samples must be homogenized before they are subjected to sFIDA, we first established a suitable homogenization buffer and protocol. Due to the complex and individually varying composition of feces, we tested the reproducibility of homogenization and sample dilution (1:5 in sample buffer) using normalized pixel counts of three fecal samples (initial low, intermediate, high readout) to calculate percentage reproducibility. Figure S2 demonstrates that the homogenization and sample dilution resulted in a high degree of reproducibility, as most of the normalized pixel counts fell within the predefined tolerance range of ±25%. Only two of the observed values have exceeded the tolerance range with a slight deviation of ±0.8% (Figure S2A).

sFIDA features dilution linearity of Aβ-coated SiNaPs, IQC Samples, and fecal samples

Next, we analyzed dilution linearity by subjecting an Aβ-coated SiNaPs and IQC dilution series to sFIDA

analysis, ranging from 0.32 fM − 10 pM (molar particle concentration) and 3.2 pM − 31 nM (total Aβ concentration), respectively. The percent dilution linearity was determined using blank-corrected pixel counts and was accepted within a tolerance range of 80 − 120%. The results showed high dilution linearity for both targets, with an average linearity of 107% for Aβ-coated SiNaPs and 97.6% for IQC samples. Furthermore, for two fecal samples possessing high endogenous Aβ aggregate concentrations, high parallelism of 99.9% and 85.2%, respectively, was determined as depicted in Figure S3.

Repeated freeze-thaw cycles do not affect stability of homogenized fecal samples

In order not to compromise the sample stability during transport or assay preparation, we first performed a thermostability study. The results indicated that a temperature of 4 °C or lower did not compromise sample stability for up to 18 h, as depicted in Figure S4. In addition, we investigated the influence of freeze/thawing on crude and homogenized fecal samples since repeated freezing and thawing of clinical samples is known to compromise sample stability [43, 45, 46]. To this end, we subjected three fecal samples to repeated freeze-thaw cycles and determined the level of Aβ aggregates. As shown in Figure S5, the stability of the crude fecal samples was indeed affected by multiple thawing and freezing but remained intact in the homogenized fecal samples.

sFIDA is selective for aggregated Aβ species

To evaluate the selectivity of the sFIDA assay, we measured the percent signal reduction of capture, autofluorescence, and cross-reactivity control, and compared it to a standard assay setup (Fig. 3A). In this analysis, the sFIDA assay showed a selectivity of about 100% for both Aβ-coated SiNaPs and IQC samples. Thus, unspecific interference with the used blocking agent, autofluorescent components, and cross-reactivity can be excluded for both targets. In contrast, a selectivity of about 77% was determined for fecal Aβ aggregates. Both capture and cross-reactivity control showed about 19.2% and 24.8% remaining pixel counts, respectively. However, since the absence of the detection probe from the fecal samples also led to a comparable result (24.3% of remaining pixels), higher background intensities of the matrix and no interference with assay surface or cross-reactivity with α-synuclein directed antibodies can be assumed. Despite this increased background noise, the signal reduction down to 25% remaining pixels in the fecal samples was still sufficient.

Assay readouts are specifically attributed to Aβ

Immunodepletion was performed to demonstrate that the observed pixel counts by sFIDA can be specifically attributed to Aβ aggregates. Following Aβ immunodepletion, supernatants were subjected to sFIDA analysis, and depletion effectivity was calculated by the percent signal reduction compared to non-depleted sample (reference sample). Nab228-depleted Aβ-coated SiNaPs and

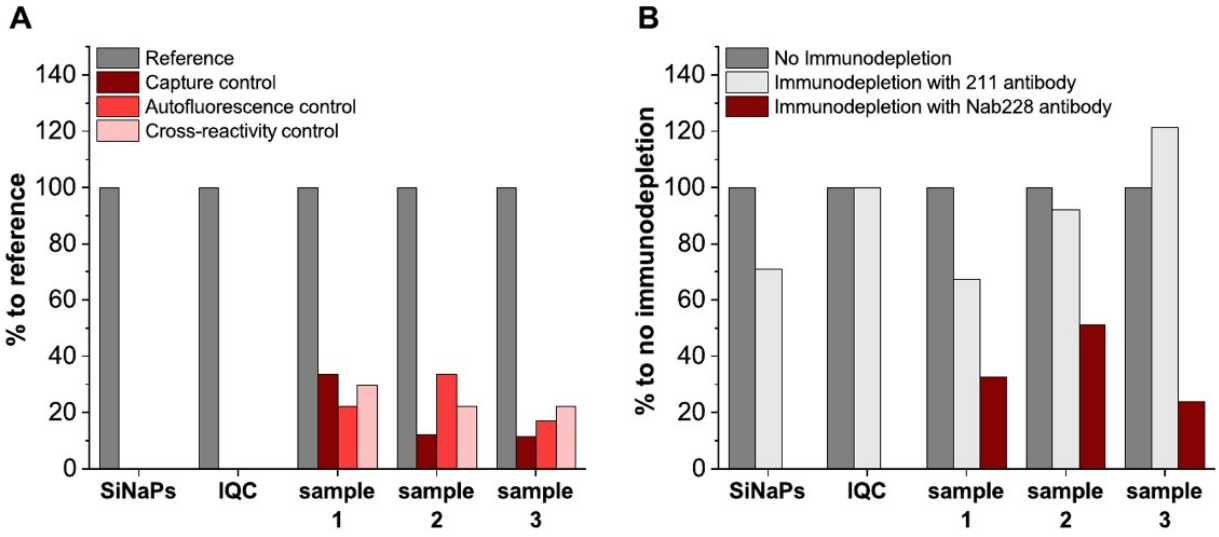

Fig. 3 Percent signal reduction of different assay controls for the assessment of assay selectivity. **A**) Aβ-coated SiNaPs, IQC, and Aβ aggregates in three fecal samples were analyzed by sFIDA. Based on the observed pixel counts, the percent signal reduction of each assay control (no capture antibody: capture control, dark red; no detection probe: autofluorescence control, light red; detection probe against α-synuclein: cross-reactivity control, rose) in comparison to reference (standard assay setup) were calculated. (**B**) All samples were subjected to immunodepletion using magnetic beads linked to Aβ-specific antibody (Nab228) and control beads linked to α-synuclein-specific antibody (211). Based on the observed pixel counts of non-depleted (dark gray), 211-depleted (light gray), and Nab228-depleted (red) samples, percent signal reduction was calculated

IQC showed depletion-dependent signal reduction close to 100% (Fig. 3B), whereas, for Nab228-depleted fecal samples, a mean signal reduction of 72.6% was determined. As a control, α-synuclein immunodepletion with 211-coated magnetic beads was performed, resulting in only negligible signal reduction of IQC (0%) and fecal samples (6.5%). However, for Aβ-coated SiNaPs a signal reduction of 28.9% was observed, suggesting some non-specific adherence of Aβ-coated SiNaPs to bead surface since cross-reactivity between 211 and Aβ-coated SiNaPs was previously excluded (Fig. 3A). To qualitatively confirm the presence of Aβ in human fecal samples, we detected Aβ species in two fecal samples (HC and AD) using a commercial ELISA kit (Figure S6). However, differentiation of fecal Aβ levels between the two subjects was only achievable after complex and sample-consuming pretreatment including homogenization, immunoprecipitation, and spiking. In the spike and recovery experiments, the percentage recovery of monomeric 100 pg/mL Aβ1−42 spiked in human fecal samples was also increased by eliminating the sample matrix using immunoprecipitation. However, the mean percentage recoveries of the ELISA were only 8.8% (homogenized samples: HC=3.5%, AD=14.1%) for homogenized samples and 13.1% (HC=10.0%, AD=16.2%) for precipitated samples, indicating substantial assay interference of matrix components that cannot be removed by immunoprecipitation. It is also important to note that the commercial ELISA used in this study was not validated for the analysis of Aβ in fecal samples, which also might explain the rather low recovery rate. In contrast, the sFIDA assay shown here was optimized for the use of stool as sample matrix (cf. homogenization procedure, homogenization buffer and assay-specific sample dilution), so that even at a lower concentration of aggregated Aβ1−42 (45 pg/mL spiked in stool sample) a mean percentage recovery of 82.3% was obtained.

Independent measurements yield comparable results

We investigated the inter-assay variability of Aβ-coated SiNaPs, IQC samples, and 13 fecal samples in two different assays (Fig. 4). All three targets showed high comparability, indicated by Spearman's coefficient of correlations (ρ: 1.0 for Aβ-coated SiNaPs and IQC samples and ρ: 0.929 (p-value: 8.63×10^{-4}) for fecal samples).

Aβ aggregates are present in fecal samples and are elevated in AD patients

After completion of preanalytical and selectivity studies, a proof-of-concept study was performed using dilution series of Aβ-coated SiNaPs for calibration and LoD calculation, a dilution series of IQC samples and 57 fecal samples comprising two diagnostic groups (Table 1). In detail, we quantified fecal Aβ aggregate concentrations of HC subjects having no subjective cognitive decline (n=31) and patients diagnosed with clinical AD (n=26). Because the data mainly did not show normal distribution (Table S2), we performed statistical analysis using non-parametric tests like the Mann−Whitney U test or Spearman correlation.

Due to the high number of assay points, the measurements were performed on two 384-well microtiter plates (experiment 1: 48 samples, experiment 2: 9 samples), each carrying both a dilution series of Aβ-coated SiNaPs for calibration and LoD calculation and a dilution series of IQC samples, respectively. We determined a femtomolar mean LoD of 1.68 fM for Aβ-coated SiNaPs, indicating high analytical sensitivity. The mean CV% for Aβ-coated SiNaPs was 13.4% and 11.1% for IQC samples. A mean intra-assay variability of 18.7% was observed for fecal samples (for individual results of each experiment see Table S3). Representative TIRFM images of Aβ-coated SiNaPs, IQC sample, patient sample and the sample buffer control are shown in Fig. 5A.

Using Aβ-coated SiNaPs standards, pixel counts of fecal samples were calibrated into molar particle concentrations (Table S4). We determined Aβ aggregate concentrations ranging from 1.3 fM−3.4 pM (Fig. 5B). Despite a substantial overlap between both groups, Aβ aggregate levels of AD patients were significantly elevated (p-value: 0.009). ROC curve were determined to evaluate the use of fecal Aβ aggregates as a diagnostic biomarker (Fig. 5C). Discrimination of AD patients versus HC showed a specificity of 90.3% and a sensitivity of 53.8% with an AUC of 0.703.

Since HC samples were collected anonymously, we could not match the sample with the demographic information of the respective donor. Thus, only the mean age and proportion of female donors was calculated. Therefore, a direct correlation to the determined fecal Aβ aggregate concentration could only be established for the AD cohort. Since we are aware that the samples used from HC do not match with samples of AD patients (Table 1), we investigated for the AD cohort whether fecal Aβ aggregate concentrations might be influenced by age or sex. However, no correlation between AD patients' age and Aβ aggregate concentration was found using Spearman correlation (ρ: 0.163, p-value: 0.426). In addition, no difference was found in Aβ aggregate concentrations in fecal samples from male and female AD patients using a two-sided Mann−Whitney U test with a confidence interval of 5% (p-value: 0.959).

Aβ aggregate quantification is not affected by sample consistency or endogenous substances

To investigate whether the feces consistency, indicated by Bristol scale, affects the measured fecal Aβ aggregate concentrations, we performed a Spearman correlation

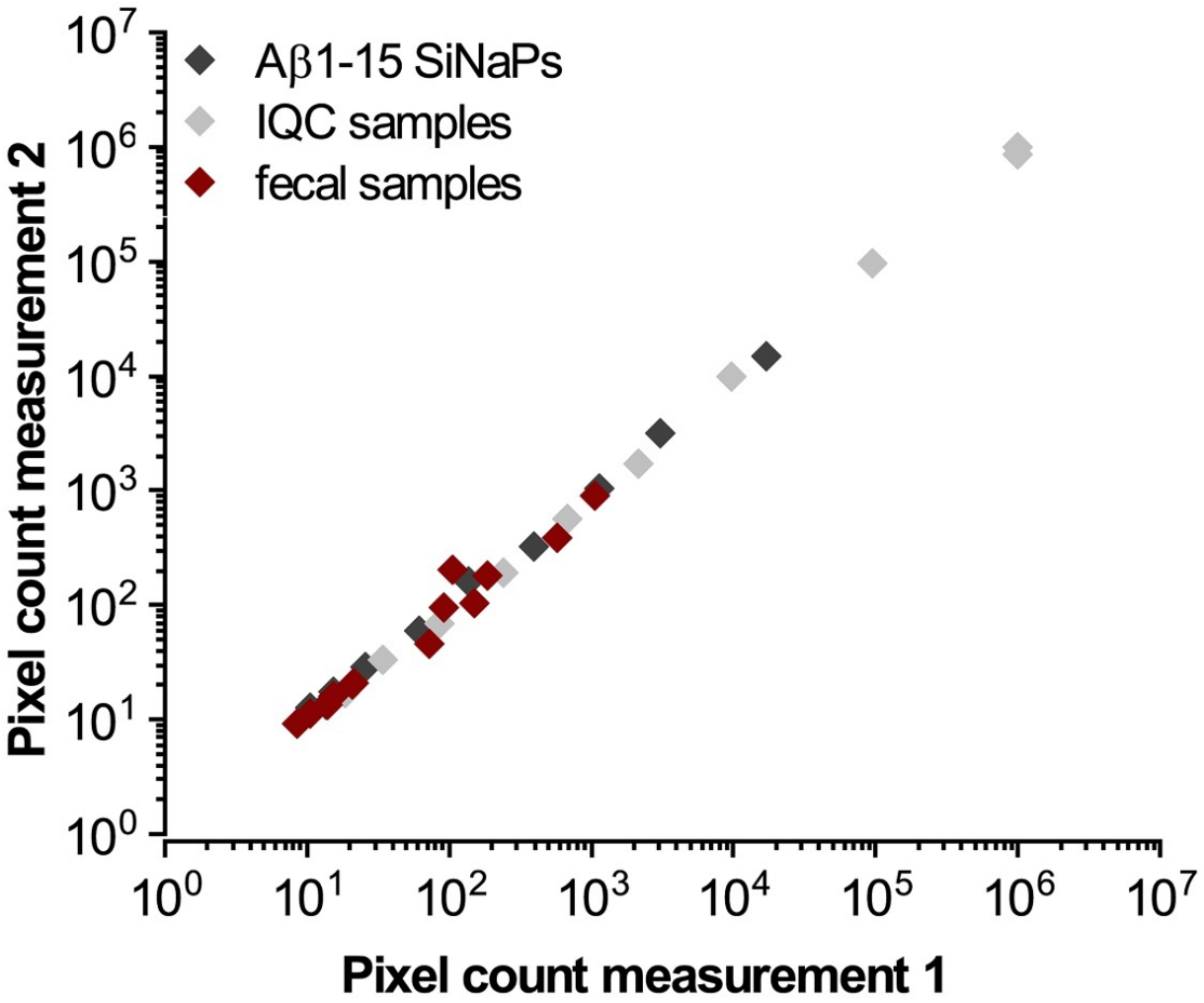

Fig. 4 Independent measurements of aggregated Aβ yield high comparability. For Aβ-coated SiNaPs (dark grey), IQC sample (light gray), and 13 fecal samples (red), pixel counts of the second measurement were plotted against pixel counts of the first measurement. Because the second measurement was carried out months later, there were minor changes in used reagent lots, e.g., manufacturing date of washing buffers, and the used homogenized fecal samples were subjected to an additional freeze-thaw cycle. Please note the logarithmic scaling

Table 1 Demographic and clinical information on AD patients and HC that donated fecal samples

Characteristics	AD	HC
Number	26	31
Female	42.3%	64.5%
Age [years ± SD]	71.1 ± 8.6	49.2 ± 16.4
Bristol scale [score ± SD]	4.4 ± 0.9	5.1 ± 0.8

[a]Abbreviations: AD, Alzheimer's disease; HC, healthy controls; SD, standard deviation

for all 57 samples. Here, we did not find a significant correlation, indicating that the quantification was not affected by feces consistency (ρ: −0.176, *p*-value: 0.191). Since we found significant differences in feces consistency between AD patients and HC (*p*-value: 0.003, Table 1), we performed additional Spearman correlation for HC and AD patient groups separately. Here, we also did not find any correlation between the Bristol scale and the signals of fecal Aβ-aggregate (AD patients: ρ: −0.087, *p*-value: 0.672; HC: ρ: 0.073, *p*-value: 0.696). Spearman correlation between fecal albumin, hemoglobin, calprotectin, IgA, bile acid, α-1-antitrypsin, lipids, and fecal Aβ aggregate concentrations were investigated to assess interfering effects. As shown in Table S5, Spearman correlation coefficients between −0.38 and +0.36 were observed. However, since they were not significant, only minute interfering effects of endogenous substances on quantification can be assumed. In addition, we investigated whether the levels of all seven biomarkers were different between AD patients and HC. As shown in Table S6, no significant differences between both cohorts were observed.

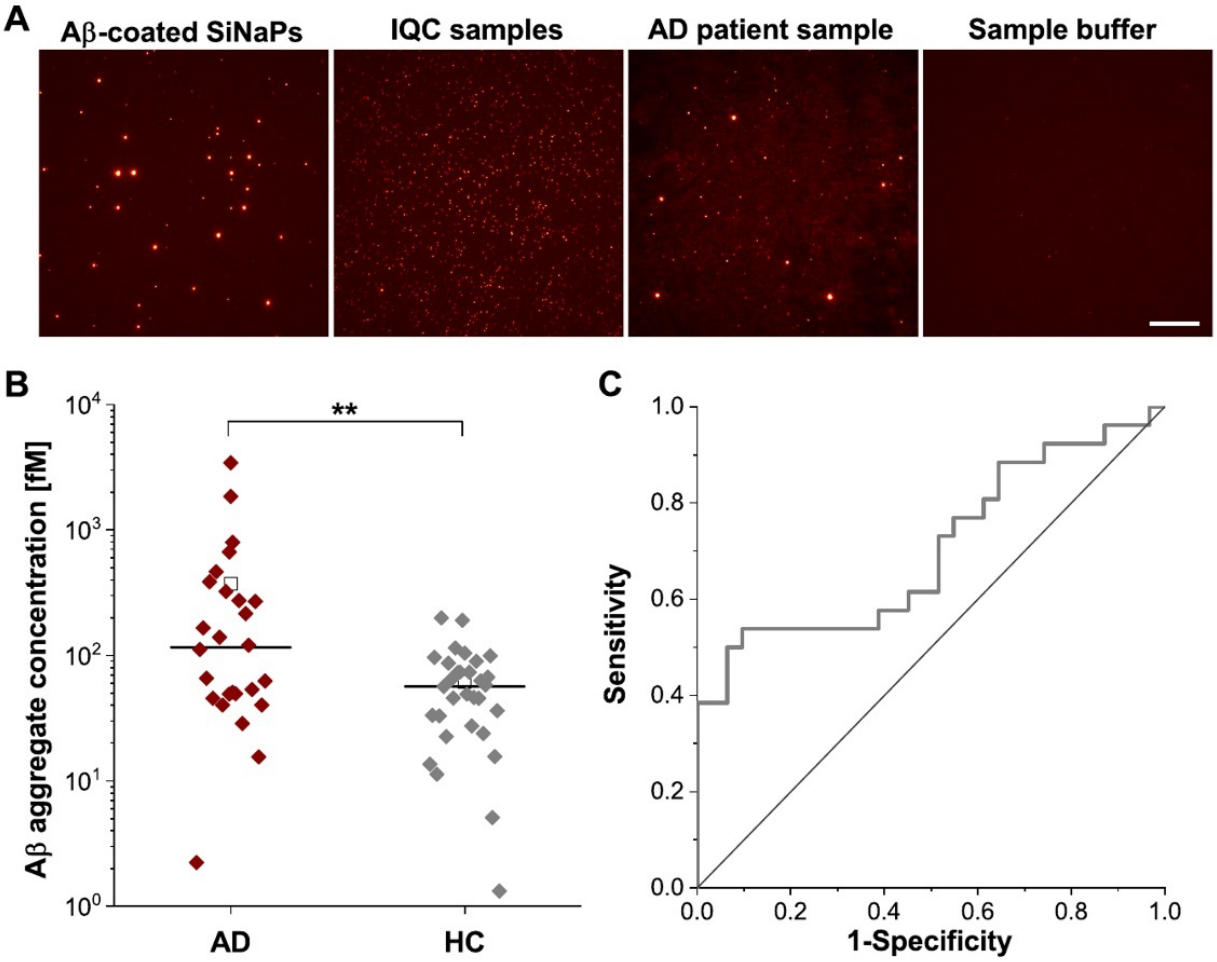

Fig. 5 Representative TIRFM images, molar particle concentration of fecal Aβ aggregates and receiver operating characteristic. (**A**) Representative TIRFM images for the red channel (IC16-CF633, excitation 635 nm, emission 705 nm, exposure time 1000 ms, gain 1000) of 1 pM Aβ-coated SiNaPs, 100 pM synthetic Aβ1 – 42 oligomers (based on total Aβ concentration), fecal sample (AD patient) and sample buffer control. For better illustration of 14-bit images, color and contrast were adjusted using ImageJ software (colormap: red hot, contrast: maximum grayscale value 8000). Scale bar: 20 µm. (**B**) Concentrations of fecal Aβ aggregates of AD patients were significantly elevated with a *p*-value of 0.009 compared to HC. Significant differences between both cohorts were calculated with a Mann – Whitney U test (**p: ≤ 0.01). Please note the logarithmic scaling (line = median, square = mean). (**C**) In receiver operating characteristic (ROC) analysis, discrimination of AD patients versus HC showed a specificity of 90.3% and a sensitivity of 53.8% with an AUC of 0.703

Discussion

AD is the most common age-related cause of dementia and among the most critical public health problems in industrialized countries due to increasing life expectancy [47]. In AD pathology, small soluble Aβ oligomers are the most toxic Aβ species that damage neurons and compromise synaptic function. Aβ oligomers form probably decades before clinical symptoms of AD manifest in humans. We hypothesized that clearance mechanisms are likely to exist to protect the brain from toxic effects. The deposition of Aβ oligomers into amyloid plaques is likely just one clearance mechanism, while the sequestration of Aβ oligomers out of the brain could be another mechanism [12, 13, 16]. Given that the liver plays a crucial role in detoxifying the blood, it is reasonable to assume that Aβ oligomers are sequestered from the bloodstream by the liver and then transported to the gut via bile. We and others have provided compelling evidence indicating that disturbances along the brain-gut-microbiota axis may substantially contribute to the pathogenesis of neurodegenerative diseases such as AD because gastrointestinal metabolic, endocrine, neuronal, and immunological pathways are critical for the maintenance of brain homeostasis [5, 6, 9–11]. Although the bidirectional communication between the brain and gut and its microbiome is not yet fully understood, it is clear that changes in the gut microbiome can induce an immune activation resulting in a systematic inflammation, which in turn may compromise the intestinal barrier (leaky gut) and the blood-brain barrier [5, 6, 10, 11, 15]. Combined with a dysregulated

Aβ homeostasis, brain-derived Aβ aggregates could thus directly enter the enteric nervous system by crossing the blood-brain barrier or by neuron-to-neuron, distal neuron spreading, or other cells like astrocytes, fibroblasts, microglia and immune system cells [5]. Conversely, Aβ species produced by enteric neurons [18] may also enter the brain. Moreover, due to the permeability of the intestinal barrier caused by systematic inflammation, it can be assumed that Aβ aggregates in blood or originating in enteric neurons enter the intestinal lumen and are excreted with feces, as we have observed for α-synuclein aggregates in patients with isolated rapid eye movement sleep behavior disorder, a prodromal form of parkinsonism [28]. Besides, circulating Aβ is predominantly cleared by degradation in hepatocytes and secreted into the gut in bile [12–14, 16], which in turn could increase intestinal and fecal Aβ concentrations. Initial studies have confirmed this association between AD and increased intestinal or fecal Aβ concentrations, irrespective of Aβ conformation [17–20]. One may assume, however, that only Aβ species that are resistant to proteases in the gut may become observable in feces.

The clinical assessment of AD is supported by neurological evaluation, imaging, and biomarkers in patients' CSF [1, 4]. Due to the invasiveness and burden of a lumbar puncture on patients, CSF is not routinely collected [48, 49]. Identifying non-invasive biomarkers that can be used for sensitive detection of AD years or even decades before clinical onset is of utmost importance [22, 50]. Therefore, we used sFIDA technology to verify whether Aβ aggregates exist in feces and, more importantly, whether Aβ aggregate concentrations in fecal samples of HC and AD differ.

As this was a pilot project to use sFIDA for the quantification of fecal Aβ aggregates, we first had to overcome several preanalytical hurdles due to a complex sample matrix in addition to already existing challenges of oligomer-based diagnostics. Because the fecal samples must be processed before they are subjected to sFIDA, we first established a reproducible homogenization procedure. Various homogenization methods for fecal samples are described in the literature, with the required sample quantity being determined either by weighing or using tubes with an integral dosing system [51–55]. For our study, we opted to use Simplix tubes, which facilitated simple, clean, and efficient sample handling, and accurate dosing, as confirmed by our results.

The easiest way to overcome matrix effects in immunoassays is to dilute samples in a dilution buffer that ensures high discrimination between negative and positive samples [56]. In this study, a 1:5 dilution of the fecal homogenates was found optimal (data not shown) and reproducible in sFIDA assay development. Furthermore, as dilution linearity or parallelism, respectively, were observed for Aβ-coated SiNaPs, IQC sample, and fecal samples, we can exclude strong interferences due to, e.g., heterophilic antibodies as these are typically reflected in insufficient dilution linearity [42]. Therefore, samples containing high levels of endogenous fecal Aβ can be diluted within a linear range, and still yield reliable outcomes.

Chemical, microbial, and physical factors influence an analyte's stability and measurable concentration in a complex sample and can significantly falsify a measurement [43, 45]. Because our thermostability study showed that incubation at temperatures above 4 °C did affect sample stability, we adjusted the sFIDA procedure for fecal analysis accordingly. In addition, we have developed a homogenization buffer, which combined with the homogenization process, leads to stable Aβ aggregates in feces, even when they are exposed to several freeze-thaw cycles. In contrast, crude samples reacted to freeze-thaw cycles with a signal reduction. These results are similar to those reported for CSF, where the stability of Aβ42 was analyzed, and a signal loss of 20% was observed after three freeze-thaw cycles [46, 57]. Especially, the signal of Aβ aggregates was further reduced with increasing cycle numbers, which is in accordance with our study in the case of crude fecal samples.

Despite complex matrix, using a suitable homogenization and sample dilution buffer ensured a high consistency within the sample replicates implicated by low intra-assay variability. Furthermore, Aβ-coated SiNaPs, IQC sample and fecal samples demonstrated low inter-assay variability, indicating a highly precise assay. In particular, the comparability of both sample measurements of the inter-assay study should be emphasized since the homogenates used for the second measurement were stored at −80 °C for nine months. Thus, besides sufficient stability against freeze-thaw cycles, the homogenization buffer also allows aggregate stability over an extended period. Additionally, the sFIDA assay displayed a high level of selectivity for fecal Aβ aggregates.

After preanalytical and analytical validation, we determined the Aβ aggregate concentrations in the feces of AD patients and HC. All feces contained Aβ aggregates in the femtomolar range, a few samples even above. Although it is not clear whether the Aβ aggregates found in feces have been secreted by the liver/bile system or have been directly secreted into the gut, e.g., from neurons of the enteric system, this study supports the presence of clearance mechanisms that reduce Aβ oligomer concentration in the body. Here, we demonstrated that sFIDA is suitable to measure low femtomolar (1.3 fM) to low picomolar (3.4 pM) concentrations of Aβ aggregates in fecal samples, which is slightly higher than the previously reported concentration range of Aβ aggregates in CSF (aM-fM) [58, 59]. We also demonstrated that fecal

samples of AD patients with proven amyloid-positivity in the CSF or brain showed significantly elevated levels of Aβ aggregates compared to HC, which has been previously shown for Aβ aggregate concentrations in CSF [27, 58–62]. Due to a high specificity for aggregated Aβ species, the sFIDA assay developed in the present study could discriminate between fecal samples from HC and AD patients with a specificity of 90.3%. Because potential clearance mechanisms can be expected to yield increased Aβ aggregate concentrations also in (still) HC, not surprisingly, we observed an overlap between both cohorts, resulting in an assay sensitivity of only 54%, which limits the clinical use at the current stage of development. In this context, longitudinal samples may help to determine possible changes in the fecal Aβ aggregate concentration before and during disease. The correlation between fecal Aβ aggregate concentration and clinical symptoms within the AD cohort could not be thoroughly evaluated in this study, as it only involved four patients with dementia and 22 with MCI. However, if future studies indeed confirm a correlation between fecal Aβ aggregate concentrations and cognitive abilities, it will represent a significant advancement toward non-invasive early detection of AD.

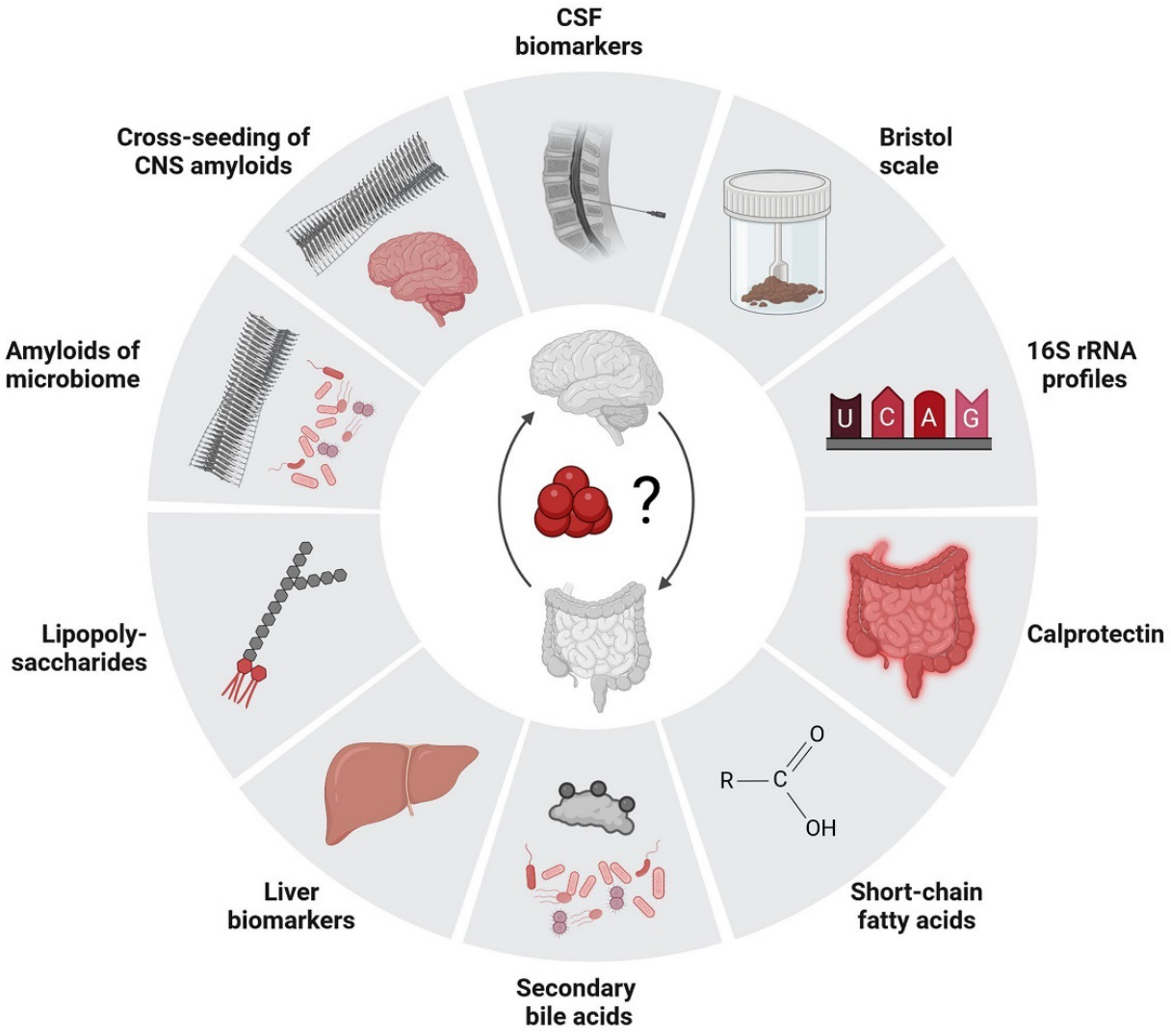

Fig. 6 Association of fecal Aβ aggregates with additional biomarkers affecting AD pathology. The combination of fecal Aβ aggregates with further biomarkers may provide new insights into mechanism of brain-gut-microbiota axis and AD pathogenesis. Therefore, in addition to CSF biomarkers (Aβ40, Aβ42, phosphorylated and total Tau) and Bristol scale, 16 S rRNA profiles, fecal calprotectin, short-chain fatty acids, secondary bile acids, liver biomarkers, and lipopolysaccharides should be determined in the future. Because amyloids produced by gut microbiome share similarities in tertiary structure with CNS amyloids, they may act in a prion-like manner and induce misfolding, aggregation, and deposition of Aβ and may cross-seed with neuronal amyloids once they have entered the brain due to increased permeability of the blood-brain barrier. Created with BioRender.com

Since this is a proof-of-concept study, there are certain limitations to our findings, primarily due to the restricted availability of samples, resulting in small sample sizes. While we could demonstrate statistically significant ($p<0.01$) elevation of fecal Aβ aggregates in AD vs. HC, it is crucial to replicate this result in larger validation studies employing independent cohorts. While in this study we did not observe any correlation between the age and Aβ aggregate concentration, we acknowledge that the samples obtained from HC were not matched in age with those from AD patients, which should be addressed in future work. Additionally, it would be intriguing to explore the link of fecal Aβ aggregates with additional biomarkers related to AD pathology, gut microbiota, and liver function (Fig. 6). Additional data on these biomarkers in combination with a larger cohort of patients across the AD continuum have the potential to enhance our comprehension of the fundamental disease pathology and enable early diagnosis at a stage when clearance mechanisms may be starting to malfunction.

Conclusion

In conclusion, we developed a sFIDA assay for the quantitation of fecal Aβ aggregates, showing high reproducibility of preanalytical procedures, high analytical sensitivity, and specificity. In this work we delivered a proof-of-concept study, that Aβ aggregate are present in human feces and that AD patients exhibited elevated levels of fecal Aβ aggregates compared to HC. Future studies will need to confirm our results with more extensive cohort of participants, encompassing various AD stages, along with longitudinal samples and more comprehensive biomarker analysis. Finally, this work underscores the promising potential of fecal Aβ aggregates as a non-invasive biomarker for AD from which clinical routine and the development of therapeutic interventions might benefit in the future.

Abbreviations

Aβ	Amyloid β
AD	Alzheimer's disease
ADL	Abilities of daily living
AF	Autofluorescence control
APTES	3aminopropyl(triethoxysilane)
AUC	Area under the curve
BC	Blank control
BSA	Bovine serum albumin
CC	Capture control
CSF	Cerebrospinal fluid
CV%	Coefficient of variation
DMSO	Dimethyl sulfoxide
EDC	1-ethyl-3-(3-dimethylaminopropyl)carbodiimide
HC	healthy controls
HFIP	1,1,1,3,3,3-hexafluoro-2-propanol
IQC	Internal quality control
IVDs	In-vitro diagnostics
LoD	Limit of detection
MCI	Mild cognitive impairment
MES	2-(N-morpholino)ethanesulfonic acid
MIHA	Maleimido hexanoic acid
NHS	N-hydroxysuccinimid
OD	Optical density
PBS	10× phosphate-buffered saline
ROC	Receiver operating characteristic
SD	Standard deviation
sFIDA	Surface-based fluorescence intensity distribution analysis
SiNaP	Silica nanoparticle
TBS	1× Tris-buffered saline
TBST	1× Tris-buffered saline containing 0.05% Tween20
TIRFM	Total internal reflection fluorescence microscopy

Supplementary Information

The online version contains supplementary material available at https://doi.org/10.1186/s13195-024-01597-3.

Supplementary Material 1

Acknowledgements

The authors thank Carsten Korth (Institute of Neuropathology, Universitätsklinikum Düsseldorf, 40225 Düsseldorf, Germany) for providing the IC16 antibody. The authors thank Volker Nischwitz (Central Institute for Engineering, Electronics and Analytics, Analytics (ZEA-3), Forschungszentrum Jülich, 52428, Jülich, Germany) for determining the silicon concentration of the used Aβ-coated SiNaPs using inductively coupled plasma mass spectrometry. The authors confirm that these results have not currently been presented at any conference or reviewed or published in any other journal.

Author contributions

Conceptualization, M.P., O.B., D.W. and G.T.; Methodology, M.P.; Validation, M.P.; L.B., T.B. and V.K.; Formal Analysis, M.P., L.B. and F.R.; Investigation, M.P. and M.T.; Resources, i.e., coordination of sample collection, transport, and biobanking M.P., A.S., G.T., M.HT.S., H.G., G.R.F., M.T.B., and O.A.O.; Writing – Original Draft, M.P.; Writing – Review & Editing, O.B., D.W., H.G., O.A.O, M.T.B., G.R.F. and G.T; Visualization, M.P.; Supervision, O.B., G.T., J.K. and D.W.; Project Administration, O.B., D.W. and G.T.; Funding Acquisition, O.B., G.T., D.W., G.R.F and O.A.O. All authors participated in the discussion of the data, provided critical feedback, and contributed to the manuscript. All authors read and approved the final manuscript.

Funding

sFIDA was supported by the programs "Biomarkers Across Neurodegenerative Diseases I + II" of The Alzheimer's Association, Alzheimer's Research UK, and the Weston Brain Institute [11084, BAND-19-614337]. We are also grateful for support from The Michael J. Fox Foundation for Parkinson's Research [14977, 009889], the ALS Association, and the Packard Center [19-SI-476]. We received further funding from the Deutsche Forschungsgemeinschaft [INST 208/616-1 FUGG, INST 208/794-1 FUGG], Helmholtz Association [HVF0079], Förderstiftung Dierichs, and Deutsche Alzheimer Gesellschaft e.V. Selbsthilfe Demenz (DalzG). G.R.F. and O.A.O. were supported by the Marga and Walter Boll Foundation. H.G. was supported by the Cologne Clinician Scientist Program (CCSP) / Faculty of Medicine / University of Cologne and received funding from Deutsche Forschungsgemeinschaft [DFG, FI 773/15 – 1]. Open Access funding enabled and organized by Projekt DEAL.

Data availability

All data generated or analysed during this study are included in this published article and its Supplementary Information. For image data analysis, we used the sFIDAta software application, which can be made available upon request.

Declarations

Ethics approval and consent to participate

The study was approved by the local ethics committee (Ethics Commission of the Faculty of Medicine of the University of Cologne, approval number 19-1644) and carried out in accordance with the Declaration of Helsinki and its later amendments. All participants agreed to be a participant in this study and gave their written informed consent to participate. All participants were aware

of what this study involves, that each participant was at least 18 years old, and have received a copy of this informed consent.

Consent for publication
No identifying information about participants is available in the article.

Competing interests
D.W. and O.B. are cofounders and shareholders of attyloid GmbH. D.W. is member of attyloid's supervisory board. M.P., O.B., G.T. and D.W. are inventors of patent DE102020114278A1 (determination of disease-specific protein aggregates in fecal samples). These factors did not influence the interpretation of the data. Remaining authors declare no conflicts of interest.

Received: 27 June 2023 / Accepted: 5 October 2024
Published online: 14 October 2024

References

1. Jack CR Jr, Bennett DA, Blennow K, Carrillo MC, Dunn B, Haeberlein SB, et al. NIA-AA research framework: toward a biological definition of Alzheimer's disease. Alzheimers Dement. 2018;14(4):535–62.
2. Brown MR, Radford SE, Hewitt EW. Modulation of β-Amyloid fibril formation in Alzheimer's disease by Microglia and infection. Front Mol Neurosci. 2020;13:609073.
3. Hampel H, Hardy J, Blennow K, Chen C, Perry G, Kim SH, et al. The amyloid-β pathway in Alzheimer's disease. Mol Psychiatry. 2021;26(10):5481–503.
4. Kulenkampff K, Wolf Perez AM, Sormanni P, Habchi J, Vendruscolo M. Quantifying misfolded protein oligomers as drug targets and biomarkers in Alzheimer and Parkinson diseases. Nat Reviews Chem. 2021;5(4):277–94.
5. Kowalski K, Mulak A. Brain-gut-microbiota Axis in Alzheimer's Disease. J Neurogastroenterol Motil. 2019;25(1):48–60.
6. Ferreiro AL, et al. Gut microbiome composition may be an indicator of preclinical Alzheimer's disease. Sci Transl Med. 2023;15(700):eabo2984.
7. Varesi A et al. The Potential Role of Gut Microbiota in Alzheimer's Disease: From Diagnosis to Treatment. Nutrients, 2022. 14(3).
8. Laske C, et al. Signature of Alzheimer's Disease in Intestinal Microbiome: results from the AlzBiom Study. Front Neurosci. 2022;16:792996.
9. Sun M, Ma K, Wen J, Wang G, Zhang C, Li Q, et al. A review of the brain-gut-microbiome axis and the potential role of microbiota in Alzheimer's disease. J Alzheimers Dis. 2020;73(3):849–65.
10. Leblhuber F, et al. Elevated fecal calprotectin in patients with Alzheimer's dementia indicates leaky gut. J Neural Transm. 2015;122(9):1319–22.
11. Fink A, Doblhammer G, Tamgüney G. Recurring gastrointestinal infections increase the risk of Dementia. J Alzheimers Dis. 2021;84:797–806.
12. Cheng Y, Tian DY, Wang YJ. Peripheral clearance of brain-derived Aβ in Alzheimer's disease: pathophysiology and therapeutic perspectives. Transl Neurodegener. 2020;9(1):16.
13. Wang J, Gu BJ, Masters CL, Wang YJ. A systemic view of Alzheimer disease - insights from amyloid-β metabolism beyond the brain. Nat Rev Neurol. 2017;13(10):612–23.
14. Ullah R, et al. Abnormal amyloid beta metabolism in systemic abnormalities and Alzheimer's pathology: insights and therapeutic approaches from periphery. Ageing Res Rev. 2021;71:101451.
15. Jiang C, et al. The gut microbiota and Alzheimer's Disease. J Alzheimers Dis. 2017;58(1):1–15.
16. Wu S, Hu L, Lin J, Li K, Ye S, Zhu S, et al. Excretion of amyloid-β in the gastrointestinal tract and regulation by the gut microbiota. J Alzheimers Dis. 2022;90:1153–62.
17. Pellegrini C et al. Prodromal Intestinal Events in Alzheimer's Disease (AD): Colonic Dysmotility and Inflammation Are Associated with Enteric AD-Related Protein Deposition. Int J Mol Sci, 2020. 21(10).
18. Manocha GD, Floden AM, Miller NM, Smith AJ, Nagamoto-Combs K, Saito T, et al. Temporal progression of Alzheimer's disease in brains and intestines of transgenic mice. Neurobiol Aging. 2019;81:166–76.
19. Puig KL, Manocha GD, Combs CK. Amyloid precursor protein mediated changes in intestinal epithelial phenotype in vitro. PLoS ONE. 2015;10(3):e0119534.
20. Joachim CL, Mori H, Selkoe DJ. Amyloid beta-protein deposition in tissues other than brain in Alzheimer's disease. Nature. 1989;341(6239):226–30.
21. Willbold D, Strodel B, Schröder GF, Hoyer W, Heise H. Amyloid-type protein aggregation and prion-like properties of amyloids. Chem Rev. 2021;121(13):8285–307.
22. Kulawik A, Heise H, Zafiu C, Willbold D, Bannach O. Advancements of the sFIDA method for oligomer-based diagnostics of neurodegenerative diseases. FEBS Lett. 2018;592(4):516–34.
23. Herrmann Y, Kulawik A, Kühbach K, Hülsemann M, Peters L, Bujnicki T, et al. sFIDA automation yields sub-femtomolar limit of detection for Aβ aggregates in body fluids. Clin Biochem. 2017;50(4–5):244–7.
24. Hülsemann M, et al. Biofunctionalized silica nanoparticles: standards in Amyloid-β oligomer-based diagnosis of Alzheimer's Disease. J Alzheimers Dis. 2016;54(1):79–88.
25. Pils M, Dybala A, Rehn F, Blömeke L, Bujnicki T, Kraemer-Schulien V, et al. Development and implementation of an internal quality control sample to standardize oligomer-based diagnostics of Alzheimer's disease. Diagnostics. 2023;13(10):1702.
26. Blömeke L, et al. Quantitative detection of α-Synuclein and tau oligomers and other aggregates by digital single particle counting. NPJ Parkinsons Dis. 2022;8(1):68.
27. Wang-Dietrich L, et al. The amyloid-β oligomer count in cerebrospinal fluid is a biomarker for Alzheimer's disease. J Alzheimers Dis. 2013;34(4):985–94.
28. Schaffrath A, et al. Patients with isolated REM-sleep behavior disorder have elevated levels of alpha-synuclein aggregates in stool. NPJ Parkinsons Dis. 2023;9(1):14.
29. Kass B, et al. Aβ oligomer concentration in mouse and human brain and its drug-induced reduction ex vivo. Cell Rep Med. 2022;3(5):100630.
30. Kalbe E, et al. DemTect: a new, sensitive cognitive screening test to support the diagnosis of mild cognitive impairment and early dementia. Int J Geriatr Psychiatry. 2004;19(2):136–43.
31. Beck AT, et al. Comparison of Beck Depression inventories -IA and -II in psychiatric outpatients. J Pers Assess. 1996;67(3):588–97.
32. Crook TH 3rd, Feher EP, Larrabee GJ. Assessment of memory complaint in age-associated memory impairment: the MAC-Q. Int Psychogeriatr. 1992;4(2):165–76.
33. Pfeffer RI, et al. Measurement of functional activities in older adults in the community. J Gerontol. 1982;37(3):323–9.
34. Albert MS, et al. The diagnosis of mild cognitive impairment due to Alzheimer's disease: recommendations from the National Institute on Aging-Alzheimer's Association workgroups on diagnostic guidelines for Alzheimer's disease. Alzheimers Dement. 2011;7(3):270–9.
35. Lewis SJ, Heaton KW. Stool form scale as a useful guide to intestinal transit time. Scand J Gastroenterol. 1997;32(9):920–4.
36. Dornieden S, et al. Characterization of a single-chain variable fragment recognizing a linear epitope of aβ: a biotechnical tool for studies on Alzheimer's disease? PLoS ONE. 2013;8(3):e59820.
37. Qian XH, Xie RY, Liu XL, Tang HD. Mechanisms of short-chain fatty acids derived from Gut microbiota in Alzheimer's disease. Aging Dis. 2022;13(4):1252–66.
38. Vogt NM, et al. Gut microbiome alterations in Alzheimer's disease. Sci Rep. 2017;7(1):13537.
39. Vandeputte D, et al. Stool consistency is strongly associated with gut microbiota richness and composition, enterotypes and bacterial growth rates. Gut. 2016;65(1):57–62.
40. Vanderstichele H, et al. Potential sources of interference on Abeta immunoassays in biological samples. Alzheimers Res Ther. 2012;4(5):39.
41. Dimeski G. Interference testing. Clin Biochem Rev. 2008;29(Suppl 1):S43–8.
42. Park JY, Kricka LJ. Chap. 5.3 - *Interferences in Immunoassay*. The Immunoassay Handbook (Fourth Edition). Oxford: Elsevier; 2013. pp. 403–16. D. Wild, Editor.
43. Andreasson U, et al. A practical guide to Immunoassay Method Validation. Front Neurol. 2015;6:179.
44. Armbruster DA, Pry T. Limit of blank, limit of detection and limit of quantitation. Clin Biochem Rev. 2008;29(Suppl 1):S49–52.
45. van de Merbel N, et al. Stability: recommendation for best practices and harmonization from the Global Bioanalysis Consortium Harmonization Team. Aaps j. 2014;16(3):392–9.
46. Vanderstichele HM, et al. Optimized standard operating procedures for the analysis of Cerebrospinal Fluid Aβ42 and the ratios of Aβ isoforms using low protein binding tubes. J Alzheimers Dis. 2016;53(3):1121–32.
47. Salvadores N, et al. Detection of misfolded Aβ oligomers for sensitive biochemical diagnosis of Alzheimer's disease. Cell Rep. 2014;7(1):261–8.
48. Teunissen CE, et al. Blood-based biomarkers for Alzheimer's disease: towards clinical implementation. Lancet Neurol. 2022;21(1):66–77.

49. Paraskevaidi M et al. Diagnostic Biomarkers for Alzheimer's Disease Using Non-Invasive Specimens. J Clin Med, 2020. 9(6).
50. Lewczuk P, Łukaszewicz-Zając M, Mroczko P, Kornhuber J. Clinical significance of fluid biomarkers in Alzheimer's disease. Pharmacol Rep. 2020;72(3):528–42.
51. Phadia-AB. *Stool Extraction Kit plus / Stool Extraction Buffer plus, instruction for use: 200/250/2500/5000-6665-020 / UK, version 2021-09-14.*. 2021; Available on https://dfu.phadia.com/Data/Pdf/6130cb9570eec660e274806b.pdf [Accessed 23 January 2023].].
52. ORGENTEC-Diagnostika-GmbH. Calprotectin, instruction for use: ORG 580_4, version ORG 580_IFU_EN_QM140866_2022-03-08_4. 2022; Available on https://products.orgentec.com/pdfs/ifu/ORG%20580_IFU_EN_QM140866_2022-03-08_4.pdf [Accessed 23 January 2023].].
53. Immundiagnostik-AG. *IDK Hemoglobin ELISA: For the in vitro determination of hemoglobin in stool, instruction for use: K 7816D, K7816D.20, version 2022-02-22*. 2022; Available on https://www.immundiagnostik.com/media/pages/testkits/k-7816d/9a63870b70-1663639307/k7816d_2022-02-22_haemoglobin.pdf [Accessed 23 January 2023].].
54. Demeditec-Diagnostics-GmbH. *Calprotectin ELISA, instruction for use: DE849 V211014/DLB, version 2021-11-25*.. 2021; Available on https://www.demeditec.de/de/produkte/calprotectin-elisa-de849/ifu-de849-calprotectin-elisa-211125-e.pdf [Accessed 23 January 2023].].
55. Bühlmann-Laboratories. Bühlmann Smart-Prep - Faecal sample preparation kit, Instruction for use: B-CAL-RD, version 2010-11-10. 2010; Available on https://www.buhlmannlabs.ch/wp-content/uploads/2015/01/B-CAL-RD_101110.pdf [Accessed 23 January 2023].].
56. Minic R, Zivkovic I. *Optimization, Validation and Standardization of ELISA*. 2020.
57. Schoonenboom NS, et al. Effects of processing and storage conditions on amyloid beta (1–42) and tau concentrations in cerebrospinal fluid: implications for use in clinical practice. Clin Chem. 2005;51(1):189–95.
58. Yang T, et al. A highly sensitive novel immunoassay specifically detects low levels of soluble Aβ oligomers in human cerebrospinal fluid. Alzheimers Res Ther. 2015;7(1):14.
59. Savage MJ, et al. A sensitive aβ oligomer assay discriminates Alzheimer's and aged control cerebrospinal fluid. J Neurosci. 2014;34(8):2884–97.
60. Herskovits AZ, et al. A Luminex assay detects amyloid β oligomers in Alzheimer's disease cerebrospinal fluid. PLoS ONE. 2013;8(7):e67898.
61. Fukumoto H, et al. High-molecular-weight beta-amyloid oligomers are elevated in cerebrospinal fluid of Alzheimer patients. Faseb j. 2010;24(8):2716–26.
62. Hölttä M, et al. Evaluating amyloid-β oligomers in cerebrospinal fluid as a biomarker for Alzheimer's disease. PLoS ONE. 2013;8(6):e66381.

Publisher's note

2.2.4 IAPP-oligomerisation levels in plasma of people with type 2 diabetes

Autoren:	**Fabian Rehn*,** Victoria Kraemer-Schulien*, Tuyen Bujnicki, Oliver Bannach, Diethelm Tschoepe, Bernd Stratmann, Dieter Willbold ***Autoren sind gleichberechtigt**
Journal:	*Scientific Reports, 14(1), 19556 (August, 2024)* *DOI: 10.1038/s41598-024-70255-3*
Beitrag:	Anwendung der Auto-Cutoff-Methode Aufbereitung, Kalibration und Normierung der Rohdaten Statistische Analyse Anfertigung von Abbildungen Verfassen des Manuskripts
Druckgenehmigung:	Siehe Anhang 11.

www.nature.com/scientificreports

scientific reports

Check for updates

OPEN

IAPP - oligomerisation levels in plasma of people with type 2 diabetes

Fabian Rehn[1,2,3,6], Victoria Kraemer-Schulien[2,6], Tuyen Bujnicki[2], Oliver Bannach[1,2,3], Diethelm Tschoepe[4,5], Bernd Stratmann[4,7]✉ & Dieter Willbold[1,2,3,7]✉

Islet amyloid polypeptide (IAPP) is co-secreted with insulin from pancreatic ß-cells. Its oligomerisation is regarded as disease driving force in type 2 diabetes (T2D) pathology. Up to now, IAPP oligomers have been detected in affected tissues. IAPP oligomer concentrations in blood have not been analysed so far. Using the IAPP single-oligomer-sensitive and monomer-insensitive surface-based fluorescence intensity distribution analysis (sFIDA) technology, levels of IAPP oligomers in blood plasma from healthy controls and people with T2D in different disease stages where determined. Subsequently, the level of IAPP oligomerisation was introduced as the ratio between the IAPP oligomers determined with sFIDA and the total IAPP concentration determined with ELISA. Highest oligomerisation levels were detected in plasma of people with T2D without late complication and without insulin therapy. Their levels stand out significantly from the control group. Healthy controls presented with the lowest oligomerisation levels in plasma. In people with T2D without complications, IAPP oligomerisation levels correlated with disease duration. The results clearly demonstrate that IAPP oligomerisation in insulin-naïve patients correlates with duration of T2D. Although a correlation per se does not identify, which is cause and what is consequence, this result supports the hypothesis that IAPP aggregation is the driving factor of T2D development and progression. The alternative and conventional hypothesis explains development of T2D with increasing insulin resistance causing exhaustion of pancreatic ß-cells due to over-secretion of insulin, and thus IAPP, too, resulting in subsequent IAPP aggregation and fibril deposition in the pancreas. Further experiments and comparative analyses with primary tissues are warranted.

Keywords IAPP, Diabetes, Disease driven protein expression, Oligomers, sFIDA

Type 2 diabetes (T2D) is a metabolic disorder that progresses continuously and is characterised by insulin resistance, often in conjunction with impaired insulin secretion. With increasing resistance, β-cells respond with augmented insulin secretion to overcome the resistance (hyperinsulinaemia)[1]. Over time, a decline in insulin secretion is observed as a signal of pancreas exhaustion. One possible cause is the diminishment in β-cell mass, resulting in decreased insulin secretion[2]. Due to the resulting lack of functional regulatory mechanisms for glucose, along with a potentially increasing gluconeogenesis in the liver, this can further aggravate hyperglycaemia, which in turn can favour various diseases, named diabetic late complications[3]. Multiple potential risk factors such as obesity or advancing age[4], as well as genetic factors contribute to its development[5]. In recent decades, the number of T2D cases, which account for more than 90% of diabetes cases[6], worldwide has risen considerably, posing an increasingly significant burden on healthcare systems[7]. However, compared to the other types of diabetes, less pronounced hyperglycaemia and decrease in β-cell mass occurs in T2D opening the window for non-insulin based, but ß-cell protective therapies[8,9].

[1]Institut für Physikalische Biologie, Heinrich-Heine-Universität Düsseldorf, Universitätsstr. 1, 40225 Düsseldorf, Germany. [2]Institute of Biological Information Processing (Structural Biochemistry: IBI-7), Forschungszentrum Jülich GmbH, Wilhelm-Johnen-Straße, 52428 Jülich, Germany. [3]attyloid GmbH, Merowingerplatz 1A, 40225 Düsseldorf, Germany. [4]Herz- und Diabeteszentrum Nordrhein-Westfalen, Universitätsklinik der Ruhr-Universität Bochum, Medizinische Fakultät OWL (Universität Bielefeld), Georgstr. 11, 32545 Bad Oeynhausen, Germany. [5]Stiftung DHG (Diabetes I Herz I Gefäße) in der Deutschen Diabetes Stiftung, c/o Deutsches Diabetes-Zentrum (DDZ), Auf´m Hennekamp 65, 40225 Düsseldorf, Germany. [6]These authors contributed equally: Fabian Rehn and Victoria Kraemer-Schulien. [7]These authors jointly supervised this work: Bernd Stratmann and Dieter Willbold. ✉email: bstratmann@hdz-nrw.de; d.willbold@fz-juelich.de

Alongside the periodically increased insulin production, insulin resistance also elevates the level of IAPP monomer, as both are co-secreted[10], with a potentially disproportionate increase in the latter[11]. IAPP, initially existing in monomeric state, possesses the potential to aggregate into small soluble oligomers, as well as to accumulate into insoluble fibrils, also called islet amyloid[12]. Due to the decrease in the ß-cell mass, the amount of monomers available for aggregation changes during the course of the disease. In the case of T2D, islet amyloid formation occurs within the islet cells, extracellularly between ß-cells, as well as between ß-cells and endothelial cells[13]. However, experiments with transgenic mice indicate that extracellular amyloid does not induce β-cell apoptosis[8]. In contrast, smaller, soluble IAPP oligomers are believed to exhibit cytotoxic properties[8,14]. Insights from mouse models and human insulinoma suggest that, differing from fibrils, oligomers may also form intracellularly within the β-cells rather than solely extracellularly[8,15,16]. While in vivo the precise impact of the IAPP oligomers on β-cells and hence the reason for their cytotoxicity are not conclusively elucidated, it has been demonstrated that certain oligomer species disrupt the cell membrane[17]. Furthermore, IAPP is a potent activator of the NLRP3 inflammasome, leading to the production of the proinflammatory cytokine IL-1β, which is known to promote insulin resistance and ultimately damage β-cells in the long term[18].

Aggregation of proteins is a hallmark of many neurodegenerative diseases[19], but also for systemic protein misfolding diseases. IAPP aggregation may also play a role in the development and progression of T2D[20]. It has been reported that T2D is a risk factor for Alzheimer's disease (AD) and, vice versa, AD is a risk factor for T2D. One potential explanation for this observation is that IAPP forms fibrils that are very similar to amyloid-beta fibrils[21,22] suggesting that they potentially can seed each other's formation and growth[23].

Hypothetically, IAPP oligomers, once formed, may induce further IAPP aggregation either upon release from β-cells or even inside β-cells even before release into the extracellular space. In order to investigate, whether such a scenario is supported by IAPP oligomer levels in blood of people with T2D compared with healthy controls, we set out to measure IAPP oligomerisation levels in donor blood samples.

We previously developed the sFIDA (surface-based fluorescence intensity distribution analysis) platform method for the quantitative and absolute specific measurement of oligomer species, irrespective of their conformation, morphology, and size, while being insensitive to monomers. This allows quantitation of oligomers even at low femtomolar (fM) concentrations, as demonstrated in human cerebrospinal fluid[24,25] and complex matrices such as brain homogenates[26]. For this study, we adapted sFIDA for the detection of IAPP aggregates in human plasma EDTA samples. Using the adapted method, oligomers were quantified in samples from individuals clinically diagnosed with T2D, and control samples from metabolically healthy people. Samples from people with T2D were divided into individuals without late complications and those with late complications. Complications comprised nephropathy, retinopathy, and cardiovascular diseases mainly.

The objectives of this study were to elucidate potential differences of IAPP oligomerisation levels in plasma between healthy individuals and people with type 2 diabetes. The acquired insights also aim to resolve whether IAPP oligomers are a cause or a consequence of the disease.

Methods and materials

Sampling

Plasma and serum of 29 people with T2D (13 without complications, 16 with complications) and 21 non-diabetic healthy controls were selected from existing samples within the HDZ Biomaterialbank, at the Herz- und Diabeteszentrum Nordrhein-Westfalen in Bad Oeynhausen, Germany. Healthy controls were collected among clinical staff at the hospital after consent in fasting state.

Briefly, blood was centrifuged within two hours after sampling (10 min, 3000 × g) and frozen at − 80 °C until analysis after overnight fasting. The ethics committee of the Ruhr University of Bochum, located in Bad Oeynhausen approved this study (AZ: 2024-1216). All methods were performed in accordance with the relevant guidelines and regulations (Declaration of Helsinki). The diagnosis of diabetes was made based on anamnesis. Data on comorbidities, medication and laboratory values were accessible from regular visits during which sampling occurred, data from healthy donors were freshly accessed at sampling.

Measurement of total IAPP in human serum

Serum IAPP concentrations were determined by using commercially available ELISA (human Islet Amyloid Polypeptide, cat. No. NBP2-76733, Novus Biologicals, Bio-Techne Europe, UK). Briefly, human serum was diluted 1:4 and measured according to manufacturer's instructions. The standard used in this kit is the monomeric form of human IAPP 34-70aa (Accession number P10997), against which the detecting antibodies are directed. Specification data are as follows: Sensitivity 37.50 pg/ml, detection range: 62.50–400 pg/ml. Optical density was measured with a micro-plate reader (Tecan, Switzerland) set to 450 nm.

Measurement of IAPP oligomer in human plasma

To determine the concentration of IAPP-aggregates in human plasma EDTA samples we adapted the sFIDA platform technology to IAPP oligomer (see Fig. 1). The general principle of sFIDA was previously described by Blömeke et al.[24] and Kravchenko et al.[27].

Antibodies and labelling

Thorough selection of antibodies is crucial for a successful assay development. To ensure that only soluble oligomers are detected and monomers are excluded, only antibodies with overlapping or even identical linear epitopes are used in sFIDA. For this purpose, the antibody EPR-22556-138 (ABCAM, Cambridge, UK), which has its epitope at the C-terminal end of the IAPP structure, was used as a capture and fluorescence labelled detection antibody in the present study.

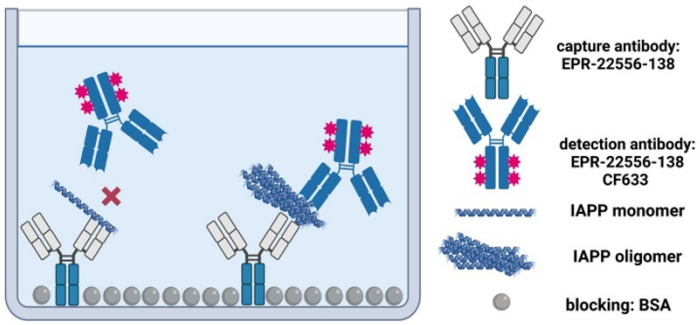

Figure 1. Scheme of surface-based fluorescence intensity distribution analysis. The capture antibody against IAPP (EPR-22556-138) is immobilised on the glass surface of a 384-well plate. IAPP oligomers and monomers can bind the capture antibodies, but only IAPP oligomers can be detected by the fluorescence labelled detection antibody EPR-22556-138 CF633, as the epitope of the monomers is already masked by the capture antibody. Created with BioRender.com.

The detection antibody was labelled with CF633 succinimidyl ester (Sigma Aldrich, St. Louis, Missouri, USA) and purified with a polyacrylamide bead suspension (Bio-Gel P-30, Bio-Rad Laboratories, Hercules, USA) according to the manufacturer's protocol. The concentration was determined with UV–Vis (Shimadzu, Kyōto, Japan) and the degree of labelling was determined for quality assurance.

Silica-nanoparticles conjugation

We have previously developed silica nanoparticles (SiNaPs) as a standard that can be conjugated with various peptides[24]. For the present work, we conjugate carboxylated SiNaPs (cSiNaPs) with full length IAPP-momomers. Therefore, we solved 1 mg of full-length lyophilised IAPP (Bachem, Bubendorf Switzerland) in 1 ml HFIP and evaporated it in the SpeedVac. Meanwhile, the cSiNaPs were activated with EDC/NHS and added to the evaporated IAPP. After overnight incubation and two washing steps the concentration of the standard was determined by ICP-MS[24].

Surface-based fluorescence intensity distribution analysis method

A pretreated 384 glass bottom microtiterplate (Sensoplate plus, Greiner Bio-One GmbH, Frickenhausen, Germany) and immobilised antibody EPR-22556–138 in a concentration of 1.25 µg/ml in 0.1 M carbonate buffer (Carl Roth, Karlsruhe, Germany) was used for capturing. After an overnight incubation at 4 °C the plate was washed five times with TBS containing 0.05% Tween (TBS-T) and TBS, each. A blocking solution consisting of 3% BSA in TBS with 0.03% ProClin™ 300 (Sigma Aldrich, St. Louis, Missouri, USA) was added to the plate and incubated for 1.5 h at room temperature.

The plate was washed as described above and 20 µl of 1:5 diluted plasma EDTA samples in low cross buffer (LC; Candor Bioscience, Wangen, Germany) were added. In addition, the same volume of an IAPP-SiNaPs calibration dilution was applied, each. For this purpose, the dilution buffer was prepared from plasma EDTA that had previously been diluted 1:5 with LC to ensure comparability with the samples. As negative control 20 µl of 20 pM Aβ-SiNaPs was applied. Subsequently, 20 µl of 0.315 µg/ml EPR-22556-138 CF633 in LC was added to each well after washing five times with TBS and incubated for 1 h at room temperature. To remove excess antibody a final washing step was applied and 80 µl of TBS containing 0.03% ProClin™ was added (Supplementary Fig. 1).

Image data acquisition and readout generation

By using a TIRF microscope (Leica Camera AG, Wetzlar, Germany) measurement (excitation: 635 nm, emission filter: 705/22 nm) was carried out with an oil immersion objective in 100 × magnifications as previously described by Kass et al.[26].

Each sample was applied on 4 wells, from which 25 individual 14-bit grayscale images with a size of 1000 × 1000 pixels were generated. Using the in-house developed sFIDAta software (version 0.61.3), images containing visual artefacts were sorted out. To convert the images into a numerical readout, the number of pixels with intensities above a certain cut-off was counted for each remaining image. Afterwards, outlier detection was conducted at the well level, filtering out all images with a readout of 1.5 interquartile ranges above or below the median of the well. Using the Hodges-Lehman estimator, a single value for each well was calculated. Finally, the average of the four wells is computed to obtain the final readout for a sample. In the following, the generated readout is referred to as the pixel count.

Cut-off optimisation

During a fully automated optimisation process, cut-offs are applied to the dilution series at regular intensity intervals of 100. For each cut-off, metrics are computed from the resulting pixel counts to assess the functional quality of the dilution series. The cut-off that, on average, yields the best performance across these metrics, is selected for the analysis, thereby ensuring the most reliable measurement and unbiased analysis of the individual samples. The optimisation metrics are elaborated on below.

Metrics

Dilution linearity. To achieve optimal distinguishability of pixel counts across various oligomer concentration levels, we employed dilution linearity as an evaluation metric. For this purpose, the dilution linearity of all successive dilution steps, i.e. a concentration c_i and the further diluted concentration c_{i+1} of the SiNaPs series was calculated and subsequently converted into the absolute deviation from the optimum (100%) using Eq. (1). Afterwards, the mean was calculated, normalised using min–max scaling, and transformed into a score using a sigmoid curve (Eq. 2).

$$Dilution\ linearity = 100 - abs\left(\frac{pixel\ count_{c_{i+1}}}{\left(\frac{c_{i+1}}{c_i} * pixel\ count_{c_i}\right)} \times 100\%\right), \tag{1}$$

$$x\prime = \frac{1}{1 + e^{-(x-0.5)*8}} \forall 0 < x < 1. \tag{2}$$

Inter-well CV%. Given that the pixel count of each sample is aggregated from 4 replicates, individual replicates with stronger deviations can potentially adversely affect measurement accuracy and reproducibility. To minimize such negative influence, Eq. (3) was used to calculate the coefficient of variation (CV%) between the pixel counts of individual wells at each dilution step within the dilution series. Afterwards, the mean was calculated, normalised using min–max scaling, and transformed into a score using a sigmoid curve (Eq. 2). As the intensity of almost all pixels can exceed very low cut-off values due to background noise, the CV% initially rises with increasing cut-offs. However, this should not be misinterpreted as deterioration, as the actual signal only becomes evident through the reduction of noise associated with an increase in CV%. Therefore, only cut-offs above the cut-off leading to the first local maximum of the CV% are considered.

$$CV\% = \frac{\sigma}{\overline{x}} \times 100\%. \tag{3}$$

wMSE. As the individual experiments are to be aligned using a weighted linear calibration, the weighted mean square error (wMSE) of such a regression on the SiNaPs dilution series is used as an additional metric. To minimise the residuals even in the low concentration range it was weighted with the reciprocal of the concentration (Eq. 4). Afterwards, the wMSE was normalised using min–max scaling, and transformed into a score using an exponential function (Eq. 5).

$$wMSE = \frac{1}{N}\sum_{i=0}^{N}(\hat{y} - y)^2 \times \frac{1}{y} \tag{4}$$

$$x' = \frac{100^{x-1}}{99} \forall 0 < x < 1 \tag{5}$$

Minimal readout. Another important factor for the evaluation of a cut-off is the minimal pixel count of the dilution series. A high value suggests that the cut-off is set too low, allowing excessive background signal. Conversely, a very low value suggests that the cut-off is set too high, resulting in signal loss and complicating the calibration and analysis process by risking samples without signal. Unlike the previous metrics, no weighting is applied. Instead, a score of one is assigned if the pixel count falls below 1000 while all cut-offs leading to a pixel count below ten are excluded. Further assessment within this range has shown to be ineffective.

QScore

Since an increase/decrease of the cut-off does not necessarily lead to improvement/deterioration in all metrics, as some metrics may partly develop inversely, a good compromise between the individual metrics must be found. This is achieved by calculating the average of all metric scores, referred to as the Quality Score (QScore) in the following. Since all metrics included in the average calculation have been normalised, the QScore also falls within the range between zero and one, where one represents the best possible and zero the worst possible value. The cut-off that leads to the highest QScore is subsequently used for the analysis of the individual samples. The results of the optimisation are depicted in the Supplementary Fig. 2.

Calibration
To equalise the pixel count level of both experiments by calibration, a linear regression was carried out using the SiNaPs dilution series between 0 and 2 pM. The individual dilution points were weighted with the reciprocal of their concentration to minimise residuals even in the low concentration range. Both regressions delivered a very high coefficient of determination of *0.998* and *0.990*. When applying the regression model, the intercept was subtracted from the prediction.

Oligomerisation level
Given that IAPP monomer is co-secreted with insulin in β-cells, whose amount diminishes at differing rates and extents depending on the progression of diabetes, the quantity of available monomer for aggregation consequently fluctuates in accordance with the unique course of the disease. For this reason, it does not seem reasonable to directly compare the oligomer titres of different individuals without considering the total amount of monomers available for aggregation, due to the fluctuation of total IAPP during disease progression. Therefore, the IAPP oligomer concentration, measured by sFIDA (2.3) was normalised by the total IAPP concentration (2.2). The result of this normalisation will be referred to as the oligomerisation level in the subsequent text.

Statistics
To select the appropriate statistical test for each investigation, various tests for normal distribution were conducted, namely the Shapiro–Wilk test, Kolmogorov–Smirnov test, and D'Agostino's K-squared test. In the case of not normal distribution data, non-parametric tests are employed for data analyses. Statistical analysis as well as the calibration were performed and illustrated using python 3.9.7 (Python software foundation, Wilmington, USA; packages: pandas 1.3.4, numpy 1.26.3, scipy 1.7.1, sklearn 1.0.2, seaborn 0.11.2).

Ethics approval and consent to participate
All local institutional review boards and ethical committees approved the study protocol. All participants gave informed consent before inclusion in the study.

Results
The aim of the present study was to investigate IAPP oligomerisation levels in human plasma samples of healthy controls and of people with type 2 diabetes.

Descriptive analysis of individual groups
Samples were selected from HDZ NRW Biomaterialbank comprising individuals with T2D with or without late complications (mainly nephropathy, defined by presence of albuminuria), and healthy controls sampled among employees of the HDZ NRW. Basic characteristics are given in Table 1.

To select appropriate statistical tests, an assessment was made to determine if the data aligned with a normal distribution. Given the deviation from normal distribution (Supplementary Table 1), subsequent statistical analyses were conducted using non-parametric tests.

To exclude the influence of demographic factors such as age or sex on the data, statistical investigations were conducted. Spearman analyses within each diagnostic group demonstrated that there is no significant correlation between age and oligomerisation levels in any group (Supplementary Table 2). Additionally, it has been shown that there is no significant sex-specific difference in the oligomerisation level for any diagnostic group (Supplementary Table 3).

People with T2D without complications showed significantly higher IAPP oligomerisation levels compared to controls
First, we investigated the levels of IAPP oligomerisation within the different groups using two-sided Mann–Whitney *U* test. For people with T2D without complications, a statistically significant elevation in the oligomerisation level was observed compared to the control group (*P* value: 0.037, Fig. 2) with an effect size, measured as the percentage increase of the median, being 412% higher than the control group. Although the median of the T2D group with complications is elevated compared to the control group (by 231%), there is no significant difference to the other groups due to heterogenous value distribution. A ROC curve was generated to enable a further evaluation of the diagnostic quality (Supplementary Fig. 3).

Positive correlation between oligomerisation level and disease duration in people with T2D without complications
In addition to inter-group comparisons of oligomerisation levels, an investigation into the temporal dynamics of oligomerisation level increase was undertaken. Specifically, an assessment was conducted within each cohort to ascertain whether a correlation exists between the oligomerisation level and the duration of diabetes. For this purpose, the two-sided Spearman correlation test was performed. For the entirety of the T2D subgroups, no correlation is observed between the years of disease and oligomerisation level (r value: – 0.122, *P* value: 0.528). However, when the analysis is restricted to the first 10 years, a moderately strong positive correlation emerges, although it is not statistically significant (r value: 0.392, *P* value: 0.097). A further refinement into the T2D subgroups shows a strong, positive, and significant correlation for the T2D group without complications (r value: 0.617, *P* value: 0.033). Conversely, the T2D group with complications does not exhibit any correlation within the same time frame (r value: – 0.054, *P* value: 0.908). Subsequently, a Huber regression, which is robust against outliers, was fitted to the oligomerisation levels and diabetes duration of T2D group without complications. The

Parameter	Healthy control	T2D without complications	T2D with complications
Number	21	13	16
Age [yrs]	48.9 ± 7.2	56.9 ± 9.9	62.9 ± 18.2
BMI [kg/m^2]	27.1 ± 4.2	28.2 ± 3.6	29.8 ± 4.0
Diabetes duration [yrs]	0.0 ± 0.0	5.2 ± 4.4	16.1 ± 12.5
HbA1c [%]	5.3 ± 0.2	7.9 ± 1.2	8.4 ± 1.0
C-peptide [pmol/l]	1067 ± 557	1275 ± 439	1100 ± 832
HDL-cholesterol [mg/dl]	53.0 ± 11.1	45.1 ± 8.8	44.3 ± 9.3
LDL-cholesterol [mg/dl]	142.4 ± 23.8	134.2 ± 48.8	93.7 ± 27.4
GFR [ml/min]	–	82.2 ± 13.7	78.3 ± 18.8
Urine albumine [mg/l]	–	16.0 ± 18.4	75.9 ± 46.8
Blood pressure systolic [mm Hg]	–	128.0 ± 7.0	144.0 ± 14.0
Blood pressure diastolic [mm Hg]	–	77.0 ± 8.0	84.0 ± 11.0
IAPP [pg/ml]	3701 ± 4771	1165 ± 647	4906 ± 6457
Insulin in mU/l (includes insulin therapy)	15.2 ± 10.7	17.6 ± 27.5	33.9 ± 21.5
SPISE-INDEX	5.9 ± 1.5	5.1 ± 1.3	4.7 ± 1.0
Therapy			
Insulin (U/day/kg BW)			0.538 ± 0.219
Metformin [N]		10	6
SGLT2 [N]		3	4
DPPIV [N]		6	3
Statin [N]		3	10
Omega-3-fatty acids [N]		4	4
Ezetimibe [N]		1	0
Fibrate [N]		0	2
Co-morbidities			
Hypertension [N]		6	14
PAD [N]		0	4
CVD [N]		0	5
CAD [N]		0	8
DFU [N]		0	4

Table 1. Basic characteristics of analysed cohort comprising clinical data, therapy and co-morbidities.

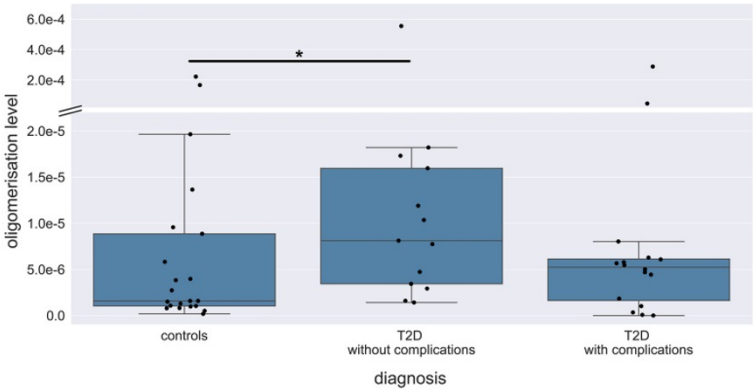

Figure 2. Oligomerisation levels based on diabetes subgroups. Oligomerisation levels of T2D group without complications are significantly elevated compared to the controls (*P* value: 0.037). ● indicates single individuals. – indicates the median. A two-sided Mann–Whitney *U* Test (confidence interval: 0.05) was carried out to investigate differences between the groups. Significant differences were labelled with *. Please, note the two-part y-axis, which removes free space.

median value of the control group closely aligns with the intercept of the Huber regression displayed in Fig. 3 (Median = 1.59e−6, Intercept = 2.78e−6). However, due to the limited data set of T2D without complications, especially with a disease duration of more than seven years it is not possible to reliably estimate if and when the oligomerisation level will peak. Further correlations are listed in Supplementary Tables 4–7.

Discussion

The main focus of this research was to demonstrate a relation between the stage of the disease without comorbidities and complications and insulin applications—and IAPP oligomerisation levels. To create the oligomerisation level, we quantified concentrations of IAPP oligomers in plasma using sFIDA and normalised them to the total IAPP concentration in serum to account for the individually very different total IAPP levels. People with T2D without complications presented with the highest IAPP oligomerisation levels whereas healthy controls showed the lowest levels as expected. In T2D group without complications, oligomerisation levels were significantly elevated compared to the control group. In T2D group with complications, mainly albuminuria with preserved GFR, the median oligomerisation level is also elevated compared to the control group; however, statistical significance could not be established. These observations support that elevated IAPP aggregation exists in people with T2D. Within the first 10 years of the disease, oligomerisation level of T2D group was in correlation to the duration of the disease as long as no confounding conditions, like comorbidities and/or insulin applications are present. Although this cannot prove that IAPP oligomerisation is the driving factor of type 2 diabetes development and progression, one would expect that the IAPP oligomerisation level is increasing with disease duration. This might open the opportunity to determine the real disease onset, long before the disease becomes diagnosed. Next to the lower oligomerisation levels in T2D group with complications, there is also no correlation between oligomerisation levels and the duration of the disease.

There are various plasma components that are supposed to have a stabilising effect on IAPP oligomers or inhibit their aggregation. Camargo et al.[28] show that sucrose (glucose, fructose) has a stabilising effect on IAPP oligomers. In contrast, we were unable to demonstrate that HbA1c influences the oligomerisation level. This could be due to the possibility that only short-term effects exist, which are not detectable by long-term glycaemic markers. Insulin, on the other hand, is a potential inhibitor for the aggregation of IAPP oligomers[29,30]. In accordance with this, we observed an inverse correlation between insulin and the oligomerisation levels of all samples, which was particularly pronounced and significant in the control group (Supplementary Table 8). However, no such correlation was found for people with T2D. The absence of this correlation supports the hypothesis that additional factors must be involved in T2D, or that the binding of insulin to IAPP is influenced. Whether insulin therapy might destabilise IAPP oligomers and result in their partial reduction remains an open question[31]. IAPP fibrils and plaques form not only in the pancreas of persons with T2D but also in the brain, which is not the case for healthy people[32]. Furthermore, IAPP can form fibrils that are very similar to amyloid-beta fibrils[21,22] suggesting that T2D and AD potentially can seed each other's formation and growth[23]. Taken together with our results, which demonstrate that the aggregation of IAPP into soluble oligomers is increased

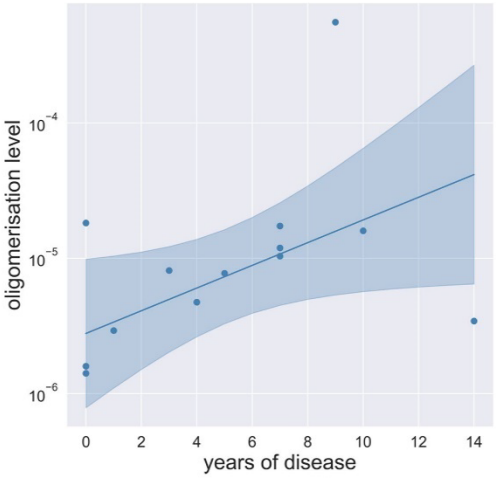

Figure 3. Relationship between oligomerisation level and disease duration in people with T2D without complications. In the first 10 years the oligomerisation level of T2D group without complications correlates strongly positive with the duration of the disease (Spearman *r* value: 0.617, *P* value: 0.033). The line represents a fitted Huber regression. The surrounding marked area represents the confidence interval. Data for the entirety of the T2D subgroups are shown in Supplementary Fig. 4.

in T2D and progresses over the course of the disease, this may be one potential explanation, why T2D is a risk factor for Alzheimer's disease[33,34].

Based on our results, it is neither possible to use the oligomerisation level to assess the severity of the disease, nor to determine whether IAPP oligomerisation can lead to the occurrence of complications. Due to the lack of data from a T2D group without complications with high diabetes duration, it is currently not possible to make a reliable statement about the duration at which the oligomer progression reaches its peak and how it behaves thereafter. We have chosen different matrices for the measurement of total IAPP and IAPP oligomers because serum is recommended for metabolomic measurements[35] and the commercially available ELISA as well, but results in a lower signal-to-noise ratio and consequently lower accuracy in sFIDA measurements compared to plasma, making plasma the better choice for this assay. As the composition of serum and plasma differs, this might influence the results. Moreover, it should be considered that IAPP in plasma can potentially bind to other plasma components such as apolipoproteins[36] and beta-amyloid[37]. Even if this does not lead to false positive signals in the sFIDA assay, it should be considered when interpreting the results.

To clarify the open questions, a longitudinal observation of a larger group of people with T2D would be useful. The further development of the level of oligomerisation could be clarified, and if complications develop in some people over time, conclusions could be drawn from the previously recorded oligomerisation levels. Because IAPP oligomerisation levels were increased in T2D patients without complications in comparison to healthy controls, determination of IAPP oligomers in clinically healthy but obese people might become a tool to identify people at risk to develop T2D. Furthermore, the correlation between oligomerisation levels and the duration of diabetes, might open the possibility to determine the real diabetes time, before overt hyperglycaemia is diagnosed. This, of course, requires many more studies to investigate this potential. IAPP oligomers have been widely detected in pancreatic tissue and oligomerisation is regarded as main contributor to loss of ß-cell function and number. Whether plasma concentrations correlate to pancreatic levels remains elusive as pancreatic biopsies have not been analysed in parallel, and therefore require further investigation.

Conclusion

Taken together we have shown for the first time that the sFIDA technology works in blood plasma from people with type 2 diabetes to determine IAPP oligomer concentrations down to the fM range. Additional work has to be done to prove the results in a higher number of individuals in different disease stages, according to comorbidities and background therapy. Comparative tissue analysis is warranted to rule out issues on secretion and serum stability of IAPP. Highly sensitive analysis methods for systemic detection of organ-specific misfolded proteins may develop as a future analysis method to identify early organ damage.

Data availability

The authors confirm that the data supporting the findings of this study are available within the article and its supplementary materials.

Received: 13 May 2024; Accepted: 14 August 2024
Published online: 22 August 2024

References

1. Polonsky, K. Dynamics of insulin secretion in obesity and diabetes. *Int. J. Obes.* **24**, S29–S31 (2000).
2. Butler, A. E. *et al.* β-cell deficit and increased β-cell apoptosis in humans with type 2 diabetes. *Diabetes* **52**, 102–110 (2003).
3. Meir, J. *et al.* The vascular complications of diabetes: A review of their management, pathogenesis, and prevention. *Expert Rev. Endocrinol. Metab.* **19**, 11–20 (2024).
4. Orozco, L. J. *et al.* Exercise or exercise and diet for preventing type 2 diabetes mellitus. *Cochrane Database Syst. Rev.* https://doi.org/10.1002/14651858.CD003054.pub3 (2008).
5. Sladek, R. *et al.* A genome-wide association study identifies novel risk loci for type 2 diabetes. *Nature* **445**, 881–885 (2007).
6. Chatterjee, S., Khunti, K. & Davies, M. J. Type 2 diabetes. *Lancet* **389**, 2239–2251 (2017).
7. Abdul Basith Khan, M. *et al.* Epidemiology of type 2 diabetes—Global burden of disease and forecasted trends. *J. Epidemiol. Glob. Health* **10**, 107–111 (2020).
8. Haataja, L., Gurlo, T., Huang, C. J. & Butler, P. C. Islet amyloid in type 2 diabetes, and the toxic oligomer hypothesis. *Endocr. Rev.* **29**, 303–316 (2008).
9. DiMeglio, L. A., Evans-Molina, C. & Oram, R. A. Type 1 diabetes. *Lancet* **391**, 2449–2462 (2018).
10. Kahn, S. E. *et al.* Evidence of cosecretion of islet amyloid polypeptide and insulin by β-cells. *Diabetes* **39**, 634–638 (1990).
11. Mulder, H., Ahren, B., Stridsberg, M. & Sundler, F. Non-parallelism of islet amyloid polypeptide (amylin) and insulin gene expression in rat islets following dexamethasone treatment. *Diabetologia* **38**, 395–402 (1995).
12. Westermark, P., Engström, U., Johnson, K. H., Westermark, G. T. & Betsholtz, C. Islet amyloid polypeptide: Pinpointing amino acid residues linked to amyloid fibril formation. *Proc. Natl. Acad. Sci.* **87**, 5036–5040 (1990).
13. Kahn, S. E., Andrikopoulos, S. & Verchere, C. B. Islet amyloid: A long-recognized but underappreciated pathological feature of type 2 diabetes. *Diabetes* **48**, 241–253 (1999).
14. Janson, J., Ashley, R. H., Harrison, D., McIntyre, S. & Butler, P. C. The mechanism of islet amyloid polypeptide toxicity is membrane disruption by intermediate-sized toxic amyloid particles. *Diabetes* **48**, 491–498 (1999).
15. Gurlo, T. *et al.* Evidence for proteotoxicity in β cells in type 2 diabetes: Toxic islet amyloid polypeptide oligomers form intracellularly in the secretory pathway. *Am. J. Pathol.* **176**, 861–869 (2010).
16. Lin, C.-Y. *et al.* Toxic human islet amyloid polypeptide (h-IAPP) oligomers are intracellular, and vaccination to induce anti-toxic oligomer antibodies does not prevent h-IAPP–induced β-cell apoptosis in h-IAPP transgenic mice. *Diabetes* **56**, 1324–1332 (2007).
17. Kanatsuka, A., Kou, S. & Makino, H. IAPP/amylin and β-cell failure: Implication of the risk factors of type 2 diabetes. *Diabetol. Int.* **9**, 143–157 (2018).
18. Masters, S. L. *et al.* Activation of the NLRP3 inflammasome by islet amyloid polypeptide provides a mechanism for enhanced IL-1β in type 2 diabetes. *Nat. Immunol.* **11**, 897–904 (2010).
19. Willbold, D., Strodel, B., Schröder, G. F., Hoyer, W. & Heise, H. Amyloid-type protein aggregation and prion-like properties of amyloids. *Chem. Rev.* **121**, 8285–8307 (2021).

20. Moreno-Gonzalez, I. *et al.* Molecular interaction between type 2 diabetes and Alzheimer's disease through cross-seeding of protein misfolding. *Mol. Psychiatry* **22**, 1327–1334 (2017).
21. Röder, C. *et al.* Cryo-EM structure of islet amyloid polypeptide fibrils reveals similarities with amyloid-β fibrils. *Nat. Struct. Mol. Biol.* **27**, 660–667 (2020).
22. Gremer, L. *et al.* Fibril structure of amyloid-β (1–42) by cryo–electron microscopy. *Science* **358**, 116–119 (2017).
23. Hu, R., Zhang, M., Chen, H., Jiang, B. & Zheng, J. Cross-seeding interaction between β-amyloid and human islet amyloid polypeptide. *ACS Chem. Neurosci.* **6**, 1759–1768 (2015).
24. Blömeke, L. *et al.* Quantitative detection of α-Synuclein and Tau oligomers and other aggregates by digital single particle counting. *NPJ Parkinson's Dis.* **8**, 68 (2022).
25. Blömeke, L. *et al.* Aβ oligomers peak in early stages of Alzheimer's disease preceding tau pathology. *Alzheimer's Dement. Diagn. Assess. Dis. .Monit.* **16**, e12589 (2024).
26. Kass, B. *et al.* Aβ oligomer concentration in mouse and human brain and its drug-induced reduction ex vivo. *Cell Rep. Med.* **3**, 100630 (2022).
27. Kravchenko, K. *et al.* Analysis of anticoagulants for blood-based quantitation of amyloid β oligomers in the sFIDA assay. *Biol. Chem.* **398**, 465–475 (2017).
28. Camargo, D. C. R. *et al.* hIAPP forms toxic oligomers in plasma. *Chem. Commun.* **54**, 5426–5429 (2018).
29. Larson, J. L. & Miranker, A. D. The mechanism of insulin action on islet amyloid polypeptide fiber formation. *J. Mol. Biol.* **335**, 221–231 (2004).
30. Baram, M., Gilead, S., Gazit, E. & Miller, Y. Mechanistic perspective and functional activity of insulin in amylin aggregation. *Chem. Sci.* **9**, 4244–4252 (2018).
31. Gilead, S., Wolfenson, H. & Gazit, E. Molecular mapping of the recognition interface between the islet amyloid polypeptide and insulin. *Angew. Chem.* **118**, 6626–6630 (2006).
32. Jackson, K. *et al.* Amylin deposition in the brain: A second amyloid in Alzheimer disease?. *Ann. Neurol.* **74**, 517–526 (2013).
33. Amidei, C. B. *et al.* Association between age at diabetes onset and subsequent risk of dementia. *JAMA* **325**, 1640–1649 (2021).
34. Athanasaki, A. *et al.* Type 2 diabetes mellitus as a risk factor for Alzheimer's disease: Review and meta-analysis. *Biomedicines* **10**, 778 (2022).
35. Liu, L. *et al.* Differences in metabolite profile between blood plasma and serum. *Anal. Biochem.* **406**, 105–112 (2010).
36. Ly, H. *et al.* Brain microvascular injury and white matter disease provoked by diabetes-associated hyperamylinemia. *Ann. Neurol.* **82**, 208–222 (2017).
37. Kotiya, D. *et al.* Rapid, scalable assay of amylin-β amyloid co-aggregation in brain tissue and blood. *J. Biol. Chem.* **299**, 104682 (2023).

Author contributions

VK developed the assay and performed the experiments. VK carried out the artefact detection. FR analysed the data together with VK. FR developed the cut-off optimisation and carried out the statistics. FR and VK wrote the manuscript together with TB, DW and BS. DT and DW initiated the project and TB, DW, BS and OB supervised the project. All authors agree to the publication.

Funding

Open Access funding enabled and organized by Projekt DEAL. To develop the sFIDA technology in general, we received funding from The Michael J. Fox Foundation for Parkinson's Research (14977, 009889), from the ALS Association and from the Packard Center (19-SI-476). We are also grateful for support funding from the Deutsche Forschungsgemeinschaft (INST 208/616-1 FUGG, INST 208/794-1 FUGG), the Helmholtz Association (HVF0079) and the Helmholz Innovation lab (DB001822).

Competing interests

BS has none to declare. DW and OB are co-founder and co-owner of attyloid GmbH, which is commercializing the sFIDA technology. This did not influence any data interpretation. All the remaining authors declare no conflict of interest.

Additional information

Supplementary Information The online version contains supplementary material available at https://doi.org/10.1038/s41598-024-70255-3.

Correspondence and requests for materials should be addressed to B.S. or D.W.

2.2.5 Quantitative detection of α-Synuclein and Tau oligomers and other aggregates by digital single particle counting

Autoren:	Lara Blömeke, Marlene Pils, Victoria Kraemer-Schulien, Alexandra Dybala, Anja Schaffrath, Andreas Kulawik, **Fabian Rehn**, Anneliese Cousin, Volker Nischwitz, Johannes Willbold, Rebecca Zack, Thomas F. Tropea, Tuyen Bujnicki, Gültekin Tamgüney, Daniel Weintraub, David Irwin, Murray Grossman, David A. Wolk, John Q. Trojanowski, Oliver Bannach, Alice Chen-Plotkin, Dieter Willbold
Journal:	*npj Parkinsons Dis. 8(1), 68 (Juni, 2022)* *DOI: 10.1038/s41531-022-00330-x*
Beitrag:	Implementierung des Bootstrapping Ansatzes Durchführung der multivariablen Logistischen Regressionen Erstellung der ROC-Curven Diskussion der Ergebnisse Prüfung des Manuskriptes
Druckgenehmigung:	Siehe Anhang 11

npj | parkinson's disease

www.nature.com/npjparkd

ARTICLE OPEN

Check for updates

Quantitative detection of α-Synuclein and Tau oligomers and other aggregates by digital single particle counting

Lara Blömeke[1,2], Marlene Pils[2,3], Victoria Kraemer-Schulien[1], Alexandra Dybala[2,3], Anja Schaffrath[1], Andreas Kulawik[1,2,3], Fabian Rehn[1], Anneliese Cousin[1], Volker Nischwitz[4], Johannes Willbold[1], Rebecca Zack[5], Thomas F. Tropea[5,6], Tuyen Bujnicki[1], Gültekin Tamgüney[1,3], Daniel Weintraub[6,7,8], David Irwin[5,6], Murray Grossman[5,6], David A. Wolk[5], John Q. Trojanowski[6,9], Oliver Bannach[1,2,3], Alice Chen-Plotkin[5,6] and Dieter Willbold[1,3]✉

The pathological hallmark of neurodegenerative diseases is the formation of toxic oligomers by proteins such as alpha-synuclein (aSyn) or microtubule-associated protein tau (Tau). Consequently, such oligomers are promising biomarker candidates for diagnostics as well as drug development. However, measuring oligomers and other aggregates in human biofluids is still challenging as extreme sensitivity and specificity are required. We previously developed surface-based fluorescence intensity distribution analysis (sFIDA) featuring single-particle sensitivity and absolute specificity for aggregates. In this work, we measured aSyn and Tau aggregate concentrations of 237 cerebrospinal fluid (CSF) samples from five cohorts: Parkinson's disease (PD), dementia with Lewy bodies (DLB), Alzheimer's disease (AD), progressive supranuclear palsy (PSP), and a neurologically-normal control group. aSyn aggregate concentration discriminates PD and DLB patients from normal controls (sensitivity 73%, specificity 65%, area under the receiver operating curve (AUC) 0.68). Tau aggregates were significantly elevated in PSP patients compared to all other groups (sensitivity 87%, specificity 70%, AUC 0.76). Further, we found a tight correlation between aSyn and Tau aggregate titers among all patient cohorts (Pearson coefficient of correlation $r = 0.81$). Our results demonstrate that aSyn and Tau aggregate concentrations measured by sFIDA differentiate neurodegenerative disease diagnostic groups. Moreover, sFIDA-based Tau aggregate measurements might be particularly useful in distinguishing PSP from other parkinsonisms. Finally, our findings suggest that sFIDA can improve pre-clinical and clinical studies by identifying those individuals that will most likely respond to compounds designed to eliminate specific oligomers or to prevent their formation.

npj Parkinson's Disease (2022)8:68 ; https://doi.org/10.1038/s41531-022-00330-x

INTRODUCTION

Tauopathies and synucleinopathies are characterized by abnormal aggregation of microtubule-associated protein tau (Tau) and alpha-synuclein (aSyn), respectively. From the clinical perspective there is some overlap in the phenotypic presentation of the resulting diseases, with parkinsonism characterizing multiple diseases, including Parkinson's disease (PD), dementia with Lewy bodies (DLB), and progressive supranuclear palsy (PSP)[1,2]. While protein aggregation is the pathological key event in these disorders, ultimately resulting in the formation of aSyn and Tau deposits, the neurotoxic effect is thought to be exerted by small oligomeric intermediates within the aggregation pathway[3–5]. Consequently, a number of drug candidates have been designed to interfere with the aggregation pathway aiming to eliminate existing oligomers or to prevent their formation[6]. Since aggregate formation reflects pathophysiological changes inside the brain, oligomers have also been proposed as promising biomarker candidates[7–9]. However, quantitative measurement of oligomers is technically challenging and mainly hampered by three technical issues. First, the minute amount of oligomers in human biofluids such as cerebrospinal fluid (CSF) requires extreme sensitivity. Secondly, the presence of a vast excess of monomers demands high selectivity for oligomers over monomeric species. Quantitation of oligomeric aSyn by ELISA-like techniques, which employ overlapping epitopes or antibody probes directed against structural motifs, render these assays insensitive towards monomers[10]. Our previously developed sFIDA technology (surface-based fluorescence intensity distribution analysis) employs a similar biochemical setup using the same capture and detection antibody (Fig. 1) but features single-particle sensitivity through a microscopy-based readout[11]. Thirdly, the structural diversity of aggregates renders their detection technically challenging[12]. sFIDA uses linear epitopes and therefore detects and counts all subtypes of aggregated protein irrespectively of higher-ordered structures, while assays using structural epitopes only determine a subfraction of oligomers, fibrils, or other aggregates from a heterogeneous pool of structures. Because the assay itself is not yet discriminating between small oligomers and larger, but still soluble assemblies, like protofibrils, seeding competent fibrillar oligomers or fibrils, we refer to the analytes measured by sFIDA as aggregates, irrespectively, whether they are on or off pathway to fibrils[13].

While our prior work establishes the technical concept of sFIDA[11,14,15], its utility in clinical samples from neurodegenerative

[1]Institute of Biological Information Processing (Structural Biochemistry: IBI-7), Forschungszentrum Jülich, 52428 Jülich, Germany. [2]attyloid GmbH, 40225 Düsseldorf, Germany. [3]Institut für Physikalische Biologie, Heinrich-Heine-Universität Düsseldorf, 40225 Düsseldorf, Germany. [4]Central Institute for Engineering, Electronics and Analytics, Analytics (ZEA-3), Forschungszentrum Jülich, 52428 Jülich, Germany. [5]Department of Neurology, Perelman School of Medicine, University of Pennsylvania, Philadelphia, PA, USA. [6]Center for Neurodegenerative Disease Research, Perelman School of Medicine, University of Pennsylvania, Philadelphia, PA, USA. [7]Department of Psychiatry, Perelman School of Medicine, University of Pennsylvania, Philadelphia, PA, USA. [8]Parkinson's Disease and Mental Illness Research, Education, and Clinical Centers, Philadelphia Veterans Affairs Medical Center, Philadelphia, PA, USA. [9]Department of Pathology and Laboratory Medicine, Perelman School of Medicine, University of Pennsylvania, Philadelphia, PA, USA.
✉email: d.willbold@fz-juelich.de

Published in partnership with the Parkinson's Foundation

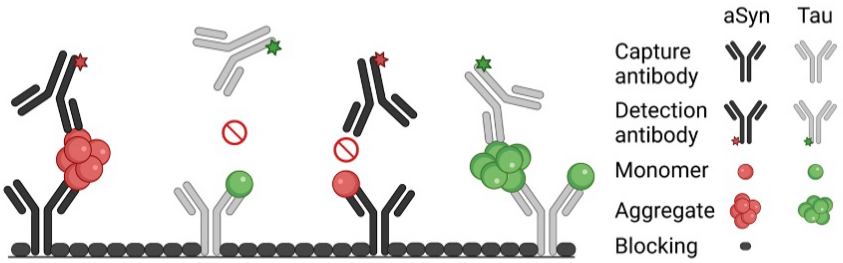

Fig. 1 Scheme of the sFIDA assay. Antibodies directed against linear epitopes of aSyn (211) or Tau (Tau5) are immobilized on the glass surface of a microtiter plate. Monomers and aggregates of the sample can bind to the capture antibodies, but only aggregates are detected with fluorescently labeled probes (211 CF633 and Tau5 CF488A) because capture and detection antibodies bind the same epitope. For monomeric protein, this epitope is masked by the capture antibody and can therefore not be bound by a probe antibody. Finally, the assay surface is imaged by dual-color fluorescence microscopy and single particles on the well surface are counted by image-data analysis. *Created with BioRender.com*.

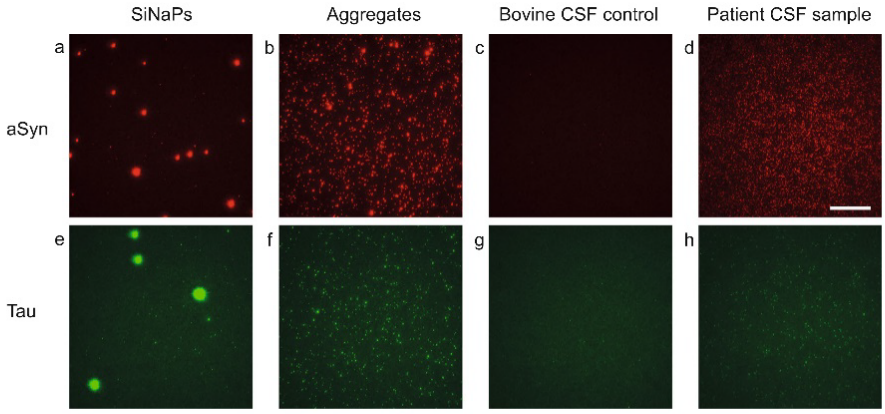

Fig. 2 TIRFM images of aSyn and Tau SiNaPs, synthetic aggregates, and samples. Shown are characteristic TIRFM images for the red fluorescence channel (211 CF633) of **a** 629 fM aSyn SiNaPs in buffer, **b** 8 nM aSyn aggregates in buffer (the concentration is based on the monomer concentration), **c** a bovine CSF control, **d** a CSF sample of a PD patient as well as for the green fluorescence channel (Tau5 CF488) of **e** 645 fM Tau SiNaPs in buffer, **f** 200 nM Tau aggregates in buffer (the concentration is based on the monomer concentration), **g** a bovine CSF control, **h** a CSF sample of a PSP patient. The scale bar is 25 µm. For illustration of the 14-bit images, the contrast was adjusted to a maximum grayscale value of 5000.

disease patients is yet to be established. In the present work, we apply sFIDA to quantitate aSyn and Tau aggregates in CSF from 237 individuals, demonstrating its applicability in clinical settings and drug development.

RESULTS

In this work, we have developed an sFIDA assay for simultaneous quantification of aSyn and Tau aggregates. Development and validation of immunoassays require determination of crucial parameters including limit of detection (LOD), coefficient of variation, inter-assay and inter-laboratory correlation and cross reactivity, which are described in the first part of the results chapter.

sFIDA displays low intra-assay variance for measurements of SiNaPs and samples

The sFIDA technology was used to determine the concentrations of aggregated aSyn and aggregated Tau in a total of 237 CSF samples. Due to the high number of assay points, the measurements were performed on a total of eight 384 well microtiter plates. For calibration of the samples and determination of the LOD, we used our previously developed silica nanoparticle (SiNaP) standard[14] (TEM image and size distribution in Supplementary Fig. 1). Exemplary images of SiNaPs, aggregates, bovine CSF and patient samples are shown in Fig. 2. The intra-assay variance among all experiments was calculated from the pixel counts of the four replicates. The intra-assay variance for the calibration standard was 15.8% for aSyn SiNaPs and 19.1% for Tau SiNaPs for the concentrations included in the calibration range. The intra-assay variance of the samples was 16.8% for aSyn aggregates and 13.0% for Tau aggregates, respectively (individual results for each experiment in Supplementary Table 1).

Independent measurements of aSyn and Tau aggregates in CSF samples yield comparable results

The inter-assay variance was studied in 20 samples on two different runs that were executed at a four-month interval. We analyzed each sample in four replicates and determined an intra-assay variation for the 20 CSF samples of 22.6% for aSyn aggregates and 20.4% for Tau aggregates. A linear correlation between the two measurements was observed for the detection of aSyn aggregates with a Pearson coefficient of correlation of $r = 0.964$. Although the concentration of Tau aggregates was less than that of aSyn aggregates and very close to the LOD, the two

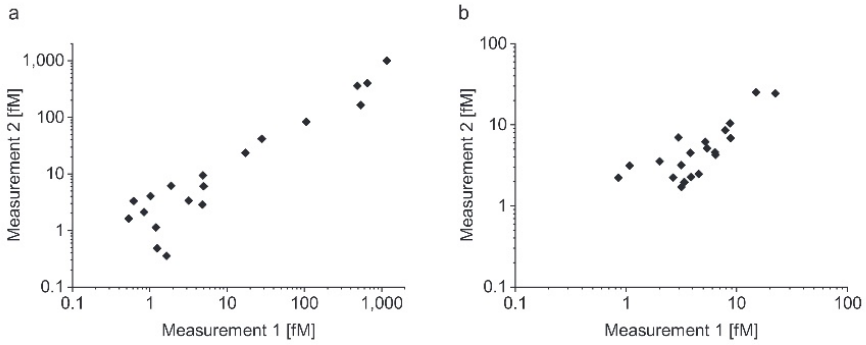

Fig. 3 Repeated measurements of aSyn and Tau aggregates in CSF yield highly reproducible results. We tested the inter-assay variance of the sFIDA assay for **a** aSyn and **b** Tau aggregates. Two independent measurements of 20 CSF samples by the same technician in the same laboratory on different days were highly reproducible with a Pearson coefficient of correlation of $r = 0.96$ for aSyn aggregates and $r = 0.92$ for Tau aggregates.

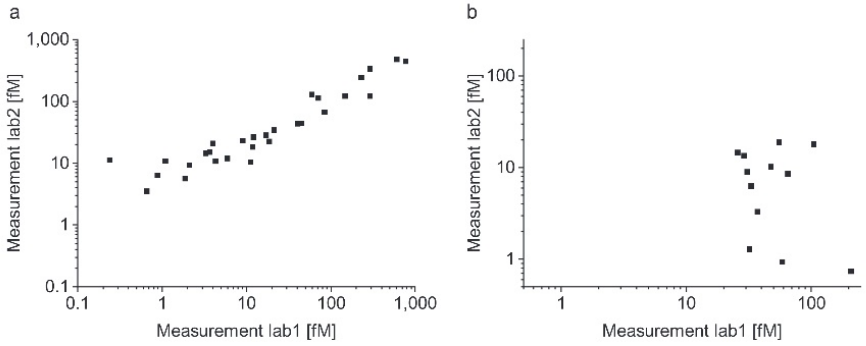

Fig. 4 Measurements of aSyn but not Tau aggregates in CSF correlated well when measured in a different laboratory. The CSF samples were measured by sFIDA by two different technicians in two different laboratories. The first sFIDA experiment was prepared and run by a technician at the Forschungszentrum Jülich, while the second sFIDA was performed by another technician at the Heinrich-Heine-Universität Düsseldorf. **a** Concentrations of aSyn aggregates correlated well between both experiments with a Pearson coefficient of correlation of $r = 0.95$, **b** while for Tau aggregates no correlation was observed ($r = 0.03$).

measurements showed a significant correlation with a Pearson coefficient of correlation of $r = 0.920$ (Fig. 3).

The inter-laboratory variance was studied in a laboratory at the Forschungszentrum Jülich and another laboratory at the Heinrich-Heine-Universität in Düsseldorf. The calibrated results for the detection of aSyn aggregates showed a high correlation with a Pearson coefficient of correlation of $r = 0.950$. In this study, no correlation for Tau aggregates was observed (Pearson coefficient of correlation of $r = 0.033$, Fig. 4).

sFIDA features femtomolar sensitivity for the detection of aSyn and Tau SiNaPs

We determined the sensitivity of the assay based on aSyn and Tau SiNaPs. After application of t-test, Mann-Whitney U test, LOD and standardization of the calibration range for all experiments, the upper limit of the calibration curve was 1.99 pM for aSyn and 2.04 pM for Tau SiNaPs, and the lower limit was set to 63 fM and 204 fM for aSyn and Tau SiNaPs, respectively. In all experiments a linear correlation between pixel count and concentration with a mean coefficient of determination of 0.98 for aSyn and 0.96 for Tau SiNaPs was observed. The calibration resulted in a mean LOD of 6.72 fM for the detection of aSyn SiNaPs and a mean LOD of 33.7 fM for the detection of Tau SiNaPs (individual LOD values for each experiment are shown in Supplementary Table 2). For aSyn aggregates, 66% of samples were above the LOD of the individual experiment and for Tau aggregates 44% (Supplementary Table 3).

sFIDA shows negligible cross reactivity for measurements of aSyn, amyloid beta, and Tau

To determine the selectivity of the sFIDA assay, amyloid beta SiNaPs with a concentration of 6 pM were used as a control. The amyloid beta SiNaPs were coated with amino acid residues 1–15 of the amyloid beta protein. We observed a very low cross reactivity with 0.1% of the signal for amyloid beta SiNaPs when compared to the signal obtained with aSyn SiNaPs and 0.2% of the signal obtained with Tau SiNaPs when used at a comparable concentration (data not shown). Detection of synthetic Tau aggregates with the 211 antibody and detection of synthetic aSyn aggregates with the Tau5 antibody resulted in a pixel count as negligible as for the buffer control (Fig. 5). The pixel count of the buffer control (BC) showed an increased background signal compared to the CSF control for aSyn (capture and detection antibody: 211) and Tau (capture and detection antibody: Tau5) (Fig. 5). Therefore, the CSF control was used as negative control for the calibration of the samples. The buffer control showed no autofluorescence signal (data not shown). The recovery of aSyn SiNaPs spiked in bovine CSF was 79%. For Tau SiNaPs the recovery in CSF was 36%. Another control was to run the assay without a capture antibody, which is an indication for unspecific binding of silica nanoparticles or proteins to the surface, and is described as the signal compared to the same concentration of silica nanoparticles/protein on an antibody surface. For aSyn, the signal originating from 6 pM silica nanoparticles without the use of a

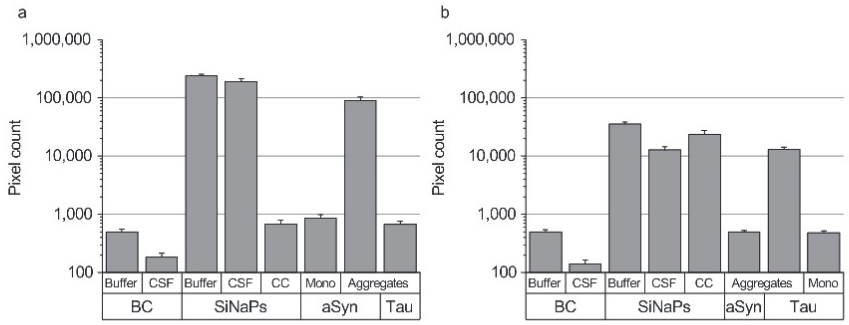

Fig. 5 Pixel counts of assay controls for the detection of aSyn and Tau aggregates. a aSyn SiNaPs showed a recovery of 79% in CSF, whereas **b** Tau SiNaPs showed a recovery of 36% in CSF. Synthetic aSyn and Tau aggregates served as positive controls. The pixel counts of the aSyn aggregates when detected with the Tau5 antibody as well as the pixel counts of the Tau aggregates when detected with the 211 antibody were as low as the blank control (BC). The pixel count of 8 nM monomeric (Mono) aSyn as well as 200 nM monomeric Tau was reduced by 99.5% compared to the same concentration of monomer units in aggregated aSyn or Tau. When the capture antibody was omitted (capture control, CC), no signal was detected for aSyn SiNaPs, whereas the signal for Tau SiNaPs was still at 67%. Standard deviation was calculated from the four replicates.

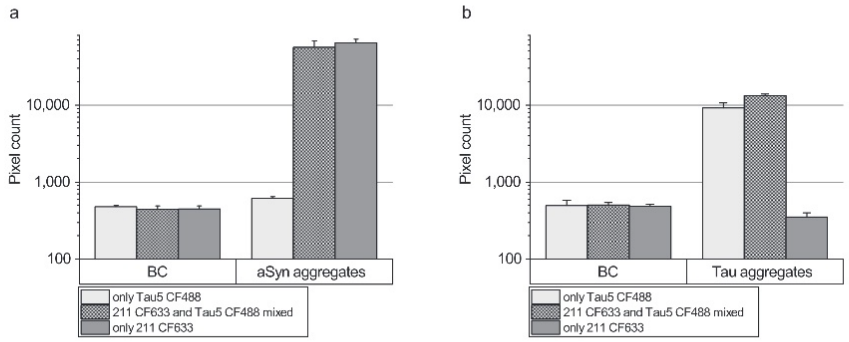

Fig. 6 Analysis of probe interference. To analyze the effect of detection probe interference on the signal, we performed an additional experiment in which we added either only one detection antibody or both detection antibodies. Using only the relevant antibody probe did not show an increased pixel count for the detection of aggregated aSyn (**a**, 211 CF633) or Tau (**b**, Tau5 CF488), respectively. Standard deviation was calculated from the four replicates.

capture antibody was below 0.1% of that when a capture antibody was used. For Tau, the signal was still at 67% without a capture antibody and, presumably, originating from large particles which non-specifically stick to the glass surface. Furthermore, we investigated the effect of monomeric aSyn and Tau on the sFIDA readout.

We found that the pixel counts of both aSyn and Tau monomers, respectively, were decreased by about 99.5% compared to the signal of aSyn or Tau aggregates indicating that endogenous monomers in the CSF samples have a neglectable effect on the sFIDA readout (Fig. 5).

To address the question whether addition of the mixture of two antibodies might impair assay sensitivity, we added just the relevant detection antibody or a mixture of both detection antibodies, and compared the correspondent sFIDA readouts. As shown in Fig. 6, applying just a single detection antibody did not increase the readout. Moreover, absence of confounding autofluorescence signals was demonstrated, because aggregated aSyn and Tau did not show any non-specific signal when the relevant antibody probe was not applied.

aSyn and Tau aggregates are removed by immunodepletion

To show that the signal measured by sFIDA is specifically attributed to aSyn and Tau aggregates and not to matrix interference, we performed immunodepletion in five CSF samples and the silica nanoparticle standard. To remove the analytes, samples were incubated in presence of magnetic beads linked to 211 antibody, Tau5 antibody or no antibody. After magnetic separation, the supernatants were subjected to sFIDA analysis. For aSyn, 211-depleted samples showed a mean decrease of the readout by 97.0% (Fig. 7b), while in the controls without 211 antibody, the readout was not reduced (−0.6%). Although the readout for Tau aggregates in the samples was comparatively low and close to that of the bovine CSF control, depletion with Tau5 decreased the readout by 38.6% (Fig. 7c, d). Incubation of the samples with magnetic beads alone led to an average decrease of the pixel count by only 19.5% (Fig. 7d). Still, the less efficient reduction in the samples compared to the standards can be attributed to a lower signal-to-noise ratio. The Tau-coated silica nanoparticle standard was depleted even without Tau5 antibody, suggesting non-specific adherence to the surface as observed in the capture control experiment (Fig. 5b).

Analysis of potential heterophilic anti-mouse antibodies (HAMAs) interference

Although one may expect absence of high antibody titers in CSF, we investigated whether HAMAs could possibly compromise the sFIDA assay result, and whether this is potentially relevant for the interpretation of the study results. HAMAs are a well-described interfering factor in immunoassays especially for blood-based

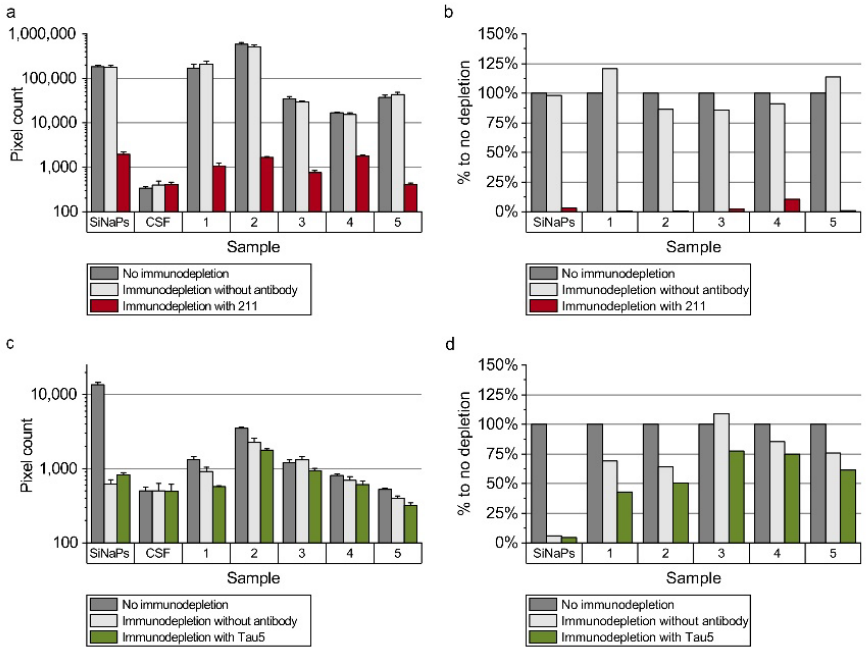

Fig. 7 Immunodepletion of aSyn and Tau in CSF samples. The SiNaP standard and five CSF samples were subjected to immunodepletion with magnetic beads with and without antibody. **a**, **b** Immunodepletion of samples with 211 antibody decreased the pixel counts for aSyn on average by 97%, while incubation with magnetic beads without antibody did not affect the signal. **c**, **d** For aggregated Tau, incubation with magnetic beads without antibody decreased the pixel count by 94% for Tau SiNaPs and on average by 19.5% for samples. Using Tau5 antibody, the decrease of the pixel count for Tau SiNaPs was 95% and for samples 38.6%, respectively. The *% to no depletion* value (Fig. 7 **b**, **d**) was calculated by the ratio the pixel counts of depleted to non-depleted samples. Standard deviation was calculated from the four replicates.

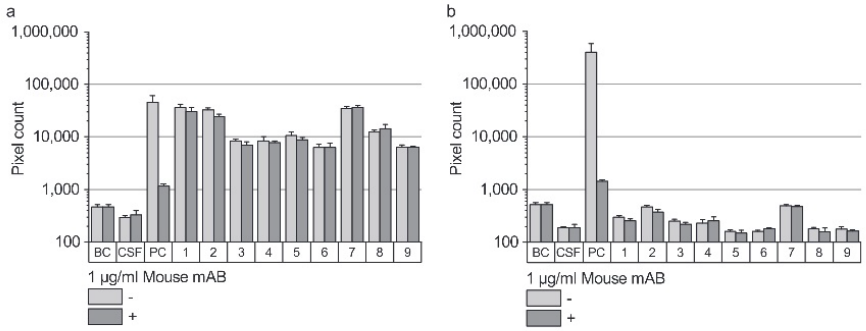

Fig. 8 Influence of heterophilic anti-mouse antibodies. To test, if the signal obtained by sFIDA was possibly caused by heterophilic anti-mouse antibodies, nine CSF samples were incubated with or without 1 µg/ml MOPC-21. As a HAMA model and positive control (PC), we used a goat anti-mouse antibody. The interference of this anti-mouse antibody was reduced by about 98.4% for aSyn (211 CF633, **a**) and 99.7% for Tau (Tau5 CF488, **b**) when adding MOPC-21 while for the CSF samples the signal remains unaffected. Standard deviation was calculated from the four replicates.

assays[16,17]. HAMAs can crosslink capture and detection mouse antibodies leading to false positive signals. Recent research indicates, that HAMAs can also interfere with measurements of CSF samples[18,19]. To analyze HAMA interference in our assay, we used an anti-mouse antibody as a HAMA model. As expected, sFIDA analysis of a blank control spiked with the anti-mouse antibody shows an increased signal in both detection channels (Fig. 8, PC). Addition of the same concentration of a competitor mouse antibody (MOPC-21) reduces the signal by 98.4% for 211 CF633 and by 99.7% for Tau5 CF488. Additionally, we tested nine CSF samples, which yielded high sFIDA readouts, for possible presence of HAMAs. Incubation of the samples with MOPC did not influence sFIDA readouts (p-value of two-sided Mann-Whitney-U for 211 CF633: 0.470, Tau5 CF488: 0.800) suggesting that the observed signal indeed originates from aggregate-bound probes and is not due to HAMA interference.

Contamination with blood did not affect the quantification of aSyn and Tau aggregates in CSF

As blood shows an increased concentration of total aSyn, the contamination of CSF even with low amounts of blood can interfere with the detection of aSyn monomers in CSF[20,21]. To investigate, whether the results in sFIDA were affected by blood contamination as well, we classified the samples into five groups according to their contamination level. Most of the samples (57%)

Table 1. Demographic information on patients and controls that donated CSF samples.

	PD	AD	DLB	PSP	*N*
Number	115	28	19	30	45
Female	41 (36%)	10 (36%)	5 (26%)	15 (50%)	20 (44%)
Age [years]	65.7 (±7.6)	68.2 (±6.3)	69.7 (±7.2)	67.5 (±6.2)	69.0 (±8.9)
Education [years]	16.3 (±2.3)	14.9 (±3.2)	15.5 (±2.8)	15.2 (±2.7)	16.6 (±3.6)
Deceased	17%	32%	32%	37%	13%

PD Parkinson's disease, *AD* Alzheimer's disease, *DLB* Dementia with Lewy bodies, *PSP* Progressive supranuclear palsy, *N* Normal control.

showed no contamination with blood (negative test result), 11% were classified to contamination level 1 (~10 Ery/µL), 7% to level 2 (~25 Ery/µL), and 8% to level 3 (~50 Ery/µl). A contamination of level 4 (> 250 Ery/µL) was observed in 18% of CSF. We further investigated, whether there is a correlation between high read-outs in sFIDA and the blood contamination level. We could not observe a significant increase of aSyn ($p = 0.776$) or Tau ($p = 0.628$) aggregate concentrations in CSF contaminated with blood using Kruskal-Wallis ANOVA (scatterplot in Supplementary Fig. 2). Therefore, no samples were excluded from analysis.

Descriptive analysis of the patient and control cohorts

The samples comprised five diagnostic groups (Table 1). Applying the Kruskal-Wallis test, no significant differences between groups was found for age and gender. For education, PD patients received longer education than AD patients, and normal controls received longer education than the AD and PSP cohorts. Individual information and results of each patient are listed in Supplementary Table 4.

aSyn and Tau aggregate levels distinguish patients with different neurodegenerative diseases

First, we tested the calibrated results of all groups for normal distribution. As the data showed non-normal distributions (*p*-value < 0.05, Supplementary Table 5), statistical analysis was performed using non-parametric tests like the Kruskal-Wallis or Mann-Whitney U test. The results of the Kruskal-Wallis test showed significant differences between the diagnostic groups for aggregated aSyn ($p = 6.92*10^{-3}$) as well as for aggregated Tau ($p = 2.17*10^{-6}$). The results of pairwise comparisons are shown in Table 2. Concentrations of aSyn aggregates in CSF samples of PD patients were significantly increased compared to the control group. Moreover, patients with DLB showed elevated levels of aSyn aggregates in their CSF. Interestingly, CSF samples of AD patients also showed significantly increased levels of aSyn aggregates compared to normal controls. In the scatterplot (Fig. 9a) as well as in the receiver operating characteristic (ROC) curve (Fig. 9c) we observed a great overlap between synucleinopathies like PD and DLB and the control group (sensitivity and specificity values and AUC in Table 3).

The concentrations of Tau aggregates in PSP samples were significantly elevated compared to all other groups (PD, DLB, AD and controls; Fig. 9b). ROC analysis (Fig. 9d) for this model showed a sensitivity and specificity of 87 and 70% (AUC 0.76) for distinguishing PSP from all other subjects based on Tau sFIDA alone. Moreover, patients with DLB had elevated levels of Tau aggregates compared to the control group ($p = 0.006$) and to PD patients ($p = 0.024$). Interestingly, no significant increase in Tau aggregate concentration for AD patients was observed. The performance of ROC analysis for the tauopathies PSP and AD versus non-tauopathies (DLB, PD, N) revealed a decreased sensitivity and specificity compared to PSP alone. AD alone showed no distinguishability to PD, DLB, and N (Table 2).

Table 2. *P*-values of two-sided Mann-Whitney U test for pairwise comparisons of measured aSyn and of Tau aggregate concentrations.

		PD	DLB	PSP	AD	*N*
aSyn	PD	1				
	DLB	0.992	1			
	PSP	0.292	0.326	1		
	AD	0.811	0.887	0.561	1	
	N	$3.6*10^{-4}$	0.007	0.109	0.010	1
Tau	PD	1				
	DLB	0.024	1			
	PSP	$2.0*10^{-6}$	0.022	1		
	AD	0.418	0.167	$3.4*10^{-4}$	1	
	N	0.243	0.006	$9.7*10^{-6}$	0.123	1

PD Parkinson's disease, *AD* Alzheimer's disease, *DLB* Dementia with Lewy bodies, *PSP* Progressive supranuclear palsy, *N* Normal control.

Aggregate concentrations show comparable discrimination to conventional biomarkers

In CNS biomarker research and clinical routine, total Tau protein (tTau) and phosphorylated Tau protein (pTau) are frequently used as a measure of neurodegeneration. For the present study, we received pTau and tTau concentrations of 88% of the CSF samples and compared sensitivity, specificity and AUC values for each biomarker alone and as combination of three biomarkers (for PD and DLB: pTau, tTau and aSyn aggregates, for AD and PSP: pTau, tTau and Tau aggregates). For PD vs. N, tTau, aSyn aggregates and the combination of pTau, tTau and aSyn aggregates showed nearly the same AUC but differences in specificity and sensitivity (Fig. 10 and Table 4). Due to the reduced number of samples and adaption of the method for the analysis of DLB vs. N, the AUC for aSyn aggregates was decreased compared to the first analysis with all samples (Fig. 9 and Table 3). Consequently, in this analysis, discrimination is only possible based on tTau values. Like in the first analysis, Tau aggregate levels did not discriminate AD vs. N, while AD patients showed increased concentrations of pTau and tTau and can be discriminated with an AUC of 0.78 and 0.75, respectively. For PSP vs. N, pTau and Tau aggregates separated the diseases with an AUC of 0.74 and 0.73. Here, the combination of the three biomarkers showed the largest AUC of 0.80.

aSyn and Tau aggregate concentrations significantly correlate between all patient cohorts

As a correlation between total aSyn (t-aSyn) and total Tau (tTau) has been reported in many studies[8,22–24], we investigated the correlation between aggregated forms of aSyn and Tau, respectively. A significant correlation between Tau and aSyn aggregate concentrations was observed for the whole data set (Pearson coefficient of correlation: $r = 0.81$, $p = 3.8*10^{-57}$), as well as for each individual diagnostic group (Fig. 11a). The greatest correlation was observed

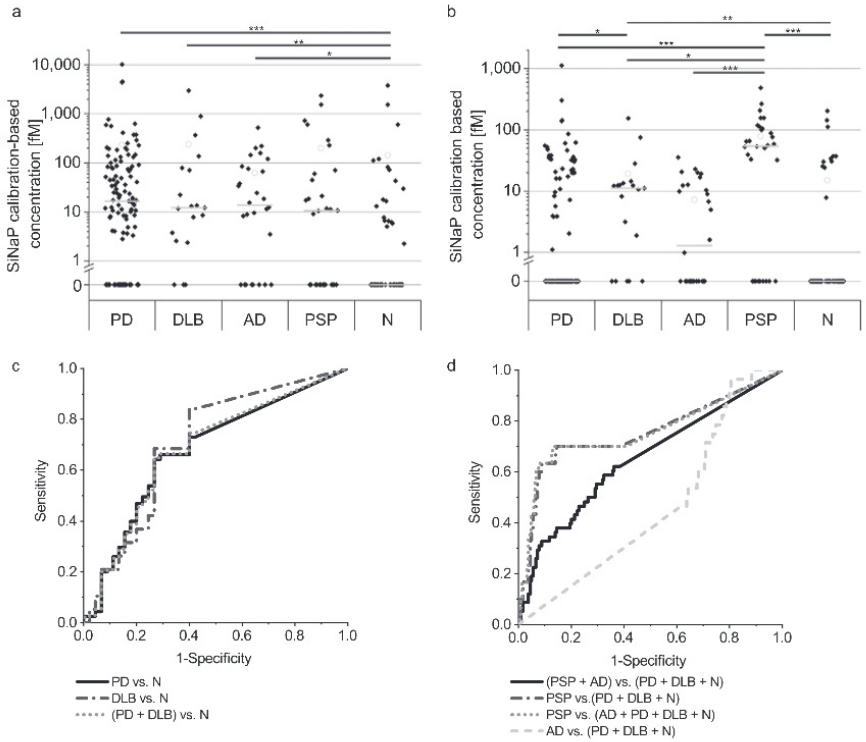

Fig. 9 Calibrated sFIDA results (a, b) and receiver operating characteristic (ROC) analysis (c, d) for the detection of aSyn and Tau aggregates in CSF samples. a For aSyn aggregates, PD, DLB, and AD samples were significantly elevated compared to normal controls (N). **c** In ROC analysis, discrimination of PD patients versus normal controls (N) showed a specificity of 73% and a sensitivity of 64% with an AUC of 0.68, while discrimination of DLB patients versus normal controls showed a specificity of 60% and a sensitivity of 84% with an AUC of 0.71. In combination, synucleinopathies (PD and DLB) can be differentiated from normal controls with a specificity of 73% and a sensitivity of 65% with an AUC of 0.68. **b**, **d** For Tau aggregates, the tauopathy PSP but not AD can be discriminated from non-tauopathies (for PSP vs. non-tauopathies: 86% specificity and 70% sensitivity with an AUC of 0.75; for other specificity and sensitivity values s. Table 3). DLB samples showed significantly increased Tau aggregate concentrations compared to normal controls and PD patients (*p*-values of Mann-Whitney U test for aSyn and Tau aggregates are shown in Table 2). Values below the LOD were set to 0. "-" indicates the median and "○" the mean. Significant differences between cohorts were calculated with Mann-Whitney U test and signed with * ($*p = 0.01–0.05$; $**p = 0.001–0.01$; $***p < 0.001$). Please, note the logarithmic concentration scales.

Table 3. Results of ROC analysis for specificity, sensitivity and area under the curve (AUC) for aSyn and Tau aggregates in CSF.

		Specificity	Sensitivity	AUC
aSyn	PD vs. N	73.3%	64.3%	0.678
	DLB vs. N	60.0%	84.2%	0.705
	(PD + DLB) vs. N	73.3%	64.9%	0.682
Tau	(PSP + AD) vs. (PD + DLB + N)	67.6%	58.6%	0.649
	PSP vs. (PD + DLB + N)	85.5%	70.0%	0.753
	PSP vs. (AD + PD + DLB + N)	87.0%	70.0%	0.755
	AD vs. (PD + DLB + N)	19.6%	96.4%	0.462

PD Parkinson's disease, *AD* Alzheimer's disease, *DLB* Dementia with Lewy bodies, *PSP* Progressive supranuclear palsy, *N* Normal control, *AUC* Area under the curve.

for DLB samples with a Pearson coefficient of correlation of 0.98 ($p = 8.5*10^{-13}$). PD ($r = 0.87$, $p = 6.5*10^{-36}$), PSP ($r = 0.74$, $p = 3.4*10^{-6}$), and normal control ($r = 0.90$, $p = 2.5*10^{-17}$) CSF samples also showed a positive correlation. For AD patients, the correlation was weaker ($r = 0.52$, $p = 0.005$).

Age, sex and disease duration do not correlate with aggregate concentrations in CSF

As age and gender are risk factors for PD, AD, DLB and PSP[25], the correlation between the concentration of aSyn and Tau aggregates to age and sex are interesting parameters. Across all cohorts, there was no detectable significant effect specific to age, sex, or disease duration (Pearson coefficient of correlation in Supplementary Table 6). For Tau, we observed an inverse correlation between aggregate concentration and education.

DISCUSSION

Our study explored the ability of the sFIDA technology to detect and quantitate aSyn and Tau aggregates in CSF samples and its applicability for the diagnosis of neurodegenerative diseases. aSyn oligomers are thought to be the major toxic species in synucleinopathies like PD and DLB[4,26] but the detection of such oligomers in human biofluids is still challenging due to the low concentration of oligomers and the interference with monomers. The principle of sFIDA allows the sensitive detection and quantitation of oligomers and other aggregates in the presence of monomers with an LOD in the low femtomolar region. Approximately 66% of the CSF samples tested here showed concentrations above the LOD with a wide concentration range of up to 10 pM. Most samples harbored concentrations of aSyn

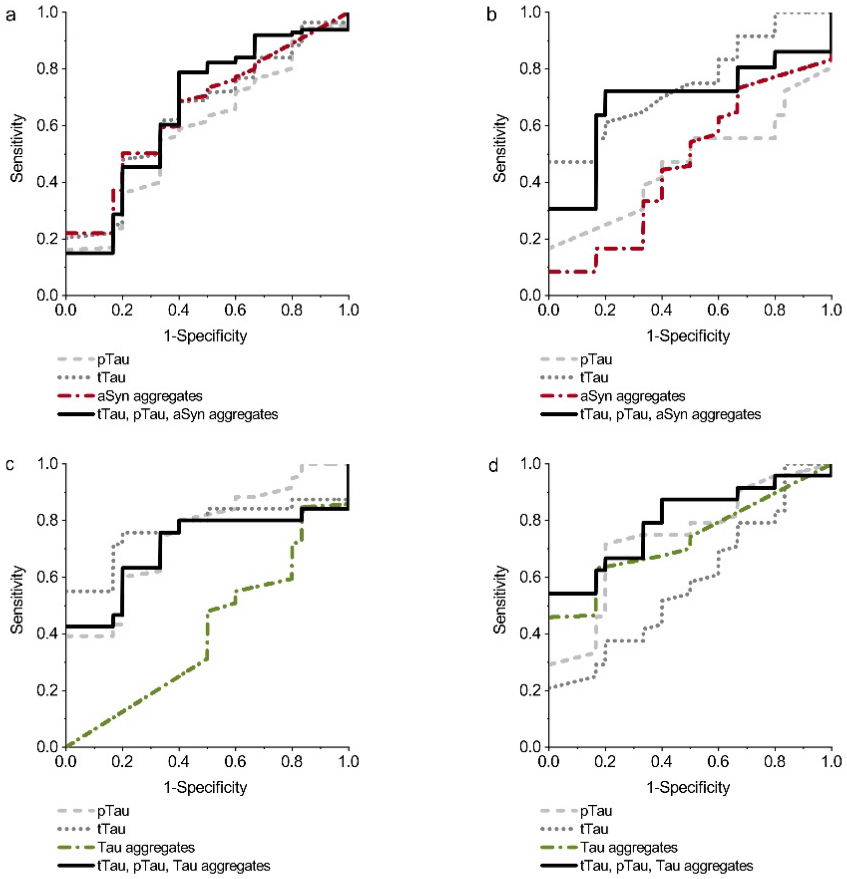

Fig. 10 ROC of pTau, tTau, aSyn and Tau aggregates and their combination. We compared the performance of different biomarkers and analyzed, if the combination of biomarkers improves the discrimination of neurodegenerative diseases compared to normal control (**a**: PD vs. N, **b**: DLB vs. N, **c**: AD vs. N, **d**: PSP vs. N). Sensitivity, Specificity and AUC values are listed in Table 4.

aggregates between 5 fM and 500 fM. For Tau aggregates, 44% of the CSF samples were above the LOD. It has to be considered that a single SiNaP led on average to more pixels with fluorescence above the cutoff value than compared to the average aggregate from real samples. This is presumably due to a higher amount of accessible binding sites for detection antibodies or due to agglomeration of our silica nanoparticle standard. Probably, both aspects influence the average apparent size distribution of our standard particles. With the term size, we therefore do not refer to the actual size, as all particles can be expected to be below the optical resolution limit, but instead to the number of pixels that are illuminated above the cutoff value. The evaluation accounts at least partially for that, because the exact fluorescence intensity of a pixel is not affecting the readout, only the digital decision, whether the fluorescence intensity of a pixel is above the cutoff threshold or not. Nevertheless, the differences in particle size may influence the calibration, so we described the calibrated concentrations as *SiNaP calibration-based concentration*. In this study, we calculated an average apparent particle size of 11.2 pixels per particle for aSyn SiNaPs (obtained from the 63 fM calibration), while for aggregated aSyn in patient samples, the apparent average particle size was 5.2 pixels. For Tau, 204 fM SiNaPs and samples yielded an average apparent particle size of 10 pixels and 2.6 pixels, respectively.

As expected, CSF samples of PD and DLB patients harbored significantly elevated levels of aSyn aggregates compared to normal controls. This is in agreement with several other studies quantifying aSyn oligomers in CSF[8,27,28]. But there is also a large overlap between synucleinopathies and normal controls, which is congruent with some previous studies aimed at discriminating both populations (Majbour: sensitivity 89%, specificity 52%[8], Tokuda: sensitivity 75%, specificity 88%[27]). The combination of aSyn aggregates with other predictive values like total aSyn (t-aSyn), phosphorylated aSyn (p-aSyn), tTau, phosphorylated Tau (pTau), or age may improve the discrimination of synucleinopathies from normal controls, as investigated in other studies[8,21,29]. In this work, we have tested the combination of aSyn aggregates as biomarker with pTau and tTau. The combination of the three biomarkers did not improve the predictive power of the analysis, but for PD vs N, aSyn aggregates alone showed the highest performance of the three biomarkers. We hypothesize that the combination with t-aSyn probably has a higher impact on the AUC, but information on total aSyn levels was not available for the samples tested in this study.

Interestingly, we found elevated levels of aSyn aggregates also in AD patients with concentrations comparable to that of PD or DLB patients. The role of aSyn in AD is still under investigation. Many studies have reported the presence of Lewy bodies in AD brains[30–33] as well as increased t-aSyn concentrations in CSF[24],

Table 4. Results of ROC analysis for specificity, sensitivity and area under the curve (AUC) for pTau, tTau, aSyn or Tau aggregates in CSF and their combination.

		Specificity	Sensitivity	AUC
PD vs. N	tTau	60.0%	68.5%	0.645
	pTau	66.6%	55.0%	0.589
	aSyn aggregates	80.0%	50.2%	0.656
	pTau + tTau + aSyn aggregates	60.0%	78.8%	0.663
DLB vs. N	tTau	100.0%	47.2%	0.752
	pTau	100.0%	16.7%	0.468
	aSyn aggregates	100.0%	8.3%	0.468
	pTau + tTau + aSyn aggregates	80.0%	72.2%	0.689
AD vs. N	tTau	80.0%	75.8%	0.775
	pTau	66.6%	74.7%	0.753
	Tau aggregates	16.6%	84.7%	0.409
	pTau + tTau + Tau aggregates	80.0%	63.3%	0.708
PSP vs. N	tTau	100.0%	20.8%	0.586
	pTau	80.0%	71.7%	0.743
	Tau aggregates	83.3%	63.2%	0.734
	pTau + tTau + Tau aggregates	100.0%	54.2%	0.800

and in an autopsy study based at UPenn, where our CSF samples were collected, more than 52% of individuals with a diagnosis of AD showed considerable Lewy body burden on neuropathology[34]. However, prior biomarker studies have also reported no difference in aSyn monomer concentrations in CSF of AD patients compared to normal controls[21], or even decreased levels of aSyn oligomers in CSF of AD and PSP compared to PD patients[27,35], which is in contrast to our results. Differences in study results might be ascribed to differences in (1) the makeup of patients recruited at different clinical sites, (2) preanalytical aspects related to sample collection or handling, or (3) quantification methods[36]. In this context, we note that all samples used in this study were single-use aliquots collected under strict standard operating procedures. For PSP, we did not measure a significant increase in aSyn aggregate concentration compared to normal controls, which agrees with other studies[21,27].

To date, limited evidence exists regarding the detectability of Tau aggregates in CSF for the diagnosis of neurodegenerative diseases. Increased Tau oligomer concentrations in postmortem PSP brain samples have been reported by Gerson et al.[37]. This is in agreement with our study, where PSP patients showed increased levels of Tau aggregates compared to all other diseases, with sensitivity and specificity of 87 and 70%, respectively. Although there is a consensus about the certainty of tTau and pTau for diagnosis of AD[38] and the presence of Tau oligomers in AD brains[9], we did not observe a statistically significant increase in the concentration of Tau aggregates in CSF samples of these patients. Up to now, most studies are focusing on the presence of tTau and pTau in neurodegenerative diseases. For PSP and AD, quite different concentrations are found in CSF: AD shows significantly increased levels of tTau and pTau[23], whereas PSP samples show no difference or even a decrease in Tau monomer concentrations[23,39]. These observations match our data showing that pTau and tTau were increased for AD, but decreased for PSP (for pTau). For PSP, Tau aggregates alone can differentiate between PSP and normal control group similar to pTau, and the combination of the biomarkers improves the specificity and AUC, which underlines the role of Tau aggregates in PSP as possible biomarker. Wagshal et al. postulate that differences between AD and PSP can probably be ascribed to differences in Tau isoforms, as PSP is known as a 4R-tauopathy, whereas AD shows equal ratios of 4 R and 3 R Tau. Different isoforms of Tau are differentially released from neuronal and glial cells and have differing affinities to antibodies[39,40]. These differences could also be relevant in interpreting our present results, which suggest that aggregated Tau species discriminate PSP vs. AD.

The importance of Tau protein in PD and DLB is still under investigation. Many studies have reported the presence of neurofibrillary tangles in PD and DLB brains[30,31,41,42] but no increase in tTau or pTau in CSF samples of PD patients[8,21]. Our study implicates no relation of increased Tau aggregate concentrations in CSF and the presence of PD. Interestingly, DLB samples showed elevated levels of Tau aggregates compared to those of normal controls and compared to PD patients, but less than those observed in PSP samples.

We also correlated aSyn and Tau aggregate concentrations in CSF samples between individual groups. For correlation of t-aSyn and tTau evidence in the literature is inconcise. Parnetti et al. reported an inverse correlation of aSyn and Tau[29], while several others have observed a positive correlation[22–24]. For aSyn and Tau aggregates, we observed a highly significant positive correlation (Fig. 11a), which is in agreement with several other studies showing the coexistence of the two proteins in Lewy bodies[30,41] and even the existence of hetero-aggregates[33]. Despite substantial overlap, median values of the individual disease groups suggest a mixed pathology ranging from rather pure aSyn pathology in PD via AD and DLB to PSP which shows decreased aSyn and increased Tau pathology (Fig. 11b). Additional correlations with other potential biomarkers, e.g. Amyloid beta and TDP43 aggregates, may further complement the view on these diseases on the molecular level. Determining whether aSyn-Tau hetero-aggregates might be detected by sFIDA in human biofluids is a promising area of future investigation that might add to our understanding on the molecular basis of phenotypic overlap among neurodegenerative diseases.

Naturally occurring oligomers and other aggregates differ in size, morphology and posttranscriptional modifications[4,43]. For detection and quantification, we used the same capture and detection antibody directed against linear epitopes that are expected to be accessible in all aggregated species, in order to quantitate all isoforms, irrespectively of their structural conformation. In future studies, we will further characterize the exact nature of the analytes by introducing size standards and structural probes. Possibly, not all aSyn assemblies in human brain are neurotoxic or disease-specific, and it was strongly discussed if aSyn physiologically occurs as a globular tetramer or as an intrinsically disordered monomer[4,44,45]. Future research will show, if the complex pathology of neurodegenerative diseases limits the diagnostic specificity of measuring the whole soluble aggregate fraction. Nevertheless, we are convinced that the possibility to finally measure aggregate concentrations is essential not only in understanding the underlying pathology, but also for developing therapeutic compounds against these species. Here we showed, that total aggregate concentrations differentiate i.e. PD or PSP from normal control, which further emphasizes the usefulness of quantifying aggregates in CSF for diagnosis of neurodegenerative diseases. For sufficient accuracy, surely, sensitivity and specificity need to be improved, i.e., by combining the concentration of aSyn or Tau aggregates with other biomarkers like t-aSyn, tTau, pTau, or Aβ1-42. Taking further into consideration that perhaps not all naturally occurring aggregates are disease-relevant, it might be interesting to compare or combine the results of total aggregates measured by sFIDA with seeding assays like the RT-QuIC or assays that measure a specific fraction of aggregates.

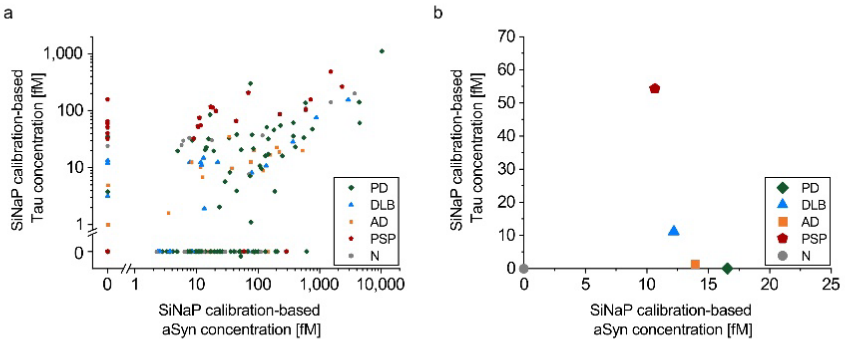

Fig. 11 Correlation of aSyn and Tau aggregate concentration. a aSyn and Tau aggregate concentrations measured by sFIDA show a highly significant correlation across all samples tested (Pearson coefficient of correlation $r = 0.81$, $p = 3.8*10^{-57}$) as well as for each individual cohort. Correlation of the median values for the disease groups is plotted in **b**.

Moreover, we note that, aside from diagnostic applications, sFIDA may be a valuable tool in clinical studies, to select, stratify, and monitor patients for therapies targeting aSyn or Tau oligomers, since sFIDA allows for direct assessment of the mechanism of action and is able to measure target engagement, irrespectively of the structural conformation. Finally, treatment success can be validated on the molecular level by monitoring aggregate titers over the course of medication.

METHODS

Synthesis of protein-coated silica nanoparticles

For assay calibration we have developed a nanoparticle calibration standard based on a silica core[14]. These silica nanoparticles (SiNaPs) were synthesized via Stöber process and afterwards modified with 3-aminopropyl(triethoxysilane) (APTES, Sigma-Aldrich, St. Louis, USA) to generate an aminated surface. Proteins were crosslinked to the aminated surface by maleimido hexanoic acid (MIHA, abcr GmbH, Karlsruhe, Germany). After activation with 200 mM 1-ethyl-3-(3-dimethylaminopropyl)carbodiimide (EDC, Sigma Aldrich, St. Louis, USA) and 50 mM N-hydroxysuccinimid (NHS, Sigma Aldrich, St. Louis, USA) for 10 min at room temperature (RT), the carboxy group of MIHA was coupled covalently to the amines of the silica nanoparticles. Following incubation for 1 h at RT, the resulting SiNaPs were centrifuged (7000 x *g*, 2 min) and redispersed in PBS and 10% dimethylformamid (DMF, Sigma Aldrich, St. Louis, USA). The washing step was repeated three times, where after the pellet was redispersed in PBS containing 10% DMF and 50 mM ethylendiamintetraacetic acid disodium salt (Na_2EDTA, AppliChem, Darmstadt, Germany) in the last step. Protein fragments of aSyn (aa115-130, Peptides and Elephants, Henningsdorf, Germany) and Tau (aa 210-230, Peptides and Elephants, Henningsdorf, Germany) are functionalized with cysteamine on the C-terminus to enable reacting with the maleimide group of the SiNaPs. For synthesis of protein-conjugated silica nanoparticles, 10% of the possible binding sites were functionalized by adding protein to the redispersed SiNaPs. The dispersion was shaken at RT and 650 rpm. After 1 h, 50 µL of 1 M Tris-(2-carboxyethyl)-phosphine (TCEP, abcr GmbH, Karlsruhe, Germany) was added to prevent oxidation of the protein. The reaction was quenched by adding 20 µL of a 1 M 2-mercaptoethanol solution. The functionalized SiNaPs were washed two times by centrifugation (10,000 x *g*, 4 min) and redispersed in ddH_2O. Finally, the silicon concentration was determined using ICP-MS (inductively coupled plasma – mass spectrometry) and the resulting molar SiNaPs concentration was calculated based on size, density as well as particle shape. Prior to use, the protein-conjugated silica nanoparticles were subjected to ultra-sonification for 10 min.

Tau and aSyn monomers were isolated prior to sFIDA measurement using size exclusion chromatography (Bio SEC3, pore size 150 Å, Agilent, Santa Clara, USA) to ensure that the sample does not contain any aggregates. After SEC purification, we determined the monomer concentration using UV-Vis spectroscopy. We calculated the signal reduction of monomers versus aggregates as described in Eq. (1):

$$Signal\ reduction[\%] = \left(1 - \frac{pixel\ count_{monomer} - pixel\ count_{BC}}{pixel\ count_{aggregates} - pixel\ count_{BC}}\right) * 100\% \quad (1)$$

Characterization of silica nanoparticles

Size and particle shape of the aminated silica nanoparticles were analyzed using transmission electron microscopy (TEM) as previously described by Hülsemann et al.[14]. Mean particle size was 18.5 nm for the aminated silica core (TEM image and size distribution in Supplementary Fig. 1).

Finally, the silicon concentration was determined using inductively coupled plasma – mass spectrometry (ICP-MS). SiNaPs were diluted in 3% nitric acid and analyzed in helium collision cell mode with an Agilent 7500 (Agilent Technologies, Japan). External calibration with rhodium as the internal standard was performed using NIST traceable commercial standard solution (VWR International, PA, USA). Complete dissociation of silica nanoparticles in the plasma without the need for digestion prior to analysis was shown in earlier studies up to a particle diameter of 500 nm[46–48]. The molar SiNaPs concentration was calculated based on the silicon concentration determined by ICP-MS and the known size, density as well as shape of the particles.

Labeling of antibodies

For microscopic detection of aggregates, we used fluorescent antibodies. The mouse anti-aSyn monoclonal antibody 211 (Santa Cruz Biotechnology, Inc., Dallas, USA) was labeled with CF633 (Biotium, Freemont, USA), whereas the anti-tau Tau5 antibody (Biolegend, San Diego, USA) was labeled with CF488A (Biotium, Freemont, USA). The labeling process was performed as described in the manufacturer's protocol. The dyes were activated as succinimidyl esters to react covalently with the amines of the antibody in carbonate buffer. For purification of each labeled antibody, a polyacrylamide bead suspension (Bio-Gel P-30 Gel, Bio-Rad Laboratories, Inc., Hercules, USA) was used. The concentration and the degree of labeling was determined according to the manufacturer's protocol.

Assay protocol

The biochemical principle of the sFIDA assay was previously described by Kravchenko et al., and Herrmann et al.[11,49]. In the present study, we used Nunc MicroWell 384-Well plates (Thermo Fisher Scientific, Waltham, USA) functionalized with 211 and Tau5 antibodies as captures, each at 5 µg/mL in 1 x PBS buffer. After washing five times with 80 µL TBS-T (1x TBS (Serva, Duisburg, Germany) and 0.05% Tween20 (AppliChem, Darmstadt, Germany)) and afterwards five times with 1 x TBS, the wells were blocked with 1% BSA (AppliChem, Darmstadt, Germany) in TBS containing 0.03% ProClin (Sigma Aldrich, Missouri, USA) for 1.5 h at RT. The plate was washed again with TBS-T and TBS (see above) and 20 µl protein-conjugated SiNaPs diluted in TBS-ProClin containing 0.5% BSA and 0.05% Tween, and 20 µl of the samples were incubated for 2 h at RT. After washing five times with TBS and changing the buffer to TBS-ProClin, the wells were incubated for 2 h

with the fluorescent detection antibodies 211-CF633 (0.4 µg/mL) and Tau5-CF488 (4 µg/mL) in TBS, after which the wells were washed with TBS again. For measurement, the buffer in the wells was changed against TBS-ProClin. Each concentration and sample were pipetted fourfold. All washing steps were carried out by an automated microplate washer (405 LS Microplate Washer, BioTek, VT, USA).

Inter-assay and inter-laboratory measurements

For inter-assay measurement of the calibration curve and the samples, the same assay was repeated four months later by the same technician with the same antibodies and materials but minor changes in washing conditions, such as the use of a different microplate washer and washing and blocking reagents with a different manufacturing date. Repeatedly assayed samples were subjected to an additional freeze-thaw cycle.

For inter-laboratory analysis, the assay was prepared and measured by a different operator in a different laboratory. The first measurement took place at the Forschungszentrum Jülich, and the second measurement at the Heinrich-Heine-Universität in Düsseldorf two months after the first measurement with the same changes as described above for inter-assay analysis.

Immunodepletion

For immunodepletion, 211 and Tau5 antibody were covalently coated to carboxylated magnetic dynabeads (Invitrogen, Waltham, USA) according to the manufacturer's protocol. Shortly, dynabeads were washed twice with 2.5 mM 2-(N-morpholino)ethanesulfonic acid (MES, pH 5, Roth, Karlsruhe, Germany) and applied to a magnet to remove the supernatant. Carboxy groups were activated with 50 µg/ml EDC and 50 µg/ml NHS in MES for 30 min at RT while rotating. After activation, the dynabeads were washed again with MES and coated with 211 or Tau5 antibody to a concentration of 20 µg/ml dynabeads, respectively. To ensure that signal loss is not due to unspecific binding of sample components to dynabeads, we run a third synthesis without antibody. After incubation for 1 h at RT, dynabeads were washed again and quenched with 50 mM ethanolamine in MES for 1 h at RT followed by a last washing step.

For immunodepletion, we applied 0.5 mg of antibody coated dynabeads to the magnet and removed the supernatant. 100 µl sample were added and incubated for 1 h at RT while rotating. After incubation, dynabeads were applied to the magnet again and the supernatant was transferred to a fresh tube. The immunodepleted samples were analyzed using sFIDA as described above. To consider for possible effects of magnetic beads on the pixel count, we normalized the signals by using an individual cutoff based on the CSF control. Please, note that the CSF control used for immunodepletion and HAMA interference experiments differed from the CSF control used for calibrating the results of the big data set of the study and showed an increased fluorescence signal for Tau5 CF488.

Influence of heterophilic antibodies

The potential influence of heterophilic antibodies, specifically anti-mouse antibodies (HAMAs), was analyzed using the purified mouse IgG isotype control MOPC-21 as a competitor (Biolegend, San Diego, USA). Possibly existing HAMAs in CSF can bind to MOPC instead to the assay antibodies which prevents false positive signals. A total of nine samples that yielded high sFIDA signals were spiked with 1 µg/ml MOPC-21. As positive control, we used buffer spiked with 1 µg/ml goat anti-mouse IgG (Thermo Fisher Scientific, Waltham, USA) with or without MOPC-21.

Determination of blood contamination

Contamination of CSF samples with blood was determined semi-quantitatively using Combur10-Test-Analysis (Hoffmann-La Roche, Basel, Switzerland) as described in Barkovits et al.[20]. Test stripes were incubated with 50 µL CSF for 60 s and the amount of contamination was analyzed according to the manufacture's protocol.

Image-data acquisition

Imaging was performed on a total internal reflection microscope (TIRFM, Leica DMI6000B, Wetzlar, Germany) as previously described by Kravchenko et al.[49] (excitation: 635 nm, emission filter: 705/22 nm; excitation: 488 nm, emission filter: 525/36 nm; exposure time: 1000 ms; gain: 1300). A total of 25 images per well with 1000×1000 pixels each were measured, which covers 3.14% of the total area per well. For unbiased and automated image-data analysis, we have used our previously developed sFIDAta software tool[15]. The analysis includes the automated detection and elimination of artefact containing images and counting of aggregate indicating pixels. The *pixel count* is referred to as the average number of pixels in an image that exceed a pre-defined cutoff value. The *cutoff* is defined as the grey-scale value at which the ratio of the positive versus the total number of pixels in the buffer control equals a pre-defined value. The cutoff is used to compensate fluctuations in the absolute fluorescence intensities among experiments and different conditions within one experiment (i.e., antibody dilutions) and is determined for each experiment based on a buffer control sample. To further ensure that differences in fluorescence intensity do not affect assay robustness, we run a calibration in each 384-microtiter plate and converted pixel counts into SiNaP calibration-based fM concentrations.

For inter-assay measurement, a cutoff of 0.001% was chosen, while the cutoff for the analysis of the whole dataset of 237 samples was 0.05%. This difference is due to a new lot of detection antibodies with a lower degree of labeling. To further ensure that all artificial images are excluded from the analysis, min-max filtering was applied, which removed 10% of the images per well with the highest and 10% of the images per well with the lowest pixel counts.

Statistics

General statistics. Statistical analysis was performed using OriginPro 2020 SR1 (OriginLab Corporation, MA, USA) and matlab2019b (The MathWorks, MA, USA) software. Mean and standard deviation was calculated based on the pixel counts of the four replicates. Intra-assay variation is described by the CV% value. To determine inter-assay and inter-laboratory variation, the Pearson coefficient of correlation was calculated for the replicate measurements of the samples.

Calibration. For calculation of the calibration curve, only the concentrations of the silica nanoparticle standard were included that significantly differed from the blank control and were above the limit of detection (LOD). To this end, a one-sided Mann-Whitney U test was carried out with a confidence interval of 5%. After calculation of the calibration range for each experiment, a universal calibration range for all of the experiments was established. The LOD is defined based on Eq. (2):

$$LOD[pixel] = pixel\,count(blank\,control) * 2\sigma \quad (2)$$

For linear regression, the pixel counts were weighted with 1/readout. The bovine CSF control was used as a negative control for the calibration as well as for calculation of the LOD.

Logistic regression and ROC analysis. Logistic regression was performed to evaluate the ability of each biomarker to classify the diagnostic groups. To this end, we used scikit-learn library (version 1.0.2). Since the use of multiple features increases the risk of overfitting, the k-fold cross-validation method was used to generate Fig. 10, in order to provide unbiased results. Deviations between Fig. 9 and Fig. 10 can be explained not only by the modified method but also by a divergent data basis. Since tTau and pTau values were not available for all samples, these were excluded for the creation of the Fig. 10. By forming the average of the k results, a single receiver operating characteristic (ROC) curve was generated. The optimal combination of sensitivity and specificity for a ROC curve was calculated with a maximized Youden's index.

Patient samples

Patients were recruited from the University of Pennsylvania (UPenn) Parkinson's Disease and Movement Disorder Center (PDMDC), Alzheimer's Disease Center (ADC), or Frontotemporal Dementia Center (FTDC). Written, informed consent was obtained from each study participant at enrollment and biofluids were collected and stored for future research as approved by the UPenn Institutional Review Board (FWA00004028). Participants were diagnosed with Parkinson's disease (PD, $n = 115$), Alzheimer's disease (AD, $n = 28$), progressive supranuclear palsy (PSP, $n = 30$), or dementia with Lewy bodies (DLB, $n = 19$) according to clinical criteria as previously described[50]. Participants with no known neurological disorder were also enrolled (normal control, N, $n = 45$). Cerebrospinal fluid (CSF) was collected by trained neurologists via lumbar puncture, and aliquots of 0.5 mL were stored at −80 °C until analysis. Demographic information was collected by trained research staff. Samples were collected between August of 2005 and November 2019, with the exception of one sample, which was

collected in March of 1999. Samples included in the analysis were matched for age across diagnosis groups. Initially, a subset of PSP ($n = 30$), PD ($n = 30$), and N ($n = 30$) samples were analyzed as an exploratory cohort. The remainder of the samples were analyzed to investigate differences between disease groups. Researchers were blinded to clinical data at the time of sFIDA measurement.

Concentrations of pTau and tTau were measured using Luminex xMAP immunoassay platform (Luminex, Austin, USA)[51,52] and provided by Integrated Neurodegenerative Disease Database (INDD).

After unblinding, the data points of each group were first tested for normal distribution (Shapiro Wilk, Lilliefors, Kolmogorov-Smirnov, Anderson Darling). Afterwards, a Kruskal-Wallis test was executed to identify differences between the groups. In case of significant differences ($p < 0.05$) a pairwise comparison using the two-sided Mann-Whitney U test with a confidence interval of 0.05 was performed.

DATA AVAILABILITY

The authors confirm that the data supporting the findings of this study are available within the article and its supplementary materials.

CODE AVAILABILITY

For image data analysis, we used the sFIDAta software tool, which can be made available upon request from the corresponding author.

Received: 27 November 2021; Accepted: 10 May 2022;
Published online: 02 June 2022

REFERENCES

1. Dickson, D. W. Parkinson's disease and parkinsonism: neuropathology. *Cold Spring Harb. Perspect Med.* **2**, https://doi.org/10.1101/cshperspect.a009258 (2012).
2. Foguem, C. & Manckoundia, P. Lewy Body Disease: Clinical and Pathological "Overlap Syndrome" Between Synucleinopathies (Parkinson Disease) and Tauopathies (Alzheimer Disease). *Curr. Neurol. Neurosci. Rep.* **18**, 24 (2018).
3. Haass, C. & Selkoe, D. J. Soluble protein oligomers in neurodegeneration: lessons from the Alzheimer's amyloid beta-peptide. *Nat. Rev. Mol. Cell Biol.* **8**, 101–112 (2007).
4. Bengoa-Vergniory, N., Roberts, R. F., Wade-Martins, R. & Alegre-Abarrategui, J. Alpha-synuclein oligomers: A new hope. *Acta Neuropathol.* **134**, 819–838 (2017).
5. Prots, I. et al. alpha-Synuclein oligomers induce early axonal dysfunction in human iPSC-based models of synucleinopathies. *Proc. Natl Acad. Sci. USA* **115**, 7813–7818 (2018).
6. Willbold, D. & Kutzsche, J. Do we need anti-prion compounds to treat Alzheimer's Disease? *Molecules* **24**, https://doi.org/10.3390/molecules24122237 (2019).
7. Majbour, N. K. et al. Cerebrospinal alpha-Synuclein oligomers reflect disease motor severity in DeNoPa longitudinal cohort. *Mov. Disord.* https://doi.org/10.1002/mds.28611 (2021).
8. Majbour, N. K. et al. Oligomeric and phosphorylated alpha-synuclein as potential CSF biomarkers for Parkinson's disease. *Mol. Neurodegener.* **11**, 7 (2016).
9. Sengupta, U. et al. Tau oligomers in cerebrospinal fluid in Alzheimer's disease. *Ann. Clin. Transl. Neurol.* **4**, 226–235 (2017).
10. Kulenkampff, K., Wolf Perez, A.-M., Sormanni, P., Habchi, J. & Vendruscolo, M. Quantifying misfolded protein oligomers as drug targets and biomarkers in Alzheimer and Parkinson diseases. *Nat. Rev. Chem.* **5**, 277–294 (2021).
11. Herrmann, Y. et al. Nanoparticle standards for immuno-based quantitation of alpha-synuclein oligomers in diagnostics of Parkinson's disease and other synucleinopathies. *Clin. Chim. Acta* **466**, 152–159 (2017).
12. Alam, P., Bousset, L., Melki, R. & Otzen, D. E. alpha-synuclein oligomers and fibrils: A spectrum of species, a spectrum of toxicities. *J. Neurochem.* **150**, 522–534 (2019).
13. Willbold, D., Strodel, B., Schroder, G. F., Hoyer, W. & Heise, H. Amyloid-type protein aggregation and prion-like properties of amyloids. *Chem. Rev.* **121**, 8285–8307 (2021).
14. Hülsemann, M. et al. Biofunctionalized Silica nanoparticles: Standards in amyloid-beta oligomer-based diagnosis of Alzheimer's Disease. *J. Alzheimers Dis.* **54**, 79–88 (2016).
15. Kühbach, K. et al. Application of an Amyloid Beta Oligomer Standard in the sFIDA Assay. *Front Neurosci.* **10**, 8 (2016).
16. Bolstad, N. et al. Heterophilic antibody interference in commercial immunoassays; a screening study using paired native and pre-blocked sera. *Clin. Chem. Lab Med.* **49**, 2001–2006 (2011).
17. Vanderstichele, H., Stoops, E., Vanmechelen, E. & Jeromin, A. Potential sources of interference on Abeta immunoassays in biological samples. *Alzheimers Res. Ther.* **4**, 39 (2012).
18. Ishii, R. et al. Decrease in plasma levels of alpha-synuclein is evident in patients with Parkinson's disease after elimination of heterophilic antibody interference. *PLoS One* **10**, e0123162 (2015).
19. Sehlin, D. et al. Interference from heterophilic antibodies in amyloid-beta oligomer ELISAs. *J. Alzheimers Dis.* **21**, 1295–1301 (2010).
20. Barkovits, K. et al. Blood Contamination in CSF and Its Impact on Quantitative Analysis of Alpha-Synuclein. *Cells* **9**, https://doi.org/10.3390/cells9020370 (2020).
21. Mollenhauer, B. et al. alpha-Synuclein and tau concentrations in cerebrospinal fluid of patients presenting with parkinsonism: a cohort study. *Lancet Neurol.* **10**, 230–240 (2011).
22. Forland, M. G. et al. The value of cerebrospinal fluid alpha-synuclein and the tau/alpha-synuclein ratio for diagnosis of neurodegenerative disorders with Lewy pathology. *Eur. J. Neurol.* **27**, 43–50 (2020).
23. van Steenoven, I. et al. alpha-Synuclein species as potential cerebrospinal fluid biomarkers for dementia with lewy bodies. *Mov. Disord.* **33**, 1724–1733 (2018).
24. Slaets, S. et al. Increased CSF alpha-synuclein levels in Alzheimer's disease: Correlation with tau levels. *Alzheimers Dement* **10**, S290–S298 (2014).
25. Savica, R., Grossardt, B. R., Bower, J. H., Ahlskog, J. E. & Rocca, W. A. Incidence and pathology of synucleinopathies and tauopathies related to parkinsonism. *JAMA Neurol.* **70**, 859–866 (2013).
26. Winner, B. et al. In vivo demonstration that alpha-synuclein oligomers are toxic. *Proc. Natl Acad. Sci. USA* **108**, 4194–4199 (2011).
27. Tokuda, T. et al. Detection of elevated levels of alpha-synuclein oligomers in CSF from patients with Parkinson disease. *Neurology* **75**, 1766–1772 (2010).
28. Park, M. J., Cheon, S. M., Bae, H. R., Kim, S. H. & Kim, J. W. Elevated levels of alpha-synuclein oligomer in the cerebrospinal fluid of drug-naive patients with Parkinson's disease. *J. Clin. Neurol.* **7**, 215–222 (2011).
29. Parnetti, L. et al. Differential role of CSF alpha-synuclein species, tau, and Abeta42 in Parkinson's Disease. *Front. Aging Neurosci.* **6**, 53 (2014).
30. Wakabayashi, K. et al. The Lewy body in Parkinson's disease and related neurodegenerative disorders. *Mol. Neurobiol.* **47**, 495–508 (2013).
31. Irwin, D. J. & Hurtig, H. I. The Contribution of Tau, Amyloid-Beta and Alpha-Synuclein Pathology to Dementia in Lewy Body Disorders. *J. Alzheimers Dis. Parkinsonism* **8**, https://doi.org/10.4172/2161-0460.1000444 (2018).
32. Hamilton, R. L. Lewy bodies in Alzheimer's disease: a neuropathological review of 145 cases using alpha-synuclein immunohistochemistry. *Brain Pathol.* **10**, 378–384 (2000).
33. Galpern, W. R. & Lang, A. E. Interface between tauopathies and synucleinopathies: A tale of two proteins. *Ann. Neurol.* **59**, 449–458 (2006).
34. Robinson, J. L. et al. Neurodegenerative disease concomitant proteinopathies are prevalent, Age-related and APOE4-associated. *Brain* **141**, 2181–2193 (2018).
35. Hansson, O. et al. Levels of cerebrospinal fluid alpha-synuclein oligomers are increased in Parkinson's disease with dementia and dementia with Lewy bodies compared to Alzheimer's disease. *Alzheimers Res. Ther.* **6**, 25 (2014).
36. Abdi, I. Y. et al. Preanalytical stability of CSF Total and Oligomeric Alpha-Synuclein. *Front. Aging Neurosci.* **13**, 638718 (2021).
37. Gerson, J. E. et al. Characterization of tau oligomeric seeds in progressive supranuclear palsy. *Acta Neuropathol. Commun.* **2**, 73 (2014).
38. Olsson, B. et al. CSF and blood biomarkers for the diagnosis of Alzheimer's disease: A systematic review and meta-analysis. *Lancet Neurol.* **15**, 673–684 (2016).
39. Wagshal, D. et al. Divergent CSF tau alterations in two common tauopathies: Alzheimer's disease and progressive supranuclear palsy. *J. Neurol. Neurosurg. Psychiatry* **86**, 244–250 (2015).
40. Karch, C. M., Jeng, A. T. & Goate, A. M. Extracellular Tau levels are influenced by variability in Tau that is associated with tauopathies. *J. Biol. Chem.* **287**, 42751–42762 (2012).
41. Zhang, X. et al. Tau pathology in Parkinson's Disease. *Front Neurol.* **9**, 809 (2018).
42. Irwin, D. J., Lee, V. M. & Trojanowski, J. Q. Parkinson's disease dementia: Convergence of alpha-synuclein, tau and amyloid-beta pathologies. *Nat. Rev. Neurosci.* **14**, 626–636 (2013).
43. Ingelsson, M. Alpha-Synuclein Oligomers-Neurotoxic Molecules in Parkinson's disease and other Lewy body disorders. *Front. Neurosci.* **10**, 408 (2016).
44. Bartels, T., Choi, J. G. & Selkoe, D. J. alpha-Synuclein occurs physiologically as a helically folded tetramer that resists aggregation. *Nature* **477**, 107–110 (2011).
45. Fauvet, B. et al. alpha-Synuclein in central nervous system and from erythrocytes, mammalian cells, and Escherichia coli exists predominantly as disordered monomer. *J. Biol. Chem.* **287**, 15345–15364 (2012).
46. Heroult, J., Nischwitz, V., Bartczak, D. & Goenaga-Infante, H. The potential of asymmetric flow field-flow fractionation hyphenated to multiple detectors for the quantification and size estimation of silica nanoparticles in a food matrix. *Anal. Bioanal. Chem.* **406**, 3919–3927 (2014).

47. Dubascoux, S. et al. Field-flow fractionation and inductively coupled plasma mass spectrometer coupling: History, development and applications. *J. Anal. At. Spectrom.* **25**, 613–623 (2010).
48. Meermann, B. & Nischwitz, V. ICP-MS for the analysis at the nanoscale – a tutorial review. *J. Anal. At. Spectrom.* **33**, 1432–1468 (2018).
49. Kravchenko, K. et al. Analysis of anticoagulants for blood-based quantitation of amyloid beta oligomers in the sFIDA assay. *Biol. Chem.* **398**, 465–475 (2017).
50. Toledo, J. B. et al. A platform for discovery: The University of Pennsylvania Integrated Neurodegenerative Disease Biobank. *Alzheimer's Dement* **10**, 477–484 e471 (2014).
51. Irwin, D. J. et al. CSF tau and beta-amyloid predict cerebral synucleinopathy in autopsied Lewy body disorders. *Neurology* **90**, e1038–e1046 (2018).
52. Berlyand, Y. et al. An Alzheimer's Disease-Derived Biomarker Signature Identifies Parkinson's Disease Patients with Dementia. *PLoS One* **11**, e0147319 (2016).

ACKNOWLEDGEMENTS

We received funding from the European Union Seventh Framework Program (FP7/2007-2013) under grant agreement 602999 (SYMPATH project), the Federal Ministry of Education and Research within the projects VIP (03V0641), KNDD (01GI1010A), JPND/BIOMARKAPD (01ED1203H), and NEUROALLIANZ (16GW0099). We were also supported by the programs "Biomarkers Across Neurodegenerative Diseases I + II" of The Alzheimer's Association, Alzheimer's Research UK and the Weston Brain Institute (11084 and BAND-19-614337). We are also grateful for support from The Michael J. Fox Foundation for Parkinson's Research (14977, 009889), from the ALS Association and from the Packard Center (19-SI-476). We further received funding from the Deutsche Forschungsgemeinschaft (INST 208/616-1 FUGG, INST 208/794-1 FUGG) and the Helmholtz Association (HVF0079). TFT is additionally funded by the NIH (K23-NS11416). In memoriam of John Q. Trojanowski.

AUTHOR CONTRIBUTIONS

LB, MP, and VK developed the assay. LB performed the experiments and analyzed the data, VK, AC and VN assisted in validation of the method. AK, FR and JW helped carry out the statistics and analysis. LB wrote the manuscript together with OB, DW and GT. OB, DW, and ACP supervised the project. DWe, DI, MG, DAW, JQT, TFT, and ACP recruited the patients. RZ, TFT, and ACP selected appropriate samples and organized the clinical data. AD, AS and TB contributed to the discussion of the results and provided critical feedback. JQT reviewed the manuscript and all data before his passing on February 8, 2022.

FUNDING

Open Access funding enabled and organized by Projekt DEAL.

COMPETING INTERESTS

The Authors declare no competing non-financial interests but the following competing financial interests: DW, OB, and AK are shareholders of attyloid GmbH. All other authors declare no competing financial interests related to this work.

ADDITIONAL INFORMATION

Supplementary information The online version contains supplementary material available at https://doi.org/10.1038/s41531-022-00330-x.

Correspondence and requests for materials should be addressed to Dieter Willbold.

Reprints and permission information is available at http://www.nature.com/reprints

Publisher's note Springer Nature remains neutral with regard to jurisdictional claims in published maps and institutional affiliations.

2.2.6 Development and Implementation of an Internal Quality Control Sample to Standardize Oligomer-Based Diagnostics of Alzheimer's Disease

Autoren:	Marlene Pils, Alexandra Dybala, **Fabian Rehn**, Lara Blömeke, Tuyen Bujnicki, Victoria Kraemer-Schulien, Wolfgang Hoyer, Detlev Riesner, Dieter Willbold, Oliver Bannach
Journal:	*Diagnostics. 13(10):1702 (Mai, 2023)* DOI: 10.3390/diagnostics13101702
Beitrag:	Datenauswertung Diskussion der Ergebnisse Prüfung des Manuskriptes
Druckgenehmigung:	Siehe Anhang 11.

diagnostics

MDPI

Article

Development and Implementation of an Internal Quality Control Sample to Standardize Oligomer-Based Diagnostics of Alzheimer's Disease

Marlene Pils [1,2], Alexandra Dybala [1,3], Fabian Rehn [1,2], Lara Blömeke [1,2], Tuyen Bujnicki [2], Victoria Kraemer-Schulien [2], Wolfgang Hoyer [2,3], Detlev Riesner [1,3], Dieter Willbold [1,2,3] and Oliver Bannach [1,2,*]

1 attyloid GmbH, Merowingerplatz 1a, 40225 Düsseldorf, Germany; m.pils@attyloid.com (M.P.); alexandra.ziemski@hhu.de (A.D.); f.rehn@attyloid.com (F.R.); l.bloemeke@attyloid.com (L.B.); detlev.riesner@hhu.de (D.R.); d.willbold@fz-juelich.de (D.W.)
2 Institute of Biological Information Processing (Structural Biochemistry: IBI-7), Forschungszentrum Jülich, 52428 Jülich, Germany; t.bujnicki@fz-juelich.de (T.B.); v.kraemer-schulien@fz-juelich.de (V.K.-S.); wolfgang.hoyer@hhu.de (W.H.)
3 Institut für Physikalische Biologie, Heinrich-Heine-Universität Düsseldorf, 40225 Düsseldorf, Germany
* Correspondence: o.bannach@attyloid.com; Tel.: +49-(0)-211-81-10377

Abstract: Protein misfolding and aggregation are pathological hallmarks of various neurodegenerative diseases. In Alzheimer's disease (AD), soluble and toxic amyloid-β (Aβ) oligomers are biomarker candidates for diagnostics and drug development. However, accurate quantification of Aβ oligomers in bodily fluids is challenging because extreme sensitivity and specificity are required. We previously introduced surface-based fluorescence intensity distribution analysis (sFIDA) with single-particle sensitivity. In this report, a preparation protocol for a synthetic Aβ oligomer sample was developed. This sample was used for internal quality control (IQC) to improve standardization, quality assurance, and routine application of oligomer-based diagnostic methods. We established an aggregation protocol for Aβ1–42, characterized the oligomers by atomic force microscopy (AFM), and assessed their application in sFIDA. Globular-shaped oligomers with a median size of 2.67 nm were detected by AFM, and sFIDA analysis of the Aβ1–42 oligomers yielded a femtomolar detection limit with high assay selectivity and dilution linearity over 5 log units. Lastly, we implemented a Shewhart chart for monitoring IQC performance over time, which is another important step toward quality assurance of oligomer-based diagnostic methods.

Keywords: Alzheimer's disease; diagnosis; dementia; biomarkers; amyloid-β peptide; oligomer-based diagnostics; immunoassays; internal quality control; atomic force microscopy; Shewhart chart

Citation: Pils, M.; Dybala, A.; Rehn, F.; Blömeke, L.; Bujnicki, T.; Kraemer-Schulien, V.; Hoyer, W.; Riesner, D.; Willbold, D.; Bannach, O. Development and Implementation of an Internal Quality Control Sample to Standardize Oligomer-Based Diagnostics of Alzheimer's Disease. *Diagnostics* **2023**, *13*, 1702. https://doi.org/10.3390/diagnostics13101702

Academic Editor: Agnieszka Kulczyńska-Przybik

Received: 30 March 2023
Revised: 5 May 2023
Accepted: 7 May 2023
Published: 11 May 2023

1. Introduction

Alzheimer's disease (AD) is a progressive brain disease that causes increasing deterioration of mental abilities. AD is mainly characterized by misfolding and aggregation of amyloid-β (Aβ) peptides and Tau proteins into amyloid plaques and neurofibrillary tangles [1,2]. For decades, these deposits were considered the primary cause of disease onset and progression. However, it is increasingly recognized that the soluble oligomeric species formed during the aggregation process are the major neurotoxic species of AD [3–6]. Consequently, these oligomers represent a primary drug target and a promising biomarker candidate for early AD diagnostics. The minute amounts of oligomeric Aβ in body fluids such as cerebrospinal fluid (CSF, aM-fM) [5] and excessive concentrations of Aβ monomers and matrix components require extremely sensitive and specific quantitation technologies [5–7].

We previously developed the surface-based fluorescence intensity distribution analysis (sFIDA) technology as an oligomer-specific quantitation method with single-particle

sensitivity [8–12]. Although the biochemical setup of the sFIDA assay is similar to sandwich ELISA (Figure 1), the readout is microscopy-based with sub-femtomolar sensitivity [7]. In sFIDA, Aβ species are captured on a glass surface by an N-terminal anti-Aβ antibody; subsequently, Aβ oligomers are detected by two different fluorescence-labeled antibodies. Monomeric Aβ is not detected because capture and detection antibodies compete for the same or overlapping epitopes [11]. Using linear epitopes, all subtypes of aggregated protein, including low- and high-molecular-weight oligomers, are detected [8]. The glass surface is imaged by dual-color total internal reflection fluorescence microscopy (TIRFM) to count the number of oligomers in a sample. Background noise is reduced by applying a cutoff, which is a predefined intensity value, and only signals above the cutoff are evaluated. Moreover, signal colocalization of both fluorescently labeled detection antibodies (called sFIDA readout) increases specificity and directly correlates with the Aβ oligomer concentration in the sample [11].

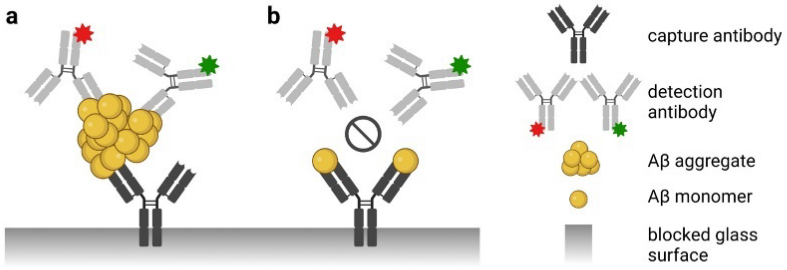

Figure 1. Scheme of the sFIDA principle. The biochemical principle of sFIDA is similar to a sandwich ELISA with capture and detection antibodies directed against the same or overlapping epitopes of the N-terminus of Aβ. Monomeric and oligomeric Aβ species of the sample bind to the capture antibodies. (**a**) However, the red or green fluorescently labeled detection antibodies only detect aggregated Aβ species such as oligomers because the assay antibodies bind to the same or overlapping epitope. (**b**) Therefore, the red or green labeled detection antibody cannot bind monomers because the capture antibody already masks the epitope. Subsequently, the assay surface is imaged using dual-color fluorescence microscopy (excitation at 635 and 488 nm), and only colocalized pixels above a defined cutoff threshold are counted by image data analysis. Abbreviations: Aβ, amyloid-β; sFIDA, surface-based fluorescence intensity distribution analysis. Created with BioRender.com (accessed on 26 April 2023).

Moreover, oligomer quantification is challenging because reliable calibration standards are required [4,5,13]. To address this issue, we recently developed and characterized stable silica nanoparticles (SiNaPs) coated with Aβ peptides, which serve as calibration standards for translating pixel-based readouts into molar particle concentrations [13]. In contrast to natural oligomers that can undergo structural changes and epitope masking in response to changes in buffer conditions or matrix effects [14,15], SiNaPs are very robust because of their artificial, silica-based nature. Nevertheless, it is necessary to have an Aβ oligomer-based internal quality control (IQC) sample that sensitively detects unfavorable or declining assay performance in response to analytical, biological, or clinical changes [16,17]. In addition, monitoring the day-to-day (between-run) precision and accuracy of the IQC sample improves assay comparability and standardizes oligomer-based diagnostic methods for routine applications [18].

Soluble Aβ oligomers are transient and very heterogeneous in size and shape. Thus, investigators have struggled to prepare a reliable Aβ oligomer sample for in vitro and in vivo studies [4,5,13,19]. Firstly, Aβ oligomers must be sufficiently stable during the assay procedure, i.e., must not dissociate to monomers or grow further into insoluble structures such as fibrils. In this context, the ease of the aggregation protocol would also be important, as it should not require complex pretreatments for stabilization, such as crosslinking or protein engineering [20]. Secondly, a suitable characterization method

must be applied to investigate the shape and size of Aβ oligomers. Several methods are described in the literature, whereby atomic force microscopy (AFM) enables size and shape characterization because of its insensitivity to buffer components and matrix effects while providing high-resolution three-dimensional morphological images [21]. Thirdly, Aβ oligomers should be stable for in vitro studies such as oligomer-based diagnostic methods to facilitate reproducibility that is evaluated using quality assurance tools such as control sheets, Shewhart charts, or Cusum charts [16–18].

In the present study, we describe detailed methods to consistently generate an Aβ1–42 oligomer-based IQC sample and characterize its shape and size using atomic force microscopy. We then demonstrate IQC applicability and monitoring using sFIDA for in vitro oligomer-based diagnostic methods. We investigated several validation parameters, such as detection and quantification limits, intra-assay variability, dilution linearity, and assay selectivity. Lastly, we demonstrate the use of Shewhart charts for monitoring the IQC performance over time at three IQC sample concentrations.

2. Materials and Methods

2.1. Monomerization Aβ1–42 Peptide Stock and Aggregation Protocol

The monomerization and aggregation protocol used to generate oligomeric Aβ species was established by considering the findings of Aβ aggregation studies [19–23]. For a graphical illustration of the preparation methods, including the monomerization and aggregation procedure, see Figure S1.

Monomerization of the Aβ1–42 peptide stock is essential for generating homogeneous oligomers [19,21]. Thus, we used a strong fluorinated alcohol, 1,1,1,3,3,3-hexafluoro-2-propanol (HFIP, Sigma-Aldrich, St. Louis, MO, USA), to remove any preexisting β-sheet secondary structure or seeds. All preparation steps that use HFIP should be performed under a fume hood or clean bench because of its volatility. We reduced the lyophilized starting material per aliquot because Aβ1–42 aggregates more spontaneously at a stock concentration higher than 90 nM. Thus, we first prepared aliquots containing 50 µg of Aβ1–42 by adding 550 µL of HFIP directly into the original vial containing 1 mg of Aβ1–42 (Bachem AG, Bubendorf, Switzerland). Complete dissolution of the Aβ1–42 peptide was achieved by 30 min incubation at room temperature (RT) and agitated at 650 rpm. The solution was then transferred into a protein low-binding reaction tube (Eppendorf, Hamburg, Germany), and the original vial was rinsed with 550 µL of HFIP. Next, this solution was quickly divided into 20 aliquots of 50 µL each using a repeating pipette or cooled Hamilton syringe (Figure S1, step 1). Subsequently, tubes were transferred into a SpeedVac and dried for ~1 h without heating until all HFIP and H_2O were removed. The monomeric stock tubes containing 50 µg of Aβ1–42 were sealed and stored at RT (Figure S1, step 2). To further reduce the initial amount of Aβ1–42, we repeated this step by adding 550 µL of HFIP to a 50 µg Aβ1–42 tube and creating 10 new aliquots of 5 µg each. These were dried and stored as described above (Figure S1, step 3).

For the preparation of the IQC sample stock solution, 5 µg of monomeric Aβ1–42 was solved in 5 µL of dimethyl sulfoxide (DMSO, Sigma-Aldrich), briefly mixed, spun down, and agitated for 10 min at 650 rpm (Thermomixer, Eppendorf) at RT (Figure S1, step 4). This step should be scheduled immediately prior to further use because a prolonged residence time of Aβ in the DMSO stock solution can lead to spontaneous protofibril formation [21]. Because physiological conditions such as salt concentration and pH facilitate the aggregation of oligomeric Aβ species [21], we subsequently diluted the DMSO stock solution with 1× phosphate-buffered saline, pH 7.4 (PBS, Sigma-Aldrich) containing 0.04% sodium azide (NaN_3, AppliChem, Darmstadt, Germany) to a concentration of 10 µM (Figure S1, step 5). The IQC sample stock solution was again briefly mixed, spun down, and agitated for 16 h at 650 rpm at RT to promote oligomerization (Figure S1, step 6).

2.2. Atomic Force Microscopy

AFM is insensitive to matrix effects and solution conditions, and it generates detailed surface information at a nanometer scale [21]. Therefore, AFM was used for the size and shape characterization of the synthesized Aβ oligomers.

The 10 µM IQC sample stock solution containing oligomeric species was diluted to 1 µM in PBS. As a control, 10 µM monomeric IQC sample stock solution was prepared analogously, but incubation after adding PBS was not performed (Section 2.1). Ten microliters of each sample was loaded onto a mica slide and incubated for 30 min at RT in a closed petri dish. A wet tissue was added to prevent drying artefacts. The slide was washed 3× with 100 µL of ddH_2O and dried with N_2 gas. The samples were measured using NanoWizard III (JPK BioAFM, Bruker Corporation, Billerica, MA, USA) with an OMCL-AC160TS cantilever (Olympus Corporation, Tokyo, Japan) in the intermittent contact mode (AC mode) in air. For size determination, three images (2 × 2 µm with a resolution of 512 × 512 pixels) were recorded with a frequency of 0.5 Hz. Assuming the oligomers are globular, the height profile of 1300 oligomers was further analyzed with ImageJ using the "Find Maxima" tool. The determined height was equated to the size of the oligomers.

2.3. sFIDA

2.3.1. Synthesis of SiNaPs Coated with Aβ1–15

In this study, SiNaPs coated with Aβ1–15 were synthesized, functionalized, and activated, as described previously [7,8,13]. Briefly, SiNaPs were synthesized via the Stöber process and silanized with 3-aminopropyl(triethoxysilane) (APTES, Sigma-Aldrich) to functionalize the surface with primary amino groups. The carboxy groups of maleimidohexanoic acid (MIHA, abcr GmbH, Karlsruhe, Germany) were then activated by 1-ethyl-3-(3-dimethylaminopropyl) carbodiimide (EDC, Sigma-Aldrich) and N-hydroxysuccinimide (NHS, Sigma-Aldrich) and coupled covalently to the amines. Aβ and maleimide groups were crosslinked using C-terminal functionalized Aβ1–15 peptides with cysteamine (Peptides and Elephants, Henningsdorf, Germany). Lastly, the molar SiNaP concentration was calculated on the basis of the silicon concentration, which was determined by inductively coupled plasma mass spectrometry, and the size, density, and shape of the particles were determined by transmission electron microscopy.

2.3.2. Labeling of Antibodies

The anti-Aβ antibody IC16 (mouse, monoclonal, amino acids (aa)2–8, Heinrich-Heine-University Düsseldorf, Düsseldorf, Germany) labeled with CF633 dye (Biotium, Freemont, CA, USA) and the anti-Aβ antibody Nab228 (mouse, monoclonal, aa1–11, Sigma-Aldrich) labeled with CF488A dye (Biotium) were used as detection probes for TIRFM. Labeling was performed according to the manufacturer's protocol. After purification via size exclusion using a polyacrylamide bead suspension (Bio-Gel P-30 Gel, Bio-Rad Laboratories, Hercules, CA, USA), the concentration and degree of labeling of both detection probes were calculated according to the manufacturer's protocols.

2.3.3. Assay Protocol

In the present study, 384-well plates (Sensoplate Plus, Greiner Bio-One, Frickenhausen, Germany) were functionalized with the Nab228 antibody (2.5 µg/mL in 0.1 M carbonate solution pH 8.4, 40 µL per well). After overnight incubation at 4 °C, plates were washed five times with Tris-buffered saline containing Tween (TBST, 1× TBS (Serva, Duisburg, Germany) and 0.05% Tween-20 (AppliChem)) and five times with 1× TBS and blocked with 0.5% bovine serum albumin (BSA, AppliChem) in 1× TBS containing 0.03% ProClin (Sigma-Aldrich,) for 1.5 h at RT. After washing the wells, as described above, 20 µL per well of SiNaPs (3.16-fold dilution, 10.26 pM–0.3 fM), assay controls, or IQC samples were applied in fourfold determination and incubated for 2 h at RT. For sample dilution, 1× PBS containing 0.05% Tween, 0.5% BSA, and 0.095% NaN_3 was used. Using the oligomeric IQC sample stock solution, a 3.16-fold dilution series ranging from 100 nM (IQC-15) to

0.01 pM (IQC-1) was used for validation studies, whereas, for the QC chart, 20 replicates of 316 pM (IQC-10), 31.6 pM (IQC-8), and 3.16 pM (IQC-6) were used. Wells were then washed five times with 1× TBS before adding 20 µL per well of the centrifuged (100,000× *g*, 4 °C, 1 h) detection antibodies mixture (IC16-CF633 + Nab228-CF488A, each at 0.625 µg/mL, in TBST + 0.1% BSA) for 1 h at RT. Lastly, wells were washed again, and the buffer was changed to 1× TBS with 0.03% ProClin. A microplate washer (405LS Microplate Washer, BioTek, Winnoski, VT, USA) was used for all washing steps.

2.3.4. Image Data Acquisition

The well surface was imaged in two different channels (channel 633: excitation 635 nm, emission filter 705/72 nm, exposure time 1000 ms, gain 1000; channel 488: excitation 488 nm, emission filter 525/36 nm, exposure time 1000 ms, gain 500) using TIRFM (Leica DMI6000B, Wetzlar, Germany). Twenty-five images per well with 1000 × 1000 pixels each were measured, representing 3.14% of the well surface.

2.4. Statistics

General statistical analyses were performed using Microsoft Excel (Microsoft, Redmond, WA, USA), and OriginPro (OriginLab Corporation, Northampton, MA, USA) and matlab2019b (The MathWorks, Natick, MA, USA) were used for calculations and graphs. Data were further analyzed for normal distributions using the Shapiro–Wilk test; for non-normal distributions, a non-parametric test was used, i.e., the Mann–Whitney U test.

2.4.1. Analysis of Image Data

Images were analyzed using in-house developed software that features artefact filtering and an automated sFIDA readout calculation [7,8]. To reduce background noise, intensity cutoffs were defined as the signal intensity exceeding 0.05% of the total pixels of the individual channels of the used blank control (dilution buffer, BC). Lastly, the number of pixels that had intensities above the defined cutoff and were colocalized in both fluorescence channels was calculated as the sFIDA readout. sFIDAta calculated the sFIDA readout on the basis of the mean value, standard deviation, and coefficient of variation (CV%) for each sample and the respective replicates.

2.4.2. Calibration

For calibrating the received sFIDA readouts, a weighted linear regression analysis with respective weights calculated as one per readout was performed with matlab2019b (The MathWorks). Therefore, all data points of the SiNaP calibration curve that differed significantly from BC and were above the limit of detection (Section 2.4.1) were included. For all further analyses, only the calibrated sFIDA readouts were shown.

2.4.3. Analytical Validation: Detection and Quantification Limits

For the calculation of the limit of blank (LoB) and limit of detection (LoD), 24 BC samples were analyzed, and parameters were calculated according to Armbruster et al. [24] using Equations (1) and (2). Afterward, values were translated into particle concentrations using the calculated calibration curve.

$$\text{LoB} = \text{mean sFIDA reaodut}_{\text{BC}} + 1.645 \times \text{standard deviation}_{\text{BC}}. \quad (1)$$

$$\text{LoD} = \text{mean sFIDA readout}_{\text{BC}} + 2 \times \text{standard deviation}_{\text{BC}}. \quad (2)$$

Using the calibrated particle concentrations of the Aβ oligomer dilution series, the linear working range was defined by calculating the lower and the upper endpoint and the dilution linearity. Therefore, the concentrations that differed significantly from the next lower concentration were determined using the one-sided Mann–Whitney U test with a confidence interval of 5%. Before calculating dilution linearity, background correction was

performed by subtracting the BC value from each IQC sample value. Subsequently, the percentage dilution linearity of each dilution step was calculated using Equation (3).

$$\text{Dilution linearity}[\%] = \frac{\text{observed value}}{(\text{expected value}/\text{dilution factor})} \times 100\% \quad (3)$$

Within the working range, the mean dilution linearity should be 80–120%, and the coefficient of determination should be higher than 0.95 to be accepted. The CV% of the four replicates of the same sample within the same run was calculated to assess intra-assay variability (within-run precision).

2.4.4. Analytical Validation: Analytical Selectivity

The selectivity of sFIDA indicated by the percentage signal reduction (Equation (4)) was carried out by measuring the IQC-13 (10 nM monomer concentration) sample in different assay setups. Nonspecific binding to the blocking agent used was excluded by performing capture control, where the capture antibody was omitted. As an autofluorescence control, the assay was performed using only TBST + 0.1% BSA without detection probes. In addition, the cross-reactivity of anti-Tau antibodies against the produced Aβ oligomers was tested. To this end, the Tau12 antibody (mouse, monoclonal, aa6–18, Biolegend, San Diego, CA, USA) was conjugated with CF633 and CF488A according to the protocol in Section 2.3.2 and diluted in TBST + 0.1% BSA to 0.625 µg/mL. The insensitivity of sFIDA against monomeric Aβ species was evaluated by applying 10 nM of freshly diluted monomeric Aβ1–42. IQC-13 was spiked in bovine CSF to simulate matrix effects, and the sFIDA readouts, generated using 0.05% cutoff-based CSF-blank, were compared to an equal concentration in the dilution buffer.

$$\text{Signal reduction}[\%] = \left(1 - \frac{\text{observed readout assay control}}{\text{readout reference}}\right) \times 100\% \quad (4)$$

Furthermore, sFIDA readouts of the respective assay control were compared to the readouts of the standard assay setup using the one-sided Mann–Whitney U test with a confidence interval of 5%.

2.4.5. Establishment of QC-Tool

A Shewhart chart, the most widely used tool for IQC [18], was used to monitor the readouts of IQC-10, IQC-8, and IQC-6. The oligomeric IQC sample stock solution (Section 2.1) was serially diluted 20 times to corresponding monomer concentrations of 316 pM (IQC-10), 31.6 pM (IQC-8), and 3.16 pM (IQC-6) to simulate 20 observations of each IQC sample. Subsequently, each dilution underwent a fourfold sFIDA analysis, and the observed sFIDA readouts were calibrated into particle concentrations. Lastly, observed particle concentrations were plotted as absolute values against the number of analyses. Using the mean and the standard deviation of the 20 observations, the lower and upper control limits (LCL/UCL) and action limits (LAL/UAL), respectively, were calculated according to Equations (5)–(8) and were integrated into the control chart.

$$\text{LCL} = \text{mean} - 2 \times \text{standard deviation} \quad (5)$$

$$\text{UCL} = \text{mean} + 2 \times \text{standard deviation} \quad (6)$$

$$\text{LAL} = \text{mean} - 3 \times \text{standard deviation} \quad (7)$$

$$\text{UAL} = \text{mean} + 3 \times \text{standard deviation} \quad (8)$$

In general, values within the control limits are considered satisfactory. Even if values are located between control and action limits, they are still accepted if they do not affect more than 10% of the measured values. However, if one result of a sample occurs outside the action limit, or if nine consecutive results create a trend (decreasing or increasing) or lie on

one side of the central line, the operator's intervention becomes necessary [18,25]. Between-run precision was considered satisfactory when all results were unbiased, all results lay within the warning limits, and the mean CV% of the 20 replicates was below 20%.

3. Results

The aim of this study was to develop and characterize an IQC sample for oligomer-based diagnostic assays. The first part of the results describes the characterization of the IQC sample, which was prepared using the protocol established in Section 2.1. In the second part, we used the IQC sample in the sFIDA assay and determined several validation parameters. Lastly, application of the Shewhart chart to monitor IQC performance was demonstrated with three IQC samples.

3.1. Aβ Oligomer-Based IQC Sample Displays High Homogeneity

The size distribution and morphology of the Aβ oligomers were determined by AFM. The analysis showed that the oligomers were monodisperse and globular in shape (Figure 2a). In contrast, we observed no particles in the monomer control containing a 10-fold higher protein concentration. Size distribution analysis revealed that the median height of all 1300 oligomers was 2.67 nm, with a minimum size of 1.07 nm. Only 2% of the detected oligomers were ≥5 nm (Figure 2b).

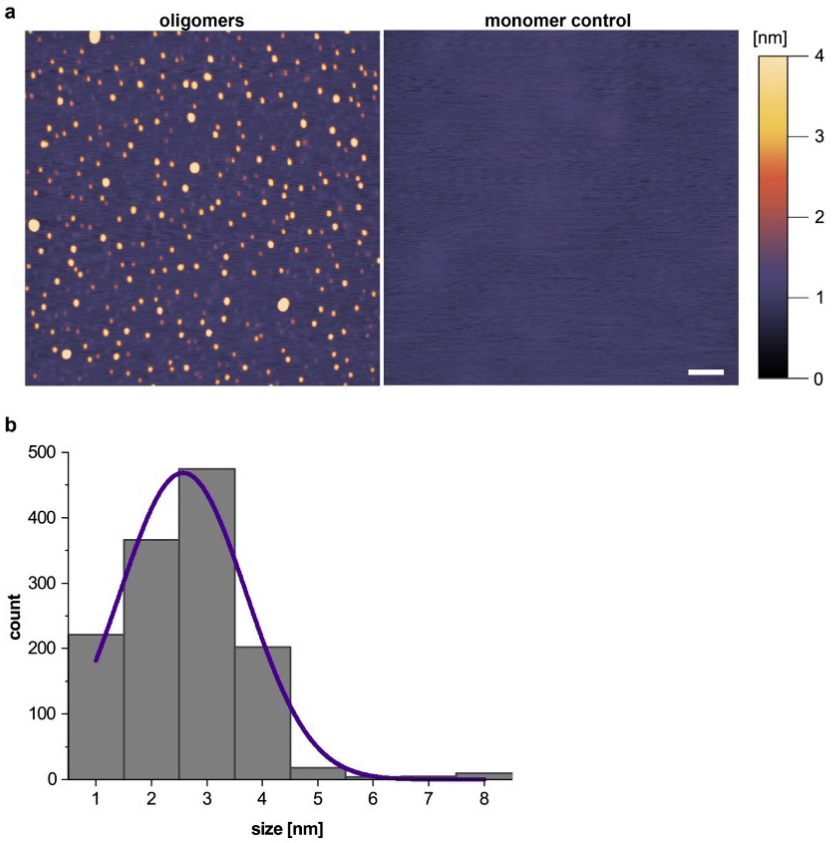

Figure 2. Analysis of the Aβ oligomers measured by AFM. (**a**) AFM images of the monomer control and Aβ oligomer samples. The color scale indicates the height profile. Scale bar = 200 nm. (**b**) Histogram showing the size distribution of 1300 oligomers. Abbreviations: Aβ, amyloid-β; AFM, atomic force microscopy.

3.2. Successful Application of the Aβ Oligomer-Based IQC Sample in the sFIDA Assay

The applicability of the prepared Aβ oligomers as an IQC sample for in vitro oligomer-based diagnostic methods using the sFIDA assay was investigated. We prepared a 3.16-fold concentration series of the oligomers in dilution buffer and subjected each sample to sFIDA analysis in quadruplicate determination. The molar concentrations represent monomer concentrations ranging from 0.01 pM (IQC-1) to 100 nM (IQC-15). Using the SiNaPs calibration curve ($y = 5.08x - 0.25$), we calculated the Aβ oligomer concentrations in each IQC sample from the sFIDA readouts. Individual sFIDA readouts and calibrated particle concentrations for each IQC sample are listed in Table S1.

Figure 3 illustrates the sFIDA IQC performance, which exhibits a 5 log dynamic range and an analytical sensitivity below the femtomolar level (LoB: 0.25 fM, LoD: 0.28 fM). The lower limit of quantification (LLoQ), upper limit of quantification (ULoQ), and acceptable dilution linearity (acceptance range of 80–120%, Section 2.4.1) defined the working range of the used IQC samples. Data were not normally distributed (p-value: 6.97×10^{-6}). Thus, the two quantification limits were identified using the one-sided Mann–Whitney U test with a confidence interval of 5% (Table S1) and were set to a particle concentration of 0.36 fM (IQC-3) and 197 pM (IQC-14). Within this range, a mean percentage dilution linearity of 107% was determined (Table S2). Interestingly, a coefficient of determination of 0.73 indicated that the dilution linearity could be improved. A closer inspection of the data indicated that the IQC-14 readout was an outlier with a similar readout to that of IQC-13. Removing IQC-14 from the fit yielded a coefficient of determination of 0.99. This refit resulted in a change in the percentage dilution linearity; however, the value of 109% was still acceptable. Furthermore, within this linear working range of 0.36 fM–196 pM, a mean CV% of 18.4% was determined, indicating acceptable intra-assay variance for single-particle analysis.

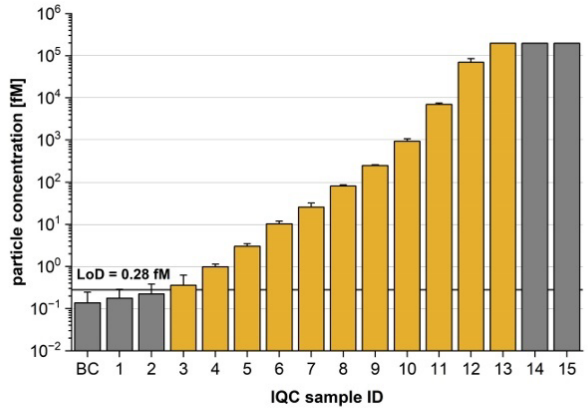

Figure 3. Molar particle concentration of internal quality control (IQC) samples and blank control (BC). On the basis of 24 replicates of the BC, the limit of detection (LoD) was calculated and translated into a particle concentration of 0.28 fM using the calibration curve. The linear working range (yellow) was identified by acceptable dilution linearity between the upper (196 pM) and lower (0.36 fM) limits of quantification. Note the logarithmic scale. Data are presented as the mean and standard deviation of four replicates.

3.3. sFIDA Features High Selectivity for the Aβ Oligomer-Based IQC Sample

Testing different assay controls confirmed that sFIDA is highly selective for aggregated Aβ species and robust against false-positive signals because of matrix interference and cross-reactivities. Figure 4a shows sFIDA readouts of IQC-13 applied on different assay setups. For all controls, a signal reduction of almost 100% was observed (Table S3a). Because data showed a non-normal distribution (Shapiro–Wilk test p-value: 2.53×10^{-4}), we applied the nonparametric one-sided Mann–Whitney U test with a confidence interval of 5% to

Diagnostics **2023**, *13*, 1702

investigate differences between the sFIDA readouts of the respective assay control and the reference. For all controls, significantly lower sFIDA readouts were observed compared to the reference (for individual *p*-values, see Table S3). Aβ oligomers were only detected when captured on the assay surface via the anti-Aβ antibodies, whereas no detection was observed in the absence of the capture antibody. In addition, the capture control readout was significantly lower than the reference values (*p*-value: 0.0152). Moreover, false-positive signals generated by the autofluorescence of chemicals and buffers were not detected because the sFIDA readout of the autofluorescence control was significantly lower than the sFIDA readout of the reference, as indicated by the *p*-value of 0.0147. Using anti-Tau antibodies as the detection probe or monomers (Figure 4b, Table S3b) as the target yielded no false-positive signals caused by cross-reactivity. For both controls, significantly lower sFIDA readouts compared to the reference were observed (*p*-value of 0.0152).

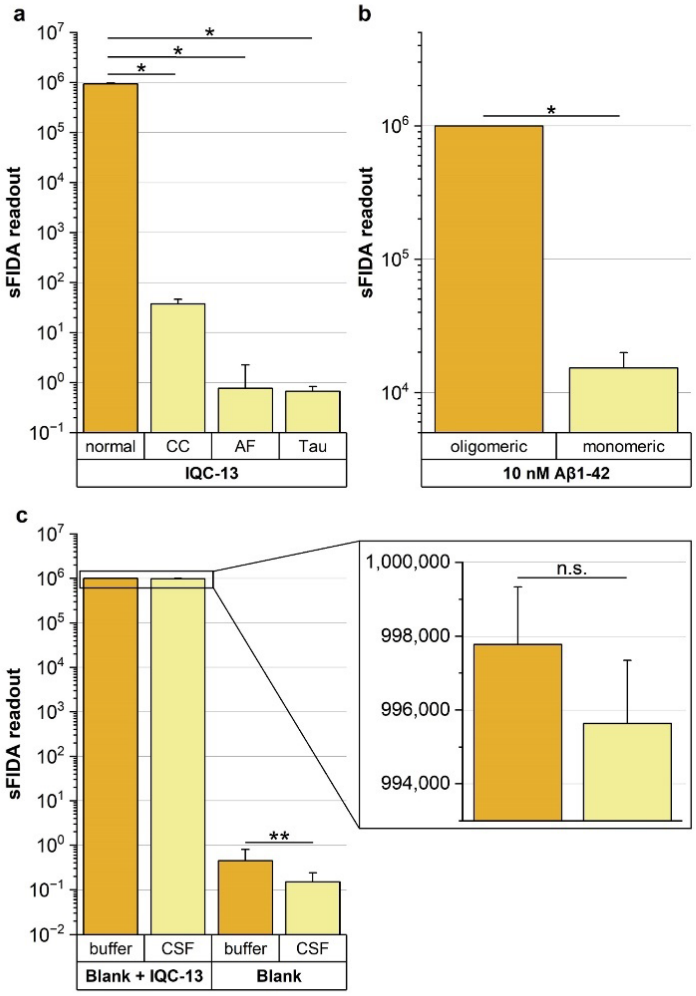

Figure 4. Comparison of sFIDA readout of IQC-13 applied on different assay setups. (**a**) sFIDA readouts of the normal assay setup were compared to assay setups without the capture antibody (capture control, CC), without Aβ-specific detection probes (TBST + 0.1% BSA without any detection probes, autofluorescence control, AF) or with Tau-specific detection probes (equimolar mixture of Tau12 antibodies labeled with CF633 and CF488A in TBST + 0.1% BSA, Tau). A signal reduction of almost 100% and significantly lower sFIDA readouts compared to the standard assay setup (normal,

p-values between 0.0152 and 0.0147) were observed for all controls. (**b**) In addition, equal molar concentrations of monomeric Aβ1–42 were applied on the assay surface to demonstrate that the assay is insensitive toward monomers. A signal reduction of nearly 99% and significantly lower sFIDA readouts compared to the standard assay setup were observed (*p*-value: 0.0152), showing that interference from monomeric Aβ can be excluded. (**c**) To evaluate the matrix effects of CSF, IQC-13 was spiked into bovine CSF, and sFIDA readouts were calculated on the basis of the background signal of the additionally applied bovine CSF-blank. For IQC-13, no significant difference in the sFIDA readouts was observed (*p*-value: 0.108), and only a slight signal reduction of 0.2% was observed. In contrast, the sFIDA readout of CSF-blank was significantly lower compared to the buffer control (*p*-value: 0.002, signal reduction: 67%). Note the logarithmic scale. Data are presented as the mean and standard deviation of four replicates. Significant differences between groups were calculated using the one-sided Mann–Whitney U test with a confidence interval of 5%. Significant differences are marked as follows: * $0.01 \leq p < 0.05$; ** $0.001 \leq p < 0.01$; n.s. not significant. Abbreviations: CSF, cerebrospinal fluid; IQC, internal quality control.

Furthermore, after spiking the Aβ oligomers in CSF, only negligible matrix effects were observed, with a minor signal reduction of 0.2% and no significant difference in the readouts (*p*-value: 0.108) (Figure 4c, Table S3c). In addition, matrix components in the CSF-blank reduced the background signal more efficiently than the dilution buffer, indicated by a signal reduction of approximately 67% and significantly lower readouts indicated by a *p*-value of 0.002 (CSF-blank vs. BC). Consequently, the signal-to-noise ratio between IQC-13 and the respective blank was three times higher in CSF than in the dilution buffer.

3.4. Shewhart Chart as a Reliable QC-Tool for Monitoring IQC Performance

Control charts are a valuable tool for monitoring assay performance and can be used by any laboratory [25]. In this work, we demonstrated the use of a Shewhart chart to monitor the performance of three IQC samples in sFIDA (for respective TIRFM images showing co-localized pixel above cutoff values, see Figure S2) by integrating values of 20 observations of each IQC sample into a separate chart (Table S4). Charts were then interpreted analogously to defined rules (Section 2.4.3).

All three IQC samples showed low inter-assay variability as the calculated mean CV% of the respective 20 observations was below 20% (IQC-6 = 16.2%, IQC-8 = 16.5%, IQC-10 = 17.6%). As illustrated in Figure 5, none of the IQC samples exceeded the action limit. In addition, neither IQC-6 nor IQC-8 exceeded the control limits, but one value of sample IQC-10 occurred between the control and action limit. Nonetheless, assay performance was considered acceptable within the predefined range because this was the only deviation. No ascending or descending trend of the nine consecutive observation points was seen in IQC samples. Even if no out-of-control situation could be determined in IQC samples, IQC-6 should be monitored further as a general downward progression became apparent. Moreover, an out-of-control situation may arise in the foreseeable future if the next three observation points of IQC-6 also occur between the central line and the lower control limit.

In particular, for those assays subjected to quality management, such as sFIDA technology, troubleshooting out-of-order situations can be monitored rapidly, as possible causes related to the operator, instruments, manufacturing protocols, and/or lot numbers of assay components are regularly documented.

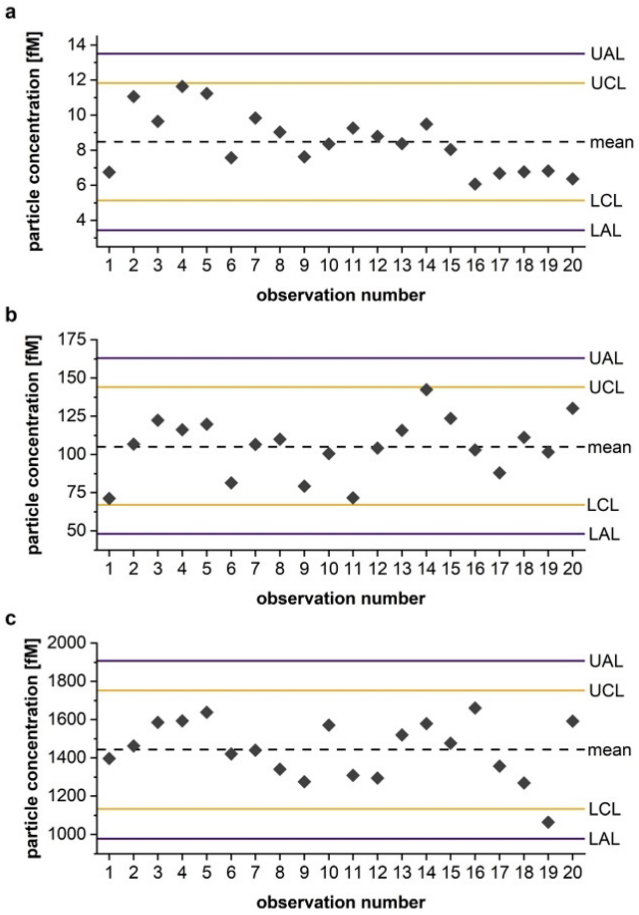

Figure 5. Shewhart chart monitoring the performance of IQC-6 (**a**), IQC-8 (**b**) and IQC-10 (**c**). The calibrated particle concentrations of 20 observations of each IQC sample (gray dots) were plotted to simulate assay performance in chronological order. Mean: central dashed line; upper and lower control limit (UCL, LCL): yellow line; upper and lower action limit (UAL, LAL): purple line. Data are presented as the mean of four replicates (gray data points). Abbreviation: IQC, internal quality control.

4. Discussion

In the present study, we developed a homogeneous and reproducible Aβ oligomer-based IQC sample for sFIDA and established a QC-tool for monitoring assay performance.

We characterized the formation of Aβ oligomers by AFM, which revealed globular-shaped oligomers with a median size of 2.67 nm, whereby AFM analysis revealed the size of a dried oligomer and not the hydrodynamic size. Oligomers are in thermodynamic equilibrium with monomers and larger aggregates, such as amyloid fibrils. In vitro produced oligomers have been shown to dissociate into monomers within a few hours, with only a small fraction of oligomers converting to fibrils [26]. Conversion to fibrils can be excluded herein because no fibrillary morphologies were detected by AFM. Noteworthily, the sFIDA assay currently does not discriminate oligomers from larger yet still soluble aggregates because of the diffraction limit of the optical detection system. However, as larger particles bind more fluorescent probes, a size determination of sub-resolution particles should be possible based on pixel intensity. For this purpose, the oligomers developed can serve as a size standard. In addition to established AD biomarkers, such as monomeric Aβ1–42, the ratio of Aβ1–42 to Aβ1–40, phosphorylated Tau, and total Tau in CSF, and magnetic

resonance imaging and positron emission tomography (PET), i.e., Amyloid-PET or Tau-PET [2,27,28], oligomeric forms of Aβ represent a promising biomarker candidate for early AD diagnosis [5,6,29]. Consequently, in vitro, oligomer-based diagnostics are the subject of current biomarker research.

We detected and quantified oligomers at sub-femtomolar concentrations, down to 0.28 fM (LoD), which qualifies the sFIDA assay for biofluid-based in vitro oligomer-based diagnostic methods [5]. We previously showed that Aβ oligomers and aggregates are detectable in human CSF samples [10] and complex matrices such as murine and human brain homogenate samples [9] using sFIDA. Due to further development of the assay protocol, including the use of synthetic Aβ oligomers shown herein, the analytical sensitivity was further improved compared to our previously published data [7]. The potential of this analytical sensitivity to improve diagnostic performance must be validated using a large set of clinical samples. In comparison to other oligomer-specific Aβ assays, sFIDA ensures single-particle sensitivity. Although a direct comparison of sensitivity among different assays is challenging because of variations in assay design, calibration standards, and detection limit calculations, we evaluated the sensitivity ranges of various assays (Table 1).

Table 1. Comparison of several Aβ oligomer quantification assays according to their sensitivity level. For this purpose, the respective weight concentrations pg/mL were converted into femtomolar oligomer concentrations using the approximate molecular weights of the used calibration standards.

Reference	Assay Setup	Calibration Standard	Sensitivity [fM]
sFIDA	Single-particle analysis with fluorescence microscopy, overlapping epitopes capture: Nab228 aa1–11 detection: IC16 aa2–8 + Nab228 aa1–11	Aβ1–15 SiNaPs	LoD = 0.28
Savage et al. [30]	Single particle analysis with bead-based assay capture: 19.3 oligomer-specific detection: 82E1 aa1–16	Aβ1–42 oligomers (MW 1117 kDa)	LoD = 0.08
IBL [31]	ELISA capture: 82E1 aa1–16 detection: 24B3 oligomer-specific	E22P–Aβ40 Dimer	31.4 (N/A)
Hölttä et al. [32]	ELISA, overlapping epitopes capture and detection: 82E1 aa1–16	Dimer Aβ1–11	LLoQ = 90.9
Kasai et al. [33]	ELISA, overlapping epitopes capture and detection: Ban50 aa1–10	MAP 16-mer (lysine core)	LoD = 190
Esparza et al. [34]	Single particle analysis with bead-based assay overlapping epitopes capture and detection: HJ3.4 aa1–13	Aβ1–40Ser26Cys dimer	LLoQ = 720

Only the assay described by Savage et al. (0.08 fM) [30] or the commercial ELISA assay from Immuno-Biological Laboratories Co. Ltd. (IBL, Fujioka, Japan) [31] (31.4 fM), which also claims to detect single particles, offers sensitivity in the low femtomolar range, which is presumably because of the combined use of N-terminal and oligomer-specific assay antibodies. In contrast, all listed homotypic assays, using the same antibody for capture and detection, showed insufficient sensitivity levels between 91 and 720 fM. However, because of epitope competition, these assays [32–34] and the sFIDA assay are insensitive toward monomers.

Through our experiments, we demonstrated that Aβ oligomer-based IQC samples are reproducible, homogeneous, and suitable in oligomer-based diagnostic methods such as sFIDA. However, as our studies were performed in an artificial sample matrix, further

validation data from authentic biological sample matrices such as the plasma or CSF should be obtained, including extensive recovery and parallelism studies [35]. In addition, the critical concentration at which endogenous components compromise the readout and lead to false-positive or false-negative results must be investigated. For sFIDA analysis of α-synuclein and Tau aggregates in CSF, we showed that blood contamination and HAMAs can affect the sFIDA readout [8]. In particular, for CSF, validation should be straightforward because we determined a signal loss of only 0.2% for IQC-15 due to matrix effects. The Aβ oligomer IQC can also facilitate the development of a blood-based sFIDA assay, which is currently in progress. However, the complex plasma matrix could make validation more challenging, as strong matrix effects such as interference between Aβ and human serum albumin or between circulating human antibodies with the assay antibodies are expected [6,15,36,37]. In addition to matrix effects, sample stability and sample tubing can also influence the measurement signal [38,39]. For future routine applications and regulatory approval of the sFIDA technology, the IQC sample should ideally be available as a ready-to-use kit component. Hence, the benchtop stability and long-term stability of the IQC sample should be investigated by testing different sample tubes, storage temperatures and durations, and the effects of repetitive freeze–thaw cycles [2,35,40].

5. Conclusions

Since protein misfolding and aggregation are pathological hallmarks for a variety of neurodegenerative diseases, it is necessary to establish additional IQC samples, e.g., based on Tau or α-synuclein oligomers that improve the routine application of oligomer-based diagnostic methods such as sFIDA. Transitioning from research use to in vitro diagnostics (IVD) has various regulatory requirements [11]. The Aβ oligomer-based IQC sample implemented represents an important step toward the standardization, routine application and ultimately, registration of sFIDA as a diagnostic tool of AD for the IVD market.

Supplementary Materials: The following supporting information can be downloaded at https://www.mdpi.com/article/10.3390/diagnostics13101702/s1: Figure S1. Scheme of monomerization and oligomerization procedure; Figure S2. TIRFM-images of colocalized pixels of IQC-6, IQC-8, and IQC-10 samples with intensities above blank control-based cutoff; Table S1. Individual sFIDA readouts, calibrated molar particle concentrations, and CV% for each IQC sample; Table S2. Calculation of dilution linearity of Aβ oligomer-based IQC samples within working range; Table S3. Selectivity and recovery of the sFIDA assay to IQC-13; Table S4. Raw data used to generate Shewhart charts in Figure 5.

Author Contributions: Conceptualization, M.P., A.D. and O.B.; formal analysis, M.P., A.D. and F.R.; funding acquisition, D.W. and O.B.; investigation, M.P. and A.D.; methodology, M.P., A.D., L.B., T.B. and V.K.-S.; project administration, D.R., D.W. and O.B.; supervision, D.R., D.W. and O.B.; validation, M.P. and A.D.; writing—original draft, M.P. and A.D.; writing—review and editing, W.H., D.R., D.W. and O.B. All authors have read and agreed to the published version of the manuscript.

Funding: This research was funded by the Helmholtz Association, grant number HVF0079.

Institutional Review Board Statement: Not applicable.

Data Availability Statement: The data presented in this study are available in the article and its Supplementary Materials.

Acknowledgments: The authors thank Volker Nischwitz (Central Institute for Engineering, Electronics and Analytics, Analytics (ZEA-3), Forschungszentrum Jülich, 52428, Jülich, Germany) for determining silicon concentrations in the Aβ1–15 SiNaPs using inductively coupled plasma mass spectrometry. The authors also thank Carsten Korth (Institute of Neuropathology, Universitätsklinikum Düsseldorf, 40225 Düsseldorf, Germany) for providing the IC16 antibody. Jürgen Rehage, Maike Heppelmann, and Ioannis Proios (University of Veterinary Medicine Hannover, 30559 Hannover, Germany) kindly provided the bovine CSF used for the spiking experiment. Lastly, the authors thank Andrew Dingley for proofreading the manuscript.

Conflicts of Interest: Dieter Willbold and Oliver Bannach are cofounders and shareholders of attyloid GmbH. Dieter Willbold and Detlev Riesner are members of attyloid's supervisory board. These factors did not influence the interpretation of the data. The remaining authors declare no conflicts of interest.

References

1. Brettschneider, J.; Del Tredici, K.; Lee, V.M.; Trojanowski, J.Q. Spreading of pathology in neurodegenerative diseases: A focus on human studies. *Nat. Rev. Neurosci.* **2015**, *16*, 109–120. [CrossRef] [PubMed]
2. Dulewicz, M.; Kulczyńska-Przybik, A.; Mroczko, P.; Kornhuber, J.; Lewczuk, P.; Mroczko, B. Biomarkers for the Diagnosis of Alzheimer's Disease in Clinical Practice: The Role of CSF Biomarkers during the Evolution of Diagnostic Criteria. *Int. J. Mol. Sci.* **2022**, *23*, 8598. [CrossRef] [PubMed]
3. Tolar, M.; Abushakra, S.; Sabbagh, M. The path forward in Alzheimer's disease therapeutics: Reevaluating the amyloid cascade hypothesis. *Alzheimers Dement.* **2020**, *16*, 1553–1560. [CrossRef] [PubMed]
4. Lotz, G.P.; Legleiter, J. The role of amyloidogenic protein oligomerization in neurodegenerative disease. *J. Mol. Med.* **2013**, *91*, 653–664. [CrossRef]
5. Kulenkampff, K.; Wolf Perez, A.-M.; Sormanni, P.; Habchi, J.; Vendruscolo, M. Quantifying misfolded protein oligomers as drug targets and biomarkers in Alzheimer and Parkinson diseases. *Nat. Rev. Chem.* **2021**, *5*, 277–294. [CrossRef]
6. Mroczko, B.; Groblewska, M.; Litman-Zawadzka, A.; Kornhuber, J.; Lewczuk, P. Amyloid β oligomers (AβOs) in Alzheimer's disease. *J. Neural. Transm.* **2018**, *125*, 177–191. [CrossRef]
7. Herrmann, Y.; Kulawik, A.; Kühbach, K.; Hülsemann, M.; Peters, L.; Bujnicki, T.; Kravchenko, K.; Linnartz, C.; Willbold, J.; Zafiu, C.; et al. sFIDA automation yields sub-femtomolar limit of detection for Aβ aggregates in body fluids. *Clin. Biochem.* **2017**, *50*, 244–247. [CrossRef]
8. Blömeke, L.; Pils, M.; Kraemer-Schulien, V.; Dybala, A.; Schaffrath, A.; Kulawik, A.; Rehn, F.; Cousin, A.; Nischwitz, V.; Willbold, J.; et al. Quantitative detection of α-Synuclein and Tau oligomers and other aggregates by digital single particle counting. *NPJ Parkinsons Dis.* **2022**, *8*, 68. [CrossRef]
9. Kass, B.; Schemmert, S.; Zafiu, C.; Pils, M.; Bannach, O.; Kutzsche, J.; Bujnicki, T.; Willbold, D. Aβ oligomer concentration in mouse and human brain and its drug-induced reduction ex vivo. *Cell. Rep. Med.* **2022**, *3*, 100630. [CrossRef]
10. Wang-Dietrich, L.; Funke, S.A.; Kühbach, K.; Wang, K.; Besmehn, A.; Willbold, S.; Cinar, Y.; Bannach, O.; Birkmann, E.; Willbold, D. The amyloid-β oligomer count in cerebrospinal fluid is a biomarker for Alzheimer's disease. *J. Alzheimers Dis.* **2013**, *34*, 985–994. [CrossRef]
11. Kulawik, A.; Heise, H.; Zafiu, C.; Willbold, D.; Bannach, O. Advancements of the sFIDA method for oligomer-based diagnostics of neurodegenerative diseases. *FEBS Lett.* **2018**, *592*, 516–534. [CrossRef] [PubMed]
12. Schaffrath, A.; Schleyken, S.; Seger, A.; Jergas, H.; Özdüzenciler, P.; Pils, M.; Blömeke, L.; Cousin, A.; Willbold, J.; Bujnicki, T.; et al. Patients with isolated REM-sleep behavior disorder have elevated levels of alpha-synuclein aggregates in stool. *NPJ Parkinsons Dis.* **2023**, *9*, 14. [CrossRef] [PubMed]
13. Hülsemann, M.; Zafiu, C.; Kühbach, K.; Lühmann, N.; Herrmann, Y.; Peters, L.; Linnartz, C.; Willbold, J.; Kravchenko, K.; Kulawik, A.; et al. Biofunctionalized Silica Nanoparticles: Standards in Amyloid-β Oligomer-Based Diagnosis of Alzheimer's Disease. *J. Alzheimers Dis.* **2016**, *54*, 79–88. [CrossRef] [PubMed]
14. Zielinski, M.; Röder, C.; Schröder, G.F. Challenges in sample preparation and structure determination of amyloids by cryo-EM. *J. Biol. Chem.* **2021**, *297*, 100938. [CrossRef] [PubMed]
15. Vanderstichele, H.; Stoops, E.; Vanmechelen, E.; Jeromin, A. Potential sources of interference on Abeta immunoassays in biological samples. *Alzheimers Res. Ther.* **2012**, *4*, 39. [CrossRef]
16. Blacksell, S.D.; Cameron, A.R.; Chamnanpood, C.; Chamnanpood, P.; Tatong, D.; Monpolsiri, M.; Westbury, H.A. Implementation of internal laboratory quality control procedures for the monitoring of ELISA performance at a regional veterinary laboratory. *Vet. Microbiol.* **1996**, *51*, 1–9. [CrossRef]
17. Sturgeon, C.M. Chapter 6.2—Quality Assurance. In *The Immunoassay Handbook*, 4th ed.; Wild, D., Ed.; Elsevier: Oxford, UK, 2013; pp. 441–454.
18. Lock, R.J. My approach to internal quality control in a clinical immunology laboratory. *J. Clin. Pathol.* **2006**, *59*, 681–684. [CrossRef]
19. Ryan, D.A.; Narrow, W.C.; Federoff, H.J.; Bowers, W.J. An improved method for generating consistent soluble amyloid-beta oligomer preparations for in vitro neurotoxicity studies. *J. Neurosci. Methods* **2010**, *190*, 171–179. [CrossRef]
20. Kotler, S.A.; Ramamoorthy, A. Preparation of Stable Amyloid-β Oligomers Without Perturbative Methods. *Methods Mol. Biol.* **2018**, *1777*, 331–338. [CrossRef]
21. Stine, W.B.; Jungbauer, L.; Yu, C.; LaDu, M.J. Preparing synthetic Aβ in different aggregation states. *Methods Mol. Biol.* **2011**, *670*, 13–32. [CrossRef]
22. Brener, O.; Dunkelmann, T.; Gremer, L.; van Groen, T.; Mirecka, E.A.; Kadish, I.; Willuweit, A.; Kutzsche, J.; Jürgens, D.; Rudolph, S.; et al. QIAD assay for quantitating a compound's efficacy in elimination of toxic Aβ oligomers. *Sci. Rep.* **2015**, *5*, 13222. [CrossRef]
23. Novo, M.; Freire, S.; Al-Soufi, W. Critical aggregation concentration for the formation of early Amyloid-β(1–42) oligomers. *Sci. Rep.* **2018**, *8*, 1783. [CrossRef] [PubMed]

24. Armbruster, D.A.; Pry, T. Limit of blank, limit of detection and limit of quantitation. *Clin. Biochem. Rev.* **2008**, *29* (Suppl. S1), S49–S52. [PubMed]
25. Reichenbächer, M.; Einax, J.W. *Challenges in Analytical Quality Assurance*; Springer: Berlin/Heidelberg, Germany, 2011.
26. Michaels, T.C.T.; Šarić, A.; Curk, S.; Bernfur, K.; Arosio, P.; Meisl, G.; Dear, A.J.; Cohen, S.I.A.; Dobson, C.M.; Vendruscolo, M.; et al. Dynamics of oligomer populations formed during the aggregation of Alzheimer's Aβ42 peptide. *Nat. Chem.* **2020**, *12*, 445–451. [CrossRef] [PubMed]
27. Jack, C.R., Jr.; Bennett, D.A.; Blennow, K.; Carrillo, M.C.; Dunn, B.; Haeberlein, S.B.; Holtzman, D.M.; Jagust, W.; Jessen, F.; Karlawish, J.; et al. NIA-AA Research Framework: Toward a biological definition of Alzheimer's disease. *Alzheimers Dement.* **2018**, *14*, 535–562. [CrossRef] [PubMed]
28. Lewczuk, P.; Łukaszewicz-Zając, M.; Mroczko, P.; Kornhuber, J. Clinical significance of fluid biomarkers in Alzheimer's Disease. *Pharmacol. Rep.* **2020**, *72*, 528–542. [CrossRef]
29. Shea, D.; Colasurdo, E.; Smith, A.; Paschall, C.; Jayadev, S.; Keene, C.D.; Galasko, D.; Ko, A.; Li, G.; Peskind, E.; et al. SOBA: Development and testing of a soluble oligomer binding assay for detection of amyloidogenic toxic oligomers. *Proc. Natl. Acad. Sci. USA* **2022**, *119*, e2213157119. [CrossRef]
30. Savage, M.J.; Kalinina, J.; Wolfe, A.; Tugusheva, K.; Korn, R.; Cash-Mason, T.; Maxwell, J.W.; Hatcher, N.G.; Haugabook, S.J.; Wu, G.; et al. A sensitive aβ oligomer assay discriminates Alzheimer's and aged control cerebrospinal fluid. *J. Neurosci.* **2014**, *34*, 2884–2897. [CrossRef]
31. IBL-International. Human Amyloid β Toxic Oligomer Assay Kit—IBL. Instruction for Use Code No. 27709. Available online: https://www.ibl-japan.co.jp/files/topics/4751_ext_02_en_0.pdf (accessed on 29 March 2023).
32. Hölttä, M.; Hansson, O.; Andreasson, U.; Hertze, J.; Minthon, L.; Nägga, K.; Andreasen, N.; Zetterberg, H.; Blennow, K. Evaluating amyloid-β oligomers in cerebrospinal fluid as a biomarker for Alzheimer's disease. *PLoS ONE* **2013**, *8*, e66381. [CrossRef]
33. Kasai, T.; Tokuda, T.; Taylor, M.; Nakagawa, M.; Allsop, D. Utilization of a multiple antigenic peptide as a calibration standard in the BAN50 single antibody sandwich ELISA for Aβ oligomers. *Biochem. Biophys Res. Commun.* **2012**, *422*, 375–380. [CrossRef]
34. Esparza, T.J.; Zhao, H.; Cirrito, J.R.; Cairns, N.J.; Bateman, R.J.; Holtzman, D.M.; Brody, D.L. Amyloid-β oligomerization in Alzheimer dementia versus high-pathology controls. *Ann. Neurol.* **2013**, *73*, 104–119. [CrossRef] [PubMed]
35. Andreasson, U.; Perret-Liaudet, A.; van Waalwijk van Doorn, L.J.; Blennow, K.; Chiasserini, D.; Engelborghs, S.; Fladby, T.; Genc, S.; Kruse, N.; Kuiperij, H.B.; et al. A Practical Guide to Immunoassay Method Validation. *Front. Neurol.* **2015**, *6*, 179. [CrossRef] [PubMed]
36. Kuo, Y.M.; Kokjohn, T.A.; Kalback, W.; Luehrs, D.; Galasko, D.R.; Chevallier, N.; Koo, E.H.; Emmerling, M.R.; Roher, A.E. Amyloid-beta peptides interact with plasma proteins and erythrocytes: Implications for their quantitation in plasma. *Biochem. Biophys Res. Commun.* **2000**, *268*, 750–756. [CrossRef] [PubMed]
37. Sehlin, D.; Söllvander, S.; Paulie, S.; Brundin, R.; Ingelsson, M.; Lannfelt, L.; Pettersson, F.E.; Englund, H. Interference from heterophilic antibodies in amyloid-β oligomer ELISAs. *J. Alzheimers Dis.* **2010**, *21*, 1295–1301. [CrossRef] [PubMed]
38. Vanderstichele, H.M.; Janelidze, S.; Demeyer, L.; Coart, E.; Stoops, E.; Herbst, V.; Mauroo, K.; Brix, B.; Hansson, O. Optimized Standard Operating Procedures for the Analysis of Cerebrospinal Fluid Aβ42 and the Ratios of Aβ Isoforms Using Low Protein Binding Tubes. *J. Alzheimers Dis.* **2016**, *53*, 1121–1132. [CrossRef]
39. Schoonenboom, N.S.; Mulder, C.; Vanderstichele, H.; Van Elk, E.J.; Kok, A.; Van Kamp, G.J.; Scheltens, P.; Blankenstein, M.A. Effects of processing and storage conditions on amyloid β(1–42) and tau concentrations in cerebrospinal fluid: Implications for use in clinical practice. *Clin. Chem.* **2005**, *51*, 189–195. [CrossRef]
40. van de Merbel, N.; Savoie, N.; Yadav, M.; Ohtsu, Y.; White, J.; Riccio, M.F.; Dong, K.; de Vries, R.; Diancin, J. Stability: Recommendation for best practices and harmonization from the Global Bioanalysis Consortium Harmonization Team. *Aaps J.* **2014**, *16*, 392–399. [CrossRef]

2.2.7 Digital direct detection of single biomolecules revealed femtomolar sensitivity

Autoren:	Tuyen Bujnicki, Anneliese Cousin, Melanie Schwarten, Karen Hänel, **Fabian Rehn**, Bernd König, Victoria Kraemer-Schulien, Marlene Pils, Lara Blömeke, Oliver Bannach, Abhishek Cukkemane, Dieter Willbold
Journal:	*The Journal of Molecular Diagnostics* *(Eingereicht im Februar 2025)*
Beitrag:	Kalibration der Rohdaten Datenauswertung Diskussion der Ergebnisse Prüfung des Manuskriptes
Druckgenehmigung:	Siehe Anhang 11.

Digital direct detection of single biomolecules revealed femtomolar sensitivity

Tuyen Bujnicki,[1] Anneliese Cousin,[1] Melanie Schwarten,[1] Karen Hänel,[1] Fabian Rehn,[3,1,2] Bernd König,[1] Victoria Kraemer-Schulien,[1] Marlene Pils,[1,2] Lara Blömeke,[1,] Oliver Bannach,[2] Abhishek Cukkemane, [1,3] Dieter Willbold,[1,3]

[1]Forschungszentrum Jülich GmbH, Institute of Biological Information Processing (Structural Biochemistry: IBI-7), 52428 Jülich, Germany;

[2]attyloid GmbH, Merowingerplatz 1a, 40225 Düsseldorf, Germany;

[3]Heinrich-Heine-Universität Düsseldorf, Institut für Physikalische Biologie, 40225 Düsseldorf, Germany

number of pages: 25

number of figures: 6

number of tables: 2

Running Head: Digital direct detection

Grant numbers and sources of support: HIL-A13 from Helmholtz Association

Name, mailing address, phone, fax, and email address of the corresponding author(s): Dieter Willbold, d.willbold@fz-juelich.de and Tuyen Bujnicki, t.bujnicki@fz-juelich.de

23

24 Disclosures: Dieter Willbold and Oliver Bannach are co-founders and shareholders of attyloid GmbH.

25 This had no influence on the interpretation of the data. All other authors declare no competing interests

26 related to this work.

Abstract

There is a high demand for robust assays for biomarker detection in the sub-picomolar range particularly for neurodegenerative diseases, cardiovascular diseases, and tumor detection. Recent advancements in digital ELISA techniques addresses this demand, however, these techniques are characterized by a high level of complexity in sample application and measurement protocols. In order to offer a simpler alternative, we present a new, improved version of sandwich ELISA in combination with single molecule fluorescence counting using total internal reflection fluorescence (TIRF) microscopy. This method enables detection sensitivity down to the femtomolar range in a non-disruptive and straightforward manner, allowing for seamless integration into a laboratory setting. The effectiveness of this method is illustrated using two model targets. Firstly, a simplified version of the assay with a fluorescence-labelled streptavidin-biotin pair demonstrates its capacity to achieve femtomolar sensitivity. Secondly, capture nanobody immobilized ALFA-GFP is detected and counted by a fluorescence-labelled nanobody using TIRF microscopy, also achieving femtomolar sensitivity. TIRF-based single molecule detection of immune sandwiches is a promising technique for biomarker detection in the femtomolar range.

Introduction

The enzyme-linked immunosorbent assay (ELISA) serves as an essential tool for detection of biomarkers in basic research and clinical diagnostics (1, 2). The traditional and classical ELISA has a sensitivity that is typically in the order of 10^{-12} mol/l (3). However, the detection of disease in early stages and difficult-to-diagnose diseases, often require measurement of lower concentrations of protein biomarkers. Assays with single-molecule sensitivity allow the detection of ultralow protein concentrations (4, 5).

Here, the technology **d**irect **d**igital **d**etection (ThreeD) of single particles is described which enables single-molecule counting by using total internal reflection fluorescence (TIRF) microscopy in a microtiter plate format (Figure 1). ThreeD builds on the well-established principles of sFIDA (surface fluorescence intensity distribution analysis), a technology designed to quantify protein oligomers and aggregates (6-8). The ThreeD assay employs a capture antibody and a fluorescence-labelled detection antibody which bind to different epitopes of the target protein. Following assay preparation, the well surface is imaged with a TIRF microscope and the resulting images are analysed with the in-house developed software sFIDAta. This software then enumerates the number of individual fluorescence-labelled detection antibodies that correspond to single target molecules. The ThreeD technology can be used for the detection of labelled target molecules in a simple assay setup. In principle, ThreeD enables the detection of each individual labelled single molecule on the plate surface.

In various existing "digital" measurement techniques which are capable of ultralow detection, entail the confinement of individual molecules within ultra-small containers or droplets to produce a signal at locally high concentration, thereby enabling single molecule counting. One example is the single molecule array (SIMOA) technology, which uses magnetic beads to capture immunocomplexes, which are then dispensed into individual microwells on a chip (4, 9). However, the signal readout for this technology requires a proprietary device. Another such immunoassay method involves the use of

66 microdroplets with tens of femtoliter volume for confining one single bead-immunocomplex in one
67 droplet (10, 11). These droplets are then incubated on a chip, and the resultant fluorescent products
68 are detectable via a fluorescence microscope. Although this technology can achieve sub-femtomolar
69 sensitivity, the generation of the tiny femtoliter droplets remains a challenging endeavour (3). Another
70 recently introduced molecular on-bead signal amplification for individual counting (MOSAIC)
71 technology (5) represents a new type of digital ELISA. In this process, individual target molecules are
72 captured on antibody-coated magnetic beads. Detection is achieved using biotinylated antibodies
73 labelled with streptavidin-DNA conjugates. Rolling circle amplification results in immunocomplex
74 sandwiches with long DNA concatemers, which are then hybridized to fluorescently labelled DNA
75 probes. The final step involves counting both fluorescent and non-fluorescent beads by flow cytometry
76 (5).
77 In contrast, the ThreeD technology employs minimal sample preparation and detects single molecules
78 directly by fluorescence microscopy and that without amplification. The system requires neither beads
79 for prior binding of the target nor sorting of the immunocomplex into individual compartments. In a
80 nutshell, the target molecules can be captured directly on the plate surface.
81 In this paper, we present a simplified assay with a basic setup. Firstly as model, the biotin-streptavidin
82 pair is being use to characterize the sensitivity and explore the dynamic range of the ThreeD technology.
83 Next, the assay development process is demonstrated using the model construct ALFA-GFP, wherein
84 two nanobodies are used for target capture und detection. After fine-tuning of the buffer conditions
85 and concentrations for the nanobodies, the reagents and conditions for sample dilution were also
86 assessed.
87

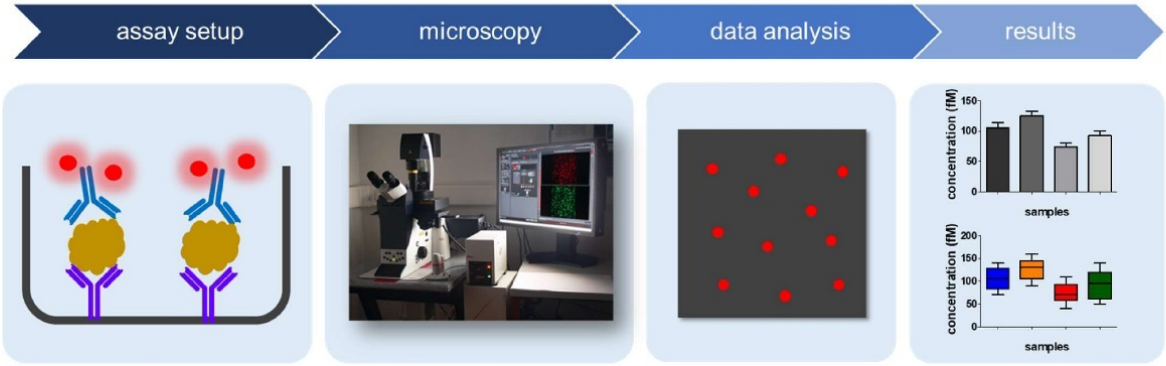

Figure 1 Schematic representation of ThreeD technology.

For the assay, capture antibodies are immobilized on the glass surface of a 384-well plate. This is followed by blocking wherein a blocking agent is added to the plate and excess is washed off. In the next step target proteins from the samples are bound to the capture surface. After washing off unbound components, target proteins are bound by fluorescence-labelled antibodies. By using high resolution fluorescence microscopy, single molecules are detected and counted individually. The images are analysed with in-house developed software with various analysis functions like automatic artefact detection, particle counting, statistics and different display formats.

Materials and Methods

Cloning, expression and purification of ALFA-GFP protein

The synthetically produced gene (Biocat, Heidelberg, Germany) for the target ALFA-GFP (N-terminus: ALFA-tag1_20aa-Linker_ALFA-tag2_20aa-Linker_eGFP1_20aa-Linker_eGFP2_6xHis-Tag) was introduced into the multiple cloning site of the expression vector pET15b (Novagen) via the restriction sites NcoI and XhoI. The ALFA epitope consists of 14 amino acids (aa) (SRLEEELRRRLTE) and human eGFP with the UniProt code 5MKY7 was used as GFP domain.

For expression, a pre-culture was prepared with 50 ml Luria Broth (LB) medium (Carl Roth, Karlsruhe, Germany) with 100 µg/ml ampicillin (Carl Roth, Karlsruhe, Germany) and 30 µg/ml chloramphenicol (Applichem, Darmstadt, Germany) (Amp/Cam) inoculated with ALFA-GFP-pET15b transformed *E. coli* Lemo21 (DE3) cells (New England Biolabs, Frankfurt, Germany) and incubated in a shaking incubator at 37 °C overnight. The overnight grown culture was pelleted by centrifugation at 4,000 x g for 5 minutes (min) at 10 °C and resuspended in LB media. For expression culture, 500 ml LB media (Amp/Cam) were inoculated with the pre-culture to an OD_{600} of 0.3 and incubated under shaking at 37 °C. Induction was performed with 0.4 mM isopropyl β-D-galactopyranoside (IPTG, UBP Bio, Dallas, USA) at an OD_{600} of 0.7. The cells were then cultivated overnight at 22 °C. After 22 hours (h) the culture was incubated for additional 6 h at 4 °C without shaking and then harvested by centrifugation at 5,000 x g for 12 min (10 °C). The bacterial pellet was stored at -80 °C until use.

For purification of ALFA-GFP the bacterial cells from a 500 ml expression culture were resuspended in 50 ml buffer A (50 mM Na_3PO_4 pH 8, 300 mM NaCl, 5 mM dithiothreitol (DTT, Applichem, Darmstadt, Germany), two tablets of cOmplete EDTA-free protease inhibitor cocktail (Roche, Basel, Swiss) using a glass homogeniser and disrupted twice at 1.7 bar using a cell disruptor. The cell debris was then pelleted at 27,500 x g for 20 min (4 °C) and the supernatant was applied to a Ni-NTA (nickel-nitrilotriacetic,

120 Cytvia, Freiburg, Germany) column equilibrated with 1 column volume (CV) buffer A. The column was
121 then washed with 10 CV buffer B (50 mM Na_3PO_4 (pH 8), 300 mM NaCl, 1 mM DTT), 10 CV buffer B with
122 10 mM imidazole (Applichem, Darmstadt, Germany) and 10 CV buffer B with 20 mM imidazole. Elution
123 was performed using 5 CV buffer B with 350 mM imidazole.
124 For further purification of the protein, the eluate from the Ni-NTA was applied to a SEC Superdex 75,
125 16/600 (Cytiva, Freiburg, Germany) equilibrated with buffer C (25 mM Na_3PO_4 (pH 8.0), 100 mM NaCl,
126 1 mM DTT). The run was performed with a flow rate of 1 ml/min at room temperature (RT) and the
127 elution fractions were analysed using SDS-Page with a TGX-Gel stainfree 4 - 20 % (BioRAD, Feldkirchen,
128 Germany). The protein-containing fractions were pooled and stored in aliquots at -80 °C.
129

130 ## ThreeD protocol

131 The steps for the assay preparation were carried out under the clean bench to avoid dust and microbial
132 contamination on a Nunc MicroWell 384-Well plate (Thermo Fisher Scientific, Waltham, USA).
133

134 *Prototype of ThreeD assay protocol for Streptavidin*
135 The setup involves preparation similar to the traditional and classical ELISA: In the first step 40 µl of 1 %
136 bovine serum albumin (BSA) (AppliChem, Darmstadt, Germany) in PBS was incubated overnight on the
137 384-well microtiter plate. This was followed by washing five times with 80 µl 1x TBS (Serva, Duisburg,
138 Germany) with 0.05 % Tween 20 (AppliChem, Darmstadt, Germany) (TBS-T) then five times washing
139 with TBS. Subsequently, 1 mM EZ-Link NHS-PEG4-Biotin (Thermo Fisher Scientific, Waltham, USA) in
140 PBS was incubated on the plate for 30 min at RT, followed by five times washing with TBS-T and TBS,
141 respectively. In the next step, the wells were blocked with 1 % BSA (AppliChem, Darmstadt, Germany)
142 in PBS for 1 h at RT followed by washing five times with TBS-T and TBS, respectively. 20 µl of

Streptavidin-AlexaFluor633 at different concentrations were then added and incubated overnight at 4 °C. Prior to the TIRF measurements, the plate was washed five times with TBS, followed by buffer change to TBS with 0.03 % ProClin (Sigma-Aldrich, Darmstadt, Germany).

ThreeD assay protocol for model protein ALFA-GFP

For capturing, 40 µl anti-GFP nanobody (Chromotek, Planegg-Martinsried, Germany) at 5 µg/ml in 0.1 M sodium hydrogen carbonate buffer ($NaHCO_3$, Carl Roth, Karlsruhe, Germany) was incubated overnight on the 384-well plate. After washing five times with 80 µl TBS-T and with 80 µl TBS, respectively, the plate was blocked with 1 % BSA in TBS-ProClin for 1.5 h at RT. The wells were washed again five times with TBS-T and TBS, respectively. Then 20 µl of ALFA-GFP were added and incubated overnight at RT. After washing five times with TBS, labelled detection nanobody anti-ALFA-AF647 (Nanotag, Göttingen, Germany) at 0.5 µg/ml was applied and incubated for 1 h at RT. The plate was washed again five times with TBS followed by a buffer change to TBS-ProClin for TIRF measurement.

TIRF setup and Image-data acquisition

Imaging was performed on a total internal reflection microscope (TIRFM, Leica DMI6000B, Wetzlar, Germany) using excitation at 635 nm with emission filter at 705/22 nm and excitation at 488 nm with emission filter at 525/36 nm. The exposure time was 1000 ms with a gain of 1300. For each well a total of 25 images with 1000 × 1000 pixels each were captured, which covers 3.14 % of the total area per well. For automated image-data analysis, we used our previously developed sFIDAta software tool (7, 12, 13). The analysis includes the automated detection and elimination of images containing obvious artefacts due to dust or crystals, and also blurred images. For the analysis, an intensity cut-off was defined and only pixels or groups of directly (not diagonal) connected pixels with intensities above this

166 cut-off were counted as individual particles. The cut-off was defined as the grey-scale value at which
167 the ratio of the positive versus the total number of pixels in the buffer control equals a pre-defined
168 value.
169
170 *Analysis*
171 Mean and standard deviation was calculated based on the particle counts of four replicates. Intra-assay
172 variation is described by the coefficient of variation (CV%) value.
173 Given the non-linear nature of the standard curves, a second-degree polynomial regression was
174 employed to determine the limit of detection (LOD) and lower limit of quantification (LLOQ) values,
175 ensuring the best possible fit for the regression model. To enhance the accuracy of data points in the
176 low concentration range, individual data points were weighted. These weights were calculated using
177 the reciprocal of the particle counts. The regression was performed using the Python packages NumPy
178 (version 1.20.3) and scikit-learn (version 0.24.2).
179 The LOD is defined as the analyte concentration corresponding to the mean particle count of blank plus
180 three times of its standard deviation (mean+3σ). The LLOQ is defined as the analyte concentration
181 corresponding to the mean particle count of blank plus ten times of its standard deviation (mean+10σ).
182 Data imaging was performed using GraphPad Prism 9 (Dotmatics, USA) or OriginPro 2019 (OriginLab
183 Corporation, USA).

184 ## Results

185 ### Prototype of ThreeD for determination of single molecule TIRF sensitivity

186 In order to establish the proof-of-principle, a simple, straightforward assay set-up was set up to
187 determine the detection limits of the ThreeD system by using the high-affinity streptavidin-biotin
188 binding pair (Figure 2 A). For this purpose, biotin was covalently binding to BSA on the plate surface.
189 Subsequently, Streptavidin-Alexa633 was added to the plate at concentrations ranging from 1 fM to 10
190 pM, thus yielding a 1 to 10 dilution series. Four wells were loaded for each concentration. After another
191 washing step, the plate bottom was scanned using a TIRF microscope. A total of 25 images was recorded
192 per well, amounting to 100 images per sample. The generated images were analysed with the in-house
193 developed software sFIDAta. The Analysis is based on a noise cut-off threshold applied to each pixel of
194 the image, leaving image pixels above the noise threshold that originate from a single fluorescence dye
195 labelled detection probe (here Streptavidin-AlexaFluor633, Figure 2D). The results obtained
196 demonstrate a dose response up to 1 pM with a limit of detection (LOD) of 1.4 fM and a lower limit of
197 quantification (LLOQ) of 5.3 fM (Figure 2 B, C). The mean intra-assay variance (indicated as CV% in
198 Supplemental Table 1) for all concentrations is below 10 %. The dynamic range extends across five
199 orders of magnitude.
200 In the experiment the direct binding of the target streptavidin labelled with fluorophore Alexa-633 to
201 BSA-Biotin on the glass surface of the wells was employed. This configuration establishes optimal
202 conditions for the experiment, thereby ensuring the highest sensitivity for the detection of single
203 particles by TIRF microscopy.

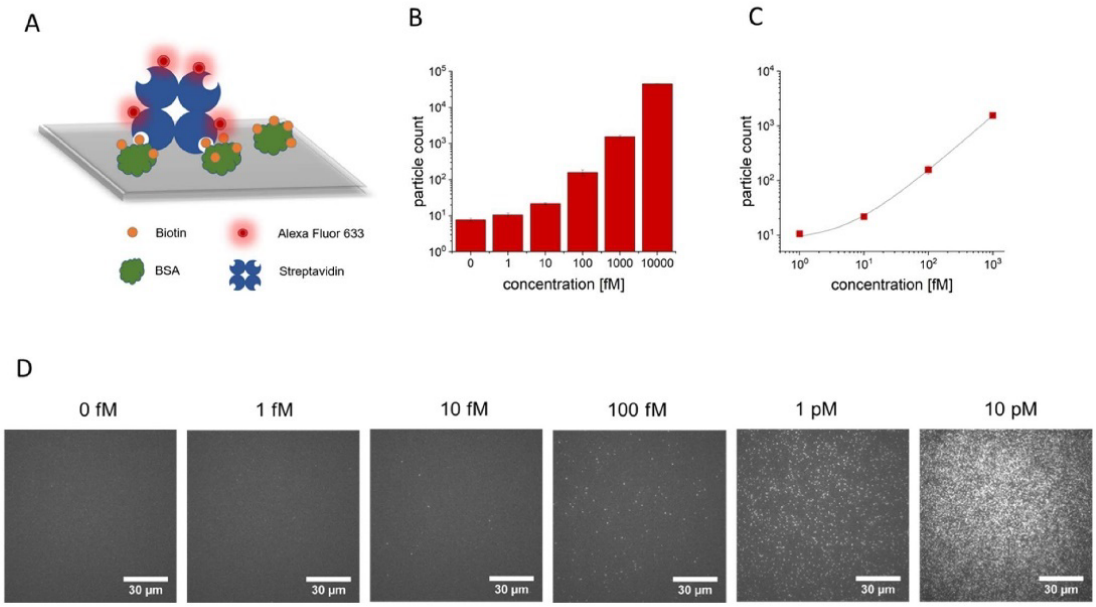

Figure 2 Prototype of the ThreeD technology for determination of single molecule TIRF sensitivity. A: Schematic representation of the assay setup. BSA and Biotin were incubated on the glass surface followed by addition of Streptavidin-Alexa633 in increasing concentrations. The fluorophore was directly detected with a TIRF microscope. B: Results of the measurements in bar chart with log y-scale: mean particle count for each sample concentration. C: plot of the data with fit to the data points up to 1 pM in double log-scale. Standard deviations were calculated from four replicates. D: Selected RAW images of different concentrations of Streptavidin-Alexa633.

Immunoassay development for model system ALFA-GFP

In the next step, a sandwich immunoassay was developed to validate the findings on single molecule sensitivity and for the establishment of the ThreeD method. The ALFA-GFP construct was selected as a model protein due to the inherent fluorescence ability of GFP, which allows direct detection of the protein itself at an excitation wavelength of 488 nm. This approach allowed the determination of the

amount of target molecules directly bound to the plate surface as a control. Detection of the target molecule was achieved by the addition of a fluorescence-labelled detection antibody. In addition, we used commercially available nanobodies for GFP and for ALFA for capture and detection, respectively (for schematics see Figure 3).

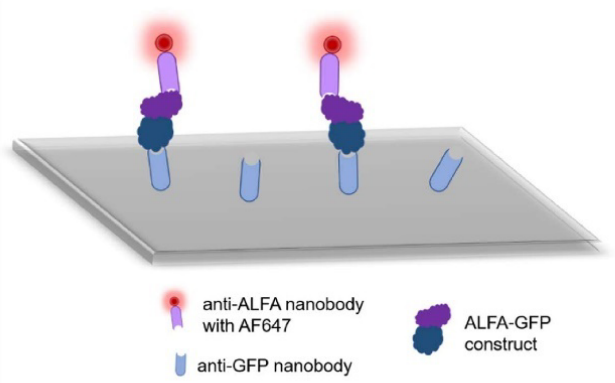

Figure 3 Assay setup for ALFA-GFP

Anti-GFP nanobody was used as capture. After applying the target ALFA-GFP in different concentrations, anti-ALFA-AF647 nanobody was added for detection.

The development of the immune assay for ALFA-GFP as the target molecule included numerous conditions and reagent concentration variations. The objective of each experiment was to achieve the highest signal intensity readout of the target. Initially, the concentration of the capture molecule, represented by the anti-GFP nanobody, was varied from 1 to 10 µg/ml, yielding the highest intensity readout with 5 µg/ml capture molecule concentration (Figure 4 A). This concentration was employed for all subsequent experiments. In the next step, a series of incubation times for the target molecule were examined, including 1 h, 2 h, 4 h, overnight and 27 h. It was observed that the signal intensity exhibited a consistent increase over time (Figure 4B). The overnight incubation was selected for further

experiments due to the marginal enhancement in signal intensity observed between the overnight and 27 h incubation.

The subsequent stage of the experiment involved the investigation of the impact of various application buffers on the outcome of the setup. Various sample buffers were tested, including PBS with 0.5% BSA, TBS with 0.5% BSA, and low cross buffer (CANDOR Bioscience, Wangen, Germany). The use of PBS-0.5% BSA resulted in a significant reduction of signal intensity (Figure 5 A). Conversely, the highest signal intensity was observed with TBS-0.5% BSA, which was selected for subsequent experiments. The variation of the detection buffer resulted in different signal levels of the detected target concentrations (Figure 5 B). The supplementation of TBS with either 0.05% detergent Tween-20 (TBS-T) or 0.1% BSA resulted in enhance signal intensity in comparison with TBS alone. The effect was most pronounced for TBS-T where, where a nearly tenfold signal increase was observed.

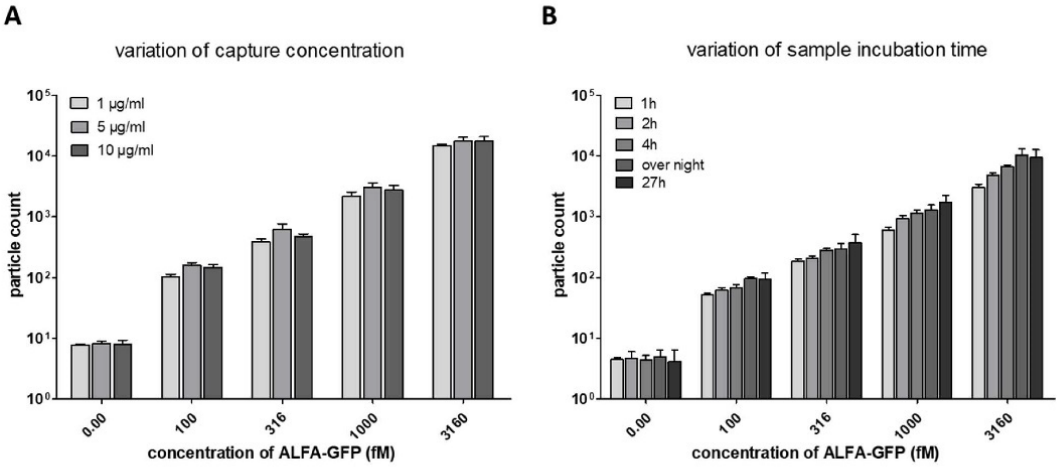

Figure 4 ThreeD assay development for ALFA-GFP by variation of capture concentration and target incubation time.

The capture nanobody was incubated on the plate overnight. After washing, the target ALFA-GFP was added in different concentrations and incubated for various time periods. After another washing step the plate was imaged by TIRF microscopy. A: Capture nanobody anti-GFP was incubated on the well surface at different concentrations: 1 µg/ml, 5 µg/ml, and 10 µg/ml in carbonate buffer. The target ALFA-GFP was incubated for 2 h at RT. B: Capture nanobody anti-GFP was applied at 5 µg/ml. The incubation time of the target ALFA-GFP was varied from 1 h to 27 h. All other parameters are unchanged. Standard deviations were calculated from four replicates.

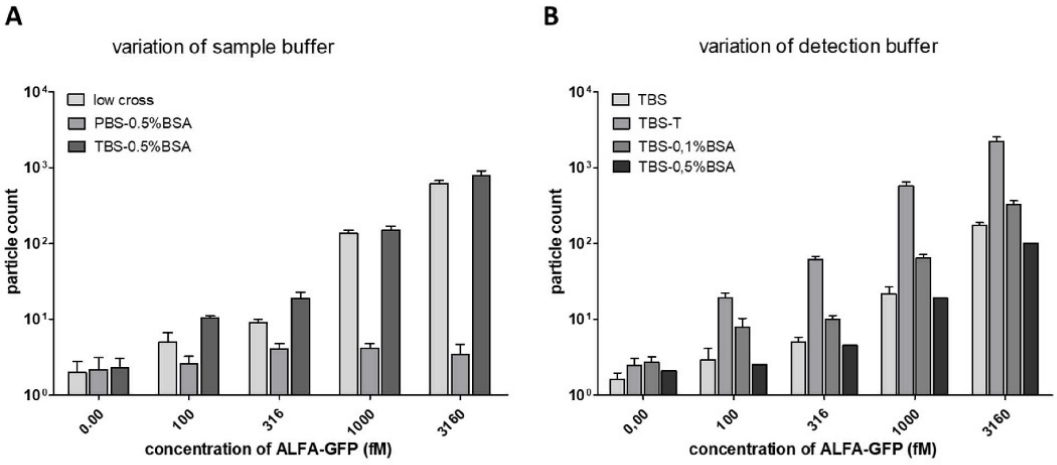

Figure 5 ThreeD assay development by variation of sample buffer and detection buffer.

The capture nanobody was incubated on the plate overnight. After washing, the target ALFA-GFP was added at different concentrations and incubated overnight. After another washing step antiALFA-647 nanobody was applied for detection. After washing, the plate was imaged by using TIRF microscopy. A: The target ALFA-GFP were diluted in various buffers: low cross, PBS-0,5% BSA and TBS-0,5% BSA. B: In this experiment the detection nanobody antiALFA-647 was tested in different buffers: TBS, TBS-T,

266 TBS-0.1% BSA and TBS-0.5% BSA. All other parameters remained the same. Standard deviations were
267 calculated from four replicates.
268

269 ThreeD assay for ALFA-GFP revealed femtomolar sensitivity

270 In the final protocol, anti-GFP nanobody in carbonate buffer was applied for capturing. Following this,
271 the plate was washed with TBS and TBS-T, and blocked with TBS containing 1% BSA and ProClin.
272 Thereafter, the target ALFA-GFP diluted in TBS with 0.5% BSA was added. For detection of the target,
273 anti-ALFA-AF647 nanobody in TBS-T was applied.
274 Figure 6 A displays the particle count for the protein directly bound to the surface via the capture
275 nanobody, as indicated by the green fluorescence channel, alongside the particle count for the protein
276 detected by the anti-ALFA nanobody, represented in the red fluorescence channel. The correlation of
277 the two channels demonstrated a significant Pearson correlation with $r=0.998$ and $p<0.0001$ (Figure 6
278 B).
279 A notable strength of the setup is its capacity for multiplexing, enabled by the utilisation of different
280 fluorescence channels. In this instance, the use of the red and green fluorescence channels permitted
281 generation of colocalization readout by combining these two channels (Figure 6 C). A key benefit of this
282 colocalization is the reduction of the background signal.
283 For data calibration, the femtomolar concentration ranges up to 1000 fM were taken into
284 consideration, since the objective was to determine the sensitivity within this range. The result
285 obtained demonstrated an LOD of 2.4 fM and an LLOQ of 5.8 fM for the directly bound proteins (Figure
286 6 D) and an LOD of 5.1 fM and LLOQ of 18.0 fM for the proteins detected with the detection nanobody
287 (Figure 6 E). The fit for the colocalized particles showed a reduced LOD value of 0.8 fM and a LLOQ of
288 1.8 fM.

The mean inter-assay variance (indicated as CV% in Supplemental Table 2) for particles directly binding on the plate surface as well as particles detected by antibody Anti-ALPHA-AF647 is below 10.

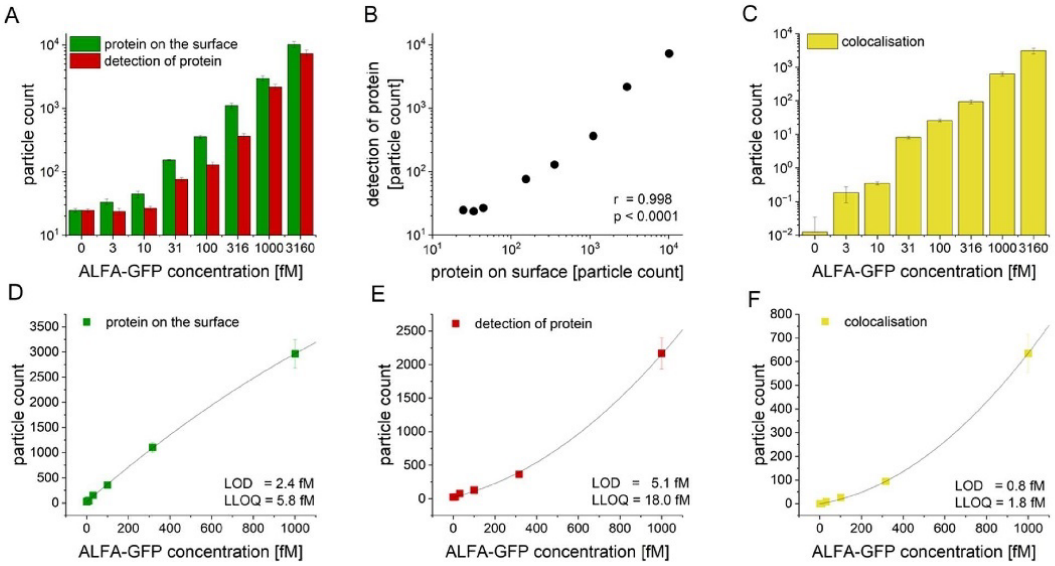

Figure 6 Optimized assay conditions for target ALFA-GFP revealed femtomolar sensitivity. A: Log particle counts of proteins binding to the capture nanobodies on the surface (green) and the particle count of the proteins recognized by the anti-ALFA-AF647 detection nanobody (red). B: Pearson correlation of the proteins on the surface and the detected proteins. C: Particle count of the colocalized particles. D-F: Plot of the data with fit from 0 to 316 fM. D: Fit curve for the proteins on the surface E: Fit curve for the detected proteins. F: Fit curve for the colocalized particles. Standard deviations were calculated from four replicates.

300 **Discussion**

301 The ThreeD method is a single molecule detection technique that allows digital counting of target
302 molecules down to femtomolar concentrations. ThreeD exploits the single molecule sensitivity of TIRF
303 microscopy for detection of individual, immobilized, fluorescently labelled molecules. The basic design
304 of the ThreeD experiment resembles a classical ELISA. For the assembly of a sandwich ELISA, two high-
305 affinity antibodies with non-overlapping epitopes on the target molecules are required. One antibody
306 molecule serves as capture and immobilizes the target on the surface of a microtiter plate. The other
307 one carries a fluorescent label for detection. Careful selection of the antibodies is crucial for high
308 specificity of target detection. Non-specific binding of detection antibody to the microtiter well surface
309 or to the capture must be avoided to the highest possible degree to ensure high sensitivity of the assay.
310 This is typically accomplished through meticulous optimisation of the assay conditions (e.g., buffers,
311 antibodies, blocking reagents) for each novel target.
312 Image analysis is a crucial part of single molecule counting methods based on TIRF microscopy. The in-
313 house developed software sFIDAta does not only apply digital image filtering and counting of the
314 particles but also contains tools for artefact detection and statistics analysis.
315 In principle, the ThreeD method can be used for the detection of each individual labelled single
316 molecule on the plate surface in a simple assay setup. In case of the simplified assay variant with the
317 biotin-streptavidin pair it was possible to quantify the target streptavidin down to the single digit
318 femtomolar range (LOD ~ 2 fM) with a range up to 1 pM (Figure 2 D). A similar sensitivity was achieved
319 in the ThreeD detection of the model protein ALFA-GFP with a LOD of ~6 fM for the range up to 1 pM
320 (Figure 6 E). Employing colocalization permitted the reduction of the LOD to 0.8 fM (Figure 6 F). ThreeD
321 is over three orders of magnitude more sensitive than the traditional sandwich ELISA which features
322 picomolar sensitivity. Starting with the SIMOA technology introduced in 2010 (4) a diverse range of

digital ELISA setups has emerged (for a recent review see (14)). These setups are based on micro-compartmentalization, enzyme reactions, single molecule detection and are quite complex. The sensitivity of these digital ELISA setups ranges from femto- to even attomolar levels. In ThreeD we opted for a simple assay design without microcompartments and enzyme-based signal amplification. Although ThreeD does not reach the attomolar sensitivity that was claimed by some variants of digital ELISA formats (15, 16), it compares very favourably with standard ELISA and allows quantification of clinically relevant diagnostic biomarkers.

The detection of single molecule of surface immobilized immune complexes by TIRF microscopy has been previously reported by others (17, 18). However, their experimental setup was more complicated than that of the present study. Macdonald et al. used a sample reloading approach to concentrate the immune complexes prior to detection thereby enhancing the sensitivity (18). Hariri et al. labelled detection and capture antibodies, respectively, with orthogonal fluorescent probes and based the detection of the immune complex on the colocalization of both probes (17). Their Single Molecule Colocalization Assay (SIMCA) greatly mitigated the effect of non-specific binding on data analysis and reduced LOD values by a factor of 3 (17). Comparable to their approach we also could reduce the LOD values by a factor of ~3 (for the proteins on the surface) or ~8 (for the detected proteins) by using colocalization. The imaging of the samples with two different fluorescent dyes in ThreeD enables not only a colocalization approach but could also be used for multiplexing, i.e., the detection of different target molecules in one sample.

In conclusion, ThreeD is a single molecule counting technology that enables the direct quantification of proteins at low femtomolar concentrations. Single particle counting as a diagnostic tool is more sensitive than measuring the integrated signal of the particles. Therefore, this method can be used to quantify low abundance biomarkers in biological fluids.

346 **Acknowledgment**

347 We received funding from the Helmholtz Association (HIL-A13).

348

349 **Author contributions**

350 A.C. and MS. performed the experiments and T.B. analysed the data. T.B., M.S., and K.H. designed the

351 experiments. F.R performed the statistics. T.B. wrote the manuscript together with B.K.. T.B and D.W.

352 supervised the project. V. K.-S., M.P., L.B., O.B., and A.Cu carefully revised the manuscript.

References

1. Belanger L, Sylvestre C, Dufour D. 1973. Enzyme-linked immunoassay for alpha-fetoprotein by competitive and sandwich procedures. *Clin Chim Acta* 48: 15-8
2. Farajollahi MM, Cook DB, Hamzehlou S, Self CH. 2012. Reduction of non-specific binding in immunoassays requiring long incubations. *Scand J Clin Lab Invest* 72: 531-9
3. Wu Y, Fu Y, Guo J, Guo J. 2023. Single-molecule immunoassay technology: Recent advances. *Talanta* 265: 124903
4. Rissin DM, Kan CW, Campbell TG, Howes SC, Fournier DR, Song L, Piech T, Patel PP, Chang L, Rivnak AJ, Ferrell EP, Randall JD, Provuncher GK, Walt DR, Duffy DC. 2010. Single-molecule enzyme-linked immunosorbent assay detects serum proteins at subfemtomolar concentrations. *Nat Biotechnol* 28: 595-9
5. Wu C, Dougan TJ, Walt DR. 2022. High-Throughput, High-Multiplex Digital Protein Detection with Attomolar Sensitivity. *ACS Nano* 16: 1025-35
6. Kulawik A, Heise H, Zafiu C, Willbold D, Bannach O. 2018. Advancements of the sFIDA method for oligomer-based diagnostics of neurodegenerative diseases. *FEBS Lett* 592: 516-34
7. Herrmann Y, Kulawik A, Kuhbach K, Hulsemann M, Peters L, Bujnicki T, Kravchenko K, Linnartz C, Willbold J, Zafiu C, Bannach O, Willbold D. 2017. sFIDA automation yields sub-femtomolar limit of detection for Abeta aggregates in body fluids. *Clin Biochem* 50: 244-7
8. Kravchenko K, Kulawik A, Hulsemann M, Kuhbach K, Zafiu C, Herrmann Y, Linnartz C, Peters L, Bujnicki T, Willbold J, Bannach O, Willbold D. 2017. Analysis of anticoagulants for blood-based quantitation of amyloid beta oligomers in the sFIDA assay. *Biol Chem* 398: 465-75

9. Chang L, Rissin DM, Fournier DR, Piech T, Patel PP, Wilson DH, Duffy DC. 2012. Single molecule enzyme-linked immunosorbent assays: theoretical considerations. *J Immunol Methods* 378: 102-15

10. Shim JU, Ranasinghe RT, Smith CA, Ibrahim SM, Hollfelder F, Huck WT, Klenerman D, Abell C. 2013. Ultrarapid generation of femtoliter microfluidic droplets for single-molecule-counting immunoassays. *ACS Nano* 7: 5955-64

11. Sakakihara S, Araki S, Iino R, Noji H. 2010. A single-molecule enzymatic assay in a directly accessible femtoliter droplet array. *Lab Chip* 10: 3355-62

12. Pils M, Dybala A, Rehn F, Blomeke L, Bujnicki T, Kraemer-Schulien V, Hoyer W, Riesner D, Willbold D, Bannach O. 2023. Development and Implementation of an Internal Quality Control Sample to Standardize Oligomer-Based Diagnostics of Alzheimer's Disease. *Diagnostics (Basel)* 13

13. Kuhbach K, Hulsemann M, Herrmann Y, Kravchenko K, Kulawik A, Linnartz C, Peters L, Wang K, Willbold J, Willbold D, Bannach O. 2016. Application of an Amyloid Beta Oligomer Standard in the sFIDA Assay. *Front Neurosci* 10: 8

14. Noji H, Minagawa Y, Ueno H. 2022. Enzyme-based digital bioassay technology - key strategies and future perspectives. *Lab Chip* 22: 3092-109

15. Kim D, Garner OB, Ozcan A, Di Carlo D. 2016. Homogeneous Entropy-Driven Amplified Detection of Biomolecular Interactions. *ACS Nano* 10: 7467-75

16. Wu C, Garden PM, Walt DR. 2020. Ultrasensitive Detection of Attomolar Protein Concentrations by Dropcast Single Molecule Assays. *J Am Chem Soc* 142: 12314-23

17. Hariri AA, Newman SS, Tan S, Mamerow D, Adams AM, Maganzini N, Zhong BL, Eisenstein M, Dunn AR, Soh HT. 2022. Improved immunoassay sensitivity and specificity using single-molecule colocalization. *Nat Commun* 13: 5359

18. Macdonald PJ, Ruan Q, Tetin SY. 2019. Direct single-molecule counting for immunoassay applications. *Anal Biochem* 566: 139-45

2.2.8 Artifact detection in fluorescence microscopy using convolutional autoencoder

Autoren:	**Fabian Rehn**, Marlene Pils, Tuyen Bujnicki, Oliver Bannach, Dieter Willbold
Journal:	*Scientific Reports* *(Eingereicht im Dezember 2024)*
Beitrag:	Erstellung der Datensätze Konzeption, Entwicklung sowie Evaluierung der Daten-Vorverarbeitung und des CAE-Models Statistische Analyse Anfertigung der Abbildungen Hauptverfasser des Manuskriptes
Druckgenehmigung:	Siehe Anhang 11.

Artifact detection in fluorescence microscopy using convolutional autoencoder

Fabian Rehn[1,2,3], Marlene Pils[3], Tuyen Bujnicki[2], Oliver Bannach[2,1,3], Dieter Willbold[2,1,3,*]

[1]Institut für Physikalische Biologie, Heinrich-Heine-Universität Düsseldorf, Universitätsstr. 1, 40225 Düsseldorf, Germany.

[2]Institute of Biological Information Processing (Structural Biochemistry: IBI-7), Forschungszentrum Jülich GmbH, Wilhelm-Johnen-Straße, 52428 Jülich, Germany.

[3]attyloid GmbH, Merowingerplatz 1A, 40225 Düsseldorf, Germany.

*Corresponding Author:

Prof. Dr. Dieter Willbold, Forschungszentrum Jülich GmbH, Institute of Biological Information Processing (IBI-7), Forschungszentrum Jülich, Wilhelm-Johnen-Straße, 52428 Jülich, Germany

Tel.: +49 2461 61 2100; E-Mail: d.willbold@fz-juelich.de

Abstract

Background: To ensure analytical accuracy in fluorescence microscopy image analysis, robust artifact detection is essential. For large datasets or time-sensitive analyses, automation is advisable, as it not only reduces time and costs but also eliminates human bias and enhances reproducibility. Although artificial intelligence is commonly employed for artifact detection, it is typically limited to recognizing artifact types that have been previously learned, often necessitating large training datasets. This study proposes an approach for an automated detection of previously unseen artifacts without the need for a training set of artifact-laden images.

Methods: Multiple datasets were assembled using images generated by our surface-based intensity distribution analysis (sFIDA) technology during different experiments. A convolutional autoencoder was trained on a dataset of artifact-free images to reproduce preprocessed images accurately. Artifact-laden images are subsequently detected by computing the difference between the input and output of a model, with increased discrepancies indicating the presence of artifacts.

Results: The proposed model is capable of classifying artifacts across different datasets with an average accuracy of 95.5%. Additionally, the model was able to detect unseen artifacts of various types, including differences in cause, structure, size and intensity.

Conclusion: The findings demonstrate that convolutional autoencoders provide a lightweight, but effective method for detecting artifact-laden images. The generalizability of this approach, along with the elimination of the need for an artifact-specific training set, makes it potentially interesting for a broad range of microscopy applications.

1. Background

In all types of microscopic imaging, the detection of artifacts is essential for ensuring analytical accuracy. This is particularly critical in quantitative fluorescence microscopy, where artifacts can markedly distort assay readouts. There are various types of artifacts, which can be categorized into three main groups: microscope-related artifacts, material-related artifacts, and sample-related artifacts. The first type is highly dependent on the type of microscopy used. For example, striping artifacts are common in light-sheet fluorescence microscopy [1] and air bubbles in the immersion oil can cause artifacts in TIRF microscopy [2]. General examples of artifacts in this category include out-of-focus images and motion-induced distortions. Material-related artifacts arise from hardware issues, such as scratches on the plate or are related to glue, which can induce autofluorescence or lead to motion artifacts if the glue fails. Sample-related artifacts can be caused by contamination with dust leading to nonspecific binding, bacterial contamination, intrinsic fluorescence of the sample, or oversaturation. Some microscope-related artifacts, such as optical aberrations, might be detected directly by the microscope software. However, this is not the case for material or sample-related artifacts. Manual inspection of images to identify and discard those containing artifacts is often an inefficient solution, especially for assays that generate large volumes of data or where quick data evaluation is desirable. Besides the excessive time required, a manual approach is susceptible to human error, and even worse, human bias. Since artifacts are not always easy to identify, leaving room for interpretation, manual evaluation also reduces the reproducibility of the analysis. Ultimately, these factors impede the efficient up-scaling of assay throughput.

One example of a high throughput assay based on fluorescence microcopy is the surface-based fluorescence intensity distribution analysis (sFIDA) technology. sFIDA was developed to quantify various types of protein oligomers which serve as biomarkers for different protein misfolding diseases [3-6]. This method typically generates at least 100 images per sample, resulting in large amount of data, making manual artifact detection the bottleneck of the analysis. As an assay quantifying fluorescence microscopy signals, artifacts can markedly distort assay readouts. Consequently, for reasons of quality, time, and cost, an automated solution for the detection of images containing artifacts is preferable.

Automatic approaches for artifact detection typically rely on kernel-based methods[7], or leverage machine learning algorithms. In the latter, convolutional neural networks, which focus on the detection of predefined and learned artifact structures [8, 9], are commonly used, sometimes in conjunction with segmentation [10]. While specializing in predefined artifacts is an effective approach, given that machine learning techniques can be used to learn and recognize structures in images with high accuracy, it does not address all potential issues. By limiting detection to specific artifact structures, previously unknown artifact types, such as those arising from contamination or compromised material, may remain undetected. This is particularly problematic in the context of scaled, automated workflows, as it could lead to persistent distorted results until the issue is noticed. Moreover, to achieve the highest possible accuracy, a broad dataset of images containing various artifacts is important for training the models [11].

Training a model without a large dataset of artifact-laden images is possible by designing the model to recognize authentic signals rather than artifacts. Every structure that cannot be confirmed to be an authentic signal, consequently, can be assumed to be an artifact and can be ignored during subsequent analysis. The circumstance that real signals are often easier to

identify, based on their known characteristics, and that a large volume of training images is easy to collect further supports this approach. One possible implementation, is the combination of segmentation techniques and deep learning classification algorithms [12]. Single structures are first identified and then classified individually. Depending on the number of elements to be identified and classified, the method is time-consuming, and models involved are usually complex. Furthermore, pixel-level labels are usually required, which substantially increases the effort required to create a dataset. Although there are segmentation approaches that allow image-level labelling [10], they usually results in a decline in performance. Another approach is the utilization of a convolutional autoencoder (CAE). CAEs are closely related to convolutional neural networks, with the key distinction that they are typically symmetrically designed to first reduce the dimensionality of the input and subsequently reproduce it. This reduction process focuses on learning essential patterns [13], making it particularly useful for denoising images [14].

CAEs are already employed for denoising medical and biological image data [15, 16] and for the removal of certain types of artifacts, such as stripes [17]. However, artifact removal is feasible only for artifacts covering small areas, where minimal reconstruction is required. In cases where artifact removal and subsequent reconstruction are unsuitable for image analysis, artifact-laden images should be identified and excluded. To this end, CAE principles can be adapted for artifact detection. This involves training a CAE solely on artifact-free input with the objective of precisely reproducing the input after dimensionality reduction. Consequently, the CAE should exhibit low error in reproducing artifact-free input while showing higher deviation for input containing artifacts. As a result, the discrepancy between the CAE's input and output images is expected to be greater for images with artifacts. Based on this reproduction error artifacts can be detected. An equivalent approach has already been applied for anomaly detection in MRI images [18]. The requirements for the CAE thus depend strongly on the specific application and may necessitate varying levels of complexity based on the intricacy of the structures involved.

The objective of this work is to demonstrate based on sFIDA-generated images that CAEs can be effectively used for the detection of artifact-laden images without requiring artifact-laden images for training.

2. Methods

2.1 sFIDA

Previously, we developed the sFIDA platform technology, which enables monomer-insensitive quantification of protein oligomers immobilized on the glass surface of a microtiter plate [19]. Individual oligomers are detected and quantified by using fluorescent antibody probes and imaging with a Leica AM total internal reflection fluorescence (TIRF) microscope, which produces 1000×1000 pixel, 14-bit grayscale images. In these images, each pixel has an intensity represented as a grayscale value. Pixels, or clusters of neighboring pixels, with intensities distinguishable from the background are referred to as signals. Figure 1 illustrates the basic principle of sFIDA, along with an example of an artifact-free sFIDA image. Furthermore, we have developed silicon nanoparticles (SiNaPs) that serve as artificial targets for the sFIDA assay

and can be used to calibrate the assay readout [20]. All images presented in this work were generated using sFIDA assays.

Protein oligomers, typically 2 to 10 nm in size, are smaller than the approximately 120 nm resolution of the TIRF microscope. As a result, oligomers occupy less space than a single pixel in a TIRF microscopy image, preventing sFIDA from capturing structural details of individual oligomers. Larger oligomers, though below the resolution limit, can emit enough fluorescence to affect neighboring pixels. With more available binding sites, these larger oligomers bind more labeled antibodies, thereby increasing fluorescence intensity and creating a broader emission radius in sFIDA images. When signals from nearby oligomers overlap, complex signal shapes may emerge.

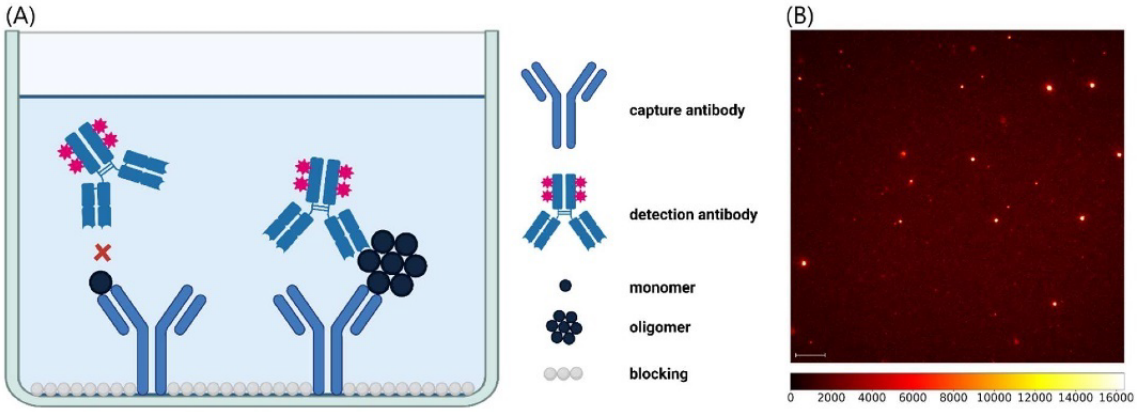

Figure 1: A) Schematic representation of sFIDA technology. The capture antibody is immobilized on the glass surface. Both oligomers and monomers can bind to the capture antibodies. However, only oligomers can be detected by fluorescence signalling, as the epitope of the monomers is masked by the capture antibody, preventing fluorescently labeled detection antibodies from binding. Created with BioRender.com. B) Example of sFIDA-generated image, showing signals from Aβ-coated SiNaPs. The image was colorized and contrast has been increased to enhance visibility. The scalebar is equal to 10 µm.

2.2 Data Preparation

To avoid using limited model capacity on learning random background noise patterns, background was removed from the images. The challenge in distinguishing signal from background lies in the variance of the background noise. A Gaussian blur with a kernel size of 5x5 pixels was applied, to align the intensity of individual pixels to their surroundings, thereby reducing variance while preserving strong signals or those that span multiple pixels. Since most of the area in a typical sFIDA-generated image is background, resulting in low intensities, signal can be effectively separated from the background using an intensity threshold. For this, a value equal to the mean intensity of an image plus five standard deviations has proven effective. Intensities below this threshold are set to zero, while those above remain unchanged.

The processing time in a convolutional network is influenced by several factors, one of which is the size of the input. The number of operations required in each layer is proportional to the size of the input. Consequently, reducing the image size from 1000x1000 pixels to 500x500 pixels leads to a considerable decrease in processing time. To realize this, a 2x2 block reduction

technique was applied, where each block was aggregated into a single pixel by calculating the blocks mean intensity. Due to the prior application of a threshold and the resulting substantial difference between signal and background intensities, signals are preserved despite the size reduction. Finally, the images are normalized to a signal strength between zero and one to facilitate the fitting process and subsequent predictions by the convolutional autoencoder.

The Gaussian blur is implemented using the Python library *OpenCV (version 4.6.0)*. Size reduction was performed using python lib *scikit-image (version 0.23.1)*.

2.3 Convolutional Autoencoder

In sFIDA-generated images, the signals lack complex structural characteristics but display large variability in signal strength (Figure 1). This makes a convolutional autoencoder (CAE) with a relatively small number of layers and a moderate number of filters a suitable choice. To minimize processing time and mitigate the risk of overfitting, hyperparameter optimization was initiated with a single layer and a minimal number of filters, which were progressively increased until no further performance improvements were observed.

Models were trained using dataset 1 (cf. below), comprising exclusively artifact-free sFIDA images of artificial Aβ-coated SiNaPs. These artificial samples offer higher reliability in artifact identification compared to human specimens, while maintaining identical signal characteristics, thereby ensuring the highest data quality during training. Hyperparameter optimization was carried out using a validation set based on artificial SiNaPs, with final hyperparameters selected based on a test set of SiNaP images both with and without artifacts. Due to the small size of the model and training dataset, training for only eight epochs was sufficient (Supplemental Figure 1). Table 1 presents the architecture of the CAE.

The CAE was implemented using Python's Keras package, version (2.3.1).

Table 1: The individual Keras layers of the CAE and their specifications are listed below.

Layer	Filter	Kernel Shape, strides	Activation function	Output Shape
Input Layer				(500,500,1)
Conv2D	126	(2,2)	RELU	(500,500,126)
MaxPooling2D		(2,2)		(250,250,126)
Conv2D	256	(5,5)	RELU	(250,250,256)
MaxPooling2D		(2,2)		(125,125,256)
Conv2DTranspose	256	(5,5),2	RELU	(250,250,256)
Conv2DTranspose	126	(2,2),2	RELU	(500,500,126)
Conv2D	1	(2,2)	RELU	(500,500,1)

2.4 Image reproduction error

To assess whether an image contains artifacts, the input and output images of the CAE are compared. Since the model has been trained exclusively on artifact-free images, it is not expected to accurately reproduce artifacts. The squared error is calculated for each pixel between the input image I and the output image O of the CAE. Given that artifacts typically occupy only a small portion of the image, most pixels should exhibit squared errors in an

inconspicuous range. As a result, smaller artifacts may not be detected if using a mean deviation across all pixels as metric. To enhance sensitivity to small artifacts, the image reproduction error (IRE) is defined as the 99.99th percentile of the squared pixel errors (Equation 1).

$$IRE = Percentile\left(\{(I_{x,y} - O_{x,y})^2 \,\middle|\, x = 1, \dots, 500\,, y = 1, \dots, 500\,\}, 0.9999\right) \quad (1)$$

To assess whether an image contains artifacts or not, a threshold must be established beyond which an image is considered as artifact-laden. A careful balance is required to minimize the false-negative classification of artifact-laden images as artifact-free while also ensuring that as few artifact-free images as possible are classified as false-positives and consequently discarded. In this work, we adjusted the 1.5 interquartile range method for outlier detection to achieve this balance. The threshold is defined as the 3-fold distance between the 0.25 and 0.5 quantiles of all IRE, added to the 0.5 quantile of the IRE for each dataset. By using the distance between the 0.25 and 0.5 quantiles, it is ensured that the threshold is not influenced by artifacts, even in datasets with a high artifact load. Since the distance used is half of the usual interquartile range, the multiplier is doubled as compensation. It is assumed that potential artifacts in images below this threshold are negligible and do not significantly affect the analysis results.

2.5 Datasets

Six different datasets were used for the training, validation, and testing of the developed model. All datasets originate from previously evaluated experiments which were not conducted specifically for this work. Each non-artificial dataset includes sFIDA images from blinded selected individuals, i.e. independently of further information, such as demographic information or clinical diagnoses. During the selection process, care was only taken to ensure that a sufficiently large number of artifact-laden image was included. Additionally, images that could not be definitively classified as either artifact-free or artifact-laden using the four-eyes principle were excluded, resulting in varying numbers of images across the datasets. The specifications of the datasets are listed below.

- ***Dataset 1***: sFIDA images of artificial Aβ-SiNaPs in two-fold dilution in buffer ranging from 128 to 2 fM [5]. A total of 407 images were used, comprising 224 artifact-free images for training, 48 for validation, and 48 for testing. Additionally, 87 artifact-laden images were used for testing. This dataset is employed for training and validating the CAE.
- ***Dataset 2***: sFIDA images of human Aβ oligomers in plasma of 5 individuals [5]. This dataset was generated in the same experiment as the artificial SiNaPs presented in **Dataset 1**. The set comprises 318 artifact-free images and 97 artifact-laden images. It will be used to investigate whether a model trained on artificial signals can be transferred to human data, enabling unbiased artifact detection in human samples.
- ***Dataset 3+4***: Identical assay as ***Dataset2***, but images are generated from different experiments with other samples. The sets contain 276 and 308 artifact-free images, respectively, and 97 and 61 artifact-laden images, respectively. These sets will be used to examine whether a model trained on a different experiment of the same assay can be applied to other experiments, allowing the use of a single model for scaled applications.

- ***Dataset 5***: sFIDA images of human IAPP oligomers in plasma of 10 individuals [6]. The number of individuals was doubled to compensate for the lower number of artifacts in the dataset. This set includes 943 artifact-free images and 56 artifact-laden images. It will be used to determine whether the model can be applied to assays using the same matrix but targeting different antigens, allowing a single model to be used across a broad range of assays.
- ***Dataset 6***: sFIDA images of human Aβ in CSF of 10 individuals [3]. The number of individuals was doubled to compensate for the low number of artifacts in the dataset. This set includes 721 artifact-free images and 25 artifact-laden images. It will be used to investigate whether the model can be transferred to other matrices and target different antigens, enabling a universal application of a single model.

All methods were performed in accordance with the relevant guidelines and regulations (Declaration of Helsinki).

2.6 Statistics

Due to the large size of datasets, a normal distribution is assumed based on the central limit theorem. For this reason, two-sided t-tests were applied.

To further evaluate the predictive power of IRE between input and output images of the CAE, ROC curves and their corresponding area under the curve (AUC) were calculated. Randomized and stratified subsets were used to account for the imbalance between the higher number of artifact-free images and the fewer artifact-laden images, which could otherwise bias the evaluation. Due to the dependence of ROC curves on the randomly selected subsets, sampling was performed 10000 times, generating an individual ROC curve for each subset. The mean AUC value across all iterations was then computed.

Logistic regression was used to generate the ROC curves, and both the logistic regression and ROC curve calculations were performed using the Python package scikit-learn (version 1.0.2). The t-tests were performed using Python package scipy (version 1.7.3).

3. Results

The aim of this study was to investigate whether CAEs can be used to identify sFIDA images containing artifacts. To this end, sFIDA images were first preprocessed, and a CAE was subsequently trained to reproduce artifact-free images. The trained CAE was then applied to both artifact-free and artifact-laden images. Figure 2 presents example images from the different stages of the data pipeline. It shows that the CAE reproduces authentic signal with minimal error, while its performance declines for images containing artifacts, resulting in an increased IRE. This increase in IRE is more pronounced for artifacts that significantly differ from the authentic signal compared to those with only minor deviations.

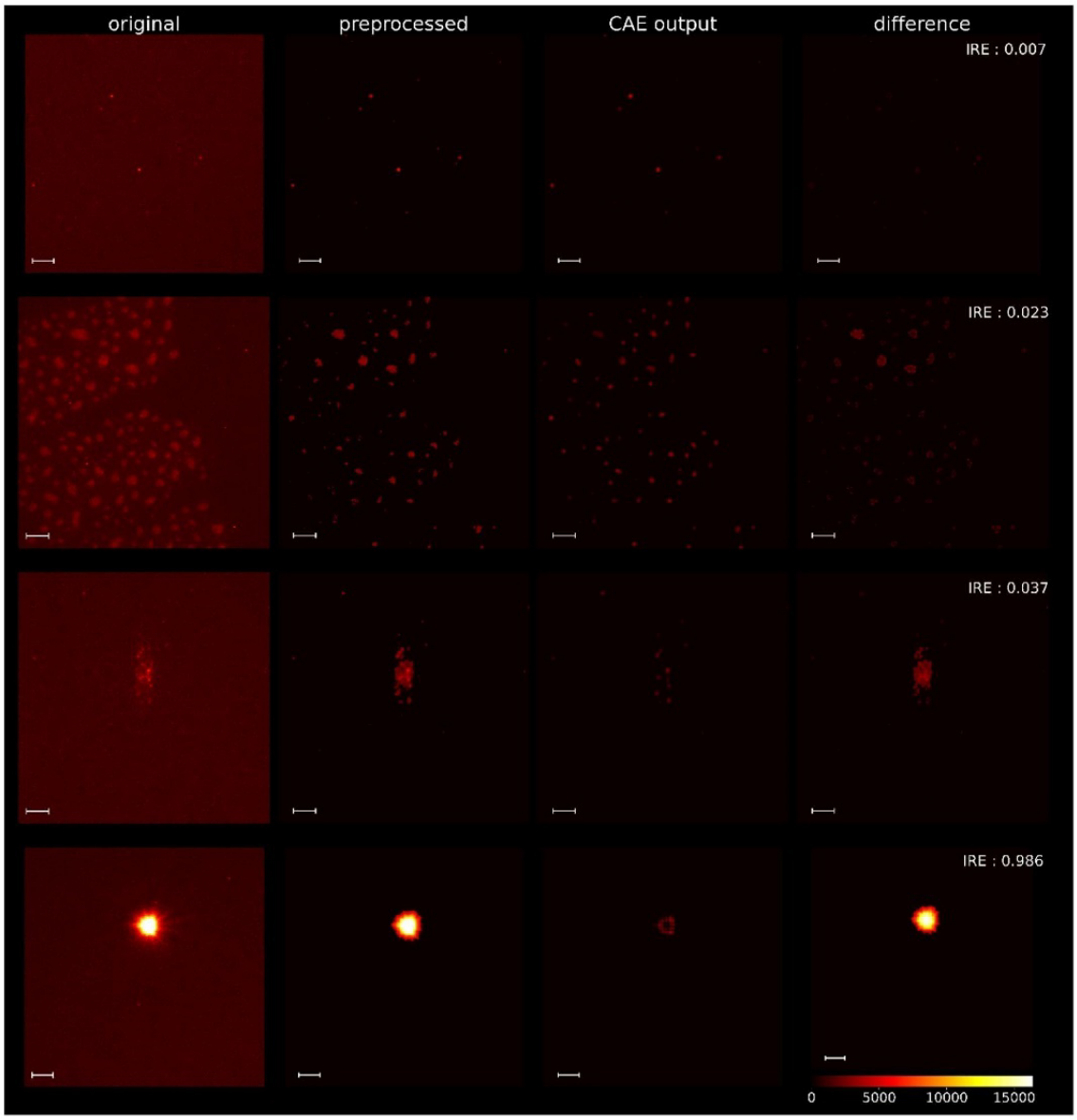

Figure 2: Examples illustrate the image processing by the preprocessing steps and the CAE. The first column shows unprocessed zoomed-in sections from some of the images in Figure 3. The second column displays these sections after applying the preprocessing steps. The third column shows the output of the CAE. The fourth column presents the absolute difference between the input and the output of the CAE. The first row shows the processing of an artifact-free image, while the remaining rows present artifact-laden images. The scalebar is equal to 5 µm.

Figure 3 shows a larger set of original images containing artifacts, along with the IRE values resulting from applying the CAE. The selected images represent all three types of artifacts: microscope-related artifacts, material-related artifacts, and sample-related artifacts. It is noticeable that larger or stronger signals lead to a higher IRE compared to more subtle artifacts.

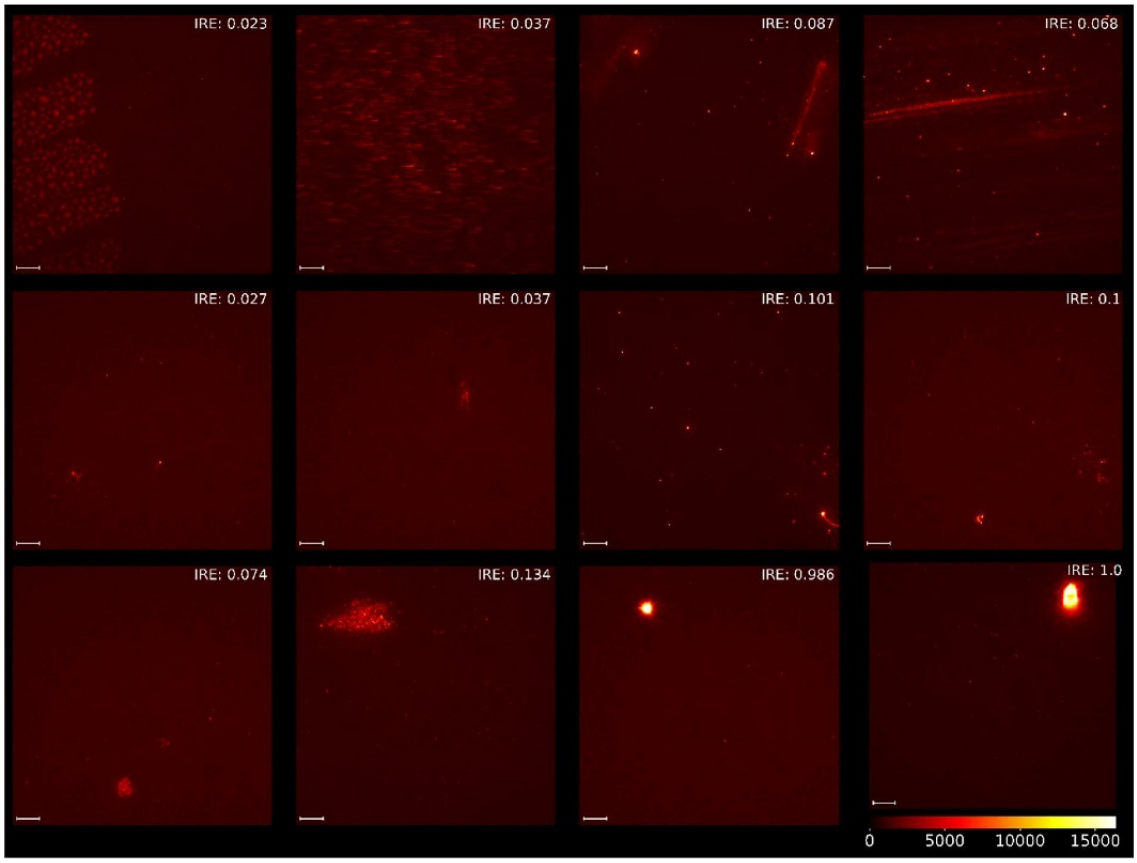

Figure 3: Examples of sFIDA generated images. The first row contains images with microscope or material-related artifacts, such as glue on the plate, motion artifacts and scratches on the plate. The second row contains small-sized sample-related artifacts. The third row contains larger sample-related artifacts. The scalebar is equal to 10 µm.

3.1 Image reproduction errors are significantly increased in artifact-laden images

To assess the suitability of IRE values derived from the CAE for detecting artifact-laden images, images from all dataset were manually classified as either artifact-free or artifact-laden and subsequently processed using the methods previously described. IRE values for artifact-laden images were consistently higher across all datasets compared to artifact-free images (Figure 4). Furthermore, the IRE values for artifact-free images from the datasets 2,3 and 4, which were based on different experiments using the same assay, were at comparable levels. In contrast, the

IRE values for artifact-free images from other datasets, which were based on different assays, were at varying levels.

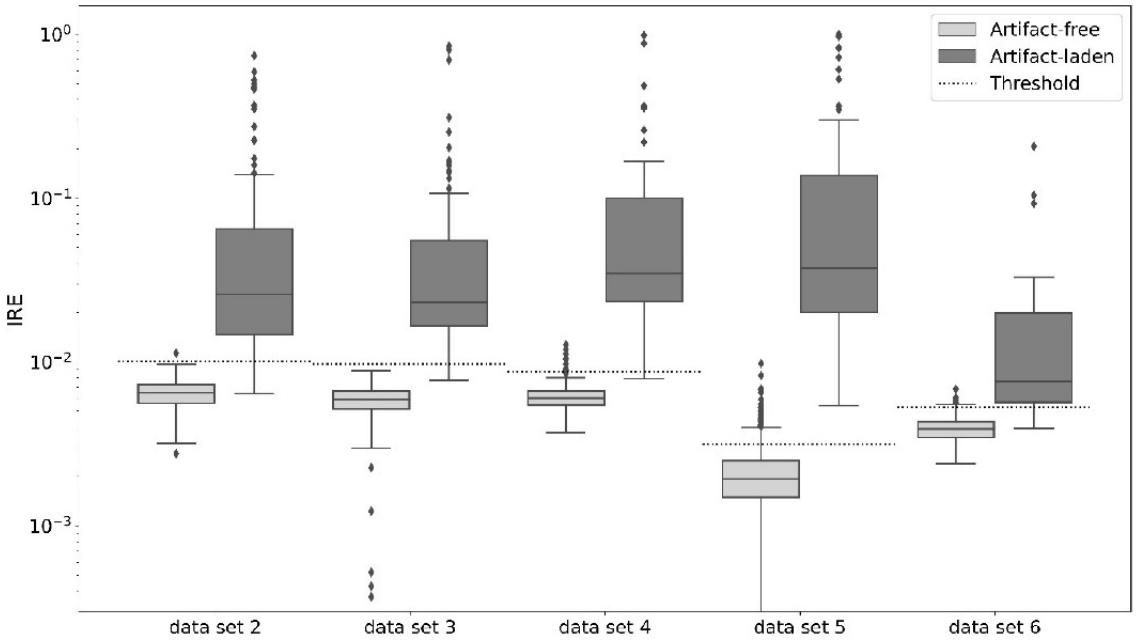

Figure 4: For each dataset, the IRE of the images with and without artifacts are shown. Note: Logistic scaling was used. The dotted line represents the dataset-specific threshold, which will be used to classify images as artifact-free or artifact-laden. The considered range was limited downwards due to irrelevance.

Table 2 presents the *P*-values of a two-sided t-test between IRE of artifact-free and artifact-laden images for each dataset. With a maximum *P*-value of 6.78e-13, the values are far below the significance level of 0.05. Consequently, the differences are highly significant across all datasets. To further evaluate prediction accuracy, ROC curves and their corresponding AUCs were generated repeatedly for randomized subsets of each dataset. The average AUC across the individual datasets ranged from 0.9644 to 0.9998.

Table 2: For each dataset, the differentiability between the IRE values of images with and without artifacts is shown using the P-value of a two-sided t-test, along with the AUC score of an ROC curve.

Dataset	P Value t-Test	AUC-Score
2	1.67e-20	0.9841
3	6.78e-13	0.9989
4	7.90e-19	0.9986
5	1.49e-68	0.9998
6	8.41e-34	0.9644

3.2 IRE-based classification

After demonstrating that the IRE has potential for accurate detection of artifact-laden images, the threshold described under 2.4 was applied to classify the samples as artifact-free or artifact-laden. For all test sets, an average accuracy of 95.5% was achieved, indicating that the chosen threshold is effective in distinguishing between artifact-laden and artifact-free images (Table 3). Artifacts are detected with a sensitivity of 94.2% on average. The mean specificity value of 96.1% indicates that artifact-free images are not excessively excluded. Dataset 6, based on CSF instead of plasma samples, yields the lowest values, especially in terms of sensitivity. To enable further evaluation, supplemental table 1 presents a confusion matrix.

Table 3: For each dataset, the sensitivity, specificity and accuracy of classification into artifact-free or artifact-laden are shown.

Dataset	Sensitivity	Specificity	Accuracy
2	88.7%	99.7%	97.1%
3	95.9%	100.0%	98.9%
4	98.4%	96.8%	97.0%
5	100.0%	85.9%	86.7%
6	88.0%	98.2%	97.9%
Mean	94.2%	96.1%	95.5%

4. Discussion

In this study, we have demonstrated that CAEs are a powerful tool for identification of artifacts in imaging-based methods, such as the sFIDA technology. The image reconstruction error between input and output of CAEs can effectively discriminate between artifact-free and artifact-laden images, making it a robust feature for classification. We showed that a classification, based on dataset-specific thresholds, achieves high mean accuracy of 95.5% in categorizing these images. Furthermore, the probability of detecting artifacts increases with increasing structural deviation from authentic signals. This makes strong distortions of the readouts and consequential the statistics, due to single artifacts less likely. The method's effectiveness across various artifact types in diverse assays with different targets and matrices, without requiring model retraining, highlights its broad applicability.

A further major advantage of the method is the small size of the training set, requiring only easily captured, artifact-free images and no artifact-laden images. This versatility suggests that our approach is not only valuable for scaling existing assays but also facilitating the development of new ones. In contrast, other approaches necessitate artifact images for training and are constrained by the specific artifact types present in the training dataset or by the existence of specific expert models [8, 9, 21, 22]. Since artifact images are not required for the training dataset, the data augmentation step, commonly involving transformations such as image rotation to facilitate the detection of identical artifacts across various orientations, becomes unnecessary, thereby accelerating the training process.

Other approaches, which were considered as very accurate, including network-based methods and support vector machines, achieved accuracies ranging from 91.25% to over 99% [8, 9, 21,

22]. It is important to note that these values are not necessarily directly comparable. This is due to variations within the datasets, including factors such as the extent of noise, the complexity of non-artifact structures, the size and detection complexity of artifacts, as well as operational differences, such as pixel-level versus image-level analysis. However, the fact that the achieved accuracy of the presented method falls within the range considered as highly accurate in other studies on artifact detection in microscopy images reinforces our assessment of its suitability for the intended application. This assessment is further supported by the fact that the datasets used in this work contained comparatively small artifacts of different types, which complicates their detection. Lastly, it must be also considered that, in the context of artifact detection, a small proportion of false positives or false negatives is generally regarded as inevitable, particularly for artifacts that are not readily detectable due to their size [21].

A limitation of the threshold-based method for classification into artifact-free or artifact-laden categories is the possible influence of artifacts on the threshold itself. This issue arises if more than 50% of the images contain artifacts. For sFIDA, this is not a problem as the usual proportion of artifact-laden images is much lower. For other applications, a high occurrence rate of artifact images would result in an elevated mean IRE level. Since different experiments of the same assay have yielded comparable IRE values, the problem could be detected through the discrepancy of mean IRE levels. Furthermore, given the comparable IRE levels of artifact-free images for different experiments of an assay, it would be feasible to establish an assay-optimized and specific threshold to effectively mitigate this unlikely, yet potential, issue. Another limitation of the proposed method is its inability to detect artifacts with very low signal strength, as these may be removed during the background removal step in preprocessing. As a result, such artifacts cannot be detected by the CAE. In the case of sFIDA, this is not particularly relevant, as background noise is also removed during the quantitative analysis of signals. However, if such removal does not occur for analysis, it can be assumed that artifact-laden images, whose IRE does not significantly differ from that of artifact-free images, would have only a negligible impact on the overall analysis, as the IRE increases with the strength and size of the artifact.

To further enhance the accuracy of the method in the future, exploring additional techniques for generating an optimal threshold will be beneficial. Additionally, investigating the potential of incorporating supplementary features and utilizing meta-learners for classification may also be of interest. Since no signal structures are visible for sFIDA images, the presented method is likely transferable to different kinds of assays, operating sub-resolution. Examples of this may include analyses of individual cells or molecules [23, 24].

5. Conclusion

We have demonstrated that CAEs represent a promising approach for fully automated and effective artifact detection. Our results show that the method, exemplified by sFIDA images, delivers high performance in distinguishing between artifact-laden and artifact-free images, irrespective of the antibody used or the matrix employed. However, in the future, this method should be tested on other types of microscopy images to verify its applicability across different microscopy modalities.

6. Declarations

6.1. Ethics approval and consent to participate

All local institutional review boards and ethical committees approved the study protocol. All participants gave informed consent before inclusion in the study.

6.2. Consent for publication

All authors agree to the publication.

6.3. Availability of data and materials

The authors confirm that the data supporting the findings of this study are available within the article and its supplementary materials. The original images as well as the preprocessed images are freely accessible online under the DOI: 10.5281/zenodo.13884860

6.4. Competing interests

DW and OB are co-founder and co-owner of attyloid GmbH, which is commercializing the sFIDA technology. This did not influence any data interpretation. All the remaining authors declare no conflict of interest.

6.5. Funding

To develop the sFIDA technology in general, we received funding from The Michael J. Fox Foundation for Parkinson's Research (14977, 009889), from the ALS Association and from the Packard Center (19-SI-476). We are also grateful for support funding from the Deutsche Forschungsgemeinschaft (INST 208/616-1 FUGG, INST 208/794-1 FUGG), the Helmholtz Association (HVF0079) and the Helmholz Innovation lab (DB001822).

6.6. Author contribution

FR created the datasets together with MaP. FR developed the data pipeline and the CAE Model. FR carried out the data analysis. FR wrote the manuscript together with OB and DW. FR, OB, DW, MaP, TB discussed the results. OB and DW supervised the project.

6.7. Acknowledgments

Not applicable

References

1. Ricci, P., et al., *Removing striping artifacts in light-sheet fluorescence microscopy: a review.* Progress in biophysics and molecular biology, 2022. **168**: p. 52-65.
2. Trache, A. and G.A. Meininger, *Total Internal Reflection Fluorescence (TIRF) microscopy: microscopy.* Current protocols in microbiology, 2008. **10**(1): p. 2A. 2.1-2A. 2.22.
3. Blömeke, L., et al., *Aβ oligomers peak in early stages of Alzheimer's disease preceding tau pathology.* Alzheimer's & Dementia: Diagnosis, Assessment & Disease Monitoring, 2024. **16**(2): p. e12589.

4. Blömeke, L., et al., *Quantitative detection of α-Synuclein and Tau oligomers and other aggregates by digital single particle counting.* npj Parkinson's Disease, 2022. **8**(1): p. 68.
5. Blömeke, L., et al., *Blood-based quantification of Aβ oligomers indicates impaired clearance from brain in ApoE ε4 positive subjects.* [Submitted] Communications Medicine, 2024.
6. Rehn, F., et al., *IAPP-oligomerisation levels in plasma of people with type 2 diabetes.* Scientific Reports, 2024. **14**(1): p. 19556.
7. Mayerich, D., B.H. McCormick, and J. Keyser. *Noise and artifact removal in knife-edge scanning microscopy*. in *2007 4th IEEE International Symposium on Biomedical Imaging: From Nano to Macro*. 2007. IEEE.
8. Hossain, M.S., et al., *Tissue artifact segmentation and severity assessment for automatic analysis using wsi.* IEEe Access, 2023. **11**: p. 21977-21991.
9. Sharma, V. and A. Yakimovich, *A deep learning dataset for sample preparation artefacts detection in multispectral high-content microscopy.* Scientific Data, 2024. **11**(1): p. 232.
10. Ali, M.A., et al., *ArtSeg: rapid artifact segmentation and removal in brightfield cell microscopy images.* bioRxiv, 2022: p. 2022.01. 24.477467.
11. Luo, C., et al. *How does the data set affect cnn-based image classification performance?* in *2018 5th international conference on systems and informatics (ICSAI)*. 2018. IEEE.
12. Laugero, K., et al., *Peripherally administered amylin inhibits stress-like behaviors and enhances cognitive performance.* Physiology & Behavior, 2022. **244**: p. 113668.
13. Hinton, G.E. and R.R. Salakhutdinov, *Reducing the dimensionality of data with neural networks.* science, 2006. **313**(5786): p. 504-507.
14. Masci, J., et al. *Stacked convolutional auto-encoders for hierarchical feature extraction*. in *Artificial Neural Networks and Machine Learning–ICANN 2011: 21st International Conference on Artificial Neural Networks, Espoo, Finland, June 14-17, 2011, Proceedings, Part I 21*. 2011. Springer.
15. Gondara, L. *Medical image denoising using convolutional denoising autoencoders*. in *2016 IEEE 16th international conference on data mining workshops (ICDMW)*. 2016. IEEE.
16. Alvarado, W., et al., *Denoising autoencoder trained on simulation-derived structures for noise reduction in chromatin scanning transmission electron microscopy.* ACS Central Science, 2023. **9**(6): p. 1200-1212.
17. Wei, Z., et al., *Elimination of stripe artifacts in light sheet fluorescence microscopy using an attention-based residual neural network.* Biomedical Optics Express, 2022. **13**(3): p. 1292-1311.
18. Chen, X. and E. Konukoglu, *Unsupervised detection of lesions in brain MRI using constrained adversarial auto-encoders.* arXiv preprint arXiv:1806.04972, 2018.
19. Kulawik, A., et al., *Advancements of the sFIDA method for oligomer-based diagnostics of neurodegenerative diseases.* FEBS letters, 2018. **592**(4): p. 516-534.
20. Hülsemann, M., et al., *Biofunctionalized silica nanoparticles: standards in amyloid-β oligomer-based diagnosis of Alzheimer's disease.* Journal of Alzheimer's Disease, 2016. **54**(1): p. 79-88.
21. Shakhawat, H.M., et al., *Automatic quality evaluation of whole slide images for the practical use of whole slide imaging scanner.* ITE Transactions On Media Technology And Applications, 2020. **8**(4): p. 252-268.
22. Babaie, M. and H.R. Tizhoosh. *Deep features for tissue-fold detection in histopathology images*. in *Digital Pathology: 15th European Congress, ECDP 2019, Warwick, UK, April 10–13, 2019, Proceedings 15*. 2019. Springer.
23. Xu, L., et al., *Virtual microfluidics for digital quantification and single-cell sequencing.* Nature methods, 2016. **13**(9): p. 759-762.
24. Sako, Y., S. Minoghchi, and T. Yanagida, *Single-molecule imaging of EGFR signalling on the surface of living cells.* Nature cell biology, 2000. **2**(3): p. 168-172.

3 Diskussion

Im Folgenden werden die einzelnen veröffentlichten sowie unveröffentlichten Ergebnisse dieser Arbeit in einen Kontext gesetzt und diskutiert. Für eine klarere Strukturierung werden die einzelnen Ergebnisse dabei anhand der Zielsetzung gegliedert.

3.1 Erkenntnisse zur Pathologie verschiedener Proteinfehlfaltungserkrankungen

Ein Ziel dieser Arbeit lag in der Gewinnung neuer Erkenntnisse zur Pathologie verschiedener Proteinfehlfaltungserkrankungen durch die Anwendung von Data-Science sowie statistischen Methoden auf sFIDA-generierte Daten verschiedener Studien. Der Fokus lag dabei insbesondere auf der AD sowie dem T2D.

Im Rahmen der DELCODE-Studie wurden sowohl CSF- als auch Plasma-Proben von AD-Patienten in unterschiedlichen Krankheitsstadien entnommen[130]. Die darin enthaltenen Aβ-Oligomere wurden anschließend mittels sFIDA quantifiziert. Durch die sequenzielle Anwendung zweier Regressionsmethoden wurde ein Modell entwickelt, das auf Basis der Aβ42- und pTau-Monomer-Konzentrationen sowie der Aβ-Oligomer-Level im CSF einen generalisierten, lückenlosen Verlauf der Aβ-Oligomer-Level in verschiedenen Krankheitsstadien bestimmte (siehe Kapitel 2.2.1)[106]. Die für APOE-ε4-positive und -negative Patienten generierten Verlaufsdaten wurden mit weiteren Biomarker-Daten kombiniert. Die Resultate unterstreichen die Auswirkung des APOE-ε4-Status auf die Aβ-Aggregation, da für APOE-ε4-positive Patienten deutlich erhöhte Aβ-Oligomer-Level bestimmt wurden, wobei der Peak leicht verzögert auftrat. Die unterschiedlichen Höchstwerte sowie die frühzeitige Abnahme der Aβ-Oligomer-Level, die je nach APOE-ε4-Status bereits im MCI-Stadium stark ausgeprägt war, könnte dabei eine mögliche Erklärung für die teils widersprüchlichen Ergebnisse verschiedener Studien zur Quantifizierung von Aβ-Oligomeren liefern. So konnten einige Studien in späten Krankheitsphasen erhöhte Aβ-Oligomer-Level bei Patienten im Vergleich zur Kontrollgruppe nachweisen, während andere keine signifikanten Unterschiede aufzeigen konnten[140,141]. Darüber hinaus verdeutlicht der Verlauf der Aβ-Oligomer-Level die Wichtigkeit einer frühzeitigen Diagnose und Behandlung, idealerweise noch vor dem Auftreten erster Symptome und somit vor dem Erreichen des Peaks. Dies gilt insbesondere für Therapien mit Wirkstoffen, die auf die Auflösung von Aβ-Oligomeren abzielen, da diese besonders neurotoxisch sind und daher so früh wie möglich eliminiert werden sollten.

Zur Ermöglichung einer frühzeitigen Diagnose sollten präventive Untersuchungen bevorzugt anhand von Proben durchgeführt werden, die mit minimalem Risiko oder gar risikolos gesammelt werden können. Durch die DELCODE-Studie (siehe Kapitel 2.2.2) sowie eine weitere Studie zur Quantifizierung der Aβ-Oligomer-Level im Stuhl von AD-Patienten (siehe Kapitel 2.2.3) konnte gezeigt werden, dass Plasma und Stuhl vielversprechende Matrizes für diesen Zweck darstellen[131,142]. Während die Aβ-Oligomer-Level im Stuhl von AD-Patienten im Vergleich zur Kontrollgruppe signifikant erhöht sind, sind sie im Plasma signifikant reduziert, was auf eine Beeinträchtigung der Clearance-Mechanismen hinweist.

Dass die Aggregation von Proteinen nicht nur für neurodegenerative Erkrankungen von Bedeutung ist, sondern auch eine Rolle in der Pathologie weiterer Proteinfehlfaltungserkrankungen, wie beispielsweise in der Stoffwechselerkrankung T2D spielt, konnte in Kapitel 2.2.4 belegt werden. Durch die Quantifizierung der IAPP-Oligomer-Konzentrationen und deren Normierung anhand der monomeren IAPP-Konzentration konnte nachgewiesen werden, dass der Oligomerisierungsgrad (Verhältnis zwischen IAPP-Oligomer und IAPP-Monomer) bei Personen mit T2D ohne Komplikationen signifikant erhöht war[143]. Zudem konnte eine signifikante Korrelation zwischen dem Oligomerisierungsgrad und der Krankheitsdauer während der ersten zehn Krankheitsjahre aufgezeigt werden. Diese Ergebnisse stützen die Hypothese, dass die Aggregation von IAPP-Oligomeren ein treibender Faktor in der Pathologie von T2D ist. Darüber hinaus liefert der festgestellte zunehmende Oligomerisierungsgrad in Kombination mit der angenommenen Möglichkeit des sogenannten Cross-Seedings zwischen IAPP- und Aβ-Aggregaten aufgrund ihrer ausgeprägten strukturellen Ähnlichkeit[144,145], eine mögliche Erklärung dafür, warum die AD und der Typ-2-Diabetes gegenseitige Risikofaktoren darstellen[64].

Die Auswertungen der durch sFIDA generierten Daten lieferten somit wertvolle Erkenntnisse über die Pathologie verschiedener Proteinfehlfaltungserkrankungen und erfüllen daher das erste Ziel dieser Arbeit. Zwischen den Patienten- und Kontrollgruppen zeigte sich jedoch häufig eine Überschneidung der Oligomer-Level, sodass weitere Optimierungen der sFIDA-Technologie erforderlich sind, um Oligomer-Level als alleiniges diagnostisches Kriterium nutzen zu können. Nichtsdestotrotz konnte im Rahmen einer Studie zur Quantifizierung von aSyn- und Tau-Oligomeren im CSF von Patienten mit Parkinson, AD, Lewy-Körper-Demenz oder progressiver supranukleärer Blickparese mittels ROC-Kurven, basierend auf multiplen logistischen Regressionsanalysen, nachgewiesen werden, dass die durch sFIDA bestimmten Oligomer-Level trotz dieser Einschränkungen einen diagnostischen Wert besitzen (siehe

Kapitel 2.2.5)[146]. In bestimmten Fällen erzielen sie eine ähnliche diagnostische Leistung wie monomere Biomarker oder erhöhen in Kombination mit diesen die diagnostische Genauigkeit. Die sFIDA-Technologie liefert darüber hinaus einen großen Mehrwert in der Entwicklung neuer Wirkstoffe zur Auflösung von Aggregaten, da die Wirksamkeit dieser Wirkstoffe unabhängig von der zuvor klinisch definierten Patientenkohorte effektiv evaluiert werden kann. Um dieses Potenzial vollständig auszuschöpfen, sind Messungen mit höchstmöglichen Qualitätsstandards, Genauigkeit und Präzision erforderlich, die zudem Zeit-, Kosten- und Qualitätsvorteile einer Automatisierung nutzen. Erstere wurden durch neu entwickelte Kontrollproben zur Qualitätssicherung gewährleistet (siehe Kapitel 2.2.6)[105], während weitere Optimierungen durch die im Rahmen dieser Arbeit entwickelten und im Folgenden diskutierten Methoden realisiert wurden.

3.2 Erhöhung der Genauigkeit und Präzision der sFIDA Technologie

Die Erhöhung der Genauigkeit und Präzision der sFIDA-Technologie stellt ein weiteres Ziel dieser Arbeit dar. Diese wurden insbesondere bei Verwendung des roten Fluoreszenzkanals sowie der Kolokalisation durch FPS beeinträchtigt. Zu diesem Zweck wurde eine Methode entwickelt, um FPS in sFIDA-generierten Bildern zu reduzieren. Hierbei wurde der markierungsbasierte sFIDA-Assay durch eine zusätzliche Messung im niedrigen Wellenlängenbereich (405 nm) ergänzt, in dem die eingesetzten Detektionsantikörper kein Signal emittieren. Diese zusätzliche Messung ermöglicht die Identifikation von Bereichen der Glasoberfläche, in denen autofluoreszierende Matrixkomponenten unspezifisch gebunden sind und somit auch die unspezifische Bindung von Detektionsantikörpern potenziell möglich ist. Durch Exklusion dieser Bereiche in den antikörperspezifischen Detektionskanälen während der quantitativen Analyse konnten sowohl die Präzision als auch die Genauigkeit des sFIDA-Assays erhöht werden. Diese Erhöhung hat darüber hinaus zur Folge, dass eine genauere Kalibration ermöglicht wird, was besonders im Falle groß angelegter Studien mit mehreren Experimenten von Bedeutung ist, da dies zur Verringerung der Inter-Assay-Varianz beiträgt. Von der Anwendung der Methode profitierten humane Proben mit hoher SD besonders, da eine signifikante Korrelation zwischen der ursprünglichen SD sowie der SD-Reduktion festgestellt werden konnte. Dies unterstreicht die Effektivität der Methode, insbesondere bei weniger präzisen Messdaten und hebt ihre Bedeutung für die Erhöhung der Messgenauigkeit in anspruchsvollen Matrizes hervor.

Zu den Vorteilen der Methode gegenüber anderen Ansätzen, wie Bleaching oder chemischer Behandlung zählt, dass die zusätzliche Messung nach den Messungen der markierten Detektionsantikörper durchgeführt werden kann. Dadurch wird das ursprüngliche Signal nicht beeinflusst und über die Anwendung der FPS-Reduzierungsmethode kann retrospektiv entschieden werden. Da chemische Behandlungen und zeitaufwändige Bleaching-Prozeduren entfallen, ist diese Methode zudem zeit- und kostensparend und die Integrität der Aggregate wird bewahrt. Einer der größten Vorteile liegt jedoch in ihrer universellen Anwendbarkeit. Da im Gegensatz zu anderen Methoden weder Zeitabstände zwischen Anregung und Detektion (Time-Gated Detection)[100,101], noch Detektionsbereiche angepasst werden müssen[98] und auch keine Probenmatrix- bzw. antigenspezifischen Anpassungen erforderlich sind, kann die Methode ohne Anpassungen in jeden sFIDA-Assay integriert werden.

Eine Limitation der Methode besteht darin, dass für den Detektionskanal spezifisches FPS nur indirekt identifiziert werden kann. Neben den Detektionsantikörpern müssen auch endogene Fluorochrome unspezifisch gebunden sein, die darüber hinaus im blauen Wellenlängenbereich emittieren müssen. Ist jedoch genügend Fläche für zahlreiche Bindungen vorhanden, ist dies als nicht unwahrscheinlich zu erachten. Zum einen ist die Bindung endogener Moleküle wahrscheinlicher als die der Detektionsantikörper, da diese zuerst und mit zeitlichem Abstand induziert werden, zum anderen tritt AF durch endogene Moleküle am häufigsten im niedrigen Wellenlängenbereich auf[94]. Eine weitere Limitation besteht darin, dass innerhalb der durch einen Pixel abgedeckten Fläche sowohl unspezifisch gebundene Moleküle als auch spezifisch an Detektionsantikörper gebundene Antigene existieren können. Dies birgt das Risiko einer Fehlklassifizierung und kann folglich zur unbeabsichtigten Entfernung von Nutzsignal führen. Wird jedoch beachtet, dass nur ein Teil der endogenen Moleküle autofluoreszierende Eigenschaften aufweist, welche darüber hinaus im blauen Wellenlängenbereich liegen müssen, ist die Wahrscheinlichkeit für derart kleinflächige Szenarien gering. Diese Einschätzung wird dadurch untermauert, dass Partikel, die im blauen Fluoreszenzkanal detektiert werden, in der Regel größer als ein einzelner Pixel sind.

Neben der Erhöhung der Präzision und Genauigkeit durch die Reduktion von FPS sollten diese auch durch die Implementierung von Aggregationsmethoden erhöht werden, welche robust gegenüber einzelnen Ausreißern in den Readout-Werten eines Wells sind. Zu diesem Zweck wurden während der Entwicklung der Auto-Cutoff-Methode verschiedene Aggregationsmethoden verglichen. Es zeigte sich, dass jede untersuchte Methode zur Ausreißer-Entfernung, unabhängig davon, ob sie auf statischen oder dynamischen

Grenzwerten, robusten Schätzern oder einer Kombination beider Ansätze basierte, gleichwertige Ergebnisse lieferte. Alle Methoden führten insbesondere zu einer erhöhten Genauigkeit, gemessen an der Differenzierbarkeit einzelner Verdünnungs- bzw. Spike-Schritte im Vergleich zur Nichtentfernung von Ausreißern.

Sowohl die Methode zur Reduzierung des FPS als auch die AE-HL-Aggregationsmethode konnten bereits in der Praxis erfolgreich angewendet werden[131,143]. Folglich konnte das zweite Ziel dieser Arbeit, die Erhöhung der Präzision und Genauigkeit der sFIDA-Technologie, ebenfalls erreicht werden. Neben der Erweiterung der etablierten sFIDA-Technologie, wurde auch an der Adaption der Technologie für ein weiteres Anwendungsfeld, die Detektion nicht aggregierter Proteine, mitgewirkt (siehe Kapitel 2.2.7).

Die Präzision und Genauigkeit des sFIDA-Assays werden ebenfalls maßgeblich durch den für die Analyse verwendeten Cutoff beeinflusst. Bei einem zu niedrigen Cutoff wird die Analyse durch Hintergrundrauschen beeinflusst, während ein zu hoher Cutoff den Ausschluss von Nutzsignalen zur Folge hat. Da sich jedoch der direkte Vergleich mit der bisherigen Methode als wenig zielführend erweist, da sich die aus den Perzentilen resultierenden Cutoffs über den gesamten möglichen Graustufenbereich erstrecken können, wird die Methode unter dem Ziel der Erhöhung des Automationsgrades aufgeführt.

3.3 Steigerung des Automationsgrades des Analyseprozesses

Zur automatischen Optimierung des kritischen Cutoffs wurde die Auto-Cutoff-Methode entwickelt, die für einen spezifischen Cutoff eine qualitative und objektive Bewertung in Form des QScores erstellt. Der QScore ergibt sich dabei aus einer Sammlung verschiedener Metriken und Kriterien, welche die Qualität der SiNaPs-Verdünnungsreihe bewerten bzw. sicherstellen. Analysen von humanen Proben, die verdünnt oder mit Aggregaten gespiked wurden, belegten, dass der QScore stark negativ und hochsignifikant mit der Differenzierbarkeit zwischen den einzelnen Verdünnungs- bzw. Spikestufen, gemessen am *P*-Wert eines Mann-Whitney-U-Tests, korreliert. Da zudem signifikante Korrelationen zwischen Genauigkeit und Präzision, gemessen an VDL und CV% zwischen der SiNaPs-Verdünnungsreihe und den humanen Proben belegt werden konnten, kann der Cutoff für humanen Proben folglich objektiv durch den QScore der SiNaPs-Verdünnungsreihe optimiert werden.

Im Rahmen der Methodenentwicklung wurde festgestellt, dass die Optimierungsziele Präzision und Genauigkeit unterschiedlich mit dem Cutoff korrelieren. Die Genauigkeit nimmt mit steigendem Cutoff zu, während die Präzision abnimmt. Daher ist ein Kompromiss erforderlich,

um eine ausgewogene Analysequalität zu gewährleisten. Die Auto-Cutoff-Methode erreichte einen solchen Kompromiss in verschiedenen Datensätzen und berücksichtigt zusätzlich weitere Bedingungen, wie das Vorhandensein eines Mindestmaßes an Signal. Dadurch wird sichergestellt, dass jeder ermittelte Cutoff funktional geeignet ist, was die bisherige Notwendigkeit wiederholter manueller Auswertung der Analyseergebnisse eliminiert. Ein weiterer Nutzen des QScores liegt darin, dass er als zusätzliches Qualitätskriterium verwendet werden kann, indem er die Vergleichbarkeit einzelner Experimente innerhalb desselben Assays ermöglicht und somit plötzlich auftretende Qualitätsprobleme offenbaren kann.

Eine Limitation ist jedoch, dass die derzeitige Datengrundlage zu gering ist, um exakte Aussagen darüber zu erlauben, ab welchem QScore eine Differenzierung von humanen Proben potenziell möglich wäre.

Obwohl die Auto-Cutoff-Methode die Berechnung des QScores aller möglichen Cutoffs bzw. Cutoff-Kombinationen (im Fall der Kolokalisation) erfordert, um den Cutoff mit dem größten Potenzial zu identifizieren, konnte gezeigt werden, dass dies nicht zwingend notwendig ist, um Cutoffs zu identifizieren, welche zu hochwertigen QScores führen. So konnte durch den Einsatz eines Firefly-Algorithmus der Berechnungsaufwand erheblich reduziert werden, ohne dass Abweichungen von mehr als einem Prozent des maximal möglichen QScores des Datensatzes auftraten. Zwar muss hierbei beachtet werden, dass die QScores in definierten Intensitätsabständen und nicht für jeden möglichen Cutoff berechnet wurden, da die Unterschiede zwischen den QScores benachbarter Cutoffs jedoch minimal ausfielen, ist nicht zu erwarten, dass diese Einschränkung die Gültigkeit der zuvor getroffenen Aussagen beeinträchtigt.

Neben der Auto-Cutoff-Methode wurde ebenfalls eine Methode zur automatischen Artefaktdetektion entwickelt (siehe Kapitel 2.2.8)[147]. Hierbei wurde ein *Convolutional Neural Network* als *Auto-Encoder* (englisch: *Convolutional autoencoder,* CAE) verwendet, um die Struktur und Intensitäts-Eigenschaften von Nutzsignal zu erlernen und dieses in Bildern reproduzieren zu können. Da der CAE ausschließlich auf artefaktfreien Bildern trainiert wurde, kann das CAE diese mit geringer Abweichung reproduzieren. Sind jedoch Artefakte im Bild enthalten, entsteht eine signifikant höhere Abweichung zwischen dem Original und dem durch das CAE reproduzierten Bild. Es konnte belegt werden, dass das CAE auf diese Weise in der Lage ist, Artefakte unterschiedlicher Quellen zu identifizieren. So konnten unter anderem Artefakte die durch ihre Fläche oder durch (Bewegungs-)Unschärfe charakterisiert sind, identifiziert werden, wofür zuvor mehrere Detektionstypen erforderlich waren. Darüber hinaus

konnten Artefakte detektiert werden, die zuvor unbemerkt geblieben wären. Im Gegensatz zu anderen Ansätzen aus dem Bereich des überwachten Lernens ist das CAE in der Lage bisher unbekannte Artefakte zu detektieren.

Obwohl beide Methoden eine längere Laufzeit in Anspruch nehmen, als es eine einzelne Durchführung der bereits zuvor etablierten Methoden tun würde, muss beachtet werden, dass diese iterativ wiederholt werden mussten, bis ein zufriedenstellendes Ergebnis erzielt wurde. Darüber hinaus ist durch die nicht gegebene Notwendigkeit einer Nutzerinteraktion der Analyst während der Bearbeitungsdauer frei für andere Tätigkeiten. Da sowohl die entwickelte Auto-Cutoff-Methode, welche bereits erfolgreich praktisch eingesetzt wurde[143], als auch der CAE ohne Nutzerinteraktion, oder vom Analysten zu definierende Parameter auskommen und gleichzeitig die Qualitätsanforderungen erfüllen, ist auch das dritte Ziel dieser Arbeit, die Erhöhung des Automatisierungsgrads, erfüllt worden.

Im Rahmen dieser Arbeit wurde darüber hinaus die sFIDAta-Software (siehe Kapitel 1.5) neu konzipiert und programmiert. Alle entwickelten Methoden wurden über diese Software bereitgestellt. Der Entwicklungsprozess wird in Anhang 2 erläutert.

4 Zusammenfassung/Fazit

Im Rahmen dieser Dissertation konnte gezeigt werden, dass durch die sFIDA-Technologie erzeugte Bilddaten durch FPS belastet werden. Durch Anwendung der entwickelten FPS-Reduktionsmethode konnten die Genauigkeit und Präzision der sFIDA-Technologie gesteigert und die Anwendbarkeit in komplexen Probenmatrizes erhöht werden. Darüber hinaus konnte gezeigt werden, dass die sFIDA-Technologie wichtige Beiträge zum Verständnis der Pathologie von Proteinfehlfaltungserkrankungen leisten kann. Besonders hervorzuheben sind dabei die neugewonnenen Erkenntnisse über die Entwicklung der Aβ-Oligomer-Level im Krankheitsverlauf der AD, die Beeinflussung der Clearance-Mechanismen durch die AD sowie die Unterstützung der Hypothese, dass IAPP-Oligomere einen Treiber des T2D darstellen. Darüber hinaus lieferte die sFIDA-Technologie wertvolle Einblicke in weitere neurodegenerative Erkrankungen und bietet großes Potenzial für die Entwicklung innovativer Therapeutika sowie diagnostischer Anwendungen. Zur Ausschöpfung des vollen Potenzials wurden mehrere Automatisierungsmethoden entwickelt. Dazu zählen die Auto-Cutoff-Methode, die eine objektive und reproduzierbare Optimierung des Cutoffs basierend auf repräsentativen SiNaPs-Verdünnungsreihen ermöglicht, sowie die Entwicklung

der CAE-basierten Artefaktdetektion, die eine zuverlässige Identifikation von Artefakten verschiedenster Typen gewährleistet. Durch diese methodischen Fortschritte wurde der Automatisierungsgrad der sFIDA-Technologie erheblich erhöht und alle notwendigen Voraussetzungen für eine vollständige Automatisierung der Datenanalyse geschaffen. Alle definierten Zielsetzungen (siehe Kapitel 1.6) wurden somit erreicht.

Die präsentierten Ergebnisse eröffnen vielfältige Perspektiven für zukünftige Forschungsarbeiten. Dies betrifft besonders die Weiterentwicklung des CAE-Modells durch die Integration zusätzlicher Bildmerkmale sowie die Einbindung eines Meta-Modells, um die Klassifikationsgenauigkeit weiter zu steigern. Zudem könnte die zugrundeliegende Logik der Erlernung von Signalcharakteristiken und der nachfolgende Abgleich adaptiert werden, um eine diagnostische Anwendbarkeit zu prüfen. Ein weiteres mögliches Ziel zukünftiger Forschung ist die Entwicklung und Evaluierung eines vollständig automatisierten sFIDA-Prozesses, der sowohl die experimentellen Laboraktivitäten als auch die Analyseprozesse umfasst. Ein solcher Prozess hätte das Potenzial, den Durchsatz und die Reproduzierbarkeit der Experimente weiter zu steigern. Zuletzt bietet die verstärkte Anwendung von ML zur Ergänzung lückenhafter Datenverläufe eine vielversprechende Methode, um kontinuierliche Biomarker-Verlaufskurven zu erstellen und dadurch die Pathologie weiterer Krankheiten genauer zu charakterisieren, was zu einem vertieften Verständnis der Krankheitsdynamiken beitragen könnte.

5 Referenzen

1. Crick, F. H. On protein synthesis. in *Symp Soc Exp Biol* vol. 12 8 (1958).
2. Hartl, F. U. Protein misfolding diseases. *Annu. Rev. Biochem.* **86**, 21–26 (2017).
3. Creighton, T. E. Protein folding. *Biochem. J.* **270**, 1 (1990).
4. Anfinsen, C. B. Principles that govern the folding of protein chains. *Science* **181**, 223–230 (1973).
5. Gregersen, N., Bross, P., Vang, S. & Christensen, J. H. Protein misfolding and human disease. *Annu Rev Genomics Hum Genet* **7**, 103–124 (2006).
6. Chiti, F. & Dobson, C. M. Protein misfolding, functional amyloid, and human disease. *Annu Rev Biochem* **75**, 333–366 (2006).
7. Soto, C. Protein misfolding and disease; protein refolding and therapy. *FEBS Lett.* **498**, 204–207 (2001).
8. Rostagno, A., Holton, J., Lashley, T., Revesz, T. & Ghiso, J. Cerebral amyloidosis: amyloid subunits, mutants and phenotypes. *Cell. Mol. Life Sci.* **67**, 581–600 (2010).
9. Soto, C. Unfolding the role of protein misfolding in neurodegenerative diseases. *Nat. Rev. Neurosci.* **4**, 49–60 (2003).
10. Brettschneider, J., Tredici, K. D., Lee, V. M.-Y. & Trojanowski, J. Q. Spreading of pathology in neurodegenerative diseases: a focus on human studies. *Nat. Rev. Neurosci.* **16**, 109–120 (2015).
11. Dickson, D. W. Parkinson's disease and parkinsonism: neuropathology. *Cold Spring Harb. Perspect. Med.* **2**, a009258 (2012).
12. Chiu, M.-J., Chen, T.-F., Yip, P.-K., Hua, M.-S. & Tang, L.-Y. Behavioral and psychologic symptoms in different types of dementia. *J. Formos. Med. Assoc.* **105**, 556–562 (2006).
13. Rizzi, L., Rosset, I. & Roriz-Cruz, M. Global epidemiology of dementia: Alzheimer's and vascular types. *BioMed Res. Int.* **2014**, 908915 (2014).
14. Jia, J. *et al.* The cost of Alzheimer's disease in China and re-estimation of costs worldwide. *Alzheimers Dement.* **14**, 483–491 (2018).
15. Kalaria, R. N. *et al.* Alzheimer's disease and vascular dementia in developing countries: prevalence, management, and risk factors. *Lancet Neurol.* **7**, 812–826 (2008).

16. Zhu, X.-C. *et al.* Rate of early onset Alzheimer's disease: a systematic review and meta-analysis. *Ann. Transl. Med.* **3**, (2015).
17. Panegyres, P. K. & Chen, H.-Y. Differences between early and late onset Alzheimer's disease. *Am. J. Neurodegener. Dis.* **2**, 300 (2013).
18. Jack, C. R. & Holtzman, D. M. Biomarker modeling of Alzheimer's disease. *Neuron* **80**, 1347–1358 (2013).
19. Chen, G. *et al.* Amyloid beta: structure, biology and structure-based therapeutic development. *Acta Pharmacol. Sin.* **38**, 1205–1235 (2017).
20. Jack Jr, C. R. *et al.* NIA-AA research framework: toward a biological definition of Alzheimer's disease. *Alzheimers Dement.* **14**, 535–562 (2018).
21. Chávez-Gutiérrez, L. *et al.* The mechanism of γ-secretase dysfunction in familial Alzheimer disease. *EMBO J.* **31**, 2261–2274 (2012).
22. Jarrett, J. T., Berger, E. P. & Lansbury Jr, P. T. The carboxy terminus of the. beta. amyloid protein is critical for the seeding of amyloid formation: Implications for the pathogenesis of Alzheimer's disease. *Biochemistry* **32**, 4693–4697 (1993).
23. Scheltens, P. *et al.* Alzheimer's disease. *The Lancet* **388**, 505–517 (2016).
24. Ayodele, T., Rogaeva, E., Kurup, J. T., Beecham, G. & Reitz, C. Early-onset Alzheimer's disease: what is missing in research? *Curr. Neurol. Neurosci. Rep.* **21**, 1–10 (2021).
25. Wingo, T. S., Lah, J. J., Levey, A. I. & Cutler, D. J. Autosomal recessive causes likely in early-onset Alzheimer disease. *Arch. Neurol.* **69**, 59–64 (2012).
26. Corder, E. H. *et al.* Gene dose of apolipoprotein E type 4 allele and the risk of Alzheimer's disease in late onset families. *Science* **261**, 921–923 (1993).
27. Strittmatter, W. J. *et al.* Apolipoprotein E: high-avidity binding to beta-amyloid and increased frequency of type 4 allele in late-onset familial Alzheimer disease. *Proc. Natl. Acad. Sci.* **90**, 1977–1981 (1993).
28. Povova, J. *et al.* Epidemiological of and risk factors for Alzheimer's disease: a review. *Biomed Pap Med Fac Univ Palacky Olomouc Czech Repub* **156**, 108–114 (2012).

29. Butterfield, D. A., Di Domenico, F. & Barone, E. Elevated risk of type 2 diabetes for development of Alzheimer disease: a key role for oxidative stress in brain. *Biochim. Biophys. Acta BBA-Mol. Basis Dis.* **1842**, 1693–1706 (2014).

30. Irie, F. *et al.* Enhanced risk for Alzheimer disease in persons with type 2 diabetes and APOE ε4: the Cardiovascular Health Study Cognition Study. *Arch. Neurol.* **65**, 89–93 (2008).

31. Geldmacher, D. S. & Whitehouse, P. J. Evaluation of dementia. *N. Engl. J. Med.* **335**, 330–336 (1996).

32. Koedam, E. L. *et al.* Early-versus late-onset Alzheimer's disease: more than age alone. *J. Alzheimers Dis.* **19**, 1401–1408 (2010).

33. James, B. D. *et al.* Contribution of Alzheimer disease to mortality in the United States. *Neurology* **82**, 1045–1050 (2014).

34. Ganguli, M., Dodge, H. H., Shen, C., Pandav, R. S. & DeKosky, S. T. Alzheimer disease and mortality: a 15-year epidemiological study. *Arch. Neurol.* **62**, 779–784 (2005).

35. Knopman, D. S. *et al.* The National Institute on Aging and the Alzheimer's Association research framework for Alzheimer's disease: perspectives from the research roundtable. *Alzheimers Dement.* **14**, 563–575 (2018).

36. Jessen, F. *et al.* A conceptual framework for research on subjective cognitive decline in preclinical Alzheimer's disease. *Alzheimers Dement.* **10**, 844–852 (2014).

37. Jack, C. R. *et al.* Hypothetical model of dynamic biomarkers of the Alzheimer's pathological cascade. *Lancet Neurol.* **9**, 119–128 (2010).

38. Hardy, J. & Selkoe, D. J. The amyloid hypothesis of Alzheimer's disease: progress and problems on the road to therapeutics. *science* **297**, 353–356 (2002).

39. Hardy, J. A. & Higgins, G. A. Alzheimer's disease: the amyloid cascade hypothesis. *Science* **256**, 184–185 (1992).

40. Verma, M., Vats, A. & Taneja, V. Toxic species in amyloid disorders: Oligomers or mature fibrils. *Ann. Indian Acad. Neurol.* **18**, 138–145 (2015).

41. Yang, M. & Teplow, D. B. Amyloid β-protein monomer folding: free-energy surfaces reveal alloform-specific differences. *J. Mol. Biol.* **384**, 450–464 (2008).

42. Blennow, K., de Leon, M. J. & Zetterberg, H. Alzheimer's disease. *The Lancet* **368**, 387–403 (2006).
43. Iqbal, K. *et al.* Tau pathology in Alzheimer disease and other tauopathies. *Biochim. Biophys. Acta BBA-Mol. Basis Dis.* **1739**, 198–210 (2005).
44. Blennow, K., Bogdanovic, N., Alafuzoff, I., Ekman, R. & Davidsson, P. Synaptic pathology in Alzheimer's disease: relation to severity of dementia, but not to senile plaques, neurofibrillary tangles, or the ApoE4 allele. *J. Neural Transm.* **103**, 603–618 (1996).
45. van Harten, A. C. *et al.* Tau and p-tau as CSF biomarkers in dementia: a meta-analysis. *Clin. Chem. Lab. Med.* **49**, 353–366 (2011).
46. He, Y. *et al.* Soluble oligomers and fibrillar species of amyloid β-peptide differentially affect cognitive functions and hippocampal inflammatory response. *Biochem. Biophys. Res. Commun.* **429**, 125–130 (2012).
47. Shankar, G. M. *et al.* Natural oligomers of the Alzheimer amyloid-β protein induce reversible synapse loss by modulating an NMDA-type glutamate receptor-dependent signaling pathway. *J. Neurosci.* **27**, 2866–2875 (2007).
48. Sperling, R. A. *et al.* Toward defining the preclinical stages of Alzheimer's disease: Recommendations from the National Institute on Aging-Alzheimer's Association workgroups on diagnostic guidelines for Alzheimer's disease. *Alzheimers Dement.* **7**, 280–292 (2011).
49. Pini, L. *et al.* Brain atrophy in Alzheimer's disease and aging. *Ageing Res. Rev.* **30**, 25–48 (2016).
50. Scheltens, P. *et al.* Alzheimer's disease. *The Lancet* **397**, 1577–1590 (2021).
51. DeFronzo, R. A. The triumvirate: β-cell, muscle, liver: a collusion responsible for NIDDM. *Diabetes* **37**, 667–687 (1988).
52. Association, A. D. Diagnosis and classification of diabetes mellitus. *Diabetes Care* **37**, S81–S90 (2014).
53. Vinik, A. I. & Vinik, E. Prevention of the complications of diabetes. *Am. J. Manag. Care* **9**, S63–S80 (2003).
54. Bloomgarden, Z. T. Diabetes complications. *Diabetes Care* **27**, 1506–1514 (2004).
55. IDF, D. A. International diabetes federation. *Diabetes Res. Clin. Pract.* **102**, (2021).

56. Galicia-Garcia, U. *et al.* Pathophysiology of type 2 diabetes mellitus. *Int. J. Mol. Sci.* **21**, 6275 (2020).

57. International Diabetes Federation. IDF Diabetes Atlas, 10th Edition. https://diabetesatlas.org/idfawp/resource-files/2021/07/IDF_Atlas_10th_Edition_2021.pdf (Stand 02.10.2024). (2021).

58. Deshpande, A. D., Harris-Hayes, M. & Schootman, M. Epidemiology of diabetes and diabetes-related complications. *Phys. Ther.* **88**, 1254–1264 (2008).

59. DeFronzo, R. A. *et al.* Type 2 diabetes mellitus. *Nat. Rev. Dis. Primer* **1**, 1–22 (2015).

60. Warshauer, J. T., Bluestone, J. A. & Anderson, M. S. New frontiers in the treatment of type 1 diabetes. *Cell Metab.* **31**, 46–61 (2020).

61. Matveyenko, A. V. & Butler, P. Relationship between β-cell mass and diabetes onset. *Diabetes Obes. Metab.* **10**, 23–31 (2008).

62. McCulloch, D. K., Koerker, D. J., Kahn, S. E., Bonner-Weir, S. & Palmer, J. P. Correlations of in vivo β-cell function tests with β-cell mass and pancreatic insulin content in streptozocin-administered baboons. *Diabetes* **40**, 673–679 (1991).

63. Sinha, R. *et al.* Assessment of skeletal muscle triglyceride content by 1H nuclear magnetic resonance spectroscopy in lean and obese adolescents: relationships to insulin sensitivity, total body fat, and central adiposity. *Diabetes* **51**, 1022–1027 (2002).

64. Janson, J. *et al.* Increased risk of type 2 diabetes in Alzheimer disease. *Diabetes* **53**, 474–481 (2004).

65. Butler, A. E. *et al.* β-Cell Deficit and Increased β-Cell Apoptosis in Humans With Type 2 Diabetes. *Diabetes* **52**, 102–110 (2003).

66. Christensen, A. A. & Gannon, M. The beta cell in type 2 diabetes. *Curr. Diab. Rep.* **19**, 1–8 (2019).

67. Kahn, S. E. *et al.* Evidence of cosecretion of islet amyloid polypeptide and insulin by β-cells. *Diabetes* **39**, 634–638 (1990).

68. Mulder, H., Ahren, B., Stridsberg, M. & Sundler, F. Non-parallelism of islet amyloid polypeptide (amylin) and insulin gene expression in rat islets following dexamethasone treatment. *Diabetologia* **38**, 395–402 (1995).

69. Haataja, L., Gurlo, T., Huang, C. J. & Butler, P. C. Islet Amyloid in Type 2 Diabetes, and the Toxic Oligomer Hypothesis. *Endocr. Rev.* **29**, 303–316 (2008).

70. Kahn, S. E., Andrikopoulos, S. & Verchere, C. B. Islet amyloid: a long-recognized but underappreciated pathological feature of type 2 diabetes. *Diabetes* **48**, 241–253 (1999).

71. Lin, C.-Y. *et al.* Toxic human islet amyloid polypeptide (h-IAPP) oligomers are intracellular, and vaccination to induce anti-toxic oligomer antibodies does not prevent h-IAPP–induced β-cell apoptosis in h-IAPP transgenic mice. *Diabetes* **56**, 1324–1332 (2007).

72. Gurlo, T. *et al.* Evidence for proteotoxicity in β cells in type 2 diabetes: toxic islet amyloid polypeptide oligomers form intracellularly in the secretory pathway. *Am. J. Pathol.* **176**, 861–869 (2010).

73. Costes, S., Langen, R., Gurlo, T., Matveyenko, A. V. & Butler, P. C. β-Cell failure in type 2 diabetes: a case of asking too much of too few? *Diabetes* **62**, 327–335 (2013).

74. Westermark, P., Andersson, A. & Westermark, G. T. Islet amyloid polypeptide, islet amyloid, and diabetes mellitus. *Physiol. Rev.* **91**, 795–826 (2011).

75. Li, X., Wan, M., Gao, L. & Fang, W. Mechanism of inhibition of human islet amyloid polypeptide-induced membrane damage by a small organic fluorogen. *Sci. Rep.* **6**, 21614 (2016).

76. Kanatsuka, A., Kou, S. & Makino, H. IAPP/amylin and β-cell failure: implication of the risk factors of type 2 diabetes. *Diabetol. Int.* **9**, 143–157 (2018).

77. Camargo, D. C. R. *et al.* hIAPP forms toxic oligomers in plasma. *Chem. Commun.* **54**, 5426–5429 (2018).

78. Larson, J. L. & Miranker, A. D. The mechanism of insulin action on islet amyloid polypeptide fiber formation. *J. Mol. Biol.* **335**, 221–231 (2004).

79. Baram, M., Gilead, S., Gazit, E. & Miller, Y. Mechanistic perspective and functional activity of insulin in amylin aggregation. *Chem. Sci.* **9**, 4244–4252 (2018).

80. Carter, T. C. *et al.* Validation of a metabolite panel for early diagnosis of type 2 diabetes. *Metabolism* **65**, 1399–1408 (2016).

81. Sevigny, J. *et al.* The antibody aducanumab reduces Aβ plaques in Alzheimer's disease. *Nature* **537**, 50–56 (2016).

82. Budd Haeberlein, S. *et al.* Two randomized phase 3 studies of aducanumab in early Alzheimer's disease. J Prev Alzheimers Dis 2022; 9: 197-210. *Copyrightcopyright 2022 Mass. Med. Soc.* (2022).

83. Cizas, P. *et al.* Size-dependent neurotoxicity of β-amyloid oligomers. *Arch. Biochem. Biophys.* **496**, 84–92 (2010).

84. Rosén, C., Hansson, O., Blennow, K. & Zetterberg, H. Fluid biomarkers in Alzheimer's disease–current concepts. *Mol. Neurodegener.* **8**, 1–11 (2013).

85. Birkmann, E. *et al.* Counting of single prion particles bound to a capture-antibody surface (surface-FIDA). *Vet. Microbiol.* **123**, 294–304 (2007).

86. Funke, S. A. *et al.* Single particle detection of Aβ aggregates associated with Alzheimer's disease. *Biochem. Biophys. Res. Commun.* **364**, 902–907 (2007).

87. Funke, S. A., Wang, L., Birkmann, E. & Willbold, D. Single-particle detection system for Aβ aggregates: adaptation of surface-fluorescence intensity distribution analysis to laser scanning microscopy. *Rejuvenation Res.* **13**, 206–209 (2010).

88. Gan, S. D. & Patel, K. R. Enzyme immunoassay and enzyme-linked immunosorbent assay. *J. Invest. Dermatol.* **133**, 1–3 (2013).

89. Hornbeck, P. Enzyme-linked immunosorbent assays. *Curr. Protoc. Immunol.* **1**, 2–1 (1992).

90. Kulawik, A., Heise, H., Zafiu, C., Willbold, D. & Bannach, O. Advancements of the sFIDA method for oligomer-based diagnostics of neurodegenerative diseases. *FEBS Lett.* **592**, 516–534 (2018).

91. Haringsma, J. & Tytgat, G. Fluorescence and autofluorescence. *Best Pract. Res. Clin. Gastroenterol.* **13**, 1–10 (1999).

92. Shrirao, A. B. *et al.* Autofluorescence of blood and its application in biomedical and clinical research. *Biotechnol. Bioeng.* **118**, 4550–4576 (2021).

93. Monici, M. Cell and tissue autofluorescence research and diagnostic applications. *Biotechnol. Annu. Rev.* **11**, 227–256 (2005).

94. Campbell, J. M. *et al.* Label-Free Assessment of Key Biological Autofluorophores: Material Characteristics and Opportunities for Clinical Applications. *Adv. Mater.* 2403761 (2024).

95. Croce, A. C. & Bottiroli, G. Autofluorescence spectroscopy and imaging: a tool for biomedical research and diagnosis. *Eur. J. Histochem. EJH* **58**, (2014).

96. Hüpfel, M., Yu. Kobitski, A., Zhang, W. & Nienhaus, G. U. Wavelet-based background and noise subtraction for fluorescence microscopy images. *Biomed. Opt. Express* **12**, 969–980 (2021).

97. Sakr, N. *et al.* Characterizing and quenching autofluorescence in fixed mouse adrenal cortex tissue. *Int. J. Mol. Sci.* **24**, 3432 (2023).

98. Johnston, N. W. & Bienenstock, J. Abolition of non-specific fluorescent staining of eosinophils. *J. Immunol. Methods* **4**, 189–194 (1974).

99. Neumann, M. & Gabel, D. Simple method for reduction of autofluorescence in fluorescence microscopy. *J. Histochem. Cytochem.* **50**, 437–439 (2002).

100. Rich, R. M. *et al.* Elimination of autofluorescence background from fluorescence tissue images by use of time-gated detection and the AzaDiOxaTriAngulenium (ADOTA) fluorophore. *Anal. Bioanal. Chem.* **405**, 2065–2075 (2013).

101. Beeby, A. *et al.* Luminescence imaging microscopy and lifetime mapping using kinetically stable lanthanide (III) complexes. *J. Photochem. Photobiol. B* **57**, 83–89 (2000).

102. Murphy, C. L. & Lever, M. J. A ratiometric method of autofluorescence correction used for the quantification of Evans blue dye fluorescence in rabbit arterial tissues. *Exp. Physiol.* **87**, 163–170 (2002).

103. Steinkamp, J. A. & Stewart, C. C. Dual-laser, differential fluorescence correction method for reducing cellular background autofluorescence. *Cytom. J. Int. Soc. Anal. Cytol.* **7**, 566–574 (1986).

104. Van de Lest, C., Versteeg, E., Veerkamp, J. H. & Van Kuppevelt, T. H. Elimination of autofluorescence in immunofluorescence microscopy with digital image processing. *J. Histochem. Cytochem.* **43**, 727–730 (1995).

105. Pils, M. *et al.* Development and implementation of an internal quality control sample to standardize oligomer-based diagnostics of Alzheimer's disease. *Diagnostics* **13**, 1702 (2023).

106. Blömeke, L. *et al.* Aβ oligomers peak in early stages of Alzheimer's disease preceding tau pathology. *Alzheimers Dement. Diagn. Assess. Dis. Monit.* **16**, e12589 (2024).

107. Yang, L. *et al.* Detection and quantification of bacterial autofluorescence at the single-cell level by a laboratory-built high-sensitivity flow cytometer. *Anal. Chem.* **84**, 1526–1532 (2012).

108. Huffman, J. A. *et al.* Real-time sensing of bioaerosols: Review and current perspectives. *Aerosol Sci. Technol.* **54**, 465–495 (2020).

109. Pan, Y.-L. *et al.* Fluorescence spectra of atmospheric aerosol particles measured using one or two excitation wavelengths: Comparison of classification schemes employing different emission and scattering results. *Opt. Express* **18**, 12436–12457 (2010).

110. Knight, A. E. Single-molecule fluorescence imaging by total internal reflection fluorescence microscopy (IUPAC Technical Report). *Pure Appl. Chem.* **86**, 1303–1320 (2014).

111. Trache, A. & Meininger, G. A. Total Internal Reflection Fluorescence (TIRF) microscopy: microscopy. *Curr. Protoc. Microbiol.* **10**, 2A – 2 (2008).

112. Aubreville, M. *et al.* Deep learning-based detection of motion artifacts in probe-based confocal laser endomicroscopy images. *Int. J. Comput. Assist. Radiol. Surg.* **14**, 31–42 (2019).

113. Soulet, D., Paré, A., Coste, J. & Lacroix, S. Automated filtering of intrinsic movement artifacts during two-photon intravital microscopy. *PLoS One* **8**, e53942 (2013).

114. Canale, C., Torre, B., Ricci, D. & Braga, P. C. Recognizing and avoiding artifacts in atomic force microscopy imaging. *At. Force Microsc. Biomed. Res. Methods Protoc.* 31–43 (2011).

115. Kühbach, K. *et al.* Application of an amyloid beta oligomer standard in the sFIDA assay. *Front. Neurosci.* **10**, 8 (2016).

116. Marr, D. & Hildreth, E. Theory of edge detection. *Proc. R. Soc. Lond. B Biol. Sci.* **207**, 187–217 (1980).

117. Bansal, R., Raj, G. & Choudhury, T. Blur image detection using Laplacian operator and Open-CV. in *2016 International Conference System Modeling & Advancement in Research Trends (SMART)* 63–67 (IEEE, 2016).

118. Bi, W. L. *et al.* Artificial intelligence in cancer imaging: clinical challenges and applications. *CA. Cancer J. Clin.* **69**, 127–157 (2019).

119. Panayides, A. S. *et al.* AI in medical imaging informatics: current challenges and future directions. *IEEE J. Biomed. Health Inform.* **24**, 1837–1857 (2020).

120. Cunningham, P., Cord, M. & Delany, S. J. Supervised learning. in *Machine learning techniques for multimedia: case studies on organization and retrieval* 21–49 (Springer, 2008).

121. Shorten, C. & Khoshgoftaar, T. M. A survey on image data augmentation for deep learning. *J. Big Data* **6**, 1–48 (2019).

122. Hossain, M. S. *et al.* Tissue artifact segmentation and severity assessment for automatic analysis using wsi. *IEEe Access* **11**, 21977–21991 (2023).

123. Wei, Z. *et al.* Elimination of stripe artifacts in light sheet fluorescence microscopy using an attention-based residual neural network. *Biomed. Opt. Express* **13**, 1292–1311 (2022).

124. Luo, C. *et al.* How does the data set affect cnn-based image classification performance? in *2018 5th international conference on systems and informatics (ICSAI)* 361–366 (IEEE, 2018).

125. Sharma, V. & Yakimovich, A. A deep learning dataset for sample preparation artefacts detection in multispectral high-content microscopy. *Sci. Data* **11**, 232 (2024).

126. Ronneberger, O., Fischer, P. & Brox, T. U-net: Convolutional networks for biomedical image segmentation. in *Medical image computing and computer-assisted intervention–MICCAI 2015: 18th international conference, Munich, Germany, October 5-9, 2015, proceedings, part III 18* 234–241 (Springer, 2015).

127. Hülsemann, M. *et al.* Biofunctionalized silica nanoparticles: standards in amyloid-β oligomer-based diagnosis of Alzheimer's disease. *J. Alzheimers Dis.* **54**, 79–88 (2016).

128. Herrmann, Y. *et al.* Nanoparticle standards for immuno-based quantitation of α-synuclein oligomers in diagnostics of Parkinson's disease and other synucleinopathies. *Clin. Chim. Acta* **466**, 152–159 (2017).

129. Mattheyses, A. L., Simon, S. M. & Rappoport, J. Z. Imaging with total internal reflection fluorescence microscopy for the cell biologist. *J. Cell Sci.* **123**, 3621–3628 (2010).

130. Jessen, F. *et al.* Design and first baseline data of the DZNE multicenter observational study on predementia Alzheimer's disease (DELCODE). *Alzheimers Res. Ther.* **10**, 1–10 (2018).

131. Blömeke, L. *et al.* Blood-based quantification of Aβ oligomers indicates impaired clearance from brain in ApoE ε4 positive subjects. *Commun. Med.* **4**, 1–13 (2024).

132. Reed, G. F., Lynn, F. & Meade, B. D. Use of coefficient of variation in assessing variability of quantitative assays. *Clin. Vaccine Immunol.* **9**, 1235–1239 (2002).

133. Hernando, L., Mendiburu, A. & Lozano, J. A. Hill-Climbing algorithm: let's go for a walk before finding the optimum. in *2018 IEEE Congress on Evolutionary Computation (CEC)* 1–7 (IEEE, 2018).

134. Prügel-Bennett, A. Benefits of a population: Five mechanisms that advantage population-based algorithms. *IEEE Trans. Evol. Comput.* **14**, 500–517 (2010).

135. Shi, Y. & others. Particle swarm optimization: developments, applications and resources. in *Proceedings of the 2001 congress on evolutionary computation (IEEE Cat. No. 01TH8546)* vol. 1 81–86 (IEEE, 2001).

136. Dorigo, M., Birattari, M. & Stutzle, T. Ant colony optimization. *IEEE Comput. Intell. Mag.* **1**, 28–39 (2006).

137. Karaboga, D. & Basturk, B. Artificial bee colony (ABC) optimization algorithm for solving constrained optimization problems. in *International fuzzy systems association world congress* 789–798 (Springer, 2007).

138. Yang, X.-S. Firefly algorithms for multimodal optimization. in *International symposium on stochastic algorithms* 169–178 (Springer, 2009).

139. Yang, X.-S. & He, X. Firefly algorithm: recent advances and applications. *Int. J. Swarm Intell.* **1**, 36–50 (2013).

140. Hölttä, M. *et al.* Evaluating amyloid-β oligomers in cerebrospinal fluid as a biomarker for Alzheimer's disease. *PloS One* **8**, e66381 (2013).

141. Yang, T. *et al.* A highly sensitive novel immunoassay specifically detects low levels of soluble Aβ oligomers in human cerebrospinal fluid. *Alzheimers Res. Ther.* **7**, 1–16 (2015).

142. Pils, M. *et al.* Elevated Aβ aggregates in feces from Alzheimer's disease patients: a proof-of-concept study. *Alzheimers Res. Ther.* **16**, 223 (2024).

143. Rehn, F. *et al.* IAPP-oligomerisation levels in plasma of people with type 2 diabetes. *Sci. Rep.* **14**, 19556 (2024).

144. Hu, R., Zhang, M., Chen, H., Jiang, B. & Zheng, J. Cross-seeding interaction between β-amyloid and human islet amyloid polypeptide. *ACS Chem. Neurosci.* **6**, 1759–1768 (2015).

145. Röder, C. *et al.* Cryo-EM structure of islet amyloid polypeptide fibrils reveals similarities with amyloid-β fibrils. *Nat. Struct. Mol. Biol.* **27**, 660–667 (2020).

146. Blömeke, L. *et al.* Quantitative detection of α-Synuclein and Tau oligomers and other aggregates by digital single particle counting. *Npj Park. Dis.* **8**, 68 (2022).

147. Rehn, F., Marlene, P., Bujnicki, T., Bannach, O. & Willbold, D. Artifact detection in fluorescence microscopy using convolutional autoencoder. *Eingereicht Sci. Rep.*

6 Anhang

Anhang 1 – Weitere Informationen zu Kapitel 2

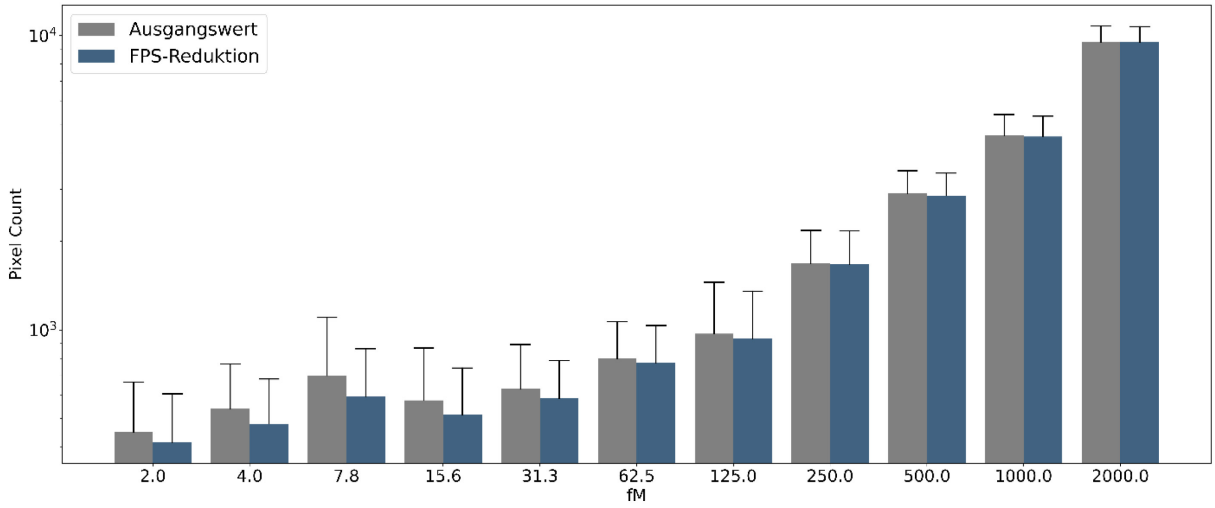

Abbildung A1: SiNaPs-Verdünnungsreihe des roten Fluoreszenzkanals. Die Abbildung zeigt die Readouts der SiNaPs-Verdünnungsreihe vor und nach Anwendung der FPS-Reduktion. Die Balken spiegeln den Mittelwert aller Wells wider. Die Whisker repräsentieren die SD zwischen den einzelnen Wells.

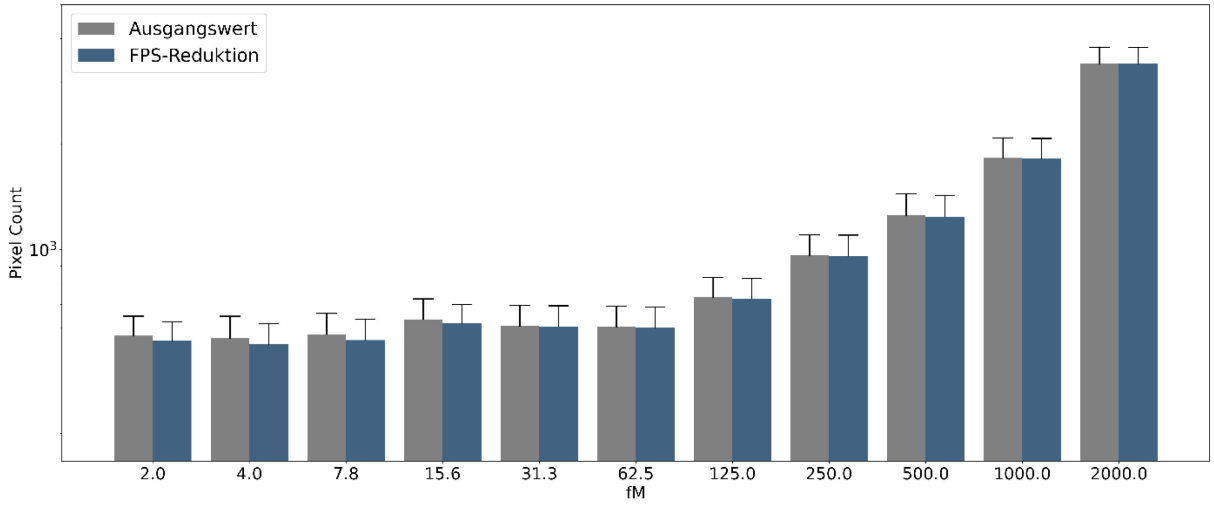

Abbildung A2: SiNaPs-Verdünnungsreihe des grünen Fluoreszenzkanals. Die Abbildung zeigt die Readouts der SiNaPs-Verdünnungsreihe vor und nach Anwendung der FPS-Reduktion. Die Balken spiegeln den Mittelwert aller Wells wider. Die Whisker repräsentieren die SD zwischen den einzelnen Wells.

Tabelle A1: Test auf Normalverteilung. Die Tabelle zeigt die Ergebnisse des Shapiro-Wilk-Tests zur Prüfung der Normalverteilung der humanen Proben für verschiedene Fluoreszenzkanäle, bzw. die Kolokalisation, vor und nach Anwendung der FPS-Reduktion. Eine Normalverteilung wird angenommen, wenn der P-Wert das Signifikanzniveau von 0.05 überschreitet.

Anwendung auf	**Fluoreszenzkanal**	***FPS-Reduktion [angewendet]***	***P*-Wert [Shapiro-Wilk-Test]**
Mittelwert	Rot	Nein	8.879e-12
	Rot	Ja	3.907e-12
	Grün	Nein	5.339e-13
	Grün	Ja	1.598e-12
	Kolokalisation	Nein	4.187e-25
	Kolokalisation	Ja	6.384e-27
SD	Rot	Nein	3.564e-23
	Rot	Ja	4.833e-28
	Grün	Nein	5.274e-17
	Grün	Ja	8.641e-18
	Kolokalisation	Nein	2.835e-22
	Kolokalisation	Ja	5.818e-23

Tabelle A2: Auswirkung der FPS auf die Verdünnungslinearität. Die Tabelle zeigt die VDL (Absolute Abweichung der Verdünnungslinearität vom Optimum (100 %) vor und nach Anwendung der FPS-Reduktion.

Fluoreszenzkanal	**Bereich [fM]**	**VDL vor FPS-Reduktion**	**VDL nach FPS-Reduktion**	**Veränderung**
Rot	2-2000	52.03 %	48.01 %	7.726 %
Rot	15.6-2000	37.15 %	27.88 %	24.953 %
Grün	2-2000	70.02 %	65.51 %	6.441 %
Grün	15.6-2000	60.81 %	52.70 %	13.337 %
Kolokalisation	2-2000	19.42 %	8.34 %	57.055 %
Kolokalisation	15.6-2000	6.13 %	1.77 %	71.11 %

Tabelle A3: Für die Auto-Cutoff-Methode verwendeten Min-Max Werte. Die Tabelle zeigt die zur Normalisierung der Metrik verwendeten Min- und Max-Werte.

Metrik	**Min-Wert**	**Max-Wert**
wMSE	0	143
VDL	0	30
CV%	0	50

***Tabelle A4: Nach Aggregationsmethode aufgeschlüsselte Korrelationen zwischen Metriken der humanen Proben und SiNaPs-Verdünnungsreihen* (Validierungsdatensatz).** Die Korrelationen wurden mittels eines zweiseitigen Spearman-Tests ermittelt. Die präsentierten Korrelationen beziehen sich auf den Validierungsdatensatz. Es wurden nur gültige Cutoffs beachtet. Bei Vergleich einer Metrik mit dem *P*-Wert wurde die Wertung verwendet, andernfalls der unbehandelte Wert (weder normalisiert noch transformiert). Anmerkung: r-Wert = Rangkorrelationskoeffizient, E.K. = Einzelkanäle, Kolok. = Kolokalisation, Signifikanzniveau: 0.05.

Aggr.	**Metrik (humane Probe)**	**Metrik (SiNaPs)**	**r-Wert [E.K.]**	***P*-Wert [E.K.]**	**r-Wert [Kolok.]**	***P*-Wert [Kolok.]**
MdM	*P*-Wert	QScore	-0.793	2.64e-92	-0.725	2.50e-113
	P-Wert	wMSE (Wertung)	-0.556	1.36e-35	-0.823	8.12e-171
	P-Wert	VDL (Wertung)	-0.077	0.114	-0.340	4.33e-20
	P-Wert	CV% (Wertung)	-0.084	0.084	0.807	1.34e-159
	VDL	VDL	0.885	4.64e-141	0.723	2.21e-112
	CV%	CV%	0.249	2.25e-07	0.864	6.28e-207
MME-MdM	*P*-Wert	QScore	-0.873	4.01e-132	-0.756	6.47e-124
	P-Wert	wMSE (Wertung)	-0.717	3.56e-67	-0.850	3.74e-186
	P-Wert	VDL (Wertung)	-0.153	1.73e-03	-0.385	7.62e-25
	P-Wert	CV% (Wertung)	0.000	1.0	0.864	3.38e-199
	VDL	VDL	0.924	2.98e-176	0.581	3.65e-61
	CV%	CV%	0.243	4.93e-07	0.871	3.35e-206
AE-MdM	*P*-Wert	QScore	-0.870	4.72e-141	-0.731	4.22e-111
	P-Wert	wMSE (Wertung)	-0.710	6.55e-71	-0.822	3.99e-163
	P-Wert	VDL (Wertung)	-0.233	4.96e-07	-0.359	1.60e-21
	P-Wert	CV% (Wertung)	0.204	1.16e-05	0.825	1.55e-165
	VDL	VDL	0.894	4.23e-160	0.549	3.93e-53
	CV%	CV%	0.419	9.94e-21	0.891	6.08e-228
HL	*P*-Wert	QScore	-0.909	1.22e-169	-0.765	1.50e-129
	P-Wert	wMSE (Wertung)	-0.756	1.83e-83	-0.854	2.15e-191
	P-Wert	VDL (Wertung)	-0.183	1.03e-04	-0.356	2.12e-21
	P-Wert	CV% (Wertung)	0.142	2.76e-03	0.855	1.06e-191
	VDL	VDL	0.928	1.66e-191	0.630	3.05e-75
	CV%	CV%	0.288	6.43e-10	0.855	5.51e-192
AE-HL	*P*-Wert	QScore	-0.874	6.29e-144	-0.697	1.33e-96
	P-Wert	wMSE (Wertung)	-0.719	1.81e-73	-0.771	1.89e-130
	P-Wert	VDL (Wertung)	-0.238	2.74e-07	-0.330	4.40e-18
	P-Wert	CV% (Wertung)	0.222	1.78e-06	0.808	1.51e-152
	VDL	VDL	0.880	6.74e-149	0.529	1.35e-48
	CV%	CV%	0.469	3.10e-26	0.889	3.90e-224

Tabelle A5: Nach Aggregationsmethode aufgeschlüsselte Korrelationen zwischen Metriken der humanen Proben und SiNaPs-Verdünnungsreihen (beide Datensätze). Die Korrelationen wurden mittels eines zweiseitigen Spearman-Tests ermittelt. Die präsentierten Korrelationen beziehen sich auf alle Kanäle beider Datensätze. Es wurden nur gültige Cutoffs beachtet. Bei Vergleich einer Metrik mit dem P-Wert wurde die Wertung verwendet, andernfalls der unbehandelte Wert (weder normalisiert noch transformiert). Anmerkung: r-Wert = Rangkorrelationskoeffizient, Signifikanzniveau: 0.05.

Aggr.	**Metrik (humane Probe)**	**Metrik (SiNaPs)**	**r-Wert**	***P*-Wert**
MdM	*P*-Wert	QScore	-0.573	4.89e-162
	P-Wert	wMSE (Wertung)	-0.564	8.24e-156
	P-Wert	VDL (Wertung)	-0.109	2.87e-06
	P-Wert	CV% (Wertung)	0.450	6.34e-93
	VDL	VDL	0.346	3.80e-53
	CV%	CV%	0.866	0.0
MME-MdM	*P*-Wert	QScore	-0.632	2.18e-192
	P-Wert	wMSE (Wertung)	-0.687	1.11e-240
	P-Wert	VDL (Wertung)	-0.358	2.95e-53
	P-Wert	CV% (Wertung)	0.682	1.46e-235
	VDL	VDL	0.393	1.31e-64
	CV%	CV%	0.724	1.42e-279
AE-MdM	*P*-Wert	QScore	-0.643	3.10e-204
	P-Wert	wMSE (Wertung)	-0.686	1.26e-242
	P-Wert	VDL (Wertung)	-0.399	8.19e-68
	P-Wert	CV% (Wertung)	0.679	2.34e-236
	VDL	VDL	0.424	6.79e-77
	CV%	CV%	0.770	0.0
HL	*P*-Wert	QScore	-0.636	2.14e-201
	P-Wert	wMSE (Wertung)	-0.694	8.28e-255
	P-Wert	VDL (Wertung)	-0.380	8.32e-62
	P-Wert	CV% (Wertung)	0.705	1.22e-265
	VDL	VDL	0.420	1.11e-76
	CV%	CV%	0.763	0.0
AE-HL	*P*-Wert	QScore	-0.619	1.16e-183
	P-Wert	wMSE (Wertung)	-0.663	3.55e-220
	P-Wert	VDL (Wertung)	-0.387	5.03e-63
	P-Wert	CV% (Wertung)	0.684	9.98e-240
	VDL	VDL	0.405	2.24e-69
	CV%	CV%	0.786	0.0

Anhang 2 – Neukonzeption und Entwicklung von sFIDAta

Um die Analysten bei der Auswertung von sFIDA-Experimenten zu entlasten, wurde am Forschungszentrum Jülich eine Inhouse-Software namens „sFIDAta“ entwickelt. Im Rahmen dieser Dissertation wurde diese Legacy-Software neu konzipiert und programmiert, um eine leistungsfähige Basis für die Integration zusätzlicher, im Verlauf der Arbeit entwickelter Funktionen zu schaffen. Zu Beginn der Neuentwicklung wurden in enger Zusammenarbeit mit den Stakeholdern die Anforderungen ermittelt. Dabei wurde festgelegt, welche Funktionen der bestehenden Software im operativen Betrieb weiterhin relevant und welche zugunsten einer verringerten Komplexität und intuitiveren Benutzeroberfläche entfernt werden konnten. Des Weiteren wurden bisher nicht implementierte, jedoch gewünschte Funktionen identifiziert und hinsichtlich ihres Potenzials sowie ihrer Machbarkeit bewertet. Auf Basis einer detaillierten Analyse der Stakeholder-Anforderungen konnten thematische Schwerpunkte für die Entwicklungsarbeit definiert werden. Ziel dieser Fokussierung war es, Entwicklungsbereiche mit Erweiterungspotenzial flexibel zu gestalten, während bereits klar definierte Bereiche unter dem Aspekt der Effizienzmaximierung geplant wurden.

Nach dem Entwurf der System- und Datenbankarchitektur wurden im Rahmen einer technischen Machbarkeitsprüfung die komplexesten Systemkomponenten implementiert. Nach erfolgreicher Prüfung wurde ein agiler Projektplan erstellt, der zwei wesentliche Meilensteine enthielt. Die Bereitstellung eines Minimum Viable Products (MVP) sowie die Veröffentlichung der Release-Version. Das MVP umfasste die grundlegende Systemstruktur sowie alle erforderlichen Funktionen zur Projekterstellung und -verwaltung, Artefaktdetektion, Berechnung von Cutoffs und Durchführung erster quantitativer Analysen, wie Pixel Counts und Histogrammen. Mit der Release-Version wurde die Bildanalyse erheblich erweitert. Neben dem Particle Count wurde eine Einzelpartikelanalyse integriert, die es ermöglichte, die durchschnittliche Partikelgröße zu bestimmen. Darüber hinaus wurde die Funktion implementiert, hochgradig individualisierbare Abbildungen auf Basis einzelner oder kombinierter Analyseergebnisse zu generieren. Dies beseitigte eine potenzielle Fehlerquelle, die zuvor durch den Datentransfer in externe Programme bestand. Zusätzlich wurde die Funktion eingeführt, die Analyseergebnisse mithilfe verschiedener Regressionsmethoden (lineare, polynomiale Regression) sowohl gewichtet als auch ungewichtet zu kalibrieren.

Um eine flexible und schnelle Entwicklung zu gewährleisten sowie eine möglichst hohe Performance zu erreichen, wurde in das auf C++ basierende sFIDAta2 ein Python-Interpreter integriert. Dadurch ist die Software in der Lage, zur Erstellung von Abbildungen

Python-Skripte nach dem Baukastenprinzip eigenständig zu erstellen und auszuführen. Hierdurch wurde die Verwendung der umfangreichen Python-Visualisierungsbibliotheken ermöglicht, welche nicht im selben Umfang in C++ verfügbar sind. Gleichzeitig liefert sFIDAta2 aufgrund der durch C++ optimierten Speicher- und Prozessorzugriffe hohe Performance bei Analysen. Das durch C++ gegebene Leistungspotential wurde durch den konsequenten Einsatz von Multithreading in allen Bereichen ausgeschöpft. Die Anzahl der verwendeten Prozessorkerne kann dabei vom Nutzer flexibel angepasst werden, um die Hardware parallel für andere Aufgaben nutzen zu können.

Nach der Produktivsetzung der Release-Version wurde ein Ticketsystem eingeführt und die Software wurde in enger Abstimmung mit den Stakeholdern laufend weiterentwickelt, um die Benutzerfreundlichkeit zu optimieren und neue Funktionen hinzuzufügen. Zur Sicherstellung der Softwarequalität wurden Unit-Tests und komplette Workflows mittels gTest (Google Test) durchgeführt.

Zum aktuellen Zeitpunkt sind in sFIDAta2 alle in dieser Arbeit beschriebenen Methoden implementiert.

Anhang 3 – Weitere Informationen zu Kapitel 2.2.1

Aβ oligomers peak in early stages of Alzheimer's disease preceding Tau pathology

Supplementary Information

Authors: Lara Blömeke, Fabian Rehn, Victoria Kraemer-Schulien, Janine Kutzsche, Marlene Pils, Tuyen Bujnicki, Piotr Lewczuk, Johannes Kornhuber, Silka D. Freiesleben Luisa-Sophie Schneider, Lukas Preis, Josef Priller, Eike J. Spruth, Slawek Altenstein, Andrea Lohse, Anja Schneider, Klaus Fliessbach, Jens Wiltfang, Niels Hansen, Ayda Rostamzadeh, Emrah Düzel, Wenzel Glanz, Enise I. Incesoy, Michaela Butryn, Katharina Buerger, Daniel Janowitz, Michael Ewers, Robert Perneczky, Boris-Stephan Rauchmann, Stefan Teipel, Ingo Kilimann, Doreen Goerss, Christoph Laske, Matthias H. Munk, Carolin Sanzenbacher, Annika Spottke, Nina Roy-Kluth, Michael T. Heneka, Frederic Brosseron, Michael Wagner, Steffen Wolfsgruber, Luca Kleineidam, Melina Stark, Matthias Schmid, Frank Jessen, Oliver Bannach, Dieter Willbold, Oliver Peters

Supplementary Table 1. Mean coefficient of variation (CV%) values of the SiNaPs and the samples over the four replicates for Aβ and Tau.

	Aβ		Tau	
Experiment	SiNaPs [%]	Samples [%]	SiNaPs [%]	Samples [%]
1	15.6	15.6	13.5	10.4
2	11.2	12.8	10.8	8.6
3	14.8	12.0	12.7	8.5
4	12.1	13.0	10.7	9.8
5	15.6	12.0	17.1	13.7
6	10.5	11.5	8.9	9.2
7	14.3	13.3	15.0	11.2
8	15.0	13.8	12.7	9.7
9	12.3	13.9	12.0	8.7
10	12.5	14.2	9.6	8.0
11	18.2	12.7	14.5	8.9
12	12.3	11.4	10.2	7.2
13	10.5	13.0	9.5	6.6
14	17.6	13.5	11.3	8.9
15	12.1	12.8	9.9	7.1
16	14.5	11.9	12.4	8.4
Mean	13.7	13.0	11.9	9.1

Supplementary Fig. 1. Assay controls for measurement of Aβ (A, C) and Tau (B, D) oligomer levels.

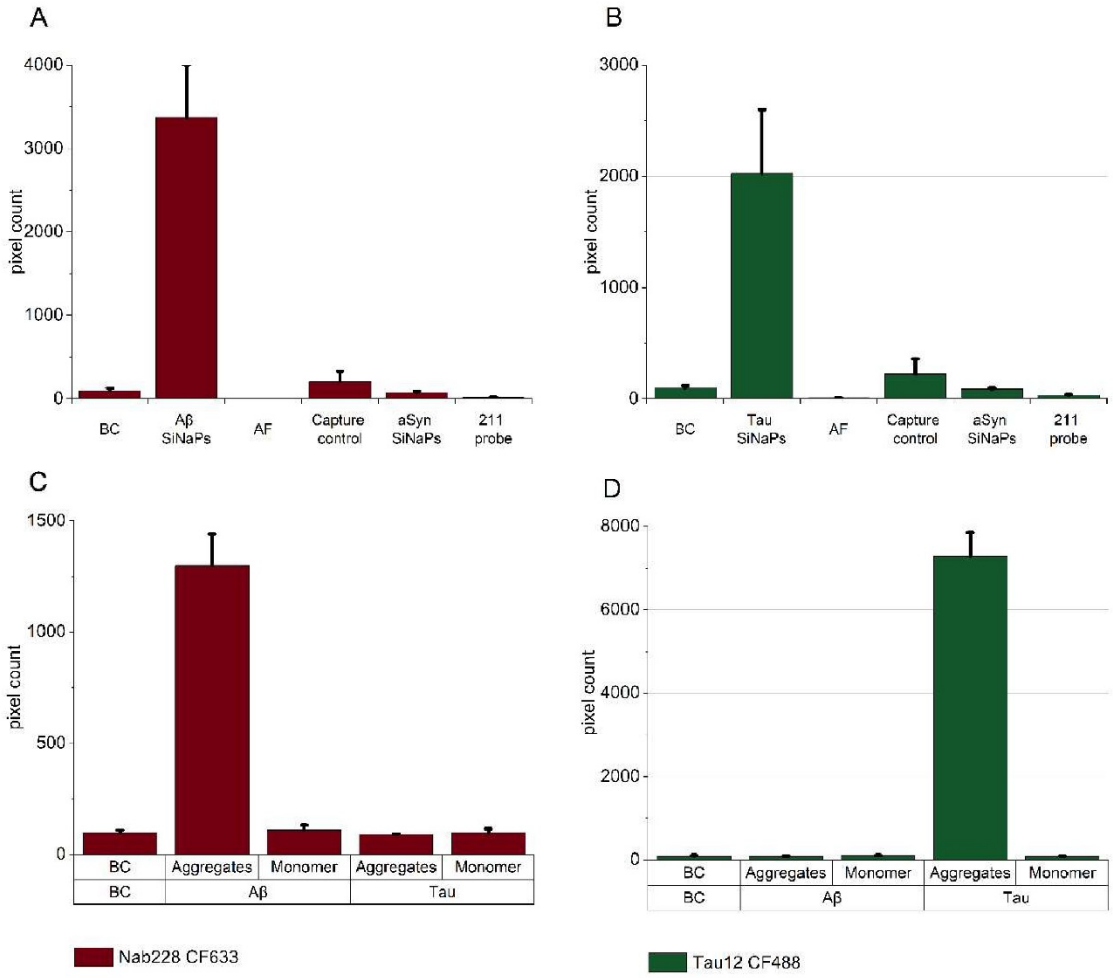

For Aβ (A) as well as for Tau (B), none of the assay components showed an autofluorescence signal (AF, signal < 0.1%). The signal of SiNaPs when leaving of the capture antibody was reduced to 2.8% for Aβ and 7.4% for Tau, respectively. When applying α-Synuclein (αSyn) SiNaPs or when detecting Aβ and Tau SiNaPs with an αSyn specific antibody (211), pixel counts were at blank control (BC) level. Recombinant Aβ aggregates of 1 nM (concentration depends on the monomer concentration) showed an increased fluorescence signal for detection with Nab228 CF633 (C), but were not detected with Tau12 CF488A (D). Likewise, Tau aggregates of 250 pM

(concentration depends on the monomer concentration) were detected with Tau12 CF488A, but not with Nab228 CF633. Neither presence of monomeric Aβ nor the presence of monomeric Tau showed a fluorescence signal above the blank control when applied in the same concentration like the aggregates with a signal reduction by more than 99% compared to the same concentration of monomer units in aggregates. Standard deviation was determined across the four replicates

Supplementary Table 2. Scaling factors of the individual experiments for Aβ and Tau oligomer pixel counts used to perform scaling.

Experiment	Scale Factor Aβ	Scale Factor Tau
1	1.459	1.224
2	0.938	0.977
3	0.938	0.977
4	1.236	1.597
5	1.300	1.688
6	1.108	1.510
7	1.077	1.306
8	0.798	1.129
9	1.237	0.689
10	1.084	0.934
11	0.965	0.985
12	1.020	1.037
13	0.893	0.850
14	1.004	0.723
15	0.810	0.643
16	0.822	0.998

Supplementary Fig 2. Measured Aβ (A, C) and Tau (B, D) pixel counts before scaling. To increase readability, the y-axis was limited to the range between 20−350 for Aβ (C) and 20−200 for Tau (D). Especially for Tau considerable fluorescence fluctuations between the 16 individual plates can be observed. As the samples were applied in the blinded state, the distribution of the diagnostic groups on the plates is not uniform and consequently a distortion of statistical results could occur if values are used without scaling.

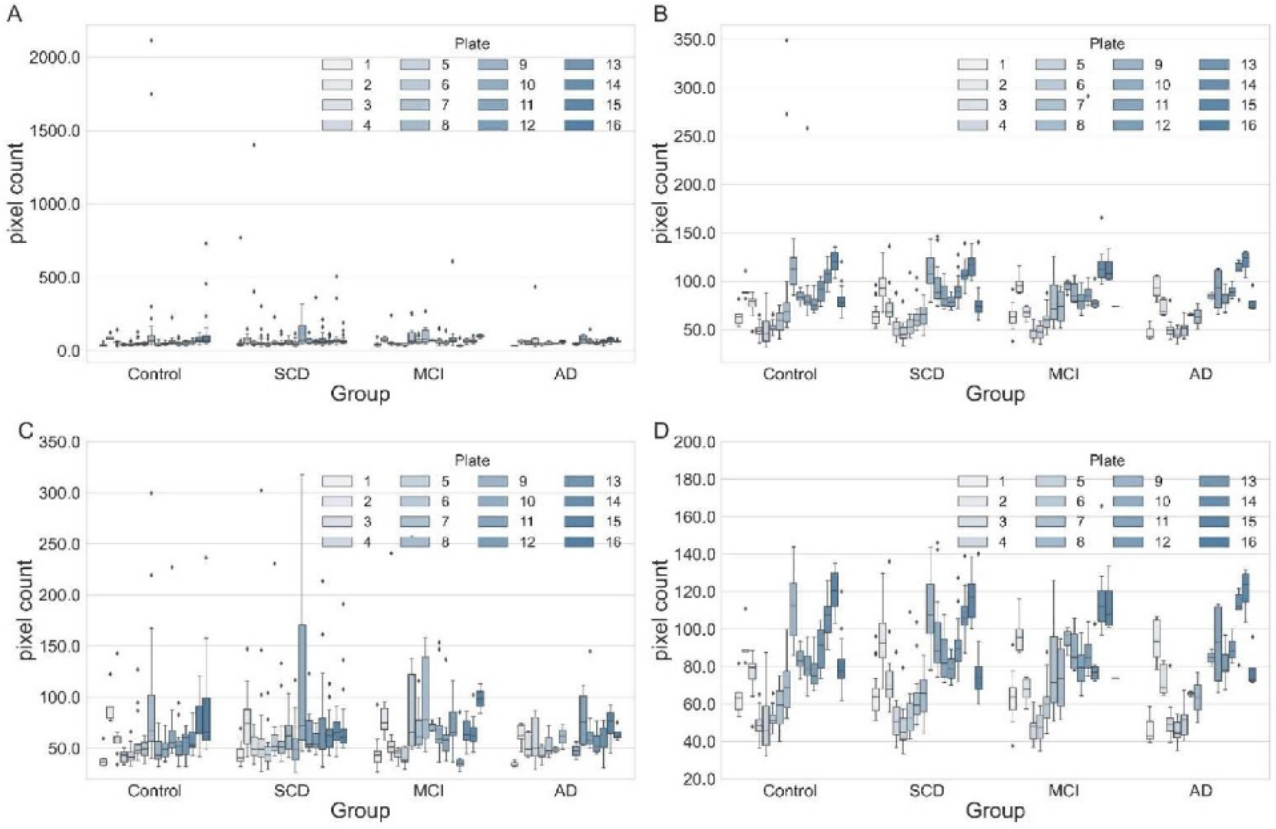

Supplementary Fig 3. Measured Aβ (A, C) and Tau (B, D) oligomer pixel counts after scaling. To increase readability, the y-axis was limited to the range between 20−350 for Aβ (C) and 20−200 for Tau. Since the fluorescence fluctuations between the individual plates are now reduced to an acceptable level, it is now possible to carry out statistical analyses without distorting the results.

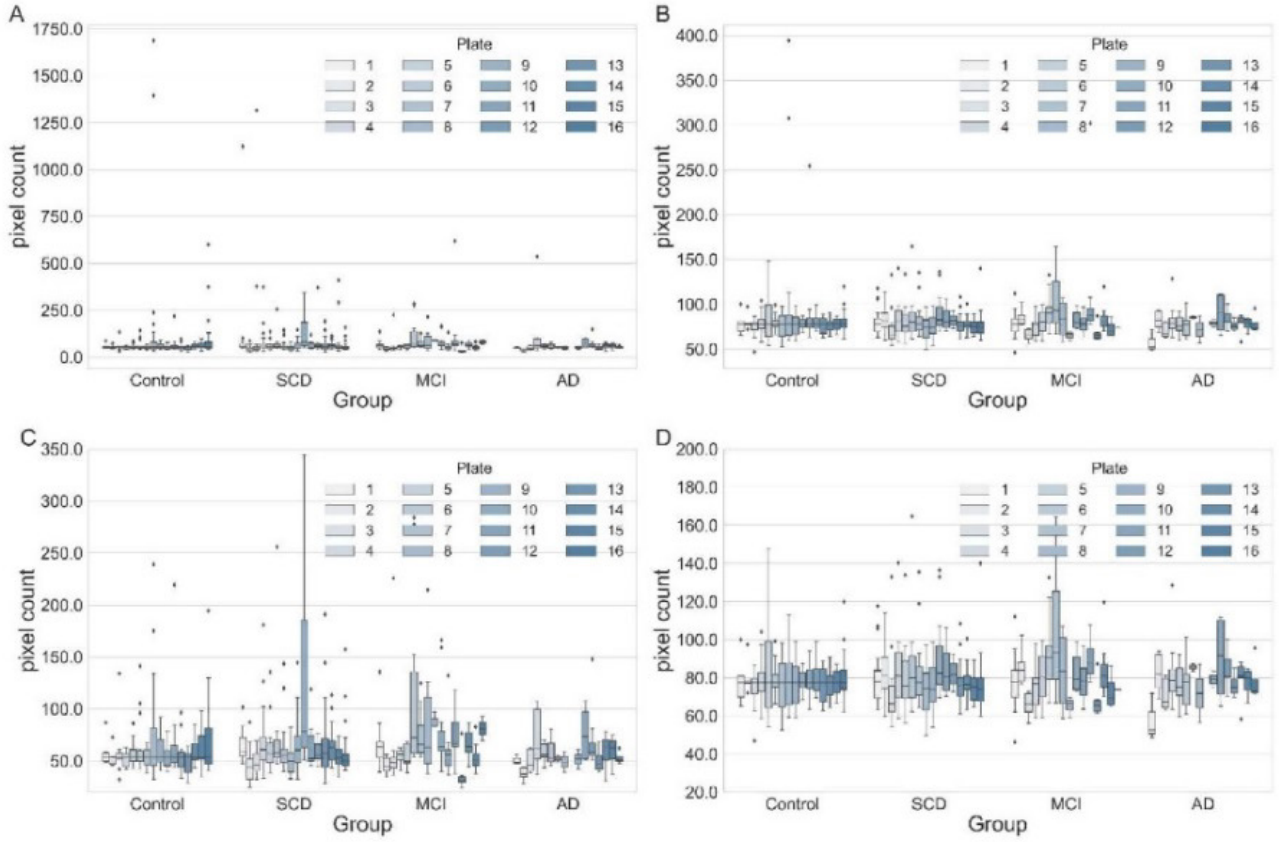

Supplementary Table 3. Effect size, among groups significantly differing from each other

Groups	Median Difference Ratio [%]
Control vs. MCI	8.57
Control [A-] vs. SCD [A+]	8.65
Control [A-] vs. MCI [A+]	13.26
SCD [A-] vs. SCD [A+]	5.06
A-T- vs. A+T-	9.31
A+T- vs. A+T+	-8.65

Supplementary Table. 4. Bootstrapped median AUC scores.

Groups	Bootstrapped median AUC score
Control vs. MCI	0.54
Control [A-] vs. SCD [A+]	0.56
Control [A-] vs. MCI [A+]	0.57
SCD [A-] vs. SCD [A+]	0.57
A-T- vs. A+T-	0.60
A+T- vs. A+T+	0.60

Supplementary Fig. 4. ROC-Curves of classifications between groups significantly differing from each other.

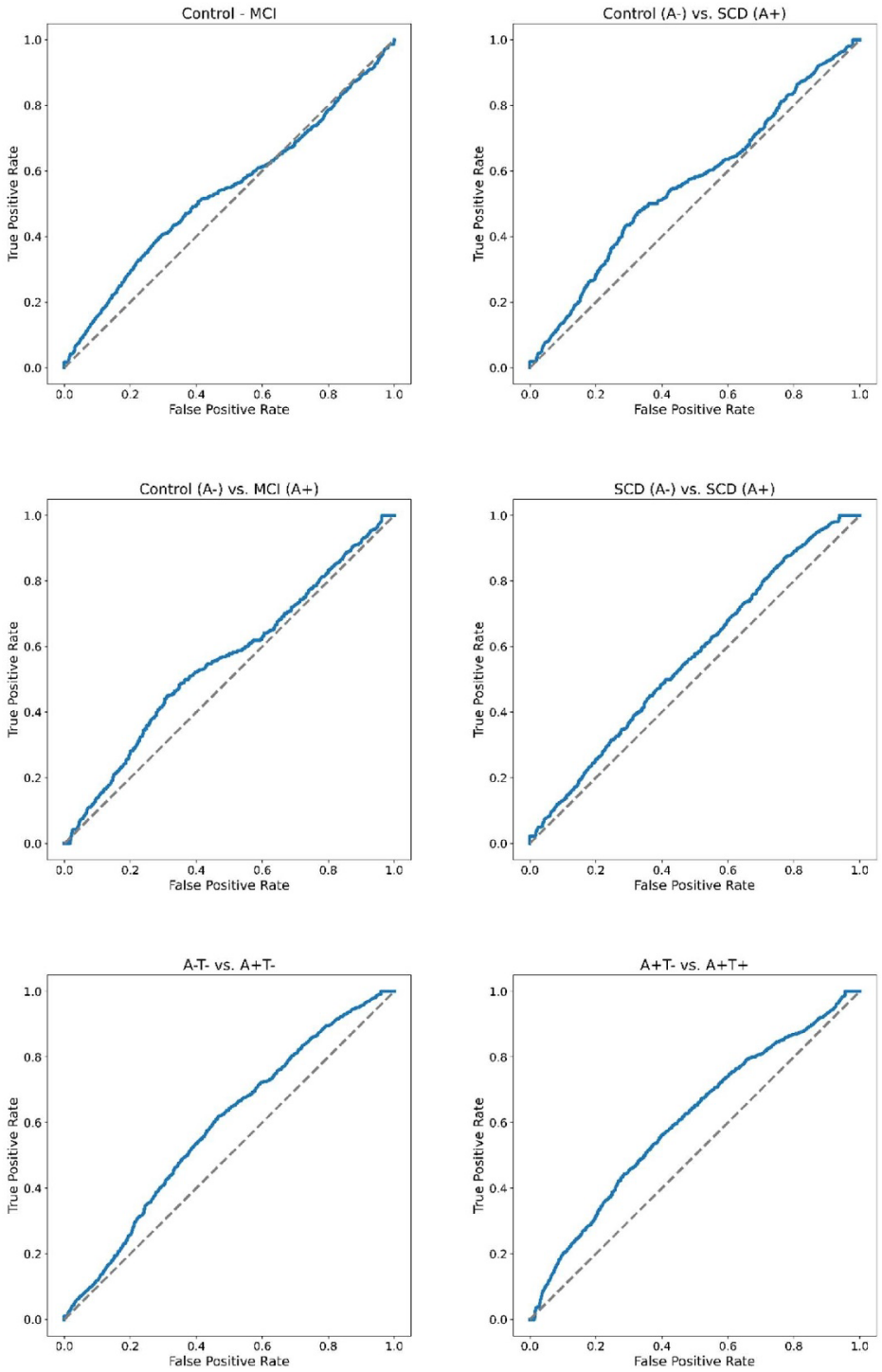

For all group pairs showing a significant difference according to Mann-Whitney-U a ROC-Curve and AUC-Score was calculated. To account for the variance and consequent uncertainty arising from a train-test split, a strictly stratified bootstrapping approach with N=500 was chosen, where for each iteration, a randomized subset of data was determined using random sampling with replacement. This subset was then divided into training and test sets, and a logistic regression was trained and used to classify the test data. For each of the N regressions, an ROC curve and AUC were computed. Since the dispersion of the AUC scores was very high, the median of all scores was used to avoid the inclusion of outliers. To visualize a single curve, the FPR and TPR values were calculated for each of the N iterations, interpolated at intervals of 0.001 steps, and then the median of all N FPR values for each TPR value was computed.

The AUC scores were found to be in a range between 0.54 and 0.57, which, while not particularly high, was not unexpected. This can be partly attributed to the considerable overlap among the groups, together with the illustrated progression of Aβ oligomers depicted in Figure 4. The values do not monotonically increase but instead reach their maximum in the SCD (ApoE4-) or MCI (ApoE4+) stage before subsequently decreasing. However, logistic regression, building the foundation of ROC analysis, need constantly increasing or decreasing levels over the disease progression and therefore cannot accurately depict the described development.

Supplementary Table 5. Regression Error

Model	nMAE
All Data	0.16
ApoeE4+	0.24
ApoE4-	0.15

The MAE was normalized by the standard deviation.

Supplementary Fig. 5. Binned Aβ oligomer pixel counts plotted as a function of Aβ42 and pTau concentrations.

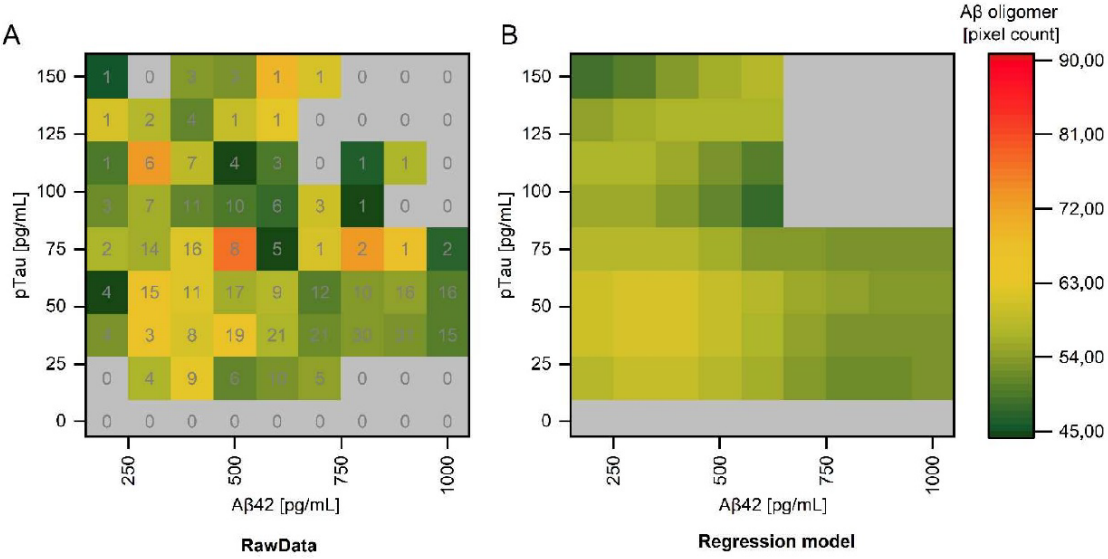

The heatmap shows a 2D plot with Aβ42 and pTau concentrations on the x any y axis, respectively. (A) measured Aβ oligomer pixel counts were binned and median oligomer pixel counts were plotted based on Aβ42 and pTau concentrations. Numbers in the squares represent the number of measurement points. (B) Results of the regression model were binned and plotted equal to (A). Highest Aβ oligomer pixel counts are found at low Aβ42 and pTau concentrations for the raw data as well as for the regression data.

Anhang 4 – Weitere Informationen zu Kapitel 2.2.2

Blood-based quantification of Aβ oligomers indicates impaired clearance from brain in ApoE ε4 positive subjects

Lara Blömeke, Fabian Rehn, Marlene Pils, Victoria Kraemer-Schulien, Anneliese Cousin, Janine Kutzsche, Tuyen Bujnicki, Silka D. Freiesleben, Luisa-Sophie Schneider, Lukas Preis, Josef Priller, Eike J. Spruth, Slawek Altenstein, Anja Schneider, Klaus Fliessbach, Jens Wiltfang, Niels Hansen, Ayda Rostamzadeh, Emrah Düzel, Wenzel Glanz, Enise I. Incesoy, Katharina Buerger, Daniel Janowitz, Michael Ewers, Robert Perneczky, Boris-Stephan Rauchmann, Stefan Teipel, Ingo Kilimann, Christoph Laske, Matthias H. Munk, Annika Spottke, Nina Roy, Michael T. Heneka, Frederic Brosseron, Michael Wagner, Sandra Roeske, Alfredo Ramirez, Matthias Schmid, Frank Jessen, Oliver Bannach, Oliver Peters, Dieter Willbold

Supplementary Figures and Tables

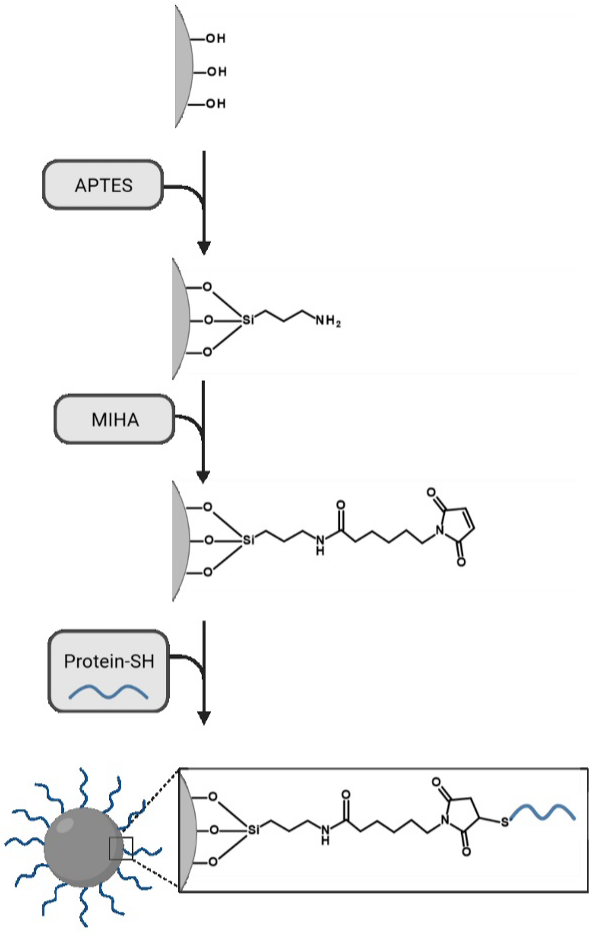

Supplementary Fig. 1 Synthesis of protein conjugated SiNaPs.

The process of protein conjugation of SiNaPs consists of three main steps. First, the silica core is functionalized with APTES. As a second step, MIHA is added as a crosslinker between the SiNaPs core and the protein. The use of maleimide as functional group in combination with the reaction conditions allows a directed coupling with the thiol group at the modified C-terminus of the protein. The resulting protein conjugated SiNaPs imitate a protein aggregate with multiple binding sites for the antibody but showing a unique size distribution, high stability, and defined epitope number [1].

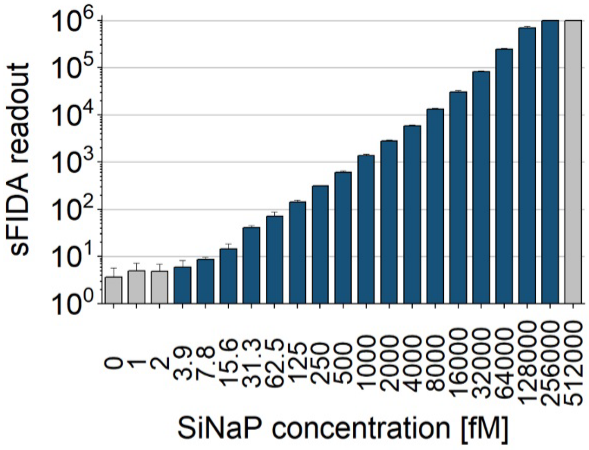

Supplementary Fig. 2 Dynamic range of SiNaP calibration

In an independent experiment, the dynamic range of SiNaP calibration standard spiked in plasma was determined. Two-fold serial dilutions were performed starting at 512 pM down to 1 fM. ULOQ was determined at 256 pM. The average dilution linearity between 3.9 fM and 256 pM was 0.91. The standard deviation was calculated across the four replicates. Please, note the logarithmic scale.

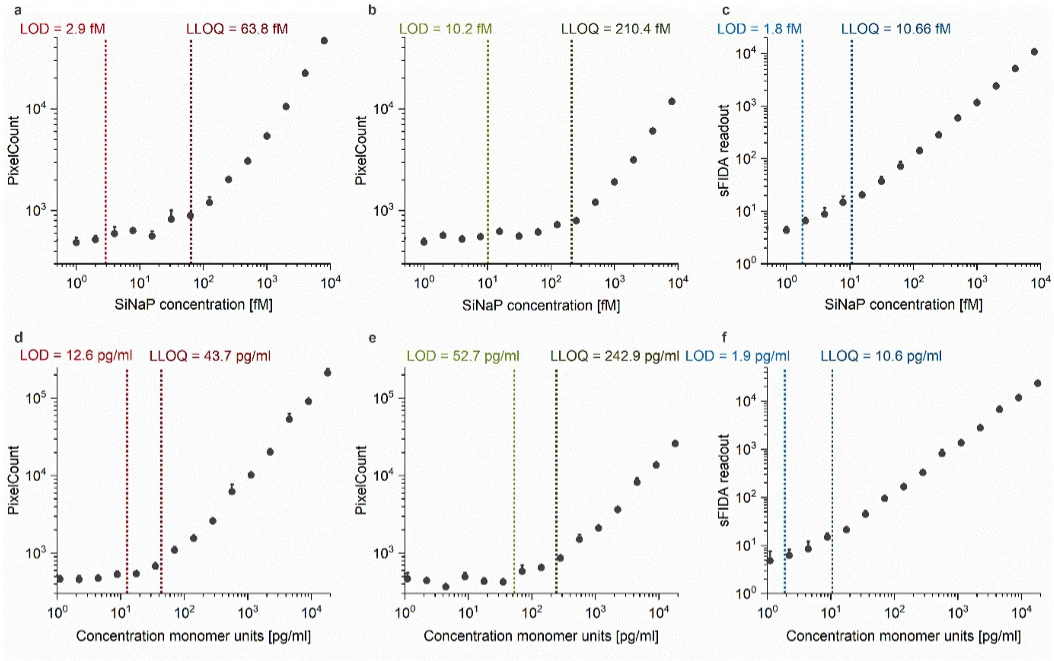

Supplementary Fig. 3 Linear dilution of $A\beta_{1-15}$ SiNaPs and $A\beta_{1-42}$ aggregates spiked in plasma. Shown are dilution series for $A\beta_{1-15}$ SiNaPs for the red (CF 633) **a** and green (CF488) **b** fluorescence channels, and the colocalization **c** and the corresponding limit of detection (LOD) and lower limit of quantification (LLOQ). Similarly, dilution series of synthetic $A\beta_{1-42}$ aggregates for the red (CF633) **d** and green (CF488) **e** fluorescence channels and colocalization **f** with calculated LOD and LLOQs are shown. The standard deviation was calculated across the four replicates. Please, note the logarithmic scale.

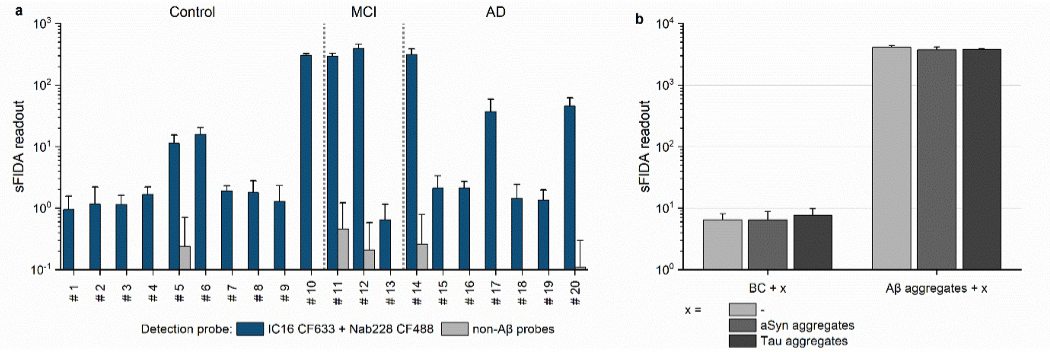

Supplementary Fig. 4 Assay controls with non-Aβ probes (a) and αSyn and Tau aggregates.

a sFIDA readouts of the samples (#1 to #20) of the validation cohort for detection with anti-Aβ detection antibodies IC16 CF633 in combination with Nab228 CF488 (blue) and non-Aβ probes MOPC-21 CF633 in combination with 211 CF488 (grey). While the samples detected with anti-Aβ antibodies showed an sFIDA readout ranging from approximately 1 pixel to 500 pixels, the samples did not give a signal when detected with antibodies who do not recognize Aβ. **b** Neat plasma and 1 nM (18 ng/ml) Aβ aggregates (concentration based on the monomer unit concentration) were spiked with 1 nM of αSyn and Tau aggregates, respectively. Standard deviation was calculated across the four replicates. Please, note the logarithmic scaling.

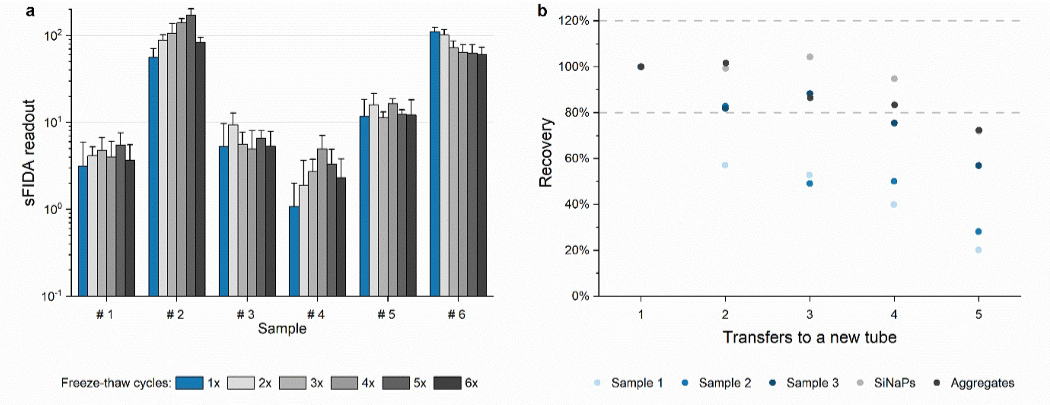

Supplementary Fig. 5 Evaluation of freeze-thaw cycles (a) and influence of tube transfers (b).

a Six patient plasma samples were thawed for 2 h at RT and then refrozen. The sFIDA readout for half of the samples remained unaffected (mean recovery 103%–129%), whereas additional freeze-thaw cycles caused an increase in the sFIDA readout for two samples and a decrease in the readout for one sample. Please, note the logarithmic scaling. Standard deviation is calculated across the four replicates. **b** After centrifugation, the supernatants of the plasma samples were transferred to a new tube (one transfer). One additional transfer reduced the sFIDA readout for the samples, whereas that of SiNaPs and recombinant aggregates remains constant for at least two additional transfers. Standard deviation was calculated across the four replicates. Please, note the logarithmic scale.

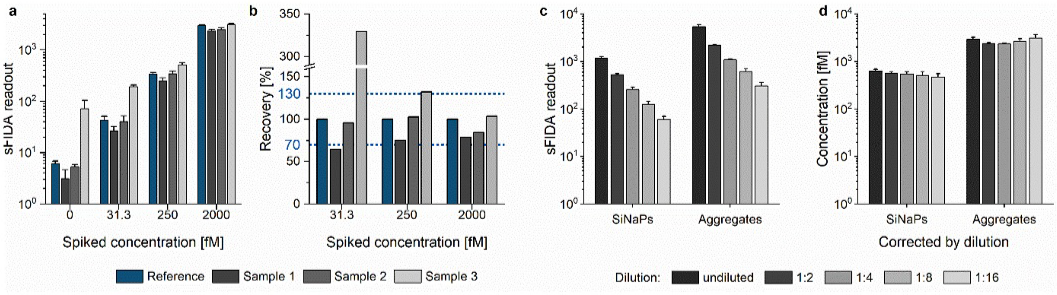

Supplementary Fig. 6 Recovery of SiNaPs in different matrices (a, b) and dilution of SiNaPs and aggregates spiked in plasma (c, d).

a Three samples with an initial low (sample 1), medium (sample 2) and high concentration (sample 3) of Aβ oligomers were spiked with three different concentrations of SiNaPs to examine whether the recovery of SiNaPs is dependent on the individual plasma matrix. **b** The obtained sFIDA readouts were initially normalized with the non-spiked sample and then compared to the readout of the same concentration of SiNaPs in the reference plasma sample. Samples 1 and 2 showed a mean recovery of 73% and 94%, respectively. For sample 3, the lowest concentration of 31.3 fM was beyond the acceptable range (dashed blue line), whereas medium and high concentrations of SiNaPs spiked in sample 3 showed a mean recovery of 118%. Mean recovery of all samples and concentrations (except sample 3 spiked with a low concentration) was 92%. **c** SiNaPs and recombinant $A\beta_{1-42}$ aggregates were spiked in plasma and diluted two-fold with TBS. **d** After calibration and correction for dilution, calculated stock concentrations for SiNaPs and aggregates differed on average by 15.9% and 8.9%, respectively. Standard deviations are calculated across the four replicates. Please, note the logarithmic scaling in a, c and d.

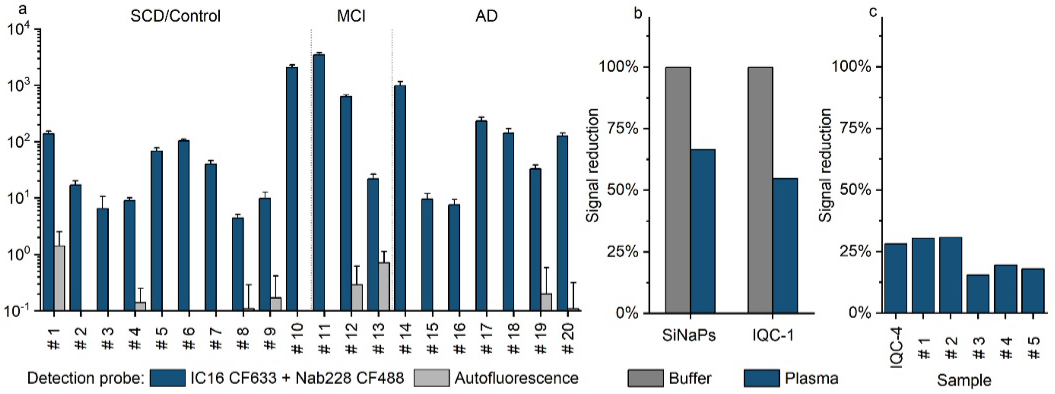

Supplementary Fig. 7 Autofluorescence of plasma samples

a Autofluorescence of 20 plasma samples was evaluated by incubation with the detection buffer without adding the capture antibody. Mean sFIDA readout was 0.61% compared to the signal with detection antibodies IC16 CF633 and Nab228 CF488 while all autofluorescence signals were below LOD. The experiment was carried out as part of the assay development, which is why there are slight deviations from the final protocol with regard to capture antibody (Nab228 at 2.5 µg/ml), blocking concentration (3% BSA) and washing steps after sample and detection antibody incubation (washing steps only with TBS). **b** To test unspecific binding of the analyte to the assay surface, sFIDA assay was performed with and without capture antibody with capture control refereing to the signal without capture antibody. Leaving of the capture antibody lead to a signal reduction of >99% for 8 pM SiNaPs and Aβ1−42 aggregates (IQC-1 with 18 ng/ml Aβ1−42 monomer concentration) spiked in low cross buffer while the same concentration spiked in a plasma samples resulted in a signal reduction of 33.5% and 54.7%, respectively. **c** Signal reduction for capture control for a lower concentration of Aβ1−42 aggregates (IQC-4 with 4.45 ng/ml Aβ1−42 monomer concentration) was at 28.1% while signal reduction in capture control for plasma samples ranged from 15.5% to 30.7% with a mean signal reduction of 22.8%, respectively. Standard deviation was calculated across the four replicates. Please, note the logarithmic scaling.

Supplementary Table 1 Mean Spearman coefficient of correlation r of the bootstrapping analysis of Aβ oligomers in plasma with demographics and biomarkers in CSF and plasma (*p*-value of Spearman distribution * 0.01 – 0.05, ** *p*-value 0.001 – 0.01)

		Control/Relatives /SCD	p-value	MCI/AD	p-value
	Age	−0.100	0.078	0.047	0.313
	MMSE	−0.053	0.242	0.011	0.451
CSF	$A\beta_{1-40}$	−0.037	0.314	0.219*	0.015
	$A\beta_{1-42}$	0.103	0.083	0.236**	0.005
	$A\beta_{1-42}/A\beta_{1-40}$	0.166*	0.013	0.196*	0.022
	tTau	−0.160*	0.015	0.023	0.410
	pTau	−0.203**	0.002	0.051	0.302
	Aβ Oligomers	0.186**	0.005	−0.217**	0.009
	Tau Oligomers	0.201**	0.002	−0.096	0.165
Plasma	$A\beta_{1-40}$	−0.067	0.205	0.158	0.111
	$A\beta_{1-42}$	−0.044	0.300	0.054	0.336
	$A\beta_{1-42}/A\beta_{1-40}$	0.034	0.337	−0.233*	0.031

Supplementary references

1 Herrmann, Y. *et al.* Nanoparticle standards for immuno-based quantitation of alpha-synuclein oligomers in diagnostics of Parkinson's disease and other synucleinopathies. *Clin Chim Acta* **466**, 152-159 (2017). https://doi.org:10.1016/j.cca.2017.01.010

Anhang 5 – Weitere Informationen zu Kapitel 2.2.3

Elevated Aβ aggregates in feces from

Alzheimer's disease patients: a proof-of-concept study

Supplementary Information

Marlene Pils, Alexandra Dybala, Anja Schaffrath, Fabian Rehn, Janine Kutzsche, Lara Blömeke, Markus Tusche, Pelin Özdüzenciler, Tuyen Bujnicki, Victoria Kraemer-Schulien, Hannes Gramespacher, Maximilian H.T. Schmieschek, Michael T. Barbe, Oezguer A. Onur, Gereon R. Fink, Gültekin Tamgüney, Oliver Bannach and Dieter Willbold

Supplementary Methods

Homogenization of fecal samples for sFIDA analysis

In this study, we used Tris buffer (20 mM Tris and 250 mM NaCl, both AppliChem, Darmstadt, Germany, pH 8.3), which was previously applied to quantify Aβ aggregates in homogenized brain tissue using sFIDA technology [1]. As during homogenization release of proteases and phosphatases cannot be excluded, we added cOmplete EDTA-free protease inhibitor and PhosStop phosphatase inhibitor (both Roche, Basel, Switzerland) as described in the study of Kass et al. [1]. To reduce non-specific binding of Aβ aggregates to the homogenization tubes, we added 1% bovine serum albumin (BSA, AppliChem). Furthermore, the properties of glycerol (Carl Roth, Karlsruhe, Germany) were used to further stabilize the analyte, especially during repeated freezing and thawing [2], using a concentration of 5%. Because about a quarter of the solid fecal components comprises bacteria and other microorganisms that may still be viable [3, 4], we added NaN_3 (AppliChem) at a concentration of 0.05%.

Various feces homogenization methods are described in the literature, with the required sample quantity being determined either by weighing or using tubes with an integral dosing system [5-9]. We decided to use such a dosing system, i.e., Simplix tubes (polypropylene, Gaudlitz, Coburg, Germany), allowing for simple, clean, and fast sample handling and accurate dosing. The homogenization procedure used in this study (Supplementary Figure 1) was adapted by combining already established instructions of *in-vitro* diagnostics (IVDs) using feces as sample matrix for the quantification of other biomarkers, e.g., fecal IgA, hemoglobin, or calprotectin [5, 6, 8, 9].

Preanalytics

Reproducibility of preanalytical procedures

Due to the complex and individually varying composition of feces, we tested the reproducibility of homogenization and sample dilution using three fecal samples with an initial low, intermediate, and high readout. To this end, six homogenates of each of the three samples were prepared, whereby the weight of the sample was additionally calculated based on the previously recorded empty weight (homogenization tube with buffer). Based on these data and using the reference weight of 17 mg according to the manufacturer's specifications of the Simplix tubes, the sample dosage's precision and trueness were calculated. Each homogenate was subjected to sFIDA assay in quadruplicates. In addition, the reproducibility of sample dilution was investigated by preparing four dilutions from one homogenate of each sample and assaying them also in quadruplicate within sFIDA. Afterward, pixel counts of individual replicates of each sample were normalized based on Eq.1. Values within the tolerance range of ± 25% indicated sufficient reproducibility.

$$(1)\quad \text{Normalized pixel count } [\%] = \frac{\text{pixel count}_{\text{replicate x}}}{\text{pixel count}_{\text{mean all replicates}}} \times 100\ \%$$

Dilution linearity

In this study, the dilution linearity of Aβ-coated SiNaPs and IQC in dilution buffer was investigated. Before calculating the dilution linearity of both targets, background correction was performed by subtracting the BC value from each value. Subsequently, the percent dilution linearity of each calibration or IQC sample

was calculated using Eq.2. Dilution linearity was accepted when the mean percent dilution linearity was between 80−120%.

$$(2)\quad \text{Dilution linearity or parallelism } [\%] = \frac{\text{observed concentration}}{(\text{previous observed value}/\text{dilution factor})} \times 100\ \%$$

For investigating parallelism, two fecal samples with high endogenous concentrations of Aβ aggregates were homogenized and diluted 1:5 with sample dilution buffer. Subsequently, these samples were serially diluted four times by a factor of two, and all prepared dilutions were applied on sFIDA surface. Because parallelism and dilution linearity are conceptually similar [10], the percent parallelism of each dilution step was also calculated using Eq.2. In the case of fecal samples, acceptance criteria for the mean dilution linearity were increased up to ± 25%.

Sample stability

To assess thermostability, three crude fecal samples with low, intermediate, and high readouts were stored at −20 °C, 4 °C, or 20 °C for 3, 6, or 18 h to simulate sample transport and bench top conditions, respectively. To this end, nine Simplix tubes were prefilled with the respective fecal sample, and the individual homogenization tubes were stored according to the storage condition mentioned above. At the end of each storage period, the aliquots were frozen at −80 °C. As a reference, another Simplix tube was prefilled with the corresponding sample and stored directly at −80 °C. On the day of the sFIDA experiment, all Simplix tubes were thawed simultaneously, the homogenization tubes were filled with homogenization buffer, and the samples were homogenized and diluted 1:5 with sample dilution buffer. Finally, all samples were measured by sFIDA, and the normalized pixel counts were calculated (Eq.1), where values within a tolerance range of ± 25% were accepted. Values outside the tolerance range indicated that sample stability was compromised.

For CSF samples, it is known that repeated thawing and refreezing can drastically reduce the measurable concentration of Aβ. In order to test whether similar effects can be observed in crude and already homogenized fecal samples, the effect of multiple freeze-thaw cycles (none, one, two, three, five, or seven) on the stability of the three samples was investigated according to Andreasson et al. [10]. To this end, six Simplix tubes each were prefilled with the respective crude sample and then stored at −80 °C. In contrast, for the investigation of fecal homogenates, homogenates of three samples were prepared at the beginning of the stability study, whereby the supernatant obtained after centrifugation was divided into six aliquots of 100 µL each. For this purpose, 1.5 mL polypropylene low-binding Eppendorf reaction tubes were used as containers, and all aliquots were frozen at −80 °C. Subsequently, the individual Simplix tubes and the fecal homogenates were thawed successively, while the reference aliquots did not undergo a thaw-freezing process during the study. After an incubation time of 2 h at RT, samples were frozen again for at least 12 h at −80 °C. At the end of the study period, all aliquots were thawed simultaneously and diluted 1:5 with sample buffer, while the crude fecal samples were first homogenized. The data acquisition and analysis of the image data were carried out analogously to the thermostability study.

Assay selectivity

Assay selectivity – investigation of assay controls

To evaluate the selectivity of the sFIDA assay in detecting Aβ-coated SiNaPs (molar particle concentration of 10.26 pM), IQC samples (100 nM, Aβ monomer subunit concentration), and three fecal samples with intermediate to high readouts, we measured the percent signal reduction of capture, autofluorescence, and cross-reactivity control, and compared it to a standard assay setup. To exclude unspecific binding of Aβ to the blocking agent, a capture control (CC) was performed in which no capture antibody was added to the surface. The assay was performed without adding any fluorescent probes to exclude autofluorescence (AF) events from assay components or samples. In addition, we also tested the cross-reactivity of anti-α-synuclein antibodies (detection antibody 211) against the immobilized Aβ species. For each assay control setup, the ratio of observed and expected (standard assay setup) values and the percentage amount of reduced signal were calculated according to Eq.3. Values between 80−120% were accepted for Aβ-coated SiNaPs and IQC sample. In comparison, the tolerance range for fecal samples was increased up to ± 25%.

$$(3)\quad \text{Signal reduction}\,[\%] = \left(1 - \frac{\text{observed readout assay control}}{\text{readout reference}} \times 100\%\right)$$

Assay selectivity – immunodepletion

Immunodepletion was performed on three fecal samples with intermediate to high readouts, Aβ-coated SiNaPs, and IQC samples to determine if the observed pixel counts were specifically attributed to Aβ aggregates and not to interfering fecal matrix components. To this end, the Nab228 antibody was covalently coated on the surface of carboxylated magnetic dynabeads (Invitrogen, Waltham, USA), as previously described by Blömeke et al. [11]. Briefly, the dynabeads were washed twice with 2.5 mM 2-(N-morpholino)ethanesulfonic acid (MES, pH 5.0, Carl Roth, Karlsruhe, Germany) before being applied to a magnet to remove the supernatant. Afterward, carboxy groups of the dynabeads were activated for 30 min at RT using 50 µg/mL EDC and 50 µg/mL NHS in MES, and the dynabeads were rewashed with MES and coated with Nab228 antibody to a concentration of 20 µg/mL dynabeads. The control dynabeads were coated with an α-synuclein-specific antibody 211 to investigate Aβ specificity of the depletion protocol. After antibody incubation for 1 h at RT, coated dynabeads were rewashed, and still activated carboxy groups were quenched with 50 mM ethanolamine in MES for 1 h at RT, followed by a final washing step. We applied 0.5 mg of antibody-coated dynabeads to the magnet for immunodepletion and removed the supernatant. 100 µL sample (10.26 pM Aβ-coated SiNaPs, 100 nM synthetic Aβ1−42 oligomers, and three fecal samples, which were diluted 1:5 in sample buffer before depletion) were added and incubated for 1 h at RT while rotating. After incubation, dynabeads were applied to the magnet again and the supernatant was transferred into a fresh tube and stored at −80 °C until sFIDA analyses. To assess assay selectivity, the efficiency of the immunodepletion was calculated according to Eq.3. The acceptance criteria were the same as for the assay control setup described above.

Assay selectivity – detection of Aβ using ELISA

To confirm whether Aβ species are present in human fecal samples, we used a human amyloid β (1−42) ELISA Assay kit (IBL International, Hamburg, Germany), where total Aβ (monomers and aggregates) was analyzed. Since the ELISA only includes plasma, CSF or cell culture supernatants as sample matrix, the use of fecal samples is not intended. Consequently, it cannot be assumed that the calibration of the optical density (OD) values in molar concentrations is still valid for fecal samples. However, it should at least be applicable for the qualitative detection of Aβ in the feces by comparing the OD values. We investigated two fecal samples (HC and AD donor) which were as follows:

Homogenized: For sample homogenization, 15 mg of each sample were transferred into a low binding Eppendorf tube, which was prefilled with 20 µL H_2O containing protease inhibitor. After homogenization using vortex mixer, homogenates were incubated for 10 min at 95 °C at 600 rpm in order to free as many epitopes as possible. To separate insoluble digestive residues, homogenates were centrifuged for 5 min at 3000× *g*, 4 °C, and supernatants were used for ELISA analysis.

Precipitated: In another preparation approach, we eliminated and enriched Aβ from the sample matrix using immunoprecipitation. To this end, 1.5 g feces per donor were required to obtain 100 µL supernatant. Protein-G magnetic dynabeads (Invitrogen, Waltham, USA) were functionalized with IC16 antibody and homogenized samples were precipitated according to manufactures protocol. Afterward, Aβ was eluted using 10 mM acetic acid, resuspended in H_2O containing protease inhibitor and supernatants were used for ELISA analysis.

Spiked + precipitated: To be sure that Aβ1−42 in stool samples can be determined by the applied ELISA assay, we spiked 100 pg/mL monomeric Aβ1−42 (Bachem, Bubendorf, Switzerland) to the homogenates prior to immunoprecipitation in a third preparation approach. In addition, we conducted a spike and recovery experiment to assess matrix effects. To this end, 100 pg/mL Aβ1−42 were spiked into assay buffer and into homogenized human fecal samples. The recovery rate in percent was calculated for spiked test samples by comparison to the measured recovery of spiked assay buffer control (reference) (see Eq. 4).

$$(4)\quad \text{Recovery rate } [\%] = \frac{\text{assay readout}_{\text{spiked samples}}}{\text{assay readout}_{\text{Reference}}} \times 100\%$$

The ELISA was performed according to manufactures protocol and OD values of the fecal samples of HC and AD were compared.

5

Supplementary Figures

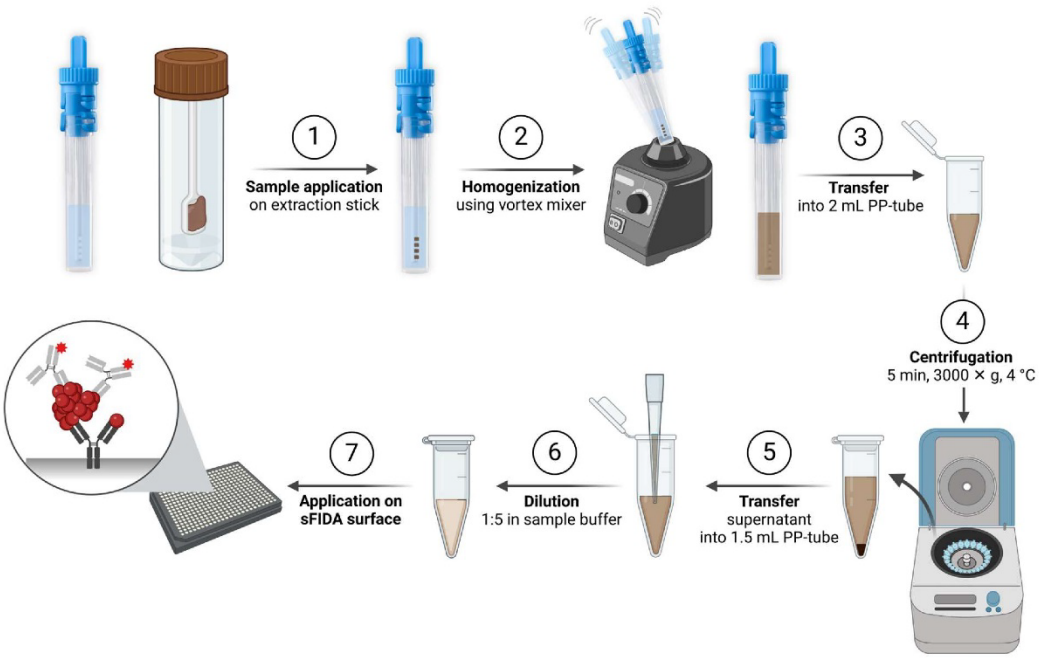

Figure S1. Schematic illustration of the preanalytical processing of fecal samples prior sFIDA analysis, related to Methods. Step1: Simplix tubes were prefilled with cold 1300 µL homogenization buffer. Afterward, thawed fecal samples were applied on a sample stick, whereby the integrated dosing system ensured a sample weight of approximately 17 mg. Due to the liquid consistency, fecal samples with Bristol scale seven were weighted into Simplix tubes. Step 2: samples were homogenized completely using a vortex mixer and incubated for 10 min at RT. Step 3: homogenates were transferred into 2 mL polypropylene low-binding tubes (Eppendorf, Hamburg, Germany). Step 4: since dead bacteria can also show autofluorescence, these and solid components, e.g., undigested food residues, were mechanically separated from the liquid phase by centrifugation (5 min, 3000× g, 4 °C). Step 5: the supernatants were transferred into fresh 1.5 mL polypropylene low-binding tubes and stored at −80 °C before sFIDA analysis. Step 6: homogenates were diluted 1:5 in sample buffer (PBS containing 0.05% Tween, 0.095% NaN3 (AppliChem) and 0.5% BSA). Step 7: diluted homogenates were applied in fourfold determination on sFIDA surface where Aβ aggregates are immobilized by the capture antibody and labeled for microscopy using detection probes.

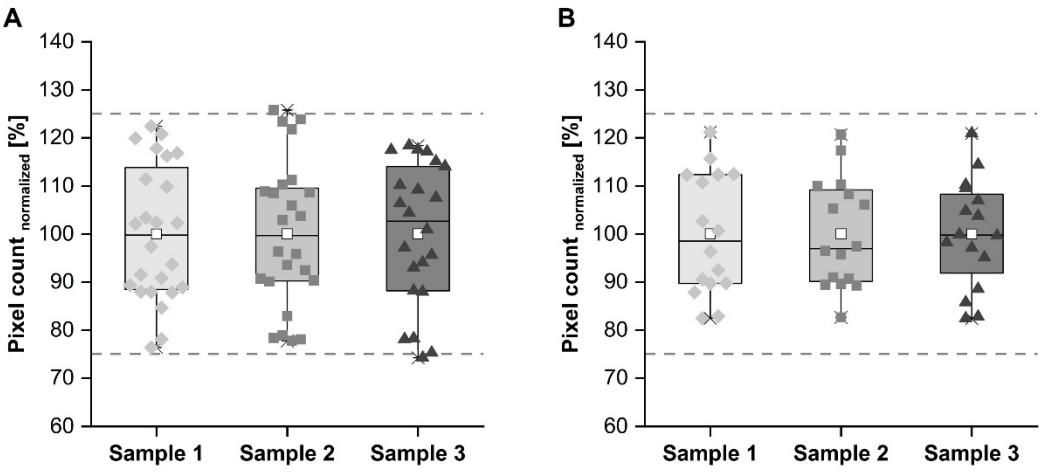

Figure S2. Evaluation of the reproducibility of sample homogenization and dilution for three different fecal samples, related to Results. (**A**) To evaluate the reproducibility of sample homogenization, we prepared six homogenates from each of three different fecal samples. Each homogenate was diluted 1:5 and was measured by sFIDA in 4-fold replicates, and reproducibility was determined based on normalized pixel counts. In detail, the mean pixel count of the 24 data points was calculated. Afterward, the pixel count of each data point was divided by the mean value and multiplied by 100% according to Eq.1. The normalized pixel counts were illustrated as box plot. Consequently, there were 24 data points per box for each of the three samples (except for sample 3, where only 22 data points were available due to measurement artifacts in the affected wells). Intra-assay variances described by CV% of about 15% were recorded for all three samples confirming the reproducibility of the homogenization procedure. Based on documented sample weight, a precision of 98.6% and a trueness of 99.4% were calculated for the sample dosing using Simplix tubes. (**B**) We prepared a 1:5 dilution of each sample homogenate four times and subjected each dilution to sFIDA in quadruplicates. In general, we observed a high reproducibility with normalized pixel counts of the three fecal samples not exceeding the predefined tolerance range of ± 25% and showing low intra-assay variance (CV% of sample 1: 12.6%, samples 2 and 3: 11.3% each). For all replicates, a precision of 88.3% was determined, indicating a high reproducibility of the sample dilution (tolerance range 80−120%). Box plots include the median as a line and the mean of normalized pixel counts as a square. The tolerance range of ± 25% is depicted as dashed gray lines. sample 1 = diamonds, low readout; sample 2 = squares, intermediate readout, and sample 3 = triangles, high readout.

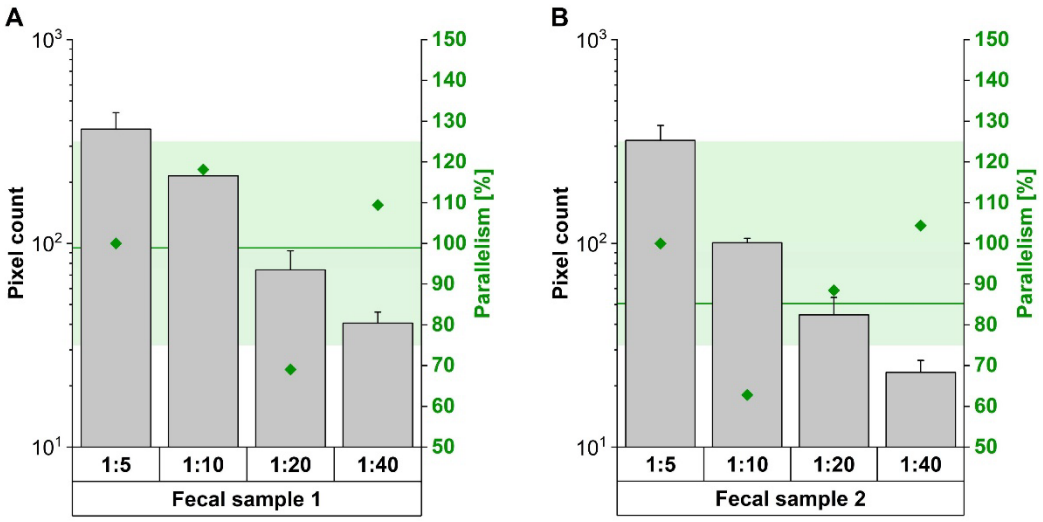

Figure S3. Parallelism of endogenous Aβ aggregates in fecal sample 1 and sample 2, related to Results. We performed a parallelism study using two fecal samples (sample 1 (**A**), sample 2 (**B**) with high endogenous Aβ aggregate concentrations to test whether samples can be diluted linearly. The pixel counts (left y-axis, gray bars) and the calculated percent parallelism (dilution linearity, right y-axis, dark green diamonds) were plotted against the used sample dilution. The acceptance range for percent parallelism was 75−125%, indicated by light green background shading. Mean percent dilution linearities of 99.9%, for sample 1, and 85.2%, for sample 2, were observed, although two values exceeded the lower tolerance limit (1:20 dilution of sample 1, 1:10 dilution of sample 2). Thus, we can exclude strong interferences due to, e.g., heterophilic antibodies, which typically affect dilution linearity [12]. Consequently, samples with a high Aβ aggregate level can be diluted within a linear range and yield reliable results. Data are represented as mean with standard deviation.

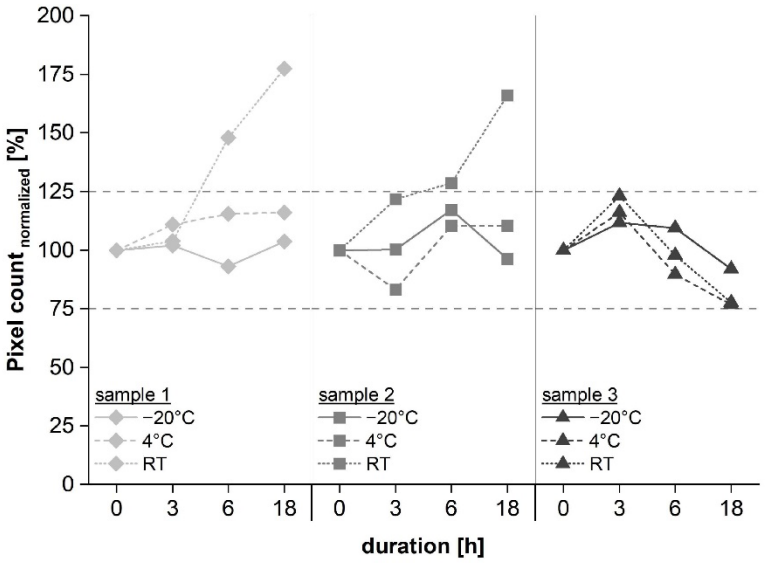

Figure S4. Evaluation of thermostability during transport or bench-top handling, related to Results. To investigate thermostability, three crude fecal samples (sample 1 = diamonds, low readout; sample 2 = square, intermediate readout; sample 3 = triangle, high readout) were stored at −20 °C, 4 °C or 20 °C for 3, 6, or 18 h before they were frozen at −80 °C. Afterward, crude samples were homogenized, diluted 1:5 with sample buffer, and subjected to sFIDA analysis in quadruplicates. Normalized pixel counts were calculated using a non-stressed reference sample and plotted against storage time. Dashed lines indicate the tolerance range of ± 25%. Because none of the samples showed normalized pixel counts outside the tolerance, we assumed that sample stability at −20 °C and 4 °C is not affected within the analyzed time period of 3 to 18h. In contrast, simulated transport or bench-top handling at 20 °C exceeded the tolerance limit after 3 h (sample 1 and sample 2). A signal increase was observed for both samples, which can be explained by increasing autofluorescence caused by decay processes and bacterial growth at this temperature. Consequently, we have decided not to transport or handle the sample at RT and adapted the sFIDA procedure accordingly, i.e., by sufficiently cooling the fecal samples during the preanalytics.

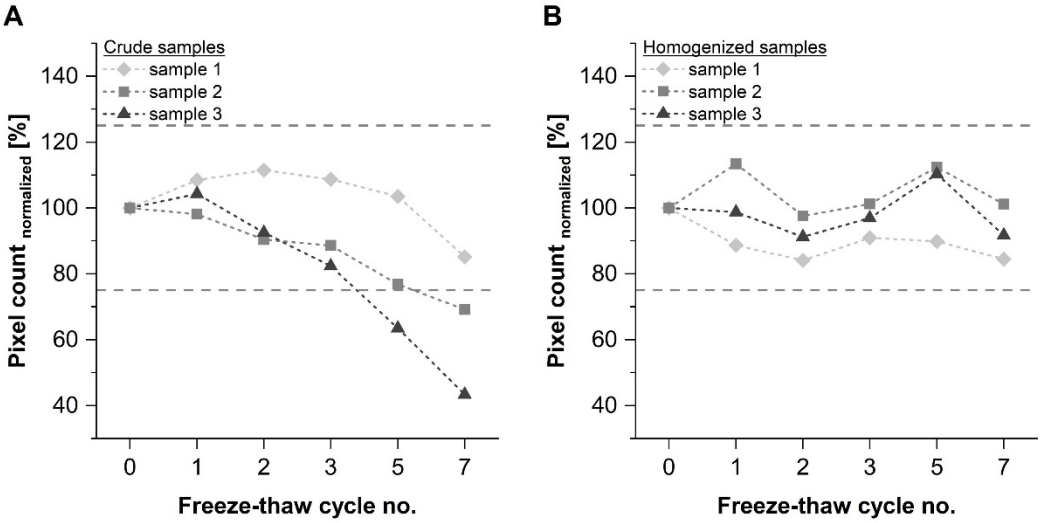

Figure S5. Influence of repeated freeze-thaw cycles on the stability of Aβ aggregates. Normalized pixel counts of three crude (A) or homogenized (B) fecal samples (sample 1 = diamonds, low readout; sample 2 = square, intermediate readout; sample 3 = triangle, high readout) were plotted against freeze-thaw cycles. The tolerance range of ± 25% is depicted as dashed gray lines. In detail, for the crude control sample (sample 1, low readout), neither a signal reduction due to decreased sample stability nor a signal increase was observed. In contrast, a decreasing effect of the number of freeze-thaw cycles on the signal was determined for samples 2 and 3. In particular, repetitive freeze-thaw cycles dramatically reduced the stability of high-readout sample 3. Compared to the reference (no freeze-thaw cycle), a signal loss of 57% was recorded for this sample after thawing and freezing seven times. Considering crude sample 2, an out-of-tolerance value was also recorded at the seventh freeze-thaw cycle, with the measured signal dropping by 31% compared to the reference. In contrast to the crude fecal samples, no signal decrease was observed for the homogenized samples over all freeze-thaw cycles indicating high sample stability after homogenization.

10

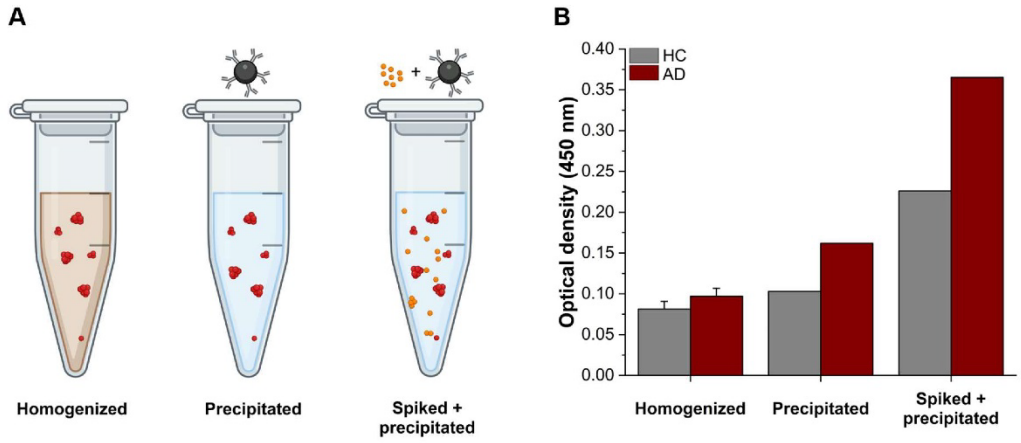

Figure S6. Schematic illustration of sample treatment and confirming the presence of fecal Aβ species in those samples using ELISA, related to Results. To determine total Aβ (monomers and aggregates) in feces, two samples (gray: HC, red: AD patient) were analyzed using a human amyloid β (1−42) ELISA Assay kit (IBL International, Hamburg, Germany). While this ELISA was developed for plasma, CSF, and cell culture supernatants [13], it should at least be applicable for the qualitative detection of Aβ in the feces. We tested the effect of different sample treatments ("homogenized", "precipitated", and "spiked + precipitated", schematic illustration in (**A**), *created with BioRender.com*.) on the discrimination between AD and HC. Signals (**B**) could be detected in those samples that were only homogenized, but no differentiation between both samples was possible. Sensitivity could only be increased by accumulation and elimination of the matrix by immunoprecipitation. This difference between control and AD could be further enhanced by adding Aβ1−42. NOTE. For the immunoprecipitation, a total of 1.5 g feces per donor were required to obtain 100 µL supernatant. Due to the limited amount of feces, only a single determination by ELISA was possible. Therefore, no standard deviation is shown. In case of homogenized samples, data are represented as mean with standard deviation.

Supplementary Tables

Table S1. Overview of the clinical diagnosis of cognitively impaired study participants based on DemTect, Functional Activities Questionnaire (FAQ), Beck Depression Inventory II (BDI-II) or Memory Assessment Clinic-Questionnaire (MAC-Q) and assessment of functional abilities of daily living (ADL, preserved or impaired), related to Methods.

Sample ID	Cohort	DemTect[b]	FAQ	BDI-II	MAC-Q	Functional ADL	Clinical diagnosis
1	AD	4	NA	NA	NA	P	MCI
2	AD	NA	NA	NA	NA	I	dementia
3	AD	NA	NA	NA	NA	P	MCI
4	AD	9	NA	4	NA	P	MCI
5	AD	10	0	2	NA	P	MCI
6	AD	9	NA	25	NA	I	dementia
7	AD	5	NA	30	NA	P	MCI
8	AD	12	NA	29	NA	P	MCI
9	AD	9	NA	29	NA	P	MCI
10	AD	9	5	11	NA	P	MCI
11	AD	2	2	3	10	P	MCI
12	AD	5	15	5	30	I	dementia
13	AD	4	0	6	24	P	MCI
14	AD	7	0	1	22	P	MCI
15	AD	12	2	7	26	P	MCI
16	AD	10	5	9	31	P	MCI
17	AD	5	26	NA	34	I	dementia
18	AD	10	6	9	27	P	MCI
19	AD	9	2	9	33	P	MCI
20	AD	12	0	14	25	P	MCI
21	AD	3	0	3	21	P	MCI
22	AD	11	4	6	24	P	MCI
23	AD	1	18	4	27	P	MCI
24	AD	12	5	8	26	P	MCI
25	AD	11	4	3	25	P	MCI
26	AD	18	0	14	29	P	MCI

[a]NOTE. Raw scores were transformed as described by Kalbe et al. [14].

[b]Abbreviations: AD, Alzheimer's disease; BDI-II, Beck Depression Inventory II; F, female; FAQ, Functional Activities Questionnaire; I, impaired; M, male; MAC-Q, Memory Assessment Clinic-Questionnaire; MCI, mild cognitive impairment; NA, not applicable; P, preserved.

Table S2. Results of normal distribution tests for molar Aβ aggregate concentrations in fecal samples, related to Results.

Normal distribution test	All samples	AD samples	HC samples
Shapiro−Wilk	$2.51*10^{-14}$	$3.37*10^{-8}$	0.003
Lilliefors	$3.99*10^{-19}$	$9.71*10^{-7}$	0.109
Kolmogorov Smirnov	$1.24*10^{-6}$	0.012	0.513
Anderson−Darling	$7.11*10^{-31}$	$6.43*10^{-12}$	0.018

[a]Abbreviations: AD, Alzheimer's disease; HC, healthy controls

Table S3. The coefficient of variation, calculated calibration curve, coefficient of determination and the limit of detection of each experiment for Aβ-coated SiNaPs, IQC samples, and fecal samples, related to Results.

	Experiment 1	Experiment 2	Mean
CV%	S: 11.54	S: 15.15	S: 13.35
	I: 10.91	I: 11.30	I: 11.11
	F: 19.36	F: 18.13	F: 18.74
Calibration curve	Range: 0.32 fM − 1026 fM	Range: 1.03 fM − 1026 fM	-
	y = 1.536x + 6.984	y = 1.118x + 10.88	-
	R^2 = 0.9709	R^2 = 0.9886	R^2 = 0.9798
LoD [fM]	2.27	1.09	1.68

[a]NOTE. CV% are defined as the ratio of standard deviation and the mean of the respective sample quadruplicates. The calibration curve was calculated based on the pixel counts of Aβ-coated SiNaPs using linear regression (readouts were weighted with 1/readout).

[b]Abbreviations: CV%, coefficient of variation; S, Aβ-coated SiNaPs; I, IQC samples; F, fecal samples; R^2, coefficients of determination; LoD, the limit of detection.

Table S4. Clinical information, Bristol scale scores, and mean Aβ aggregate concentrations with the standard deviation of the individual subjects, related to Results, Figure 5B and Figure 5C.

Sample ID	Cohort	Cognition	Clinical symptoms	Sex	Age [years]	Bristol scale	Aβ40 [pg/mL]	Aβ42 [pg/mL]	Ratio Aβ40/Aβ42	tTau [pg/mL]	pTau pg/mL]	Amyloid PET	Tau PET	Fecal Aβ aggregate concentration ± SD [fM]
1	AD	impaired	MCI	M	75	5	NA	475	NA	280	46	pos	pos	1852.5 ± 174.7
2	AD	impaired	dementia	F	84	4	NA	NA	NA	NA	NA	pos	pos	3430.8 ± 773.7
3	AD	impaired	MCI	M	60	4	7224	550.4	0.076	426.9	59	NA	NA	50.9 ± 3.53
4	AD	impaired	MCI	M	68	5	5172	321.3	0.06	479.4	86	NA	NA	49 ± 6.31
5	AD	impaired	MCI	M	79	3	NA	NA	NA	NA	NA	pos	NA	49.4 ± 8.63
6	AD	impaired	dementia	M	76	3	8537	586.4	0.07	671.1	119	NA	NA	798.9 ± 364.6
7	AD	impaired	MCI	M	67	5	4905	248.5	0.051	468.4	69	NA	NA	322.4 ± 45.6
8	AD	impaired	MCI	M	48	5	NA	435	NA	NA	84	NA	NA	273.3 ± 33.9
9	AD	impaired	MCI	F	76	5	9592	851.6	0.089	364.7	68	NA	NA	40.1 ± 3.78
10	AD	impaired	MCI	M	69	3	NA	NA	NA	NA	NA	pos	NA	28.7 ± 3.97
11	AD	impaired	MCI	F	79	4	6890	515.1	0.075	583.7	99	NA	NA	139.7 ± 44.1
12	AD	impaired	dementia	M	79	4	7483	635.77	0.085	614.43	83	NA	NA	215.3 ± 26.2
13	AD	impaired	MCI	F	71	5	10362	621.89	0.06	561.73	110	NA	NA	462.9 ± 143.9
14	AD	impaired	MCI	M	72	3	12703	1138.1	0.09	602	100	NA	NA	120.6 ± 15.7
15	AD	impaired	MCI	M	69	5	4961	401.4	0.081	548	118	NA	NA	45.5 ± 6.66
16	AD	impaired	MCI	F	75	4	8941	806.8	0.09	799	139	NA	NA	53.6 ± 12.4
17	AD	impaired	dementia	F	67	4	8982	787.7	0.088	815	131	NA	NA	387.1 ± 46.2
18	AD	impaired	MCI	F	81	4	6935	566.4	0.082	674	97	NA	NA	268.7 ± 48.4

15

19	AD	impaired	MCI	M	65	4	6507	488.8	0.075	641	129	NA	NA	665.9 ± 312.8
20	AD	impaired	MCI	F	83	5	5272	487.4	0.092	458	65	NA	NA	65.6 ± 4.59
21	AD	impaired	MCI	F	67	3	9276	749.1	0.081	887	164	NA	NA	15.5 ± 1.66
22	AD	impaired	MCI	F	73	6	12451	806	0.065	753	98	NA	NA	165.2 ± 46.4
23	AD	impaired	MCI	M	81	6	7248	537	0.074	531	100	NA	NA	40.3 ± 4.51
24	AD	impaired	MCI	M	64	4	10503	850.2	0.081	699	106	NA	NA	111.5 ± 11.6
25	AD	impaired	MCI	M	60	5	11101	1003.6	0.09	640	126	NA	NA	62.6 ± 12.5
26	AD	impaired	MCI	F	60	6	12364	681.5	0.055	778	125	NA	NA	2.2 ± 0.24
27	HC	normal	no	A	A	5	NA	NA	NA	NA	NA	NA	NA	104 ± 25.7
28	HC	normal	no	A	A	6	NA	NA	NA	NA	NA	NA	NA	190.7 ± 53.2
29	HC	normal	no	A	A	5	NA	NA	NA	NA	NA	NA	NA	49.2 ± 8
30	HC	normal	no	A	A	5	NA	NA	NA	NA	NA	NA	NA	73.3 ± 6.7
31	HC	normal	no	A	A	5	NA	NA	NA	NA	NA	NA	NA	73.6 ± 7.9
32	HC	normal	no	A	A	5	NA	NA	NA	NA	NA	NA	NA	72.9 ± 22.2
33	HC	normal	no	A	A	4	NA	NA	NA	NA	NA	NA	NA	27.4 ± 3.9
34	HC	normal	no	A	A	4	NA	NA	NA	NA	NA	NA	NA	114.9 ± 27.3
35	HC	normal	no	A	A	3	NA	NA	NA	NA	NA	NA	NA	46.2 ± 14.5
36	HC	normal	no	A	A	5	NA	NA	NA	NA	NA	NA	NA	45.7 ± 9
37	HC	normal	no	A	A	5	NA	NA	NA	NA	NA	NA	NA	89.6 ± 15.4
38	HC	normal	no	A	A	5	NA	NA	NA	NA	NA	NA	NA	64 ± 12.4
39	HC	normal	no	A	A	6	NA	NA	NA	NA	NA	NA	NA	45.4 ± 5.7
40	HC	normal	no	A	A	6	NA	NA	NA	NA	NA	NA	NA	86.7 ± 15
41	HC	normal	no	A	A	6	NA	NA	NA	NA	NA	NA	NA	62.7 ± 12.1
42	HC	normal	no	A	A	5	NA	NA	NA	NA	NA	NA	NA	22.6 ± 4.4
43	HC	normal	no	A	A	6	NA	NA	NA	NA	NA	NA	NA	23.9 ± 7.1
44	HC	normal	no	A	A	6	NA	NA	NA	NA	NA	NA	NA	56.6 ± 12.7

16

45	HC	normal	no	A	A	5	NA	NA	NA	NA	NA	NA	NA	58 ± 14.7
46	HC	normal	no	A	A	6	NA	NA	NA	NA	NA	NA	NA	198.5 ± 49.6
47	HC	normal	no	A	A	4	NA	NA	NA	NA	NA	NA	NA	67.1 ± 7.4
48	HC	normal	no	A	A	6	NA	NA	NA	NA	NA	NA	NA	32.9 ± 5.8
49	HC	normal	no	A	A	5	NA	NA	NA	NA	NA	NA	NA	99.3 ± 20.2
50	HC	normal	no	A	A	4	NA	NA	NA	NA	NA	NA	NA	11.3 ± 3.2
51	HC	normal	no	A	A	5	NA	NA	NA	NA	NA	NA	NA	5.1 ± 1.2
52	HC	normal	no	A	A	5	NA	NA	NA	NA	NA	NA	NA	96.4 ± 16.6
53	HC	normal	no	A	A	6	NA	NA	NA	NA	NA	NA	NA	15.6 ± 2
54	HC	normal	no	A	A	6	NA	NA	NA	NA	NA	NA	NA	33.2 ± 4.6
55	HC	normal	no	A	A	6	NA	NA	NA	NA	NA	NA	NA	36.3 ± 6.5
56	HC	normal	no	A	A	5	NA	NA	NA	NA	NA	NA	NA	13.6 ± 1.6
57	HC	normal	no	A	A	4	NA	NA	NA	NA	NA	NA	NA	1.3 ± 0.5

[a]Abbreviations: A, anonymized, Aβ, amyloid-beta, AD, Alzheimer's disease; MCI, mild cognitive impairment; HC, healthy controls; NA, not applicable, PET, Positron emission tomography, SD, standard deviation.

17

Table S5. Spearman coefficient of correlation values for the analyses between fecal Aβ aggregate levels and seven fecal biomarkers indicating gut inflammation and increased permeability of intestinal membranes (bile acid, lipids, calprotectin, IgA, α-1-antitrypsin, hemoglobin, and albumin), related to Results.

Biomarker	Bile acid	Lipids	Calpro-tectin	IgA	α1-Anti-trypsin	Hemo-globin	Albumin	Aβ aggregates
Bile acid	1	0.5181*	−0.1580	−0.1596	−0.0164	0.2236	0.0039	−0.1108
Lipids		1	−0.2998	0.0778	−0.2737	0.0854	0.1134	−0.3805
Calprotectin			1	0.5941*	0.5845*	0.4669	0.5911*	0.1489
IgA				1	0.2336	0.2423	0.6071*	−0.0118
α1-Antitrypsin					1	0.3872	0.0731	0.3564
Hemoglobin						1	0.5965*	−0.0121
Albumin							1	−0.3665
Aβ aggregates								1

[a]NOTE. Significant correlations are indicated by * p: ≤ 0.05.

Table S6. *p*-values of two-sided Mann−Whitney U test for pairwise comparisons of measured fecal biomarker concentrations, related to Results.

Biomarker	AD (n = 7)	HC (n = 8)	*p*-value
Bile acid [mmol/100 g]	350 ± 91.7	272 ± 70.5	0.1321
Lipids wt%	1.6 ± 0.7	1.6 ± 0.6	0.8608
Calprotectin [µg/g]	40.3 ± 27.5	53.5 ± 32.5	0.3524
IgA [µg/g]	1444 ± 2041	1716 ± 1433	0.2699
α1-Antitrypsin [µg/g]	39.1 ± 22.7	61.8 ± 47.6	0.1753
Hemoglobin [µg/g]	0.3 ± 0	0.4 ± 0.3	0.2036
Albumin [µg/g]	4.1 ± 2.0	9.8 ± 10.9	0.1870

[a]NOTE. No significant differences of fecal biomarker concentrations between AD patients and HC were found. [b]Abbreviations: AD, Alzheimer's disease; HC, healthy controls.

Supplemental References

[1] Kass, B., et al., *Aβ oligomer concentration in mouse and human brain and its drug-induced reduction ex vivo.* Cell Rep Med, 2022. **3**(5): p. 100630.

[2] Vagenende, V., M.G. Yap, and B.L. Trout, *Mechanisms of protein stabilization and prevention of protein aggregation by glycerol.* Biochemistry, 2009. **48**(46): p. 11084-96.

[3] Rose, C., et al., *The Characterization of Feces and Urine: A Review of the Literature to Inform Advanced Treatment Technology.* Crit Rev Environ Sci Technol, 2015. **45**(17): p. 1827-1879.

[4] Stephen, A.M. and J.H. Cummings, *The microbial contribution to human faecal mass.* J Med Microbiol, 1980. **13**(1): p. 45-56.

[5] Phadia-AB. *Stool Extraction Kit plus / Stool Extraction Buffer plus, instruction for use: 200/250/2500/5000-6665-020 / UK, version 2021-09-14.* . 2021; Available on https://dfu.phadia.com/Data/Pdf/6130cb9570eec660e274806b.pdf [Accessed 23 January 2023].].

[6] ORGENTEC-Diagnostika-GmbH. *Calprotectin, instruction for use: ORG 580_4, version ORG 580_IFU_EN_QM140866_2022-03-08_4.* 2022; Available on https://products.orgentec.com/pdfs/ifu/ORG%20580_IFU_EN_QM140866_2022-03-08_4.pdf [Accessed 23 January 2023].].

[7] Bühlmann-Laboratories. *Bühlmann Smart-Prep - Faecal sample preparation kit, Instruction for use: B-CAL-RD, version 2010-11-10.* 2010; Available on https://www.buhlmannlabs.ch/wp-content/uploads/2015/01/B-CAL-RD_101110.pdf [Accessed 23 January 2023].].

[8] Immundiagnostik-AG. *IDK Hemoglobin ELISA: For the in vitro determination of hemoglobin in stool, instruction for use: K 7816D, K7816D.20, version 2022-02-22.* 2022; Available on https://www.immundiagnostik.com/media/pages/testkits/k-7816d/9a63870b70-1663639307/k7816d_2022-02-22_haemoglobin.pdf [Accessed 23 January 2023].].

[9] Demeditec-Diagnostics-GmbH. *Calprotectin ELISA, instruction for use: DE849 V211014/DLB, version 2021-11-25.* . 2021; Available on https://www.demeditec.de/de/produkte/calprotectin-elisa-de849/ifu-de849-calprotectin-elisa-211125-e.pdf [Accessed 23 January 2023].].

[10] Andreasson, U., et al., *A Practical Guide to Immunoassay Method Validation.* Front Neurol, 2015. **6**: p. 179.

[11] Blömeke, L., et al., *Quantitative detection of α-Synuclein and Tau oligomers and other aggregates by digital single particle counting.* NPJ Parkinsons Dis, 2022. **8**(1): p. 68.

[12] Park, J.Y. and L.J. Kricka, *Chapter 5.3 - Interferences in Immunoassay*, in *The Immunoassay Handbook (Fourth Edition)*, D. Wild, Editor. 2013, Elsevier: Oxford. p. 403-416.

[13] IBL-international. *Amyloid-beta (1-42) (FL) ELISA Instruction for use Code No. 27719, version 2.* 2016; Available on https://www.ibl-america.com/content/elisa/27719.pdf [Accessed 23 January 2023].].

[14] Kalbe, E., et al., *DemTect: a new, sensitive cognitive screening test to support the diagnosis of mild cognitive impairment and early dementia.* Int J Geriatr Psychiatry, 2004. **19**(2): p. 136-43.

Anhang 6 – Weitere Informationen zu Kapitel 2.2.4

IAPP - oligomerisation levels in plasma of people with type 2 diabetes

Authors: Fabian Rehn[a,1,2,3], Victoria Kraemer-Schulien[a,2], Tuyen Bujnicki[2], Oliver Bannach[2,1,3], Diethelm Tschoepe[4,5], Bernd Stratmann[b,4*], Dieter Willbold[b,2,1,3*]

a: All authors contributed equally. The order was set randomly.

b: Lead Contact, shared last authorship

[1]Institut für Physikalische Biologie, Heinrich-Heine-Universität Düsseldorf, Universitätsstr. 1, 40225 Düsseldorf, Germany.

[2]Institute of Biological Information Processing (Structural Biochemistry: IBI-7), Forschungszentrum Jülich GmbH, Wilhelm-Johnen-Straße, 52428 Jülich, Germany.

[3]attyloid GmbH, Merowingerplatz 1A, 40225 Düsseldorf, Germany.

[4]Herz- und Diabeteszentrum Nordrhein-Westfalen, Universitätsklinik der Ruhr-Universität Bochum, Medizinische Fakultät OWL (Universität Bielefeld), Georgstr. 11, D-32545 Bad Oeynhausen, Germany

[5]Stiftung DHG (Diabetes I Herz I Gefäße) in der Deutschen Diabetes Stiftung c/o Deutsches Diabetes-Zentrum (DDZ), Auf´m Hennekamp 65, 40225 Düsseldorf, Germany

*Corresponding Authors:

Prof. Dr. Dieter Willbold, Forschungszentrum Jülich GmbH, Institute of Biological Information Processing (IBI-7), Forschungszentrum Jülich, Wilhelm-Johnen-Straße, 52428 Jülich, Germany

Tel.: +49 2461 61 2100; E-Mail: d.willbold@fz-juelich.de

PD Dr. rer. nat. Bernd Stratmann, Herz- und Diabeteszentrum Nordrhein-Westfalen, Universitätsklinik der Ruhr-Universität Bochum, Medizinische Fakultät OWL (Universität Bielefeld), Georgstr. 11, D-32545 Bad Oeynhausen, Germany

Tel. 05731 973768, E-Mail: bstratmann@hdz-nrw.de

Supplement

Sup. Table 1: Test for normal distribution

Test	*P* value
Shapiro-Wilk	*1.306e-13*
Kolmogorov-Smirnov	*4.393e-12*
D'Agostino's K-squared	*7.980e-18*

To select suitable statistical methods, the oligomerisation level was analysed using various tests for normal distribution. None of the tests indicated a normal distribution.

Sup. Table 2: Confounding factor: Age

Diagnosis group	r value	*P* value
control	-0.207	0.368
T2D without complications	-0.069	0.823
T2D with complications	-0.142	0.600

Using a two-sided Spearman correlation test, it was investigated whether there is a correlation between oligomerisation level and age in any of the diagnostic groups. No significant correlation was found in any of the groups.

3

Sup. Table 3: Confounding factor: Gender

Diagnostic group	*P* value
control	0.916
T2D without complications	0.231
T2D with complications	0.417

Using a two-sided Mann-Whitney U test, it was investigated whether there are significant differences in oligomerisation levels depending on gender within the diagnostic groups. No significant differences were found in any of the groups.

Sup. Table 4: Correlation of IAPP with disease years

T2D group	IAPP Type	r value	*P* value
Without complications	Oligomerisation level	0.439	0.133
Without complications	Oligomer concentration	0.433	0.139
Without complications	Total IAPP concentration	-0.189	0.537
With complications	Oligomerisation level	-0.394	0.132
With complications	Oligomer concentration	-0.619	0.011
With complications	Total IAPP concentration	-0.389	0.137

Using a two-sided Spearman correlation test, the correlation between various IAPP types and the duration of the disease in years was investigated.

4

Sup. Table 5: Correlation of IAPP with disease years during first 10 years

T2D group	IAPP Type	r value	*P* value
Without complications	Oligomerisation level	0.617	0.033
Without complications	Oligomer concentration	0.688	0.013
Without complications	Total IAPP concentration	-0.298	0.347
With complications	Oligomerisation level	-0.054	0.908
With complications	Oligomer concentration	0.162	0.728
With complications	Total IAPP concentration	-0.391	0.386

Using a two-sided Spearman correlation test, the correlation between various IAPP types and the duration of the disease in years was investigated. Data is limited to a maximum disease duration of 10 years.

Sup. Table 6: Correlation of IAPP with HbA1c [in % (4,3-6,1)]

T2D group	IAPP Type	r value	*P* value
Without complications	Oligomerisation level	0.320	0.287
Without complications	Oligomer concentration	0.163	0.596
Without complications	Total IAPP concentration	-0.661	0.014
With complications	Oligomerisation level	0.279	0.295
With complications	Oligomer concentration	-0.007	0.978
With complications	Total IAPP concentration	-0.231	0.389

Using a two-sided Spearman correlation test, the correlation between various IAPP types and HbA1c in serum was investigated.

5

Sup. Table 7: Correlation of IAPP with HbA1c [in % (4,3-6,1)] during first 10 years

T2D group	IAPP Type	r value	*P* value
Without complications	Oligomerisation level	0.340	0.280
Without complications	Oligomer concentration	0.196	0.541
Without complications	Total IAPP concentration	-0.690	0.013
With complications	Oligomerisation level	-0.143	0.760
With complications	Oligomer concentration	-0.571	0.180
With complications	Total IAPP concentration	-0.198	0.670

Using a two-sided Spearman correlation test, the correlation between various IAPP types and the HbA1c in serum was investigated. Data is limited to a maximum disease duration of 10 years.

Sup. Table 8: Correlation of IAPP oligomerisation levels with Insulin mU/l in serum

Group	r value	*P* value
All Samples	-0.277	0.052
Control	-0.517	0.017
T2D (both subgroups)	-0.249	0.193

Using a two-sided Spearman correlation test, the correlation between IAPP oligomerisation level and insulin in serum was investigated.

6

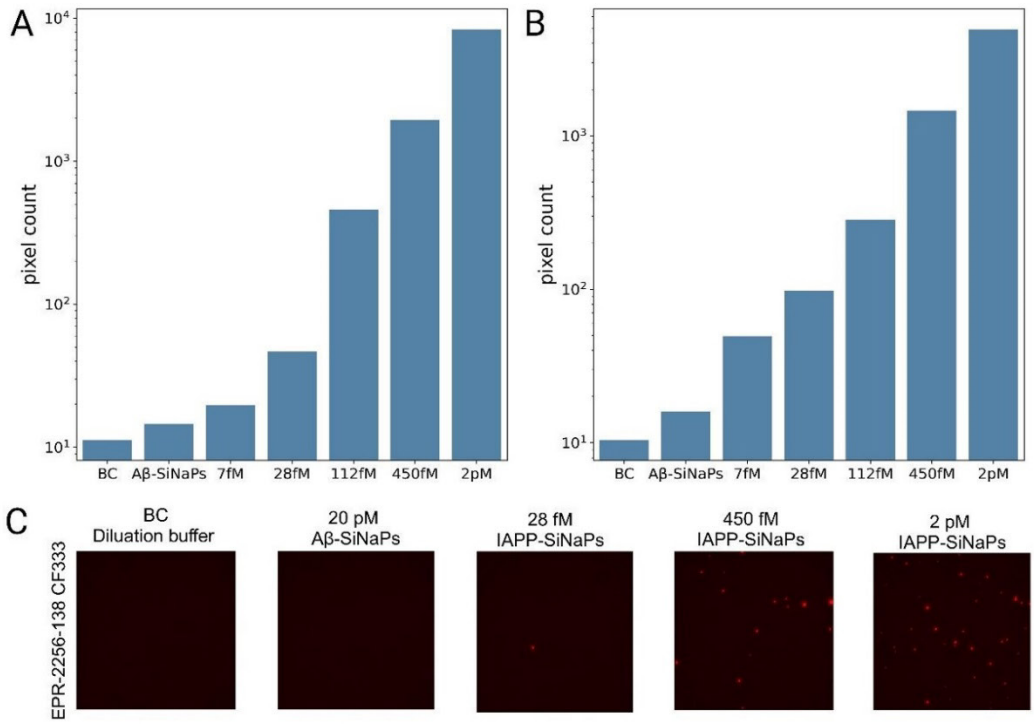

Sup. Figure 1: Assay Controls

Figure A) and B) shows assay controls for the two individual experiments. For both experiments, the BC provides the lowest signals. Aβ-SiNaPs lead to a slight increase in signal in both cases, however, it should be noted that non-physiologically high concentrations (20 pM) were used here, which means that no influence on the results is to be expected at physiological concentrations. It is also shown that the signal increases considerably with increasing concentrations (7 fM – 2 pM) of IAPP SiNaPs. Figure C) show the corresponding TIFFs Images.

7

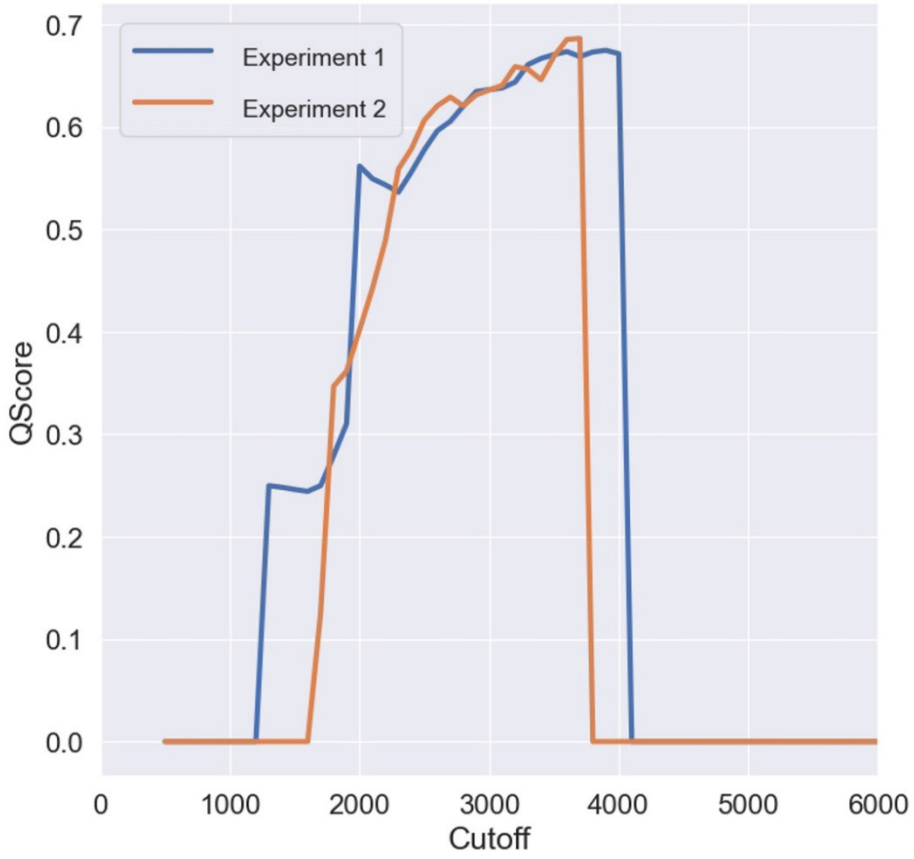

Sup. Figure 2: Cut-off optimisation results

QScores of the individual experiments in relation to the applied cut-off. It shows that the QScore develops very similarly in both experiments. The maximum QScore of 0.675 and 0.686 is reached at a cut-off of 3900 and 3700 respectively.

8

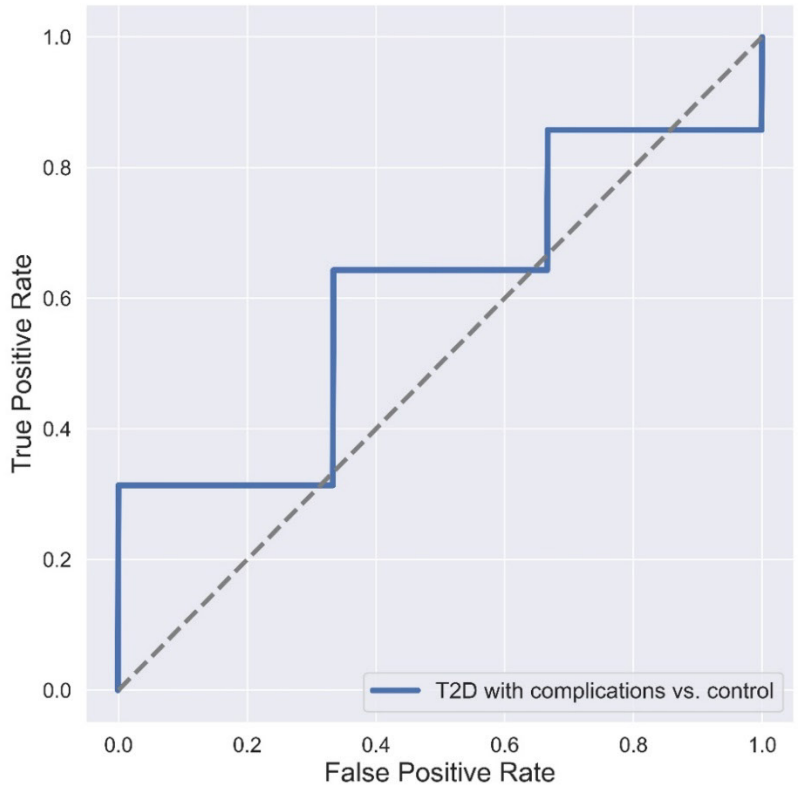

Sup. Figure 3: ROC-Curves

ROC analysis was carried out to assess the ability to classify individuals based on the oligomerisation level. For this purpose, a randomised and stratified split into training and test set was carried out. ROC curves were then created using a logistic regression. Due to the small group size, the result depends heavily on the split. Therefore, the procedure was repeated a thousand times with different random seeds to determine the mean ROC curve and the mean AUC (0.61).

9

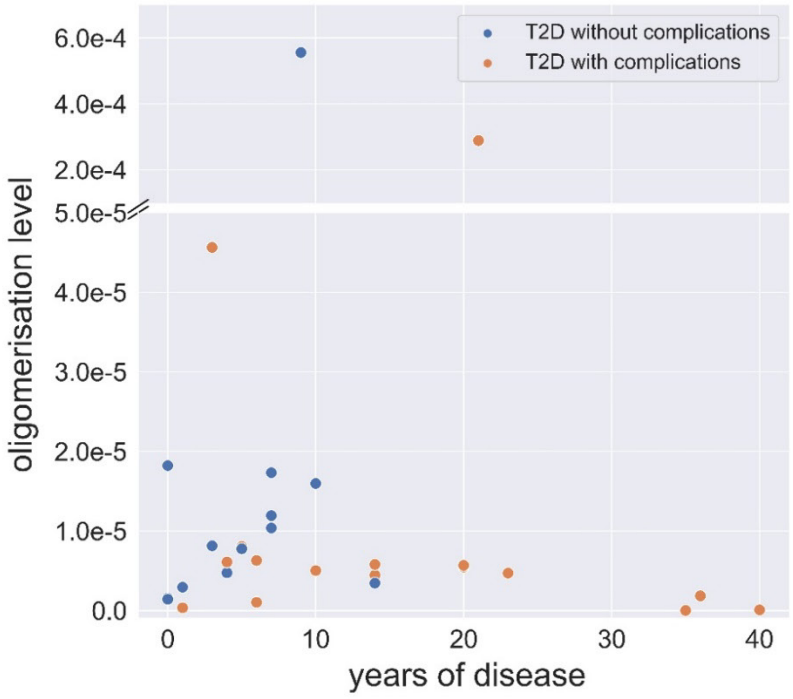

Sup. Figure 4: T2D oligomerisation level in relation to the years of disease

Relation between oligomerisation level and years of disease of both T2D subgroups. Please, note the two-part y-axis, which removes free space.

References

1 Polonsky, K. Dynamics of insulin secretion in obesity and diabetes. *International journal of obesity* **24**, S29-S31 (2000).

2 Butler, A. E. *et al.* β-cell deficit and increased β-cell apoptosis in humans with type 2 diabetes. *Diabetes* **52**, 102-110 (2003).

3 Meir, J. *et al.* The vascular complications of diabetes: a review of their management, pathogenesis, and prevention. *Expert Review of Endocrinology & Metabolism* **19**, 11-20 (2024).

4 Orozco, L. J. *et al.* Exercise or exercise and diet for preventing type 2 diabetes mellitus. *Cochrane database of systematic reviews* (2008).

5 Sladek, R. *et al.* A genome-wide association study identifies novel risk loci for type 2 diabetes. *Nature* **445**, 881-885 (2007).

6 Chatterjee, S., Khunti, K. & Davies, M. J. Type 2 diabetes. *The lancet* **389**, 2239-2251 (2017).

7 Abdul Basith Khan, M. *et al.* Epidemiology of type 2 diabetes—global burden of disease and forecasted trends. *Journal of epidemiology and global health* **10**, 107-111 (2020).

8 Haataja, L., Gurlo, T., Huang, C. J. & Butler, P. C. Islet amyloid in type 2 diabetes, and the toxic oligomer hypothesis. *Endocrine reviews* **29**, 303-316 (2008).

9 DiMeglio, L. A., Evans-Molina, C. & Oram, R. A. Type 1 diabetes. *The Lancet* **391**, 2449-2462 (2018).

10 Kahn, S. E. *et al.* Evidence of cosecretion of islet amyloid polypeptide and insulin by β-cells. *Diabetes* **39**, 634-638 (1990).

11 Mulder, H., Ahren, B., Stridsberg, M. & Sundler, F. Non-parallelism of islet amyloid polypeptide (amylin) and insulin gene expression in rat islets following dexamethasone treatment. *Diabetologia* **38**, 395-402 (1995).

12 Westermark, P., Engström, U., Johnson, K. H., Westermark, G. T. & Betsholtz, C. Islet amyloid polypeptide: pinpointing amino acid residues linked to amyloid fibril formation. *Proceedings of the National Academy of Sciences* **87**, 5036-5040 (1990).

13 Kahn, S. E., Andrikopoulos, S. & Verchere, C. B. Islet amyloid: a long-recognized but underappreciated pathological feature of type 2 diabetes. *Diabetes* **48**, 241-253 (1999).

14 Janson, J., Ashley, R. H., Harrison, D., McIntyre, S. & Butler, P. C. The mechanism of islet amyloid polypeptide toxicity is membrane disruption by intermediate-sized toxic amyloid particles. *Diabetes* **48**, 491-498 (1999).

15 Gurlo, T. *et al.* Evidence for proteotoxicity in β cells in type 2 diabetes: toxic islet amyloid polypeptide oligomers form intracellularly in the secretory pathway. *The American journal of pathology* **176**, 861-869 (2010).

16 Lin, C.-Y. *et al.* Toxic human islet amyloid polypeptide (h-IAPP) oligomers are intracellular, and vaccination to induce anti-toxic oligomer antibodies does not prevent h-IAPP–induced β-cell apoptosis in h-IAPP transgenic mice. *Diabetes* **56**, 1324-1332 (2007).

17 Kanatsuka, A., Kou, S. & Makino, H. IAPP/amylin and β-cell failure: Implication of the risk factors of type 2 diabetes. *Diabetology international* **9**, 143-157 (2018).

18 Masters, S. L. *et al.* Activation of the NLRP3 inflammasome by islet amyloid polypeptide provides a mechanism for enhanced IL-1β in type 2 diabetes. *Nature immunology* **11**, 897-904 (2010).

19 Willbold, D., Strodel, B., Schröder, G. F., Hoyer, W. & Heise, H. Amyloid-type protein aggregation and prion-like properties of amyloids. *Chemical reviews* **121**, 8285-8307 (2021).

20 Moreno-Gonzalez, I. *et al.* Molecular interaction between type 2 diabetes and Alzheimer's disease through cross-seeding of protein misfolding. *Molecular psychiatry* **22**, 1327-1334 (2017).

21 Röder, C. *et al.* Cryo-EM structure of islet amyloid polypeptide fibrils reveals similarities with amyloid-β fibrils. *Nature structural & molecular biology* **27**, 660-667 (2020).

22 Gremer, L. *et al.* Fibril structure of amyloid-β (1–42) by cryo–electron microscopy. *Science* **358**, 116-119 (2017).

23 Hu, R., Zhang, M., Chen, H., Jiang, B. & Zheng, J. Cross-seeding interaction between β-amyloid and human islet amyloid polypeptide. *ACS chemical neuroscience* **6**, 1759-1768 (2015).

24 Blömeke, L. *et al.* Quantitative detection of α-Synuclein and Tau oligomers and other aggregates by digital single particle counting. *npj Parkinson's Disease* **8**, 68 (2022).

25 Blömeke, L. *et al.* Aβ oligomers peak in early stages of Alzheimer's disease preceding tau pathology. *Alzheimer's & Dementia: Diagnosis, Assessment & Disease Monitoring* **16**, e12589 (2024).

26 Kass, B. *et al.* Aβ oligomer concentration in mouse and human brain and its drug-induced reduction ex vivo. *Cell Reports Medicine* **3** (2022).

27 Kravchenko, K. *et al.* Analysis of anticoagulants for blood-based quantitation of amyloid β oligomers in the sFIDA assay. *Biological chemistry* **398**, 465-475 (2017).

28 Camargo, D. C. R. *et al.* hIAPP forms toxic oligomers in plasma. *Chemical Communications* **54**, 5426-5429 (2018).

29 Larson, J. L. & Miranker, A. D. The mechanism of insulin action on islet amyloid polypeptide fiber formation. *Journal of molecular biology* **335**, 221-231 (2004).

30 Baram, M., Gilead, S., Gazit, E. & Miller, Y. Mechanistic perspective and functional activity of insulin in amylin aggregation. *Chemical science* **9**, 4244-4252 (2018).

31 Gilead, S., Wolfenson, H. & Gazit, E. Molecular mapping of the recognition interface between the islet amyloid polypeptide and insulin. *Angewandte Chemie* **118**, 6626-6630 (2006).

32 Jackson, K. *et al.* Amylin deposition in the brain: a second amyloid in Alzheimer disease? *Annals of neurology* **74**, 517-526 (2013).

33 Amidei, C. B. *et al.* Association between age at diabetes onset and subsequent risk of dementia. *Jama* **325**, 1640-1649 (2021).

34 Athanasaki, A. *et al.* Type 2 diabetes mellitus as a risk factor for Alzheimer's disease: Review and meta-analysis. *Biomedicines* **10**, 778 (2022).

35 Liu, L. *et al.* Differences in metabolite profile between blood plasma and serum. *Analytical biochemistry* **406**, 105-112 (2010).

36 Ly, H. *et al.* Brain microvascular injury and white matter disease provoked by diabetes-associated hyperamylinemia. *Annals of neurology* **82**, 208-222 (2017).

37 Kotiya, D. *et al.* Rapid, scalable assay of amylin-β amyloid co-aggregation in brain tissue and blood. *Journal of Biological Chemistry* **299** (2023).

Anhang 7 – Weitere Informationen zu Kapitel 2.2.5

Quantitative Detection of α-Synuclein and Tau Oligomers and other Aggregates by Digital Single Particle Counting

Lara Blömeke, Marlene Pils, Victoria Kraemer-Schulien, Alexandra Dybala, Anja Schaffrath, Andreas Kulawik, Fabian Rehn, Anne Cousin, Volker Nischwitz, Johannes Willbold, Rebecca Zack, Thomas F. Tropea, Tuyen Bujnicki, Gültekin Tamgüney, Daniel Weintraub, David Irwin, Murray Grossman, David A. Wolk, John Q. Trojanowski, Oliver Bannach, Alice Chen-Plotkin, Dieter Willbold

Supplementary Information

Supplementary Table 1 CV% values of each experiment for SiNaPs and CSF samples

	aSyn		Tau	
Experiment	Calibration	Samples	Calibration	Samples
1	18.05	22.08	20.42	18.62
2	22.18	32.86	30.27	19.45
3	17.33	20.71	23.00	15.66
4	14.63	12.58	18.60	10.81
5	11.71	9.16	12.54	8.66
6	14.87	12.70	16.01	9.58
7	16.99	13.86	15.15	10.15
8	10.29	10.58	16.77	10.84
Mean	15.76	16.82	19.10	12.97

Supplementary Table 2 LOD values for aSyn- and Tau silica nanoparticles [fM] for each experiment

Experiment	aSyn	Tau
1	9.59	36.69
2	20.72	70.09
3	6.76	32.04
4	1.67	10.09
5	6.08	-
6	2.43	-
7	3.53	-
8	2.98	19.41
Mean	6.72	33.7

Supplementary Table 3 Number of samples above the LOD for each individual experiment

Experiment	aSyn	Tau
1	11	8
2	13	6
3	18	19
4	23	9
5	17	5
6	27	24
7	20	15
8	27	18
Sum	156	104

Supplementary Table 4 Demographic information, aSyn and Tau aggregate concentrations and blood contamination level of each individual patient CSF sample

Sample	*Diagnosis*	*Sex*	*Deceased*	*Education (years)*	*Age at Sample*	*aSyn aggregate concentration [fM]*	*StdDev aSyn*	*Tau aggregate concentration [fM]*	*StdDev Tau*	*Blood contamination level*
1	AD	Male	True	16	72.00	0.00	0.00	0.00	0.00	0
2	AD	Female	True	12	68.00	3.51	0.30	1.60	0.23	0
3	AD	Male	False	18	75.00	8.84	0.36	0.00	0.00	0
4	AD	Male	True	18	75.00	24.20	3.20	0.00	0.00	0
5	AD	Female	False	6	65.00	75.75	12.31	12.70	0.38	0
6	AD	Female	True	15	65.00	0.00	0.00	0.00	0.00	0
7	AD	Female	False	18	65.00	521.47	116.08	20.11	2.04	4
8	AD	Male	False	11	77.00	9.52	1.14	0.00	0.00	0
9	AD	Female	False	16	76.00	18.48	1.37	0.00	0.00	4
10	AD	Male	True	16	61.00	144.55	14.95	0.00	0.00	0
11	AD	Male	True	12	68.00	0.00	0.00	0.00	0.00	0
12	AD	Male	False	18	66.00	66.46	7.84	0.00	0.00	0
13	AD	Male	False	20	81.00	202.30	16.43	22.69	2.87	0
14	AD	Female	False	16	75.00	156.65	32.57	16.87	2.12	0
15	AD	Male	True	12	69.00	15.41	1.25	0.00	0.00	2
16	AD	Female	False	18	70.00	0.00	0.00	0.00	0.00	1
17	AD	Female	False	20	75.00	0.00	0.00	0.00	0.00	0
18	AD	Male	False	12	64.00	0.00	0.00	0.00	0.00	3
19	AD	Male	False	12	73.00	221.12	31.78	19.19	1.78	4
20	AD	Male	False	12	63.00	12.42	2.29	6.79	0.53	4
21	AD	Male	True	16	66.00	37.81	6.06	9.82	0.83	0
22	AD	Male	False	18	68.00	33.69	2.30	35.38	3.16	1
23	AD	Female	False	15	69.00	0.00	0.00	4.93	0.50	4
24	AD	Male	False	12	56.00	0.00	0.00	0.99	0.06	1
25	AD	Male	True	14	55.00	11.58	1.01	10.33	1.09	0
26	AD	Female	False	12	68.00	120.74	16.88	8.98	0.83	0
27	AD	Male	False	16	66.00	8.32	0.66	12.36	0.66	2
28	AD	Male	False	16	59.00	85.40	9.02	20.72	1.71	4

29	DLB	Male	True	12	73.00	12.20	1.76	11.07	1.02	0
30	DLB	Male	False	12	67.00	8.52	1.31	0.00	0.00	0
31	DLB	Female	False	18	68.00	2.57	0.36	0.00	0.00	3
32	DLB	Male	False	16	79.00	886.05	65.57	75.02	4.34	0
33	DLB	Female	False	20	58.00	0.00	0.00	12.05	0.74	0
34	DLB	Female	True	12	66.00	13.02	1.20	14.56	2.10	0
35	DLB	Female	False	14	87.00	2.38	0.22	0.00	0.00	2
36	DLB	Male	False	18	66.00	70.49	6.04	0.00	0.00	0
37	DLB	Male	True	20	66.00	3.75	0.15	0.00	0.00	0
38	DLB	Male	False	14	74.00	0.00	0.00	3.14	0.51	2
39	DLB	Male	True	19	65.00	7.88	0.84	12.38	0.96	0
40	DLB	Male	True	12	70.00	0.00	0.00	13.39	0.53	0
41	DLB	Male	False	12	72.00	370.27	51.32	27.96	3.86	0
42	DLB	Male	False	16	68.00	22.03	3.69	12.43	0.76	0
43	DLB	Male	True	18	63.00	78.99	3.33	8.12	0.60	2
44	DLB	Male	False	14	84.00	13.47	1.75	1.89	0.14	1
45	DLB	Male	False	16	68.00	2949.10	470.68	153.28	17.66	0
46	DLB	Male	False	16	63.00	136.01	24.98	10.69	1.15	2
47	DLB	Female	False	16	68.00	11.73	1.42	12.32	0.51	0
48	N	Female	False	18	70.00	0.00	0.00	0.00	0.00	3
49	N	Female	False	18	73.00	81.98	22.45	0.00	0.00	0
50	N	Male	False	16	57.00	0.00	0.00	0.00	0.00	0
51	N	Male	False	12	61.00	0.00	0.00	36.89	7.70	2
52	N	Male	False	18	74.00	0.00	0.00	0.00	0.00	0
53	N	Female	True	20	70.00	0.00	0.00	0.00	0.00	0
54	N	Male	True	19	83.00	0.00	0.00	0.00	0.00	4
55	N	Female	False	18	74.00	0.00	0.00	24.30	4.41	1
56	N	Male	False	18	75.00	0.00	0.00	0.00	0.00	3
57	N	Female	False	16	58.00	43.36	8.97	0.00	0.00	0
58	N	Male	False	16	67.00	119.16	46.24	37.25	5.88	1
59	N	Female	False	20	69.00	0.00	0.00	0.00	0.00	3
60	N	Male	False	20	60.00	72.13	8.67	7.79	0.62	0
61	N	Male	False	12	62.00	0.00	0.00	0.00	0.00	0
62	N	Male	False	20	77.00	0.00	0.00	0.00	0.00	0

63	N	Female	False	18	63.00	0.00	0.00	0.00	0.00	0
64	N	Female	False	12	59.00	602.80	231.60	110.63	16.15	3
65	N	Female	False	20	57.00	13.13	2.78	0.00	0.00	1
66	N	Male	True	12	93.00	0.00	0.00	0.00	0.00	4
67	N	Female	False	18	80.00	0.00	0.00	0.00	0.00	2
68	N	Male	False	20	70.00	5.00	0.27	0.00	0.00	0
69	N	Male	False	20	71.00	0.00	0.00	0.00	0.00	1
70	N	Female	False	20	71.00	17.92	1.72	30.74	1.94	2
71	N	Female	False	20	71.00	0.00	0.00	0.00	0.00	1
72	N	Female	True	14	89.00	0.00	0.00	0.00	0.00	0
73	N	Female	False	20	66.00	0.00	0.00	0.00	0.00	4
74	N	Female	False	16	64.00	0.00	0.00	0.00	0.00	0
75	N	Male	False	18	70.00	0.00	0.00	0.00	0.00	4
76	N	Male	True	20	90.00	112.50	45.08	0.00	0.00	4
77	N	Male	False	12	71.00	0.00	0.00	0.00	0.00	0
78	N	Male	False	4	56.00	0.00	0.00	0.00	0.00	0
79	N	Male	False	20	74.00	0.00	0.00	0.00	0.00	3
80	N	Male	False	9	66.00	0.00	0.00	0.00	0.00	0
81	N	Male	True	20	80.00	1536.16	572.99	142.57	33.72	4
82	N	Female	False	16	57.00	16.57	1.15	0.00	0.00	0
83	N	Male	False	18	70.00	0.00	0.00	0.00	0.00	4
84	N	Female	False	18	66.00	6.64	1.21	0.00	0.00	4
85	N	Male	False	18	69.00	29.53	5.15	0.00	0.00	3
86	N	Female	False	14	65.00	7.74	0.55	33.95	2.42	0
87	N	Female	False	18	64.00	5.78	0.41	25.09	2.54	3
88	N	Male	False	12	62.00	0.00	0.00	0.00	0.00	2
89	N	Female	False	14	66.00	2.25	0.23	0.00	0.00	4
90	N	Male	False	12	57.00	6.19	0.34	30.29	3.81	4
91	N	Male	False	16	74.00	3742.12	361.11	202.57	17.10	4
92	N	Male	False	18	63.00	6.47	0.46	0.00	0.00	4
93	PD	Female	False	16	63.00	0.00	0.00	34.76	12.08	0
94	PD	Male	True	16	76.00	49.27	9.72	0.00	0.00	0
95	PD	Male	True	12	75.00	10229.34	5666.03	1117.47	181.59	4

96	PD	Male	False	16	63.00	621.44	232.23	0.00	0.00	0
97	PD	Male	True	16	64.00	0.00	0.00	0.00	0.00	1
98	PD	Male	False	18	64.00	3.75	0.43	0.00	0.00	0
99	PD	Female	True	18	80.00	147.24	46.97	32.26	5.74	4
100	PD	Male	True	12	84.00	86.24	19.19	0.10	0.02	4
101	PD	Male	True	14	62.00	131.68	14.47	16.11	1.62	0
102	PD	Female	False	18	66.00	248.19	44.48	16.14	1.21	4
103	PD	Male	False	20	58.00	193.78	91.25	0.00	0.00	4
104	PD	Male	False	16	62.00	75.01	15.85	302.30	78.63	0
105	PD	Male	False	18	87.00	52.49	6.61	0.08	0.01	0
106	PD	Female	False	18	59.00	10.72	1.55	0.00	0.00	4
107	PD	Male	True	16	72.00	146.89	17.61	17.27	1.07	2
108	PD	Male	True	11	77.00	107.68	22.31	10.75	0.51	0
109	PD	Female	False	16	57.00	53.46	6.75	20.61	2.53	3
110	PD	Male	False	18	64.00	4.85	0.54	0.00	0.00	4
111	PD	Male	False	18	67.00	0.00	0.00	0.00	0.00	4
112	PD	Male	False	18	64.00	17.19	5.94	0.00	0.00	0
113	PD	Male	False	16	65.00	766.49	320.78	47.45	4.65	0
114	PD	Male	True	14	79.00	0.00	0.00	0.00	0.00	3
115	PD	Male	False	13	67.00	372.84	98.84	61.82	10.50	2
116	PD	Female	False	19	60.00	138.14	46.83	51.90	10.04	0
117	PD	Male	False	16	66.00	289.85	75.62	0.00	0.00	1
118	PD	Male	False	13	59.00	83.84	18.40	0.00	0.00	2
119	PD	Male	False	18	60.00	0.00	0.00	0.00	0.00	0
120	PD	Male	False	16	59.00	40.33	19.68	0.00	0.00	4
121	PD	Male	False	14	56.00	0.00	0.00	0.00	0.00	1
122	PD	Female	True	18	63.00	8.36	1.42	0.00	0.00	2
123	PD	Male	True	16	73.00	0.00	0.00	0.00	0.00	1
124	PD	Female	False	17	70.00	0.00	0.00	0.00	0.00	4
125	PD	Female	False	16	63.00	0.00	0.00	0.00	0.00	0
126	PD	Male	True	20	70.00	0.00	0.00	0.00	0.00	0
127	PD	Female	False	18	67.00	0.00	0.00	0.00	0.00	0
128	PD	Male	False	18	68.00	0.00	0.00	0.00	0.00	0
129	PD	Male	False	16	62.00	16.54	1.44	85.32	5.46	0

130	PD	Female	False	14	61.00	205.19	88.91	0.00	0.00	4
131	PD	Male	True	18	72.00	0.00	0.00	0.00	0.00	3
132	PD	Male	True	12	64.00	84.34	12.81	21.78	2.25	0
133	PD	Female	False	16	63.00	0.00	0.00	0.00	0.00	1
134	PD	Male	False	13	57.00	0.00	0.00	0.00	0.00	0
135	PD	Male	False	16	67.00	587.52	134.89	137.76	17.80	0
136	PD	Female	False	18	62.00	0.00	0.00	0.00	0.00	0
137	PD	Male	False	14	54.00	0.00	0.00	0.00	0.00	0
138	PD	Male	True	14	55.00	90.61	15.76	0.00	0.00	4
139	PD	Male	False	20	59.00	51.37	18.63	0.00	0.00	4
140	PD	Male	False	20	66.00	0.00	0.00	0.00	0.00	0
141	PD	Male	False	12	57.00	375.96	64.21	36.13	6.35	3
142	PD	Male	False	16	56.00	11.37	0.76	0.00	0.00	0
143	PD	Male	True	16	72.00	114.05	17.52	9.66	1.37	1
144	PD	Female	False	16	63.00	0.00	0.00	0.00	0.00	0
145	PD	Male	False	18	68.00	229.91	34.62	55.16	7.03	2
146	PD	Female	False	16	65.00	4.95	0.28	19.55	2.14	0
147	PD	Female	False	18	68.00	45.25	5.94	3.94	0.41	4
148	PD	Male	False	18	65.00	11.96	1.18	0.00	0.00	0
149	PD	Male	False	14	76.00	10.05	1.21	0.00	0.00	0
150	PD	Male	False	14	58.00	0.00	0.00	3.79	0.25	0
151	PD	Male	False	16	54.00	24.73	3.97	0.00	0.00	0
152	PD	Female	False	16	72.00	0.00	0.00	0.00	0.00	4
153	PD	Male	False	20	57.00	10.63	1.11	0.00	0.00	0
154	PD	Male	False	20	71.00	17.15	3.21	0.00	0.00	0
155	PD	Male	False	12	59.00	11.32	1.76	0.00	0.00	0
156	PD	Male	False	20	54.00	76.96	14.31	1.12	0.16	0
157	PD	Female	False	14	71.00	15.56	1.66	32.06	3.42	0
158	PD	Male	False	20	64.00	407.13	62.90	23.01	3.30	0
159	PD	Male	False	18	65.00	4.14	0.22	0.00	0.00	0
160	PD	Female	False	18	65.00	16.94	2.62	0.00	0.00	0
161	PD	Female	False	18	59.00	33.96	5.75	33.04	2.29	0
162	PD	Male	False	18	74.00	21.90	2.51	0.00	0.00	0
163	PD	Female	False	19	67.00	19.12	1.82	19.73	2.60	0

164	PD	Female	False	16	70.00	24.10	1.16	0.00	0.00	0
165	PD	Female	False	16	62.00	73.93	8.92	7.12	0.70	0
166	PD	Female	False	16	58.00	3.32	0.30	0.00	0.00	1
167	PD	Male	False	18	66.00	80.83	7.37	37.98	2.23	0
168	PD	Male	True	16	70.00	23.47	1.86	2.02	0.16	0
169	PD	Female	False	18	52.00	132.21	22.41	0.00	0.00	0
170	PD	Male	False	18	68.00	29.28	6.21	5.66	0.63	3
171	PD	Male	True	12	63.00	0.00	0.00	0.00	0.00	0
172	PD	Male	False	15	75.00	12.28	1.22	0.00	0.00	0
173	PD	Female	False	11	54.00	0.00	0.00	0.00	0.00	0
174	PD	Male	False	13	60.00	14.62	1.33	22.73	2.62	0
175	PD	Male	False	19	62.00	67.99	4.77	0.00	0.00	0
176	PD	Male	False	18	67.00	0.00	0.00	0.00	0.00	4
177	PD	Male	False	15	62.00	2.81	0.28	0.00	0.00	4
178	PD	Male	False	16	72.00	44.98	4.20	38.38	3.88	3
179	PD	Female	False	14	69.00	8.09	1.20	0.00	0.00	0
180	PD	Male	False	18	63.00	555.58	96.28	33.51	5.21	1
181	PD	Female	False	16	54.00	99.96	22.01	0.00	0.00	0
182	PD	Male	False	18	79.00	13.82	0.93	20.54	4.27	1
183	PD	Female	False	18	77.00	0.00	0.00	0.00	0.00	0
184	PD	Male	False	16	55.00	8.52	0.85	30.14	5.21	0
185	PD	Female	False	18	69.00	7.62	0.88	0.00	0.00	0
186	PD	Female	False	16	77.00	0.00	0.00	0.00	0.00	0
187	PD	Female	False	16	59.00	4.07	0.34	0.41	0.05	0
188	PD	Female	True	12	80.00	35.02	2.98	8.29	0.68	0
189	PD	Female	False	18	69.00	0.00	0.00	0.00	0.00	4
190	PD	Male	False	16	69.00	0.00	0.00	0.00	0.00	0
191	PD	Male	False	12	69.00	26.32	1.54	0.00	0.00	4
192	PD	Female	False	14	80.00	182.85	20.13	45.89	6.23	1
193	PD	Male	False	13	59.00	35.76	4.22	0.00	0.00	0
194	PD	Male	False	16	75.00	0.00	0.00	0.00	0.00	4
195	PD	Female	False	14	57.00	19.59	2.02	0.00	0.00	0
196	PD	Male	False	18	74.00	4490.78	1154.13	60.32	4.69	1
197	PD	Male	False	18	70.00	201.21	27.67	0.00	0.00	0

198	PD	Female	True	16	71.00	4384.64	901.04	142.69	16.95	0
199	PD	Female	False	20	77.00	13.83	1.27	0.00	0.00	0
200	PD	Male	False	16	65.00	8.23	0.45	0.00	0.00	0
201	PD	Male	False	18	74.00	187.24	15.78	3.85	0.32	4
202	PD	Female	False	16	54.00	7.15	0.35	0.00	0.00	1
203	PD	Female	False	18	50.00	0.00	0.00	0.00	0.00	0
204	PD	Female	False	20	55.00	40.55	9.22	0.00	0.00	0
205	PD	Male	False	18	74.00	3.64	0.13	0.00	0.00	1
206	PD	Male	False	14	65.00	9.55	0.74	0.00	0.00	0
207	PD	Male	False	18	76.00	0.00	0.00	0.00	0.00	2
208	PSP	Female	False	12	72.00	1540.61	581.89	480.18	76.40	0
209	PSP	Male	True	10	71.00	0.00	0.00	0.00	0.00	0
210	PSP	Male	True	18	58.00	0.00	0.00	0.00	0.00	0
211	PSP	Male	True	12	56.00	0.00	0.00	0.00	0.00	4
212	PSP	Male	True	12	72.00	0.00	0.00	50.59	16.29	0
213	PSP	Male	False	12	56.00	2339.34	1093.41	262.56	72.65	0
214	PSP	Male	True	20	71.00	10.56	2.99	53.03	16.28	3
215	PSP	Male	False	20	70.00	0.00	0.00	0.00	0.00	0
216	PSP	Female	False	16	72.00	0.00	0.00	0.00	0.00	1
217	PSP	Female	False	16	66.00	11.74	1.35	55.46	26.30	0
218	PSP	Female	True	16	64.00	0.00	0.00	0.00	0.00	0
219	PSP	Female	True	19	59.00	288.40	164.91	0.00	0.00	0
220	PSP	Female	False	16	68.00	59.56	26.04	0.00	0.00	1
221	PSP	Male	False	12	68.00	227.69	90.53	87.52	21.84	2
222	PSP	Female	False	12	64.00	9.07	1.28	32.81	2.97	0
223	PSP	Female	False	15	72.00	11.25	2.11	75.38	15.20	0
224	PSP	Female	False	15	71.00	44.69	8.89	65.87	12.89	0
225	PSP	Female	False	16	68.00	0.00	0.00	58.53	1.30	0
226	PSP	Female	False	14	60.00	0.00	0.00	39.49	5.90	0
227	PSP	Female	True	16	63.00	0.00	0.00	155.77	23.57	4
228	PSP	Male	True	18	75.00	0.00	0.00	0.00	0.00	0
229	PSP	Female	False	18	65.00	0.00	0.00	64.98	10.51	1
230	PSP	Female	False	19	72.00	18.51	6.31	112.82	17.52	3
231	PSP	Male	True	14	72.00	70.30	11.02	207.12	23.09	4

232	PSP	Male	False	16	67.00	603.26	166.08	104.81	24.00	0
233	PSP	Female	False	12	78.00	0.00	0.00	32.11	3.07	0
234	PSP	Male	False	16	58.00	17.12	2.93	117.12	23.41	1
235	PSP	Male	False	12	77.00	10.73	0.29	52.67	4.95	3
236	PSP	Male	False	16	65.00	720.76	132.26	156.15	15.01	0
237	PSP	Male	True	16	74.00	21.00	6.02	98.61	10.14	0

Supplementary Table 5 p-values of tests on normal distribution for aSyn and Tau aggregates in CSF

		PD	DLB	AD	PSP	N
aSyn	Shapiro Wilk	0	$7.37*10^{-8}$	$2.44*10^{-7}$	$1.81*10^{-9}$	$9.16*10^{-14}$
	Lilliefors	$7.91*10^{-57}$	$5.73*10^{-9}$	$13.85*10^{-6}$	$1.20*10^{-13}$	$5.24*10^{-26}$
	Kolmogorov Smirnov	$5.72*10^{-18}$	0.0027	0.018	$7.76*10^{-5}$	$8.45*10^{-9}$
	Anderson Darling	$4.18*10^{-76}$	$2.35*10^{-12}$	$5.94*10^{-9}$	$3.00*10^{-17}$	$1.59*10^{-33}$
Tau	Shapiro Wilk	0	$9.03*10^{-7}$	$5.54*10^{-5}$	$4.72*10^{-6}$	$6.85*10^{-12}$
	Lilliefors	$6.56*10^{-57}$	$1.40*10^{-8}$	$3.70*10^{-5}$	$9.74*10^{-4}$	$9.8*10^{-21}$
	Kolmogorov Smirnov	$5.4*10^{-18}$	0.004	0.036	0.103	$4.03*10^{-7}$
	Anderson Darling	$2.12*10^{-69}$	$3.60*10^{-9}$	$4.97*10^{-6}$	$1.35*10^{-5}$	$4.42*10^{-25}$

Supplementary Table 6 Pearson coefficient of correlation values for analysis between aSyn and Tau aggregate concentrations and age, education, sex, disease duration, and death

		All cohorts	PD	DLB	AD	PSP	N
aSyn	Age	0.096	0.157	0.026	0.049	-0.256	0.130
	Education	-0.074	-0.133	0.025	0.183	-0.268	0.009
	Sex	-0.081	-0.061	-0.210	0.179	-0.134	-0.155
	Disease duration	0.093	0.012	0.073	0.130	-0.115	–
	Deceased	0.095	0.226*	-0.225	-0.235	-0.248	0.087
Tau	Age	0.070	0.166	0.031	-0.024	0.016	0.074
	Education	-0.144*	-0.182	-0.001	0.150	-0.258	-0.060
	Sex	-0.043	-0.081	-0.195	-0.060	-0.006	-0.089
	Disease duration	0.068	-0.006	0.106	0.047	0.055	–
	Deceased	0.070	-0.193*	-0.181	-0.357	-0.211	0.085

* indicates a significant correlation with p-values between 0.01–0.05

Supplementary Figure 1 TEM image (a) and size distribution (b) of silica nanoparticles

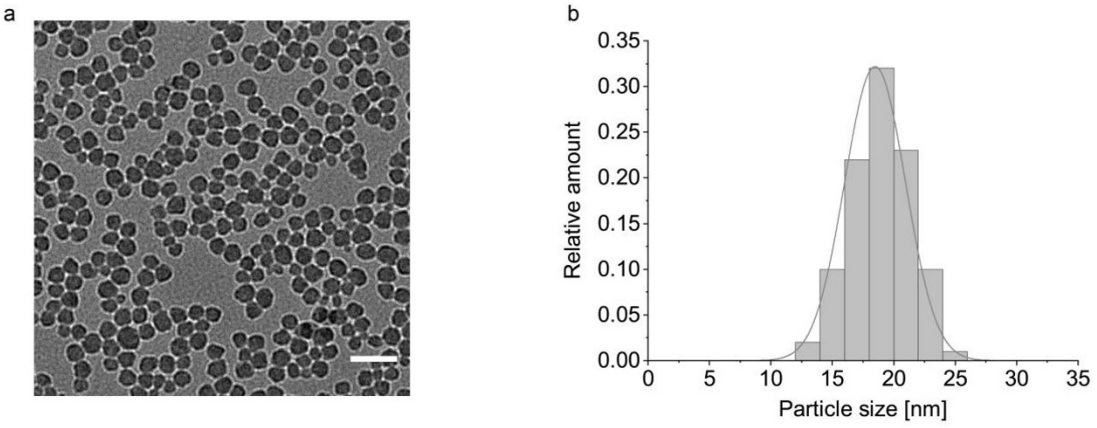

The exemplary image of an aSyn silica nanoparticle (a) shows the typical particle shape of the calibration standard. The scale bar is 50 nm. Aminated silica nanoparticles, which are the basis for peptide conjugation, show a normally distributed particle size with a mean of 18.5 nm (b, normal distribution analysed using Kolmogorov Smirnoff).

Supplementary Figure 2 aSyn (a) and Tau (b) aggregate concentrations grouped by blood-contamination levels

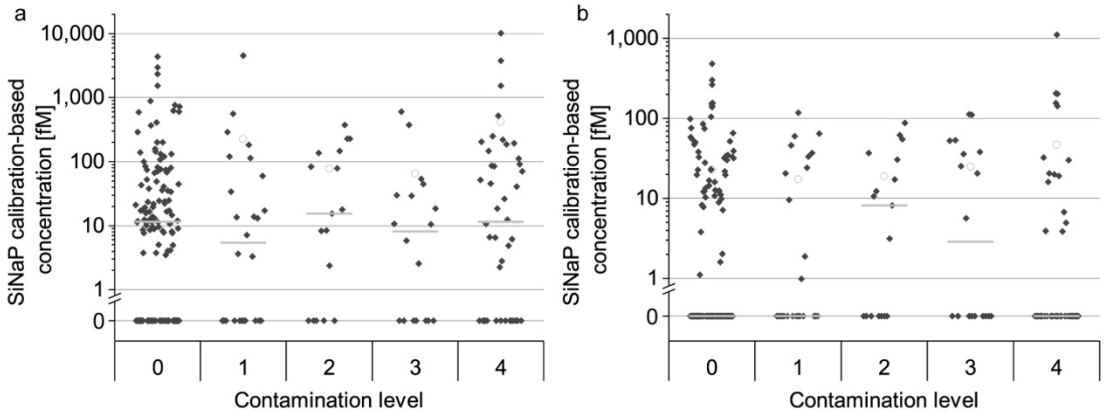

Blood contamination in CSF samples were measured with Combur10 stripes and grouped in 5 contamination levels (0: no contamination, 1: ~10 Ery/µL, 2: ~25 Ery/µL, 3: ~50 Ery/µL, 4: >250 Ery/µL). Higher contamination levels did not result in significant differences in aggregate concentrations (Kruskal-Wallis ANOVA: $p = 0.78$ for aSyn aggregates and $p = 0.63$ for Tau aggregates).

Anhang 8 – Weitere Informationen zu Kapitel 2.2.6

Development and Implementation of an Internal Quality Control Sample to Standardize Oligomer-Based Diagnostics of Alzheimer's Disease

Supplementary Material

Marlene Pils, Alexandra Dybala, Fabian Rehn, Lara Blömeke, Tuyen Bujnicki, Victoria Kraemer-Schulien, Wolfgang Hoyer, Detlev Riesner, Dieter Willbold and Oliver Bannach

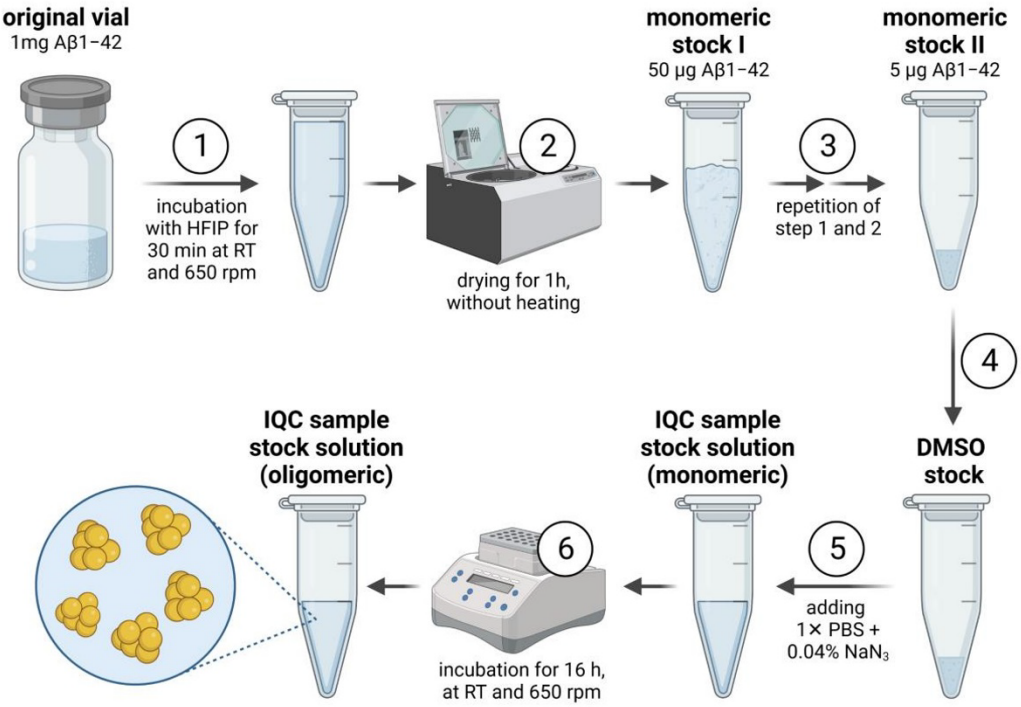

Figure S1. Scheme of monomerization and oligomerization procedure. Step 1: 1 mg Aβ1–42 is dissolved 550 µl HFIP for 1 h at RT with mixing at 650 rpm. The original sample tube is rinsed with an additional 550 µl HFIP, and the combined sample is divided into twenty aliquots containing 50 µg Aβ1–42. Step 2: aliquots are transferred to a SpeedVac and dried for ~1 h without heating until all HFIP and H_2O are removed. Step 3: the initial amount of Aβ1–42 is reduced by dissolving 50 µg Aβ1–42 with 550 µl HFIP and dividing this sample into ten aliquots containing 5 µg Aβ1–42. These aliquots are dried using a SpeedVac. Step 4: for oligomerization, 5 µg Aβ1–42 is dissolved in 5 µl DMSO, mixed briefly, centrifuged, and agitated for 10 min at RT and 650 rpm. Step 5: An IQC stock solution is prepared by adding 1× PBS containing 0.04% NaN_3. Step 6: the monomeric solution is mixed briefly, centrifuged and agitated for 16 h at 650 rpm and RT to promote oligomerization. Abbreviations: Aβ, amyloid-β; DMSO, dimethyl sulfoxide; HFIP, 1,1,1,3,3,3-hexafluoro-2-propanol; IQC, internal quality control; NaN_3, sodium azide; PBS, phosphate-buffered saline; RT, room temperature. Created with Biorender.com (accessed on 10 May 2023).

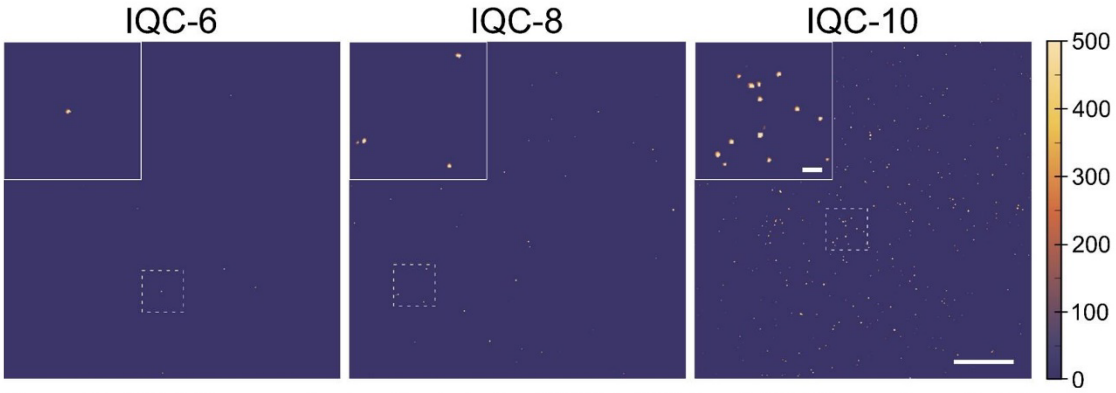

Figure S2. TIRFM-images of colocalized pixels of IQC-6, IQC-8 and IQC-10 samples with intensities above the blank control-based cutoff. The colocalized TIRFM images were created using a multi-step process. First, a global cutoff value was selected for each channel based on the blank control (0.05%). Only signals exceeding this value were considered in the consecutive analysis, enabling a distinction between signals and background noise, thereby increasing the measurement accuracy. In the next step, the matrices of both channels, representing the same area of a well, were used to create two supportive matrices. A binary matrix was generated that contains a one for all pixels whose intensity in both channel matrices is above the respective cutoff and a zero otherwise. The second matrix was the product of both channel matrices, which was scaled to the original range of values by dividing through by the maximum possible intensity value. The cutoffs were considered by multiplying the two generated supportive matrices, and the colocalization matrix for a distinct area of the well was created. For each image, a section was selected and enlarged (10×) to demonstrate differences in particle concentrations among the tested IQC samples. The color scaling was created using matlab2019b, where all pixels with an intensity equal to or higher than 500 were colored yellow. Scale bar image: 20 µm; scale bar enlarged image: 2 µm. Abbreviations: IQC, internal quality control; TIRFM, total internal reflection fluorescence microscopy.

Table S1. Individual sFIDA readouts, calibrated molar particle concentrations and CV% for each IQC sample. sFIDA readouts of each IQC sample were converted into femtomolar concentrations using the linear equation y = 5.08x – 0.25. Using the one-sided Mann-Whitney U test with a confidence interval of 5%, the molar particle concentrations of IQC samples that differed significantly from the next lower concentration were determined (marked green), and thus the lower limit of quantification (LLoQ, italic, *) and upper limit of quantification (ULoQ, italic, **) were identified. Observed sFIDA readouts are presented as the means of four replicates.

IQC sample	Monomer concentration [pM]	sFIDA readout	Particle concentration [fM]	CV%	One-sided Mann-Whitney U test *p*-value
IQC-1	0.01	0.7	0.18	61.3	0.1252
IQC-2	0.03	0.9	0.22	68.8	0.3429
IQC-3	0.1	1.6	0.36	73.3	*0.1714**
IQC-4	0.3	4.7	0.98	16.4	0.0286
IQC-5	1.0	15	3.0	15.7	0.0286
IQC-6	3.2	52	10.3	13.8	0.0143
IQC-7	10	130	25.7	24.1	0.0143
IQC-8	31.6	409	80.6	7.3	0.0143
IQC-9	100	1253	247	4.6	0.0143
IQC-10	316	4701	925	16.2	0.0143
IQC-11	1000	35,723	7031	7.7	0.0143
IQC-12	3162	351,702	69,219	23.3	0.0143
IQC-13	10,000	997,783	196,375	0.2	0.0143
IQC-14	31,622	1,000,000	196,812	0	*0.0143***
IQC-15	100,000	1,000,000	196,812	0	1

*LLoQ, ** ULoQ

Table S2. Calculation of the dilution linearity of Aβ oligomer-based internal quality control (IQC) samples within the working range. Data are presented as the means of four replicates. Molar particle concentrations were background corrected, and the percent dilution linearity of each IQC sample was calculated according to Equation (3). In addition, the average of all IQC samples (mean) was calculated. *IQC-14 was excluded from the analysis. Tolerance range: 80–120%.

IQC sample	Particle concentration [fM]	Particle concentration after background correction [fM]	Linearity [%]
IQC-3	0.36	0.22	84
IQC-4	0.98	0.84	93
IQC-5	3.0	2.9	89
IQC-6	10.3	10.2	126
IQC-7	25.7	25.5	100
IQC-8	80.6	80.5	103
IQC-9	247	247	84
IQC-10	925	925	42
IQC-11	7031	7031	32
IQC-12	69,219	69,219	111
IQC-13	196,375	196,375	316
IQC-14	196,812	196,812	316
		Mean	**107 ǀ 109***
		Coefficient of determination	**0.73 ǀ 0.99***

Table S3. Selectivity and recovery of the sFIDA assay to IQC-13. (**a**) sFIDA readouts of the IQC-13 sample were applied on different assay control setups, and the calculated percentage signal reduction was compared to the standard assay setup (normal). (**b**) Investigation of monomeric interference. (**c**) Influence of matrix effects on sFIDA readouts of the IQC-13 sample spiked in buffer or bovine CSF. Observed sFIDA readouts are presented as the means of four replicates. Using the one-sided Mann-Whitney U test with a confidence interval of 5%, the sFIDA readout of the respective assay control was compared to the readout of the standard assay setup. Abbreviations: CSF, cerebrospinal fluid; IQC, internal quality control.

(a)

Assay control setup	Observed sFIDA readout	Signal reduction [%]	One-sided Mann-Whitney U test *p*-value
Normal	941,271	-	-
Capture Control (CC)	37.27	100	0.0152
Autofluorescence control (AF)	0.77	100	0.0147
Cross-reactivity anti-Tau antibodies (Tau)	0.67	100	0.0152

(b)

Assay control setup	Observed sFIDA readout	Signal reduction [%]	One-sided Mann-Whitney U test *p*-value
Normal	941,271	-	-
Monomer control	15,231	98.38	0.0152

(c)

Assay control setup		Observed sFIDA readout	Signal reduction [%]	One-sided Mann-Whitney U test *p*-value	Signal-to-noise ratio IQC/blank
Blank	buffer	0.45	66.67	-	-
	CSF	0.15		0.002	-
Blank + IQC-13	buffer	997,783	0.21	-	2,217,295
	CSF	995,639		0.108	6,637,597

Table S4. Raw data used to generate Shewhart charts in Figure 5. Listed are the calibrated particle concentrations of 20 observations of each applied internal quality control (IQC) sample (IQC-6, IQC-8 and IQC-10) and the determined intra-assay variance described as CV%. The respective values were used to calculate the mean, standard deviation (SD) and upper/lower control (UCL/LCL) and action limits (UAL/LAL). Data from each observation represent the mean of four replicates.

	IQC-6		IQC-8		IQC-10	
Observation	**Particle concentration [fM]**	**CV%**	**Particle concentration [fM]**	**CV%**	**Particle concentration [fM]**	**CV%**
1	6.8	3.4	71.3	16.2	1397.7	24.2
2	11.1	18.5	106.8	19.9	1463.0	9.6
3	9.6	33.9	122.5	15.5	1585.6	16.5
4	11.6	10.2	116.3	24.4	1593.7	11.8
5	11.2	14.7	119.8	17.0	1638.6	20.3
6	7.6	36.2	81.4	20.8	1421.9	24.3
7	9.8	14.1	106.7	20.4	1439.7	22.6
8	9.0	11.0	110.1	15.3	1340.8	9.5
9	7.6	15.7	79.3	17.8	1276.4	20.6
10	8.4	22.9	100.7	27.6	1571.9	16.4
11	9.3	14.4	71.7	4.3	1309.4	11.8
12	8.8	29.6	104.3	25.1	1295.2	5.6
13	8.4	8.5	115.8	8.5	1520.7	32.0
14	9.5	8.4	142.3	7.9	1579.4	21.0
15	8.0	9.9	123.6	13.8	1476.9	21.9
16	6.1	8.7	103.1	18.8	1661.7	14.8
17	6.7	12.2	88.1	12.8	1356.5	12.6
18	6.8	19.5	111.2	14.2	1269.8	16.2
19	6.8	20.2	101.6	18.3	1064.7	10.8
20	6.4	12.1	130.3	10.6	1592.7	28.8
Mean	**8.5**		**105**		**1443**	
SD	**1.7**		**19**		**155**	
UCL	**11.8**		**144**		**1752**	
LCL	**5.1**		**67**		**1133**	
UAL	**13.5**		**163**		**1907**	
LAL	**3.5**		**48**		**978**	

Anhang 9 – Weitere Informationen zu Kapitel 2.2.7

Supplementary section:

Table 1: Data of simplified assay with Streptavidin-633 as target. Streptavidin-633 in several concentrations were added to Biotin-BSA on the plate wells. Streptavidin-633 itself is excited with 633 nm wavelength and detected in the 705 nm channel.

Streptavidin-633 concentration [fM]	Mean of particle count	Std-dev	Coefficient of variation CV%
0	7.7	0.8	10.8
1	10.6	1.2	11.6
10	21.7	1.4	6.4
100	157.9	28.7	18.1
1000	1551.8	137.6	8.9
10000	45551.6	523.6	1.1
			∅ 9.5

Table 2: Data of immunoassay with ALFA-GFP as target, anti-GFP as capture and anti-ALFA-647 for detection. ALFA-GFP in several concentrations were added to the plate wells. The protein itself on the plate surface were excited with 488 nm wavelength and detected in the 525 nm channel, the binding of the detection nanobody were visualized in the 633 nm channel (CV%= Coefficient of variation).

	ALFA-GFP (protein on surface)			Anti-ALFA-AF647 (detection of protein)			colocalization		
ALFA-GFP concentration [fM]	Mean of particle count	Std-dev	CV%	Mean of particle count	Std-dev	CV%	Mean of particle count	Std-dev	CV%

0	24.6	1.7	7.1	24.6	1.4	5.7	0.0	0.0	0
3.16	33.4	3.7	11	23.7	2.9	12.2	0.2	0.1	49.9
10	44.3	5.2	11.6	26.6	1.8	6.8	0.4	0.0	11.2
31.6	154.2	3.3	2.2	76.1	5.5	7.2	8.2	0.7	8.6
100	356.3	19.0	5.3	128.4	13.4	10.4	26.1	2.5	9.4
316	1104.0	98.8	9	363.3	35.3	9.7	93.6	11.6	12.4
1000	2964.1	280.8	9.5	2167.3	230.8	10.6	634.5	80.8	12.7
3160	10154.7	1143.0	11.3	7270.3	956.0	13.1	3101.3	581.0	18.7
∅			8.4			9.5			15.4

Anhang 10 – Weitere Informationen zu Kapitel 2.2.8

Supplement

Artifact detection in fluorescence microscopy using convolutional autoencoder

Fabian Rehn[1,2,3], Marlene Pils[3], Tuyen Bujnicki[2], Oliver Bannach[2,1,3], Dieter Willbold[2,1,3]

[1]Institut für Physikalische Biologie, Heinrich-Heine-Universität Düsseldorf, Universitätsstr. 1, 40225 Düsseldorf, Germany.

[2]Institute of Biological Information Processing (Structural Biochemistry: IBI-7), Forschungszentrum Jülich GmbH, Wilhelm-Johnen-Straße, 52428 Jülich, Germany.

[3]attyloid GmbH, Merowingerplatz 1A, 40225 Düsseldorf, Germany.

	Predicted Artefact-laden	Predicted Artefact-free
Dataset 2- Actual Artefact-laden	88.7%	11.3%
Dataset 2 - Actual Artefact-free	0.3%	99.7%
Dataset 3 - Actual Artefact-laden	95.9%	4.1%
Dataset 3 - Actual Artefact-free	0.0%	100.0%
Dataset 4 - Actual Artefact-laden	98.4%	1.6%
Dataset 4 - Actual Artefact-free	3.2%	96.8%
Dataset 5 - Actual Artefact-laden	100.0%	0.0%
Dataset 5 - Actual Artefact-free	14.1%	85.9%
Dataset 6 - Actual Artefact-laden	88.0%	12.0%
Dataset 6 - Actual Artefact-free	1.8%	98.2%

Sup. Table 1: Confusion Matrix of classification results.

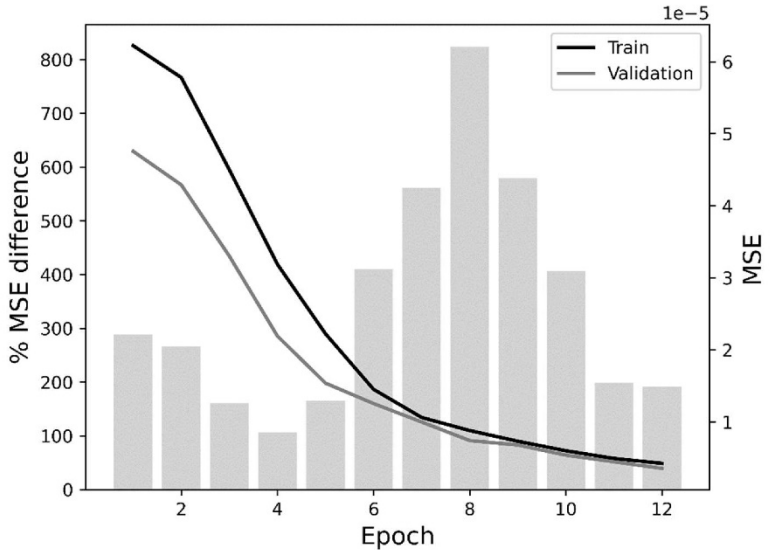

Sup. Figure 1: Metrics of the fitting process. The bars represent the average percentage difference in MSE between artifact-free and artifact-laden images in dataset 1 (left y-axis). A high value is desirable. The line plots show the average MSE during fitting (right y-axis). A low value is desirable.

Anhang 11 – Druckgenehmigung

Alle in dieser Dissertation abgebildeten Manuskripte fallen unter eine „Open Access - Creative Commons CC BY“-Lizenz, welche das Kopieren und Weiterverbreiten des Materials in jedem Medium oder Format zu nicht-kommerziellen Zwecken gestattet.

Manuskript	Lizenz	Link zur Lizenz
Quantitative detection of α-Synuclein and Tau oligomers and other aggregates by digital single particle counting	Open Access - Creative Commons CC BY 4.0	https://creativecommons.org/licenses/by/4.0/
Aβ oligomers peak in early stages of Alzheimer's disease preceding tau pathology	Open Access - Creative Commons CC BY-NC 3.0	https://creativecommons.org/licenses/by-nc/3.0/
Blood-based quantification of Aβ oligomers indicates impaired clearance from brain in ApoE ε4 positive subjects	Open Access - Creative Commons CC BY 4.0	https://creativecommons.org/licenses/by/4.0/
Elevated Aβ aggregates in feces from Alzheimer’s disease patients: a proof-of-concept study	Open Access - Creative Commons CC BY 4.0	https://creativecommons.org/licenses/by/4.0/
IAPP - oligomerisation levels in plasma of people with type 2 diabetes	Open Access - Creative Commons CC BY 4.0	https://creativecommons.org/licenses/by/4.0/
Development and Implementation of an Internal Quality Control Sample to Standardize Oligomer-Based Diagnostics of Alzheimer’s Disease	Open Access - Creative Commons CC BY 4.0	https://creativecommons.org/licenses/by/4.0/